DESIGN OF HIGH LOSS VISCOELASTIC COMPOSITES THROUGH MICROMECHANICAL MODELING AND DECISION BASED MATERIALS DESIGN

A Dissertation
Presented to
The Academic Faculty

by

Michael Richard Haberman

In Partial Fulfillment
of the Requirements for the Degree
Doctor of Philosophy in the
George W. Woodruff School of Mechanical Engineering

Georgia Institute of Technology
May 2007

DESIGN OF HIGH LOSS VISCOELASTIC COMPOSITES THROUGH MICROMECHANICAL MODELING AND DECISION BASED MATERIALS DESIGN

Approved by:

Dr. Yves H. Berthelot, Advisor
School of Mechanical Engineering
Georgia Institute of Technology

Dr. Erian Armanios
School of Aerospace Engineering
Georgia Institute of Technology

Dr. Mohammed Cherkaoui
School of Mechanical Engineering
Georgia Institute of Technology

Dr. Hamid Garmestani
Materials Science and Engineering
Georgia Institute of Technology

Dr. David L. McDowell
School of Mechanical Engineering
Georgia Institute of Technology

Date Approved: April 6, 2007

ACKNOWLEDGEMENTS

There are countless people who contribute to the success of an individual. However, the impact of the few listed here has undeniably made my success and happiness possible. I would like to first thank my thesis advisor, Dr. Y. Berthelot, and co-advisor, Dr. M. Cherkaoui. The insight, direction, and encouragement from these two individuals has driven this research and a significant amount of peripheral work. They have also provided me with a very unique educational experience by allowing me to work simultaneously at the Université Paul Verlaine in Metz and Georgia Institute of Technology for four unforgettable years. I will never be able to repay either for the positive influence they have had on my future. I am also forever grateful for the unwavering support provided by my parents throughout the years. They have inspired my achievements in countless ways and always been there to help me through whatever tough times I may have encountered. I would finally like to express my utmost thanks to my wife, Tänya, for her patience, love, and support. I couldn't have done it without you!

TABLE OF CONTENTS

LIST OF TABLES

LIST OF FIGURES

SUMMARY

This thesis focuses on the micromechanical modeling of particulate viscoelastic composite materials in the quasi-static frequency domain to approximate macroscopic damping behavior and has two main objectives. The first objective is the development of a robust frequency dependent multiscale model. For this purpose, the self-consistent (SC) mean-field micromechanical model introduced by Cherkaoui et al [J. Eng. Mater. Technol. 116, 274-278 (1994)] is extended to include frequency dependence via the viscoelastic correspondence principal. The quasi-static model is then generalized using dilute strain concentration tensor formulation and validated by comparison with complex bounds from literature, acoustic and static experimental data, and established models. The second objective is SC model implementation as a tool for the design of high loss materials. This objective is met by integrating the SC model into a Compromise Decision Support Protocol (CDSP) to explore the microstructural design space of an automobile windshield. The integrated SC-CDSP design space exploration results definitively indicate that one microstructural variable dominates structure level acoustic isolation and rigidity: negative stiffness inclusions. The work concludes with a detailed description of the fundamental mechanisms leading to negative stiffness behavior and proposes two negative stiffness inclusion designs.

CHAPTER I

INTRODUCTION

1.1 Objective and motivation

The principal objective of this thesis is the derivation, development, and validation of a multiscale model to explore microstructural aspects that lead to enhanced damping behavior for future creation, design, and development of materials with high capacity to absorb mechanical energy.

Throughout history humankind has created tools and structures to satisfy wants and needs. These structures are omnipresent in daily life and range in form and function from buildings, to cars, to computers, to airplanes. The success of any given structure depends entirely on a hierarchy of elements and the design of those elements. This hierarchy includes the structure as a whole, the individual structural elements, the components comprising each of those individual elements, the materials from which each component is fabricated, and finally the composition of those materials [1]. In other words, a structure can be viewed as a system which possesses elements that exists at multiple length scales. Behavior of the structure as a whole is governed by behavior at each individual length scale and by interactions between those length scales [2]. True engineering design must take this fact into account. It is clear, therefore, that successful

design must consider not only the design of each element at its length scale, but also the complex interaction of the hierarchy of length scales [3]. This design philosophy can ideally be extended to include even the design of the materials.

Classic design methods require the selection of materials which conform to the needs of the preconceived whole [4]. This design methodology is well developed and well understood. Unfortunately, the limiting factor in design when applying this approach is very often the lack of available materials which meet the needs of the structure, thereby limiting the entire design processes [2, 5]. The intertwined fields of composite material design, manufacture, and modeling have developed in response to this lack of available materials and have greatly supplemented the design process. Though these fields address the lack of available materials, seldom is composite material design directly integrated in to the design of the structure [6]. Even more rarely is the design methodology employed to inform the designer of useful alterations to make within the material. The latter approach, that of concurrently designing a material with the structure, represents a more elegant solution which aims to create materials specifically conceived for the demands of a given application. Such an approach not only creates materials for specific needs but also includes material creation in the design of the system as a whole. It is therefore correctly called materials design [1].

Material by design, or simply material design, is a very active area of research. One well accepted approach to material design aims to extend systems design methodologies to concurrently design materials for specific high importance components [2, 3, 6]. This approach has been pioneered by the Mechanical Properties Research Laboratory and Materials Council at Georgia Institute of Technology by employing

knowledge and tools from the fields of materials science, mechanical engineering, and engineering design [2, 6]. This extension is very natural as materials themselves can easily be viewed as multiscale structures [1, 7]. Such a strategy ensures the function of the structure and gives ultimate control to the designer. The study of material design is, however, very new and requires considerable research before being a viable option for day to day engineers. Detailed development and investigation of multiscale structures, which includes multiscale material models, is a key aspect of material design research. These investigations yield a great deal of information and understanding regarding the effects of material structure on desired structural behavior [8, 9]. This information can then be used to inform the design of materials through implementation of multi-objective design protocols.

Materials design is inherently a multiscale and multi-physics problem as the demands of a structure include thermal, electrical, and mechanical loading at all length scales. One area of interest in many engineering domains is the dissipation of energy. Applications for materials with a high capacity to absorb acoustic and vibrational energy can be found in almost every industry. For example, high loss materials are often used as a filler in structural elements such as the fuselage of an aircraft [10] or the chassis of an automobile [11]. As filler, such materials simultaneously reinforce the structure and reduce vibrations and noise. Similar energy attenuation benefits are realized when these high loss materials are used in the form of coatings and layers. Coating treatments have been employed for noise abatement in plenum chambers and ducts [12], on vibrating structures [13], and in automobile windshields [14]. Furthermore, it is known that the damping capacity of materials can be increased by introducing heterogeneities [15] into

the material, thereby creating a particulate composite material. Due to the large number of potential applications for lossy materials, constitutive modeling of viscoelastic composite materials is of great interest and has been for nearly half a century [16, 17]. Recent research suggesting the possibility of creating composites that exhibit extremely high damping [18-22] combined with advances in the design of materials [2, 5] has given renewed impetus to research in the modeling of viscoelastic composite materials. For this reason, this thesis concentrates on modeling particulate composites for damping applications and moves towards the implementation of the proposed model in a materials design scheme.

1.2 Hypothesis and strategy

This thesis proposes to satisfy the principal objective indirectly by sequentially satisfying two secondary objectives. Those secondary objectives can be paraphrased as (*i*) Perfecting the understanding of heterogeneous multiscale viscoelastic material behavior, and (*ii*) Implementing this understanding to improve the performance of structures requiring the absorption of mechanical energy. Here, two coupled hypotheses are formulated which, if accepted, equate to the satisfaction of the secondary objectives and, consequently, the principal objective.

> *Hypothesis 1:* The development of a quasi-static frequency domain self-consistent micromechanical model will provide a powerful tool for the design of absorptive materials.

Hypothesis 2: The integration of the quasi-static self-consistent model and a compromise decision support protocol will yield concrete information regarding the design of lossy materials which will inspire new research to create of highly absorptive materials.

Hypothesis 1 is accepted through the development and validation of a robust quasi-static frequency domain self-consistent (SC) micromechanical model. This model must be capable of approximating the effective frequency dependent behavior of a large range of particulate composite materials. Model inputs will be the material properties of each constituent phase and the inclusion shape and orientation. The desired model output is the effective frequency dependent stiffness tensors describing isotropic or anisotropic viscoelastic composite material behavior. Model validation will be accomplished through comparisons with theoretical bounds from complex composite media, accepted models, experimental data, and through parametric studies. The SC model must then be integrated into a multiscale structural model. *Hypothesis 2* is accepted when the SC model is integrated into a compromise decision support protocol (CDSP) to solve a material design problem and *quantify* the influence of microstructural variables on structural performance. The results inform future lossy material design when they are subsequently employed to formulate a clear set of research objectives that ultimately lead to the enhancement of macroscopic material damping. The proceeding discussion and steps to achieve the dual thesis objectives are summarized with the research plan given in. Table 1.1

Table 1.1: Overview of thesis research plan.

Principal Research Question: Can a three phase self-consistent micromechanical model be developed to aid in the design of high loss particulate composite materials?						
Questions	Can the self-consistent model be developed to calculate the effective lossy properties of "any" particulate composite material?	How does the quasi-static SC model compare with known bounds in the complex domain?	Can the SC model be used in the present state for a multiscale materials design problem?	How does the SC model map unstable inclusion behavior to the effective material properties?	Can knowledge gained from SC model mapping be used to inform decisions for inclusion parameters (geometry, σ vs. ε, orientation, etc)?	What microscale mechanisms most effectively enhance macroscopic material behavior?
Answers	**Yes**. The developed model approximates the effective viscoelastic behavior of any material that can be approximated as a combination of a matrix with *N* different coated ellipsoidal inclusion phases having known complex moduli.	The quasi-static self-consistent mean-field model **satisfies all existing complex bounds**.	**Yes**. The SC model is successfully integrated into a nested hierarchy of models predicting the behavior of an automobile windshield. Thus approximating behavior at micro, macro, part, and structural levels.	The SC model is a mean field model. As such it can only approximate the **volume averaged effects of unstable inclusion behavior as a negative stiffness domain** existing *a priori* within a positive stiffness matrix.	**Yes**. The results of CDSP-SC integration clearly indicate that negative stiffness domains are the most influential micro- or sub-microscale variable influencing macroscopic damping and stiffness.	The concept of negative stiffness is a convenient meta-model employed to approximate nonlinear small scale behavior. **Negative stiffness** and related macroscopic behavior is **the result of microscale state switching and bistability**.
Location	*Chapter III* *Chapter IV*	*Chapter IV*	*Chapter V* *Chapter VI*	*Chapter VI*	*Chapter VI* *Chapter VII*	*Chapter VI* *Chapter VII*

1.3 Thesis overview

This thesis is divided into eight chapters. The following chapter, ***Chapter II***, summarizes the principles employed throughout the thesis and notes many important works from which considerable background has been gathered. Chapter II begins with a general discussion regarding energy dissipation in both homogeneous and heterogeneous materials and recalls measures of energy dissipation. A structural vibrations approach to energy dissipation, known as the strain energy method, is then discussed. The approach employs the relationship between energy dissipation and strain energy to quantify energy dissipation. After examining strain energy dissipation approximations the chapter then discusses acoustic scattering in particulate composites, its fundamental physical principles, and related modeling methods. Chapter II terminates with a detailed bibliographical review of the two prominent research areas covered in this thesis: (*i*) homogenization techniques for modeling effective particulate composite material behavior from both the static (micromechanical) and the dynamic (acoustic scattering) perspectives, and (*ii*) important developments in materials design research using a multiscale and multi-physics approach.

Chapter III derives a SC micromechanical model in the quasi-static frequency domain for a composite consisting of a viscoelastic host containing viscoelastic ellipsoidal coated inclusions. This is achieved by extending the static model of Cherkaoui *et al* [23, 24] to include the constitutive frequency dependence of the constituent phases. The derivation is posited on the elastic-viscoelastic correspondence principle and employs Green's formalisms and interfacial operators to arrive at a general

frequency dependent homogenization model for particulate composites. The resulting quasi-static model is then generalized using dilute strain concentration tensor (DSCT) formulation. This generalization permits the homogenization of composites containing a large array of coated inclusions, inclusion orientation distributions, and coating thicknesses.

The purpose of ***Chapter IV*** is to validate the quasi-static SC model though comparisons with accepted analytic bounds, acoustic scattering based models, and elastic and acoustic experimental data. The chapter begins with an overview of the important contributions in bounding methods for complex valued effective material behavior. Three specific complex bounding techniques are introduced and approximations from the quasi-static SC model derived in Chapter III are shown to fall within those bounds. The model is then employed in several elementary studies concerning the particulate composite lossy behavior. Next the SC model is then employed to approximate the isotropic composite material behavior of a viscoelastic material containing spherical hollow glass micro-spheres [25]. SC model results are used to calculate the transmission loss (TL) of a layer of this composite material submerged in water. These results are shown to agree with an acoustic scattering model proposed by Baird *et al* [26] and experimental TL data from the same authors. Oriented ellipsoidal coated inclusion effects are then examined via parametric studies of TL, complex wavenumber, and complex sound speed for hypothetical materials created from the same constituent phases as those studied by Baird *et al* [26]. The next validation step is an illustration of DSCT SC model generality. The DSCT SC model is first used to approximate isotropic behavior resulting from a uniform distribution of ellipsoidal inclusions embedded in a

host material. These results are compared with a model proposed by Berryman for a lossy rock-water suspension as a function of volume fraction [27]. This comparison validates the usage of the DSCT SC form to approximate the effects of varying ellipsoidal inclusion orientation on macroscopic composite material behavior. The next SC DSCT model check presents a parametric study of inclusion orientation distribution on macroscopic composite anisotropy. The DSCT SC model is next compared with the experimentally obtained and theoretically approximated stiffness values of a composite shale material studied by Jones and Wang [28] and Hornby *et al* [29], respectively. The shale material studied by these researchers consisted of several different mineral phases embedded in preferentially oriented clay platelets. Effective stiffness tensor approximations provided by the SC DSCT model show good agreement with both experimental and theoretical values provided by these researchers. The SC DSCT model is then employed to approximate the behavior of a silicon carbide – aluminum composite material. Due to fabrication processes, the microstructure of this composite is best described as consisting of two distinct length scales: (*i*) sub-micron SiC particulates embedded in an Al matrix, and (*ii*) identically oriented mesoscopic Al particulates embedded in a SiC-Al composite. The effective behavior of this composite was approximated using the SC DSCT via a nested multiscale approach (sub-micron→meso→macro) and shows good agreement with both the multiple scattering model and experimental data provided by Ledbetter and Datta [30]. Finally, the SC DSCT model is validated by returning to the analysis of the particulate composite slab TL data provided by Baird *et al* [26]. The SC DSCT model is employed to approximate the effects of coating thickness variation on the observed TL. The result of this

approximation shows large improvement in agreement with experimental data over the simple single-thickness approximation.

Chapter V investigates the feasibility of quasi-static SC model implementation as a tool for a materials design strategy. This is achieved by constructing a hierarchy of models which are valid on each length scale of a simple dynamic structure: a vibrating sandwich plate. This structural element is analogous to an automobile windshield and was chosen to show the practical implications of this approach. Modeling begins by discussing the relevant part and structure level models for a vibrating sandwich plate. Part level modeling consists of finding the effective sandwich plate bending modulus using the constrained layer damping model derived by Ross *et al* [31]. Analysis of sandwich plate behavior begins with parametric studies on the constituent material behavior and geometry of a sandwich plate to provide information about effective lossy sandwich plate behavior. Sensitivity analysis of the effective modulus yields information which can be applied to efficiently increase lossy plate behavior. This model is validated though comparison with experimental TL data from several different layered windshield samples. Next, models for a viscoelastically constrained beam and plate are employed to study the contributions of lossy plate and boundary condition behavior to the modal loss factor of a vibrating plate. The beam and plate models used for this study were derived using classic beam and plate theory. These models represent the structural level behavior of the simple multiscale example. The structure and part level models are then integrated and compared with finite element approximations of the modal loss factor for a viscoelastically constrained "cantilever" sandwich beam. Finally, SC model approximations of the behavior of a particulate composite constrained layer and/or

boundary conditions are integrated into the part and structure level models to yield a nested hierarchy of behavioral models. The integration of these models permits the study of microstructural effects on the dissipation of structural vibrations. Voided viscoelastic materials are shown to increase the structural damping of a circular sandwich plate and the increases in modal loss factor is shown to increase quadratically as a function of void fraction. Windshield TL is then approximated by integrating part level and material homogenization models combined with the analytic modified-mass law [32]. Voided interlayer materials yield TL improvements near coincidence, though they are marginal. A simple example of high loss composites employing negative stiffness inclusions [18, 19, 21], however, are shown to greatly improve TL behavior at coincidence. The results of this chapter are very encouraging and suggest that the quasi-static SC model can be implemented as tool in a materials design strategy.

Chapter VI is a continuation of the design process initiated in the feasibility study of Chapter V. This chapter implements a top-down systems design approach, known as a compromise design support protocol (CDSP), to explore the design space of an automobile windshield. The CDSP is construct that aids the designer to efficiently design a structure in the face of multiple conflicting performance goals. The present CDSP implementation yields optimal design results, though the CDSP can also be employed to provide robust design solutions. For the automobile windshield those goals are the improvement of its acoustic performance while striving for weight reduction and a minimum reduction of in-plane stiffness. The design space exploration and subsequent analysis of design results achieves two purposes. First, the results shed light on sub-microscale behavior and structure that lead to significant enhancements of the

macroscopic material damping. Second, the results validate the integration of a top-down design methodology and micromechanical techniques to concurrently design structures and their constituent materials. One very positive aspect that emerges from Chapter VI is that the coupled CDSP-SC design approach permits both an analysis of trends *and* statistical analysis of the influence of microstructural variables on structural performance. Indeed, Chapter VI results unequivocally show that a windshield having isotropic or low-level transversely isotropic interlayer and glass layers that both contain negative stiffness inclusions display a statistically significant performance enhancement over the standard windshield material configuration. The critical condition that emerges from the results is the need for minute quantities ($\leq$ 1% by volume) of heterogeneities displaying negative stiffness behavior. Chapter VI clearly demonstrates that negative stiffness regions proved to be the only means to simultaneously enhance the mechanical damping capacity of the windshield and increase its stiffness. It is in this way that the integrated CDSP-SC design approach informs material design by clearly indicating the need to understand, create, and exploit negative stiffness behavior occurring on or below the microscale. That is the subject of Chapter VII.

Chapter VII chapter goes beyond the design of lossy materials to explore negative stiffness behavior in detail. First, it gives a detailed explanation of what exactly is meant by the term negative stiffness with respect to both material and structural systems. The foundations of negative stiffness behavior and its influence on macroscopic material behavior are investigated via a discussion of the thermodynamic state of the material. The chapter clearly shows that negative stiffness behavior stems from the existence of an elevated thermodynamic energy state and the tendency of a system to

lower its internal energy. It also demonstrated that any system displaying a non-monotonic force versus displacement curve will display negative stiffness. The chapter continues by illustrating that negative stiffness usually exists as a transient, resulting from state switching between two bistable configurations, but that it can be constrained by a surrounding positive stiffness. Next, experimental and theoretical research from the literature which is pertinent to understanding negative stiffness behavior is presented and discussed. The chapter concludes by discussing several promising avenues to create negative stiffness inclusions in the future. In particular, a candidate inclusion structure and corresponding meta-modeling technique to approximate its negative stiffness behavior is proposed. The proposals and discussions of the chapter are limited to explanations of the causal mechanisms, physical principles, and potential means to generate this extraordinary behavior.

The final chapter, ***Chapter VIII***, concludes and summarizes the important results and contributions from the models and methods presented in each chapter. This chapter also presents some perspectives on the role of the work presented in this thesis and suggests avenues for future research. The chapter concludes with a brief discussion on the importance of the multiscale and multi-physics material modeling and evokes ideas on the future of material design.

CHAPTER II

BIBLIOGRAPHIC REVIEW AND PRINCIPLES

2.1 Damping Materials

Applications for materials with a high capacity to absorb acoustic and vibrational energy can be found in almost every industry. For example, high loss materials are often used as a filler in structural elements such as the fuselage of an aircraft [10] or the chassis of an automobile [11]. As filler, such materials simultaneously reinforce the structure and reduce vibrations and noise. Similar energy attenuation benefits are realized when these high loss materials are used in the form of coatings and layers. Coating treatments have been employed for noise abatement in plenum chambers and ducts [12], on vibrating structures [13], and in automobile windshields [14]. Furthermore, it is known that the damping capacity of materials can be increased by introducing heterogeneities [15] into the material, thereby creating a particulate composite material.

Due to the many different areas for application of high loss materials, constitutive modeling of viscoelastic composite materials has been, [17, 33], and remains of high interest in many different engineering fields. This work to derives, develops, validates, and explores a multiscale material model of lossy composite materials and implements the model in a top-down materials design strategy. Such material modeling begins with a

fundamental understanding of the physical processes that leading to damping behavior. This section, therefore, gives a brief overview of the mechanisms that lead to damping, the mathematical tools used to approximate lossy behavior, and the simplifying assumptions employed throughout this thesis.

In general, all materials that display damping behavior can be defined as viscoelastic materials [34]. viscoelastic behavior is fundamentally due to the intrinsic absorption of dynamic strain energy in a material by conversion to heat. Crystallographic materials, such as metals, convert strain energy to heat through internal friction while energy absorption in polymeric materials is the result of molecular chain sliding and relaxation. In general, the stress in a viscoelastic material is dependent on imposed strain rate. This rate dependence translates to a stress response in the frequency domain that is called a relaxation spectrum. The relaxation spectrum of a viscoelastic material shows that the stress level is dependent on both the magnitude and frequency of the applied strain [35]. In most cases the stress-strain relationship in crystallographic materials is very weakly rate dependent and leads to a broadband damping response in the frequency domain. The magnitude of this broadband damping capacity is also very small and for these two reasons metals are seldom referred to in the context of viscoelastic behavior. Polymeric materials, on the other hand, display both high rate dependences and high losses and are therefore classified as viscoelastic. It is important to note, however, that all small strain behavior of real materials can be classified, to a certain degree, as viscoelastic [35].

A simple method to show the principles of viscoelastic material behavior is to discuss the time dependent behavior of a one-dimensional sample: a bar. The phenomena

that typify the viscoelastic response of a bar are creep and stress relaxation. Creep is the strain increase over time due to constant applied stress and stress relaxation is the decay of the stress level in a material when subjected to a constant strain [34]. These two phenomena are shown graphically in Figure 2.1and Figure 2.2, respectively.

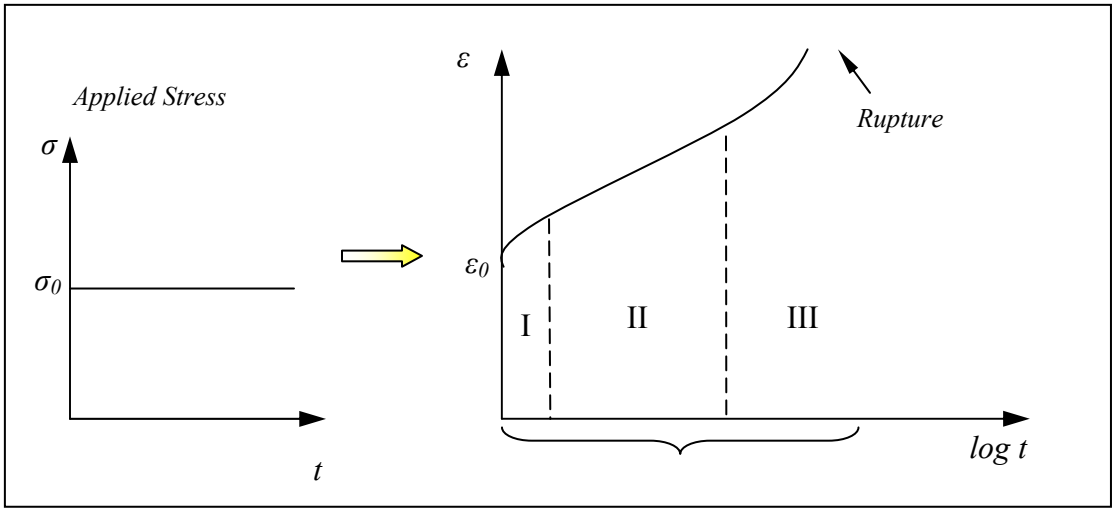

Figure 2.1: Evolution of the strain, ε, of a bar under constant stress, σ_0 (creep response). I, II, and III represent the three stages of creep. ε_0 is the value of the elastic strain.

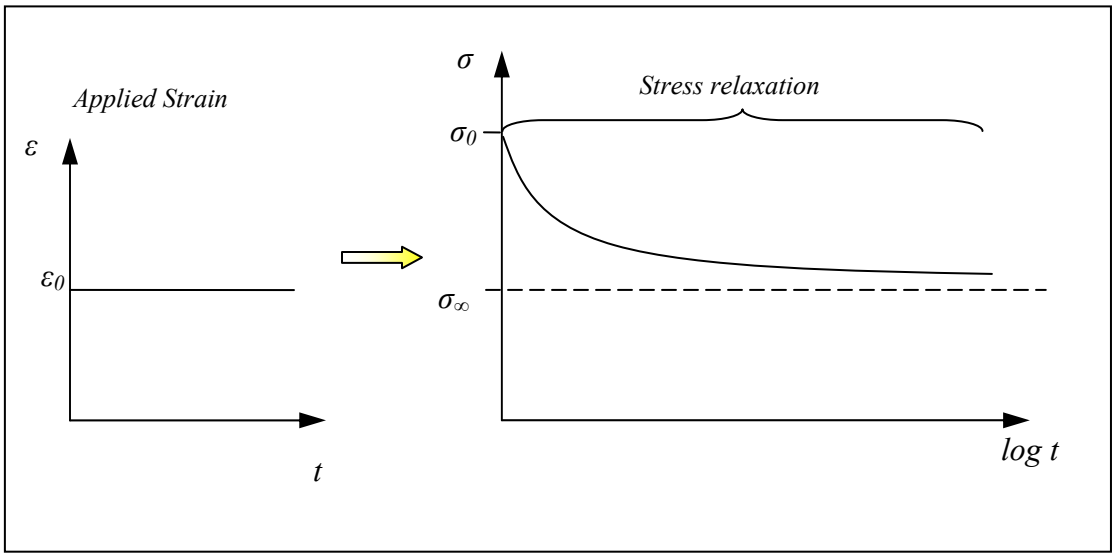

Figure 2.2: Stress relaxation, σ(t), in a bar under constant strain, ε_0. σ_0 is the value of the elastic stress and σ_∞ is the limiting value of σ(t) as $t \rightarrow \infty$.

The initial elastic response represents only an infinitesimally small fraction of the total response time in most materials and has therefore not been included in the figures above. It is also very important to stress that the viscoelastic response *is not* characterized by the whole of the responses illustrated above because they display both the elastic and plastic response of a material. viscoelastic behavior involves only recoverable deformation and therefore is more conceptually related to elasticity. However viscous behavior, which is generally associated with inelastic deformation, must be used to describe the lossy component of viscoelastic materials. These two figures clearly illustrate that the material response can be decomposed into two parts: (*i*) the elastic part and (*ii*) the viscous part [36]. Using this information, the moduli relating the time dependent stress or strain to the loading condition is written in the very general form of Eqns. (II.1.1) and (II.1.2) below.

$$\sigma(t) = \sigma_0 + \int_0^t E(t-\tau)\frac{d\varepsilon(\tau)}{d\tau}d\tau \qquad \text{(II.1.1)}$$

$$\varepsilon(t) = \varepsilon_0 + \int_0^t J(t-\tau)\frac{d\sigma(\tau)}{d\tau}d\tau \qquad \text{(II.1.2)}$$

In the above expressions, $E(t)$ is the relaxation modulus and $J(t)$ is the relaxation compliance of the material, $\sigma(t)$ and $\varepsilon(t)$ represent the total stress and strain of the material respectively at time t, σ_0 and ε_0 are the initial elastic stress and strain, and τ is the retarded time. The elastic values of stress and strain are given via the one dimensional Hooke's law as: $\sigma_0 = E_0\varepsilon_0$ and $\varepsilon_0 = \sigma_0/E_0 = J_0\sigma_0$. Expressions (II.1.1) and (II.1.2) show that the stress and strain at any given time is a function of both the initial

elastic response and some value that evolves with time according to the integral on the right-hand side (RHS). This integral represents a material memory function that takes the loading history into account in the present value and is the source of the phase lag / hysteresis observed in viscoelastic materials when submitted to cyclic loading [35].

Noting that Eqns. (II.1.1) and (II.1.2) are mathematically analogous, the following analysis will be carried out for the stress relaxation case only. Given a time varying imposed strain, $\varepsilon(t)$, the stress at any time can be determined from Eq. (II.1.3) below.

$$\sigma(t) = E^e(t)\varepsilon(t) + \int_0^t E^M(t-\tau)\frac{d\varepsilon(\tau)}{d\tau}d\tau \qquad \text{(II.1.3)}$$

In this expression, $E^e(t)$ represents the elastic part of the material response at time *t*, and $E^M(t)$ is the rate dependent material memory function. The elastic function represents the material stiffness at time *t* and the memory function is dependent on the mechanical loading history from time *t = 0* to the present time, *t*. This formulation of the material behavior is called the Boltzmann equation which takes the relaxation of the material into account [15]. From this relationship it is easy to show that Eq. (II.1.3) is the time domain representation of a *complex* Young's modulus in the frequency domain. The frequency dependent complex modulus is found by applying the Fourier transform to both sides of Eq. (II.1.3). The integral in (II.1.3) represents the convolution of $E^M(t)$ with the applied strain rate, $d\varepsilon(t)/dt$. The application of the Fourier transform and some simplification

will yield the following frequency dependent complex modulus representation of the time dependent behavior given in (II.1.3) [15, 34]:

$$\hat{\sigma}(\omega) = \hat{E}'(\omega)\left[1 - i\hat{\eta}_E(\omega)\right]\hat{\varepsilon}(\omega) \tag{II.1.4}$$

where $\hat{\eta}_E(\omega)$ represents the Young's modulus loss factor defined as $\hat{\eta}_E(\omega) \equiv \hat{E}''(\omega)/\hat{E}'(\omega)$. The exact relationships between the variables $E^e(t)$, $E^M(t)$, $E'(t)$, and $E''(t)$ depend on the material model employed and therefore are not explicitly given here (see Christensen [37]). It is important to note that the Euler's equation convention employed above is the '$e^{-i\omega t}$' convention shown in Eq. (II.1.5). This convention is employed throughout this work.

$$e^{-i\varphi} = \cos(\varphi) - i\sin(\varphi) \tag{II.1.5}$$

Equation (II.1.4) can be written in the same form as its static equivalent. The ability to describe viscoelastic material behavior by substituting complex valued variables into classic behavioral laws in place or purely real variables is called the elastic – viscoelastic correspondence principle [34]. The corresponding one dimensional viscoelastic Hooke's is given in (II.1.6).

$$\hat{\sigma}^*(\omega) = \hat{E}^*(\omega)\hat{\varepsilon}^*(\omega) \tag{II.1.6}$$

In the above expression the * indicates that the quantity is complex in general. The real part of the complex Young's modulus, $\hat{E}'(\omega)$, is called the storage modulus and represents the part of the material behavior that stores energy. The imaginary part, $\hat{E}''(\omega)$, is called the loss modulus, and describes material behavior that dissipates energy. This complex representation of the rate dependent lossy behavior of viscoelastic materials through complex moduli in the frequency domain greatly facilitates material behavior calculations. It is for this reason that the lossy behavior of a viscoelastic material is almost always represented in this simplified form and it has been shown to be applicable to micromechanical modeling [38-41].

Now consider the case where $\varepsilon(t)$ is imposed and is, therefore, a purely real function of time. Eq. (II.1.6) then simplifies to the following representation.

$$\sigma_0 e^{-i(\omega t-\varphi)} = E_0 e^{i\varphi}\varepsilon_0 e^{-i\omega t}$$
$$\sigma_0 e^{i\varphi} = E_0 e^{i\varphi}\varepsilon_0 \qquad \text{(II.1.7)}$$

Noting that the tangent of the loss angle, φ, given in Eq. (II.1.7) is the equal to the Young's modulus loss factor, $\hat{\eta}_E$.

$$\hat{\eta}_E = \tan\varphi \qquad \text{(II.1.8)}$$

All variables with a subscript "$_0$" in the above equations represent the magnitude of the corresponding variable [15].

It is important to recognize that representing viscoelastic behavior by employing the elastic-viscoelastic correspondence principle greatly simplifies mathematical models of the complex physical mechanisms leading to lossy behavior in any material. For example, when a time varying strain is imposed on a one-dimensional material sample the material immediately develops some stress depending on the strain rate and the specific material. The imposed deformation is completely recovered upon unloading, but the recovery path is not linear (as is evidenced from Eq.(II.1.2)). Just after loading, the material relaxes leading to a stress reduction. The stress relaxation results in a phase lag between the imposed cyclic strain and the resulting cyclic stress. The phase lag, clearly shown in Figure 2.3, is directly related to the loss factor of the material through relation (II.1.8). This lag corresponds to a hysteresis loop that is traced in the $\varepsilon(t) - \sigma(t)$ plane as a function of time. The area of this hysteresis loop is what quantifies the absorption of the strain energy by the viscoelastic material.

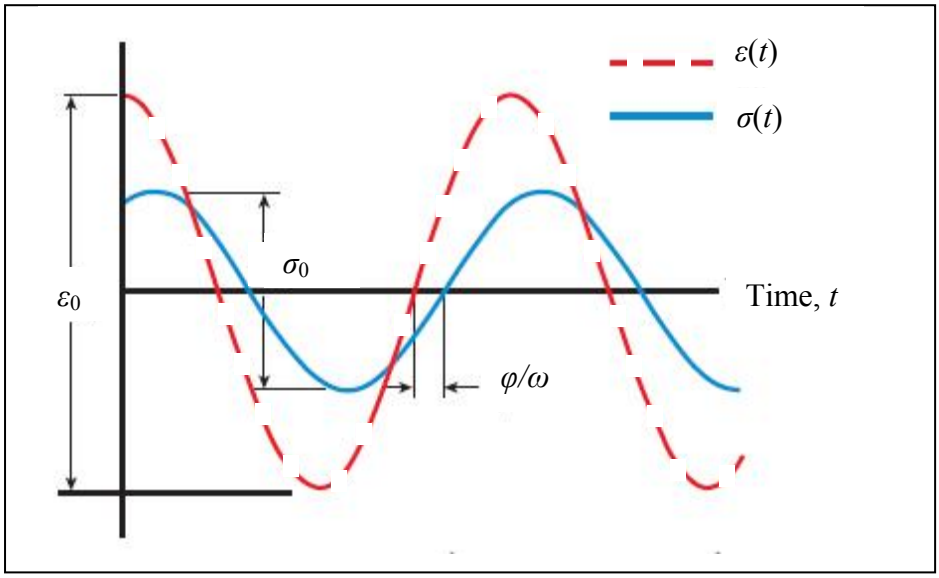

Figure 2.3: Time domain response of a one dimensional sample of viscoelastic material to an imposed cyclic strain.

Finally, it should be noted that the above simple demonstration only considered material behavior in extension, though an identical analysis could have been carried out for shear or volumetric behavior. It is therefore possible to extend the one dimensional relations given above to the more general case of viscoelastic anisotropy. As discussed above, due to the elastic-viscoelastic correspondence principle, extension of the constitutive laws of one dimensional viscoelastic behavior to behavior in three dimensions is almost trivial. Relations (II.1.9) and (II.1.10) give the constitutive viscoelastic material behavior laws for an anisotropic viscoelastic solid.

$$\hat{\sigma}^*_{ij}(\omega) = \hat{C}^*_{ijkl}(\omega)\hat{\varepsilon}^*_{kl}(\omega) \tag{II.1.9}$$

with:

$$\hat{C}^*_{ijkl}(\omega) = \hat{C}'_{ijmn}(\omega)\left[I_{mnkl} - i\hat{\eta}_{mnkl}(\omega)\right] \tag{II.1.10}$$

Where I_{ijkl} represents the fourth order identity tensor defined below.

$$I_{ijkl} = \frac{1}{2}\left(\delta_{ik}\delta_{jl} + \delta_{il}\delta_{jk}\right) \tag{II.1.11}$$

Equation (II.1.9) is the general form of the elastic-viscoelastic correspondence principle. In this form, both the frequency dependent stiffness, $\hat{C}'_{ijkl}(\omega)$, and the loss factor, $\hat{\eta}_{ijkl}(\omega)$, can depend on direction. A large part of this thesis deals with the approximation of the frequency dependent complex stiffness tensor, $\hat{C}^*_{ijkl}(\omega)$, of

viscoelastic particulate composites through micromechanical methods. The aim of this modeling is to validate a material model for future introduction into a material design strategy.

The following sections introduce two different approaches utilized to approximate the macroscopic damping behavior of a particulate composite. Section 2.1.1 presents the idea of approximating structural damping capacity through strain energy methods. This approach is wide spread in the field of structural vibrations, but the same rationale can also be applied, within certain limits, to composite material modeling. The strain energy approach approximates the damping capacity by calculating the ratio of the strain energy in lossy components to the strain energy in the non-lossy components. Section 2.1.2 presents a completely different approach based on the physics of acoustic wave propagation. This methodology is based on the mechanisms of the reflection and mode conversion of waves incident on a material heterogeneity (inclusions). These two approaches are based on very different physical concepts. However, each approach merits study since the physical mechanisms they describe are all present in the dynamic behavior of particulate composites.

2.1.1 Strain energy methods for approximating damping capacity

One well known method in the field vibrations for approximating the damping capacity of structures with lossy components is called the strain energy method. This approach consists of calculating the ratio of two different measures of strain energy. The numerator is the sum of the product of the strain energy, W_i, and material loss factor, η_i,

of all lossy elements of the structure, and the denominator is simply the sum of the strain energy in every structural element [41]. Ungar and Kerwin introduced this approach which relationship (II.1.12) summarizes [42].

$$\eta_{tot} = \frac{\sum_{i=1}^{N} \eta_i W_i}{\sum_{i=1}^{N} W_i} \qquad \text{(II.1.12)}$$

This relationship is a direct result of the complex modulus formulation employed in modeling viscoelastic materials. For the unidirectional loading case, the material's loss factor is related to the strain energy and the hysteresis area via the following relationship:

$$\eta = D/\pi\sigma_0\varepsilon_0 \qquad \text{(II.1.13)}$$

Here D represents the hysteresis area and the denominator is the total strain energy of one cycle of loading. Given the definition of specific strain energy (energy per unit volume), $W \equiv \pi\sigma_0\varepsilon_0$, and by setting $N = 1$, Eq. (II.1.12) reduces to the definition of the material loss factor for a lossy single element. Expression (II.1.12) generalizes this rationale to a system of N different elements potentially having N different damping capacities. The method described above is a simple, accurate, and very amenable to finite element (FE) calculations [39-41]. This approach is employed in many structural vibrations applications where each element can easily be modeled as a continuous material having a distinct viscoelastic response [43]. The works of Ross *et al* [31], Soni [44], and Mead

and Markus [45], are further examples of this approach and its application to the approximation of the damping capacity of multi-layered plates.

The method explained above is conceptually easy to understand and to apply at the structural level, especially though FE analysis, see the examples of Sun and Lu [46], Nashif [47], or McDaniel and Ginsberg [48]. Unfortunately, the case of particulate composites presents many difficulties to the application of this approach. The difficulty stems from the fact that the calculation of the strain distribution in each material phase is complicated by the shape, orientation, and distribution of the inclusion phases. However, since the approach has proven robust and accurate at a structural level, it is interesting to explore its potential for application to particulate composites which represent structures in a more general sense. To this end, a brief study of the strain energy of the composite sphere shown in Figure 2.4 is given. A sphere, with bulk and shear moduli of K and μ, respectively, has an outer radius b and is subject to an external pressure p_0 and boundary conditions (BC's), χ, at $r = a$.

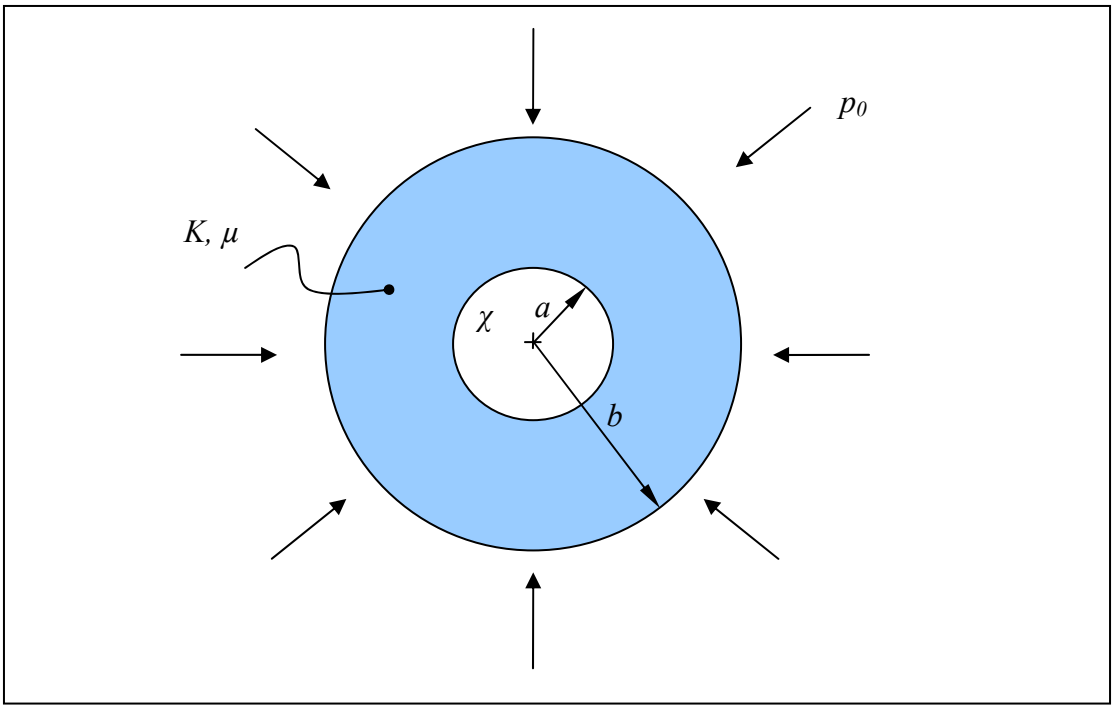

Figure 2.4: Composite sphere of inner and outer radii *a* and *b* respectively. The material has a bulk and shear moduli denoted as *K* and *μ* respectively. The boundary conditions at *r* = *a* can be changed and are designated as *χ*.

When submitted to external loading, the strain energy in the material located between $r = a$ and $r = b$ is be calculated from expression (II.1.14) below [49].

$$W = \frac{1}{2}\int_V \varepsilon_{ij} C_{ijkl} \varepsilon_{kl} dV = \frac{1}{2}\int_V \sigma_{ij} \varepsilon_{ij} dV \qquad \text{(II.1.14)}$$

The following ration is now defined in order to show the change in strain energy located between these two different radii due to different BC's imposed at $r = a$:

$$R = \frac{\int_a^b \left[\sigma_{rr}^{CpS}(r)\varepsilon_{rr}^{CpS}(r) + \sigma_{\varphi\varphi}^{CpS}(r)\varepsilon_{\varphi\varphi}^{CpS}(r) + \sigma_{\theta\theta}^{CpS}(r)\varepsilon_{\theta\theta}^{CpS}(r)\right] r^2 dr}{\int_0^b \left[\sigma_{rr}^{CS}(r)\varepsilon_{rr}^{CS}(r) + \sigma_{\varphi\varphi}^{CS}(r)\varepsilon_{\varphi\varphi}^{CS}(r) + \sigma_{\theta\theta}^{CS}(r)\varepsilon_{\theta\theta}^{CS}(r)\right] r^2 dr} \quad \text{(II.1.15)}$$

Where σ_{xx}^{CS} and ε_{xx}^{CS} represent the stress and strain in the x direction (either r, φ, or θ in the spherical coordinate system) of a continuous sphere and σ_{xx}^{CpS} and ε_{xx}^{CpS} are the same constants for the case of a composite sphere. When the loading is spherically symmetric (as is the case for an imposed external pressure) the stresses and strains in the material will only exhibit radial dependence. This dependence is derived by solving the Navier-Stokes equations whose results are given in Eqns. (II.1.16)(a)-(e) [49]. The values of coefficients α and β can then be determined from the BC's at $r = a$ and the pressure, p_0, imposed at $r = b$.

(a) $u_r(r) = \alpha r + \frac{1}{r^2}\beta$

(b) $\varepsilon_{rr}(r) = \alpha - \frac{2}{r^3}\beta$

(c) $\varepsilon_{\theta\theta}(r) = \varepsilon_{\varphi\varphi}(r) = \alpha + \frac{2}{r^3}\beta$

(d) $\sigma_{rr}(r) = 3K\alpha - 4\mu\beta\frac{1}{r^3}$

(e) $\sigma_{\theta\theta}(r) = \sigma_{\varphi\varphi}(r) = 3K\alpha + 4\mu\beta\frac{1}{r^3}$ (II.1.16)

The resulting relationship expressing the total strain energy for a continuous sphere ($a = 0$) is given below in Eq. (II.1.17):

$$W^{CS} = \frac{2}{3}\pi\left(\frac{p_0^2 b^3}{3K}\right) \quad \text{(II.1.17)}$$

To show how the boundaries at $r = a$ affect the total strain energy in the composite sphere, the following cases will be investigated and compared: (*i*) rigid boundary conditions at $r = a$ ($u_r(a) = 0$), and (*ii*) pressure release boundary conditions at $r = a$ ($\sigma_{rr}(a) = 0$). The result of the evaluation of the ratio in Eq. (II.1.15) for cases (*i*) and (*ii*) are given below in Eqns. (II.1.18) and (II.1.19) with corresponding plots in Figure 2.5 and Figure 2.6.

$$R^{i} = \frac{3\frac{K}{\mu}(1-f)}{4f - 3\frac{K}{\mu}} \tag{II.1.18}$$

$$R^{ii} = \frac{1}{(1-f)^2}\left\{1 - f\left[1 + \frac{1}{3}\ln(f)\right] + \frac{2(1+\nu)}{3(1-2\nu)} f(1-f)\right\} \tag{II.1.19}$$

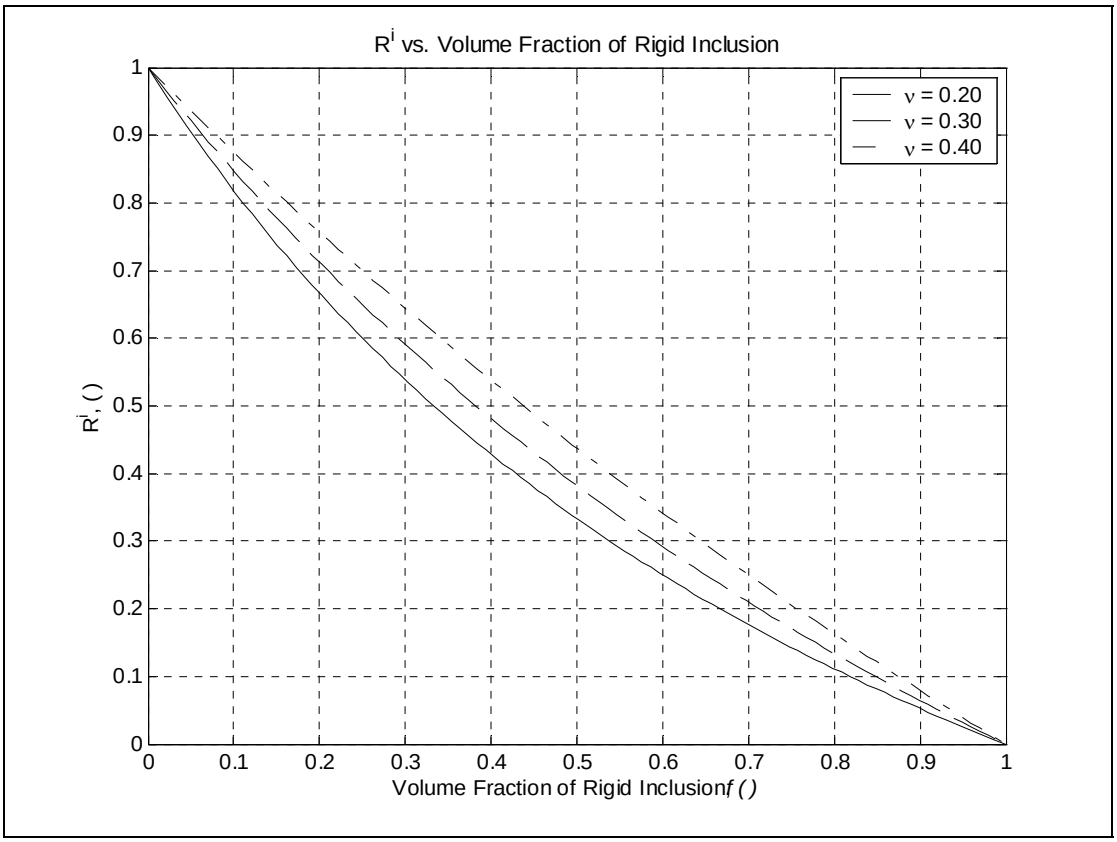

Figure 2.5: Ratio of strain energy in matrix material of composite sphere for three different values of Poisson's ratio with rigid BC's at $r = a$ as a function of volume fraction, $f = a^3/b^3$.

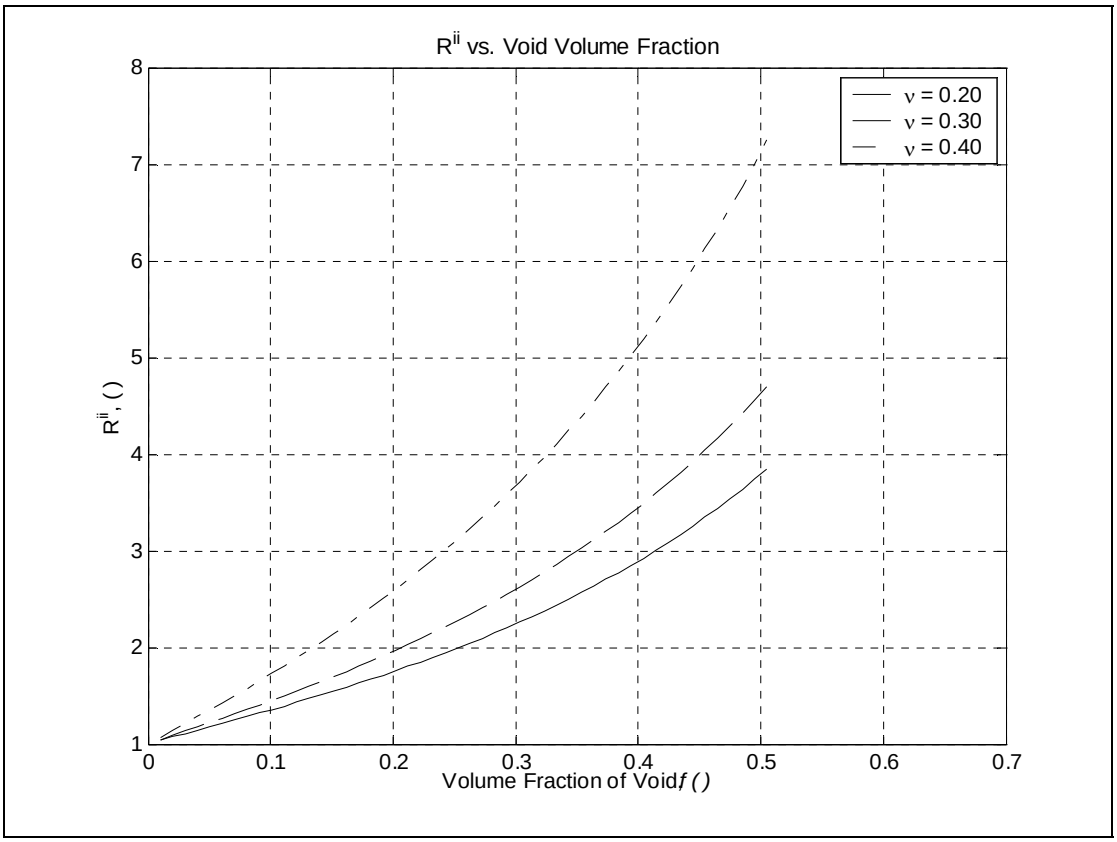

Figure 2.6: Ratio of strain energy in matrix material of composite sphere for three different values of Poisson's ratio with pressure release ($\sigma_{rr} = 0$) BC's at $r = a$ as a function of volume fraction, $f = a^3/b^3$.

In Eqns. (II.1.18) and (II.1.19) f represents the volume fraction of the composite sphere occupied by the rigid inclusion or void, $f = a^3/b^3$, and v is the Poisson's ratio of the material occupying the space between $r = a$ and $r = b$. This simple illustration demonstrates how the presence of voids in a material quickly raises the total strain energy as a function of volume fraction. This strain energy rational to approximate damping capacity implies that if the matrix material is lossy, voiding the material greatly increases the composite material's capacity to dissipate energy for a given applied *stress* (in this case p_0). Along the same lines of thought, if the voids were instead inclusions having a lower stiffness value than that of the matrix, the damping capacity of the composite would still be superior to a sphere consisting of the matrix material alone for the same

applied *stress*. It is also obvious that rigid inclusions, or indeed inclusions that are stiffer than the matrix, diminish the strain energy present in the matrix material for a fixed applied *stress*. In the case where only the matrix is lossy, this would have a negative effect on the composite's damping capacity for the imposed *stress* case. It must be noted, however, that the in wave propagation problems the effects of inertia and multiple scattering renders this statement is not necessarily true. Converse to the arguments above, if the composite sphere is loaded with a fixed *strain* imposed at $r = b$, rigid inclusions will increase the total strain energy present in the matrix material. For the imposed strain case all of the arguments given above for the voided sphere will be true for the sphere containing a rigid inclusion.

Unfortunately, for a true composite material, the calculation of the strain energy in each constituent phase is complicated by material stiffness contrasts and anisotropy along with inclusion shape and spatial orientation. Approximation of the overall loss factor of a particulate composite material through the strain energy method therefore becomes difficult. However, a micromechanical approach, which relies on the calculation of the average strain field in each constituent phase of the composite, may provide a practical means to approximate the damping capacity of particulate composites. A bibliographic review of the important contributions to micromechanics and the specific work of this thesis will be given in Section 2.2.

2.1.2 Acoustic scattering methods for approximating damping capacity

Acoustic wave absorption is the result of the four following physical mechanisms: (*i*) scattering by inhomogeneities, (*ii*) mode conversion at the interfaces of inhomogeneities, (*iii*) redirection, and (*iv*) intrinsic absorption by conversion to heat [15]. Figure 2.7 illustrates the dominant physical processes that occur when a plane wave impinges on an inhomogeneity in the form of a coated inclusion. The propagation of a harmonic longitudinal plane wave in the x_i direction is described by Eq. (II.1.20) below.

$$\hat{p}_I\left(x_i,t\right)=\hat{A}e^{-i(\omega t-k_i x_i)} \tag{II.1.20}$$

$$k=\frac{2\pi}{\lambda}=\frac{\omega}{c} \tag{II.1.21}$$

In the above equations $\hat{A}$ represents the complex magnitude of the incident wave, k is the wavenumber calculated using Eq. (II.1.21), ω is the angular frequency, λ is the wavelength (not the Lamé constant), and c is the sound speed in the material.

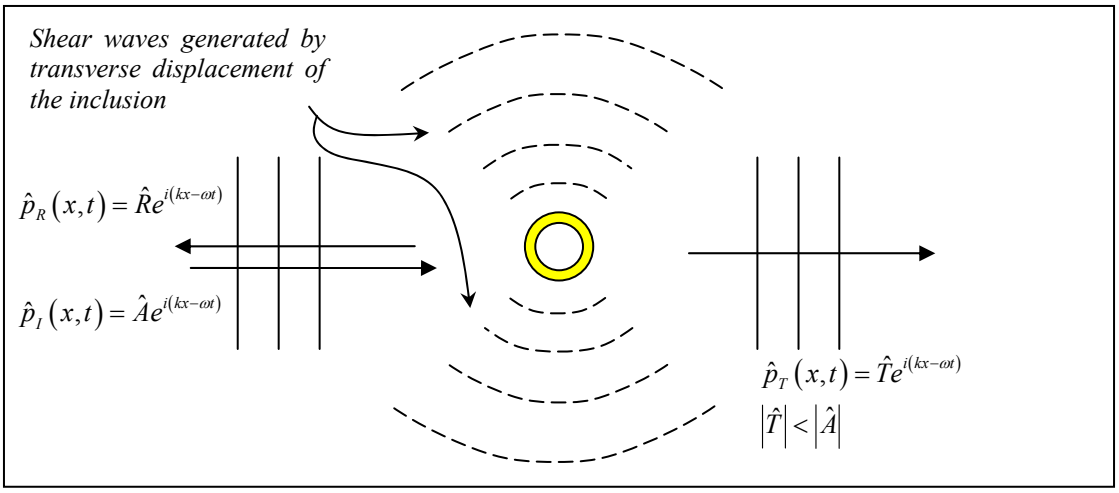

Figure 2.7: Illustration of the dominant physical mechanisms that take place when a longitudinal plane wave impinges on an material inhomogeneity.

Figure 2.7 illustrates the four mechanisms leading to energy dissipation. The first mechanism mentioned is scattering due to inhomogeneities. The incident wave is scattered when longitudinal and shear waves are generated due to reflection at the interface of the material discontinuity. These waves propagate out from the inhomogeneity in all directions with magnitudes that depends on the angle (measured with respect to the incident wave direction) and frequency of the incident wave [50]. Following scattering, the host material attenuates each new wave front and therefore the it is in this manner that scattering leads to more efficient *absorption* of wave energy and not simply redirection of that energy. This process leads to an increased damping capacity of the heterogeneous material as a whole. It is the goal of wave scattering based models of composite materials to capture this physical behavior in order to quantify the effective material stiffness and damping properties.

In general, each time a plane wave encounters an impedance difference (an inhomogeneity) a portion of the incident energy is reflected and the rest is transmitted. A portion of the reflected energy propagates as plane waves and the remaining energy

propagates in the form of different types of waves, a high percentage of which are shear waves. The amount of energy propagating in each wave depends on the specific material properties of the medium on each side of the interface and the angle of incidence [51]. This process of generating several types of waves due to the reflection of a plane wave at a material inhomogeneity is known as mode conversion, and it leads to more efficient damping. One of the reasons mode conversion increases damping efficiency is difference in the wavelength of shear waves and longitudinal waves. The wavelength of shear waves is shorter than that of longitudinal waves in the same material for the same frequency. This difference in wavelength means that a shear wave will undergo more cycles when propagating the same distance as a longitudinal wave. Since lossy material absorb a given percentage of wave energy each cycle, this process leads to more energy absorption for the same distance traveled. The fact that most materials display a higher damping capacity in shear further increases the damping capacity when mode conversion occurs. Mode conversion also creates more wave fronts. Because each wave front propagates in the absorptive material, the net result is an increase in the total damping efficiency. Mode conversion also occurs when shear waves are also generated due to the transverse displacement of the heterogeneity in the direction of propagation. This displacement results from the stress gradient of the longitudinal wave. The gradient first pushes the inclusion to the right (as sketch in the figure above) until the maximum stress level is reached, and then pulls it back to the left during rarefaction. It is obvious that this leads to shearing motion in the host material in directions that are not parallel to the propagation direction.

The way in which the redirection of wave energy leads to a reduction in energy should be clarified. For an ideal infinite lossless medium, the energy of a plane wave received at point *B* is the same as the energy when it was sent from point *A*. If an heterogeneity is placed in between these two points, part of the energy present at point *A* will never arrive at point *B* because of the reflection/scattering by the heterogeneity. The result for the lossless medium is that the total energy in the composite will remain unchanged. There will, however, be a decrease in the wave's amplitude at point *B*. The amplitude reduction due to the presence of an heterogeneity could be quantified with a measure called the Insertion Loss (IL) [12]. When the host material is lossy and many inhomogeneities are present, redirection increases absorption by increasing the distance a single wave front travels due to multiple reflections. Since the absorption of energy is a function of the distance traveled, the final result is an increase in the damping capacity [15].

Finally, in all real materials acoustic wave absorption results from viscoelastic material behavior discussed at the beginning of this section. Lossy behavior is, in general, dependent on internal friction, molecular chain relaxation, and other physical phenomena that change mechanical energy into thermal energy which ultimately heats the material [34]. The capacity of a given material to damp a traveling wave is easily quantified by complex wave number, $\hat{k}(\omega)$, calculation for propagation in the host medium using Eq. (II.1.20) [51].

$$\hat{k}_i^*(\omega) = \omega \sqrt{\frac{\rho}{\hat{C}_{ijkl}^*(\omega) n_j n_k p_l}} = \hat{k}_i'(\omega) + i\hat{\alpha}_i(\omega) \qquad \text{(II.1.22)}$$

In the above equation, ρ is the material density, $C^*_{ijkl}(\omega)$ is the complex frequency dependent stiffness described by relation (II.1.10), n_j and n_k are the normal directions as described by the Christoffel equation, $\left|C^*_{ijkl}n_j n_k - \rho c^2 \delta_{il}\right| = 0$ [51], δ_{il} is the Kronecker delta, p_l is the wave polarization describing the propagation direction, $\hat{k}_i^{'}(\omega)$ is the real part of the wave number, and $\hat{\alpha}_i(\omega)$ is the attenuation coefficient. It is important to note that for realistic values of the loss factor ($0 \le \eta \le 1$) and if the real part of the elastic moduli remains constant, the attenuation coefficient is a monotonically increasing function of the host material loss factor. By inserting (II.1.22) into (II.1.20) it becomes obvious that the wave magnitude decays exponentially as a function of α_i and the distance traveled as shown in Eq. (II.1.23).

$$\hat{p}_l(x_i,t) = \hat{A}e^{-\alpha_i x_i}e^{-i\left(\omega t - k_i^{'} x_i\right)} \tag{II.1.23}$$

The relationships presents thus far show why a homogenization scheme that correctly captures the mechanisms of scattering by finding a complex, frequency dependent, effective stiffness tensor, can yield insight into the design of lossy materials.

One problem with the method described in Section 2.1.1 is its limitation to the quasi-static case. The quasi-static domain is defined by the ratio of the incident wavelength to the descriptive inclusion dimension and is usually expressed via the non-dimensional quantity *ka* where *a* represents the largest inclusion dimension and *k* is the

wavenumber. The quasi-static domain is limited to those frequencies that render $ka << 1$ [50].

Energy dissipation due to wave scattering by the presence of a material inhomogeneity is well approximated in the quasi-static domain by the extensional strain energy in the near field of that inhomogeneity [15]. In this frequency range the "propagation" of the wave at the inclusion scale is well represented as a time varying stress/strain field. At this scale the effects of wave scattering are very small compared to the stress/strain concentration in the neighborhood of the inclusion. Using this knowledge, a strain energy based approach delivers reliable particulate composite damping capacity approximations in the frequency domain by introducing the lossy, frequency dependent, constituent material behavior into static models [38]. In order for a model to be reliable for complex particulate composites careful consideration must be taken in modeling the strain field everywhere in the composite. This is the is the case for most mean field homogenization theories [52]. If, on the other hand, the frequency of the propagating waves is such that $ka \approx 1$ or even $ka \geq 1$, models based on mean stress/strain field theories are no longer valid. For these frequencies such models neglect the physical mechanisms of scattering [53] and, therefore, single or multiple scattering homogenization approaches must be employed. The model and experimental data presented in this thesis are limited to the quasi-static domain. However, in an effort to give a complete picture of the frequency dependent behavior of particulate composites, a bibliographic review of the significant works in the area of scattering based homogenization techniques is presented in Section 2.3.

2.2 Homogenization of particulate composites through micromechanics

The most precise approach to modeling the macroscopic behavior of complex materials would be one that takes its intrinsic multiscale structure into account. This type of multiscale approach requires knowledge of the physical behavior of the material at each scale as well, as the nature of the interaction between scale levels. If a modeling approach captures the material behavior at each scale level of interest and the interaction mechanisms between scales, it is possible to approximate material behavior at all scales based on knowledge of the material's composition. The micromechanical approach is, by definition, a multiscale modeling approach. It assumes that two structural levels exist such that the effects of interfaces, heterogeneities, and other physical phenomena at the lower level can be taken into account at the upper level via an averaging approach. These structural levels are defined by length scales such that $l<<L$ where l is the descriptive dimension at the lower length scale and L describes the higher length scale. This tacitly assumes that the upper length scale properties, referred to as global or macroscopic, are the result of an average of the behavior of the lower length scales and therefore that no point to point interaction takes place between scales [33]. The idea behind this approach is illustrated by defining a Representative Volume Element (RVE). A RVE is the smallest material volume unit (element) whose effective behavior is assumed to represent the macroscopic behavior of the complex material. Selection of a RVE plays a large part in defining the limitations of any proposed micromechanical method [54]. A RVE example and associated elementary inclusion problem (EIP) illustration for a composite consisting of a matrix with identically oriented coated ellipsoidal inclusions is shown

below in Figure 2.8. This RVE and EIP represents the self-consistent (SC) model introduced by Cherkaoui *et al* [23]. This RVE assumes that the composite material behavior can be well approximated by writing the constitutive equations of a single coated inclusion embedded in the effective material, which has unknown material properties [23].

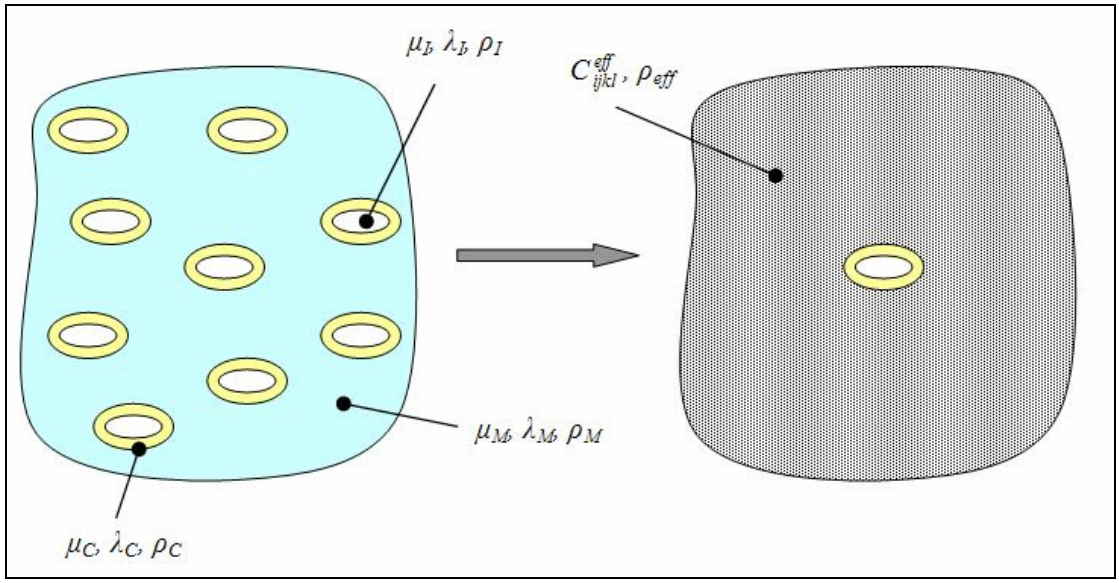

Figure 2.8: RVE for the SC model of Cherkaoui *et al* [23]. λ_x and μ_x represent the Lamé constants and ρ_x the density of material *x*. C^{eff}_{ijkl} is the effective stiffness tensor and *I, C,* and *M* specify respectively the inclusion, coating, and matrix.

Historically, all micromechanical mean field theories have been based entirely on the physical principles of continuum mechanics. The approach taken in this thesis will be no different. Since its inception nearly fifty years ago, micromechanics has become a well developed field of study which has been shown capable of addressing many different fields of science. The approach is even currently being adapted to approximate the behavior of nanomaterials (ex: [55-57]). The development of this field is the result of two distinct needs: (*i*) the need to approximate the macroscopic behavior (elastic, plastic,

thermal, electromagnetic, etc.) of materials containing micro-scale heterogeneities (micro/$\mu \rightarrow$ macro/M scale transition) and (*ii*) the need to localize macroscopically applied fields to inferior length scales (M$\rightarrow\mu$ scale transition) [33, 54]. Indeed, the approximation of the macroscopic response of an inhomogeneous material, which is an average of the microscopic behavior, requires knowledge of the spatially varying microscopic fields [58].

A good example that illustrates this point is the model proposed by Song *et al* [59] to approximate the global response of a bi-phase composite material having inclusions that can undergo phase transformation. This model applies a SC homogenization approach to approximate the macroscopic elastic and thermal material properties. The first step homogenizes the material ($\mu\rightarrow$M) thereby approximating the effective macroscopic composite properties based on its composition and thermomechanical loading. At this point, the localization of the imposed loads to the microscopic level (M$\rightarrow\mu$) is performed in order to calculate thermomechanical phase equilibrium of the inclusions via local physical laws and localized loads. Given the change in the phase composition of the inclusion, which changes the elastic and thermal properties, another homogenization step is made. This process repeats itself during the entire loading history. The micromechanical approach thus gives information of not only of the macroscopic response, but also of the thermomechanical state of the inclusions at all times during the loading history.

The specific materials and behavior just discussed are much different than those discussed in this work. However, the above example clearly shows the capacity of micromechanical models to resolve multiscale problems and give material behavior

information at multiple length scales simultaneously. Further, the example illustrates an important principle: the behavior of microscopic heterogeneities can have a significant influence on the macroscopic behavior of a material. It is for these reasons that the micromechanical modeling approach is a powerful tool that can be employed to analyze multi-scale problems.

2.2.1 Pertinent micromechanical modeling developments

The micromechanical approach employed in this work is a mean field model for particulate composite materials. All mean field models are based, in one way or another, on the seminal work of Eshelby [58]. Eshelby's results marked a great improvement over elementary techniques such as the work of Voigt [60], Reuss [61]. Voigt and Reuss used variational principles and strain energy which cannot take inclusion shape into account.

The micromechanical modeling approach initiated by Eshelby consists of two fundamental operations: (*i*) localization and (*ii*) homogenization [33, 54]. As previously stated, these operations require the existence of at least two length scales within the material. It also assumes that that the effect of material behavior and structure at the microscopic particulate length scale has only an average effect on the behavior of the material behavior at the macroscopic scale and that macroscopically applied loads can be localized to the microscopic level [33]. Eshelby's results [58] provide the insight and mathematical tools to resolve the localization problem via the equivalent inclusion method which results in localization tensor now called Eshelby's tensor, S_{ijkl}. This capability to localize macroscopically applied mechanical loading to the microscopic

level is fundamental to the approximation of volumetric average stress and strain fields in the heterogeneous material. This set of operations is called the homogenization step. Localization allows volume averaging since it permits the derivation of stress and strain fields as a function of position which depend not only on the applied load, but also inclusion forms, orientations, and properties [62-64].

Following Eshelby's fundamental contribution a large array of models, for example those of Kröner [65], Budiansky [66], Wu [64], and Mori and Tanaka [67] to name very few. All of these models employ a similar equivalent inclusion approach. Zeller and Dederichs [68], however, improved on the equivalent inclusion method by introducing a Green's function formalism that permits the calculation of the stress and strain fields at every point in a heterogeneous material at the microscopic scale. Their approach is based on the idea that the material behavior of a particulate composite can be approximated on the local, or microscopic, scale via expressions of the form shown below.

$$\mathbf{X}(\mathbf{r}) = \mathbf{X}^0 + \delta\mathbf{X}(\mathbf{r}) \qquad \text{(II.2.1)}$$

In this expression, **X** represents the material properties or fields of interest in the heterogeneous medium. The concept behind this approach is that the material properties and fields of interest are globally homogeneous, $\mathbf{X}^0$, with small perturbations due to microscopic heterogeneities scattered throughout the host material, $\delta\mathbf{X}(\mathbf{r})$. Using Green's tensors, the field generated by these heterogeneities can be approximated at every point in the material, thereby providing a good representation of the microscopic behavior. This

approach was improved upon by Mura [69] and Willis [70] to include plastic deformation and generalized for the case of two disoriented ellipsoidal plastic inclusions by Berveiller *et al* [71]. Another important improvement over the equivalent inclusion method was the introduction of interfacial operators which relate the stress and strain state across the interface of dissimilar materials [72, 73].

The combination of these two mathematic techniques provides an extremely powerful modeling tool of the physical phenomena present at the microscopic length scale which, in turn, improves the volumetric average approximation required in the homogenization step. The SC coated inclusion model of Cherkaoui *et al* [23, 24, 74], which will be extended to account for frequency dependent viscoelastic constituent phases in this work, owes its accuracy to the fact that it is derived using these tools.

It has been previously stated that all micromechanical models require the selection of a RVE. Each individual model is then derived using constitutive laws and the appropriate mathematical tools (Green's functions and interfacial operators, for example) based on the composition of the specific RVE and by solving an associated elementary inclusion problem (EIP). An EIP for a material consisting of a matrix containing coated ellipsoidal inclusions is shown below in Figure 2.9.

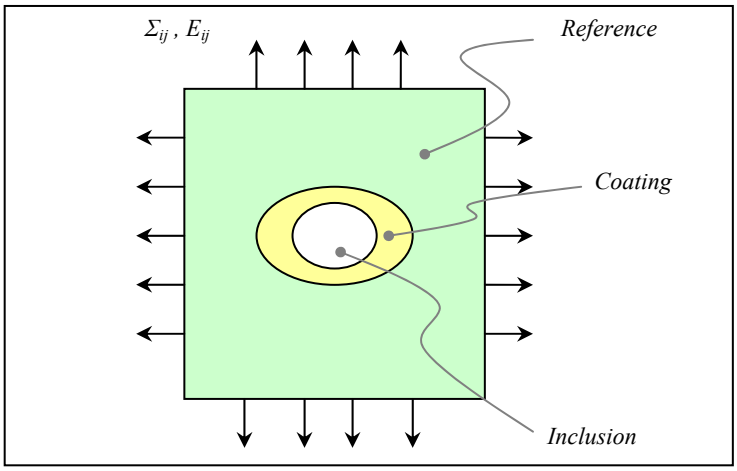

Figure 2.9: EIP of composite material consisting of a matrix containing coated ellipsoidal inclusions.

The Mori-Tanaka (MT) model, for example, assumes that the reference material of Figure 2.9 is the matrix material having elastic properties $\mathbf{C}^M$ and the imposed global strain, E_{ij}, is that of the matrix, ε_{ij}^M [67]. This results of this modeling approach at elevated volume fractions (f_I > 50%) is disputable, as are many others, due to the tacit assumption that stress and strain fields of multiple inclusions do not interact [75]. In order to overcome this limitation, several approaches can be taken. One is a computationally expensive periodic array type of approach where the interaction of heterogeneities is directly taken into account [52]. A strong example of this approach is the explicit model proposed by Molinari and El Mouden [76] which applies Berveiller *et al*'s [71] paired inclusion Green's formalism and agrees well with established models and experiment for elevated volume fractions. Another approach is the SC approach which assumes that the reference material of Figure 2.9 is an effective material having unknown elastic properties, $\mathbf{C}^{eff}$ [75]. This approach was first proposed in the area of mechanics of materials by Kröner [65] to approximate the behavior of polycrystalline materials where the definition of a matrix is unclear. This approach was later improved upon by

Budiansky [66], Hill [77, 78], and Berveiller and Zaoui [79], and finally generalized by Christensen and Lo [80].

The case of coated inclusions is of interest for several different reasons. One reason is to approximate the behavior of a bi-phase composite by assuming that the material in the neighborhood of an inclusion, the "interphase," behaves differently than the matrix material. This is the aim of the model proposed by Jasiuk and Kouider [81]. Another, more obvious, reason for choosing a coated inclusion RVE is that the composite consists of a matrix containing coated inclusions. The model proposed by Cherkaoui *et al* [23, 24, 74] can be used for either aspect of the coated inclusion problem. Hervé and Zaoui [82] extended such an approach to model the *N*-layered coated inclusion case. Approximation of the dynamic behavior of such materials by employing the elastic-viscoelastic correspondence principle, in accordance with the works of Hashin [17, 83, 84] and Christensen [16], is the subject of this thesis. This will be done by extending the work of Cherkaoui *et al* [23, 24, 74] to the quasi-static domain and further refining the model.

2.3 Homogenization of particulate composites through acoustic scattering

Homogenization models for particulate composites based on the effects of wave scattering presented in Section 2.1.2 take two general forms: *i*) single scattering models and *ii*) multiple scattering models. Both approaches are based on resolution of the problem posed by finding the acoustic field resulting when a wave traveling in a host medium that encounters an heterogeneity. The difference between the two modeling

approaches, as suggested by the naming convention, resides in the treatment of the interaction of waves reflected by the material discontinuity.

2.3.1 Single scattering models

The basis of all single scattering approaches is the assumption that inclusion concentration, usually referred to as scatterers, is low. This assumption allows the approximation of the entire acoustic displacement field in the composite as a summation of the field scattered from each individual scatterer and that no interaction between these fields takes place. The first influential single scattering model of note was proposed by Ying and Truell [85] which resolves the emulsion problem: fluid inclusions embedded in a fluid host medium. Their model introduces the important basic ideas of material homogenization via scattering methods but lacks the complexity needed to resolve the problem presented by heterogeneous solids.

The seminal work of Chaban [86] was a major contribution to the single scattering approach. It introduced two important hypotheses. The first hypothesis is that the total displacement field, $\vec{u}_{tot}$, in the heterogeneous medium can be represented as the summation of the incident displacement field, $\vec{u}_{inc}$, and the scattered field due to each scatterer, $\vec{u}_{s,i}$. This approximation requires that there can be *no* interaction between the scattered fields of the inclusions. Mathematically, this hypothesis is expressed below in Eq. (II.3.1).

$$\vec{u}_{tot}(\mathbf{x}) \approx \vec{u}_{inc}(\mathbf{x}) + \sum_{i=1}^{N} \vec{u}_{s,i}(\vec{\rho}_i); \quad \vec{\rho}_i = \mathbf{x} - \mathbf{x}_{s,i} \tag{II.3.1}$$

In the above expression, the observation point and scatterer location are represented by **x**, and $\mathbf{x}_{s,i}$, respectively [87]. The second hypothesis is the assumption that the scattered displacement field due to an inclusion having a volume, V_0, and the effective medium material properties is equivalent to the field scattered by the same volume of composite material *if* the observation point is in the far-field [26, 87-90]. Figure 2.10 shows a schematic of the "RVE" of the single scattering approach. One implication of the second hypothesis is that the center of each inclusion must be approximated as being located at the center of the scattering volume, V_0. This is mathematically expressed as: $\left|\mathbf{x} - \mathbf{x}_{s,i}\right| \approx \left|\mathbf{x} - \mathbf{x}_{V_0,center}\right|$.

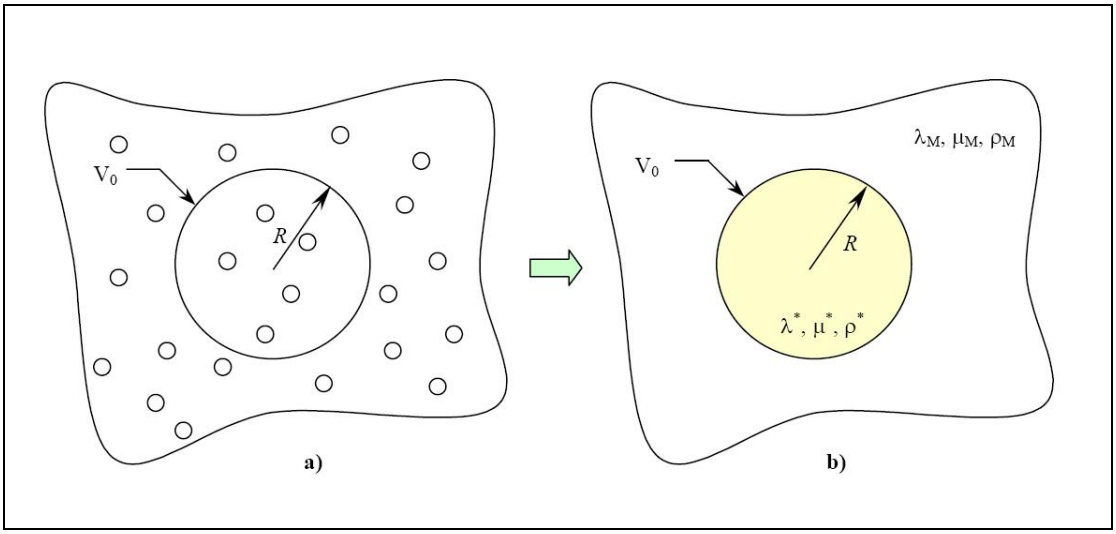

Figure 2.10: The composite material, (a), and the RVE, (b), for the single scattering approach introduced by Chaban [86].

To find the analytic solution to this problem, the equations of an incident plane wave must be decomposed as a summation of spherical waves that encounter an inclusion for the both case (a) and (b) illustrated above. The approximate solution is a series expansion with respect to *ka*, where higher order *ka* terms are truncated [26]. This truncation is only valid in the case where $ka<<1$ therefore corresponding to the quasi-static case discussed in Section 2.1. Finally, the expressions arising from the solutions of configurations (a) and (b) are set equal and it is then possible to resolve the system for the effective material properties of the heterogeneous material.

The result of all of these approximations, especially the first hypothesis, is that simple scattering models are only valid for low concentrations of inclusions, $\leq 10\%$ as a rule of thumb, and for $ka<<1$. This scattering regime is called Rayleigh scattering in honor of Lord Rayleigh [32]. However, several clever approaches have been found that provide a reliable approximation of the effective material behavior for an increased volume fraction; on the order of $\leq 30\%$ scatterer concentration. These approaches are called SC scattering models. Chaban's model incorporates the SC approximation by assuming that the scattered field from multiple non-interacting inclusions is equivalent to the field created by a single inclusion having effective material properties [86].

Another highly employed single scattering model was proposed by Kuster and Toksöz (KT) [87] which is based on the integral equations for the displacement field derived by Mal and Knopoff [91]. Their model has the capacity to approximate the effective behavior of a material containing spherical and spheroidal inclusions, but unfortunately has no dependence on the frequency outside of the frequency dependent matrix material. The absence of frequency dependence results from the fact that the

model does not take into account inclusion resonant behavior. Though this model gives reasonable approximations for several areas of study, such as geophysics, the first resonance, which is related to monopole scattering, can have an important effect on the effective behavior of the material even in the quasi-static domain [90, 92, 93]. Gaunaurd and Überall (GU) included several higher order terms in the series expansion described previously in order to address this problem [89]. The idea of including resonant behavior is a result of their work with voided materials and bubbly liquids. For such materials experimental results showed a marked deviation from theoretical values calculated using KT methods which lack resonant scattering effects [94]. It is, however, important to note that for certain types of materials, those where the inclusion has a higher stiffness value than that of the matrix, the KT approach provides a good approximation in the quasi-static domain. For this case, the monopole resonance does not have a significant effect on the global behavior. Indeed, the SC model proposed by Berryman for bi-phased composites with spherical [95] or ellipsoidal [27] inclusions shows good agreement with the KT approximation.

The work presented in this thesis focuses on the behavior of composite materials in the quasi-static domain and, therefore, single scattering models are very relevant to this discussion. Among the multitude of single scattering models, some of the most relevant to this work are highlighted below. The model described by Kerr [90] is a GU-type SC single scattering model for bi-phase composites. This model was extended to the case of coated fluid inclusions by Baird *et al* [26] and its approximations have been compared with experimental values of Transmission Loss (TL). The model of Anson and Chivers [96], also a GU-type single scattering model, deserves mention as it is probably the most

complete scattering model describing isotropic composite behavior for a material consisting of a matrix containing spherical coated micro-inclusions. Their model can approximate the effective behavior of a composite material, a suspension, or an emulsion based on the elastic, viscous, and thermal properties of the constituent phases. Though it is a very complete model, its complexity is usually superfluous as the time scales for viscoelastic and thermal processes in viscoelastic composites are very different [26]. It is for this reason that the only scattering model considered in this work is that of Baird *et al* [26].

2.3.2 Multiple scattering models

Multiple scattering models are generally employed in order to overcome two specific limitations of single scattering approaches: (*i*) the inability to provide reliable approximations of the effective behavior of composites with high scattering concentrations, and (*ii*) the inability to model effective behavior at higher frequencies [93, 97]. The first significant contribution to the multiple scattering problem was that of Foldy [98]. Foldy's work introduced a multiple scattering formalism based on a set of truncated integral equations resulting from the fields of multiple point scatterers in an isotropic host material. Lax extended this formalism to the case of anisotropic scatterers by employing a correlation function for two particles [99]. These two contributions employ a complex wavenumber and depend on the frequency, the scatterer volume fraction, and the far-field forward scattering amplitude [93]. Waterman and Truell (WT) improved these models by adding the effect of far-field back-scattering [100]. Their

approach is the basis of a large number of multiple scattering models. Models based on the WT approach include those of Bose and Mal [101], Lloyd and Berry [102], Ledbetter and Datta [30], Lu and Liaw [63], and Aggelis *et al* [93].

Another very important contribution to the multiple scattering approach was contributed by Twersky [103-105]. Twersky developed a method that takes the interaction of inclusions into account via a pair correlation function. This was done in a series of papers, most importantly for the free space [103] and two dimensional [104] cases. The same methodology has since been employed by several authors, notably Varadan *et al* [97]. These authors designate relations (II.3.2) and (II.3.3) shown below as the total displacement field for the multiple scattering case. Varadan *et al* then employ Twersky's the pair correlation function formalism to relate these fields [97].

$$\vec{u}(\mathbf{x}) = \vec{u}_{inc}(\mathbf{x}) + \sum_{i=1}^{N} \vec{u}_{s,i}(\vec{\rho}_i); \quad \vec{\rho}_i = \mathbf{x} - \mathbf{x}_i \tag{II.3.2}$$

$$\vec{u}_{s,i}(\mathbf{x}) = \vec{u}_{inc}(\mathbf{x}) + \sum_{j=i}^{N} \vec{u}_{s,j}(\vec{\rho}_j); \quad a < |\vec{\rho}_j| < 2a \tag{II.3.3}$$

In the above equations a represents the descriptive dimension of the scattering heterogeneity.

The multiple scattering models introduced above provide a very realistic picture of the physical processes taking place at the inclusion scale. One notable drawback is that they are extremely mathematically complicated even for simple cases such as an isotropic matrix containing spherical inclusions. Despite their added complexity, several of these models, [97-99, 106, 107] for example, are still only valid at *low* volume

fractions of scatterers and for spherical inclusions. Further, implementation of these models for non-spherical scatterers or anisotropic phases becomes even more complicated, if not impossible. Though methods exist to overcome these problems (see Anson and Chivers [108], Aggelis *et al* [93], or Yang [109] for example), these approaches are generally more important for applications outside the quasi-static domain represented by $ka \approx 1$ or $ka > 1$ [97] and for this reason are not considered in this work.

2.4 Materials design

Classic system and structure design require material selection for each material component. The selection depends on the foreseen physical demands: elastic, thermal, electric, *etc* [110, 111]. Unfortunately, the limiting factor in design is often material behavior of the components. A clear example of material limiting design is the microprocessor. Microprocessor performance depends on the thermal properties of the material from which it is fabricated. By assuming that the material properties cannot be changed, excellent solutions have been found to resolve the problem as a heat transfer problem. A more elegant solution, however, would be the design of a material uniquely created for the multifunctional needs of the microprocessor. This latter approach is known as *Inductive Design*, an approach studied in detail by Olsen [1, 5] and illustrated in Figure 2.11.

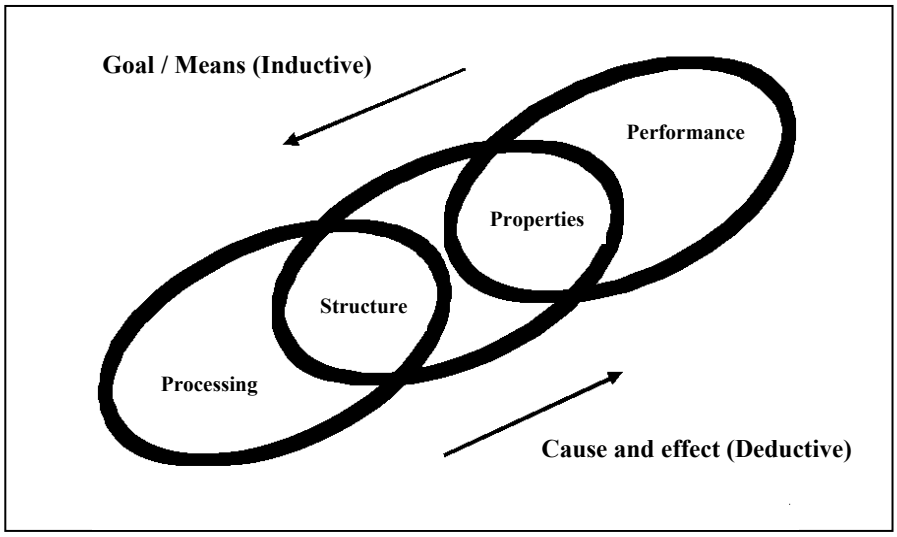

Figure 2.11: Schematic representation of the two approaches to design, adapted from Olsen [1, 5].

The concept of inductive (or top-down) design requires the ability to design materials according to the needs of a structure. In other words, inductive design represents the idea of designing for manufacture and not the classic idea of manufacture for design. The idea of material design is not entirely new (see, for example, Cohen's discussion on the reciprocity of structure and properties of a material [112] or Smith's work on hierarchical structure of materials [7]), however the scientific community still does not truly design materials [8, 113]. Material design of is therefore a very active research area. Traditional material design, however, has been somewhat inefficient due to the deductive bottom up nature of creating materials. The bottom-up methodology is not without merit. Indeed, Olsen *et al* successfully designed of high strength steels [114], and Stupp and Braun proposed designing biomaterials, ceramics, and semi-conductors using a bottom-up approaches [115].

The ever increasing depth, breadth, and precision of material modeling, however, make it feasible to employ top-down design strategies. One very interesting approach to solving material design problems in a top-down manner is the implementation of

strategies developed in the field of systems design to include material design through incorporation of existing material models [2]. Top-down methodologies are of significant interest as they favor exploration, discovery, and creation [5, 6]. One well accepted approach to material design aims to extend systems design methodologies to concurrently design materials for specific high importance components. This approach, which employs knowledge and tools from the fields of materials science, mechanical engineering, and engineering design, was pioneered by the Mechanical Properties Research Laboratory and Materials Council at Georgia Institute of Technology [2, 3, 6, 116, 117]. Such a strategy ensures the function of the structure and gives ultimate control to the designer. A particularly useful top-down design strategy is known as the Compromise Decision Support Protocol (CDSP). The technique was developed by Bras and Mistree [118] and in the context of robust design and by Mistree, Smith, and Bras for concurrent design [119]. Several strong examples of the implementation of CDSP methodology for material design exist, notably those of Seepersad *et al* on the multifunctional and multiphysics design of cellular structures [3], Karandikar *et al* [120] for the design of pressure vessel composite materials, Edwards and Deng [121] for the design of structures employing materials in combination, and for the robust design of energetic materials by Choi *et al* [117]. These references give a representative example of the range of problems that have been treated using a top-down systems design approach. The ultimate implementation of a top-down methodology requires collaboration between many different areas of research and development from economic analysis to the modeling of macroscopic behavior of materials based on micro and molecular structure [2], see Figure 2.12.

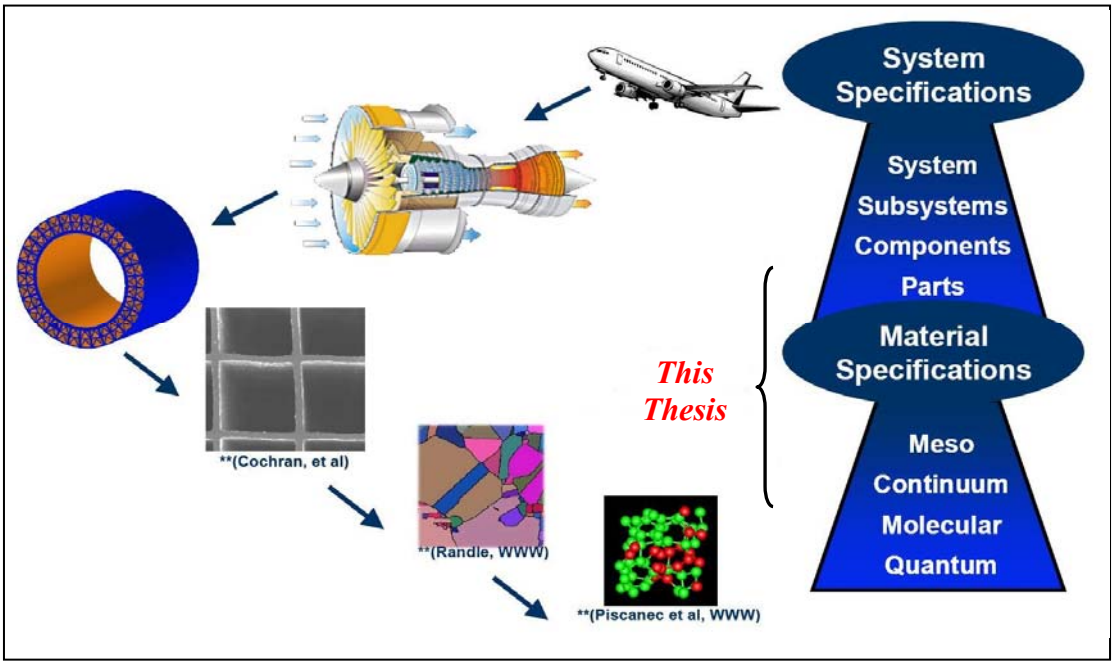

Figure 2.12: Schematic of complete system design which includes materials design. Figure from Seepersad [8], Cochran [122], Randle [123], and Piscanec [124].

2.5 Chapter summary

The previous discussion and Figure 2.12 indicate that the design of a structure requires collaboration between many different areas of research and development from economic analysis to the modeling of macroscopic behavior of materials based on micro and molecular structure. This thesis, however, does not try to put in place such an overreaching strategy. Rather it aims to implement a micromechanical model developed in this work as a tool for the design of the constituent materials of a structure where the damping of mechanical energy is a key consideration. The design results issuing from the use of micromechanical modeling as a design tool inform the design process with respect to sub-microscopic behavior. In other words, useful information and insight is

gained from the design results which is then employed to do a focused investigation of micro- and nanoscale behavior that enhances macroscopic damping. This work terminates with several micro and nanoscale material design proposals to whose successful investigation and creation will material performance in terms of passive absorption of mechanical energy and increased stiffness. These proposals are the result of the top-down material design space exploration. It is in this sense that the present work validates the exploratory nature of top-down methodologies.

CHAPTER III

MICROMECHANICAL MODELING OF VISCOELASTIC COMPOSITES CONTAINING COATED INCLUSIONS

3.1 Introduction

The previous chapter introduced the self-consistent homogenization technique and examples were given in the static (ex: Cherkaoui *et al* [23, 74]) and quasi-static (ex: Gaunaurd and Überall (GU) [89, 94] and Kuster and Toksöz (KT) [87]) domains. Both methodologies approximate macroscopic behavior by modeling physical processes at the microscopic scale and then applying averaging techniques to arrive at homogeneous material approximations of the particulate composite macroscopic behavior. The GU approach (which was employed by Kerr [90], Baird *et al* [26], and Anson and Chivers [96, 108]) is based on elastic wave propagation in heterogeneous media and is limited to the case where the wavelength of the incident wave, λ, is much larger than the inclusion's descriptive dimension, a. The same frequency dependent restriction on the wavelength also applies to the KT approach. These quasi-static scattering approaches have been shown to be applicable across a large range of length scales, from geophysics [87] to ultrasonics [26]. Further, the GU approach has the added advantage of taking inclusion resonant behavior into account, which is often important even in the quasi-static domain

[26, 89, 94]. Implementing scattering based models is, unfortunately, extremely difficult or even impossible when inclusions are non-spherical and/or constituent phases are anisotropic. This restriction greatly limits scattering model application for the wide range of existing particulate composites. The micromechanical approach, on the other hand, is not limited by the complexities presented by material anisotropy or non-spherical inclusions.

As discussed in Chapter II, the elastic-viscoelastic correspondence principle [34, 83] and strain energy arguments [42] suggest that macroscopic lossy behavior of particulate viscoelastic composites will be well approximated through micromechanical methods. It is with this rationale that the micromechanical model of Cherkaoui *et al* [23] will be extended to the quasi-static regime in an effort to approximate the macroscopic lossy behavior of particulate viscoelastic composites as a function of frequency. This chapter aims to introduce and develop the self-consistent micromechanical approach in the quasi-static domain for a composite material consisting of a homogeneous matrix containing coated ellipsoidal inclusions.

3.2 Derivation of quasi-static three phase self-consistent model

In general, micromechanical methods are based on two distinct steps: (*i*) localization, which determines the relationship between the microscopic (local) fields and the macroscopic (global) loading, and (*ii*) homogenization, which employs averaging techniques to approximate macroscopic behavior [54]. Sections 3.2.1 – 3.2.3 of this chapter show the derivation of the average strain fields in the viscoelastic inclusion and

coating materials by employing the integral equation, Green's formalism, and interfacial operators by adopting the work of Cherkaoui *et al* [23, 24] to the quasi-static domain. This is the localization step. Section 3.2.4 then applies a self-consistent scheme to find the viscoelastic particulate composite's frequency dependent effective stiffness tensors via the relationships derived in Sections 3.2.1 – 3.2.3. This is the homogenization step. Finally, the quasi-static form of the model presented by Cherkaoui *et al* will be generalized using dilute strain concentration tensors in Section 3.3.

The localization step is essentially based on the equivalent inclusion method introduced by Eshelby [58]. Eshelby's approach is modified in the present work by solving an integral equation for the displacement field at every point in an infinite homogeneous reference medium rather than by directly employing the equivalent inclusion method. The integral equation employed in this work is the result of a Green's function relating the stiffness contrast between the reference medium and a *coated* inclusion to the displacement field at each point in space [68, 71, 125]. This integral equation will be coupled with interfacial operators to modify the solution to the simpler problem of an inclusion in an infinite host medium and thereby find the solution for a coated inclusion embedded in an infinite host [72, 73].

The first requirement for the derivation of the integral equation is the definition of an elementary unit which is assumed to represent the particulate composite studied. This unit is called the representative volume element (RVE) [54]. The RVE chosen to describe the material presently studied consists of a host material containing some volume fraction, ϕ, of identically oriented coated inclusions. The problem is then solved by writing the constitutive equations for the elementary inclusion problem (EIP) of two

concentric ellipsoidal inclusions shown in Figure 3.1. The two ellipsoids represent the inclusion, *I*, and its coating, *C* [23]. In this work the coating thickness is assumed to be sufficiently thin to permit the approximation of the strain field in the coating as uniform in directions normal to the inclusion's surface. This assumption allows calculation of the average strain field in the coating via interfacial operators. These operators are applied to the strain field in the inclusion, which is assumed to be uniform in accordance with Eshelby [23, 58]. It is important to point out that the thin coating approximation simplifies the following model but limits its applicability. Fortunately, the methodology employed can be extended to the more general case of a multi-coated inclusion that does not require the thin coating approximation which is covered elsewhere, [126].

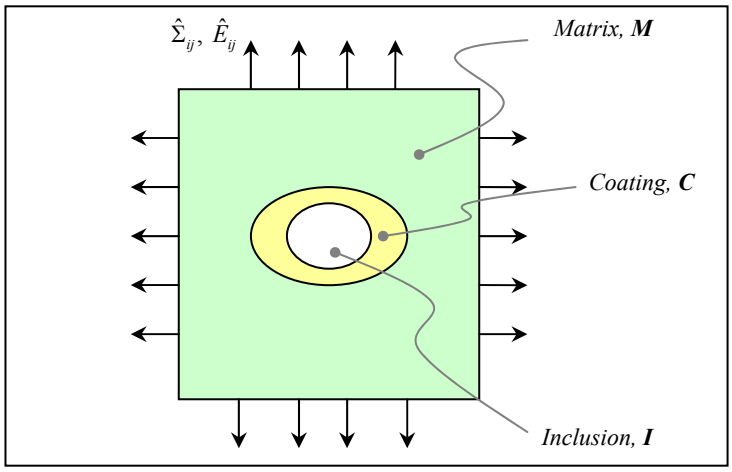

Figure 3.1: Topology of a coated inclusion embedded in a limitless matrix. Σ_{ij} and E_{ij} represent the macroscopically applied stresses and strains, respectively.

The following quasi-static self-consistent model derivation for a heterogeneous viscoelastic material closely follows Cherkaoui's derivation of the static (purely elastic) analogue [127]. The following derivation is important, however, because employs the elastic-viscoelastic correspondence principle introduced in the previous chapter and

follows the rationale of Hashin [17, 83] and Christensen [16]. The derivation will detail the physical principles captured by the model and explicitly state limitations for its application.

The topology of the present coated inclusion problem consists of an inclusion phase occupying a volume, V_I, whose frequency dependent mechanical behavior is described by the viscoelastic stiffness tensor, $\hat{\mathbf{C}}^I$. Surrounding this inclusion phase is a thin coating of another material whose viscoelastic behavior described by the tensor $\hat{\mathbf{C}}^C$ and that occupies a volume, V_C. The coated inclusion is embedded in a host material described by the viscoelastic stiffness tensor, $\hat{\mathbf{C}}^0$. The following derivation assumes that the viscoelastic stiffness tensor of *each* material is frequency dependent. The frequency dependent behavior can be approximated by material models (Kelvin-Voigt, Zener, etc) or from curve fits of experimental data (Havriliak-Negami [128], etc). For this model the exact representation of the frequency dependence it not important, it is only important to note that the model derivation does not make any restriction on the constituent material viscoelastic behavior.

At this point, several notation conventions need to be mentioned. First, tensor quantities will be denoted either with index notation or in bold, for example: $\hat{C}_{ijkl} \Leftrightarrow \hat{\mathbf{C}}$. These two representations are interchangeable and will appear throughout this thesis corresponding to the required clarity for the mathematical operations employed. The next commonly employed convention is the representation of complex frequency dependent quantities through any of the equivalent expressions shown in Eq. (III.2.1).

$$\hat{X} \Leftrightarrow \hat{X}(\omega) = X^R(\omega) - iX^I(\omega) = X^R(\omega)\left[1 - i\eta_X(\omega)\right] = \left|X(\omega)\right| e^{i\varphi(\omega)} \quad \text{(III.2.1)}$$

Where $\hat{X}(\omega)$ represents any complex variable in the frequency domain and ω is the frequency. The complex quantity consists of real, $X^R(\omega)$, and imaginary, $X^I(\omega)$, parts and has a loss factor and loss angle denoted by $\eta_X(\omega)$ and $\varphi(\omega)$ respectively. The final convention employed is the "e^{-ix}" Euler's equation: $e^{-ix} = \cos(x) - i\sin(x)$.

This derivation is further limited to the case of linear viscoelasticity and small perturbation theory. The interfaces matrix-coating and coating-inclusion interfaces are assumed to be perfect, thus ensuring continuity of traction and displacement across these boundaries [23]. One of the most limiting hypotheses for the application of this theory in the frequency domain is the small perturbation approximation [83]. This approximation assumes that inertial effects within the composite are negligible and, therefore, that the equilibrium equation (in the absence of body forces) reduces to the following:

$$\hat{\sigma}_{ij,j} - \rho \frac{\partial^2 \hat{u}_i}{\partial t^2} = 0 \quad \Rightarrow \quad \hat{\sigma}_{ij,j} = 0 \qquad \text{(III.2.2)}$$

It is this approximation that limits micromechanical methods to the quasi-static, $ka << 1$, domain and can lead to large error when inertial terms are important as those terms can lead to inclusion resonances and other important dynamic effects. Despite this limitation, the micromechanical approach provides a very accurate approximation of the frequency dependent lossy behavior of viscoelastic particulate composites when applied in the correct frequency range. This enhanced modeling freedom makes the quasi-static

micromechanical approach very interesting for application in a materials design stratagem.

3.2.1 Localization and the integral equation

Zeller and Dederichs proposed modeling the composite material shown in Figure 3.1 as a *homogeneous* material whose elastic behavior varies spatially [68]. Taking this approach, the local behavior is dictated by the constitutive laws at each point is space. Elastic-viscoelastic correspondence allows the expression of the constitutive viscoelastic material behavior at each point in space through the viscoelastic form of Hooke's law: $\hat{\sigma}_{ij}(\mathbf{r}) = \hat{C}_{ijkl}(\mathbf{r})\hat{\varepsilon}_{kl}(\mathbf{r})$. The form proposed by Zeller and Dederichs implies that local material properties can be approximated as spatially dependent variations about the properties of the reference material which are independent of position. The mathematical expression of their approach is shown in Eq. (III.2.3) for the viscoelastic stiffness tensor [71].

$$\hat{\mathbf{C}}(\mathbf{r}) = \hat{\mathbf{C}}^0 + \delta\hat{\mathbf{C}}(\mathbf{r}) \quad \text{with} \quad \mathbf{r} \in V \tag{III.2.3}$$

In the above equation $\hat{\mathbf{C}}^0$ represents the viscoelastic stiffness tensor of the reference material which is constant for all $\mathbf{r}$, $\delta\hat{\mathbf{C}}(\mathbf{r})$ denotes the spatially dependent viscoelastic stiffness tensor variation, and V represents the volume of the homogeneous medium. It is now assumed that there exists some displacement field, $\hat{u}_i^d = \hat{E}_{ij}\hat{x}_j$ imposed on the

external surface of the reference medium, *S*, where $\hat{x}_j \in S$ and $\hat{E}_{ij}$ is the macroscopically imposed strain. The localization step begins by writing the equations for the stress and strain fields at every point in the homogenous medium [127]. These relations will be derived from the local expression for equilibrium, Eq. (III.2.2), the local constitutive law, Eq. (III.2.3), and by assuming that the contrast of the viscoelastic stiffness tensors of the constituent materials can be approximated with a locally compatible strain field, $\hat{\varepsilon}_{ij}(\mathbf{r})$ [68, 71]. The local constitutive law is first substituted into the local equilibrium equation yielding:

$$\left(\hat{C}_{ijkl}(\mathbf{r})\hat{u}_{k,l}(\mathbf{r})\right)_{,j} = 0 \qquad \text{(III.2.4)}$$

where $\hat{u}_k(\mathbf{r})$ is the local compatible displacement field in the composite material at every point in *V*. For the case of small perturbations, this displacement field is related to the strain field with the classic relation: $\hat{\varepsilon}_{ij}(\mathbf{r}) = \frac{1}{2}\left[\hat{u}_{i,j}(\mathbf{r}) + \hat{u}_{j,i}(\mathbf{r})\right]$ [49]. Now, when Eq. (III.2.3) is inserted into the form of the equilibrium equation given by (III.2.4), the result is:

$$\hat{C}^0_{ijkl}\hat{u}_{k,lj}(\mathbf{r}) = \left[-\delta\hat{C}_{ijkl}(\mathbf{r})\hat{\varepsilon}_{kl}(\mathbf{r})\right]_{,j} \qquad \text{(III.2.5)}$$

The left hand side (LHS) of expression (III.2.5) can be understood to represent a distribution of fictitious volume forces [68]. It is therefore obvious that (III.2.5) can be

re-written as follows, and that the distribution of volume forces will be related to the spatial variation in the viscoelastic stiffness tensor.

$$\hat{f}_i(\mathbf{r}) = \left[\delta \hat{C}_{ijkl}(\mathbf{r}) \hat{\varepsilon}_{kl}(\mathbf{r}) \right]_{,j} \tag{III.2.6}$$

This form of the equilibrium equation makes it evident that Eq. (III.2.5) can be solved by employing Green's formalism. This is done through the second order Green's tensor, $\hat{G}^0_{km}(\mathbf{r}-\mathbf{r}')$, where the superscript *0* denotes that the resulting solution propagates the effect of the volume force distribution through the reference medium. In this case, Green's tensor calculates the displacement in the *k* direction at the point **r** due to a time varying unit force, $\hat{f}_i = \left|\hat{f}_i\right| e^{-i\omega t}$, acting in the *m* direction and located at the point $\mathbf{r}'$. This force is mathematically represented as: $\hat{f}_i = \delta_{im}\delta(\mathbf{r}-\mathbf{r}')\delta(\omega-\omega')$, where δ_{im} is the Kronecker delta, $\delta(\omega-\omega')$ is the frequency domain Dirac delta function, and $\delta(\mathbf{r}-\mathbf{r}')$ is the three dimensional Dirac delta function [71].

The second order Green's tensor $\hat{G}^0_{km}(\mathbf{r}-\mathbf{r}')$ is found by solving the differential equation below:

$$\hat{C}^0_{ijkl}\hat{G}^0_{km,lj}(\mathbf{r}-\mathbf{r}') + \delta_{im}\delta(\mathbf{r}-\mathbf{r}')\delta(\omega-\omega') = 0 \tag{III.2.7}$$

for the boundary conditions on the external surface, *S*, of the homogeneous medium [71]. Now, by modifying the work of Berveiller *et al* [71] to take the time variation of the body

force distribution into account, it can be shown that the solution to Eq. (III.2.5) is given by the two integral equivalent equations below.

$$\hat{u}_m(\mathbf{r}) = \hat{u}_m^0(\mathbf{r}) + \int_{-\infty}^{\infty}\int_V \hat{G}_{im}^0(\mathbf{r}-\mathbf{r}')\hat{f}_i(\mathbf{r}')d\mathbf{r}'d\omega' \tag{III.2.8}$$

$$\hat{u}_m(\mathbf{r}) = \hat{u}_m^0(\mathbf{r}) + \int_{-\infty}^{\infty}\int_V \hat{G}_{im}^0(\mathbf{r}-\mathbf{r}')\left[\delta\hat{C}_{ijkl}(\mathbf{r}')\hat{\varepsilon}_{kl}(\mathbf{r}')\right]_{,j'} d\mathbf{r}'d\omega' \tag{III.2.9}$$

Integrating (III.2.9) by parts, the displacement field becomes:

$$\hat{u}_m(\mathbf{r}) = \hat{u}_m^0(\mathbf{r}) - \int_{-\infty}^{\infty}\int_V \hat{G}_{im,j'}^0(\mathbf{r}-\mathbf{r}')\left[\delta\hat{C}_{ijkl}(\mathbf{r}')\hat{\varepsilon}_{kl}(\mathbf{r}')\right]d\mathbf{r}'d\omega' \tag{III.2.10}$$

Now it is important to recall the following properties of the Green's tensor.

$$\hat{G}_{im,j'}^0 = \frac{\partial\hat{G}_{im}^0(\mathbf{r}-\mathbf{r}')}{\partial x_j'} = -\frac{\partial\hat{G}_{im}^0(\mathbf{r}-\mathbf{r}')}{\partial x_j} = -\hat{G}_{im,j}^0 \tag{III.2.11}$$

And lastly, the small perturbation approximation of strain and the integral property of the Dirac delta function, $g(\omega) = \int_{-\infty}^{\infty} g(\omega')\delta(\omega-\omega')d\omega'$, can be employed to yield the simplified equation for the strain field at any point in the medium shown below [68, 125]:

$$\hat{\varepsilon}_{ij}(\mathbf{r}) = \hat{E}_{ij} - \int_V \hat{\Gamma}^0_{ijkl}(\mathbf{r}-\mathbf{r}')\,\delta\hat{C}_{klmn}(\mathbf{r}')\,\hat{\varepsilon}_{mn}(\mathbf{r}')\,d\mathbf{r}' \qquad \text{(III.2.12)}$$

In the above expression, $\hat{E}_{ij}$ represents the uniform strain field of the medium (macroscopic strain field that has no spatial dependence), and $\hat{\Gamma}^0_{ijkl}(\mathbf{r}-\mathbf{r}')$ is known as the modified Green's tensor. The modified Green's tensor is related to the second order Green's tensor given above by Eq. (III.2.13) below.

$$\hat{\Gamma}^0_{ijkl} = -\frac{1}{2}\left[\hat{G}^0_{ki,jl}(\mathbf{r}-\mathbf{r}') + \hat{G}^0_{kj,il}(\mathbf{r}-\mathbf{r}')\right] \qquad \text{(III.2.13)}$$

Relation (III.2.12) specifically shows that the strain field at the macroscopic length scale can be approximated by averaging the effects of material variations within the volume, *V*. This reinforces Christensen's statement that multi-scale modeling requires that the effects of discontinuities at the lower length scale only have an average effect on the macroscopic behavior [33].

It is now useful to define the spatial variation of the viscoelastic constants. For the topology shown in Figure 3.1, this variation can be mathematically expressed using the Heaviside step function $\theta(\mathbf{r})$ [129].

$$\delta\hat{\mathbf{C}}(\mathbf{r}) = \left(\hat{\mathbf{C}}^I - \hat{\mathbf{C}}^0\right)\theta^I(\mathbf{r}) + \left(\hat{\mathbf{C}}^C - \hat{\mathbf{C}}^0\right)\left[\theta^2(\mathbf{r}) - \theta^I(\mathbf{r})\right] \qquad \text{(III.2.14)}$$

Where the Heaviside step functions of the inclusion, $\theta^I(\mathbf{r})$, and composite inclusion, $\theta^2(\mathbf{r})$, (inclusion + coating) are defined as:

$$\begin{aligned}\theta^I(\mathbf{r}) &= \begin{cases}1 & \text{if } \mathbf{r} \in V_I \\ 0 & \text{if } \mathbf{r} \notin V_I\end{cases} \\ \theta^2(\mathbf{r}) &= \begin{cases}1 & \text{if } \mathbf{r} \in V_2 \\ 0 & \text{if } \mathbf{r} \notin V_2\end{cases}\end{aligned} \tag{III.2.15}$$

and V_2 designates the volume of the composite inclusion. Equation (III.2.14) can then be expressed in a more compact form by introducing viscoelastic stiffness contrast tensors and the variation of the Heaviside step function, $\delta\theta^I(\mathbf{r})$ [24, 74].

$$\delta\hat{\mathbf{C}}(\mathbf{r}) = \Delta\hat{\mathbf{C}}^{I0}\theta^I(\mathbf{r}) + \Delta\hat{\mathbf{C}}^{C0}\delta\theta^I(\mathbf{r}) \tag{III.2.16}$$

In the relation above, $\Delta\hat{C}^{XY}$ represents the difference (contrast) between the viscoelastic rigidity tensor of materials X and Y. The variation $\delta\theta^I(\mathbf{r})$ is defined by the first expression in Eq. (III.2.17). The second relationship will only hold true for the case of a thin inclusion coating.

$$\begin{aligned}\delta\theta^I(\mathbf{r}) &= \theta(x_i, a_i + \Delta a_i) - \theta^I(x_i, a_i) \\ &\approx \sum_i \frac{\partial\theta^I}{\partial a_i}\Delta a_i\end{aligned} \tag{III.2.17}$$

Cherkaoui *et al* [24], have further shown that for the thin coating case, $\delta\theta^I(\mathbf{r})$ can be approximated by Eq. (III.2.18).

$$\delta\theta^I(\mathbf{r}) \approx p\sum_i \frac{\Delta a_i}{a_i}\frac{x_i^2}{a_i^2}\delta(S_I) \tag{III.2.18}$$

In the above expression, x_i are the coordinates of a point on the surface of the inclusion, a_i is the radius of the ellipsoidal inclusion and Δa_i is the thickness of the inclusion coating in the direction x_i, $\delta(S_I)$ is the Dirac delta distribution for the surface of the inclusion, S_I, and p is the perpendicular distance from the center of the inclusion center to the tangent plane of the surface at the point x_i. The distance p can be calculated for any point on the surface S_I using Eq. (III.2.19).

$$p^{-1} = \sqrt{\frac{x_1^2}{a_1^4} + \frac{x_2^2}{a_2^4} + \frac{x_3^2}{a_3^4}} \tag{III.2.19}$$

Now, Eqns. (III.2.18) and (III.2.16) can be inserted into Eq. (III.2.12) to yield an expression for the strain field in the homogenous medium for the coated inclusion topology. Further, one part of the resulting volume integral can be simplified by employing the property of the Dirac delta distribution that: $\int_V g(\mathbf{r})\delta(S)d\mathbf{r} = \int_S g(\mathbf{r})dS$. The resulting equation is given below.

$$\hat{\varepsilon}_{ij}(\mathbf{r}) = \hat{E}_{ij} - \int_{V_I} \hat{\Gamma}^0_{ijkl}(\mathbf{r}-\mathbf{r}')\Delta\hat{C}^{I0}_{klmn}\hat{\varepsilon}_{mn}(\mathbf{r}')d\mathbf{r}' - \sum_{\alpha}\int_{S_I^+} \hat{\Gamma}^0_{ijkl}(\mathbf{r}-\mathbf{r}^+)\Delta\hat{C}^{C0}_{klmn}\hat{\varepsilon}_{mn}(\mathbf{r}^+)\, p\frac{\Delta a_\alpha}{a_\alpha}\frac{x_\alpha^2}{a_\alpha^2}dS \qquad \text{(III.2.20)}$$

Here, S_I^+ is the external surface of the inclusion, $\mathbf{r}^+$ is a point on the coating side of the inclusion – coating interface, and the components of $\varepsilon_{mn}(\mathbf{r}^+)$ describe the strain field inside the coating at a point very close to the inclusion – coating interface. Equation (III.2.20) is quite complicated a presents would be difficult to resolve. Fortunately, it is possible to find a relationship between the field $\varepsilon_{mn}(\mathbf{r}^+)$ and the strain field in the inclusion (which, following the results of Eshelby [58], is assumed to be uniform). This can be done by employing interfacial operators [127], which is the subject of the following section.

3.2.2 Interfacial operators

In general, the stress and strain fields in the coating material can be very complicated. This problem is exacerbated by the material discontinuity that exists at the coating – inclusion and coating – reference material interfaces. This material discontinuity leads to jumps in the stress and strain fields across material interfaces. In order to approximate the stress and strain state in the coating material, this section first makes *simplifying hypothesis that the stress and strain fields are uniform along the thickness of the coating*. This is a reasonable approximation for a *thin* coating, but care

must be taken when the ratio $\Delta a_i / a_i << 1$ no longer holds true. Then, interfacial operators studied by Walpole [73] and Hill [72] will be employed to relate these fields in the inclusion to those in the coating material.

Interfacial operators are a very convenient mathematical tool that efficiently calculates the stress or strain jump across a material interface (an interface separating two dissimilar materials). These operators are derived by writing the equations for the continuity of displacement and traction across the material interface. This derivation begins with the general case of two solid phases, *A* and *B*, with viscoelastic constants $\hat{\mathbf{C}}^A$ and $\hat{\mathbf{C}}^B$ separated by a surface with unit normal, $\vec{n}$ (see Figure 3.2).

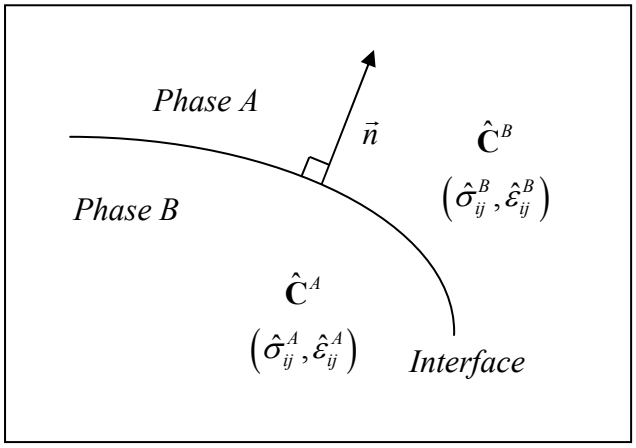

Figure 3.2 : Schematic of the interface of two viscoelastic solids used in the derivation of interfacial operators.

The interfacial operator derived below assumes that the bond between materials *A* and *B* is perfect. This leads to two requirements about the mechanical behavior across the material interface: (*i*) continuity of displacement, $\vec{u}$, and (*ii*) continuity of traction, $\sigma_{ij} n_j$. These two mechanical behaviors are mathematically represented with Eqns. (III.2.21) and (III.2.22), respectively [127].

$$\left[\hat{u}_i\right] \equiv \hat{u}_i^A - \hat{u}_i^B = \vec{0} \tag{III.2.21}$$

$$\left[\hat{\sigma}_{ij}\right] n_j \equiv \left(\hat{\sigma}_{ij}^A - \hat{\sigma}_{ij}^B\right) n_j = \vec{0} \tag{III.2.22}$$

where n_j represents the components of the unit normal vector of the surface, here assumed to be in the form of an ellipsoid. The values of the normal vector are determined from relation (III.2.23).

$$n_i = \frac{x_i}{a_i^2} p \tag{III.2.23}$$

Now, using the continuity of displacement requirement given in expression (III.2.21), it is possible to calculate the jump in the gradient of the displacement at each point $\mathbf{r}(x_i)$ on the interface. Noting $d\vec{u}_i = u_{i,j} dx_j$, Eq. (III.2.21) leads to:

$$\left[\hat{u}_{i,j}\right] dx_j = \left(\hat{u}_{i,j}^A - \hat{u}_{i,j}^B\right) dx_j = 0 \tag{III.2.24}$$

Then, given that the direction tangent to the surface is described by dx_j and that $n_j dx_j = 0$ by definition, (III.2.24) is equivalent to the following expression [24]:

$$\left[\hat{u}_{i,j}\right] \equiv \hat{u}_{i,j}^A - \hat{u}_{i,j}^B = \hat{\lambda}_i n_j \tag{III.2.25}$$

In the above expression, $\hat{\lambda}_i$ represents the jump across the interface in the complex magnitude of the gradient of the displacement field. Noting that the gradient field is symmetric with respect to indices *i* and *j*, Eq. (III.2.25) can be altered to find the strain jump across the material interface, $\left[\hat{\varepsilon}_{ij}\right]$.

$$\left[\hat{\varepsilon}_{ij}\right] = \hat{\varepsilon}_{ij}^{A} - \hat{\varepsilon}_{ij}^{B} = \frac{1}{2}\left(\hat{\lambda}_i n_j + \hat{\lambda}_j n_i\right) \tag{III.2.26}$$

Now, the continuity of traction requirement can be changed by inserting the constitutive laws of each material.

$$\hat{\sigma}_{ij}^{A} n_j = \hat{\sigma}_{ij}^{B} n_j \quad \Rightarrow \quad \hat{C}_{ijkl}^{A} \hat{\varepsilon}_{kl}^{A} n_j = \hat{C}_{ijkl}^{B} \hat{\varepsilon}_{kl}^{B} n_j \tag{III.2.27}$$

Using this form of the continuity of traction expression, it is possible to eliminate one of the strain fields in Eq. (III.2.26). For example, if phase *B* is assumed to be the reference material, $\hat{\varepsilon}_{ij}^{A}$ can be eliminated leaving:

$$\begin{gathered} \hat{C}_{ijkl}^{B} \hat{\varepsilon}_{kl}^{B} n_j = \hat{C}_{ijkl}^{A}\left(\varepsilon_{kl}^{B} + \hat{\lambda}_k n_l\right) n_j \\ \Downarrow \\ \left(\hat{C}_{ijkl}^{B} - \hat{C}_{ijkl}^{A}\right) \hat{\varepsilon}_{kl}^{B} n_j = \hat{C}_{ijkl}^{A} n_l n_j \hat{\lambda}_k \end{gathered} \tag{III.2.28}$$

Noting that the right-hand side (RHS) of the bottom equation in (III.2.28) is simply Christoffel's matrix for material A, $\hat{K}_{ik}^{A}$, times the complex magnitude of the strain jump across the interface, $\hat{\lambda}_k$. Christoffel's matrix is $\hat{K}_{ik}^{A} = \hat{C}_{ijkl}^{A} n_l n_j$. From this expression, the magnitude of the strain jump can be calculated simply from knowledge of the viscoelastic stiffness tensors of each material, the outward unit normal of the surface, and the strain field in the reference material.

$$\hat{\lambda}_i = \left(\hat{K}_{ik}^{A}\right)^{-1} n_l \left(\hat{C}_{klmn}^{B} - \hat{C}_{klmn}^{A}\right) \hat{\varepsilon}_{mn}^{B} \tag{III.2.29}$$

Using the above expression, the strain jump becomes:

$$\hat{\varepsilon}_{ij}^{A} - \hat{\varepsilon}_{ij}^{B} = \hat{\bar{P}}_{ijkl}^{A} \left(\hat{C}_{klmn}^{B} - \hat{C}_{klmn}^{A}\right) \hat{\varepsilon}_{ij}^{B} \tag{III.2.30}$$

where the interfacial operator, $\hat{\bar{P}}_{ijkl}^{A}$, follows directly from the substitution of Eq. (III.2.29) into (III.2.26). The interfacial operator, dependent only on the constituent material properties and the unit normal of the interface, is defined below in Eq. (III.2.31) [74].

$$\begin{gathered} \hat{\bar{P}}_{ijkl}^{A} \equiv \frac{1}{2}\left[\left(\hat{K}_{ik}^{A}\right)^{-1} n_j n_l + \left(\hat{K}_{jk}^{A}\right)^{-1} n_i n_l\right] \\ \Downarrow \\ \hat{P}_{ijkl}^{A} \equiv \frac{1}{4}\left[\left(\hat{K}_{ik}^{A}\right)^{-1} n_j n_l + \left(\hat{K}_{jk}^{A}\right)^{-1} n_i n_l + \left(\hat{K}_{il}^{A}\right)^{-1} n_j n_k + \left(\hat{K}_{jl}^{A}\right)^{-1} n_i n_k\right] \end{gathered} \tag{III.2.31}$$

This leads to the following general expressions that relate the strain field in phase *A* to that in phase *B*.

$$\hat{\varepsilon}_{ij}^{A} = \left[\hat{P}_{ijkl}^{A} \left(\hat{C}_{klmn}^{B} - \hat{C}_{klmn}^{A} \right) + I_{ijmn} \right] \hat{\varepsilon}_{mn}^{B}$$
$$\hat{\varepsilon}_{ij}^{B} = \left[\hat{P}_{ijkl}^{B} \left(\hat{C}_{klmn}^{A} - \hat{C}_{klmn}^{B} \right) + I_{ijmn} \right] \hat{\varepsilon}_{mn}^{A} \qquad \text{(III.2.32)}$$

where the fourth order identity tensor, I_{ijkl}, is defined as $I_{ijkl} = \frac{1}{2}\left(\delta_{ik}\delta_{jl} + \delta_{il}\delta_{jk} \right)$ and δ_{ij} is the Kronecker delta. Interfacial operators have several important mathematical properties which have been detailed by Hill [72]. For the purposes of this work, however, they will simply be used to calculate the discontinuities of the stress and strain fields across a material interface.

3.2.2.1 Application to local strain fields

The interfacial operators developed above can be used to simplify Eq. (III.2.20) which describes the local strain field in the homogeneous medium. This simplification occurs when the strain field in the coating is related to the strain field in the inclusion by applying interfacial operators. These operators permit the calculation of the strain field at the inclusion-coating interface on the coating side, $\hat{\varepsilon}_{ij}\left(\mathbf{r}^{+} \right)$, from the strain field the same interface on the inclusion side, $\hat{\varepsilon}_{ij}\left(\mathbf{r}^{-} \right)$. This strain jump calculation does not require any simplifying assumptions about the strain fields in either medium. This is done by adding

the strain jump across the interface to the strain field on the inclusion side of the interface. The strain jump is simply calculated through the interfacial operators given in Eq. (III.2.32).

$$\hat{\varepsilon}_{ij}\left(\mathbf{r}^{+}\right)=\hat{\varepsilon}_{ij}\left(\mathbf{r}^{-}\right)+\hat{P}^{C}_{ijkl}\Delta\hat{C}^{IC}_{lkmn}\hat{\varepsilon}_{mn}\left(\mathbf{r}^{-}\right) \tag{III.2.33}$$

where $\Delta\hat{\mathbf{C}}^{IC}$ is a tensor representing the contrast in the viscoelastic stiffness of the inclusion, *I*, and coating, *C*. This value is generalized for any two materials in Eq. (III.2.34) below.

$$\Delta\hat{\mathbf{C}}^{XY}=\hat{\mathbf{C}}^{X}-\hat{\mathbf{C}}^{Y} \tag{III.2.34}$$

Next Eshelby's assumption that the strain field in the inclusion, being on the smallest length scale, can be accurately approximated by a uniform strain field whose values are the volumetric average will be used [58]. Mathematically, this is represented as:

$$\hat{\varepsilon}^{I}_{ij}\equiv\frac{1}{V_I}\int_{V_I}\hat{\varepsilon}_{ij}\left(\mathbf{r}\right)d\mathbf{r}\quad\mathbf{r}\in V_I\;\Rightarrow\;\hat{\varepsilon}^{I}_{ij}\equiv\hat{\varepsilon}\left(\mathbf{r}^{-}\right) \tag{III.2.35}$$

Therefore, Eq. (III.2.33) simplifies to the following:

$$\hat{\varepsilon}_{ij}\left(\mathbf{r}^{+}\right)=\hat{\varepsilon}^{I}_{ij}+\hat{P}^{C}_{ijkl}\Delta\hat{C}^{IC}_{lkmn}\hat{\varepsilon}^{I}_{ij} \tag{III.2.36}$$

Finally, the expression above for $\hat{\varepsilon}_{ij}\left(\mathbf{r}^{+}\right)$ into the integral equation, the resulting local strain field in the heterogeneous medium becomes [24]:

$$\begin{aligned}\hat{\varepsilon}_{ij}\left(\mathbf{r}\right) = \hat{E}_{ij} &- \int_{V_I} \hat{\Gamma}^{0}_{ijkl}\left(\mathbf{r}-\mathbf{r}'\right)\Delta\hat{C}^{I0}_{klmn}\hat{\varepsilon}^{I}_{mn}d\mathbf{r}' \\ &- \sum_{\alpha}\int_{S_I^{+}} \hat{\Gamma}^{0}_{ijkl}\left(\mathbf{r}-\mathbf{r}^{+}\right)\Delta\hat{C}^{C0}_{klmn}\hat{\varepsilon}^{I}_{mn}p\frac{\Delta a_\alpha}{a_\alpha}\frac{x_\alpha^2}{a_\alpha^2}dS \\ &- \sum_{\alpha}\int_{S_I^{+}} \hat{\Gamma}^{0}_{ijkl}\left(\mathbf{r}-\mathbf{r}^{+}\right)\Delta\hat{C}^{C0}_{klmn}\hat{P}^{C}_{mnpq}\Delta C^{IC}_{pqrs}\hat{\varepsilon}^{I}_{rs}p\frac{\Delta a_\alpha}{a_\alpha}\frac{x_\alpha^2}{a_\alpha^2}dS\end{aligned} \qquad \text{(III.2.37)}$$

It is important to point out that the above integral equation only depends on the average strain field in the inclusion, the viscoelastic stiffness of the constituent materials, and the geometry of the coated inclusion. When carrying out the homogenization step, only the average strain field in each phase will be required. Given that the stiffness tensor, $\hat{\mathbf{C}}\left(\mathbf{r}\right)$, is piece-wise uniform, it will be possible to calculate the macroscopic average from Eq. (III.2.37). Then, after finding the expression for the average macroscopic strain of the medium, the strain localization tensor for the average strain in the coated inclusion will also be found [24].

3.2.3 Localization: Average strain fields in the inclusion and coating

The derivation of the integral equation in Sections 3.2.1 and 3.2.2, which used techniques introduced by Zeller and Dederichs [68], Hill [72], and Walpole [73], underlines the most basic requirements for multiscale modeling given by Christensen

[33]. The requirement is that inhomogeneities at the smallest length scale only have an average effect on the behavior observed at the macroscopic scale. Following this logic, the representation of the integral equation given in (III.2.37) for the local strain field (spatially varying strain at the smallest scale) will be used to approximate the effective behavior of the heterogeneous medium at the macroscopic scale by calculating the volumetric average of $\hat{\varepsilon}_{ij}(\mathbf{r})$.

First, the average complex strains in the inclusion and coating, $\hat{\varepsilon}_{ij}^{I}$ and $\hat{\varepsilon}_{ij}^{C}$ respectively, are defined below:

$$\begin{aligned}\hat{\varepsilon}_{ij}^{I} &= \frac{1}{V_I}\int_{V_I}\hat{\varepsilon}_{ij}(\mathbf{r})d\mathbf{r} \\ \hat{\varepsilon}_{ij}^{C} &= \frac{1}{V_C}\int_{V_C}\hat{\varepsilon}_{ij}(\mathbf{r})d\mathbf{r}\end{aligned} \tag{III.2.38}$$

By taking a volume average with respect to the inclusion, Eq. (III.2.37) becomes [24] :

$$\begin{aligned}\hat{\varepsilon}_{ij}^{I} = \hat{E}_{ij} &- \frac{1}{V_I}\int_{V_I}\int_{V_I}\hat{\Gamma}_{ijkl}^{0}(\mathbf{r}-\mathbf{r}')\Delta\hat{C}_{klmn}^{I0}\hat{\varepsilon}_{mn}^{I}d\mathbf{r}'d\mathbf{r} \\ &- \frac{1}{V_I}\sum_{\alpha}\int_{S_I^+}\left\{\int_{V_I}\hat{\Gamma}_{ijkl}^{0}(\mathbf{r}-\mathbf{r}^{+})d\mathbf{r}\right\}\Delta\hat{C}_{klmn}^{C0}\hat{\varepsilon}_{mn}^{I}p\frac{\Delta a_\alpha}{a_\alpha}\frac{x_\alpha^2}{a_\alpha^2}dS \\ &- \frac{1}{V_I}\sum_{\alpha}\int_{S_I^+}\left\{\int_{V_I}\hat{\Gamma}_{ijkl}^{0}(\mathbf{r}-\mathbf{r}^{+})d\mathbf{r}\right\}\Delta\hat{C}_{klmn}^{C0}\hat{P}_{mnpq}^{C}\Delta C_{pqrs}^{IC}\hat{\varepsilon}_{rs}^{I}p\frac{\Delta a_\alpha}{a_\alpha}\frac{x_\alpha^2}{a_\alpha^2}dS\end{aligned} \tag{III.2.39}$$

Now it is necessary to employ the simplifying assumption that the strain field in the coating is uniform along its thickness. Then by noting that $\hat{\varepsilon}_{ij}^{C}$ is equal to $\hat{\varepsilon}_{ij}(\mathbf{r}^{+})$, the

average strain field can calculated from Eq. (III.2.36). It is noted here that for the specific case of a thinly coated inclusion, the strain field in the coating only depends on the inclusion normal, the average strain in the inclusion, and the constituent material properties of the inclusion and coating as shown below.

$$\hat{\varepsilon}_{ij}^{C} = \hat{\varepsilon}_{ij}^{I} + \frac{1}{V_C}\left\{\int_{V_C} \hat{P}_{ijkl}^{C} d\mathbf{r}\right\} \Delta \hat{C}_{klmn}^{IC} \hat{\varepsilon}_{mn}^{I} \tag{III.2.40}$$

At this point, it is useful to define the following tensor denoting the volume average of the modified Green's tensor.

$$\hat{T}_{ijkl}^{I}\left(\hat{\mathbf{C}}^{0}\right) = \int_{V_I} \hat{\Gamma}_{ijkl}^{0}\left(\mathbf{r}-\mathbf{r}'\right) d\mathbf{r}' \quad \text{if } \mathbf{r} \in V_I \tag{III.2.41}$$

This tensor is related to Eshelby's tensor, **S**, as shown below [58, 71]:

$$\hat{\mathbf{S}} = \hat{\mathbf{T}}^{I}\left(\mathbf{C}^{0}\right) : \hat{\mathbf{C}}^{0} \tag{III.2.42}$$

Using interfacial operators, $\int_{V_I} \hat{\Gamma}_{ijkl}^{0}\left(\mathbf{r}^{+}-\mathbf{r}\right) d\mathbf{r}$ can be related to the relationship given in (III.2.41) as shown [24]:

$$\int_{V_I} \hat{\Gamma}_{ijkl}^{0}\left(\mathbf{r}^{+}-\mathbf{r}\right) d\mathbf{r} = \hat{T}_{ijkl}^{I}\left(\hat{\mathbf{C}}^{0}\right) - \hat{P}_{ijkl}^{0} \tag{III.2.43}$$

Equation (III.2.43) can be inserted into the expression for the average strain field in the inclusion, (III.2.39), in order to eliminate the volume integral inside the summation and the surface integral. Unfortunately, the expression is still complicated by the terms containing the projection, p, and interfacial operators, $\hat{\mathbf{P}}^*$. At this point expression (III.2.39) can be greatly simplified by through further application of the thin coating assumption and Eq. (III.2.43). This analysis will yield an expression for the average strain field based only on the viscoelastic material properties and the geometry of the coated inclusions.

First, the volume of the coating can be related to an integral on the entire representative volume, V, using the Heaviside functions given in Eq. (III.2.15).

$$V_C = \int_{V_C} d\mathbf{r} = \int_V \left[\theta^2(\mathbf{r}) - \theta^I(\mathbf{r}) \right] d\mathbf{r} \tag{III.2.44}$$

For the thin coating case, the variation of the Heaviside function, $\delta\theta^I(\mathbf{r})$, defined with relation (III.2.18) can be used to find the coating volume:

$$V_C \approx \int_V \sum_i p \frac{\Delta a_i}{a_i} \frac{x_i^2}{a_i^2} \delta(S_I) d\mathbf{r} = \sum_i \int_{S_I} p \frac{\Delta a_i}{a_i} \frac{x_i^2}{a_i^2} dS \tag{III.2.45}$$

The far RHS of the expression above partially simplifies the expression of the average strain in the inclusion. However, the expression is still complicated by the surface integral of the interfacial operators. This problem will be addressed in the following

analysis. First, Eq. (III.2.41) will be integrated with respect to the coating volume, V_C [24].

$$\int_{V_C} \hat{P}^*_{ijkl} d\mathbf{r} = V_C \hat{T}^I_{ijkl}\left(\hat{\mathbf{C}}^*\right) - \int_{V_C}\int_{V_I} \hat{\Gamma}^*_{ijkl}\left(\mathbf{r}^+ - \mathbf{r}\right) d\mathbf{r}^+ d\mathbf{r} \tag{III.2.46}$$

Since $V_C = V_2 - V_I$, the term on the right above can be decomposed as follows:

$$\int_{V_C}\int_{V_I} \hat{\Gamma}^*_{ijkl}\left(\mathbf{r}^+ - \mathbf{r}\right) d\mathbf{r}^+ d\mathbf{r} = \int_{V_2}\int_{V_I} \hat{\Gamma}^*_{ijkl}\left(\mathbf{r}^+ - \mathbf{r}\right) d\mathbf{r}^+ d\mathbf{r} - \int_{V_I}\int_{V_I} \hat{\Gamma}^*_{ijkl}\left(\mathbf{r} - \mathbf{r}'\right) d\mathbf{r} d\mathbf{r}' \tag{III.2.47}$$

And (III.2.41) can be generalized [23]:

$$\begin{aligned} \hat{T}^2_{ijkl}\left(\hat{\mathbf{C}}^*\right) &= \int_{V_2} \hat{\Gamma}^*_{ijkl}\left(\mathbf{r} - \mathbf{r}'\right) d\mathbf{r}' \quad \text{if } \mathbf{r} \in V_2 \\ \hat{T}^I_{ijkl}\left(\hat{\mathbf{C}}^*\right) &= \int_{V_I} \hat{\Gamma}^*_{ijkl}\left(\mathbf{r} - \mathbf{r}'\right) d\mathbf{r}' \quad \text{if } \mathbf{r} \in V_I \end{aligned} \tag{III.2.48}$$

Next, Eq. (III.2.48) can be shown to simplify the two terms on the RHS of (III.2.47) as shown below:

$$\begin{aligned} V_I \hat{T}^2_{ijkl}\left(\hat{\mathbf{C}}^*\right) &= \int_{V_2}\int_{V_I} \hat{\Gamma}^*_{ijkl}\left(\mathbf{r} - \mathbf{r}'\right) d\mathbf{r}^+ d\mathbf{r} \\ V_I \hat{T}^I_{ijkl}\left(\hat{\mathbf{C}}^*\right) &= \int_{V_I}\int_{V_I} \hat{\Gamma}^*_{ijkl}\left(\mathbf{r} - \mathbf{r}'\right) d\mathbf{r}' d\mathbf{r} \end{aligned} \tag{III.2.49}$$

Using these relations, Eq. (III.2.47) becomes [24]:

$$\int_{V_C}\int_{V_I} \hat{\Gamma}^{*}_{ijkl}\left(\mathbf{r}^{+}-\mathbf{r}\right)d\mathbf{r}^{+}d\mathbf{r} = V_I\left(\hat{T}^{2}_{ijkl}\left(\hat{\mathbf{C}}^{*}\right)-\hat{T}^{I}_{ijkl}\left(\hat{\mathbf{C}}^{*}\right)\right) \tag{III.2.50}$$

Next, the volume integral of the interfacial operators in the coating can be found by inserting (III.2.50) into Eq. (III.2.46).

$$\int_{V_C} \hat{P}^{*}_{ijkl}d\mathbf{r} = V_C\hat{T}^{I}_{ijkl}\left(\hat{\mathbf{C}}^{*}\right)-V_I\left(\hat{T}^{2}_{ijkl}\left(\hat{\mathbf{C}}^{*}\right)-\hat{T}^{I}_{ijkl}\left(\hat{\mathbf{C}}^{*}\right)\right) \tag{III.2.51}$$

The volume integral of the interfacial operator $\hat{\mathbf{P}}^{*}$ on V_C can be extended to an integral on the representative volume, V, and to relate Eq. (III.2.18) to the result as follows:

$$\begin{aligned}\int_{V_C} \hat{P}^{*}_{ijkl}d\mathbf{r} &= \int_{V} \hat{P}^{*}_{ijkl}\delta\theta^{I}\left(\mathbf{r}\right)d\mathbf{r} = \sum_{\alpha}\int_{S_I} \hat{P}^{*}_{ijkl}p\frac{\Delta a_\alpha}{a_\alpha}\frac{x_\alpha^2}{a_\alpha^2}dS \\ &= V_C\hat{T}^{I}_{ijkl}\left(\hat{\mathbf{C}}^{*}\right)-V_I\left[\hat{T}^{2}_{ijkl}\left(\hat{\mathbf{C}}^{*}\right)-\hat{T}^{I}_{ijkl}\left(\hat{\mathbf{C}}^{*}\right)\right]\end{aligned} \tag{III.2.52}$$

Using all of the above expressions, it is finally possible to express the average strain fields as a function of tensors $\hat{\mathbf{T}}^{I}\left(\hat{\mathbf{C}}^{*}\right)$ and $\hat{\mathbf{T}}^{2}\left(\hat{\mathbf{C}}^{*}\right)$, the geometry of the coated inclusion, and the viscoelastic stiffness tensors of the constituent materials. This is done by substituting Eqns. (III.2.45) and (III.2.52) in integral Eqns. (III.2.39) and (III.2.40) yielding expressions for the average strain field in the inclusion and coating, respectively.

$$\begin{aligned}\hat{\varepsilon}_{ij}^{I} = \hat{E}_{ij} &- \hat{T}_{ijkl}^{2}\left(\hat{\mathbf{C}}^{0}\right)\Delta\hat{C}_{klmn}^{I0}\hat{\varepsilon}_{mn}^{I} \\ &- \frac{V_C}{V_I}\hat{T}_{ijkl}^{I}\left(\hat{\mathbf{C}}^{0}\right)\Delta\hat{C}_{klmn}^{C0}\hat{T}_{mnpq}^{I}\left(\hat{\mathbf{C}}^{C}\right)\Delta\hat{C}_{pqrs}^{IC}\hat{\varepsilon}_{rs}^{I} \\ &- \frac{V_C}{V_I}\left[\hat{T}_{ijkl}^{I}\left(\hat{\mathbf{C}}^{C}\right) - \hat{T}_{ijkl}^{I}\left(\hat{\mathbf{C}}^{0}\right)\right]\Delta\hat{C}_{klmn}^{IC}\hat{\varepsilon}_{mn}^{I} \\ &+ \left[I_{ijmn} + \hat{T}_{ijkl}^{I}\left(\hat{\mathbf{C}}^{0}\right)\Delta\hat{C}_{klmn}^{C0}\right]\left[\hat{T}_{mnpq}^{2}\left(\hat{\mathbf{C}}^{C}\right) - \hat{T}_{mnpq}^{I}\left(\hat{\mathbf{C}}^{C}\right)\right]\Delta\hat{C}_{pqrs}^{IC}\hat{\varepsilon}_{rs}^{I}\end{aligned} \tag{III.2.53}$$

$$\hat{\varepsilon}_{ij}^{C} = \hat{\varepsilon}_{ij}^{I} + \left[\hat{T}_{ijkl}^{I}\left(\hat{\mathbf{C}}^{C}\right) - \frac{V_I}{V_C}\left\{\hat{T}_{ijkl}^{2}\left(\hat{\mathbf{C}}^{C}\right) - \hat{T}_{ijkl}^{I}\left(\hat{\mathbf{C}}^{C}\right)\right\}\right]\Delta\hat{C}_{klmn}^{IC}\hat{\varepsilon}_{mn}^{I} \tag{III.2.54}$$

At this point, several important aspects of the integral of the modified Green's tensor must be highlighted. First, $\hat{\mathbf{T}}^{2}\left(\hat{\mathbf{C}}^{*}\right)$ is calculated on the volume V_2 which represents the volume of the inclusion and coating together. This volume is assumed to be ellipsoidal in shape and the volume integral is dependent on the ratio of its axes, $\left(a_i + \Delta a_i\right)/\left(a_j + \Delta a_j\right)$. Likewise, $\hat{\mathbf{T}}^{I}\left(\hat{\mathbf{C}}^{*}\right)$, is calculated on the volume V_I and depends on the ratio a_i/a_j [127]. Interestingly, for the specific case where $\Delta a_i/a_i = \Delta a_j/a_j$, the following results [23]:

$$\frac{a_i + \Delta a_i}{a_i + \Delta a_i} = \frac{a_i\left(1 + \Delta a_i \big/ a_i\right)}{a_j\left(1 + \Delta a_j \big/ a_j\right)} = \frac{a_i}{a_j} \tag{III.2.55}$$

Therefore, when the ratio of the coating thickness to the inclusion axis is the same in all directions and the coating is thin the following will always be true: $\hat{\mathbf{T}}^2\left(\hat{\mathbf{C}}^*\right)=\hat{\mathbf{T}}^I\left(\hat{\mathbf{C}}^*\right)$. The remainder of this work is based on the above assumption, which further simplifies relations (III.2.53) and (III.2.54) to Eqns. (III.2.56) and (III.2.57) below.

$$\begin{aligned}\hat{\varepsilon}_{ij}^I = \hat{E}_{ij} &- \hat{T}_{ijkl}^I\left(\hat{\mathbf{C}}^0\right)\Delta\hat{C}_{klmn}^{I0}\hat{\varepsilon}_{mn}^I \\ &- \frac{V_C}{V_I}\hat{T}_{ijkl}^I\left(\hat{\mathbf{C}}^0\right)\Delta\hat{C}_{klmn}^{C0}\hat{T}_{mnpq}^I\left(\hat{\mathbf{C}}^C\right)\Delta\hat{C}_{pqrs}^{IC}\hat{\varepsilon}_{rs}^I \\ &- \frac{V_C}{V_I}\left[\hat{T}_{ijkl}^I\left(\hat{\mathbf{C}}^C\right)-\hat{T}_{ijkl}^I\left(\hat{\mathbf{C}}^0\right)\right]\Delta\hat{C}_{klmn}^{IC}\hat{\varepsilon}_{mn}^I\end{aligned} \qquad \text{(III.2.56)}$$

$$\hat{\varepsilon}_{ij}^C = \hat{\varepsilon}_{ij}^I + \hat{T}_{ijkl}^I\left(\hat{\mathbf{C}}^C\right)\Delta\hat{C}_{klmn}^{IC}\hat{\varepsilon}_{mn}^I \qquad \text{(III.2.57)}$$

These equations will be used in the following section to find the strain localization tensors, $\hat{\mathbf{A}}^I$ and $\hat{\mathbf{A}}^C$, and then the effective viscoelastic stiffness tensor for the composite material. It is important to note that calculating $\hat{\mathbf{T}}^I\left(\hat{\mathbf{C}}^*\right)$ for the general case is not trivial [54, 71, 75]. The three different methods for numerically approximating this entity are: (*i*) Fourier transforms, (*ii*) potential functions, and (*iii*) direct implementation using Eshelby's results [127]. The simplest of these methods, implementation of Eshelby's results, can only be used when the host material is isotropic. The Fourier transform technique, which is described in detail in Appendix A, has been employed in this work.

3.2.4 Homogenization and the self-consistent approximation

The integral equations derived above provide a means to calculate the local strain fields given the loading conditions imposed as infinity (at the boundaries of the RVE). From averaging operations, it is possible to use these expressions in order to approximate the macroscopic behavior or a viscoelastic particulate composite in the dilute case. Unfortunately, the assumptions implicit with the Green's function formulation of the integral equation do not take into account the interactions of the inclusions, which will be a requirement for the non-dilute case. Several different approaches exist which approximate this interaction and the method employed in this work is the self-consistent method. The SC model is derived by defining the EIP as shown below in Figure 3.3. It assumes that the reference material is the effective material, an assumption that indirectly takes inclusion interaction into account [77]. The resulting SC model is an *implicit* set of tensor equations for the effective viscoelastic stiffness tensors which must be evaluated numerically as pointed out in the previous section.

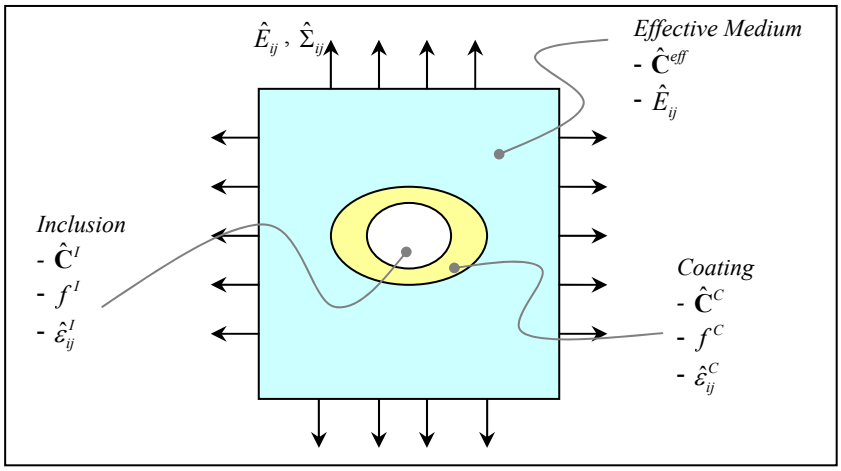

Figure 3.3: The SC model EIP consists of a coated inclusion surrounded by the homogeneous effective medium. The inclusion and coating are full described by their viscoelastic properties $\hat{\mathbf{C}}^{I}$ and $\hat{\mathbf{C}}^{C}$, an average strain field $\hat{\varepsilon}_{ij}^{I}$ and $\hat{\varepsilon}_{ij}^{C}$, and volume fractions f^{I} and f^{C}, respectively. The effective medium is submitted to macroscopic stress and strain fields, $\hat{\Sigma}_{ij}$ and $\hat{E}_{ij}$, and has viscoelastic stiffness tensor $\hat{\mathbf{C}}^{eff}$.

The volumetric composition of the composite must be defined in order to carry out the homogenization step correctly. The total volume of the particulate composite can be decomposed into portions that are occupied by the inclusion, V_I, coating, V_C, and matrix, V_M, according to $V = V_M + V_I + V_C$. This equation yields the obvious volume fraction relation below.

$$f^{M} + f^{I} + f^{C} = 1 \qquad \text{(III.2.58)}$$

where f^{X} is the volume fraction of phase X and is related to the total volume fraction of the composites by $f^{X} = V^{X}/V$.

Before beginning the homogenization step, the uniform stress and strain fields of the composite, $\hat{\Sigma}_{ij}$ and $\hat{E}_{ij}$, must be defined in terms of their local corollaries, $\hat{\sigma}_{ij}(\mathbf{r})$ and

$\hat{\varepsilon}_{ij}(\mathbf{r})$. The classic approach defines the macroscopic fields as the volumetric average of the local fields found using the following equations [54].

$$\hat{E}_{ij} = \frac{1}{V}\int_{V} \hat{\varepsilon}_{ij}(\mathbf{r})\, d\mathbf{r} \tag{III.2.59}$$

$$\hat{\Sigma}_{ij} = \frac{1}{V}\int_{V} \hat{\sigma}_{ij}(\mathbf{r})\, d\mathbf{r} \tag{III.2.60}$$

Homogenization begins by relating the macroscopic stress and strain to each other through Hooke's law for viscoelastic solids using the elastic-viscoelastic correspondence principle.

$$\hat{\Sigma}_{ij} = \hat{C}^{eff}_{ijkl}\hat{E}_{kl} \tag{III.2.61}$$

In the above equation, $\hat{\mathbf{C}}^{eff}$ is the effective viscoelastic stiffness tensor of the composite. The next step is the definition of a strain localization tensor, $\hat{\mathbf{A}}(\mathbf{r})$. This tensor relates the macroscopic strain field, applied at RVE limits, to the local strain field as shown below in Eq. (III.2.62) [69, 75].

$$\hat{\varepsilon}_{ij}(\mathbf{r}) = \hat{A}_{ijkl}(\mathbf{r})\hat{E}_{kl} \tag{III.2.62}$$

Now the average macroscopic strain and stress can be found by using relations (III.2.59) and (III.2.60) together with the average strains in each phase and Eq. (III.2.58) [54].

$$\hat{E}_{ij} = f^M \hat{\varepsilon}_{ij}^M + f^I \hat{\varepsilon}_{ij}^I + f^C \hat{\varepsilon}_{ij}^C \tag{III.2.63}$$

$$\hat{\Sigma}_{ij} = f^M \hat{\sigma}_{ij}^M + f^I \hat{\sigma}_{ij}^I + f^C \hat{\sigma}_{ij}^C \tag{III.2.64}$$

From Eq. (III.2.62) it is possible to find the two following relationships between the macroscopic strain field and the average strain in the inclusion and coating materials.

$$\hat{\varepsilon}_{ij}^I = \hat{A}_{ijkl}^I \hat{E}_{ij} \tag{III.2.65}$$

$$\hat{\varepsilon}_{ij}^C = \hat{A}_{ijkl}^C \hat{E}_{ij} \tag{III.2.66}$$

Also important are the constitutive laws for each material phase given below.

$$\hat{\sigma}_{ij}^I = \hat{C}_{ijkl}^I \hat{\varepsilon}_{kl}^I \tag{III.2.67}$$

$$\hat{\sigma}_{ij}^C = \hat{C}_{ijkl}^C \hat{\varepsilon}_{kl}^C \tag{III.2.68}$$

$$\hat{\sigma}_{ij}^M = \hat{C}_{ijkl}^M \hat{\varepsilon}_{kl}^M \tag{III.2.69}$$

Now, by substituting the relations of the form of Eqns. (III.2.65) and (III.2.66) into the constitutive law equations, a simple relation between the average local stress field in material *X* can be related to the macroscopic strain field as shown below [54].

$$\hat{\sigma}_{ij}^{X} = \hat{C}_{ijkl}^{X} \hat{A}_{klmn}^{X} \hat{E}_{mn} \tag{III.2.70}$$

Next, the average strain and stress fields in the matrix are found by first inserting Eqns. (III.2.65) and (III.2.66) into relation (III.2.63), and then by simply applying Hooke's law to the composite using Eq. (III.2.69) [24]. The results of these operations are given below in expressions (III.2.71) and (III.2.72), respectively.

$$\hat{\varepsilon}_{ij}^{M} = \frac{1}{f^{M}} \left(I_{ijkl} - f^{I} \hat{A}_{ijkl}^{I} - f^{C} \hat{A}_{ijkl}^{C} \right) \hat{E}_{kl} \tag{III.2.71}$$

$$\hat{\sigma}_{ij}^{M} = \frac{1}{f^{M}} \hat{C}_{ijkl}^{M} \left(I_{klmn} - f^{I} \hat{A}_{klmn}^{I} - f^{C} \hat{A}_{klmn}^{C} \right) \hat{E}_{mn} \tag{III.2.72}$$

The average stress in the matrix material can also be found by combining Eq. (III.2.64) and stress localization equations in the form of (III.2.70), yielding:

$$\hat{\sigma}_{ij}^{M} = \frac{1}{f^{M}} \left(\hat{C}_{ijmn}^{eff} - f^{I} \hat{C}_{ijkl}^{I} \hat{A}_{klmn}^{I} - f^{C} \hat{C}_{ijkl}^{C} \hat{A}_{klmn}^{C} \right) \hat{E}_{mn} \tag{III.2.73}$$

The effective viscoelastic stiffness tensor of the particulate composite is finally found by equating relations (III.2.72) and (III.2.73) and solving for $\hat{\mathbf{C}}^{eff}$ [24].

$$\boxed{\hat{\mathbf{C}}^{eff} = \hat{\mathbf{C}}^{M} + f^{I} \left(\hat{\mathbf{C}}^{I} - \hat{\mathbf{C}}^{M} \right) : \hat{\mathbf{A}}^{I} + f^{C} \left(\hat{\mathbf{C}}^{C} - \hat{\mathbf{C}}^{M} \right) : \hat{\mathbf{A}}^{C}} \tag{III.2.74}$$

To complete this model, the strain localization tensors, $\hat{\mathbf{A}}^I$ and $\hat{\mathbf{A}}^C$, must be found. These tensors will be dependent on the volumetric composition of the composite, the geometry of the coated inclusions, the constituent material properties, and the *effective* material properties [23]. Expressions for these terms must be solved for via integral equations derived in the previous section. The strain localization tensors are the result of re-arranging (III.2.56) and (III.2.57) as shown below in Eq. (III.2.75).

$$\hat{E}_{ij} = \left(\hat{A}^X_{ijkl}\right)^{-1} \hat{\varepsilon}^X_{kl} \tag{III.2.75}$$

Here X can represent the inclusion, I, or the coating, C. After re-arranging these expressions into the above form, the model must be made self-consistent by setting the effective material properties equal to the reference material ($\hat{\mathbf{C}}^0 = \hat{\mathbf{C}}^{eff}$) in keeping with the EIP given in Figure 3.3. The resulting strain localization equations are then:

$$\begin{aligned}\left(\hat{\mathbf{A}}^I\right)^{-1} = \mathbf{I}_4 + \hat{\mathbf{T}}^I\left(\hat{\mathbf{C}}^{eff}\right) : \Delta\hat{\mathbf{C}}^C + \frac{f_C}{f_I}\hat{\mathbf{T}}^I\left(\hat{\mathbf{C}}^{eff}\right) : \Delta\hat{\mathbf{C}}^C : \hat{\mathbf{T}}^I\left(\hat{\mathbf{C}}^C\right) : \Delta\hat{\mathbf{C}}^{IC} \\ + \frac{f_C}{f_I}\left[\hat{\mathbf{T}}^I\left(\hat{\mathbf{C}}^C\right) - \hat{\mathbf{T}}^I\left(\hat{\mathbf{C}}^{eff}\right)\right] : \Delta\hat{\mathbf{C}}^{IC}\end{aligned} \tag{III.2.76}$$

$$\hat{\mathbf{A}}^C = \left(\mathbf{I}_4 + \hat{\mathbf{T}}^I\left(\hat{\mathbf{C}}^C\right) : \Delta\hat{\mathbf{C}}^{IC}\right) : \hat{\mathbf{A}}^I \tag{III.2.77}$$

Note that Differential Effective Medium (DEM) and Mori-Tanaka (MT) models can be obtained for the coated inclusion problem from Eqs. (III.2.71), (III.2.74), (III.2.76), and (III.2.77) if $\hat{\mathbf{C}}^0 \neq \hat{\mathbf{C}}^{eff}$. This is done in Appendix D.

One further term of interest is the strain localization tensor for the matrix material. This can be useful in several applications such strain energy studies.

$$\hat{\mathbf{A}}^M = \frac{1}{1-\varphi}\left[\mathbf{I}_4 - f^I \hat{\mathbf{A}}^I - f^C \hat{\mathbf{A}}^C\right] \tag{III.2.78}$$

In the above equations, the contrast tensors are defined as $\Delta\hat{\mathbf{C}}^X = \hat{\mathbf{C}}^X - \hat{\mathbf{C}}^{eff}$ where X represents the inclusion or coating, $\mathbf{I}_4$ is the fourth order identity tensor, and φ is the volume fraction of the inclusion and coating together: $\varphi = f^I + f^C$. Eqns. (III.2.74), (III.2.76), and (III.2.77) constitute Cherkaoui's general SC micromechanical model extended to the quasi-static frequency domain through application of the elastic-viscoelastic correspondence principle.

3.3 Generalization using Dilute Strain Concentration Tensors

In reality the composition of particulate composite materials comes in an infinite number of constituent material and coated inclusion geometry combinations. Unfortunately, the model derived in Section 3.2 is limited in the types of composites that can be treated. The form of Eqns. (III.2.74), (III.2.76), and (III.2.77) will only allow the approximation of the effective material behavior for the simple case of a composite

material consisting of three material phases (matrix, inclusion, and coating) an identical shape and orientation of all coated inclusions [130]. This limitation is a direct result of the derivation of the strain localization tensors and, more specifically, the integral equation approximation. A significant improvement of the SC model derived above would be its generalization to include the effects of multiple types of coated inclusions (different materials), a variation of coating thickness, multiple coated inclusion geometries, and a variation in the coated inclusion orientation. This level of generality is achievable through the application of dilute strain concentration tensors (DSCT) [130]. Recent DSCT applications to approximate the effective behavior of polymers containing nano-tubes have shown the generality of this approach [55-57]. These applications have shown that DSCT formulation of micromechanical models accurately approximate effect the wavy shape and orientation distribution of the nanotubes on the global behavior of the composite. The DSCT approach applied in this work will expand the RVE to include all of the different coated inclusion variations. This change of RVE will lead to a SC model that is analogous to the one derived in Section 3.2. Because the SC approach assumes that the reference material surrounds each coated inclusion, it is easy to visualize calculating the fields of the expanded RVE of the DSCT approach as a summation of N different sub-EIP's as shown below in Figure 3.4.

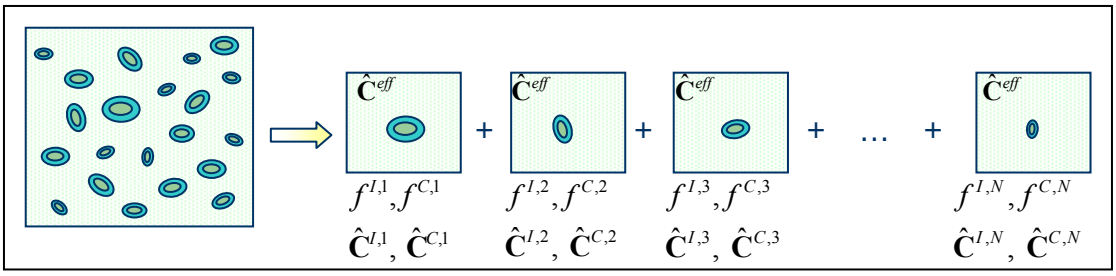

Figure 3.4: Schematic representation of DSCT formulation of the SC model as the sum of fields found from *N* different EIP's corresponding to each coated inclusion family.

The schematic representation in Figure 3.4 clearly shows the SC DSCT approach. All coated inclusions that have identical material type, spatial orientation, and shape constitute a coated inclusion family. The entire composite consists of *N* different coated inclusion families depending on the true nature of the material. For the SC approximation, each family is assumed to be surrounded by the effective material and to occupy a volume fraction, $\varphi^{\varsigma} = f^{I,\varsigma} + f^{C,\varsigma}$. The assumption of the DSCT formulation is that the effects of each coated inclusion family can be superimposed in order to arrive at a reasonable approximation of the effective behavior of the particulate composite. The DSCT approach assumes that the descriptive dimension of all coated inclusion families is of the same order of magnitude and, like all micromechanical approaches, that this dimension is much smaller than the global (macroscopic) length scale [33]. Just as in the model given in Section 3.2, all DSCT models that do not take inclusion interaction into account will be limited to low volume fraction applications [57]. In the following sections, the derivation presented in Sections 3.2.1 – 3.2.4 is adapted to the case of a composite containing multiple coated inclusions and a DSCT SC model corollary to Eqns. (III.2.74), (III.2.76), and (III.2.77) is found. The generality of the model that will be derived will allow the approximation of the effective behavior of composites

containing coated inclusions having a range of different material properties, spatial orientations, and shapes. For the sake of brevity, the following "derivation" is not a detailed repetition of all equations in Sections 3.2.1 – 3.2.4, but rather a summary of the preceding derivation adapted to the multiple coated inclusion case.

3.3.1 Localization and the integral equation

Derivation of the DSCT SC model requires several changes during the localization step. First, differences in the topology of the RVE must be addressed. The RVE shown in Figure 3.1 for a single coated inclusion is understood here to represent a single *family* of coated inclusions. In the DSCT approach, an RVE such as the one shown in Figure 3.5 will consist of N different sub-RVE's like the RVE shown in Figure 3.1.

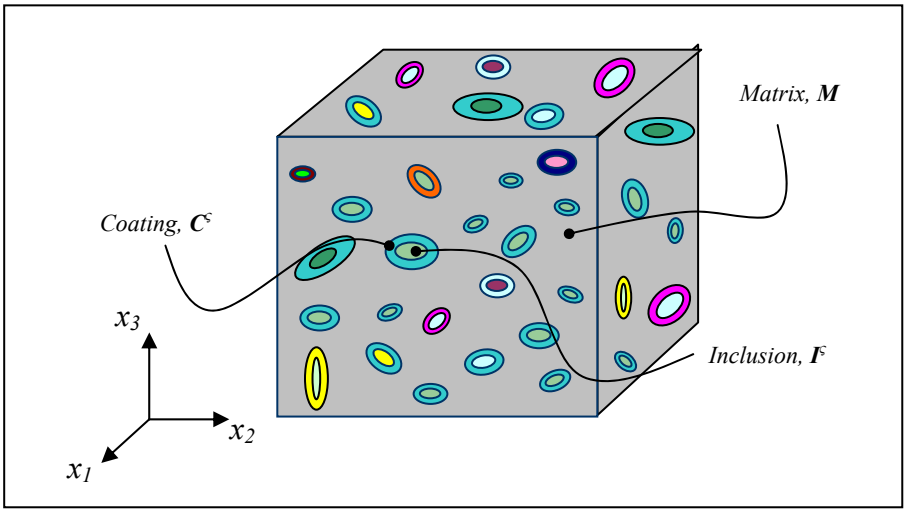

Figure 3.5: Topology of a particulate viscoelastic composite with N coated inclusion families.

The topology of the above RVE corresponds to N coated inclusion families where each family, ς, is represented with a single inclusion of volume, $V_{I,\varsigma}$, and viscoelastic stiffness, $\hat{\mathbf{C}}^{I,\varsigma}$, and is coated with another material having a volume, $V_{C,\varsigma}$, and viscoelastic stiffness, $\hat{\mathbf{C}}^{C,\varsigma}$. Each family is also assumed to have a unique ellipsoidal shape characterized by major axes, a_i^{ς}, aligned with the *local* coordinate system, $\tilde{\mathbf{x}}^{\varsigma}$. Euler angles ϑ^{ς}, ϕ^{ς}, and ψ^{ς} relate the *local* coordinate system to the *global* coordinates using the "*x*" convention (see Appendix B) [129]. As before, all coated inclusions are embedded in the reference material with viscoelastic stiffness, $\hat{\mathbf{C}}^0$. The reference material shown above is the matrix material.

It is now possible to start the derivation of the DSCT SC model beginning with the expression for the local behavior of the composite material. As in the previous section, the viscoelastic stiffness tensor of the heterogeneous material will be expressed as a homogeneous material having spatially varying viscoelastic properties. For the RVE shown in Figure 3.5 this variation is expressed identically to Eq. (III.2.3).

$$\hat{\mathbf{C}}(\mathbf{r}) = \hat{\mathbf{C}}^0 + \delta\hat{\mathbf{C}}(\mathbf{r}) \quad \text{with} \quad \mathbf{r} \in V \tag{III.3.1}$$

As before, $\hat{\mathbf{C}}^0$ represents the spatially uniform viscoelastic stiffness tensor of the reference material and V is the volume of the RVE. Unlike the previous derivation, however, the spatial variation tensor, $\delta\hat{\mathbf{C}}(\mathbf{r})$, must be modified to allow for N different

coated inclusion families. In order to do so, Eq. (III.2.14) must be generalized to the form shown below.

$$\begin{aligned}\delta\hat{\mathbf{C}}(\mathbf{r}) &= \left(\hat{\mathbf{C}}^{I,1}-\hat{\mathbf{C}}^{0}\right)\theta^{I,1}(\mathbf{r})+\left(\hat{\mathbf{C}}^{C,1}-\hat{\mathbf{C}}^{0}\right)\left[\theta^{2,1}(\mathbf{r})-\theta^{I,1}(\mathbf{r})\right] \\ &+\left(\hat{\mathbf{C}}^{I,2}-\hat{\mathbf{C}}^{0}\right)\theta^{I,2}(\mathbf{r})+\left(\hat{\mathbf{C}}^{C,2}-\hat{\mathbf{C}}^{0}\right)\left[\theta^{2,2}(\mathbf{r})-\theta^{I,2}(\mathbf{r})\right] \\ &\vdots \\ &+\left(\hat{\mathbf{C}}^{I,N}-\hat{\mathbf{C}}^{0}\right)\theta^{I,N}(\mathbf{r})+\left(\hat{\mathbf{C}}^{C,N}-\hat{\mathbf{C}}^{0}\right)\left[\theta^{2,N}(\mathbf{r})-\theta^{I,N}(\mathbf{r})\right] \\ &=\sum_{\varsigma=1}^{\mathrm{N}}\left(\Delta\hat{\mathbf{C}}^{I0,\varsigma}\theta^{I,\varsigma}(\mathbf{r})+\Delta\hat{\mathbf{C}}^{C0,\varsigma}\delta\theta^{I,\varsigma}(\mathbf{r})\right)\end{aligned} \tag{III.3.2}$$

In Eq. (III.3.2) the shorthand viscoelastic contrast tensors introduced in Eq. (III.2.34) have been employed to denote the contrast of the ς^{th} coating or inclusion and the reference material. The Heaviside step functions $\theta^{I,\varsigma}(\mathbf{r})$, $\theta^{2,\varsigma}(\mathbf{r})$, and $\delta\theta^{I,\varsigma}(\mathbf{r})$ defined below are generalizations of Eqns. (III.2.15) and (III.2.17):

$$\begin{aligned}\theta^{I,\varsigma}(\mathbf{r}) &= \begin{cases}1 & \text{si } \mathbf{r}\in V_{I,\varsigma} \\ 0 & \text{si } \mathbf{r}\notin V_{I,\varsigma}\end{cases} \\ \theta^{2,\varsigma}(\mathbf{r}) &= \begin{cases}1 & \text{si } \mathbf{r}\in V_{2,\varsigma} \\ 0 & \text{si } \mathbf{r}\notin V_{2,\varsigma}\end{cases} \\ \delta\theta^{I,\varsigma}(\mathbf{r}) &= \theta^{2,\varsigma}(\mathbf{r})-\theta^{I,\varsigma}(\mathbf{r})\end{aligned} \tag{III.3.3}$$

It is important to note that the form of Eqns. (III.3.2) and (III.3.3) assume that all viscoelastic stiffness tensors and Heaviside step functions are expressed with respect to

the global coordinate system. This fact requires the rotation of each quantity from their local coordinate system to the global coordinate system.

The derivation of the DSCT SC model can now be taken up from the modified equilibrium equation given in Eqns. (III.2.5) and (III.2.6). These equations will be used to derive the *N* different modified Green's tensors that take the shape, orientation, and stiffness contrast of each family into account. Eq. (III.3.4) below gives the equilibrium equation for the *N* coated inclusion families.

$$\begin{aligned}\hat{C}^0_{ijkl}\hat{u}_{k,lj}(\mathbf{r}) &= \left[-\delta\hat{C}_{ijkl}(\mathbf{r})\hat{\varepsilon}_{kl}(\mathbf{r})\right]_{,j} = \hat{f}_i(\mathbf{r}) \\ &= \sum_{\varsigma=1}^{N} -\left[\left\{\Delta C^{I0,\varsigma}_{ijkl}\theta^{I,\varsigma}(\mathbf{r}) + \Delta C^{C0,\varsigma}_{ijkl}\left(\theta^{2,\varsigma}(\mathbf{r}) - \theta^{I,\varsigma}(\mathbf{r})\right)\right\}\hat{\varepsilon}_{kl}(\mathbf{r})\right]_{,j} \\ &= \sum_{\varsigma=1}^{N}\hat{f}_i^{\varsigma}(\mathbf{r})\end{aligned} \quad \text{(III.3.4)}$$

For the *N* coated inclusion family case, it is obvious that the distribution of fictitious forces becomes the result of the summation of *N* distributions each described by Eq. (III.2.6). The Green's tensor solution to this differential equation, therefore, must be represented as the sum of *N* Green's tensors, $\hat{G}^{0,\varsigma}_{km}\left(\mathbf{r}-\mathbf{r}'^{,\varsigma}\right)$. Each individual Green's tensor is a function that calculates the displacement in the *k* direction at the point **r** when a time varying unit force due to the inhomogeneity of the ς^{th} family of coated inclusions, $\hat{f}_i^{\varsigma}(\mathbf{r})$, is applied at the point $\mathbf{r}'^{,\varsigma}$ in the *m* direction. Equation (III.2.7) must therefore be changed to the following form.

$$\hat{C}^{0}_{ijkl}\hat{G}^{0,\varsigma}_{km,lj}\left(\mathbf{r}-\mathbf{r}'^{,\varsigma}\right)+\delta_{im}\delta\left(\mathbf{r}-\mathbf{r}'^{,\varsigma}\right)\delta\left(\omega-\omega'\right)=0 \tag{III.3.5}$$

Given this corollary expression to (III.2.7), the resultant integral equation for the displacement field becomes a summation of *N* Green's tensors representing each coated inclusion family as shown below in Eq. (III.3.6):

$$\begin{aligned}\hat{u}_m\left(\mathbf{r}\right)&=\hat{u}^0_m\left(\mathbf{r}\right)-\sum_{\varsigma=1}^{N}\int_{-\infty}^{\infty}\int_{V}\hat{G}^{0,\varsigma}_{im,j'}\left(\mathbf{r}-\mathbf{r}'^{,\varsigma}\right)\left[\delta\hat{C}_{ijkl}\left(\mathbf{r}'^{,\varsigma}\right)\hat{\varepsilon}^{\varsigma}_{kl}\left(\mathbf{r}'^{,\varsigma}\right)\right]d\mathbf{r}'^{,\varsigma}\,d\omega'\\&=\sum_{\varsigma=1}^{N}\hat{u}^{\varsigma}_m\left(\mathbf{r}\right)\end{aligned} \tag{III.3.6}$$

Where $\hat{u}^{\varsigma}_m\left(\mathbf{r}\right)$ and $\hat{\varepsilon}^{\varsigma}_{kl}\left(\mathbf{r}\right)$ represent the compatible displacement and strain at the point **r** due to the ς^{th} family of coated inclusions. Then, by using the properties of the Dirac delta function for the frequency integral and the small strain approximation, the resulting integral equation for the strain field at every point in the heterogeneous material is given as:

$$\begin{aligned}\hat{\varepsilon}_{ij}\left(\mathbf{r}\right)&=\hat{E}_{ij}-\sum_{\varsigma=1}^{N}\int_{V}\hat{\Gamma}^{0,\varsigma}_{ijkl}\left(\mathbf{r}-\mathbf{r}'^{,\varsigma}\right)\delta\hat{C}_{klmn}\left(\mathbf{r}'^{,\varsigma}\right)\hat{\varepsilon}^{\varsigma}_{mn}\left(\mathbf{r}'^{,\varsigma}\right)d\mathbf{r}'^{,\varsigma}\\&=\sum_{\varsigma=1}^{N}\hat{\varepsilon}^{\varsigma}_{ij}\left(\mathbf{r}\right)\end{aligned} \tag{III.3.7}$$

Where the modified Green's tensor for each coated inclusion family, $\hat{\Gamma}^{0,\varsigma}_{ijkl}$, is expressed below in relation (III.3.8).

$$\hat{\Gamma}^{0,\varsigma}_{ijkl} = -\frac{1}{2}\left[\hat{G}^{0,\varsigma}_{ki,jl}\left(\mathbf{r}-\mathbf{r}'^{,\varsigma}\right)+\hat{G}^{0,\varsigma}_{kj,il}\left(\mathbf{r}-\mathbf{r}'^{,\varsigma}\right)\right] \qquad \text{(III.3.8)}$$

It is important to note that in the present form, all of the terms in the above equations are defined with respect to the global coordinate system, **x**. The simplification of the above integral equation by employing interfacial operators as described in sections 3.2.2 and 3.2.3, however, is greatly simplified by employing all operations in the local coordinate system, $\tilde{\mathbf{x}}^{\varsigma}$, and then rotating the result to the global reference system and finally performing the summation. Indeed, the entire derivation of the interfacial operators given in Section 3.2.2 remains identical for each coated inclusion family with respect to their local coordinate system. For this generalization of the SC model, it therefore suffices to restate the important results in local coordinates. In the following paragraphs all variables represented as $\tilde{X}^{\varsigma}$ represent the variable X^{ς} with respect to the local coordinates of the ς^{th} coated inclusion family.

3.3.2 Interfacial operators and average strain fields of coated inclusion families

The interfacial operators derived in Section 3.2.2 are general expressions that only assume that the reference coordinates of phases *A* and *B* are identical. Because of this, no re-derivation is necessary for the problem of multiple coated inclusions. However, for the sake of simplicity in what follows, Eqns. (III.2.31) and (III.2.32) are re-stated here with respect to the local coordinates.

$$\hat{\tilde{P}}^{A}_{ijkl} \equiv \frac{1}{4}\left[\left(\hat{\tilde{K}}^{A}_{ik}\right)^{-1}\tilde{n}_j\tilde{n}_l + \left(\hat{\tilde{K}}^{A}_{jk}\right)^{-1}\tilde{n}_i\tilde{n}_l + \left(\hat{\tilde{K}}^{A}_{il}\right)^{-1}\tilde{n}_j\tilde{n}_k + \left(\hat{\tilde{K}}^{A}_{jl}\right)^{-1}\tilde{n}_i\tilde{n}_k\right] \qquad \text{(III.3.9)}$$

and

$$\begin{aligned}\hat{\tilde{\varepsilon}}^{A}_{ij} &= \left[\hat{\tilde{P}}^{A}_{ijkl}\left(\hat{\tilde{C}}^{B}_{klmn} - \hat{\tilde{C}}^{A}_{klmn}\right) + I_{ijmn}\right]\hat{\tilde{\varepsilon}}^{B}_{mn} \\ \hat{\tilde{\varepsilon}}^{B}_{ij} &= \left[\hat{\tilde{P}}^{B}_{ijkl}\left(\hat{\tilde{C}}^{A}_{klmn} - \hat{\tilde{C}}^{B}_{klmn}\right) + I_{ijmn}\right]\hat{\tilde{\varepsilon}}^{A}_{mn}\end{aligned} \qquad \text{(III.3.10)}$$

Where $\hat{\tilde{K}}^{\chi}_{ik}$ is Christoffel's matrix for material χ with respect to the local coordinates defined as $\hat{\tilde{K}}^{\chi}_{ik} = \hat{\tilde{C}}^{\chi}_{ijkl}\tilde{n}_l\tilde{n}_j$.

Now, in order to apply the interfacial operators given above to simplify the integral equation, it is necessary to return to expression (III.3.4), and specifically the approximation of the variation in Heaviside step functions, $\delta\theta^{I,\varsigma}(\mathbf{r})$, for the case of a thinly coated inclusion, and the viscoelastic contrast tensors. As in the case of the interfacial operators, expression (III.2.18) can be adopted to the local coordinate system by simply using local variables.

$$\delta\tilde{\theta}^{I,\varsigma}(\tilde{\mathbf{r}}) \approx \tilde{p}^{\varsigma}\sum_{\alpha}\frac{\Delta\tilde{a}^{\varsigma}_{\alpha}}{\tilde{a}^{\varsigma}_{\alpha}}\frac{\left(\tilde{x}^{\varsigma}_{\alpha}\right)^2}{\left(\tilde{a}^{\varsigma}_{\alpha}\right)^2}\delta\left(\tilde{S}_{I,\varsigma}\right) \qquad \text{(III.3.11)}$$

Here $\tilde{p}^{\varsigma}$ is the perpendicular distance from the center of the ς^{th} coated inclusion to its tangent plane at the point $\tilde{\mathbf{x}}^{\varsigma}$ (represented in local coordinates identically to Eq. (III.2.19)

), $\tilde{a}_\alpha^\varsigma$ represents the α^{th} major axes, and $\tilde{S}_{I,\varsigma}$ the surface of the inclusion of the ς^{th} coated inclusion family. Using this local expression, it is now simple employ Eq. (III.3.2) to express the ς^{th} variation in viscoelastic constants as shown below:

$$\delta\hat{\tilde{\mathbf{C}}}^\varsigma(\mathbf{r}) = \left(\hat{\tilde{\mathbf{C}}}^{I,\varsigma} - \hat{\tilde{\mathbf{C}}}^0\right)\tilde{\theta}^I(\mathbf{r}) + \left(\hat{\tilde{\mathbf{C}}}^{C,\varsigma} - \hat{\tilde{\mathbf{C}}}^0\right)\tilde{p}^\varsigma \sum_\alpha \frac{\Delta\tilde{a}_\alpha^\varsigma}{\tilde{a}_\alpha^\varsigma}\frac{\left(\tilde{x}_\alpha^\varsigma\right)^2}{\left(\tilde{a}_\alpha^\varsigma\right)^2}\delta\left(\tilde{S}_{I,\varsigma}\right) \quad \text{(III.3.12)}$$

It is important to stress that the calculation of this variation requires the rotation of the *reference* material to the local coordinates. Now, Eq. (III.3.13) below results from the insertion of (III.3.12) into the integral Eq. (III.3.7) and application of the appropriate rotation matrices.

$$\begin{aligned}\hat{\varepsilon}_{ij}(\mathbf{r}) = \hat{E}_{ij} &- \sum_{\varsigma=1}^{N} R_{ir}^\varsigma R_{js}^\varsigma \int_{\tilde{V}_{I,\varsigma}} \hat{\tilde{\Gamma}}_{rskl}^{0,\varsigma}\left(\tilde{\mathbf{r}} - \tilde{\mathbf{r}}'^{,\varsigma}\right)\Delta\hat{\tilde{C}}_{klmn}^{I0,\varsigma}\hat{\tilde{\varepsilon}}_{mn}\left(\tilde{\mathbf{r}}'^{,\varsigma}\right)d\tilde{\mathbf{r}}'^{,\varsigma} \\ &- \sum_{\varsigma=1}^{N} R_{ir}^\varsigma R_{js}^\varsigma \left[\sum_\alpha \int_{\tilde{S}_{I,\varsigma}^+} \hat{\tilde{\Gamma}}_{rskl}^{0,\varsigma}\left(\tilde{\mathbf{r}} - \tilde{\mathbf{r}}^{+,\varsigma}\right)\Delta\hat{\tilde{C}}_{klmn}^{C0,\varsigma}\hat{\tilde{\varepsilon}}_{mn}\left(\tilde{\mathbf{r}}^{+,\varsigma}\right)\tilde{p}^\varsigma \frac{\Delta\tilde{a}_\alpha^\varsigma}{\tilde{a}_\alpha^\varsigma}\frac{\left(\tilde{x}_\alpha^\varsigma\right)^2}{\left(\tilde{a}_\alpha^\varsigma\right)^2}dS\right] \quad \text{(III.3.13)} \\ &= \sum_{\varsigma=1}^{N} R_{ir}^\varsigma R_{js}^\varsigma \hat{\varepsilon}_{rs}^\varsigma\left(\tilde{\mathbf{r}}\right)\end{aligned}$$

Where R_{ij}^ς is the rotation matrix determined from the Euler angles of the ς^{th} coated inclusion family. The modified Green's tensor in the local coordinate system is determined through the evaluation of Eq. (III.3.5) when the reference material and all spatial variables have been rotated to the local reference frame.

At this point, it is now possible to move towards the calculation of the average strain in the inclusion and coating of each coated inclusion family. First, it is necessary to state the local coordinate equivalent of the strain jump between the inclusion and the coating material and the average strain in each phase. The equation describing the strain at a position just outside the ς^{th} coated inclusion can be calculated via the local equivalent of Eq. (III.2.36) given below.

$$\hat{\tilde{\varepsilon}}_{ij}\left(\tilde{\mathbf{r}}^{+}\right) = \hat{\tilde{\varepsilon}}_{ij}^{I} + \hat{\tilde{P}}_{ijkl}^{C}\Delta\hat{\tilde{C}}_{lkmn}^{IC}\hat{\tilde{\varepsilon}}_{ij}^{I} \tag{III.3.14}$$

Then, the average strain in each phase is calculated using the classic equations:

$$\begin{aligned}\hat{\tilde{\varepsilon}}_{ij}^{I,\varsigma} &= \frac{1}{V_{I,\varsigma}}\int_{V_{I,\varsigma}} \hat{\tilde{\varepsilon}}_{ij}\left(\tilde{\mathbf{r}}\right)d\tilde{\mathbf{r}} \\ \hat{\tilde{\varepsilon}}_{ij}^{C,\varsigma} &= \frac{1}{V_{C,\varsigma}}\int_{V_{C,\varsigma}} \hat{\tilde{\varepsilon}}_{ij}\left(\tilde{\mathbf{r}}\right)d\tilde{\mathbf{r}}\end{aligned} \tag{III.3.15}$$

Using these expressions, the integral equation given in (III.3.13) simplifies to give the average strain in the inclusion and coating of each family with respect to the local coordinates via the two following equations.

$$\hat{\tilde{\varepsilon}}_{ij}^{I,\varsigma} = \hat{\tilde{E}}_{ij} - \frac{1}{V_{I,\varsigma}} \int_{\tilde{V}_{I,\varsigma}} \int_{\tilde{V}_{I,\varsigma}} \hat{\tilde{\Gamma}}_{ijkl}^{0,\varsigma}\left(\tilde{\mathbf{r}} - \tilde{\mathbf{r}}'^{,\varsigma}\right) \Delta\hat{\tilde{C}}_{klmn}^{I0,\varsigma} \hat{\tilde{\varepsilon}}_{mn}^{I,\varsigma} d\tilde{\mathbf{r}}'^{,\varsigma} d\tilde{\mathbf{r}}$$
$$- \frac{1}{V_{I,\varsigma}} \sum_{\alpha} \int_{\tilde{S}_{I,\varsigma}^{+}} \left\{ \int_{\tilde{V}_{I,\varsigma}} \hat{\tilde{\Gamma}}_{ijkl}^{0,\varsigma}\left(\tilde{\mathbf{r}} - \tilde{\mathbf{r}}^{+,\varsigma}\right) d\tilde{\mathbf{r}} \right\} \Delta\hat{\tilde{C}}_{klmn}^{C0,\varsigma} \hat{\tilde{\varepsilon}}_{mn}^{I,\varsigma} \tilde{p}^{\varsigma} \frac{\Delta\tilde{a}_{\alpha}^{\varsigma}}{\tilde{a}_{\alpha}^{\varsigma}} \frac{\left(\tilde{x}_{\alpha}^{\varsigma}\right)^2}{\left(\tilde{a}_{\alpha}^{\varsigma}\right)^2} d\tilde{S} \qquad \text{(III.3.16)}$$
$$- \frac{1}{V_{I,\varsigma}} \sum_{\alpha} \int_{\tilde{S}_{I,\varsigma}^{+}} \left\{ \int_{\tilde{V}_{I,\varsigma}} \hat{\tilde{\Gamma}}_{ijkl}^{0,\varsigma}\left(\tilde{\mathbf{r}} - \tilde{\mathbf{r}}^{+,\varsigma}\right) d\tilde{\mathbf{r}} \right\} \Delta\hat{\tilde{C}}_{klmn}^{C0,\varsigma} \hat{\tilde{P}}_{mnpq}^{C,\varsigma} \Delta\hat{\tilde{C}}_{pqrs}^{IC,\varsigma} \hat{\tilde{\varepsilon}}_{rs}^{I,\varsigma} \tilde{p}^{\varsigma} \frac{\Delta\tilde{a}_{\alpha}^{\varsigma}}{\tilde{a}_{\alpha}^{\varsigma}} \frac{\left(\tilde{x}_{\alpha}^{\varsigma}\right)^2}{\left(\tilde{a}_{\alpha}^{\varsigma}\right)^2} d\tilde{S}$$

$$\hat{\tilde{\varepsilon}}_{ij}^{C,\varsigma} = \hat{\tilde{\varepsilon}}_{ij}^{I,\varsigma} + \frac{1}{V_{C,\varsigma}} \left\{ \int_{\tilde{V}_{C,\varsigma}} \hat{\tilde{P}}_{ijkl}^{C,\varsigma} d\tilde{\mathbf{r}} \right\} \Delta\hat{\tilde{C}}_{klmn}^{IC,\varsigma} \hat{\tilde{\varepsilon}}_{mn}^{I,\varsigma} \qquad \text{(III.3.17)}$$

At this stage in the derivation of the *N* coated inclusion SC model, it is necessary to define the volume integral of the modified Green's tensor. In accordance with Eq. (III.2.48), this integral is defined for each family of coated inclusions using the following equation.

$$\hat{\tilde{T}}_{ijkl}^{\chi,\varsigma}\left(\hat{\tilde{\mathbf{C}}}^{*}\right) = \int_{\tilde{V}_{\chi,\varsigma}} \hat{\tilde{\Gamma}}_{ijkl}^{*,\varsigma}\left(\tilde{\mathbf{r}} - \tilde{\mathbf{r}}'^{,\varsigma}\right) d\tilde{\mathbf{r}}'^{,\varsigma} \quad \text{if } \tilde{\mathbf{r}} \in \tilde{V}_{\chi,\varsigma} \qquad \text{(III.3.18)}$$

Where $V_{\chi,\varsigma}$ represents the inclusion or composite inclusion (inclusion + coating) volume and * can represent the inclusion or coating of the ς^{th} coated inclusion family or reference material. Now, because the coating is assumed to be thin for each family, Eqns. (III.2.44) and (III.2.45) can be combined and re-stated for each family as follows:

$$V_{C,\varsigma} = \int_{V_{C,\varsigma}} \left[\theta^{2,\varsigma}(\mathbf{r}) - \theta^{I,\varsigma}(\mathbf{r})\right] d\mathbf{r}$$
$$\approx \int_{\tilde{V}} \sum_{\alpha} \tilde{p}^{\varsigma} \frac{\Delta\tilde{a}_{\alpha}^{\varsigma}}{\tilde{a}_{\alpha}^{\varsigma}} \frac{\left(\tilde{x}_{\alpha}^{\varsigma}\right)^2}{\left(\tilde{a}_{\alpha}^{\varsigma}\right)^2} \delta\left(\tilde{S}_I\right) d\tilde{\mathbf{r}} = \sum_{i} \int_{\tilde{S}_I} \tilde{p}^{\varsigma} \frac{\Delta\tilde{a}_{\alpha}^{\varsigma}}{\tilde{a}_{\alpha}^{\varsigma}} \frac{\left(\tilde{x}_{\alpha}^{\varsigma}\right)^2}{\left(\tilde{a}_{\alpha}^{\varsigma}\right)^2} d\tilde{S} \tag{III.3.19}$$

The derivation of equations equivalent to (III.2.46)-(III.2.52) for the local coordinates of the ς^{th} coated inclusion family is identical the analysis carried out in Section 3.2.3. The expressions below relating the inclusion and coating volumes to the interfacial operators and the integral of the modified Green's tensor are, therefore, given for continuity and clarity. First, the following property of the interfacial operator is important.

$$\int_{\tilde{V}_C} \hat{\tilde{P}}^{*}_{ijkl} d\tilde{\mathbf{r}} = V_C \hat{\tilde{T}}^{I}_{ijkl}\left(\hat{\tilde{\mathbf{C}}}^{*}\right) - \int_{\tilde{V}_C} \int_{\tilde{V}_I} \hat{\tilde{\Gamma}}^{*}_{ijkl}\left(\tilde{\mathbf{r}}^{+} - \tilde{\mathbf{r}}\right) d\tilde{\mathbf{r}}^{+} d\tilde{\mathbf{r}} \tag{III.3.20}$$

Then, the equivalent statements to Eqns. (III.2.51) and (III.2.52) are shown below.

$$\int_{\tilde{V}_C} \int_{\tilde{V}_I} \hat{\tilde{\Gamma}}^{*,\varsigma}_{ijkl}\left(\tilde{\mathbf{r}}^{+} - \tilde{\mathbf{r}}\right) d\tilde{\mathbf{r}}^{+} d\tilde{\mathbf{r}} = V_{I,\varsigma}\left(\hat{\tilde{T}}^{2,\varsigma}_{ijkl}\left(\hat{\tilde{\mathbf{C}}}^{*,\varsigma}\right) - \hat{\tilde{T}}^{I,\varsigma}_{ijkl}\left(\hat{\tilde{\mathbf{C}}}^{*,\varsigma}\right)\right) \tag{III.3.21}$$

$$\int_{\tilde{V}_{C,\varsigma}} \hat{\tilde{P}}^{*,\varsigma}_{ijkl} d\tilde{\mathbf{r}} = \int_{\tilde{V}} \hat{\tilde{P}}^{*,\varsigma}_{ijkl} \delta\theta^{I,\varsigma}(\tilde{\mathbf{r}}) d\tilde{\mathbf{r}} = \sum_{\alpha} \int_{\tilde{S}_{I,\varsigma}} \hat{\tilde{P}}^{*,\varsigma}_{ijkl} \tilde{p}^{\varsigma} \frac{\Delta\tilde{a}_{\alpha}^{\varsigma}}{\tilde{a}_{\alpha}^{\varsigma}} \frac{\left(\tilde{x}_{\alpha}^{\varsigma}\right)^2}{\left(\tilde{a}_{\alpha}^{\varsigma}\right)^2} d\tilde{S}$$
$$= V_{C,\varsigma} \hat{\tilde{T}}^{I,\varsigma}_{ijkl}\left(\hat{\tilde{\mathbf{C}}}^{*,\varsigma}\right) - V_{I,\varsigma}\left[\hat{\tilde{T}}^{2,\varsigma}_{ijkl}\left(\hat{\tilde{\mathbf{C}}}^{*,\varsigma}\right) - \hat{\tilde{T}}^{I,\varsigma}_{ijkl}\left(\hat{\tilde{\mathbf{C}}}^{*,\varsigma}\right)\right] \tag{III.3.22}$$

Finally, the results of applying the assumption that $\Delta a_i / a_i = \Delta a_j / a_j$ and inserting the above expressions into Eqns. (III.3.16) and (III.3.17) are given below. These two integral equations can be used to calculate the average strain field in the inclusion and coating of each family of coated inclusions due to a macroscopically applied strain.

$$\begin{aligned}\hat{\tilde{\varepsilon}}_{ij}^{I,\varsigma} = \tilde{E}_{ij} &- \hat{\tilde{T}}_{ijkl}^{I,\varsigma}\left(\hat{\tilde{\mathbf{C}}}^{0}\right)\Delta\hat{\tilde{C}}_{klmn}^{I0,\varsigma}\hat{\tilde{\varepsilon}}_{mn}^{I,\varsigma} \\ &- \frac{V_{C,\varsigma}}{V_{I,\varsigma}}\hat{\tilde{T}}_{ijkl}^{I,\varsigma}\left(\hat{\tilde{\mathbf{C}}}^{0}\right)\Delta\hat{\tilde{C}}_{klmn}^{C0,\varsigma}\hat{\tilde{T}}_{mnpq}^{I,\varsigma}\left(\hat{\tilde{\mathbf{C}}}^{C,\varsigma}\right)\Delta\hat{\tilde{C}}_{pqrs}^{IC,\varsigma}\hat{\tilde{\varepsilon}}_{rs}^{I,\varsigma} \\ &- \frac{V_{C,\varsigma}}{V_{I,\varsigma}}\left[\hat{\tilde{T}}_{ijkl}^{I,\varsigma}\left(\hat{\tilde{\mathbf{C}}}^{C,\varsigma}\right) - \hat{\tilde{T}}_{ijkl}^{I,\varsigma}\left(\hat{\tilde{\mathbf{C}}}^{0}\right)\right]\Delta\hat{\tilde{C}}_{klmn}^{IC,\varsigma}\hat{\tilde{\varepsilon}}_{mn}^{I,\varsigma}\end{aligned} \qquad \text{(III.3.23)}$$

$$\hat{\tilde{\varepsilon}}_{ij}^{C,\varsigma} = \hat{\tilde{\varepsilon}}_{ij}^{I,\varsigma} + \hat{\tilde{T}}_{ijkl}^{I,\varsigma}\left(\hat{\tilde{\mathbf{C}}}^{C,\varsigma}\right)\Delta\hat{\tilde{C}}_{klmn}^{IC,\varsigma}\hat{\tilde{\varepsilon}}_{mn}^{I,\varsigma} \qquad \text{(III.3.24)}$$

From these expressions it is now possible to move to the homogenization step and derive the SC model generalized using DSCT.

3.3.3 Homogenization and effective material properties

The next step in the derivation of the DSCT SC model requires the selection of a RVE. For the DSCT formulation of the SC model, the simplest visualization of the RVE has been given in Figure 3.4. This representation breaks the true RVE into *N* different RVE's each representing a coat inclusion family. In this case, each individual RVE is identical to that presented in Figure 3.3. The RVE consists of a single inclusion having

viscoelastic properties $\hat{\mathbf{C}}^{I,\varsigma}$ and occupying a fraction of the total volume $f^{I,\varsigma}$, coated by a different material with viscoelastic constants $\hat{\mathbf{C}}^{C,\varsigma}$ and which occupies a fraction of the total volume $f^{C,\varsigma}$. The coated inclusion is embedded in the effective infinite medium with viscoelastic rigidity tensor $\hat{\mathbf{C}}^{eff}$ which has been subjected to a time varying macroscopic strain represented by $\hat{E}_{ij}$. Further, as in Section 3.2.4, the following identity is noted for the sum of the volume fractions of all phases.

$$f^M + \sum_{\varsigma=1}^{N}\left(f^{I,\varsigma} + f^{C,\varsigma}\right) = 1 \qquad \text{(III.3.25)}$$

Now, the definitions of the macroscopic strain and stress given in Eqns. (III.2.63) and (III.2.64) can be modified for the *N* coated inclusion family case as shown below.

$$\hat{E}_{ij} = \frac{1}{V}\int_V \hat{\varepsilon}_{ij}(\mathbf{r})\,d\mathbf{r} = f^M\hat{\varepsilon}_{ij}^M + \sum_{\varsigma=1}^{N}\left(f^{I,\varsigma}\hat{\varepsilon}_{ij}^{I,\varsigma} + f^{C,\varsigma}\hat{\varepsilon}_{ij}^{C,\varsigma}\right) \qquad \text{(III.3.26)}$$

$$\hat{\Sigma}_{ij} = \frac{1}{V}\int_V \hat{\sigma}_{ij}(\mathbf{r})\,d\mathbf{r} = f^M\hat{\sigma}_{ij}^M + \sum_{\varsigma=1}^{N}\left(f^{I,\varsigma}\hat{\sigma}_{ij}^{I,\varsigma} + f^{C,\varsigma}\hat{\sigma}_{ij}^{C,\varsigma}\right) \qquad \text{(III.3.27)}$$

Where the strain and stress values on the right-hand side of the above equations denote the average value in their respective phase.

Next, the strain localization tensors for each phase are defined via the general expression (III.2.62). For the specific case studied here, equations relating the average strain in the inclusion and coating phase of each family are simply:

$$\hat{\varepsilon}_{ij}^{I,\varsigma} = \hat{A}_{ijkl}^{I,\varsigma}\hat{E}_{ij} \tag{III.3.28}$$

$$\hat{\varepsilon}_{ij}^{C,\varsigma} = \hat{A}_{ijkl}^{C,\varsigma}\hat{E}_{ij} \tag{III.3.29}$$

At this point, it is possible to express the average strain and stress fields in the matrix material. First, Eq. (III.3.26) and the strain localization relations above are employed yielding:

$$\hat{\varepsilon}_{ij}^{M} = \frac{1}{f^{M}}\left[I_{ijkl} - \sum_{\varsigma=1}^{N}\left(f^{I,\varsigma}\hat{A}_{ijkl}^{I,\varsigma} + f^{C,\varsigma}\hat{A}_{ijkl}^{C,\varsigma} \right) \right]\hat{E}_{kl} \tag{III.3.30}$$

Then by employing the local constitutive law, the average stress in the matrix is:

$$\hat{\sigma}_{ij}^{M} = \frac{1}{f^{M}}\hat{C}_{ijkl}^{M}\left[I_{klmn} - \sum_{\varsigma=1}^{N}\left(f^{I,\varsigma}\hat{A}_{klmn}^{I,\varsigma} + f^{C,\varsigma}\hat{A}_{klmn}^{C,\varsigma} \right) \right]\hat{E}_{mn} \tag{III.3.31}$$

The average stress in the matrix can also be deduced from the combination of Eq. (III.3.27), local constitutive laws, and strain localization equations of the form of Eq. (III.3.28). The result yields the following expression for the matrix stress.

$$\hat{\sigma}_{ij}^{M} = \frac{1}{f^{M}}\left[\hat{C}_{ijmn}^{eff} - \sum_{\varsigma=1}^{N}\left(f^{I,\varsigma}\hat{C}_{ijkl}^{I,\varsigma}\hat{A}_{klmn}^{I,\varsigma} + f^{C,\varsigma}\hat{C}_{ijkl}^{C,\varsigma}\hat{A}_{klmn}^{C,\varsigma} \right) \right]\hat{E}_{mn} \tag{III.3.32}$$

Setting Eqns. (III.3.31) and (III.3.32) equal and solving for the effective viscoelastic stiffness tensor yields the following expression.

$$\hat{\mathbf{C}}^{eff} = \hat{\mathbf{C}}^{M} + \sum_{\varsigma=1}^{N}\left[f^{I,\varsigma}\left(\hat{\mathbf{C}}^{I,\varsigma} - \hat{\mathbf{C}}^{M}\right) : \hat{\mathbf{A}}^{I,\varsigma} + f^{C,\varsigma}\left(\hat{\mathbf{C}}^{C,\varsigma} - \hat{\mathbf{C}}^{M}\right) : \hat{\mathbf{A}}^{C,\varsigma} \right] \quad \text{(III.3.33)}$$

This equation, coupled with the following expression for the strain localization tensors, is the DSCT form of the SC model, a generalization of the model originally derived by Cherkaoui *et al* [23].

The strain localization tensors for each phase are derived by rearranging Eqns. (III.3.23) and (III.3.24) in the form:

$$\hat{E}_{ij} = \left(\hat{A}^{X,\varsigma}_{ijkl}\right)^{-1} \hat{\varepsilon}^{X,\varsigma}_{kl} \quad \text{(III.3.34)}$$

where X can represent either the inclusion or the coating in each family. Also, the SC approximation requires that the reference material in all expressions be set equal to the effective medium. It is important to note that for each coated inclusion family the strain localization tensors derived from Eqns. (III.3.23) and (III.3.24) will yield expressions with respect to the local coordinate system of the ς^{th} coated inclusion family. In order to implement these localization tensors in Eq. (III.3.33) for correct calculation of the effective properties, it is therefore necessary to rotate the resulting tensor to the global coordinates. The local expressions of the strain localization tensors is given below

$$\left(\hat{\tilde{\mathbf{A}}}^{I,\varsigma}\right)^{-1} = \mathbf{I}_4 + \hat{\tilde{\mathbf{T}}}^{I,\varsigma}\left(\hat{\tilde{\mathbf{C}}}^{eff}\right) : \Delta\hat{\tilde{\mathbf{C}}}^{C,\varsigma} + \frac{f_{C,\varsigma}}{f_{I,\varsigma}}\hat{\tilde{\mathbf{T}}}^{I,\varsigma}\left(\hat{\tilde{\mathbf{C}}}^{eff}\right) : \Delta\hat{\tilde{\mathbf{C}}}^{C,\varsigma} : \hat{\tilde{\mathbf{T}}}^{I,\varsigma}\left(\hat{\tilde{\mathbf{C}}}^{C,\varsigma}\right) : \Delta\hat{\tilde{\mathbf{C}}}^{IC,\varsigma} + \frac{f_{C,\varsigma}}{f_{I,\varsigma}}\left[\hat{\tilde{\mathbf{T}}}^{I,\varsigma}\left(\hat{\tilde{\mathbf{C}}}^{C,\varsigma}\right) - \hat{\tilde{\mathbf{T}}}^{I,\varsigma}\left(\hat{\tilde{\mathbf{C}}}^{eff}\right)\right] : \Delta\hat{\tilde{\mathbf{C}}}^{IC,\varsigma} \tag{III.3.35}$$

$$\hat{\tilde{\mathbf{A}}}^{C,\varsigma} = \left(\mathbf{I}_4 + \hat{\tilde{\mathbf{T}}}^{I,\varsigma}\left(\hat{\tilde{\mathbf{C}}}^{C,\varsigma}\right) : \Delta\hat{\tilde{\mathbf{C}}}^{IC,\varsigma}\right) : \hat{\tilde{\mathbf{A}}}^{I,\varsigma} \tag{III.3.36}$$

Where $\Delta\hat{\mathbf{C}}^{X,\varsigma} = \hat{\mathbf{C}}^{X,\varsigma} - \hat{\mathbf{C}}^{eff}$ X representing either the inclusion or coating, and $\mathbf{I}_4$ is the fourth order identity tensor. The local expressions of the strain localization tensors given above are then rotated to the global system according to the Euler angles of the ς^{th} coated inclusion family as follows:

$$\hat{A}^{\chi,\varsigma}_{ijkl} = R^{\varsigma}_{im}R^{\varsigma}_{jn}R^{\varsigma}_{kp}R^{\varsigma}_{lq}\hat{\tilde{A}}^{\chi,\varsigma}_{nmpq} \tag{III.3.37}$$

Finally, as for the case base case of identical coated inclusions presented in Section 3.2.4, it is possible to calculate strain localization tensor for the matrix material. The expression for the DSCT case is given below in Eq. (III.3.38).

$$\hat{\mathbf{A}}^{M} = \frac{1}{1-\varphi}\left[\mathbf{I}_4 - \sum_{\varsigma=1}^{N}\left(f^{I,\varsigma}\hat{\mathbf{A}}^{I,\varsigma} + f^{C,\varsigma}\hat{\mathbf{A}}^{C,\varsigma}\right)\right] \tag{III.3.38}$$

Where φ is the total volume fraction of all coated inclusion families calculated from:

$$\varphi = \sum_{\varsigma=1}^{N} \left(f^{I,\varsigma} + f^{C,\varsigma} \right) \tag{III.3.39}$$

Equations (III.3.33), (III.3.35), and (III.3.36) constitute a generalized form of the quasi-static SC micromechanical model developed in Section 3.2 using DSCT. This generalized form of the SC model permits approximation of the effective elastic or viscoelastic properties for a wide variety of particulate composites. Indeed, the attractiveness of this formulation of the SC model is its flexibility to be employed in modeling the effective behavior for a wide variety of particulate composites including lossy composites. It presents an improvement in the static domain over the model as introduced by Cherkaoui *et al* [23, 24], and a vast improvement in the quasi-static domain for the approximation of lossy behavior over the scattering based models.

3.4 Chapter summary

This chapter successfully derived a quasi-static mean field micromechanical model describing the effective behavior of a viscoelastic matrix containing thinly coated inclusions. The model was then generalized using DSCT formulation to permit the approximation of materials with vastly different microstructures. Before employing this model in a materials design strategy, however, it is first necessary to verify its accuracy and robustness. The aim of the following chapter is to validate this model derived above in the quasi-static regime through two different methods. First, the model will be

compared to established bounds in the complex domain. This will ensure that the formulation of the model does not violate energy restrictions. Second, the model will be validated by comparing SC approximations against experimental data taken from the literature in both the static and quasi-static domain. Following this validation, Chapter V will investigate the feasibility of employing the SC model in a materials design strategy by solving an elementary multiscale materials design example employing the quasi-static SC model presented above.

CHAPTER IV

VALIDATION AND APPLICATION OF THE SELF-CONSISTENT MODEL IN THE QUASI-STATIC DOMAIN

4.1 Overview

The aim of this chapter is the validation and application of the SC model in the quasi-static regime. This will be accomplished in two steps. The first step is the comparison of the SC model with existing bounds for complex composite media. The complex bounding validation section begins with an introduction of complex bounding methods available in the literature. Following a detailed introduction, the SC is used to approximate the effective complex behavior of several different hypothetical composite media and the results are compared to accepted bounds. Agreement with existing bounds insures that the derived SC model does not violate basic physical laws. The second part of the SC model validation is done via parametric studies and comparison with experiment. That section begins by employing the general SC model to do parametric studies of the effective lossy behavior of viscoelastic composite materials containing oriented ellipsoidal inclusions. The transmission loss (TL) of a slab of a viscoelastic composite is calculated from the effective material behavior approximated using the general SC model. These results are then compared to experimental data and a SC single

scattering model of Baird, Kerr, and Townend (BKT) [26]. Following this analysis, DSCT SC model approximations are compared with experimental data for viscoelastic composite materials having varying orders of anisotropy, multiple inclusion types, multiple length scales, and varying coating thicknesses. All of the above steps will validate the use of the SC model in the quasi-static domain and will indicate the robustness of the DSCT formulation. Finally, the last section of this chapter discusses important numerical difficulties encountered and solution paths employed during implementation of the SC model.

4.2 Complex bounds and the self-consistent model

In order to properly frame the use of the SC model for such applications as quasi-static wave propagation problems, the issue of bounds must be addressed. Insight into the validity and optimality of any mean field model can be established by investigating the effective properties calculated with the model and comparing the results to well-established bounds [131]. Comparison with bounds has a two fold purpose. Bounds on the effective behavior of composite materials describe the limits of possible effective material properties due to minimal and maximal energy restrictions. They are dependent on constituent material properties, inclusion geometries, and the volume fractions of each phase. Disagreement with bounds invalidates a material model as it implies that physical laws have been violated during model derivation. Verification that a proposed effective medium theory (EMT) falls within accepted bounds is, therefore, a first order model check. The second purpose for comparison with bounds is to check model optimality.

Because bounds are derived based on upper and lower energy restrictions, the closer a model approximation lies upper or lower bounds, the closer that model is to describing optimal behavior due to composite composition, inclusion geometry, or both.

Bounding techniques for purely elastic materials (purely elastic meaning that no losses occur and all material properties are modeled as *real*) are well known; see, for example, Hashin & Shtrikman [132], Walpole [133], Hill [134, 135], and for a summary see Hashin [136]. It is well known that the *n*-phase SC model falls within accepted bounds in the purely elastic case [77]. There has been comparatively little work done on the bounds of the effective material properties of a composite with complex material properties. The subject of bounding the effective complex moduli of multiphase composites has been addressed in several papers starting with Hashin [17, 83, 84], Christensen [16], and Roscoe [137, 138]. Hashin's work proposes a method for calculating the effective complex moduli as a function in the frequency domain for elementary composites and only briefly mentions bounds which are restricted to very simple material mixtures. Christenson discusses the bounding problem, but restricts the discussion to the application of Hashin-Shtrikman (HS) bounds for a bi-phase viscoelastic matrix material containing either voids or rigid inclusions. Christenson's approach is simply the application of HS bounds to the real and imaginary parts of the effective moduli separately. Roscoe takes a similar approach to bounding effective viscoelastic behavior by applying the Voigt and Reuss bounds separately to the real and imaginary parts of a viscoelastic composite; the simplest and least restrictive complex bounding technique in the literature. These bounds were derived from variational principles expressing minimal and maximal strain energy in the viscoelastic composite,

but the interaction of the real and imaginary parts was not considered. Recent developments in bounding the effective behavior of complex composites are based on the variational techniques of Cherkaev and Gibiansky [139] (see also Milton [140] and Miller [141]) which couple contributions from the real and imaginary parts of the constitutive phases on the expressions for overall energy. Results based on this approach are detailed in series of related papers: Gibiansky & Milton [142], Milton & Berryman [143], Gibiansky & Lakes [144, 145], and Gibiansky & Torquato [146]. Many of the works referenced above were introduced for bounding the effective behavior of any complex composite medium including the effective electrical conductivity or viscoelastic moduli. The methods derived by the above authors bound the effective bulk and/or shear moduli of *bi-phase* viscoelastic composite in zones prescribed by arcs in the complex plane. These circular arcs are functions of the complex moduli of the constituent phases and the inclusion volume fraction. The variational approaches of the above authors are more restrictive than those proposed by Roscoe, Hashin, or Christensen because they relate the complex bounds of the effective moduli to the real *and* imaginary parts of the constituent phases. For the elastic case, all of these approaches reduce to the Hashin-Shtrikman bounds for an isotropic bi-phase composite.

All of the bounding methods introduced above have limitations, especially for application to the materials which are the subject of this thesis: composites containing coated ellipsoidal inclusions. The most relevant restrictions to the application of these bounds to the composites studied in this work concern the number of constituent phases in the composite and composite anisotropy. Applying bounds derived for purely elastic composites to the real and imaginary parts of a viscoelastic composite separately, as

proposed by Roscoe [137, 138] and Christenson [16], does not limit the resultant bounds to any specific number of constituent phases. However, the Reuss [61], Voigt [60], and HS [132] bounds require the constituent phases and the composite material to be isotropic. More importantly, the interaction between the real and imaginary parts, which are related by the principle of causality [147, 148], is neglected. The more restrictive bounds, which do take storage and loss moduli interactions into account, and are derived from the variational methods introduced by Cherkaev and Gibiansky are restricted to bi-phase composites and have the same problem as the aforementioned approaches of requiring both the constituent and effective materials be isotropic. Though these methods are limited in terms of the number of phases and material anisotropy, they are the most developed bounds to be found in the literature. The three most tractable approaches available (those of Roscoe [137, 138] and presented by Milton and Berryman [143] and Gibiansky and Lakes [144]) are summarized below and plotted together with SC model estimates.

4.2.1 Roscoe's complex bounds

The upper and lower bounds derived by Roscoe for a viscoelastic composite reduce to the application of Voigt and Reuss bounds separately to the real and imaginary parts of the composite [12]. These bounds provide the least restrictive limits of possible effective viscoelastic properties and can be calculated as a function of either inclusion volume fraction or frequency. Though these bounds are not restrictive they represent a good starting point for the validation of the SC model in the quasi-static domain.

The equations used to derive bounds proposed by Roscoe are analogous statements of the potential energy equations which are the basis of the extremum principles used to find the bounds for elastic composites, see Voigt [60] and Reuss [61]. The result of this analysis in the complex domain, see Appendix C, yields the bounds described by Equations (IV.2.1) and (IV.2.2) which are the weighted harmonic average and weighted average of the constituent phase properties, respectively.

$$\mu_{RL}^{*} = \left(\sum_{r} \frac{f_r}{\mu_r^{*}} \right)^{-1} \qquad \kappa_{RL}^{*} = \left(\sum_{r} \frac{f_r}{\kappa_r^{*}} \right)^{-1} \tag{IV.2.1}$$

$$\mu_{RU}^{*} = \sum_{r} f_r \mu_r^{*} \qquad \kappa_{RU}^{*} = \sum_{r} f_r \kappa_r^{*} \tag{IV.2.2}$$

In the above relationships, *RL* and *RU* denote the lower and upper bounds derived by Roscoe and are analogous to the Reuss and Voigt bounds, respectively. It is now important to note that due to energy considerations the following is true:

$$\begin{aligned} \mu_{RU}^{*} &\geq \mu_{eff}^{*} \quad \kappa_{RU}^{*} \geq \kappa_{eff}^{*} \\ j_{RL}^{*} &\geq j_{eff}^{*} \quad l_{RL}^{*} \geq l_{eff}^{*} \end{aligned} \tag{IV.2.3}$$

An important aspect of these bounds is their lack of restrictions with respect to the frequency inspected, the total number of constituent viscoelastic phases, *r*, or the total

volume fraction, φ. This logic leads to the following restrictions on the possible values for the effective viscoelastic moduli:

$$\begin{aligned} \mu'''_{RL}(\omega,\varphi) \le \mu'''_{eff}(\omega,\varphi) \le \mu'''_{RU}(\omega,\varphi) \\ \kappa'''_{RL}(\omega,\varphi) \le \kappa'''_{eff}(\omega,\varphi) \le \kappa'''_{RU}(\omega,\varphi) \end{aligned} \qquad \text{(IV.2.4)}$$

where ω is the frequency of interest. It is also useful to note that $f_{matrix} = 1 - \varphi$.

At this stage the quasi-static SC model to the will be compared to the simple bounds proposed by Roscoe and summarized above. This is achieved through two different comparisons. First, the approximations from the quasi-static SC model are compared to the upper and lower bounds for a fixed frequency while the coated inclusion volume fraction is varied from 0 to 1 for a hypothetical viscoelastic composite created from the materials studied by Baird *et al* [26]. Then the frequency dependent SC model approximation for a viscoelastic composite having fixed volume fraction will be compared the same bounds. The constituent material properties that will be employed for these studies are repeated, for convenience, in Table 4.1.

Table 4.1: Constituent material properties of the viscoelastic composites studied by Baird *et al* [26].

		"Soft" Polymer	*"Stiff" Polymer*
Bulk modulus of matrix (Pa):	K^M	3×10^9	3×10^9
Density of matrix (kg/m^3):	ρ^M	935	1090
Dynamic shear modulus coefficients:	A_0	5.93978	6.675 69
	A_1	2.6618×10^{-1}	3.954×10^{-2}
	A_2	-3.613×10^{-2}	9.39×10^{-3}
	A_3	4.1×10^{-3}	3.85×10^{-3}
Dynamic loss factor coefficients:	B_0	5.251×10^{-2}	9.792×10^{-2}
	B_1	1.9374×10^{-1}	5.9×10^{-4}
	B_2	-6.209×10^{-2}	6.89×10^{-2}
	B_3	8.19×10^{-3}	-9.25×10^{-3}
Bulk Modulus of coating (Pa):	K^C	2.1×10^9	2.1×10^9
Density of coating (kg/m^3):	ρ^C	1700	1700
Shear Modulus of coating (Pa):	μ^C	1.26×10^9	1.26×10^9
Loss factor of coating:	η^C	0.1	0.1
Bulk modulus of air at 1 atm (Pa):	K^I	1.4×10^5	1.4×10^5
Density of air at 1 atm (kg/m^3):	ρ^I	1.28	1.28
Average coating fraction:	ε	2.5 e 10^{-2}	2.5 e 10^{-2}
Average outer shell radius:	b	5×10^{-5}	5×10^{-5}

The frequency dependent shear modulus of each matrix material detailed in the above table is approximated through Eqns. (IV.2.5) – (IV.2.7) and the above information.

$$\log \mu_M^R = A_0 + A_1 \log f + A_2 (\log f)^2 + A_3 (\log f)^3 \qquad \text{(IV.2.5)}$$

$$\delta_M = B_0 + B_1 \log f + B_2 (\log f)^2 + B_3 (\log f)^3 \qquad \text{(IV.2.6)}$$

$$\mu_M(f) = \mu_M^R (1 - i \tan \delta_M) \qquad \text{(IV.2.7)}$$

These equations and coefficients were found by fitting experimental data obtained from a Dynamic Mechanical Thermal Analyzer (DMTA) [26].

The results of the two studies comparing the quasi-static SC model approximation to the elementary bounds proposed by Roscoe are given below in Figure 4.1 - Figure 4.4. The matrix material is the "soft" material given in Table 4.1.

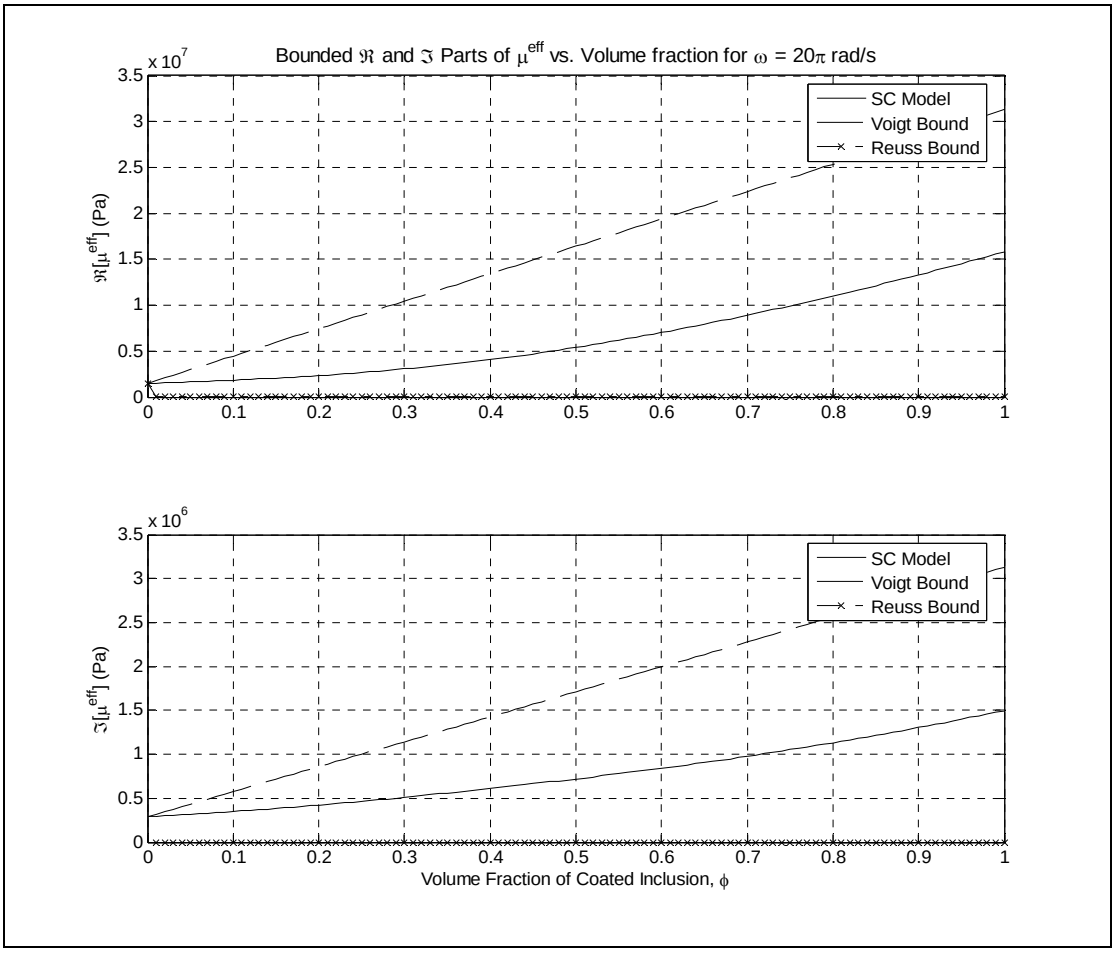

Figure 4.1: Real and imaginary parts of the effective shear modulus as function of coated inclusion volume fraction for a fixed frequency. SC model approximation shown with the upper and lower bounds proposed by Roscoe. (Lower bound of imaginary part is zero everywhere).

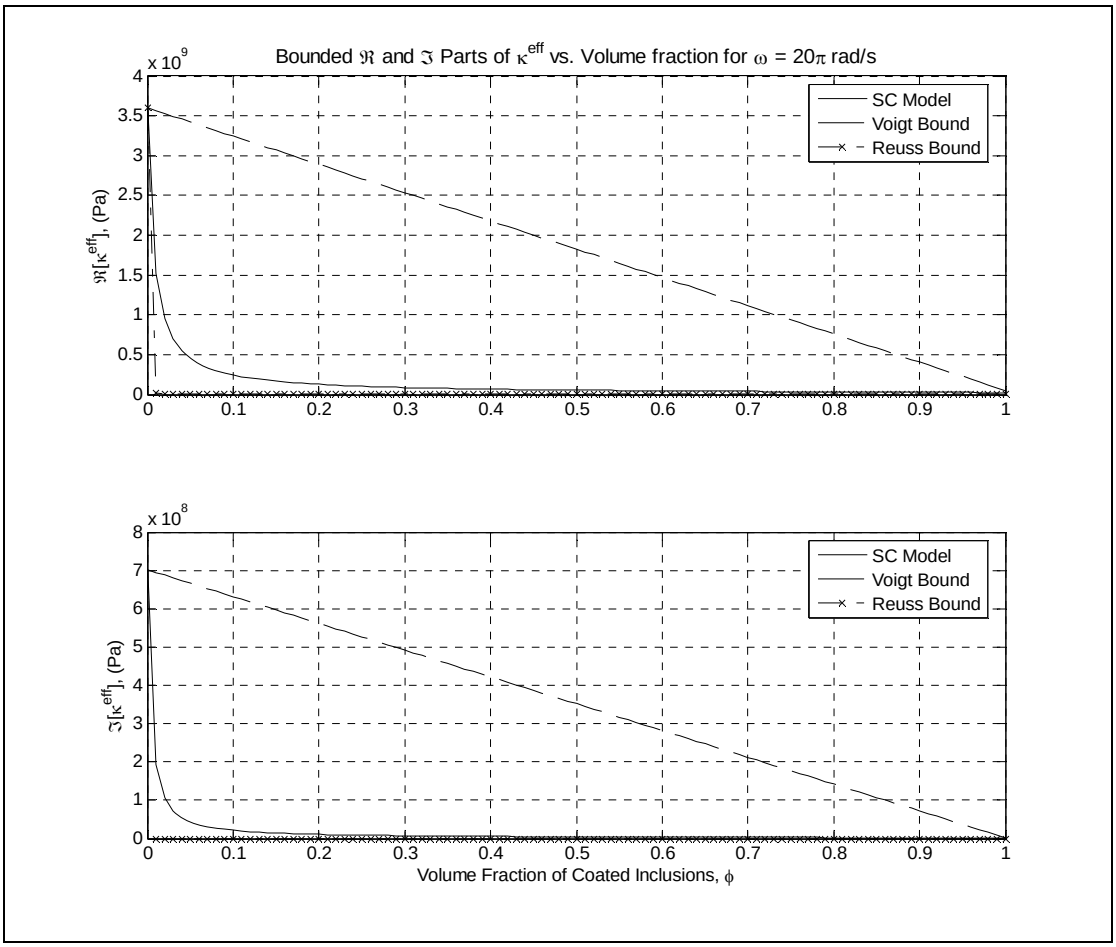

Figure 4.2: Real and imaginary parts of the effective bulk modulus as a function of coated inclusion volume fraction for a fixed frequency. SC model approximation shown with the upper and lower bounds proposed by Roscoe. (Lower bound of imaginary part is zero everywhere).

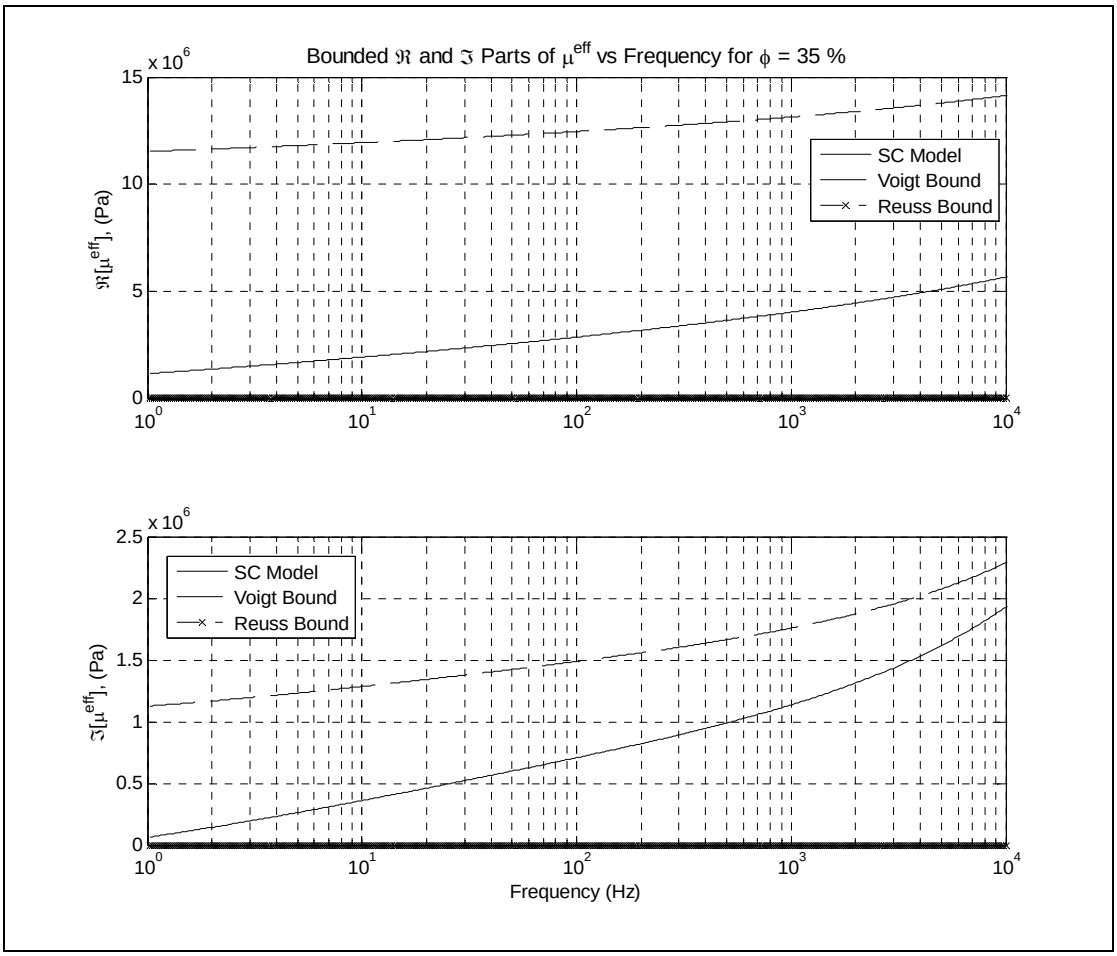

Figure 4.3: Real and imaginary parts of the effective shear modulus as a function of frequency for a fixed coated inclusion volume fraction. SC model approximation shown with the upper and lower bounds proposed by Roscoe. (Lower bound of imaginary part is zero everywhere).

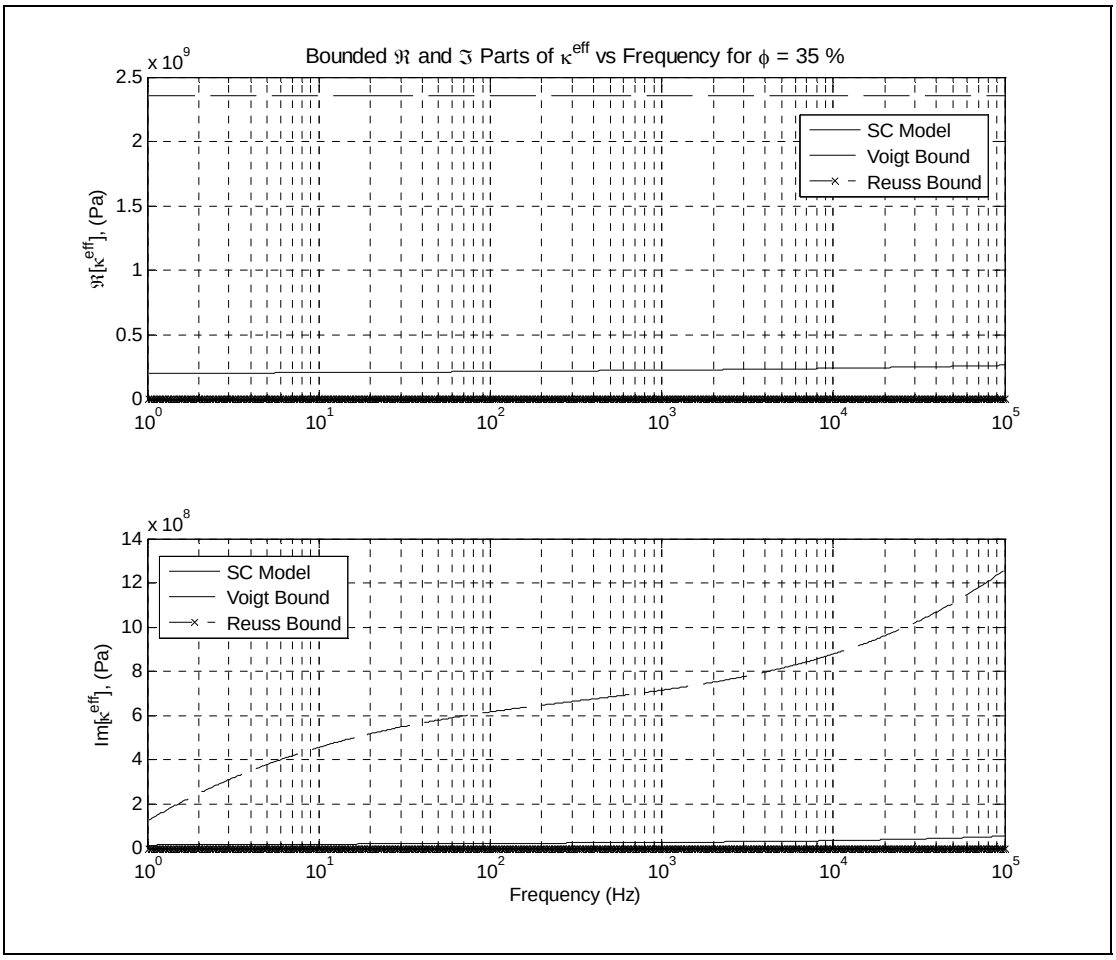

Figure 4.4: Real and imaginary parts of the effective bulk modulus as a function of frequency for a fixed coated inclusion volume fraction. SC model approximation shown with the upper and lower bounds proposed by Roscoe. (Lower bound of imaginary part is zero everywhere).

The plots above clearly show that the SC model falls within Roscoe's bounds for viscoelastic composites as a function of both frequency and coated inclusion volume fraction. Though the study was far from exhaustive and not a direct proof, the plots suggest that no physical laws have been violated during the derivation of the quasi-static model. These observations are encouraging; however, since Roscoe's bounds are the least restrictive, it is prudent to compare the SC model against more restrictive bounds. The bounds chosen for this analysis are the shear and bulk bounds for bi-phase

viscoelastic composites derived by Milton and Berryman [143] and Gibiansky and Lakes [144], respectively.

4.2.2 Complex bounds using variational and translational techniques

The two bounding techniques described in this section stem from the complementary works of Milton [140] and Cherkaev and Gibiansky [139]. The objective of their work was to simplify the algebraic calculations required to find the bounds for complex valued effective material properties resulting from heterogeneous media. This is done via a fractional-linear *Y*-transformation [146]. These methods were derived for any complex valued material property whose fields are dissipative and time varying. The resulting bounds can therefore be applied to physical properties as disparate as electrical conductivity and viscoelasticity. Using complex valued expressions of Hooke's law and strain energy density, Cherkaev and Gibiansky [139] formulated four different min-max variational principles. These principles lead to rigorous bounds for the effective viscoelastic moduli of a bi-phase composite material. This approach inspects a bi-phase viscoelastic composite at a fixed inclusion volume fraction and prescribes a zone in the complex modulus plane which bounds the set of permissible values describing effective material behavior. Their results yield coupled bounds. Coupled bounds restrict the effective complex valued moduli based on functions of both the real *and* imaginary parts of the constituent phase moduli. Gibiansky and Lakes employed this approach to find the bounds on the effective viscoelastic bulk modulus [144]. Those bounds are defined by four arcs that intercept each other at two points in the complex plane. The outer-most of

those four arcs define the limits of permissible effective complex bulk modulus values of a bi-phase viscoelastic composite. The approach derived by Milton and Berryman [143] to find bounds on the effective shear modulus is similar in its derivation and also based wholly on the work of Cherkaev and Gibiansky [139] and Milton [140]. Both of these bounding approaches, which are summarized in Appendix C, are restricted to the following cases: (*i*) bi-phase viscoelastic composites, (*ii*) isotropic behavior of both the composite and constituent phases, and (*iii*) calculation of bounds for a *single* frequency and a *single* volume fraction. These restrictions limit quasi-static SC model validation. The third restriction is the most limiting for the inspection of a wide range of material compositions and exciting frequencies. These restrictions illustrate why these methods do not easily lend themselves to inspect the validity of an effective medium theory as a function of either volume fraction or frequency. Bounds based on these variational techniques are, however, the most rigorous available. Therefore, despite these limitations, it is valuable to check SC model approximations against these bounds. The following sub-sections employ the bounds described in Appendix C and plot the bounds together with the quasi-static SC approximation. This analysis provides further validation of the SC model in the quasi-static frequency domain.

4.2.2.1 Complex bounds on the bulk modulus of bi-phase media

The bounds for the bulk modulus derived by Gibiansky and Lakes [144] are defined for a bi-phase viscoelastic composite material. The composite's composition is defined by a phase *1* which occupies volume fraction *f* and its complex bulk and shear

moduli are represented as κ_1 and μ_1, respectively. Conversely, phase *2* occupies a volume fraction $(1-f)$ and its bulk and shear moduli are represented as κ_2 and μ_2, respectively. The effective complex valued bulk modulus of the isotropic viscoelastic composite will be constrained to a "lens-shaped" region in the complex bulk modulus plane that is bounded by the outer-most pair of four circular arcs each of which correspond to the four min-max variational principles proposed by Cherkaev and Gibiansky [139] and Milton [140]. To illustrate their bounds, Gibiansky and Lakes presented a hypothetical viscoelastic comsposite material having constituent material properties defined in whose composition and constituent material properties are defined in Table 4.2. Figure 4.5 shows that the bi-phase isotropic SC model falls within the bulk modulus bounds calculated using the relations of Appendix C.

Table 4.2: viscoelastic composite composition and constituent material properties for hypothetical material presented by Gibiansky and Lakes [144].

	f	μ_1	K_1	μ_2	K_2
Figure 4.5	50%	$40 + 0i$	$100 + 0i$	$0 + 30i$	$0 + 65i$

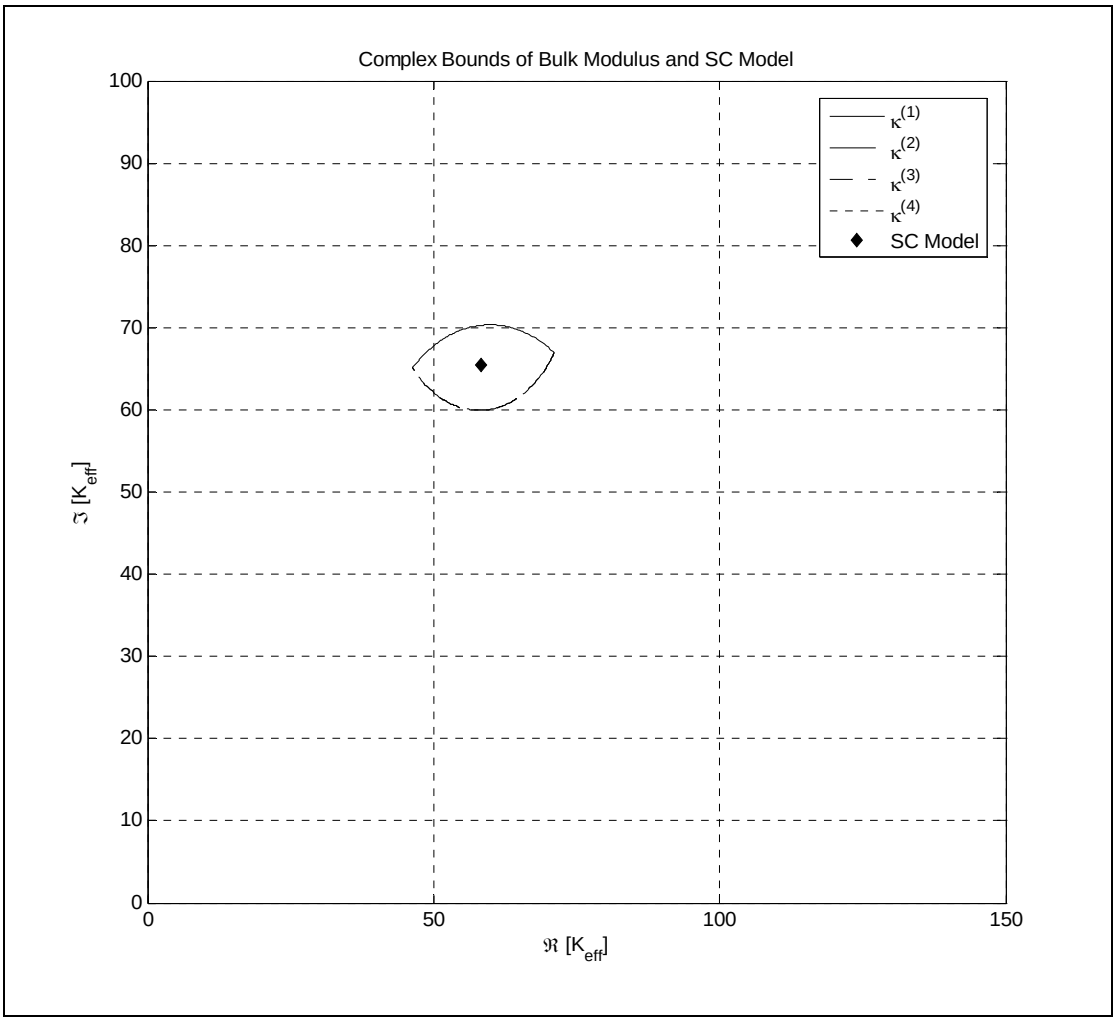

Figure 4.5: Bounds in the complex bulk modulus plane calculated from reference [144] and SC model approximation of the same composite. Bounds are delineated by four, sometimes overlapping, lines: $\kappa^{(1\text{-}4)}$.

4.2.2.2 Complex bounds on the shear modulus of bi-phase media

The bounds on the effective complex shear modulus derived by Milton and Berryman [143] are also based on the four variational principles and the *Y*-transform introduced by Cherkaev and Gibiansky [139] and Milton [140]. Their results yield arcs in the complex modulus plane which define the limits of permissible effective complex shear modulus values of a bi-phase viscoelastic composite. The bounds are best

described by an algorithm in reference [143] which is summarized in Appendix C for convenience. It must be noted that difficulties can arise in calculating these bounds because some factors may be driven to infinity while the final result is always finite. Further, these bounds are sometimes not completely closed, and tangent lines must be drawn to close the bounds. These complications make the process arduous and less than ideal for an exhaustive evaluation of model validity as a function of frequency or volume fraction, or both. Despite these difficulties, the comparison shown in Figure 4.6 of the quasi-static SC model and these bounds using constituent properties defined in given in Table 4.3 shows good agreement and further suggests that the application of the SC model in the quasi-static regime is valid.

Table 4.3: Material properties used to evaluate the complex bounds shown and SC model point in

f	μ_1	K_1	μ_2	K_2
50%	$0.5 + 0.866i$	$0.66 + 0.33i$	$1 + 1.732i$	$1.33 + 0.833i$

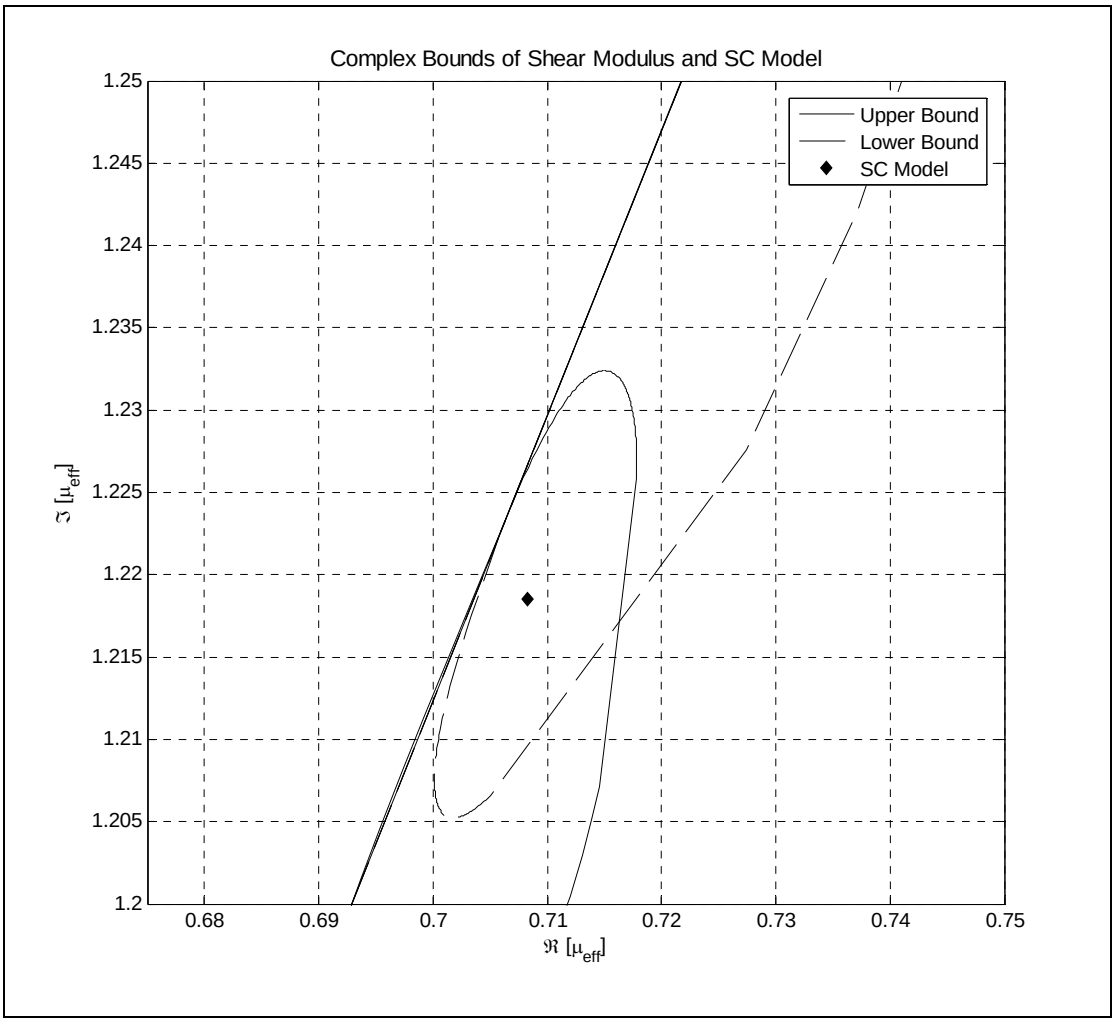

Figure 4.6: Bounds on the complex effective shear modulus given in reference [143]. Calculated SC model point is shown to fall within ellipsoidal bounded area.

4.3 Validation of the general SC model in the quasi-static domain

The previous section serves as a fundamental check of the quasi-static SC modeling approach. The fact that the SC model was shown to fall within accepted complex bounds proves that no physical laws were violated in the derivation of the model and that it is, therefore, a valid homogenization method in the quasi-static domain. Though model validation against complex bounds is very important, it yields little

information about the precision and versatility of the SC model. The purpose of this section is, therefore, to investigate the SC model for more specific information about its capacity to model the effective behavior of various viscoelastic composite materials. This information will be gathered through two methods: comparison with experiment and parametric studies. Specifically, the SC model precision will be investigated by comparing model results with experimental data and the versatility will be validated though a series of parametric studies. These two approaches will provide a clear picture of SC model precision and its adaptability to model many different types of viscoelastic composites.

4.3.1 Elementary validation of quasi-static SC model

The fundamentals detailed in Chapter II indicate that the effective lossy behavior of a viscoelastic composite in the quasi-static domain is intimately related to the strain energy in its lossy components. To illustrate this point, the increase in strain energy in the "matrix" material of a voided composite sphere was given as an example. The present section generalizes the voided sphere concept to the case of an isotropic voided viscoelastic material. The elementary parametric studies below will show trends of the effective behavior of the voided viscoelastic material as calculated by the SC model. The relationship of interest is between the composite's macroscopic lossy behavior and the void fraction. The goal of this simple study is to provide a first order validation of the quasi-static SC model by showing that the trends calculated with the SC model are in

accordance with expectations. This analysis will serve as the starting point for SC model validation in the quasi-static domain.

The viscoelastic composite studied is a hypothetical material resulting from the introduction of spherical voids in a matrix of the "soft" polymer matrix material studied by Baird *et al* [26]. The properties of the matrix (together with other material properties which will be important in examples following this one) were given by Baird *et al* and have been repeated in Table 4.1 in the previous section.

The fundamentals of the frequency dependent behavior of voided viscoelastic materials is well understood (see, for example, Jarzynski [15]). The three following trends are expected: (*i*) a decrease in the elastic moduli of the material, $\mathbf{C}_v$, with increasing void fraction, φ, (*ii*) an increased damping capacity with increasing frequency, and (*iii*) an increased damping capacity with increasing void fraction. The first trend is the result of removing material and thereby weakening the resistance of the whole to deformation. Figure 4.7 clearly shows that the SC model correctly approximates this trend across all frequencies inspected.

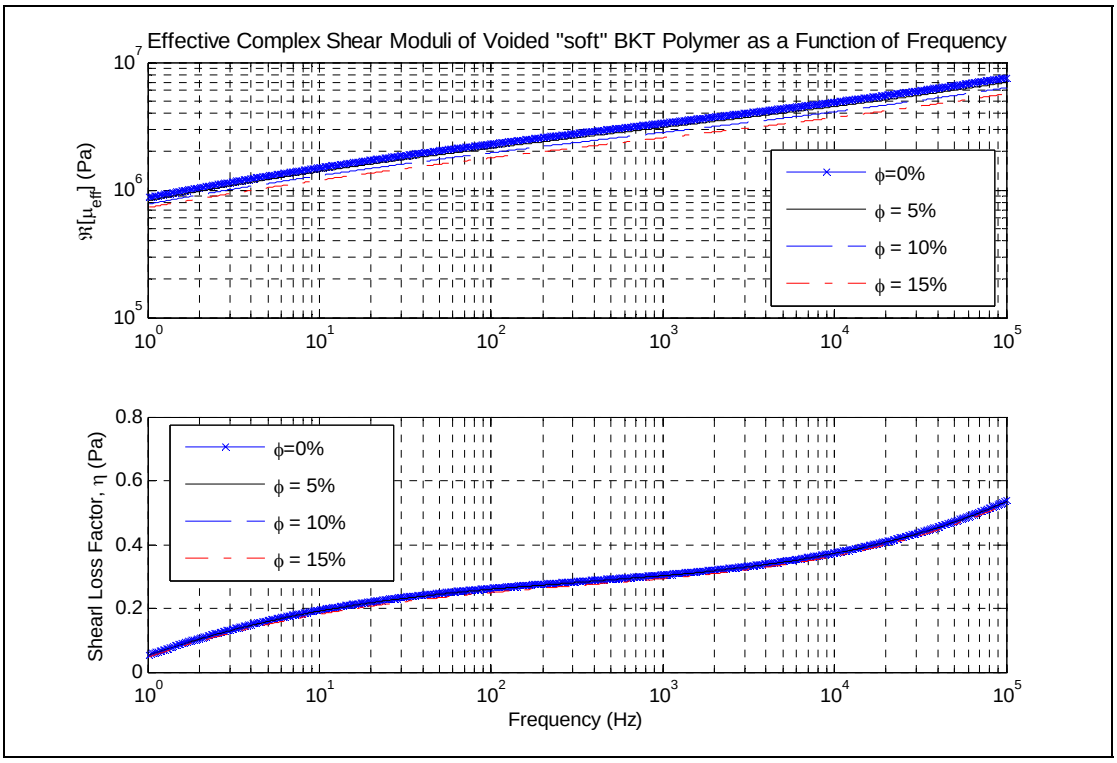

Figure 4.7: Effective complex shear modulus of a voided viscoelastic material as a function of frequency. The pure matrix response is shown together with three differnent values of void fraction.

The second trend, an increase in lossy behavior with increasing frequency, is independent of the void fraction and is simply due to constitutive material behavior. Increasing the frequency of an applied load increases the characteristic phase lag between the load and the resulting strain. This increases the area of the hysteresis loop in stress-strain space (see Section 2.1.1). It is very important to note that this is *not true for all materials at all frequencies* [149]. Typical characteristics of the frequency dependant complex shear modulus are shown below in Figure 4.8. The figure clearly shows that both the storage and loss modulus are strongly frequency dependent and that the monotonic increase in damping capacity as a function of frequency is only true for $0 < f < f_{crit}$. However, for the materials and frequency range used in this example, the damping capacity will increase monotonically as a function of frequency. The ability of the SC model to

correctly capture this behavior regardless of the void fraction is clearly shown in Figure 4.10.

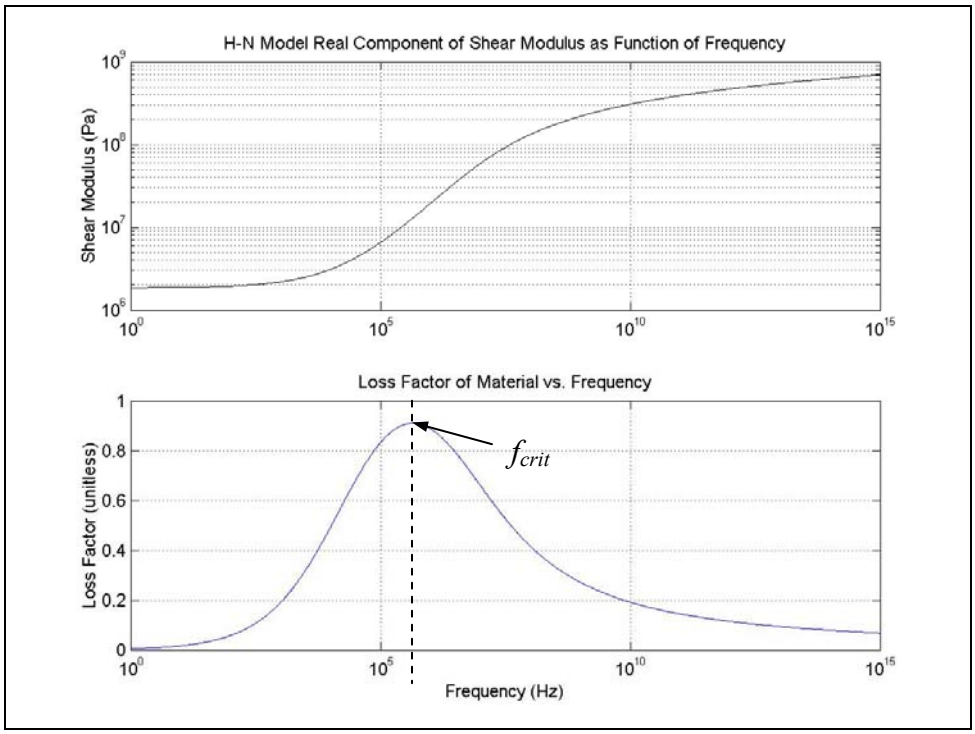

Figure 4.8: General characteristics of the frequency dependent shear modulus of viscoelastic. The modulus is approximated by the Havriliak-Negami model [128]. Damping capacity of the viscoelastic material is a monotonically increasing function of frequency for $0 < f < f_{crit}$.

The third trend, an increase in damping capacity with increasing void fraction, can be explained from two different points of view. The first is within the framework of wave scattering. As frequency increases, the relative size of voids with respect to the wavelength of traveling waves increases (the non-dimensional number, *ka*, increases). This "increase" in void size leads to more efficient reflection, re-direction, and mode conversion (scattering) of an incident wave by voids in the material and thus creates more wave-fronts which are attenuated by the host material. The ultimate result is an increase in the absorptive quality of the material. Incidentally, this argument is the same used by

Lord Rayleigh to explain why the sky is blue: blue light, having a short wavelength compared to the rest of the visible spectrum, is more efficiently scattered by particles in the air. His fundamental work in the area of wave scattering is also the reason that simple low frequency (low *ka*) scattering models are called Rayleigh scattering models. The increase in damping capacity with increasing void fraction can also be explained from the perspective of strain energy. The time varying specific strain energy (strain energy per unit volume) and specific complementary strain energy in any material can be calculated from Eq. (IV.3.1).

$$\hat{w} = \frac{1}{2}\hat{\sigma}_{ij}\hat{\varepsilon}_{ij} = \begin{cases} (1/2)\hat{\sigma}_{ij}\hat{J}_{ijkl}\hat{\sigma}_{kl} \\ (1/2)\hat{\varepsilon}_{ij}\hat{C}_{ijkl}\hat{\varepsilon}_{kl} \end{cases} \qquad \text{(IV.3.1)}$$

In the above equation $\hat{w}$ represents the specific strain energy, $\hat{\sigma}_{ij}$ the applied stress, $\hat{\varepsilon}_{ij}$ the strain, and $\hat{\mathbf{J}}$ is the compliance tensor which is the inverse of the stiffness tensor, $\hat{\mathbf{C}}$. For a propagating wave or a time-varying applied stress having a known magnitude the strain energy should be calculated with the relation $2\hat{w} = \hat{\sigma}_{ij}\hat{J}_{ijkl}\hat{\sigma}_{kl}$. As previously stated, increasing void fraction of any material leads to a decrease in the elastic constants and conversely to an *increase* in the compliance of the effective material. It is clear from this expression that for a given applied stress level an increase in the magnitude of the material's compliance translates to an increase in the specific strain energy in the effective material. Further, since voids cannot carry any load, this increase in strain energy is concentrated in the viscoelastic host material. Chapter II illustrated that an increase in strain energy of lossy materials leads to an increase in the total energy

absorbed. Figure 4.9 below illustrates the ability of the SC model to correctly approximate this expected physical behavior. The plot shows the ratio of the specific strain energy in the voided material to that in a homogeneous material for the same applied shear strain, τ. The plot clearly shows that the SC model correctly captures the increase in specific strain energy for all frequencies as the void fraction is increased.

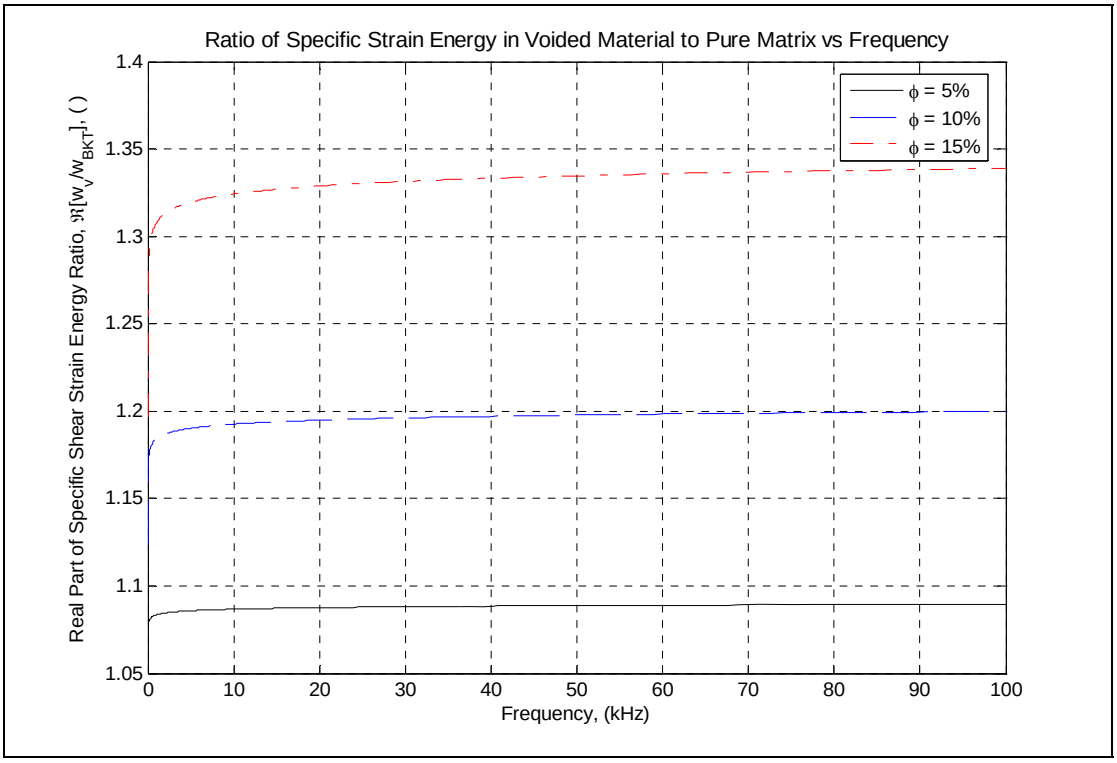

Figure 4.9: Increase in the specific strain energy of voided composites due to pure shear loading. The ratio shown is the ratio of the specific strain energy in a voided composite to the strain energy in a homogeneous material submitted to the same shear stress.

The result of the increase of strain energy in the lossy matrix material shown above is an increase in the macroscopic damping capacity of the composite. Evidence of the increase in the damping capacity is best captured through parametric studies of the attenuation coefficient of shear and longitudinal waves. The attenuation coefficient is the

imaginary part of the complex wave number and is a measure of the decay rate for a wave propagating in a medium with lossy properties. Recalling Eqs. (II.1.20) and (II.1.21), the attenuation coefficients for longitudinal and shear waves propagating in the voided polymer given here are found from the two expressions below.

$$\hat{k}_{\mu}^{*} = \omega\sqrt{\frac{\rho}{\mu^{eff}}} = \hat{k}_{\mu}^{'} + i\hat{\alpha}_{\mu} \quad \Rightarrow \quad \hat{p}_{\mu}(x,t) = \hat{A}e^{-\alpha_{\mu}x}e^{-i\left(\omega t - k_{\mu}^{'}x\right)}$$

$$\hat{k}_{L} = \omega\sqrt{\frac{\rho}{\hat{\lambda}^{eff} + 2\hat{\mu}^{eff}}} = \hat{k}_{L}^{'} + i\hat{\alpha}_{L} \quad \Rightarrow \quad \hat{p}_{L}(x,t) = \hat{B}e^{-\alpha_{L}x}e^{-i\left(\omega t - k_{L}^{'}x\right)} \tag{IV.3.2}$$

These equations show clearly that an increase in the magnitude of the attenuation coefficient leads directly to an increase in the attenuation of the propagating wave. Figure 4.10 shows that the SC model captures the increase in lossy behavior of a voided polymer both with increasing void fraction and increasing frequency. This parametric study further validates SC model use for approximating the effective lossy properties of viscoelastic composites.

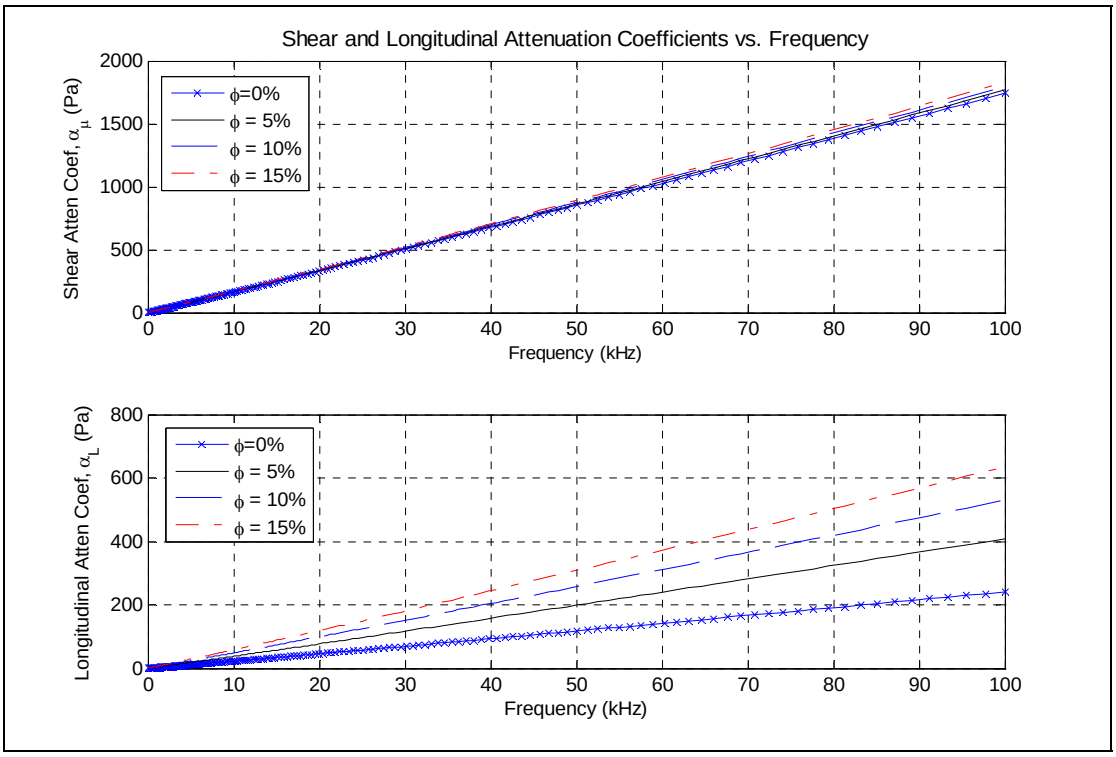

Figure 4.10: Attenuation coefficients for the propagation of shear and longitudinal waves in a pure polymer compared with the effective behavior of three different voided composites approximated by the SC model.

One very important observation about Figure 4.7 and Figure 4.10 is that the increasing lossy behavior is due to the softening of the material caused by introducing voids. This softening is best indicated by an increase in the magnitude of the compliance tensor. Given the case of an imposed stress, $\boldsymbol{\sigma}$, which is the case for a propagating wave, the strain energy will increase in the lossy component and, as a direct result, the overall damping capacity of the material will be increased. This is further illustrated by examining the increase in the inverted shear and longitudinal moduli shown in Figure 4.11 below.

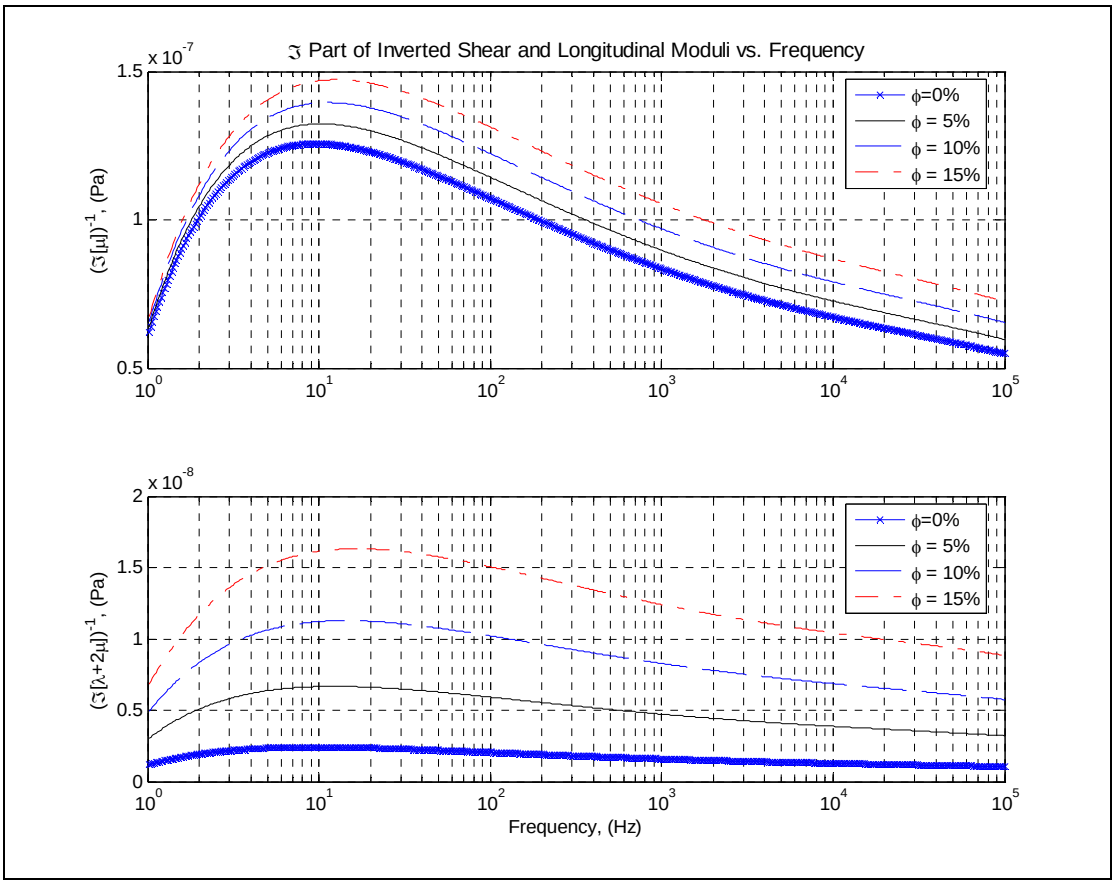

Figure 4.11: The imaginary part of the inverted shear and longitudinal moduli of a pure polymer compared with the effective behavior of three different voided composites as approximated by the SC model.

It is also important to specify that an increase in lossy properties for the case of an imposed stress (such as a propagating wave) is the result of a softening of a host material by introduction of voids and, to a lesser extent, coated inclusions having less resistance to deformation than the matrix material. However, the opposite is true for the case of an imposed time-varying strain. An increase in the overall lossy behavior of the composite will result from the reinforcement of a lossy host, thereby increasing the strain energy present in all constituent materials ($2\hat{w} = \hat{\varepsilon}_{ij}\hat{C}_{ijkl}\hat{\varepsilon}_{kl}$). *The true measure of the pure damping capacity of a composite material is therefore not its stiffness tensor loss factor, but rather the magnitude of the imaginary part of the tensor directly related to the*

loading in question. When the real part of the stiffness or compliance tensor in question does not change, then the increase of the corresponding loss factor is the important measure of the damping capacity of the composite. For the case of waves propagating in a material (representing an imposed stress), the best measure of damping capacity is the imaginary part of the effective compliance tensor and related terms. The following section presents a measure related to the compliance of a composite material, the Transmission Loss (TL). SC estimates of the effective complex moduli for a composite consisting of a viscoelastic matrix containing coated micro-inclusions are compared with Baird *et al*'s experimental data [26] and parametric studies of inclusion geometry and orientation are given.

4.3.2 Comparison of modeling results with experimental TL data: Oriented ellipsoidal inclusions

The following quasi-static SC model verification is a sound isolation application. SC model estimates of the effective complex moduli of a viscoelastic composite are used to calculate the TL of a material layer as a function of frequency. The SC estimates of the TL are compared to experimental data and the low *ka* scattering model of Baird *et al* [26]. Following this comparison, parametric studies of the inclusion geometry effects on the spatial dependence of composite material lossy properties are presented in order to explore SC model strengths.

The following short analysis details how the TL of a slab of viscoelastic composite material is calculated from the effective material properties. TL is a measure

of the sound isolation provided by an obstruction between a sound source and receiver. Specifically, TL is the ratio the energy of the incident wave to the energy transmitted through the obstruction (in this case the material layer) [12]. For the following analysis, normal incidence is assumed because it represents is the worst case (TL increases as a function of angle of incidence). By assuming normal incidence of a plane wave on the submerged composite material layer, the magnitude of the incident, reflected, and transmitted pressures can be calculated by using continuity of pressure and velocity at the two water-composite interfaces ($x_3 = 0$ and $x_3 = L$).

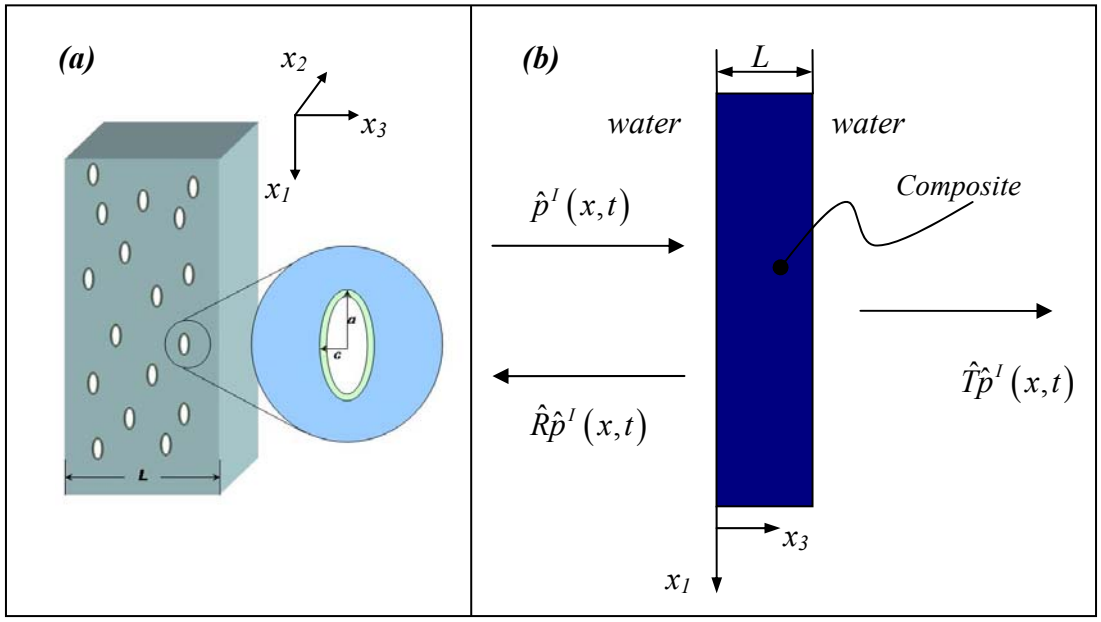

Figure 4.12: (a) Representation of viscoelastic matrix containing identically oriented ellipsoidal inclusions. (b) Incident, reflected, and transmitted plane-wave visualization used to calculate the TL of the composite material layer.

In the figure above, $\hat{p}^I$ is the magnitude of the incident pressure, $\hat{R}$ is the reflection coefficient, $\hat{T}$ is the transmission coefficient, L is the thickness of the composite, and a and c represent the major and minor axes of the oriented oblate coated inclusions.

Consider an isotropic fluid medium of density ρ and sound speed c in which an acoustic plane wave of the form $e^{i(kx_3-\omega t)}$ is normally incident on an infinitely long slab of thickness L, as shown in Figure 4.12b. The composite is composed of a viscoelastic matrix material described by the complex Lamé constants, $\hat{\lambda}_M$, $\hat{\mu}_M$ and density ρ_M and containing coated ellipsoidal inclusions. This initial study considers the orthotropic case of a slab containing oblate spheroidal inclusions all oriented such that their minor axes are along the x_3 direction of propagation. The inclusions are defined by their Lamé constants $\hat{\lambda}_I$, $\hat{\mu}_I$ and density ρ_I, and the coating by $\hat{\lambda}_C$, $\hat{\mu}_C$ and density ρ_C. The coating has a thickness Δa where $\Delta a/a$ assumed to be much less than unity. Further, it is assumed that $\Delta a/a = \Delta c/c$. In the quasi-static case, $ka << 1$, it is reasonable to model the composite as a homogeneous material defined by its complex effective elastic stiffness tensor $\hat{\mathbf{C}}^{eff}$. For plane wave transmission through the slab submerged in water along the x_3 axis, the TL, in decibels, is defined in terms of the transmission coefficient $\hat{T}$ by [50] :

$$TL = -10\log_{10}(\hat{T}\hat{T}^*) \tag{IV.3.3}$$

with

$$\hat{T} = 2\left[2\cos(\hat{k}_{33}^{eff}L) - i\left(\frac{\hat{Z}_{33}^{eff}}{(\rho c)^{water}} + \frac{(\rho c)^{water}}{\hat{Z}_{33}^{eff}}\right)\sin(\hat{k}_{33}^{eff}L)\right]^{-1} \tag{IV.3.4}$$

where the effective wavenumber in the x_3 direction is given by

$$\hat{k}_{33}^{eff} = \omega\sqrt{\frac{\rho^{eff}}{\hat{M}^{eff}}} = \hat{k}_{33}^{',eff} + i\hat{\alpha}_{33}^{eff} \tag{IV.3.5}$$

The effective density and impedance of the composite are, respectively,

$$\rho^{eff} = \rho^{M} - \phi\left[\rho^{M} - \rho^{C}\left(3\frac{\Delta a}{a}\right) - \rho^{I}\left(1 - 3\frac{\Delta a}{a}\right)\right] \tag{IV.3.6}$$

and

$$\hat{Z}_{33}^{eff} = \rho^{eff}\hat{c}_{33}^{eff} = \sqrt{\hat{M}^{eff}\rho^{eff}} \tag{IV.3.7}$$

In the above equations, $\hat{M}^{eff} = \hat{C}_{33}^{eff}$ is the complex plane wave modulus of the material in the direction of wave propagation, $\hat{c}_{33}^{eff}$ is the longitudinal phase velocity in the x_3 direction, $\hat{\alpha}_{33}^{eff}$ is the longitudinal wave amplitude attenuation coefficient in the x_3 direction, ϕ is the volume fraction of coated inclusions, $(\rho c)^{water}$ is the specific acoustic impedance of water and is known to be 1.5x10^6 Rayl, and the asterisk denotes the complex conjugate.

It was previously shown that micromechanical models can be used to approximate the global dynamic behavior of isotropic three phase lossy composites in the low frequency, or quasi-static, regime [38]. In that study, viscoelastic composite materials were created by introducing various volume fractions of spherical (*a/c = 1*) coated inclusions were introduced into the "stiff" matrix material given in Table 4.1. The TL was then measured for frequencies ranging from 0 to 100 kHz by Baird *et al* [26]. Model

estimates of the TL were calculated using the BKT model (a low *ka* scattering model) and the coated inclusion SC model which was derived in Chapter III. The results have been reproduced in Figure 4.13 below. These plots replicate Figures 2 – 6 of reference [26]. From these plots two facts are readily apparent. First, the application of the SC model in the quasi-static regime has good agreement with the low *ka* scattering model for composites containing coated inclusions. Second, the SC model provides precise estimates of the frequency dependent lossy behavior of such viscoelastic composites as a function of both frequency and volume fraction.

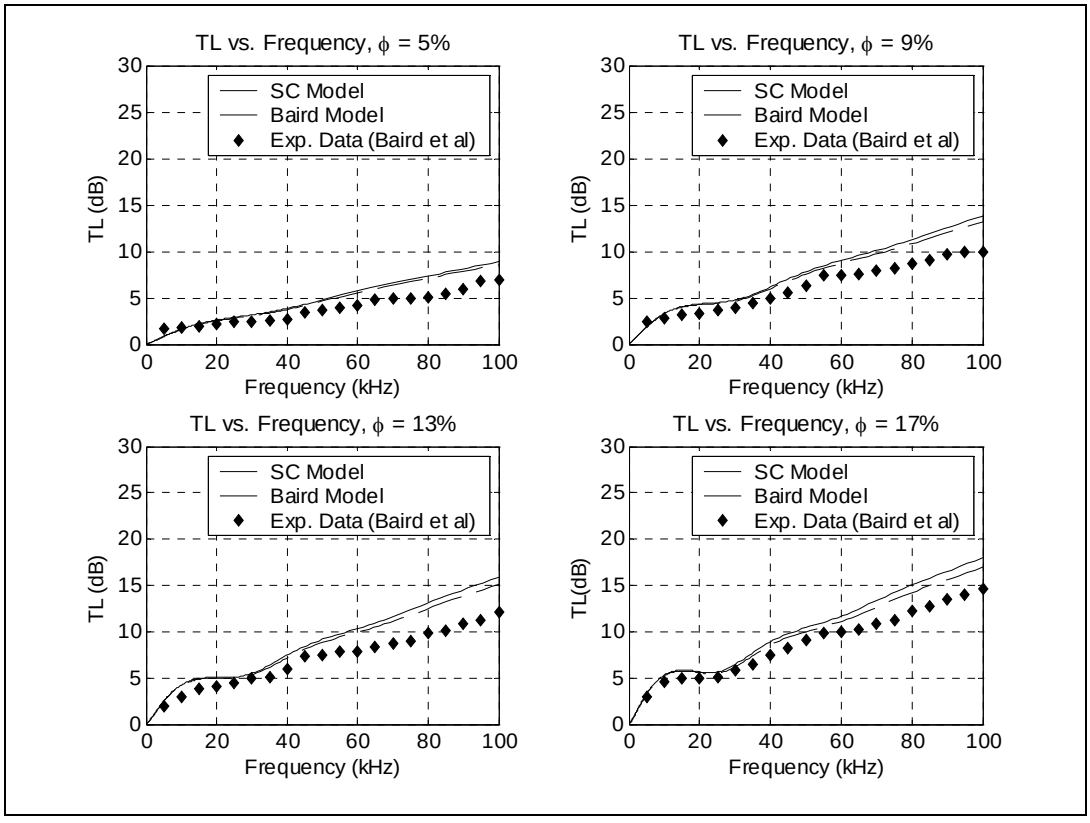

Figure 4.13: SC and BKT model estimates of TL for a 1 cm thick slab of viscoelastic composite submerged in water. Experimental data taken by Baird *et al* [26].

The precision of the SC model in the quasi-static domain is a result of the fact that the main features of the dynamics of the composite are correctly captured. Namely, the micromechanical approach takes small strains in the neighborhood of an inclusion into account using homogenization techniques. It therefore accounts for losses during propagation directly due to that strain and not by using asymptotic scattering approximations. This approach has the added advantage of being amenable to the modeling the anisotropic behavior of the material when the inclusions are no longer spherical and are similarly oriented with respect to the coordinate system of reference.

The following section employs the SC model to predict sound transmission through a 1 cm thick viscoelastic composite slab containing 13% volume fraction of coated oblate inclusions of varying aspect ratios. The constituent materials are taken to be the same as those used by Baird *et al* [26] for the case of a stiff matrix. Figure 4.14 gives the transmission loss as a function of frequency for various aspect ratios: a/c= 1 (spherical inclusions), a/c = 1.5, 2.0, and 2.5, while keeping the volume fraction constant at ϕ = 0.13.

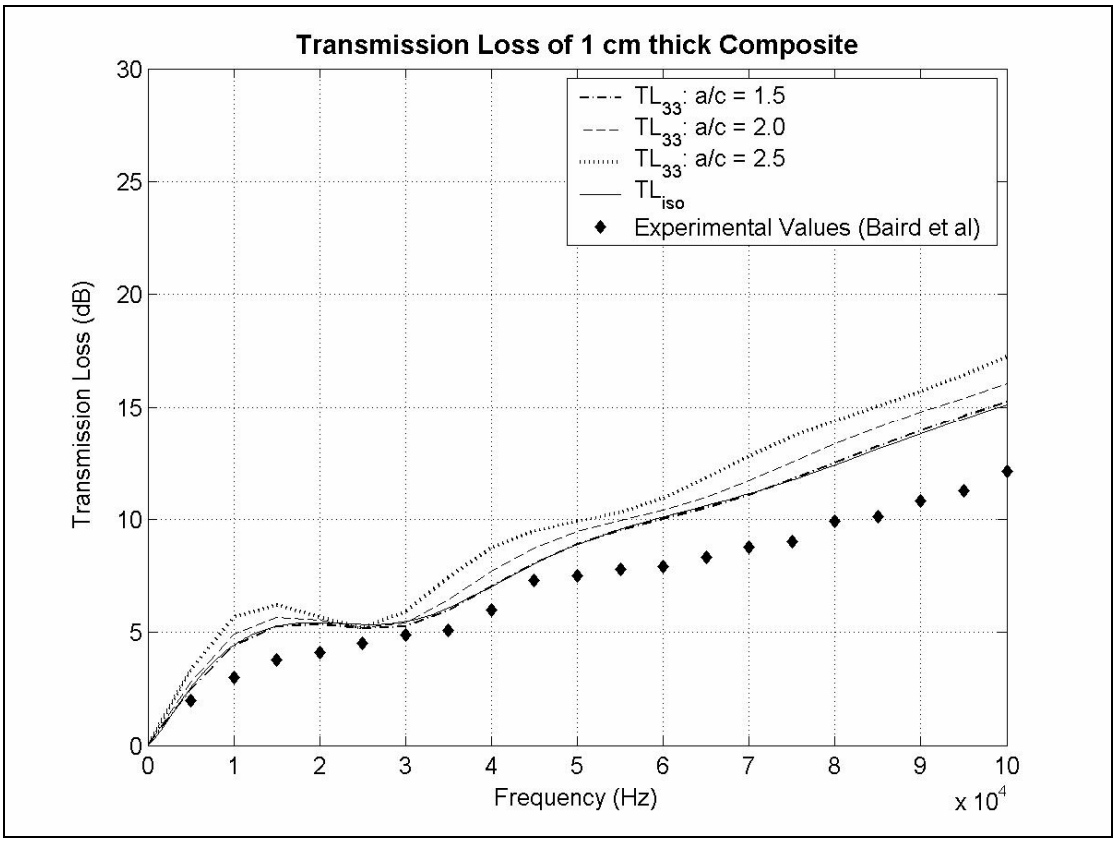

Figure 4.14: Transmission loss of 1 cm thick slab of composite material having the orientation shown in Figure 4.12 and containing 13% by volume of oblate coated inclusions of varying aspect ratios.

The oscillations in TL observed at the lower frequencies of the frequency range studied are caused by resonances in the finite thickness of the slab. Maximum transmission, i.e., minimum TL, occurs at the half-wavelength resonances while maximum transmission losses occur at the odd quarter wavelength resonances. It is observed that increasing the aspect ratio *a/c* results in a small increase in TL (less than 2 dB in the 0 to 100 kHz range) because of the increased shear strain in the neighborhood of the inclusion caused by its form. In other words, for the same traveling compressional stress wave field, more deformation occurs in the neighborhood of the oblate inclusions as compared to the spherical inclusion. Thus more mode conversion to shear occurs, with subsequent increased losses. This trend is also confirmed by plotting the attenuation coefficient,

$\hat{\alpha}^{eff}$, of the longitudinal wave number as a function of the angle in the x_1-x_3 plane, as shown in Figure 4.16. The angle is the polar angle, here denoted as θ, in spherical coordinates and the plot shows the attenuation coefficient for a longitudinal wave traveling in the direction, **n**, defined as $\mathbf{n} = \left\langle \sin\theta\cos\varphi\,\hat{\mathbf{i}}, \sin\theta\sin\varphi\,\hat{\mathbf{j}}, \cos\theta\,\hat{\mathbf{k}} \right\rangle$, in an infinite medium containing oriented ellipsoidal inclusions (where φ is the azimuthal angle), see Figure 4.15.

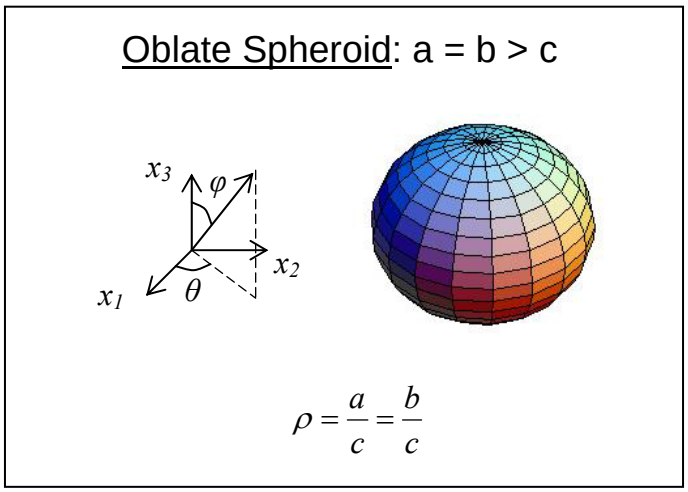

Figure 4.15: Geometry of oblate spheroids and their orientation with respect to the global coordinate system.

It is in this way that the influence of changing the orientation of inclusions with respect to the coordinate system shown in Figure 4.12a (i.e. rotating the inclusions about the x_2-axis in the material for a slab of composite material can be studied. The attenuation coefficient in the x_1-x_3 plane ($\varphi = 0$) as a function of polar angle is calculated from Eq. (IV.3.8).

$$\hat{\alpha}^2(\theta) = \hat{\alpha}_{11}^2 \sin^2\theta + \hat{\alpha}_{33}^2 \cos^2\theta \qquad \text{(IV.3.8)}$$

Both the attenuation coefficient (in Np/m) and the anisotropy factor, defined as $(\hat{\alpha}_{11} - \hat{\alpha}_{33})/\hat{\alpha}_{33}$, increase as the aspect ratio increases, as expected. One interesting point is that as the angle of propagation increases, the attenuation coefficient is seen to increase. Here it is noted that there are competing factors which tend to increase or decrease the lossy behavior with respect to the polar angle. These competing factors are the effective shearing area of the inclusions (which depends on their form) and the increase or decrease in effective material stiffness of the composite due to coated-inclusion properties. For the case shown in Figure 4.16, the oblate form of the inclusions increases the shearing area parallel to the propagation direction. This tends to increase the lossy properties of the composite and results in an increase in the composite material's damping capacity, described here by the attenuation coefficient, as a function of polar angle.

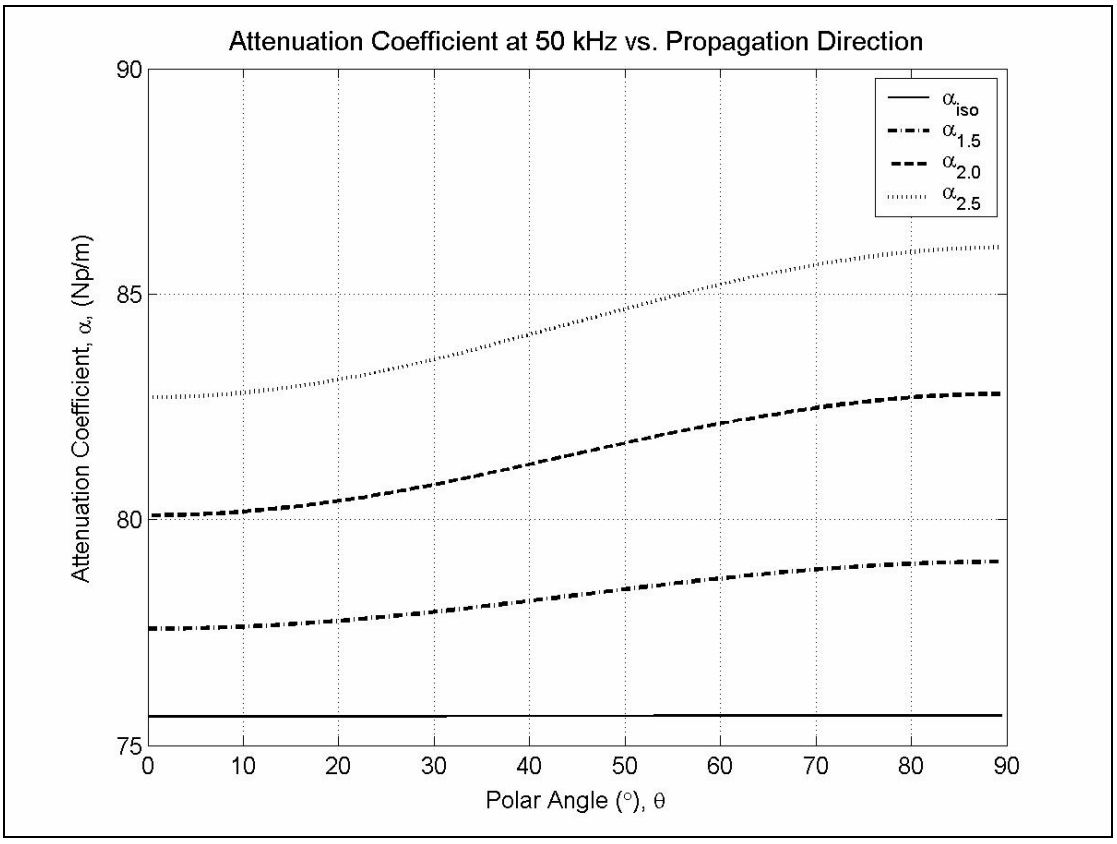

Figure 4.16: Attenuation coefficient as a function of angle in the x_1-x_3 plane of material containing oblate ellipsoidal inclusions of varying aspect ratios (θ = 0 coincides with x_3-axis). The volume fraction of inclusions is 13% and the frequency of the incident wave is 50 kHz.

In example given below, that of prolate and penny shaped Lucite inclusions, the opposite trend is observed as the inclusion and coating material properties lead to an overall increase in stiffness which will dominate the increase in shearing area related to inclusion geometry. Staying with the oblate inclusion example, Figure 4.17 plots the real and imaginary parts of the complex wave speed in the x_3 -direction as a function of frequency for aspect ratios a/c = 1, 1.5, 2.0, and 2.5, again for a fixed volume fraction ϕ = 0.13. The results show another aspect of the change in inclusion form, specifically that at a fixed frequency, the real part of the phase velocity decreases with increasing aspect ratio. This corresponds to a relative softening of the composite in the x_3-direction as the aspect ratio

increases. The softening, a result of oblate inclusion geometry, increases the specific strain energy in the neighborhood of the inclusion for the same imposed stress levels. At the same time, for single frequency, the absolute value of the imaginary part of the phase velocity also decreases with increasing aspect ratio. This decrease in the imaginary part is proportionally less than the decrease of the real part and therefore corresponds to an increase in attenuation in the x_3-direction for the oblate geometry. Otherwise stated: the magnitude of the imaginary part of the inverted plane wave modulus along x_3 increases with increasing aspect ratio. As discussed in Section 4.3.1, this causes an increase in the specific strain energy for a fixed value of imposed stress, thereby increasing the absorptive qualities of the composite along x_3.

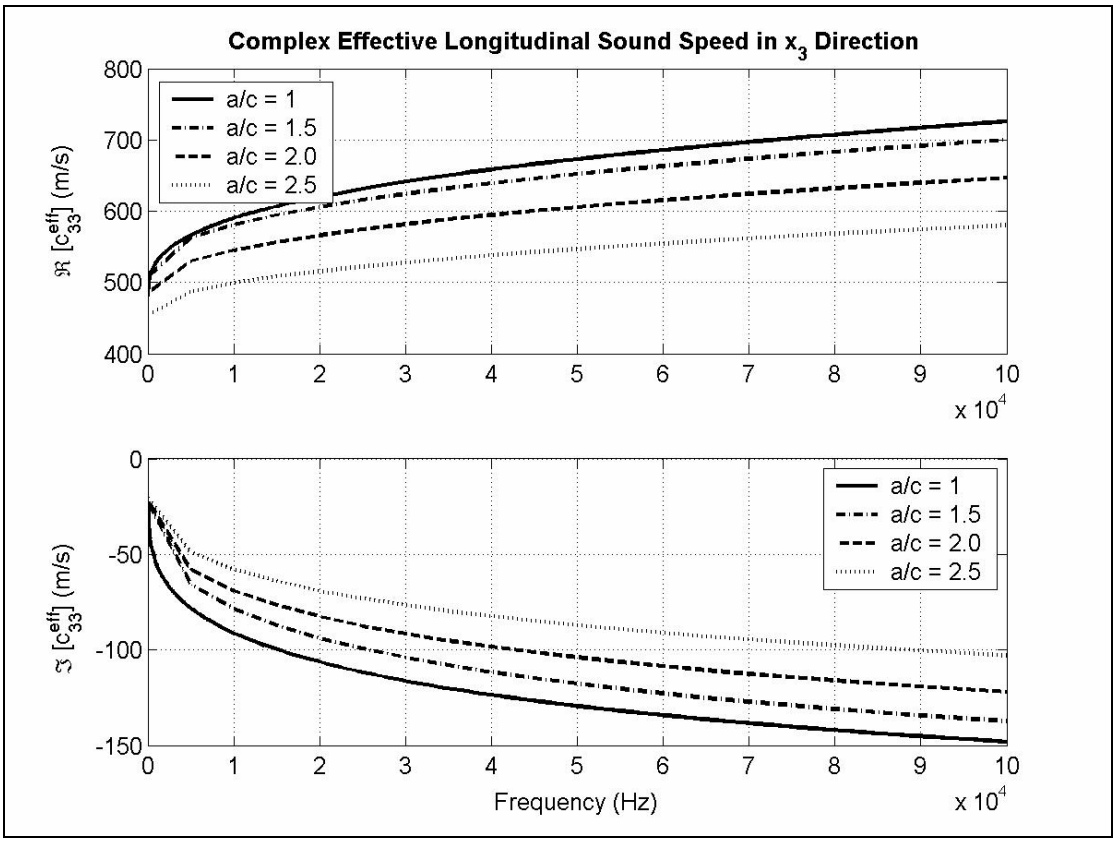

Figure 4.17: Real and imaginary parts of effective complex longitudinal wave speed in x_3-direction as function of frequency for a volume fraction inclusions of 13%.

The above discussion is for a specific case of a viscoelastic matrix containing oblate coated inclusions. The SC model is more general, however, and can be used to study the effects of prolate, needle shaped, and penny shaped inclusions (along with any variation of these forms). In what follows, the SC model is applied to the case of composite material composed of the same "stiff" viscoelastic matrix material containing inclusion and coating materials with the properties given in Table 4.4. This parametric study investigates the effects of such geometries on the overall damping properties of the composite.

Table 4.4: Material properties of coating and inclusion for material modeled in Figure 4.18.

	μ (GPa)	ν	ρ (kg/m^3)
Coating	1.40	0.40	1200
Inclusion	28.5	0.23	2300

To display the SC model's capabilities, five types of inclusions are considered: spherical, oblate, prolate, penny-shaped, and needle-shaped ellipsoids. Table 4.5 gives the minor radius ratios, *a/b* and *a/c*, for each of these cases.

Table 4.5: Minor radius ratios for composite modeled in Figure 4.18.

	Sphere	*Oblate*	*Penny*	*Prolate*	*Needle*
a/b	1	1	1	1	1
a/c	1	3	10	$\frac{1}{3}$	$\frac{1}{10}$

Figure 4.18 shows the variation of the calculated attenuation coefficient in the $x_1 - x_3$ plane as a function of polar angle. Minimum attenuation observed coincides with propagation along the x_3-axis ($\theta = 0$) for a composite containing needle shaped inclusions aligned with this axis. For the same composite, attenuation increases monotonically with increasing angle between incident plane wave and the long-axis of the needle shape inclusions. This plot also shows that attenuation diminishes for propagation along the x_1-axis (and therefore, by symmetry, the x_2-axis) of a composite containing penny-shaped inclusions whose large radii (*a* and *b*) are aligned with the x_1-x_2 plane. It was previously mentioned that this decreasing attenuation is the result of increased stiffness in the direction that coinciding with the long major axes when the composite inclusion has a higher stiffness value than the matrix. For the present material studied, this affect dominates the increase in shearing area due to inclusion geometry. Using the specific strain energy argument, the increase in composite material stiffness in certain directions

decreases the strain specific energy for stress wave of fixed magnitude propagating in the same direction. This reasoning also explains why the attenuation coefficient anisotropy factor of the oblate and penny shaped inclusions is lower than for the needle shaped inclusions. The oblate form of those inclusions renders the increase in shearing area increasingly influential with respect to the reinforcement it imparts to the composite. For the oblate and penny-shaped inclusions the increase in stiffness still dominates but the effects are reduced because the shearing area is significantly higher in this form of inclusion (compared to the needle-shape).

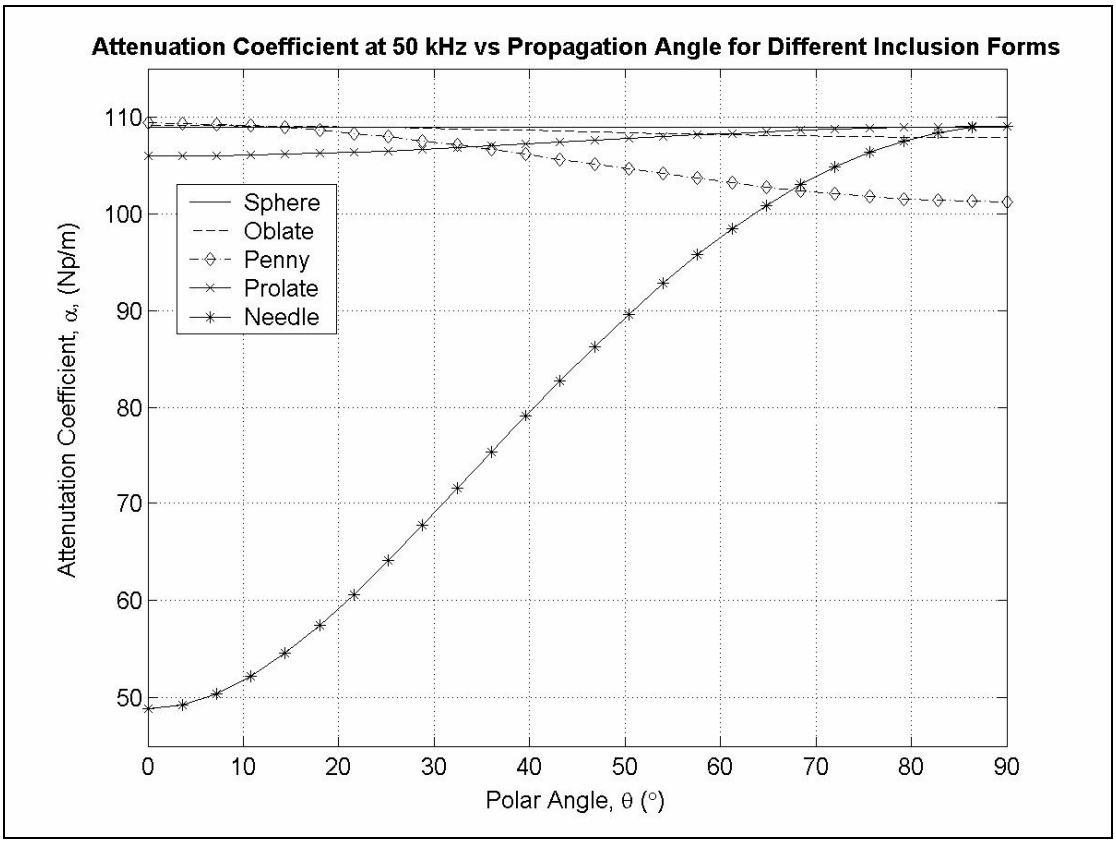

Figure 4.18: Attenuation coefficient as a function of angle in the x_1-x_3 plane for a composite consisting of a viscoelastic matrix with Lucite coated glass ellipsoidal inclusions of different forms (θ = 0 coincides with x_3-axis). The volume fraction of inclusions is 10% and the frequency of the incident wave is 50 kHz.

As expected, the composite containing spherical inclusions has a constant attenuation regardless of propagation direction, and the oblate and prolate inclusion cases fall somewhere between the limits of the penny-shape and needle-shape inclusions, respectively. One point of interest is that the attenuation coefficient for propagation along the x_3 axis for materials containing both oblate and penny-shaped inclusions is slightly superior to that of the material containing spherical inclusions. An explanation of this behavior is that the shape of the inclusion leads to stronger mode conversion at the boundaries resulting from stress concentrations related to the inclusion form.

At this point it is interesting to point out that all of the factors discussed above give a few guidelines for the design of composite materials having a desired lossy behavior. First, if inclusions are softer than the matrix material, increased inclusion aspect ratios lead to increased damping capacity in all directions compared to the same inclusion volume fraction of spherical inclusions. The highest losses will be observed in directions perpendicular to the outward normals of increased shear areas. This is illustrated with the oblate inclusion case shown in Figure 4.16. Secondly, if stiffness is required in one direction while high losses are desired in an orthogonal direction, high modulus needle shaped inclusions are an ideal solution (see for example Figure 4.18). This type of inclusion leads to low losses and high reinforcement along the longest inclusion minor axis but maintains lossy behavior nearly identical to spherical inclusions (twice the attenuation as observed along the longest axis) for propagation in all directions perpendicular to that axis. Using these two cases as guidelines and the quasi-static general SC model for design, numerous types of materials of varying lossy behavior can be conceived relatively easily.

The present section explored some of the strengths of the general SC model in the quasi-static domain. The SC model used for these calculations is limited to a single inclusion form, set of material properties, and spatial orientation. Reformulation of the SC model using dilute strain concentration tensors (DSCT) permits the approximation of the behavior of many different types of viscoelastic composite materials with relative ease. It is the purpose of the following section to show the level of generality achievable through application of the DSCT SC model derived in Section 3.3.

4.3.3 Identical coated inclusions with a known orientational distribution

The most common application of dilute strain concentration tensors cited in literature is the approximation of the globally isotropic material properties of composites containing identical non-spherical inclusions having a uniform orientation distribution. The generality of Eq. (III.3.33), however, permits the homogenization of composites containing non-spherical inclusions with a preferential orientation distribution just as easily as for the case of a uniform distribution. This is done by taking the approach discussed below. First the orientational average or a fourth order tensor quantity is defined in the following equation [56].

$$\left\{B_{ijkl}\right\} = \frac{1}{\alpha}\int_{\Omega} p(\Omega) a_{im} a_{jn} a_{kp} a_{lq} B_{nmpq} d\Omega \qquad \text{(IV.3.9)}$$

In this expression, α is an integration factor, a_{ij} is the rotation matrix determined by the appropriate Euler angles, θ, φ, and ψ, **B** is a fourth order tensor defined with respect to its local coordinate system, $\{\mathbf{B}\}$ is the orientational average of the same tensor with respect to the global coordinate system, Ω is the orientational space defined by the Euler angles, and $p(\Omega)$ is the orientation distribution function. It is now useful to define a normalized distribution function, $n(\Omega)$:

$$n(\Omega) = \frac{p(\Omega)}{\alpha} = \frac{p(\Omega)}{\int_{\Omega} p(\Omega) d\Omega} \tag{IV.3.10}$$

Equation (IV.3.10) defines a distribution which has the desirable property that its integral over the entire orientation space is unity. Substituting Eq. (IV.3.10) into Eq. (IV.3.9) yields:

$$\{B_{ijkl}\} = \int_{\Omega} n(\Omega) a_{im} a_{jn} a_{kp} a_{lq} B_{nmpq} d\Omega \tag{IV.3.11}$$

Now, in order to find the effective properties of a composite containing ellipsoidal inclusions with a known orientation distribution and a known inclusion and coating volume fraction (f^I and f^C, respectively), it is helpful to define the following tensor quantity.

$$\hat{\mathbf{C}}^{loc} = f^I \left(\hat{\mathbf{C}}^I - \hat{\mathbf{C}}^M \right) : \hat{\mathbf{A}}^I + f^C \left(\hat{\mathbf{C}}^C - \hat{\mathbf{C}}^M \right) : \hat{\mathbf{A}}^C \tag{IV.3.12}$$

$\hat{\mathbf{C}}^{loc}$ is simply the last two terms of Eq. (III.2.74) and is calculated by the SC model with respect to the local coordinate system for the family of inclusions having the same orientation in space. Then, when all coated inclusions in the composite are assumed to have identical shape and material properties, the effective material properties of the composite can be found by taking the orientational average of $\hat{\mathbf{C}}^{loc}$ and adding it to the matrix stiffness tensor, $\hat{\mathbf{C}}^{M}$, as follows:

$$\hat{C}^{eff}_{ijkl} = \hat{C}^{M}_{ijkl} + \sum_{\theta}\sum_{\phi}\sum_{\psi} n(\theta,\phi,\psi)\, a_{im} a_{jn} a_{kp} a_{lq} \hat{C}^{loc}_{nmpq} \Delta\theta \Delta\phi \Delta\psi \qquad \text{(IV.3.13)}$$

Equation (IV.3.13) is a general expression that permits the calculation of the effective properties of a composite consisting of identical oriented coated inclusions such as those studied by Haberman *et al* [150], randomly oriented inclusions such as for the composites studied by Berryman [27], and for any known preferential orientation distribution such as can be observed in shale material studied by Hornby *et al* [29] by selection of the appropriate orientation distribution. Equation (IV.3.12) for $\hat{\mathbf{C}}^{loc}$ is not, in general, an analytical expression and therefore the evaluation of the integral is approximated by a summation in Eq. (IV.3.13).

4.3.3.1 Approximation of globally isotropic properties

The section presents the verification first step of the generalized SC model using concentration tensors. The verification is simply a check on the agreement between the DSCT SC model and Berryman's model [27] for the case of ellipsoidal inclusions having a uniform orientation distribution. The effective compressional and shear wave speeds in the materials studied by Berryman have been reproduced for the prolate and oblate inclusion cases (see Figures 5b, c and 6b, c of reference [27]) in Figure 4.19 and Figure 4.20, respectively. The materials studied are suspensions of either prolate (*a/b = a/c = 10*) or oblate (*a/b =1; a/c = 10)* rock particles in water. The rock material is assumed to have the bulk and shear moduli $K_r = 44.9(1\text{-}0.004i)\ GPa$ and $\mu_r = 37.9\ GPa$, respectively and a density of $\rho_r = 2700\ kg/m^3$ while the same properties for water are $K_w = 2.18\ GPa$, $\mu_w = 1\text{-}i682\ Pa$, and $\rho_w = 1000\ kg/m^3$. The shear modulus of water is assumed to be lossy in accord with Berryman's paper and a very small (but non-zero) value is assigned to the real part in order to avoid singularity problems with calculation of the strain localization tensor, $\hat{\mathbf{A}}^1$, in the DSCT SC model.

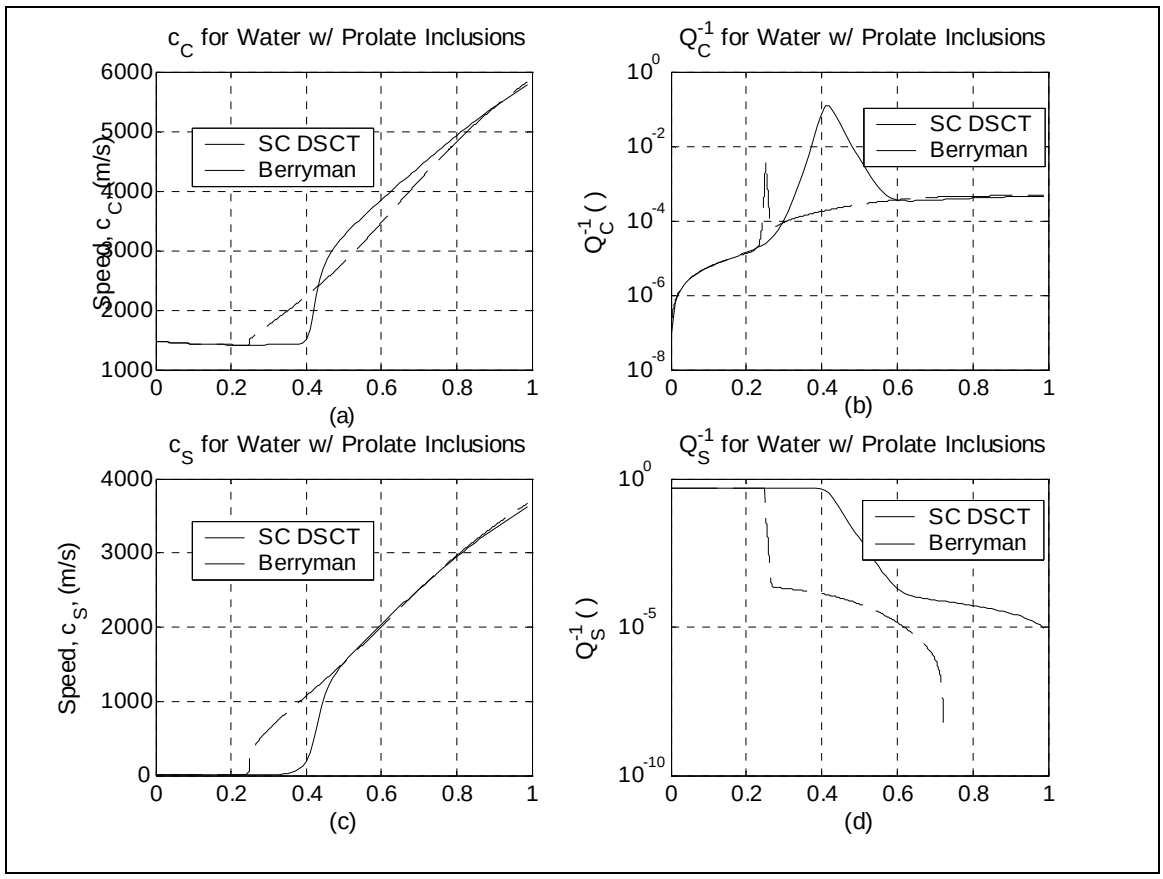

Figure 4.19: Compressional and shear wave speeds and Q^{-1} values as a function of volume fraction calculated using the DSCT SC model and Berryman's model [27] for the case of prolate rock inclusions in water where a/b = 1 and a/c = 1/10. f = 10 Hz.

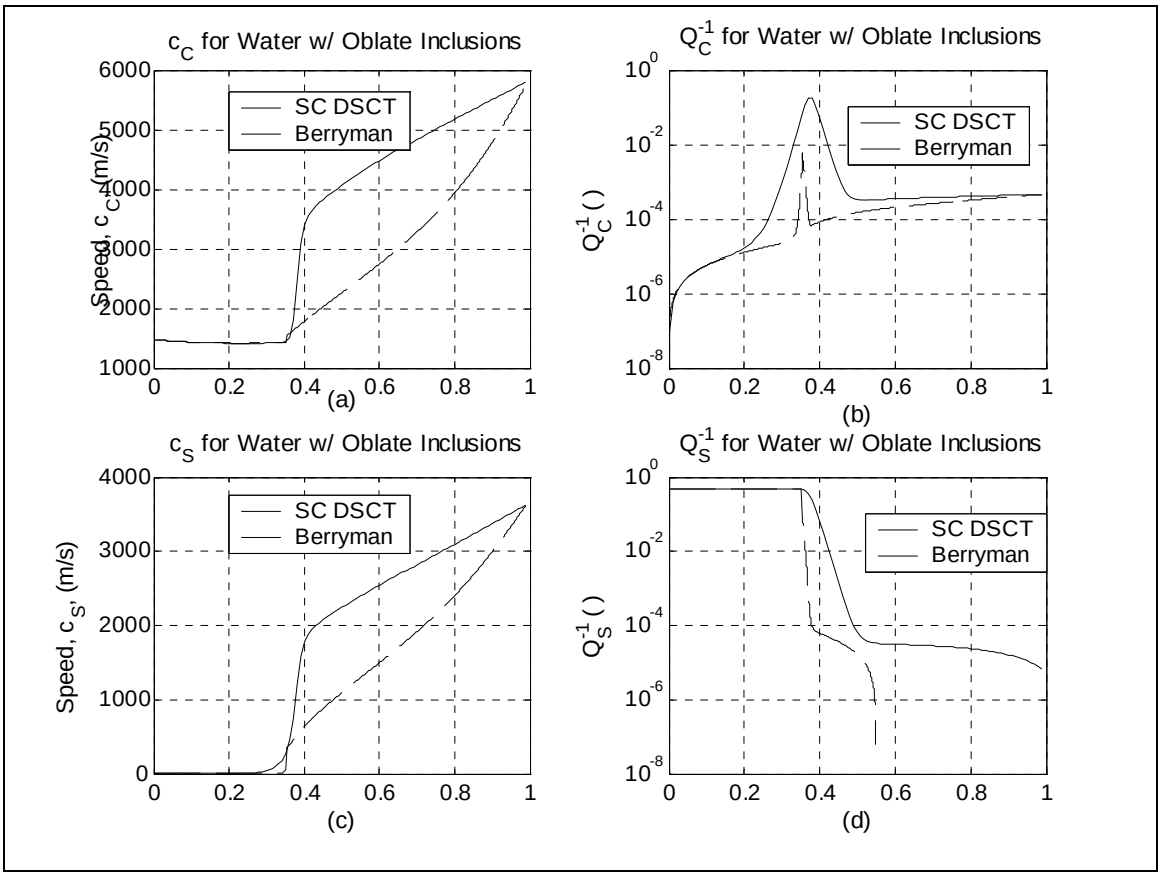

Figure 4.20: Compressional and shear wave speeds and Q^{-1} values as a function of volume fraction calculated using the DSCT SC model and Berryman's model [27] for the case of oblate rock inclusions in water where a/b = 1 and a/c = 10. f = 10 Hz.

These plots illustrate that the behavior modeled by the DSCT SC model and Berryman's model (which were reproduced for reference using the equations (32) and (33) along with the appendix of reference [27]) is qualitatively similar though there are some significant quantitative differences. Firstly, the real parts of both the compressional and shear wave speeds (c_C and c_S respectively) are nearly constant as a function of volume fraction up to a certain concentration where the effect of the rock inclusions begins to have a marked effect on the global behavior and a sharp increase in both wave speeds is observed. It is important to point out that the sharp increases in effective sound speed observed at specific model dependent concentration levels have a physical

significance and that the apparent jump (or discontinuity) is due to the numerical evaluation. The sharp increase in sound speed is directly related to the fact that the elastic constants of the constituent phases differ by several orders of magnitude. When the matrix material is significantly softer than that of the inclusion, many models will predict a similar sharp increase in the effective elastic constants at some level of concentration. This occurs at some concentration level that represents the point at which the reinforcement of the stiffer phase becomes important and, because the high contrast between the materials is high, the result is a sharp increase in effective elastic properties as a function of volume fraction. Berryman refers to this concentration as the "threshold of rigidity" and gives an excellent discussion of the physics of the modeled behavior in Section V of reference [95] in terms of different modeling approaches. Physically it is obvious that regardless of the abruptness of this transition, there can never be a true jump in material properties as a function of the volume fraction of constituent materials. Indeed, the magnitude of the observed "jump" decreases as the step size used for evaluation decreases leaving instead a very steep slope which is exacerbated by the implicit nature of the self-consistent model [95]. Smaller concentration steps have not been employed in order to reduce calculation time and because this behavior can be explained in terms of physical phenomena and the modeling approach. It is important to note that the specific volume fraction corresponding to the threshold of rigidity varies depending on the inclusion aspect ratio and the elastic contrast of the constituents for both the DSCT SC model and Berryman's model.

The threshold of rigidity discussed above coincides with another observation, the presence of a singularity in the values of $\hat{Q}_c^{-1}$ associated with the compressional wave

number for the same rock concentration value. $\hat{Q}_c^{-1}$ is related to the damping quality of the composite and calculated from the expression $\hat{k}_{c,s} = \hat{k}'_{c,s} + i/2\hat{Q}_{c,s}$, where $\hat{k}_{c,s}$ is the complex compressional or shear wave number of the effective material, indeed $\hat{Q}_{c,s}^{-1} = 2\hat{\alpha}_{c,s}$. Importantly, both the micromechanical DSCT SC model and Berryman's model show this result. For the case of prolate inclusions, the DSCT SC formulation shows the singularity at $\approx$23% rock, whereas Berryman's model displays this singularity at a concentration of $\approx$30% and for the case of oblate inclusions these values are $\approx$21% using DSCT SC and $\approx$38% using Berryman's model. Though the location of the singularity in the DSCT SC model is different from that modeled by Berryman, the behavior, as described at length by Berryman [95], is non-physical in both cases and is due uniquely to SC modeling's implicit solution formulation for composites consisting of materials with such high contrast between elastic constants. Here it is stressed, as was pointed out by Berryman [95], that the lossy component of the effective wave speeds are over predicted near this singularity and that this is a weakness of the SC modeling approach for high contrast composites. More importantly, the trends of the DSCT formulation for the SC coated inclusion model agree well with Berryman's accepted model. Indeed Berryman's SC relations were derived by using the orientational averages of Wu's "*T*-matrix" formulation [64] (which is based on Eshelby's solution) for the case of a uniform distribution of orientation of ellipsoidal inclusions. The two approaches are therefore quite similar, with Berryman's formulation falling closer to the lower bound and the DSCT SC being nearer the upper bound. The large quantitative difference between the two models is due this fact coupled with the high contrast of constituent materials for this particular case. The qualitative agreement with Berryman's approach is

pointed out here as a validation the DSCT formulation for implementation in the quasi-static regime when a composite material has a complex microstructure and yet displays globally isotropic behavior because the identical inclusions have a random orientation distribution.

At this point it is informative to show that the DSCT formulation can just as easily be used allow an increased degree of flexibility in modeling particulate composites that are globally anisotropic as a result of inherent material anisotropy, preferential orientation of ellipsoidal inclusions, or both. The advantage of the DSCT SC model is that modeling of such materials, which are globally anisotropic, is treated in the exact same manner as discussed above, and therefore no additional modeling complexity is added for homogenization of such composites. This is a marked improvement over Berryman's approach, which is limited to globally isotropic materials, or the SC model, which is limited to either spherical or identically oriented inclusions. One further improvement that can be made by using the current model, since it is valid for coated inclusions, is the implementation of the generalized SC (GSC) model for the case of bi-phase composites. The GSC model, which was introduced by Christensen and Lo [80], assumes that the inclusion phase is surrounded directly by the matrix material and that entire coated inclusion is then embedded in an effective medium of unknown properties. This modification to the SC model has been shown to yield better results than the SC, Mori-Tanaka, and differential methods for increased volume fractions [151].

4.3.3.2 Approximation of globally anisotropic properties

DSCT formulation easily lends itself to computations of the effective material properties for composite materials consisting of inclusions having non-spherical geometries with a preferential orientation (neither aligned nor randomly oriented). Such microstructures can be observed in geologic materials, such as the shales studied by Hornby *et al* [29], or in fabricated materials due to manufacturing processes. This section presents a parametric study of the attenuation coefficient as a function of propagation angle in a composite consisting of prolate inclusions in a lossy matrix in order to illustrate the capability of the DSCT SC model to capture these effects.

Consider a hypothetical material consisting of a polymer matrix having the properties of the "soft" polymer characterized by Baird *et al* [26] which is assumed to be incompressible at all frequencies and containing prolate glass inclusions ($a/b = a/c = 5$, $\mu_{glass} = 28.5\ GPa$, $\upsilon_{glass} = 0.23\ GPa$, $\rho_{glass} = 2300\ kg/m^3$). The inclusions are assumed to have an axis-symmetric preferential orientation along the x_1-axis where the level of preference is fully described by a Gaussian distribution of solid azimuthal angle, θ, having an assumed standard deviation, σ_θ (see Figure 4.21).

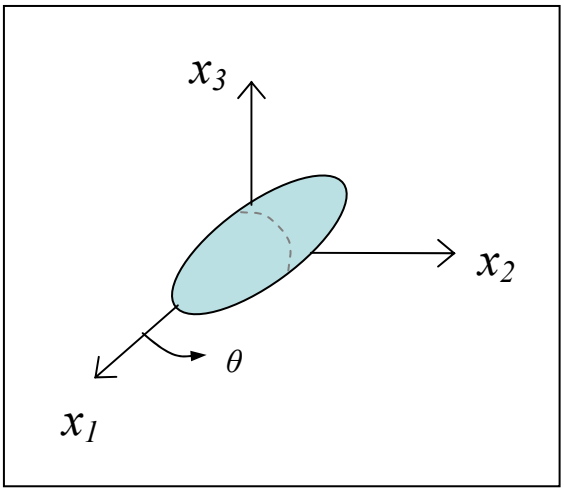

Figure 4.21: Orientation of prolate glass inclusions. θ is the azimuthal angle.

The complete orientation distribution, $n(\Omega)$, given in Eq. (IV.3.10) is then defined using the normalized Gaussian distribution for the azimuthal angle, $n_{gauss}(\theta)$, as follows:

$$n(\Omega_{ij}) = n_{gauss}(\theta_i)\, n_{gauss}(\theta_j) \qquad \text{(IV.3.14)}$$

$$\text{where: } \theta_{i,j} \in \left[\frac{-\pi}{2}, \frac{\pi}{2}\right]$$

It is important to note that the comma in Eq. (IV.3.14) *does not* denote the special derivative. This normalized distribution function can then be employed directly in Eq. (IV.3.13) to approximate the effective properties of a material having inclusions of assumed orientational preference. This was done for a composite consisting of 10% by volume glass inclusions at a frequency of 25 kHz for five different values of σ_θ ranging from 0º (all inclusions aligned along the x_1-axis) to ∞º (uniform distribution yielding a

globally isotropic composite). The results of the parametric study are given below in Figure 4.22.

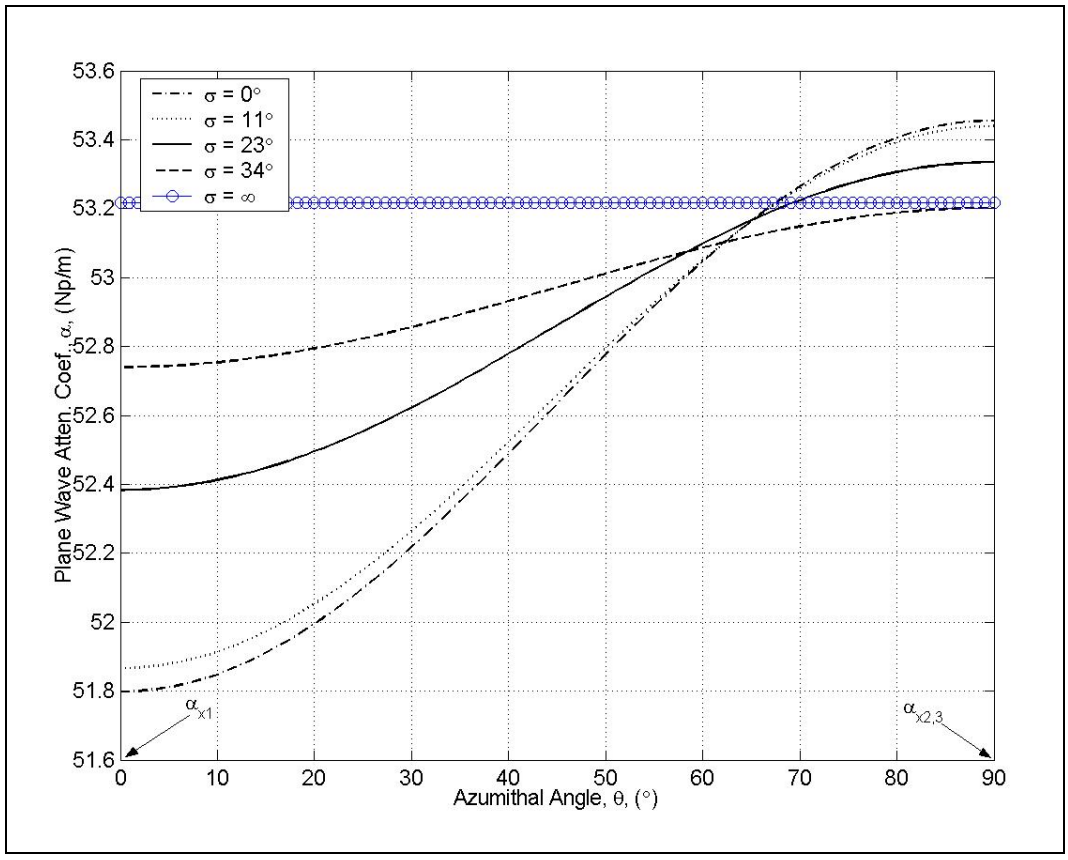

Figure 4.22: Variation of attenuation coefficient as a function of azimuthal angle for glass/polymer composite with varying degrees of anisotropy. Volume fraction of prolate inclusions φ = 10%, *a/b* = *a/c* = 5, frequency inspected *f* = 25 kHz.

Two intuitive checks are immediately obvious from the inspection of Figure 4.22. First, the magnitude of anisotropy factor, defined here as $\left(\hat{\alpha}_3 - \hat{\alpha}_1\right)/\hat{\alpha}_3$, decreases with increasing σ_θ from the case of aligned prolate inclusions ($\sigma_\theta = 0$) up to the limit of $\sigma_\theta = \infty$ where the composite is isotropic and similar to the materials studied in the previous section. Second, the minimum attenuation coefficient calculated is for propagation along the x_1-axis for the case of identically oriented glass inclusions aligned

with the x_1-axis. This yields minimal attenuation because of the high-stiffness and non-lossy material behavior of the inclusions. Several other interesting points can be observed about these calculations. An interesting feature of this plot is that for highly preferential orientation distributions one observes a slightly higher value of $\hat{\alpha}$ in directions orthogonal to the x_1-axis over the uniform distribution case. This is due to the increase in strain energy brought about by stress concentration at inclusion ends for plane wave incidence perpendicular to the major inclusion axis. Though this effect is small, it is an interesting result of orientational preference. It also illustrates the effects that can be captured by the quasi-static DSCT SC model that relate stress concentration due different inclusion geometries and orientation distributions to the macroscopic damping capacity of a viscoelastic composite. This parametric study clearly shows the capability of the DSCT SC model to capture the variation of anisotropy depending on orientational preference of like inclusions. Since, either as a natural occurrence or due to inherent variability in processing techniques, very few real materials have identically oriented particulate inclusions this additional flexibility is very useful. Indeed, the case study below shows a potential application of this specific capability.

4.3.3.3 Comparison with experiment

The effective elastic constants of the shale material studied by the Hornby *et al* [29] are approximated here using the DSCT SC model as a case study. The shale can be broadly described as a composite material consisting of a load bearing water-filled porous clay containing three distinct "spherical" mineral inclusion phases (quartz, feldspar, and

pyrite) of different concentrations (see Figure 4.23). For a more detailed description of the composition of the material see reference [29].

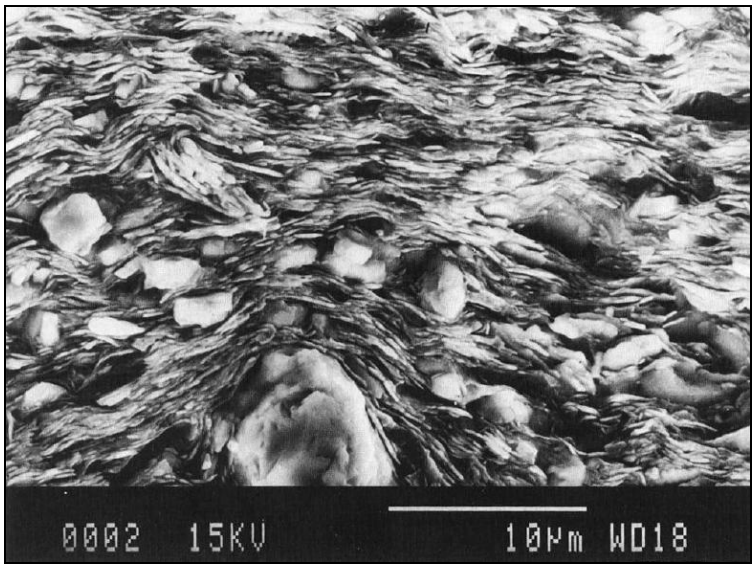

Figure 4.23: Micrograph of shale studied by Horby *et al* [29] (image from reference).

The porous clay itself is best described by fully-connected oblate clay platelets with a preferential orientation distribution (axis-symmetric about the x_3-axis) arranged such that ~11% porosity remains. For modeling purposes, it is assumed that the water-filled pores can conversely be considered as oblate inclusions ($a/b = 1$, $a/c = 20$) with preferential orientation (axis-symmetric about the x_3-axis) in an otherwise continuous isotropic clay matrix of known properties given in reference [29]. The material properties used here are summarized in Table 1 and were taken from various sources (Mavko *et al* [152] and Merkel *et al* [153],) since not all constituent phase properties were specified in reference [29].

Table 4.6: Material properties of the constituent phases of shale studied by Hornby et al. Material data taken from various sources: clay [29], quartz and feldspar [152], pyrite [153].

	K (GPa)	*μ (GPa)*	*ρ (kg/m^3)*	*φ (%)*
Clay	22.9	10.6	1826	---
Water	2.2	1 x 10^{-6}	1000	11
Quartz	36.4	45.0	2640	53
Feldspar	75.6	25.6	2630	11
Pyrite	103.7	109	5015	9

Hornby *et al*'s approximation of the effective properties of shale studied was done in three different homogenization steps. First, the effective fluid-clay composite was approximated as a transversely isotropic clay medium with 11% oblate water-filled pores. An orientational average was then taken of this medium by employing the spatial distribution of pore orientation (approximated from micrographs of the shale) yielding the effective properties of the fluid-clay matrix. Finally, the spherical mineral phases were added to this effective fluid-clay composite to get an approximation of the effective components of the stiffness tensor. For approximation of the global effective properties of this shale material the DSCT SC model yields the most accurate results when the modeling is done in two separate steps. First, a transversely isotropic matrix fluid porous clay medium is approximated using techniques described in Section 4.3.3.2 above. The pores are assumed to have an orientation distribution similar to that given in Eq. (IV.3.14), but for the case of oblate inclusions the axis of symmetry is the x_3-axis and the angular variations are for the solid polar angle, φ. The standard deviation of angular variation was assume to be $\sigma_\varphi = 30^\circ$ in accordance with the histogram show in Fig. 9 of reference [29]. This effective medium was then used as the matrix to which the three spherical mineral phases were added. The results of this modeling approach are given in Table 4.7.

Table 4.7: Experimental data and results of effective stiffness coefficients of shale (GPa) for various modeling techniques. DSCT = Dilute strain concentration tensor; SC = Self-Consistent; GSC = Generalized Self-Consistent.

	Observed (GPa)	*Hornby et al (GPa)*	*DSCT SC (GPa)*	*DSCT GSC (GPa)*
C_{11}	34.3 ± 1.4	34.7	37.3	37.1
C_{22}	34.3 ± 1.4	34.7	37.3	37.1
C_{33}	22.7 ± 0.9	22.2	21.7	21.4
C_{44}	5.4 ± 0.8	6.0	5.2	5.1
C_{55}	5.4 ± 0.8	6.0	5.2	5.1
C_{66}	10.6 ± 1.6	10.8	11.1	11.1
C_{12}	*Not reported*	*Not reported*	13.1	13.0
C_{13}	10.7 ± 5.4	11.5	12.1	12.1
C_{23}	10.7 ± 5.4	11.5	12.1	12.1

The results of the DSCT SC model are in good agreement with the properties observed by Jones and Wang [28] and modeled by Hornby *et al* [29]. Approximations have been run using both the DSCT SC model and the GSC model with DSCT formulation. It is noted that the experimental error on the mean value of components C_{13} and C_{23} is very high, and so comparison of the model with the experimental values is mostly for qualitative purposes. These results clearly show that the anisotropy of the composite shale due to the preferentially oriented oblate pores is well captured by the DSCT formulation. With regards to the accuracy of the DSCT SC and GSC model approximations with respect to the approach of Hornby *et al*, several points musts be raised. First of all, the agreement of the two models is highly dependent on the values used for the moduli of the constituent mineral phases. Due to the fact that these values were not given in the reference, this could be one source of disagreement between the results given here and those arrived at by Horby *et al*. It is also important to note that the agreement with the experimental data is partially dependent on the modulus in question. The DSCT SC and GSC models show better agreement with the values of the shear

moduli whereas the approach Hornby *et al* obviously approximates the plane wave moduli (C_{11}, C_{22}, and C_{33}) more accurately. Most importantly, the application of the DSCT SC model to approximate the effective properties of this material with good qualitative and quantitative agreement between model and experiment is a strong example of the generality of the DSCT approach.

4.3.4 Sub-micron → Micro → Macro Modeling

Another area where the DSCT SC model can be show to be applicable is in the area of multi-scale modeling. Many complex materials are most accurately modeled as having behavior that can be modeled on several scales. The main problem presented by these materials is the ability to tie behavior on multiple scales together in a manner that yields a complete picture of the material behavior at the scale of interest based on its multi-scale composition. Indeed the micromechanical approach is, by definition, a type of multi-scale modeling. The materials modeled above, however, have been for the simple case of two separate scales. In the following case the influence of the material properties and geometry of one or multiple types inclusions on the same length scale is homogenized in order to approximate the behavior of the composite on a larger length scale. For multi-scale modeling purposes, it is, in general, assumed that there exist several length scales such that the effect of inhomogeneities and interfaces at an inferior scale can be taken into account at the next highest length scale through some type of averaging technique. This tacitly assumes that the behavior at lower level length scales only have an effect on the next highest level in some average way and that no point-to-

point interactions are important between length scales [33]. For the cases presented above, for example, the effect of inclusions (whose interaction at their respective length scale is indirectly taken into account via the self-consistent scheme) on the global homogeneous behavior is done through an averaging scheme that involves finding the proper DSCT. For composites consisting of more than two scales, homogenization techniques analogous to the DSCT describe above must be developed between each length scale and the next highest length scale, starting with the smallest scale to be considered and increasing until the effective global behavior is approximated. This is a very interesting problem that applies to nano-composites and many naturally occurring materials displaying structural hierarchy. The approach requires the ability to model inhomogeneities and interfaces on the local level (at their respective length scale) with respect to the surrounding medium and then to use this information to model the global behavior (see, for example, Spearot *et al* [154]). Problems of this kind are very difficult due to the complexity of models at very small length scales, and are beyond the scope of this work. Here the emphasis is simply on showing that the DSCT SC model can be used when the effect of multiple scales must be taken into account. To do so, the results of the DSCT SC model of a silicon carbide–aluminum (SiC-Al) composite material presented by Ledbetter and Datta are shown together with the experimental and theoretical results presented in the reference [30].

4.3.4.1 Comparison with experiment

The material studied by Ledbetter and Datta is a bi-phase material with complex microstructure due to manufacturing processes. Modeling this material requires a scale transition between two different length scales. The smallest length scale is that of prolate (*a/b = a/c = 3*) SiC inclusions with a uniform orientation distribution embedded in an aluminum matrix. These prolate inclusions have sub-micron descriptive lengths (~250-750 nm) and are non-uniformly distributed within the aluminum host (see Figure 4.24a). The distribution of the SiC particles within the aluminum host is such that identically oriented oblate islands (*a/b = 1, a/c = 3*) of pure aluminum with descriptive lengths of ~2-4 μm remain. These pure aluminum islands are surrounded by a "sea" of high volume fraction SiC–Al composite. The length scale associated with the Al islands is an intermediate scale, which is referred to as the meso-scale, between the sub-micron scale and the macroscopic scale. The total volume fraction of SiC in the composite was experimentally determined to be 30%, but, because of the non-uniformity of the spatial distribution, the concentration level of SiC particles in the "sea" is approximated as being 50% [30]. For modeling purposes, the important material properties of SiC and Al were given as: $K_{SiC} = 223.4\ GPa$, $\mu_{SiC} = 188.1\ GPa$, $\rho_{SiC} = 3160\ kg/m^3$, $K_{Al} = 74.9\ GPa$, $\mu_{Al} = 26.7\ GPa$, and $\rho_{Al} = 2700\ kg/m^3$.

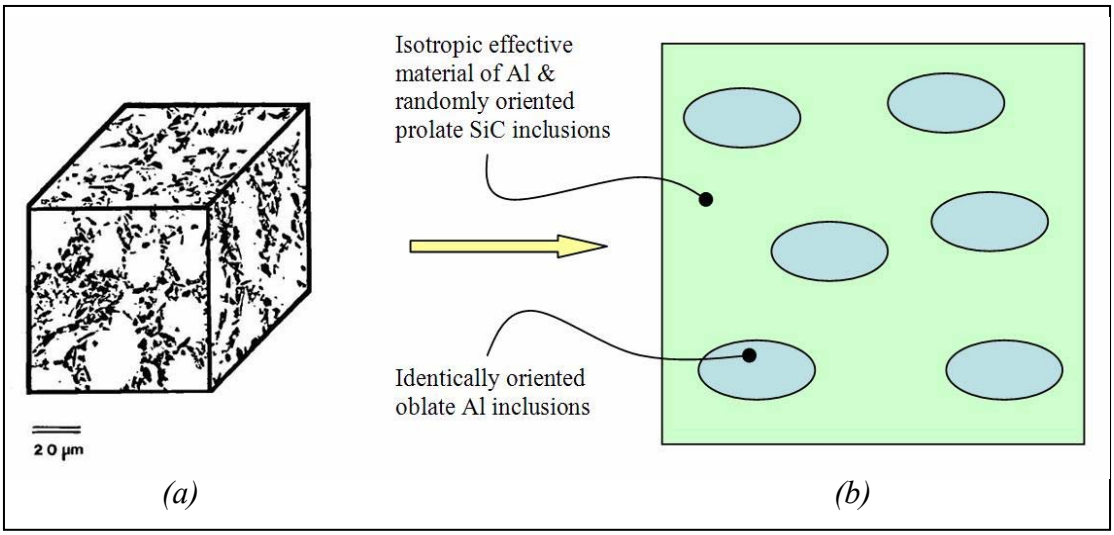

Figure 4.24: Composite material studied by Ledbetter and Datta (image taken from reference [30]). The material consists of a non-uniform distribution of sub-micron prolate SiC particles in an aluminum matrix. (a) Micrograph of material, SiC particles are dark areas, (b) Schematic of modeling approach employed.

Ledbetter and Datta proposed a scattering based model which is valid for ellipsoidal inclusions having either uniform or identically oriented orientation distribution to approximate the effective material properties of this composite which gives good results [30]. Their model illustrates the difficulty involved in finding scattering-based models for approximation of the effective properties of composites displaying complex microstructure. The modeling was done in two steps (see Figure 4.24b) the first of which involves approximating the "sea" as a homogeneous isotropic medium resulting from the 50-50 mix of uniformly oriented SiC prolate inclusions and an aluminum matrix. This isotropic medium is then idealized as the matrix material of the global composite material which has identically oriented (aligned with the x_1-x_2 plane) oblate Al inclusions with a volume fraction of 40%. The implementation of the DSCT SC model is done in an identical manner. First the sub-micron→meso transition is made by employing the DSCT formulation given in Section 4.3.3.1 to find a globally isotropic medium which

acts as the matrix for a meso→macro scale transition modeling step. The meso→macro step is done by employing the basic SC model given in Eqns. (III.2.74)-(III.2.77) where the matrix found in the previous step is assumed to contain 40% oblate Al inclusions aligned with the x_1-x_2 plane. The results of this modeling approach are tabulated in Table 4.8 together with the theoretical and experimental values given by Ledbetter and Datta [30], the DSCT GSC, and the DSCT Mori-Tanaka (MT) model results. See Appendix D for a derivation of MT and Differential Effective Medium (DEM) schemes from the local expressions derived in Chapter III.

Table 4.8: Observed and calculated values of the coefficients of the stiffness tensor (GPa) for Al-SiC composite of Ledbetter and Datta [30]. (DSCT = Dilute strain concentration tensor; GSC = Generalized Self-Consistent; MT = Mori-Tanaka; LD = Ledbetter and Datta).

	Observed	*DSCT SC*	*DSCT GSC*	*DSCT MT*	*LD*
C_{11}	165.9	172.9	170.8	240.9	172.7
C_{22}	165.1	172.9	170.8	240.9	172.7
C_{33}	148.3	161.7	160.7	118.7	148.0
C_{44}	43.3	47.9	47.3	42.9	42.9
C_{55}	43.4	47.9	47.3	42.9	42.9
C_{66}	48.7	51.7	50.6	51.3	51.3
C_{12}	68.5	69.2	69.1	99.1	70.1
C_{13}	62.2	69.1	69.0	67.9	67.7
C_{23}	62.2	69.1	69.0	67.9	67.7

The DSCT GSC and DSCT MT models were run for comparison purposes. For this particular composite, the MT model seems to greatly over-estimate the effective material properties and approximates too high of a degree of anisotropy. This is not unexpected, as the MT is known to overestimate effective material properties when the matrix material is more stiff than the inclusion phase [155, 156]. As observed in the previous section, the DSCT GSC model again shows improved agreement with the experimental values as compared to the DSCT SC model. The capability of the three-phase coated-

inclusion SC model of Cherkaoui to be extended to a GSC scheme is indeed one of the strengths which was also noted Section 4.3.3.3 that is stressed. The results indicate that the DSCT SC and GSC models both over-estimate the measured material properties and show a lower degree of anisotropy than that observed; the difference in the values of C_{12} and C_{23} is negligible and the contrast between C_{44} and C_{66} is not as marked as is the actual material or the LD model. Nevertheless, the theoretical transverse isotropy, $C_{66}^{theory} = \left(C_{11}^{SC} - C_{12}^{SC}\right)/2$, shows only a 0.5% difference between the DSCT SC model and theoretical values of C_{66}. The model is therefore shown to be giving consistent results. Here it must be noted that the LD model yields a better approximation of the observed effective properties of the SiC-Al composite than the DSCT SC model. The improved agreement more than likely stems from the fact that the LD model is derived from multiple scattering considerations and therefore is able to directly take into account high volume fractions whereas the SC formulation implicitly approximates such behavior. As the volume fraction increases, the error involved in the implicit scheme will increase and therefore leads to the SC model's lower precision approximation. It is important, however, to stress that the generality of the DSCT SC model for applications to composite materials of very different constituent phases, geometries, and orientational preferences as displayed here and in the examples above is a great advantage over models such as that proposed by Ledbetter and Datta which are restricted to heterogeneities with identical orientations or a uniform orientation distribution.

4.3.5 Distribution of coating thicknesses

The last validation of the DSCT SC model is an example of how it can be extended to capture the effect of the variation in coating thickness observed in real materials. Previous sections showed that the SC model gives very good approximations of the lossy behavior of a viscoelastic material containing hollow microspheres by comparing calculated values of TL to experimental values. One of the assumptions of that formulation is that all coated inclusions are identical. Though the effect of the relative inclusions size with respect to other inclusions can be assumed to have a negligible effect on the global properties since they are all on the same length scale and must be several orders of magnitude smaller than the wavelength of the incident wave in the host material, the distribution of coating thickness can still have a non-negligible effect. This is due to the fact that the contrast in material properties between the inclusion (which is a void) and coating (a glassy material) is significant. Indeed, the model proposed by Baird *et al* [26], included a modification for what they called a "size effect." Though the appellation of their model as capturing a "size-effect" is a misnomer as only the variation in coating thickness is taken into account, their model shows improved agreement with TL data for a 2.5 cm thick slab of viscoelastic composite. Here the SC model can is modified by using the concept of DSCT to take into account a variation in coating thickness. This is done by recognizing that each family of composite inclusions that have the same coating thickness can be modeled as representing a family of inclusions with slightly different material properties. The homogenization scheme is then represented similarly to that shown in Section 3.3, where the coating thickness of the inclusions is varied from family to family and there is no orientational effect because of the spherical symmetry of this particular case.

In order to cast the tensor relations for the effective moduli of the composite for a variation of coating thickness an approach similar to that outlined by Baird *et al* is employed. First, the coating fraction, $\gamma_{i,j}$, is defined which quantifies the percentage of the composite inclusion volume which is coating for a family of spherical coated inclusions with inner radius a_i and outer radius b_j. Here, the subscripts on γ do not denote a tensor quantity but simply the coating fraction for different values of inner and outer radii, likewise the comma does not denote a spatial derivative. For this idealized family of spherical composite inclusions, the coating fraction can then be expressed as a function of the radii as shown below.

$$\gamma_{i,j} = 1 - \left(\frac{a_i}{b_j} \right)^3 \tag{IV.3.15}$$

It is further assumed that the relative size of the inclusions has a negligible effect on the globally observed properties and that the inner radius has a constant value, a_{ave}. The coating fraction for each family of inclusions then relates the inclusion and coating volume fractions to total volume fraction of the family having the same outer radius (and therefore coating fraction) with the following relations.

$$f^{C,i} = \varphi_i \gamma_i \tag{IV.3.16}$$

$$f^{I,i} = \varphi_i - f^{C,i} = \varphi_i (1 - \gamma_i) \tag{IV.3.17}$$

It is important to note that the above relations also hold for ellipsoidal inclusions (though it would be admittedly difficult to experimentally determine the coating fraction for non-spherical inclusions). For a true composite material, it is obvious that the coating thickness will be found in some distribution that can be related to a measured distribution of outer radii through Eq. (IV.3.15). From this measured distribution, $p(\gamma)$, the normalized distribution, $n(\gamma)$, is calculated by using Eq. (IV.3.10). The resulting expression of the SC model for the case of varying coating thicknesses is then written:

$$\mathbf{C}^{eff} = \mathbf{C}^{M} + \varphi \left[\frac{\int_{-\infty}^{\infty} p(\gamma) \left\{ (1-\gamma) \Delta \mathbf{C}^{IM} : \mathbf{A}^{I}(\gamma) + \gamma \Delta \mathbf{C}^{CM} : \mathbf{A}^{C}(\gamma) \right\} d\gamma}{\int_{-\infty}^{\infty} p(\gamma) d\gamma} \right] \quad \text{(IV.3.18)}$$

$$\mathbf{C}^{eff} \approx \mathbf{C}^{M} + \varphi \sum_{j=1}^{N} n(\gamma_j) \left\{ (1-\gamma_j) \Delta \mathbf{C}^{IM} : \mathbf{A}^{I}(\gamma_j) + \gamma_j \Delta \mathbf{C}^{CM} : \mathbf{A}^{C}(\gamma_j) \right\} \Delta\gamma \quad \text{(IV.3.19)}$$

The expression given in Eq. (IV.3.18) is a continuous function of γ though the strain localization tensors, $\mathbf{A}^{\chi}$, cannot be integrated for the case of ellipsoidal inclusions since they are not analytic functions. Equation (IV.3.19) must therefore be employed for correct implementation for those cases or for simplified direct application in the case of spherical inclusions as the coating distribution function may yield integration extremely difficult or impossible for the case of spherical coated inclusions.

4.3.5.1 Comparison with experiment

The use of DSCT for the case of a distribution of coating thicknesses will be verified by implementing Eq. (IV.3.19) to calculate the TL of a 2.5 cm thick slab of viscoelastic material containing coated micro-inclusions submerged in water. The results are compared with the experimental data of Baird *et al* [26] as well as the SC approximation which only uses the average coating thickness hypothesis. The viscoelastic composite material in question is composed of the "soft" viscoelastic polymer and 10% by volume coated inclusions. The material properties of each phase are given in Table 4.1. The coating fraction distribution is assumed to be well approximated by the Rayleigh distribution given below based on heuristic grounds and through "initial measurements" by Baird *et al* [26]. The average coating fraction is $\bar{\gamma} = 2.5 \times 10^{-2}$.

$$p(\gamma) = \frac{n_0 \pi \gamma}{2\bar{\gamma}^2} \exp\left(-\frac{\pi}{4}\left(\frac{\gamma}{\bar{\gamma}}\right)^2 \right) \quad \Rightarrow \quad n(\gamma) = \frac{p(\gamma)}{\int p(\gamma) d\gamma} \qquad \text{(IV.3.20)}$$

This distribution is then used to calculate the complex effective stiffness tensor of the viscoelastic composite through Eq. (IV.3.19) and the TL is then calculated by employing relations (IV.3.3)-(IV.3.7). The material is fully described by the two Lamé coefficients since the inclusions are spherical and the composite is therefore globally isotropic. It is also important to point out that due to the distribution of shell thicknesses, the equation

expressing the effective density of the composite, (IV.3.6), must be calculated by the law of mixtures relationship below.

$$\rho^{eff} = \rho^{M}\left(1-\varphi\right)+\varphi\sum_{j=1}^{N} n\left(\gamma_j\right)\left[\left(1-\gamma_j\right)\rho^{I}+\gamma_j\rho^{C}\right]\Delta\gamma \qquad \text{(IV.3.21)}$$

Figure 4.25 shows the results of the SC model as modified with DSCT for the case of a variation in coating thickness when applied to the "soft" polymer composite material with 10% coated inclusions tested by Baird *et al* [26]. Included on the plot is the curve resulting from implementation of the uniform coating thickness model given by Haberman *et al* [38].

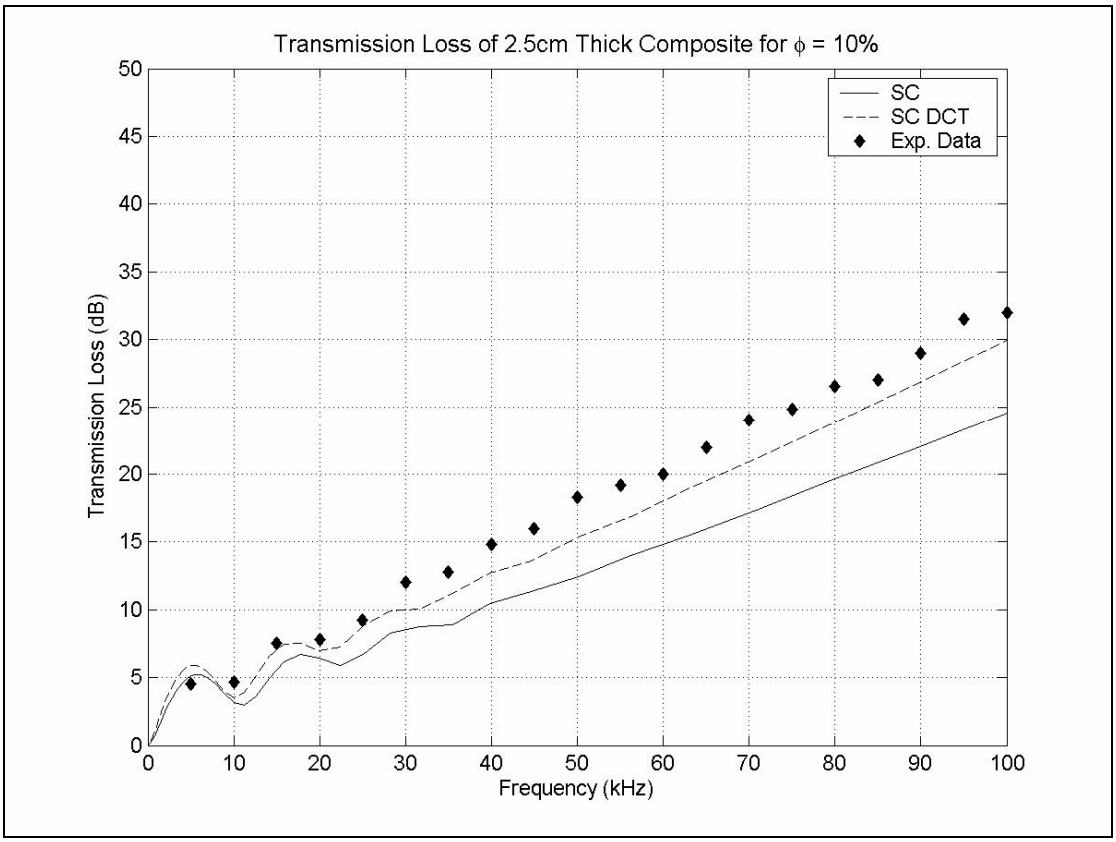

Figure 4.25: Transmission loss calculated using SC and DSCT SC with experimental data from reference [26].

As can be clearly seen in the plot, the agreement of the model with the experimental data is improved. The slope of the high frequency regime is very nearly the same as the trend observed in the data which is a marked improvement over the uniform thickness model. Further, the value of the TL approximation in general is within 2-3 dB across the full range of frequencies inspected: 0–100 kHz.

4.4 Comments on numerical implementation of SC model

Successful SC model implementation depends on the ability to numerically evaluate the implicit problem given in Eqns. (III.2.74)-(III.2.77). These equations represent a tensor relationship whose solution must be found implicitly. The implicit nature requires a careful consideration of numerical root-finding and/or minimization techniques to find the effective viscoelastic stiffness tensor, $\hat{\mathbf{C}}^{eff}$. For the case of spherical isotropic coated inclusions embedded in an isotropic matrix, the resulting effective properties will also be isotropic and Eqns. (III.2.74)-(III.2.77) can be reduced to two implicit equations for the effective Lamé constants, μ^{eff} and λ^{eff}. These relations are given in Appendix A of Haberman *et al* [38]. Solutions to this set of equations can be obtained by using a two-dimensional Newton-Raphson numerical root-finding scheme. This technique for the isotropic effective material is very robust and no convergence problems have been observed regardless of material contrasts or volume fraction of coated inclusions.

The implicit solution to the general anisotropic case is not as simple nor is it guaranteed to converge for all combinations of material stiffness contrasts, inclusion aspect ratios, or volume fractions. One approach to finding an approximate solution of the composite's effective viscoelastic properties is through minimization. The first step in the minimization process it the re-arrangement of the SC tensor equations into a vector function to be minimized to an acceptable level of accuracy. Orthotropic materials are fully described by nine independent viscoelastic constants and therefore the coefficients of the effective stiffness tensor can be re-arranged as a 9x1 vector, $\hat{\mathbf{C}}^{eff} \rightarrow \vec{\mathbf{v}}^{eff}$. The SC model and the approximate solution can then be used to create the function shown below in Eq. (IV.4.1).

$$h\left(\vec{\mathbf{v}}^{eff}\right) = SC\left(\vec{\mathbf{v}}^{eff}\right) - \vec{\mathbf{v}}^{eff} \tag{IV.4.1}$$

In this relationship, $h\left(\mathbf{v}^{eff}\right)$ is the function to be minimized and $SC\left(\mathbf{v}^{eff}\right)$ is understood to represent the result, represented in vector form, of the SC model given in Eqns. (III.2.74)-(III.2.77) for an input of $\vec{\mathbf{v}}^{eff} \rightarrow \hat{\mathbf{C}}^{eff}$. It is also important to point out that the evaluation of $\hat{\mathbf{T}}^{I}\left(\hat{\mathbf{C}}^{\chi}\right)$ is required for correct evaluation of the strain localization tensors, $\hat{\mathbf{A}}^{I}$ and $\hat{\mathbf{A}}^{C}$. This is achieved through numerical integration of the modified Green's tensor, $\hat{\Gamma}^{0}_{ijkl}\left(\mathbf{r}-\mathbf{r}'\right)$, through an *n*-point Gauss-Legendre quadrature integration, after using Fourier transform techniques to transform the ellipsoidal inclusions into spheres in the Fourier domain as outlined in the Appendix A. A nine dimensional simplex method is then used to minimize the implicit relationship given in Eq. (IV.4.1) [157]. The simplex method is robust and effective because it does not require the calculation of rates of change in the function with respect to each individual variable. The technique involves the evaluation of the SC model at ten points suspected to surround the solution in the 9-dimensional space. During implementation, these points are chosen by varying each of the nine elements of $\vec{\mathbf{v}}^{eff}$ of the previous volume fraction step by a small percentage (1% used for this evaluation) thus yielding nine initial guess points and then using the unaltered elements of $\vec{\mathbf{v}}^{eff}$ for the tenth point. The algorithm then uses a series of reflections and contractions of the ten points until an acceptable level of convergence is found. Though the technique is robust, it is not guaranteed to converge to the correct solution and calculation time can be significant for a high volume fraction of inclusions.

Several factors can cause significant problems in the convergence of the numerical evaluation of the general SC model. Therefore, a few qualitative observations may help for successful implementation of the method. The parameter that has the strongest influence on the convergence of the model is the contrast of the moduli of the constituent phases. If the moduli of the inclusion materials are significantly lower than that of the matrix (as is the case with voids or air inclusions) the numerical scheme has great difficulty in converging to the correct solution. This convergence difficulty is still observed when the inclusions are coated. Indeed, glass coated voids embedded in a soft matrix prove to be one of the most difficult set of parameters for the resolution of the general self-consistent model. Another parameter that has strong influence on the convergence of the general model is the aspect ratio of the inclusions. As the aspect ratio (either a/b or a/c) increases, the likelihood of poor convergence behavior also increases. It should be noted that poor convergence due to the inclusion aspect ratio is coupled with the contrast of the material properties, the higher the material contrast the less stable the SC method for any given aspect ratio. However, no obvious practical guidelines can be given. Here it is emphasized that, even with large aspect ratios, the model is strictly valid in the low-ka regime. Yet another parameter that can influence convergence, though to a lesser extent, is the ratio of $\Delta a/a$, i.e., the normalized coating thickness. It has been observed that values of this parameter below 10^{-3} can lead to poor convergence behavior, though, like the effect of the aspect ratio, the influence of $\Delta a/a$ on the convergence is coupled to the material contrast and therefore smaller ratios can be tolerated for lower contrast situations. Other known issues are usual user defined parameters of root-finding techniques, such as the initial values for the numerical search algorithm, the volume

fraction step size, and the number of points chosen for Gauss-Legendre evaluation of the integral of the modified Green's tensor.

4.5 Chapter summary

Despite numerical difficulties manifest in the coated-inclusion SC model, this chapter has shown, through comparison with experiment and parametric studies, both the generality and precision of the SC model. The SC model has been shown to reliably approximate the lossy behavior of many different types of viscoelastic composites. This ability is a great improvement over scattering based models because of the enhanced flexibility to include material anisotropy and the effects of inclusion orientation which is afforded by the micromechanical approach. The enhanced level of generality makes the SC micromechanical model a strong candidate to play a role in a materials design strategy. The next chapter will present a simple multi-scale modeling application that employs the SC model to enhance absorptive properties of a structure through variation of material microstructure.

CHAPTER V

TOWARDS SELF-CONSISTENT MODEL IMPLEMENTATION IN A MATERIALS DESIGN STRATEGY

5.1 Overview

Material selection, traditionally a key component of the design process [4], is a very limiting aspect of design. Indeed the systems design approach, which pervades the design community, assumes that component design will be restricted by the physical properties of materials available [8]. This paradigm is changing as the systems approach is being extended to include the design of materials for multi-functional and multi-physics applications [2, 5]. This approach is called inductive design. The inductive methodology of material design aims to design materials for manufacture, while traditional methods manufacture materials that will be used in design, a deductive approach [6]. One very important aspect of this emerging design approach is the development of robust multiscale material models that can be employed to inform the material design process [2]. For true material design, models capable of bridging disparate length and time scales (length scales ranging from atomistic to macroscopic and time scales ranging from pico-seconds to years) are far beyond the reach of current

modeling approaches. Instead, researchers currently employ a nested hierarchy of different models, each of which is capable of making one or more scale transitions [8]. One of the most prominent problems with this approach is the lack of information about, and/or the extremely complex behavior of material models in the design space [6]. These problems restrict the efficient implementation of many material models in an overarching material design scheme. One way this shortcoming can be overcome is by solving simple multiscale problems in order to observe trends that can inform future materials design strategies. Another approach would by to employ meta-models that approximate material behavior between two specific scales when models based on more rigorous physical considerations impede the design process. The meta-model approach could be employed in material design, for example, to approximate the scale transition between atomistic and continuum behavior. These modeling simplifications permit an efficient means to perform behavioral studies of a model or investigate the design space at multiple scales [9]. Regardless of the method employed, any material design process will require not only robust multiscale models, but also the profound understanding of the material behavior in the design space that a well developed model yields. The aim of this chapter is to provide an introductory level example of self-consistent (SC) model implementation in the design of a lossy structure. This is accomplished by studying the damping properties of a simple structure: a vibrating sandwich plate. The results of this study provide preliminary insight into the role the quasi-static SC model can play in a material design strategy and lay the groundwork for more detailed research.

5.2 Multiscale windshield modeling

Structural applications for layered sandwich plates are numerous and typically aim to reduce overall weight while simultaneously maintaining structural rigidity. Some examples of such sandwich structure applications include aircraft wings and fuselage [10] or reinforcement and noise isolation in automobiles [11, 14]. One consequence of sandwich plate geometry is a pronounced ability to provide acoustic and thermal isolation [158]. An example of a structural element that fulfills all of the roles highlighted above is the automobile windshield. Current windshield design is a layered structure consisting of two identical high performance glass layers sandwiching a viscoelastic layer. From a mechanical perspective, the interior viscoelastic layer serves the dual purpose of holding glass fragments in place in the event of projectile impact while simultaneously providing enhanced structural vibration dissipation and sound isolation qualities during normal operating conditions. The ability to reduce sound transmission has become one of the many requirements placed on automobile windshield. This requirement stems from a desire to reduce driver noise annoyance and to eliminate structural vibrations of the automobile frame as a whole.

The case study presented in this chapter aims to model a sandwich plate behavior as a multiscale structure. In so doing, this study introduces the key variables which define the design space and provides an important study of their interaction and influence on the behavior of the structure. Figure 5.1 illustrates the multiscale windshield modeling approach employed. The study begins with part level modeling. First, a simple sandwich plate model is introduced and the mechanisms that enhance flexural wave

damping are discussed in the context of strain energy. Several parametric studies investigating optimal damping design of a sandwich plate complete the part level modeling study. Following this analysis the structural level model considered is the modal response of a viscoelastically constrained plate and beam. The simple layered plate model is incorporated into the modal analysis and results are compared with a sophisticated finite element model. Finally, the study considers the effect of microstructural behavior on structural level damping through SC homogenization. The aim of this study is to observe the capability of microstructural behavior to increase the overall absorptive properties of the plate while limiting negative effects on its structural rigidity role thereby providing insight to multiscale modeling for damping applications.

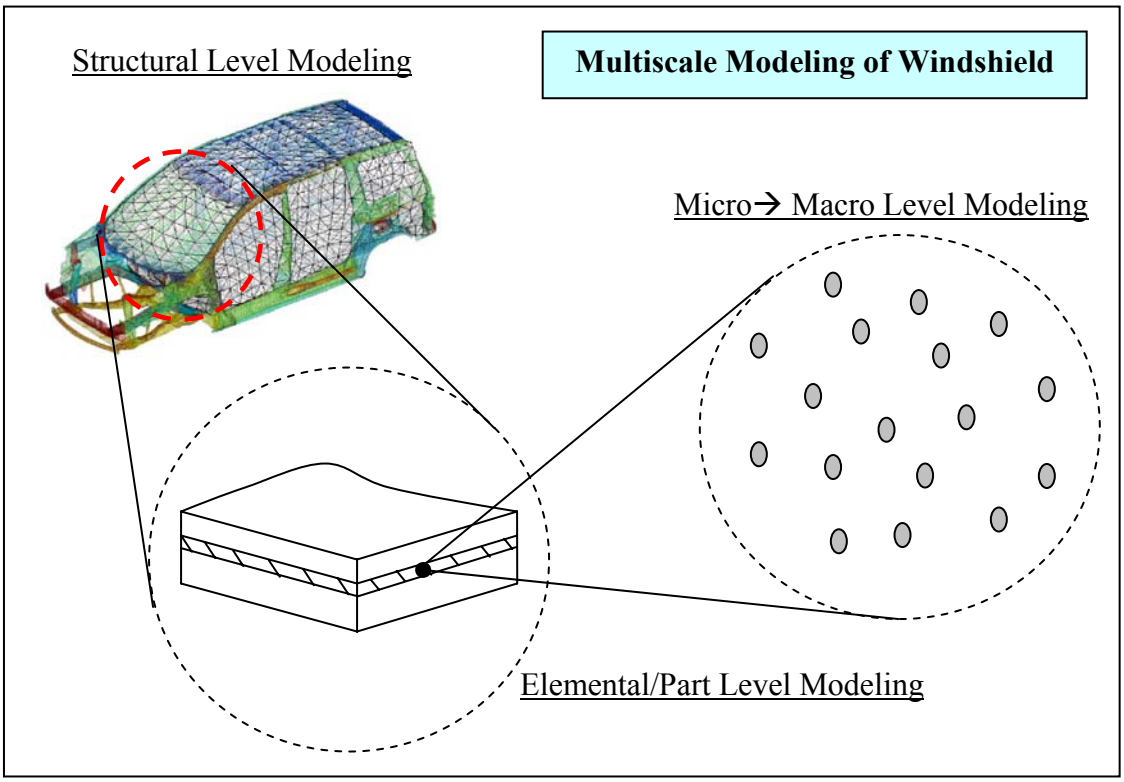

Figure 5.1: Multiscale windshield modeling approach.

5.3 Part level modeling: Damped flexural waves in a sandwich plate

The three layer structure of a windshield capitalizes on the interlayer's lossy properties by inducing high shear strains in the viscoelastic layer upon vibrational excitation [14]. The high shear strain in the interlayer results from the viscoelastic material's relatively low shear resistance as compared to that of the sandwiching plates. The high shear compliance of the constrained viscoelastic layer means that shear stresses resulting from an imposed bending moment will translate into large deformations [31]. The ultimate consequence of this geometric configuration is an increase in vibrational and acoustical energy damping capacity coupled with the structural advantage of being highly shatter resistant [11].

The study of sandwich structures is not a recent development. As early as 1959 Kerwin presented an analytic thin three-layered plate model [159]. The plates he studied consisted of three isotropic layers and had no restriction on layer thicknesses or symmetries. Following this introductory model, Ross, Kerwin, and Ungar derived a more general analytic model that describes the flexural behavior of a three layered plate to approximate the lossy behavior of structures with viscoelastic treatments (external viscoelastic layers, non-symmetric or symmetric viscoelastic sandwich structures) [31, 160]. Their model was followed by many other constrained plate analytical models that are applicable for plates having simple boundary conditions. Representative examples include Ditaranto's layered beam model [161], Mead and Markus's model of the forced vibration of a layered beam [45] , Yan and McDowell's work on the dynamic behavior of constrained layer plates [162] , and Cupial and Niziol seminal work on the damping of a

three layered plate [163]. The strength of analytical models lies in their ability to quantitatively compare the behavior of different sandwich structures with relative ease of implementation. For many cases, however, such models are not applicable because they are limited to simple geometries (flat plates, uniform thicknesses, etc) and simple boundary conditions (B.C.'s). True engineering problems often present complexities that analytical models cannot take into account. It is for this reason that many researchers have concentrated on the development of sandwich structure finite element (FE) models which approximate dynamic lossy behavior. Representative works in this area are those of Soni [44], Johnson and Kienholz [164], Rikards and Chate [165], and Daya and Potier-Ferry [166]. For an excellent review of a significant developments in constrained layer damping models, see Austin [167]. FE models are more precise and provide a richer analysis of the dynamic stress and strain states in a layered plate. Further, they can be implemented in structural analysis of higher order structures, such as the structural behavior of an automobile as a whole. However, the aim of this chapter is not to provide a detailed analysis of a complex structure but rather to give an introductory level study of the effect of microstructure on the damping properties of a multiscale approach. It is for this reason that FE studies will only be employed in this study for qualitative verification of analytical studies.

5.3.1 Approximation of the effective bending modulus of a sandwich plate

The concise study of the microstructural effects on the damping capacity of a layered plate as a structural element first requires the selection of the appropriate part-

level model. The analytic model developed by Ross, Kerwin, and Ungar (RKU) [31] is ideal for our present study. This model is computational light and provides reasonable estimates of the enhanced damping capacity due to a constrained viscoelastic layer as a function of frequency, material properties, and plate geometry [168].

The proceeding discussion has pointed out that the constrained layer geometry and material stiffness contrast lead to the enhanced damping capacity of the layered plate. These both contribute by inducing large shear deformation in the absorptive central layer. This increased deformation leads to a large increase in strain energy located in the lossy material thereby increasing the damping capacity of the layered plate as a whole [160]. Kerwin [159] showed that the flexural behavior of such a layered plate is reasonably approximated as a uniform plate having an effective complex bending (or flexural) modulus. The real part of this modulus describes the resistance to flexure due to an imposed time-varying bending moment and the imaginary part relates is a descriptor of the composite plate's capacity to absorb flexural wave energy [31, 159]. Indeed, for an out of plane flexural disturbance, $\hat{w}(x,t)$, propagating in the +x direction of a layered plate the damped wave is described using Eqns. (V.3.1) and (V.3.2) below. These expressions are analogous to Eq. (IV.3.2) for pressure wave propagation.

$$\hat{w}(x,t) = \hat{A}e^{j\left(\omega t - \hat{k}^{flex} x\right)} = \hat{A}e^{-\hat{\alpha}^{flex} x} e^{j\left(\omega t - \hat{k}^{flex,'} x\right)} \tag{V.3.1}$$

where:

$$\hat{k}^{flex} = \hat{k}^{flex,'} - j\hat{\alpha}^{flex} = \left(\frac{\omega^2 \rho^{eff} h^{tot}}{\hat{B}^{eff}} \right)^{\frac{1}{4}} \tag{V.3.2}$$

In the above expressions $\hat{A}$ is the complex amplitude, ω is the angular frequency, $\hat{k}^{flex,'}$ and $\hat{\alpha}^{flex}$ are components of the frequency dependent complex flexural wavenumber, $\hat{k}^{flex}$, ρ^{eff} is the effective density of the entire plate, h^{tot} is the thickness of the entire plate, and $\hat{B}^{eff}$ represents the layered plate's effective complex frequency dependent bending modulus. Note also that the present study treats structural vibrations. Therefore, *in keeping with the conventions of the vibrations community, the '$e^{j\omega t}$' convention is employed in this section*. The RKU model aims to provide an accurate approximation of the plate's effective bending modulus which takes the exaggerated interlayer shearing into account. This is accomplished by writing equations of motion for the plate element shown below in Figure 5.2.

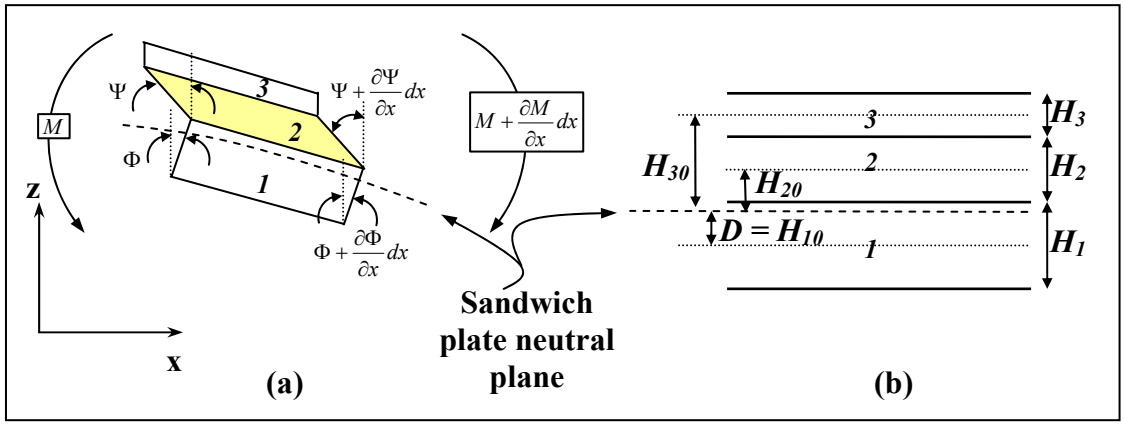

Figure 5.2: (a) Differential element of a sandwich plate; (b) Cross sectional geometry.

The RKU model results from solving the wave equation for the out of plane flexural disturbance, Eq. (V.3.3), together with the moment equation, (V.3.4), given below.

$$\nabla^4 \hat{w}(x) - \frac{\omega^2 \rho^{eff} h^{tot}}{\hat{B}^{eff}} \hat{w}(x) = \frac{\hat{p}(x)}{\hat{B}^{eff}} \qquad \text{(V.3.3)}$$

$$\hat{M}(x) = \hat{B}^{eff} \frac{\partial \hat{\Phi}(x)}{\partial x} = \sum_{i=1}^{3} \hat{M}_i(x) + \sum_{j=1}^{3} \hat{F}_j H_{j0} \qquad \text{(V.3.4)}$$

In these expressions $\hat{p}(x)$ represents the frequency dependent and spatially varying forcing pressure, $\hat{M}(x)$ denotes the total flexural moment applied to the plate, $\hat{M}_i(x)$ is the resulting moment in each layer, $\hat{F}_j(x)$ is the net transverse force in each layer, and H_{j0} represents the distance from the center j^{th} of the layer to the neutral plane of the composite [31].

This resulting model is simple and it has many restrictions for implementation. They are the following [31]:

1) The Young's modulus of the upper and lower layers (*1* and *3*) must be much larger than that of layer *2*.

2) The flexural, shear, and longitudinal wavelengths of the composite plate must be much larger than the total thickness of the plate.

3) The slope of the neutral plane must be very small, $\Phi(x) << 1$.

4) The thickness of the interlayer (layer *2*) remains fixed (no standing waves within the interlayer).

Ross *et al* derived their model for the effective bending modulus of a three layer plate using these simplifying assumptions. The resulting RKU model does not have any further restrictions regarding material or geometric symmetries. If symmetry is required, thereby creating a true "sandwich" plate, the following additional assumptions must be added [169]:

5) Layers *1* and *3* have identical material properties and geometries. The Young's modulus is denoted as E, the density ρ, and the thickness h ($H_1 = H_3 = h$).

The result of these many simplifying assumptions is the set of implicit relations below for the layered plate's complex effective bending modulus.

$$\hat{B} = \frac{1}{6}\hat{E}h^3\left(1 + 6Y\left(\frac{\hat{g}}{1+2\hat{g}}\right)\right) = \hat{B}'\left(1 + j\hat{\eta}_p\right) \qquad \text{(V.3.5)}$$

Here Y represents a variable called the geometric parameter and $\hat{g}$ is the complex shear parameter. This simple equation satisfies physical intuition about the behavior of a layered plate. The term $\hat{E}h^3/6$ is simply the bending rigidity of two plates of thickness h about their base. The term within the parenthesis increases the bending rigidity based on geometry and the interlayer's shear resistance. The geometry and shear parameters are defined in Eqns. (V.3.6) and (V.3.7) below.

$$Y = \left(1 + H\right)^2 \quad \text{with} \quad H = \frac{H_2}{h} \qquad \text{(V.3.6)}$$

$$\hat{g} = \frac{1}{h^2}\left(\frac{\hat{\mu}_2}{\hat{E}H}\right)\sqrt{\frac{1}{\omega^2}\frac{\hat{B}^{eff}}{h^{tot}\rho^{eff}}} = \hat{g}'\left(1 + j\hat{\gamma}\right) \qquad \text{(V.3.7)}$$

In the above relationships, $\hat{\mu}_2$ is the interlayer's complex shear modulus, $\hat{\mu}_2 = \hat{\mu}_2^{'}\left(1 + j\hat{\beta}\right)$, and the effective density of the composite plate is calculated from the following law of mixtures approximation.

$$\rho^{eff} = \left(1 - H_2/h^{tot}\right)\rho + \left(H_2/h^{tot}\right)\rho_2 \tag{V.3.8}$$

Ross *et al* further observed that assumption (*2*) above requires that $\hat{g}^{'}$ be larger than unity. As previously stated, this model is yields an implicit solution for the effective bending modulus. Appendix E details a numerical solution scheme for RKU model implementation.

It is now interesting to show constrained layer damping behavior as approximated by the RKU model. For this purpose, consider a symmetric plate composed of two identical glass layers sandwiching a Saflex© PVB (viscoelastic) layer [170]. The layer geometry and material properties are given in Table 5.1. The values chosen represent PVB complex moduli corresponding to observed behavior at 1 kHz (beginning of high sensitivity frequency range for human hearing) and 20ºC. The values were approximated from Havriliak-Negami (HN) fits [128] of DMTA data, see Figure 5.3. The HN model is given in Eq. (V.3.9) and the HN coefficients for this PVB material were found to be: $\mu_\infty = 2.35\times10^8$, $\mu_0 = 4.79\times10^5$, $\alpha_{HN} = 0.46$, $\beta_{HN} = 0.1946$, and $\tau_0 = 0.3979$.

$$\mu^*(\omega) = \mu_\infty + (\mu_0 - \mu_\infty)\left[1 + (j\omega\tau_0)^{1-\alpha}\right]^{-\beta} \tag{V.3.9}$$

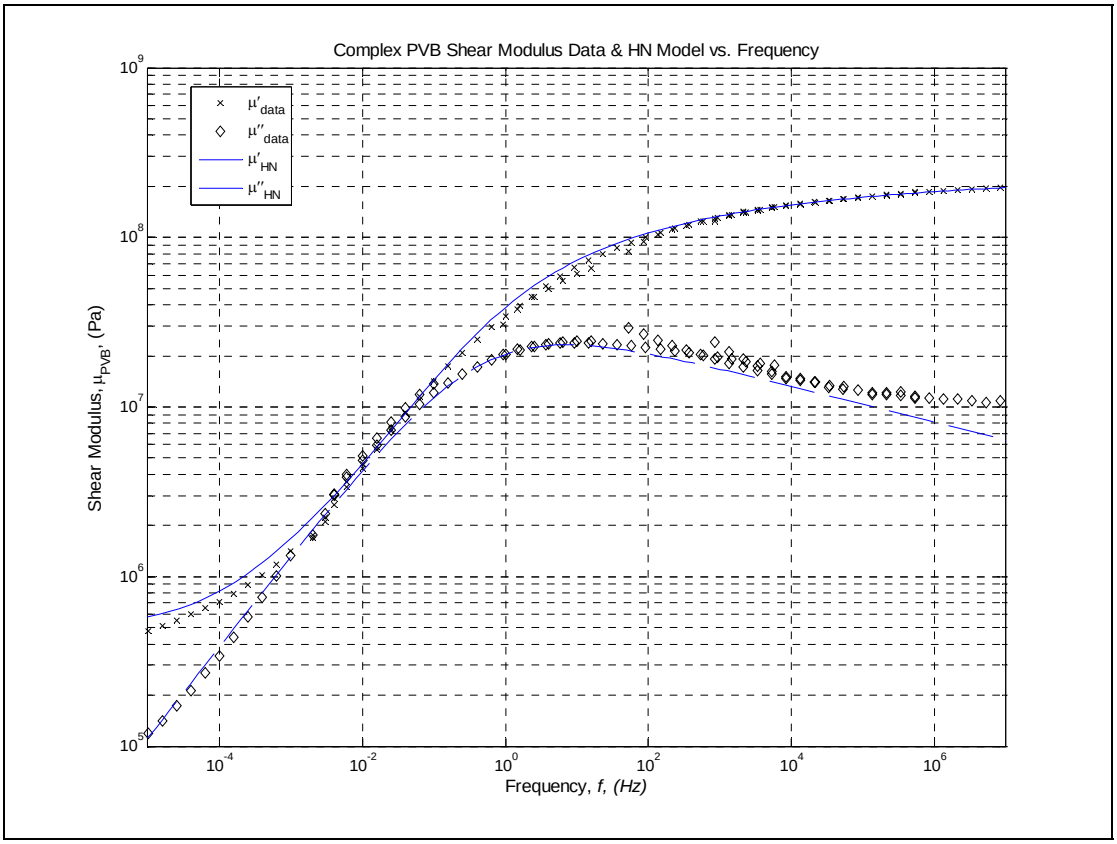

Figure 5.3: DMTA data and HN curve fits for PVB material.

Table 5.1: Layer properties representing windshield constituent properties and geometry.

	H_x (m)	$\mu'(1+j\beta)$ (GPa)	$E(1+j\eta)$ (GPa)	ρ (kg/m^3)	f (Hz)
Layers 1&3	2.0×10^{-3}	$29.5(1 + 0.02j)$	$72(1 + 0.02j)$	2469	1000
Layer 2	8.0×10^{-4}	$0.133(1 + 0.13j)$	$0.396(1 + 0.13j)$	1115	1000

The plots below show parametric studies of the effective sandwich plate bending modulus, $\hat{B}$, shear parameter, $\hat{g}$, and flexural wavenumber, $\hat{k}^{flex}$, as a function of the thickness ratio, *H*.

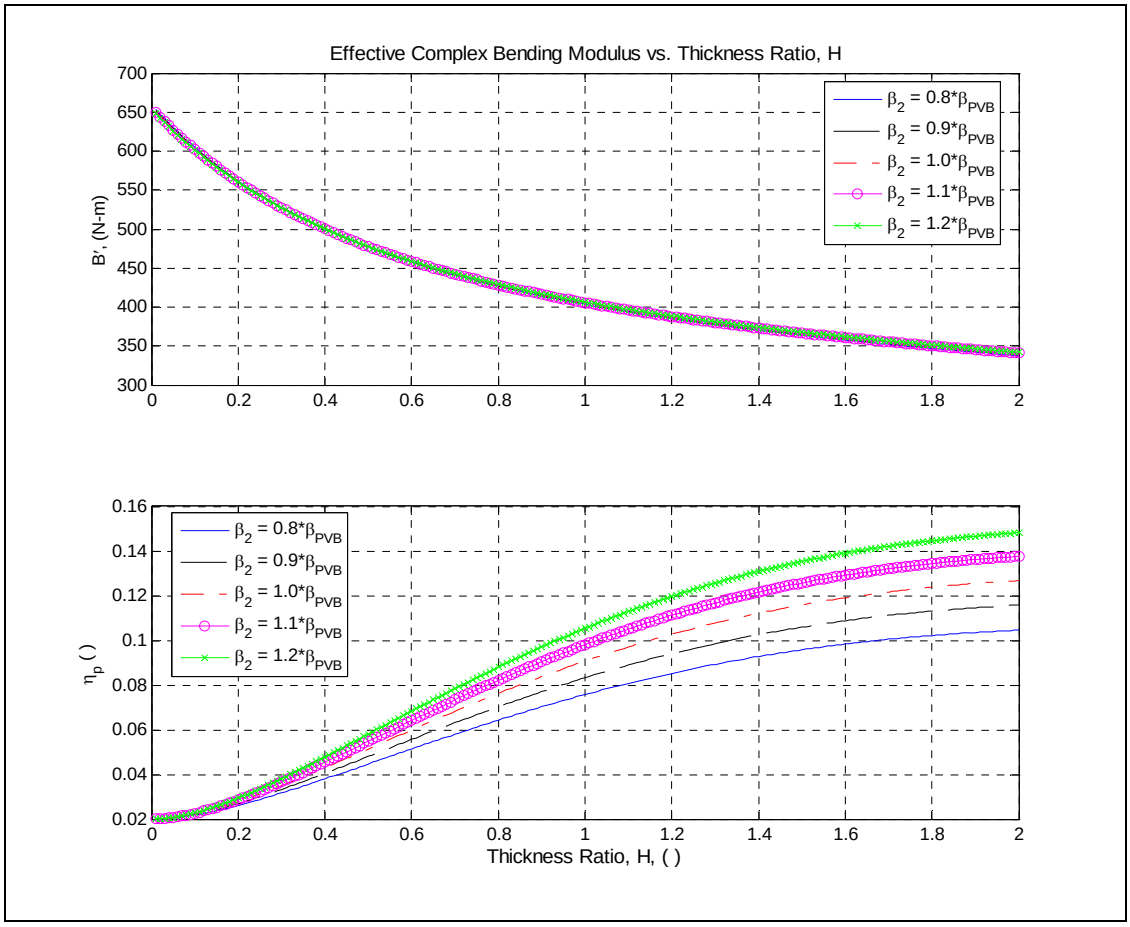

Figure 5.4: Variation of sandwich plate complex bending modulus as a function of the thickness ratio, *H*. Parametric study on the shear loss factor of the interlayer.

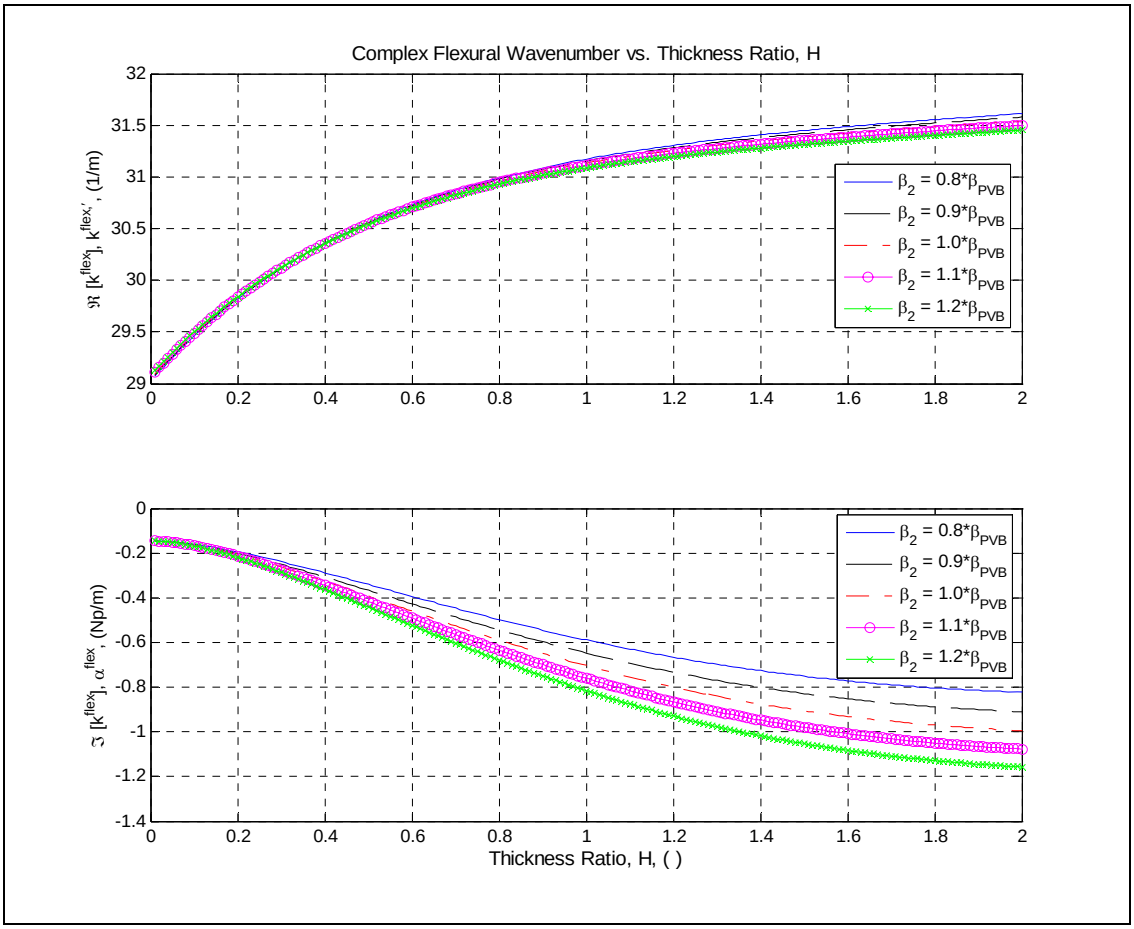

Figure 5.5: Variation of sandwich plate complex flexural wavenumber as a function of the thickness ratio, *H*. Parametric study on the shear loss factor of the interlayer.

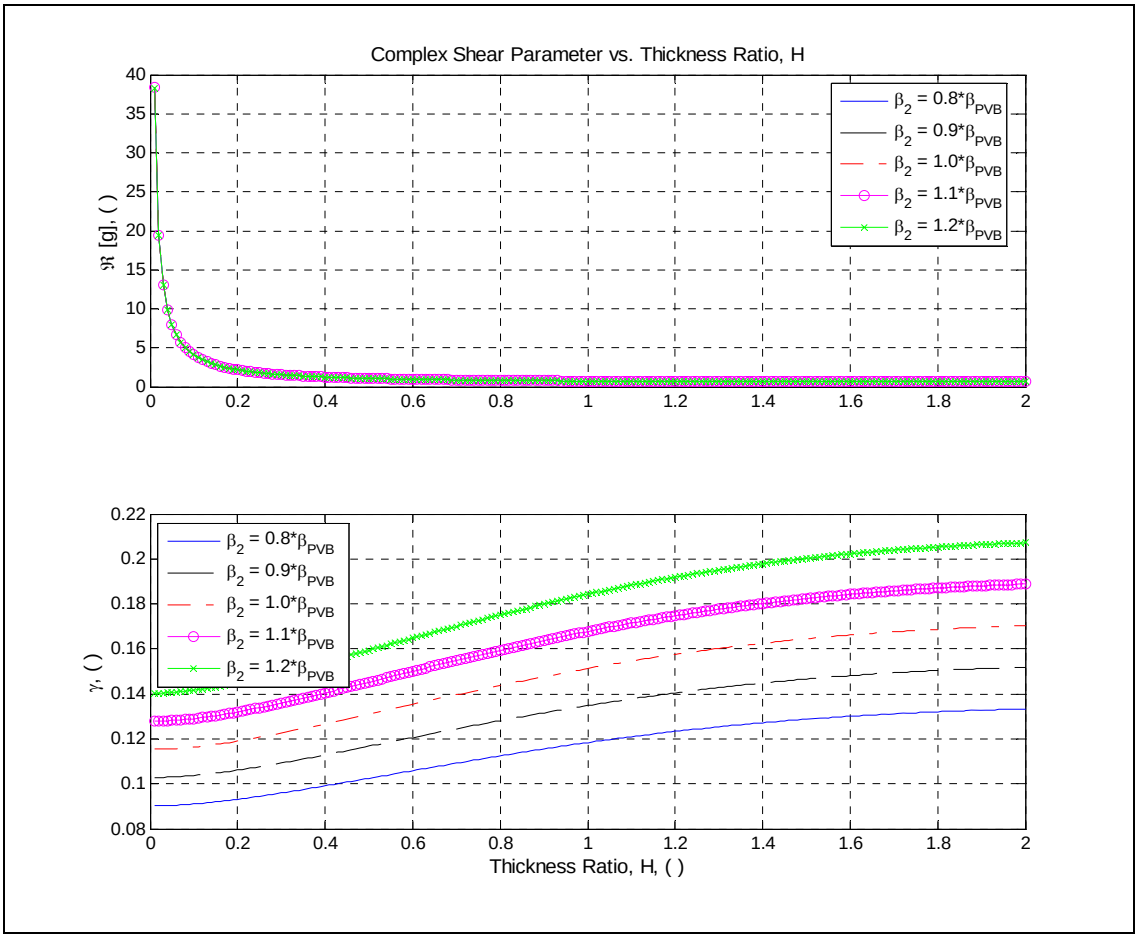

Figure 5.6: Variation of sandwich plate complex shear parameter as a function of the thickness ratio, *H*. Parametric study on the shear loss factor of the interlayer.

Several physically intuitive behaviors are apparent from these plots. Figure 5.4 shows that the plate's resistance to flexure decreases with increasing *H*. Coupled with this reduction in flexural rigidity is a loss factor increase. The increased damping capacity results from augmented strain energy located in the lossy interlayer. The increases in the magnitude of the flexural wavenumber and attenuation coefficient shown in Figure 5.5 are also direct results of the increasing compliance of the sandwich plate. Figure 5.6 illustrates that the shear parameter's loss factor also increases with increasing

H and also as the shear loss factor of the interlayer, $\hat{\beta}_2$, increases. One very important observation is that the RKU model is *not* valid for small values of $|\hat{g}|$ (assumption *2* listed above) thus limiting application of this model for these constituent material properties to values of H greater than ~0.6.

It is also interesting to inspect the flexural modulus variation as a function of the shear parameter's loss factor, $\hat{\gamma}$ while keeping H constant. Figure 5.7 shows the results of such a study.

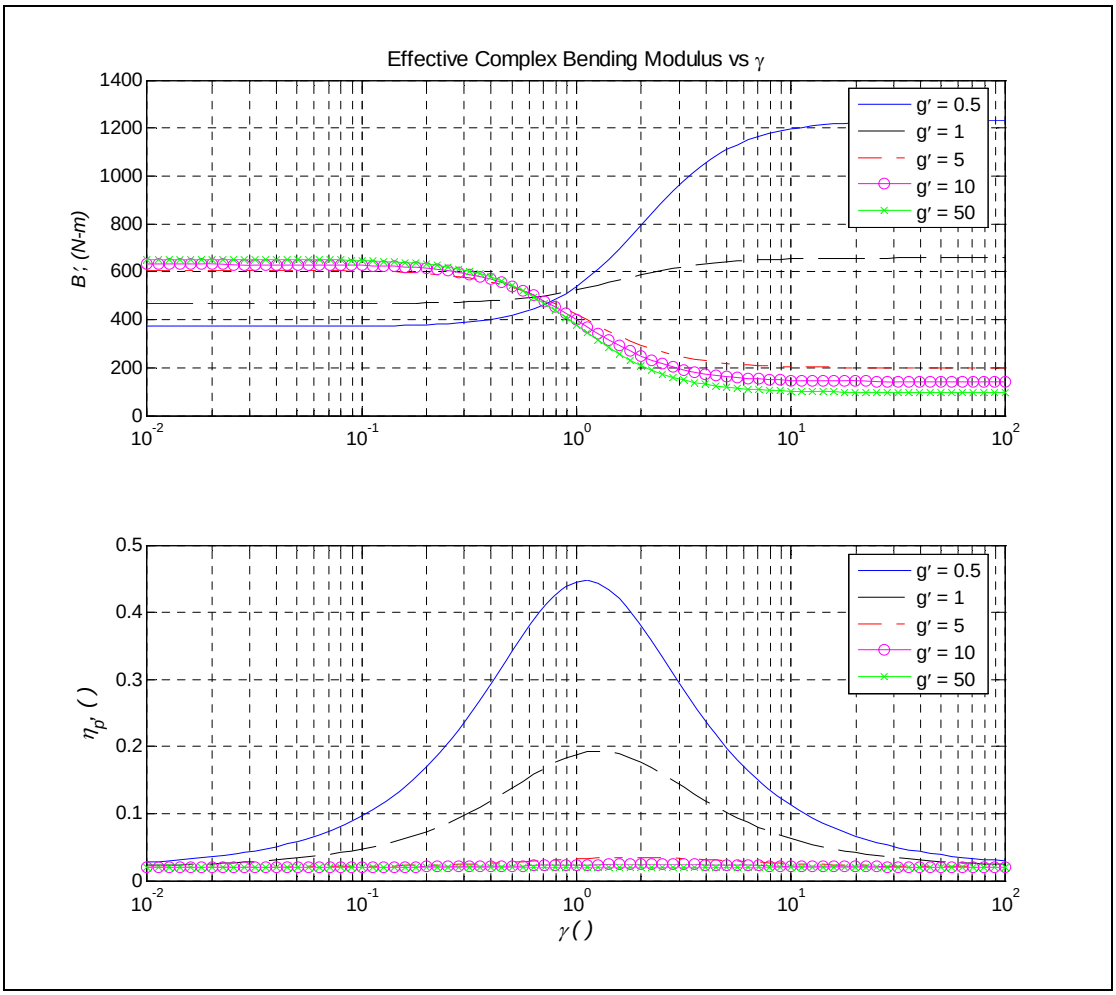

Figure 5.7: Complex effective flexural modulus calculated with BKT model as a function of the shear parameter's loss factor, γ for fixed values of g'.

This figure clearly shows that at a given frequency, ω, there exists some value of $\hat{\gamma}$ for each value of $\hat{g}'$ that yields optimal damping properties for a sandwich plate in flexure, $\hat{\eta}_p^{opt}$. If all other parameters are fixed, this optimal value of $\hat{\gamma}$ can be found through inspection of the partial derivative $\partial\hat{\eta}_p/\partial\hat{\gamma}$. Figure 5.8 shows the complex effective bending modulus for a large range of $\hat{g}'$ values when the associated value loss factor is optimal, $\hat{\gamma}^{opt}$. Mathematically stated, the value of $\hat{B}$ is calculated as a function of $\hat{g}'$ when the associated value of $\hat{\gamma}$ is such that $\partial\hat{\eta}_p/\partial\hat{\gamma}\big|_{\hat{\gamma}^{opt}} = 0$.

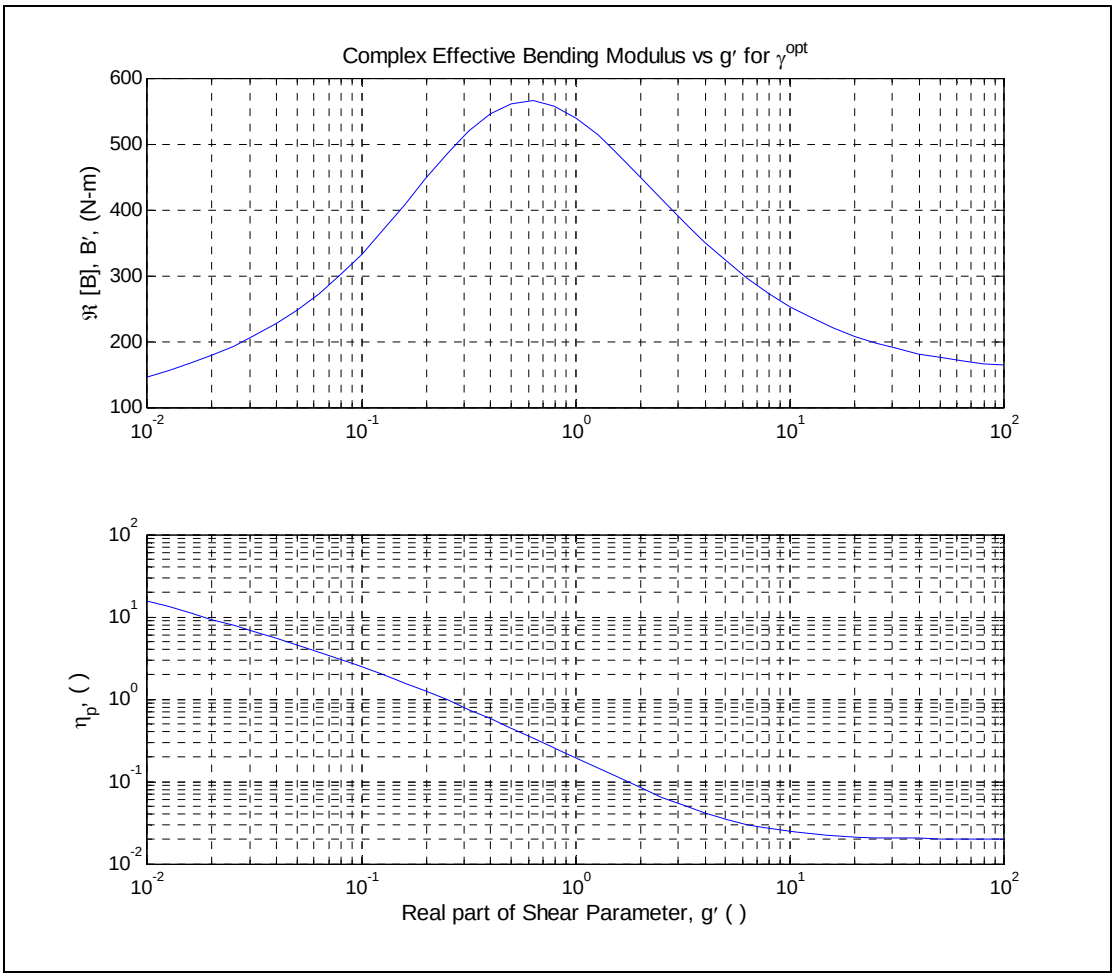

Figure 5.8: "Optimally" lossy complex effective bending modulus calculated as a function of $\hat{g}'$. The material properties employed are those given in Table 5.1

This plots clearly show that highest damping is expected with decreasing values of $\hat{g}'$. It is imperative to keep in mind, however, that the RKU model is not valid for small values of $\hat{g}'$. It is also important to observe that variations in $\hat{g}'$ have large effects on the plates overall resistance to flexural deformation. Large reductions in flexural rigidity, though ideal for damping applications, are not acceptable for such real-world applications as windshields which must fulfill multiple, often conflicting, design requirements [11]. The ideal solution for such an application is a more robust design that considers both the

flexural rigidity, $\hat{B}'$, and damping capacity, $\hat{\eta}_p$, in an effort to find the highest damping capacity with a minimal reduction in rigidity.

5.3.2 RKU model sensitivity analysis

The automobile windshield is a good example of a structural element requiring both structural rigidity and absorptive qualities. One simple manner to approach this optimization problem is through sensitivity analysis of important variables. The materials and geometry given in Table 5.1 are representative of actual values in current windshield design, however, Figure 5.6 shows that they yield a shear parameter far from optimal across all frequencies of interest ($H = 0.4$, $\hat{g}' \approx 2$, and $\hat{\gamma} \approx 0.13$ but $\hat{\gamma}^{opt} \approx 1.1$). All of the above information suggests that the most efficient means to increase the damping capacity of the plate while having a minimal effect on the flexural rigidity as a whole is to increase $\hat{\gamma}$ while minimally decreasing the real part of the shear parameter, $\hat{g}'$. It is assumed that structural design constraints require the total thickness and the real parts of the material properties remain constant. Therefore, the two remaining variables that can influence the plate's lossy behavior are the thickness ratio, H, and shear loss factor of the interlayer, $\hat{\beta}_2$. Figure 5.9 shows the results of this sensitivity analysis.

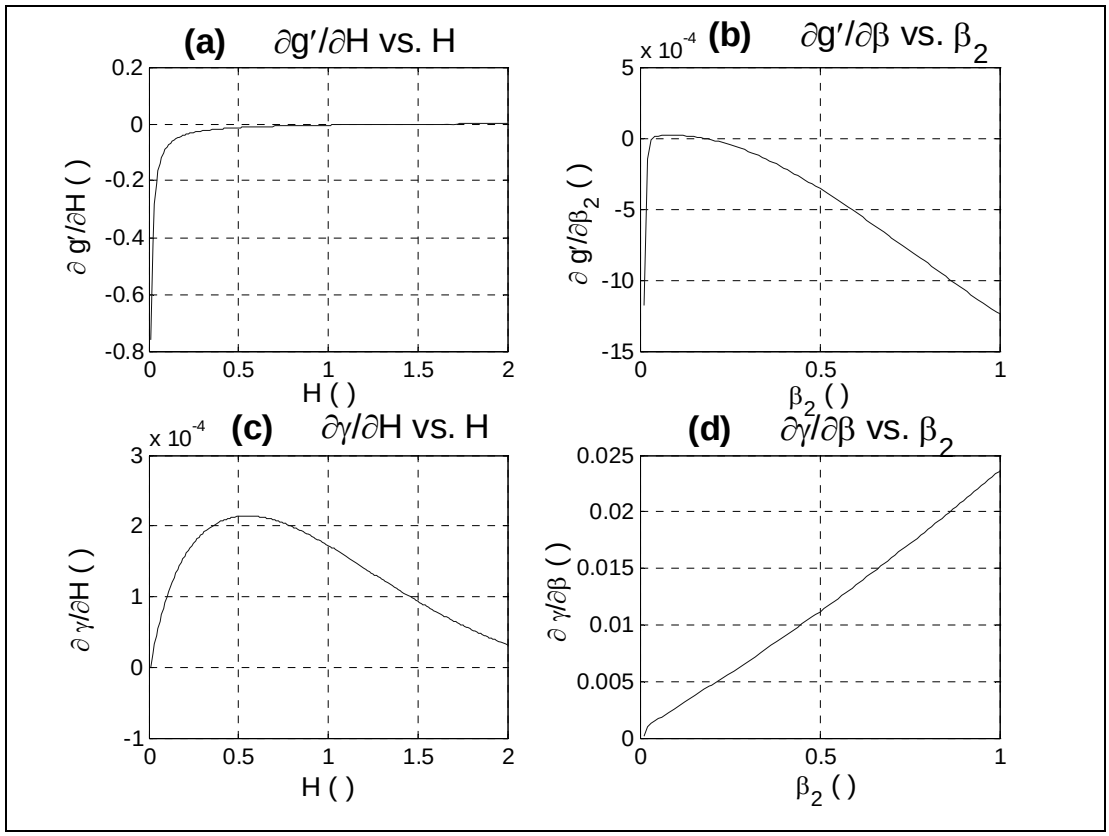

Figure 5.9: Sensitivity of the complex shear parameter to changes in the thickness ratio and the shear loss factor of the interlayer. Partial derivatives of *g'* and *γ* with respect to *H* and β_2 are shown. For (a) and (c), $\beta_2 = 0.13$; for (b) and (d), $H = 0.4$.

Plots (a) and (c) show that varying the thickness ratio has a strong negative effect on the stiffness (decrease of $\hat{g}'$) with minimal improvement of the damping capacity. On the other hand, it is obvious that an increase of the shear loss factor of the interlayer will have a notable effect on the damping capacity, $\hat{\gamma}$, ($\hat{\gamma} = f\left(\left[\hat{\beta}_2\right]^2\right)$) with a minimal increase in compliance. The previous chapter has shown that introducing inhomogeneities into a viscoelastic material can change the macroscopic damping capacity significantly. Section 5.5 will employ the SC model to investigate such microstructural effects on structural damping behavior. It should also be noted that the complex shear parameter's

dependence on the stiffness ratio, $\hat{\mu}_2^{'}/\hat{E}^{'}$ has also been studied. The results show, however, that when in the RKU's domain of applicability, specifically restriction (*1*), variations of this ratio have little influence on the plate's damping capacity as a whole.

This section has shown that a simple analytical model for the effective bending modulus of a sandwich plate can yield considerable knowledge about the design space. The influence and interaction of design space variables has been investigated resulting in several guidelines for the design of the constituent materials. In short, the part level modeling performed here has given insight and a few "handles" for lossy structure design. Further knowledge can be gained by exploring damping behavior on the structural level, the subject of the following section.

5.4 Structure level modeling

The previous section has shown that much information about constrained layer damping is gained from part level modeling and analysis. In application, however, such plates will be mounted in structures which excite structural vibration. The resulting structure level frequency response is governed by the part level behavior and the plate's boundary conditions (BC's) [171]. Both the BC's and the plate's constitutive lossy behavior have a significant effect on the damping capacity of the structure as a whole. The analysis below extends the present analysis to forced vibration of beams and plates with viscoelastic BC's. The study examines the independent influence of BC's and plate lossy behavior on structural modal damping. It is limited to the vibration of *flat* constrained layer sandwich structures with simple plate geometries. The aim of this study is to approximate the behavior of a windshield mounted in a rubbery material in

order to observe modal loss factor trends resulting from variations in the plate and B.C. material behavior. These trends are studied and it is shown how this information can be used to inform design on the part and microstructural scales. It is important to stress that the work presented here is an elementary step which gives reason to implement a materials design approach. It is submitted a proof of concept and motivation for SC model application as a tool in the materials design process than an exhaustive study. More advanced modeling techniques, such as finite elements, should be employed to approximate true B.C.'s and complex plate geometries which occur in reality. Chapter VII employs the knowledge gained in this chapter by integrating the SC modeling approach into a Decision Based Design protocol to solve a material design problem.

An initial validation of the RKU model implementation in structural level models is a comparison of resonant frequency approximations and experimental observations. The results of acoustic Transmission Loss (TL) tests of four sandwich structures can be used for this purpose. The sandwich structures, prepared by Pacific Northwest National Laboratory (PNNL), were geometrically identical (length, width, and layer thickness) each having slightly different viscoelastic interlayer materials. Generic sample geometry and material properties are given below in Table 5.2. The exact material properties of each interlayer material were not provided, but are known to be very close the PVB values provided in Table 5.2.

Table 5.2: Generic layer and plate properties used to approximate resonant behavior. ν ~ Poisson ratio, L ~ sample length, and W ~ sample width.

	$H_x\ (mm)$	$\mu^{'}(1+j\beta)\ (GPa)$	$\nu\ (\ )$	$\rho\ (kg/m^3)$	$L\ (cm)$	$W\ (cm)$
Layers 1&3	2.0	$29.5(1 + 0.02j)$	0.23	2469	30.5	30.5
Layer 2	0.8	$0.133(1 + 0.13j)$	0.49	1115	30.5	30.5

Two resonant frequency approximations, one corresponding to Law of Mixtures (LOM) homogenization and the other to RKU modeling of sandwich plate material properties, are given below in Table 5.3. See Appendix F for a derivation of elementary LOM approximations of in- and out-of-plane properties of layered plates. These values were calculated using the information in Table 5.2 and eigenvalues based on Rayleigh-Ritz methods provided by Angloulvant [172].

Table 5.3: Approximate sandwich plate resonant frequencies from LOM and RKU model homogenization.

Part-Level Model	*Resonant Frequency of 1st Six modes (Clamped Boundaries)*					
	f_{11} (*Hz*)	f_{12} (*Hz*)	f_{22} (*Hz*)	f_{13} (*Hz*)	f_{23} (*Hz*)	f_{33} (*Hz*)
LOM	580	1100	1620	1900	2390	3150
RKU	518	1418	1418	1648	2100	2780

TL testing was done for third-octave bands between 125 Hz and 8 kHz in accordance with SAE J1400 [173]. Samples were mounted in the test window between the reverberant chamber and the semi-anechoic chamber of the Integrated Acoustics Laboratory (IAL) at Georgia Tech. Figure 5.10 shows a schematic of the test setup and Figure 5.12 shows an image of the test window.

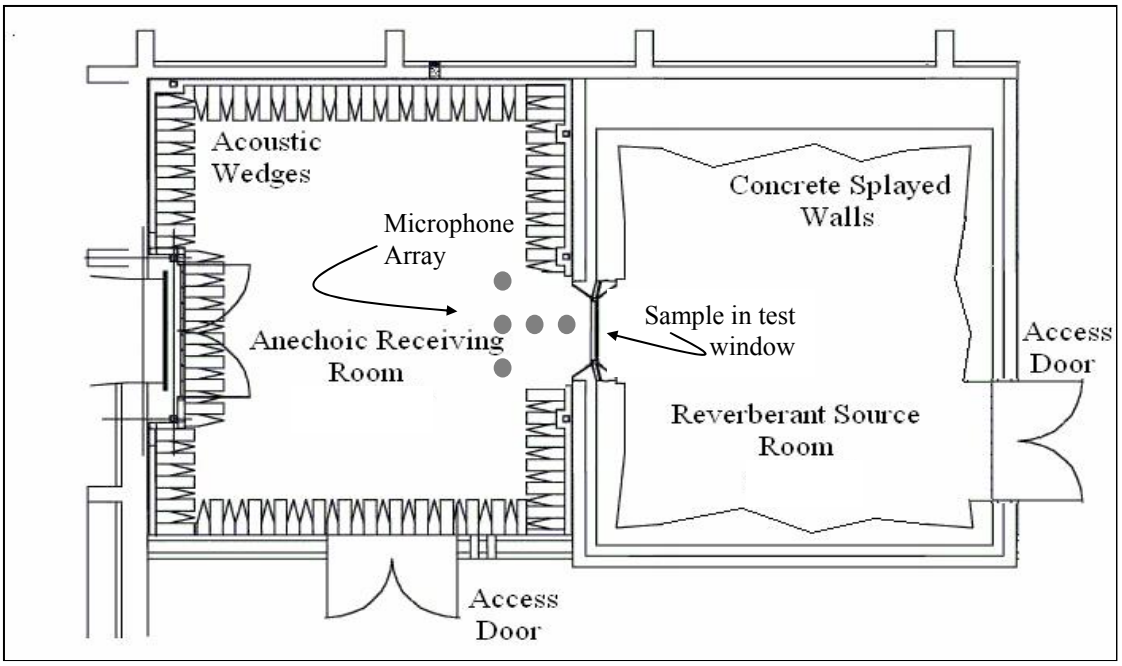

Figure 5.10: Schematic of general set-up used for SAE J1400 TL testing.

Figure 5.11 shows experimental TL results of four different glass-viscoelastic sandwich plates. This experimental data shows two important facts: (1) An increase in the interlayer damping capacity (S4) leads to a notable increase in TL and (2) Incorporation of RKU part level modeling into structural models yields increased accuracy in the approximation of the first and second resonant frequencies. The first point validates the discussion given in the previous section and the second validates the usage of the RKU model in structural models such as modal analysis.

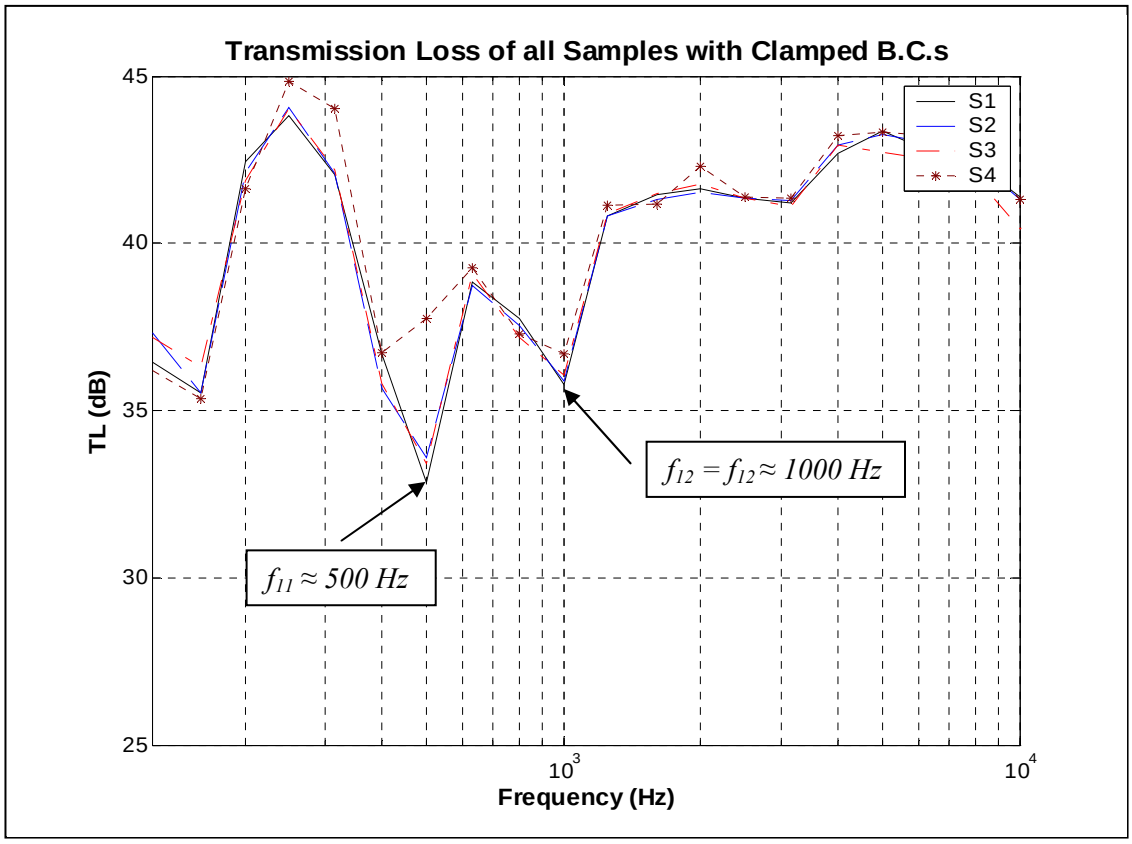

Figure 5.11: TL due to four different windshield samples. Notches in TL at ~ 500 Hz and ~ 1000 Hz agree well with RKU model approximation.

One further validation provided by these experiments is the effect of B.C.'s on observed TL. The experimental data in Figure 5.11 was taken with samples having clamped B.C.'s as shown in Figure 5.12.

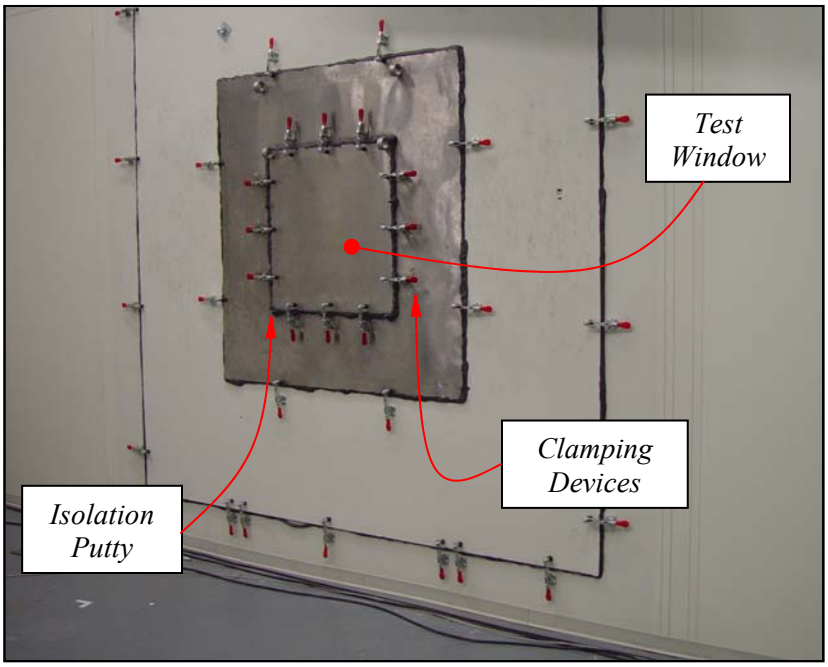

Figure 5.12: TL experimental setup. Sample window contains stainless steel plug. Note red clamps and isolation putty around exterior of test window.

The clamped conditions were modified in another set of tests by releasing the red clamps seen above in Figure 5.12 to approximate viscoelastic boundary conditions. The exact conditions are very difficult to quantify because the samples were held in place only by isolation putty whose purpose is to seal air gaps between the reverberant and semi-anechoic chambers. Though they are difficult to quantify analytically, the qualitative difference in TL near the first resonant frequency is significant (~ -4*dB re 20μPa*), see the results for S1 shown in Figure 5.13. These results also show the expected reduction in resonant frequency resulting from the decreased "stiffness" of the structure as a whole resulting from the viscoelastic B.C.'s.

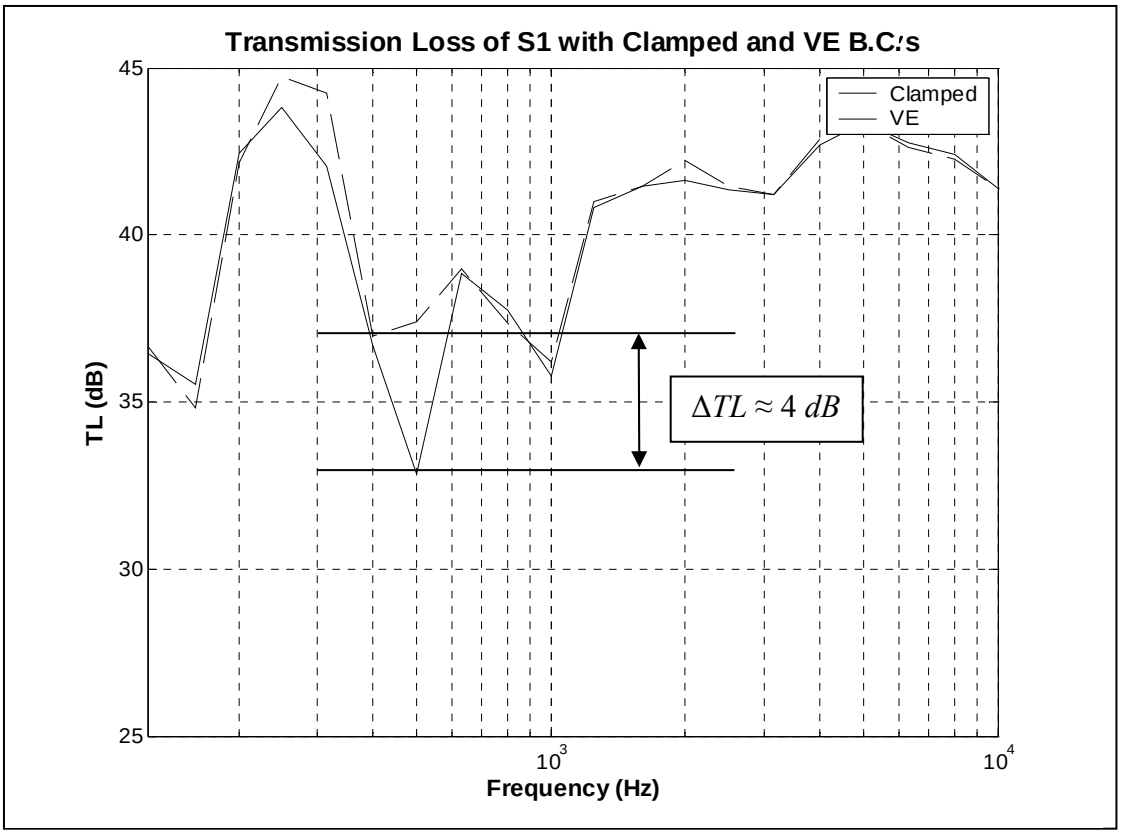

Figure 5.13: TL results for S1 with different boundary conditions. Viscoelastic B.C.'s show a substantial increase in observed TL.

5.4.1 Analysis of the lossy behavior of simplified structures

The TL study results shown in Figure 5.13 illustrate the need to incorporate plate boundary conditions into structural level models. The inclusion of influence of B.C.'s on the structural level lossy behavior adds another degree of freedom to the design space and more closely approximates real-life applications. This sub-section inspects the influence of viscoelastic boundaries on the lossy behavior of two simplified structures, a viscoelastically constrained beam and a viscoelastically constrained circular plate, through modal analysis. The aim of this study is to approximate changes in the structural level lossy behavior as a function of variations in constituent material microstructure.

Such an analysis gives a clearer picture of how microstructural variations propagate to higher length scales and thereby illustrates the value of SC micromechanical modeling in the design process.

5.4.1.1 Forced vibration of a beam with elastic boundary conditions

One of the simplest ways to quantify the modal loss factor of a uniform beam due to different boundary conditions is to find the solution for the general case of a vibrating beam with elastic boundary conditions as shown below in Figure 5.14. The present analysis finds this solution but is limited to a beam of uniform cross-section and material properties as a function of x. Further, the present work will be limited to classic plate theory discussed at length elsewhere [174].

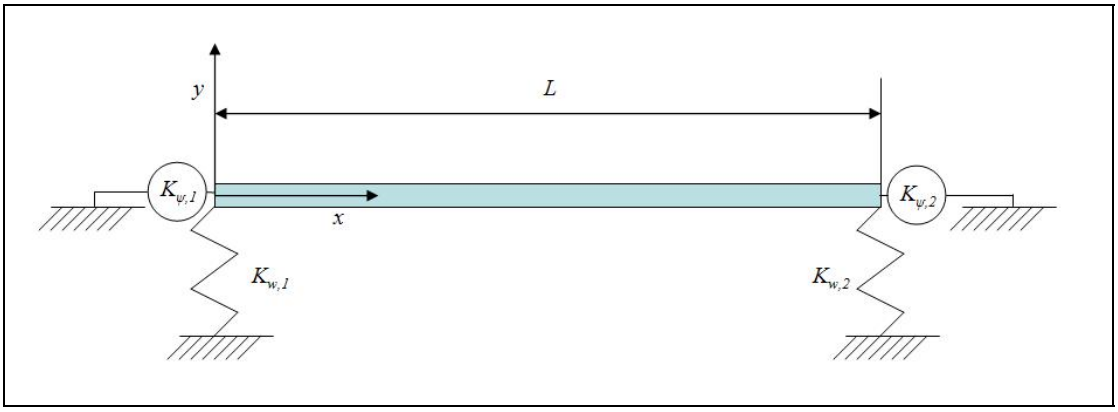

Figure 5.14: Schematic of an elastically constrained beam.

The advantage of finding a solution to the forced vibration of such a beam is that it can easily be modified to approximate many different boundary conditions by changing the

values associated with the linear displacement springs, $K_{w1,2}$ [N/m], the rotational displacement springs, $K_{\psi 1,2}$ [N·m], or both (see Appendix G for examples). Figure 5.15 shows one approach to approximating these coefficients, representing elastic boundary conditions at the extents of the beam, from the viscoelastic material constants in which the beam is embedded and the boundary geometry. Koutsawa *et al* have developed a more exact approach employing finite element methods and the same viscoelastic spring BC approximation [175]. Through application of the elastic-viscoelastic correspondence principle the boundary conditions can be altered to study the effects of different viscoelastic boundary conditions and interlayer materials on modal damping. The derivation of the general solution is given in Appendix G.

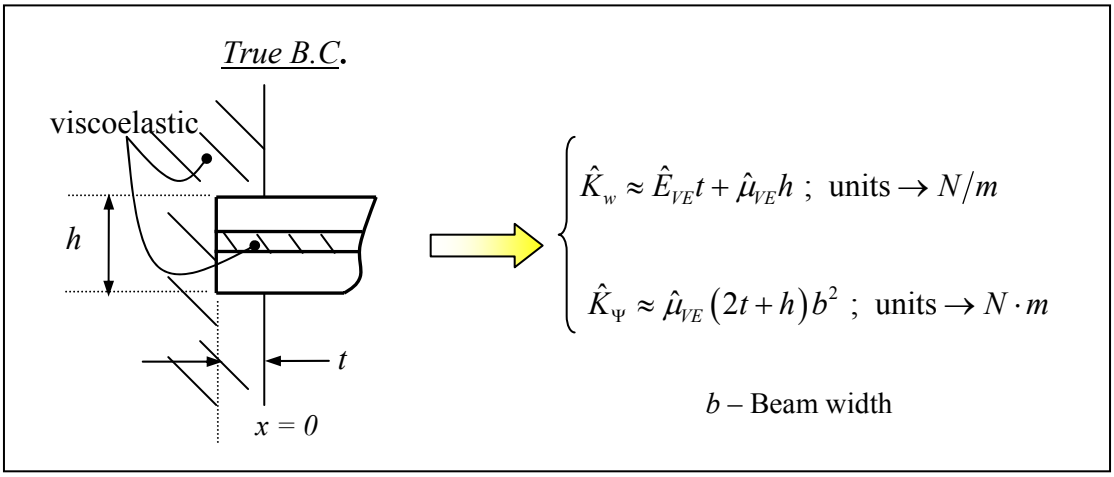

Figure 5.15: Approximation of viscoelastic boundary conditions as linear and rotational springs.

One way to check this nested analytic multiscale modeling approach is to compare modal analysis results from the analytic models above to finite element (FE) approximations. Figure 5.16 shows the results of a study that employed these two different approximations methods. The subject of study is a sandwich beam of length

$L+t$, a total thickness h, and width b. The beam is embedded at $x = 0$ in a viscoelastic medium which has the same material properties as the beam interlayer. The beam dimensions and material properties are given in Table 5.4. For this study the beam is excited using a time varying spatially uniform pressure on the top surface thereby simultaneously exciting all modes of vibration.

Table 5.4: Sandwich beam geometry and properties for analytic and FE study in Figure 5.16.

	$H\,(m)$	$L\,(m)$	$t\,(m)$	$b\,(m)$	$\mu\,(GPa)$	$v\,(\,)$	ρ (kg/m^3)
Layer 1&3	2.0×10^{-3}	0.100	1.0×10^{-2}	0.01	29.5	0.23	2469
Layer 2	1.0×10^{-3}	0.100	1.0×10^{-2}	0.01	$0.133+0.13j$	0.49	1115
B.C.	5.0×10^{-3}	---	1.0×10^{-2}	0.01	$0.133+0.13j$	0.49	1115

The analytical approach employed approximates sandwich beam behavior using the RKU model and the resulting effective bending modulus is used in model general vibrating beam model derived in Appendix G. The value used for the Poisson ratio, $v_{12,}$ can be found using the approximations given in Appendix F. The analytic model results were compared to FE analysis to validate employing such a simplified multiscale modeling approach. The FE results were calculated using the sophisticated FE model of Daya and Potier-Ferry [166] where the viscoelastic boundaries were *not* approximated as linear and rotational springs and are therefore represent reality much more closely. In both cases the modal loss factor was estimated using the half-power beam width method of the calculated beam frequency response (see any dynamic systems text, for example [171]).

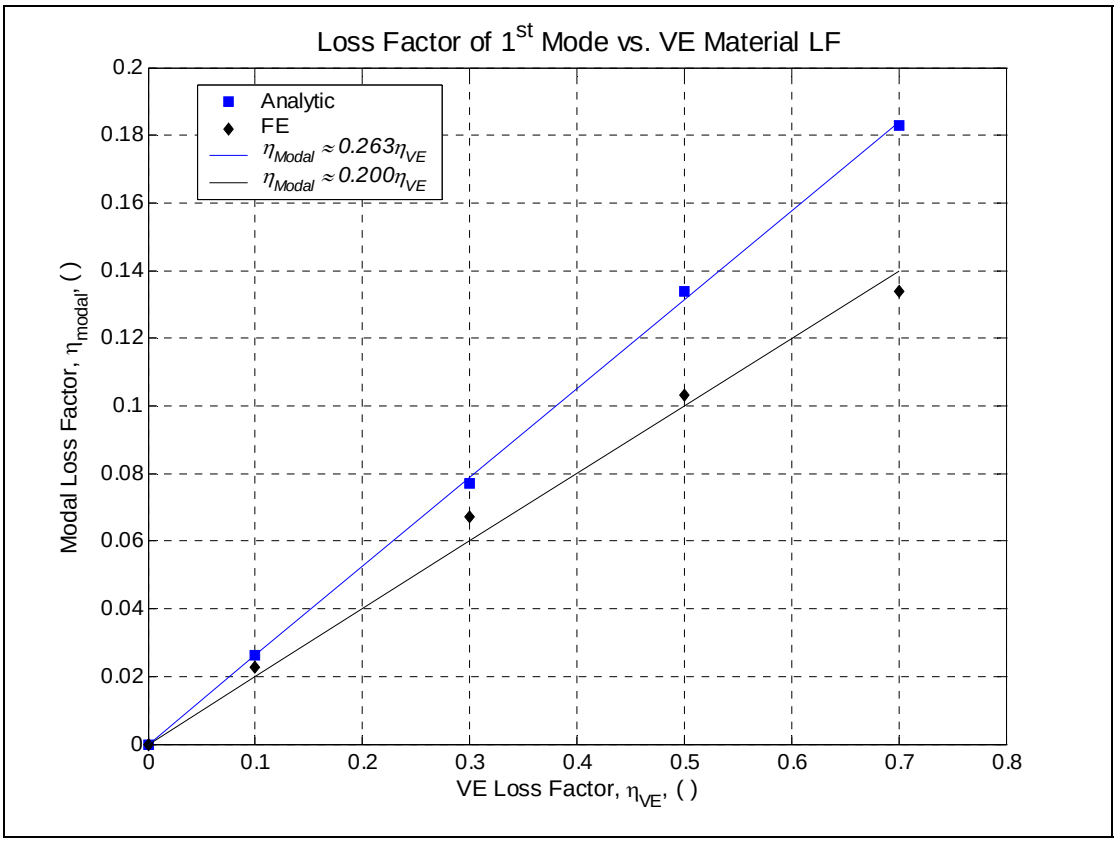

Figure 5.16: Viscoelastic constrained Beam LF as function of the LF of constraining and interlayer material. Compared to FEA model derived by Daya and Potier-Ferry [166]

The results shown above have several encouraging points. First, it is obvious that the viscoelastic material lossy behavior has a linear effect on the macroscopic damping properties of the structure for *low* loss factor values. This is to be expected [171]. When the value of the loss factor increases the analytic approach presented here will no longer be valid and more involved analytic models or FE models are required. Indeed the plot suggests that the validity of the proposed method is questionable for η_{VE} values exceeding ~ 0.5. Another encouraging point is the agreement between this simple analytic approach and the FE model, showing only a *6.3%* difference in the slope $\partial\eta_{1st}/\partial\eta_{VE}$. Considering all of the simplifying approximations, especially those concerning the viscoelastic boundaries, the estimates provided by the analytic model are

quite close. The over-estimation provided by the analytic model is in part explained by the well-known fact that the RKU model generally provides superior damping estimates to those observed in reality [167]. This comparison, more importantly, validates using the RKU model in such a multiscale approach. The analytical nature of this nested multiscale model approach permits efficient study of the effects of different B.C.'s, constituent material properties, and microstructures on structural damping behavior, thereby reducing the overall computational load. It is for this reason that it is attractive as a first step in the design of absorptive materials.

5.4.1.2 Forced vibration of an elastically constrained circular plate

It is instructive to study a two dimensional plate in order to move closer to true windshield structure. This is most easily accomplished through analytical methods by studying the vibration of a circular plate. Due to symmetries, the circular plate solution can be found through analytical methods thus eliminating the need for Rayleigh-Ritz schemes which are inherent in two-dimensional rectangular plate models [171, 174]. This fact simultaneously reduces modeling complexity and computational load. Further, the main objective of the following study is to show the effects of component viscoelasticity on the system response so the actual geometry is unimportant as long as the plate is two dimensional. As with prior beam problem, it is essential to first find the solution for the general case of a plate having uniform cross-section and material properties in the plane of the plate with elastic boundary conditions at $r = a$. Figure 5.17 illustrates this geometry. A detailed derivation of the general solution of a vibrating

circular plate with elastic B.C.'s is given in Appendix G, or see Koutsawa *et al* for a finite element method using the same approximation [175].

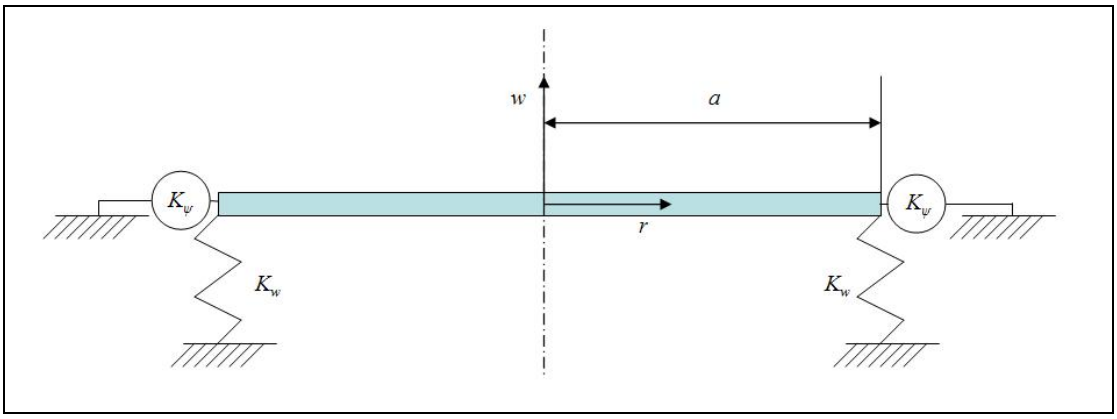

Figure 5.17: Schematic of elastically constrained circular plate.

The advantage of the resulting solution is that it is easily modified to represent many different boundary conditions by changing the values associated with the distributed linear displacement spring, K_w [N/m^2], the distributed rotational displacement spring, K_ψ [N], or both. These coefficients are chosen represent elastic boundary conditions at $r = a$ by relating them to the material constants in which the plate is embedded and the geometry of the plate-boundary interface. A simple approximation scheme is shown below in Figure 5.18. Finally, by assigning complex values to the elastic B.C.'s and plate materials, their effect on the modal damping can then be studied.

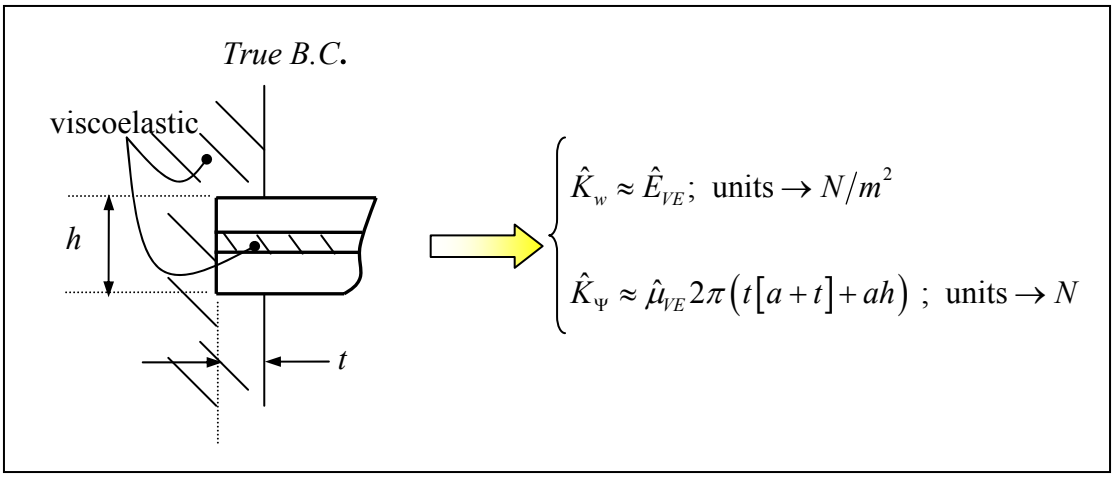

Figure 5.18: Approximation of viscoelastic boundary conditions as linear and rotational springs.

One of the main objectives of design is efficiency. Design efficiency refers to the ability to arrive at a design that fulfills all requirements though minimal design iterations and by *reducing* variables in the design space. Keeping this in mind, it is interesting to study the relative effect each "component" contributes to damping plate vibration at the first resonant frequency. The following study investigates the independent effects of plate, linear spring, and rotational spring lossy behavior on the modal loss factor of a viscoelastic constrained circular plate. This is done in an effort to shed light on the most efficient means of damping resonant behavior and is accomplished via three parametric studies. The plate geometry and material properties employed in these parametric studies are detailed in Table 5.5. It is important to note that the plate studied in each of these parametric studies *is not* a sandwich structure and therefore only the effects of lossy plate behavior are studied. In the first parametric study the plate is pinned at $r = a$ ($K_w \rightarrow \infty$) and the plate material is a homogeneous non-lossy glass. The values for the rotational spring are calculated according to the equation given in Figure 5.18 using shear modulus values given in the PS1 row of Table 5.5. Shear modulus loss factor values are varied

between *0* and *1* and the half-power bandwidth method is employed to calculate the loss factor of the first mode. For the second parametric study the plate's slope is required to be zero at $r = a$ ($K_\psi \to \infty$) and the plate material is again homogeneous non-lossy glass. The linear spring values are calculated from the equation given in Figure 5.18 using shear modulus values given in the PS2 row of Table 5.5. Again the shear modulus loss factor values are varied from *0* to *1* and the results of the structural model yield the modal loss factor of the first mode via the half-power bandwidth method. The final parametric study represents the behavior of a clamped ($K_w \to \infty$ and $K_\psi \to \infty$) viscoelastic plate where the plate material loss factor is varied between *0* and *1*. The results of these three studies are given in Figure 5.19.

Table 5.5: Plate geometry and material properties for parametric studies of component influence on structural damping.

	$a\ (m)$	$h\ (m)$	$t\ (m)$	μ_{VE} (GPa)	$\nu_{VE}(\ )$	E_p (GPa)	$\nu_p(\ )$	K_w (N/m^2)	$K_\psi\ (N)$
PS1	0.100	0.005	0.010	0.133 $(1+\eta j)$	0.49	72.0	0.23	$1x10^{10}$	calc $\in \mathbb{C}$
PS2	0.100	0.005	0.010	0.133 $(1+\eta j)$	0.49	72.0	0.23	calc $\in \mathbb{C}$	$1x10^{10}$
PS3	0.100	0.005	0.010	0.133	0.49	72.0 $(1+\eta j)$	0.23	$1x10^{10}$	$1x10^{10}$

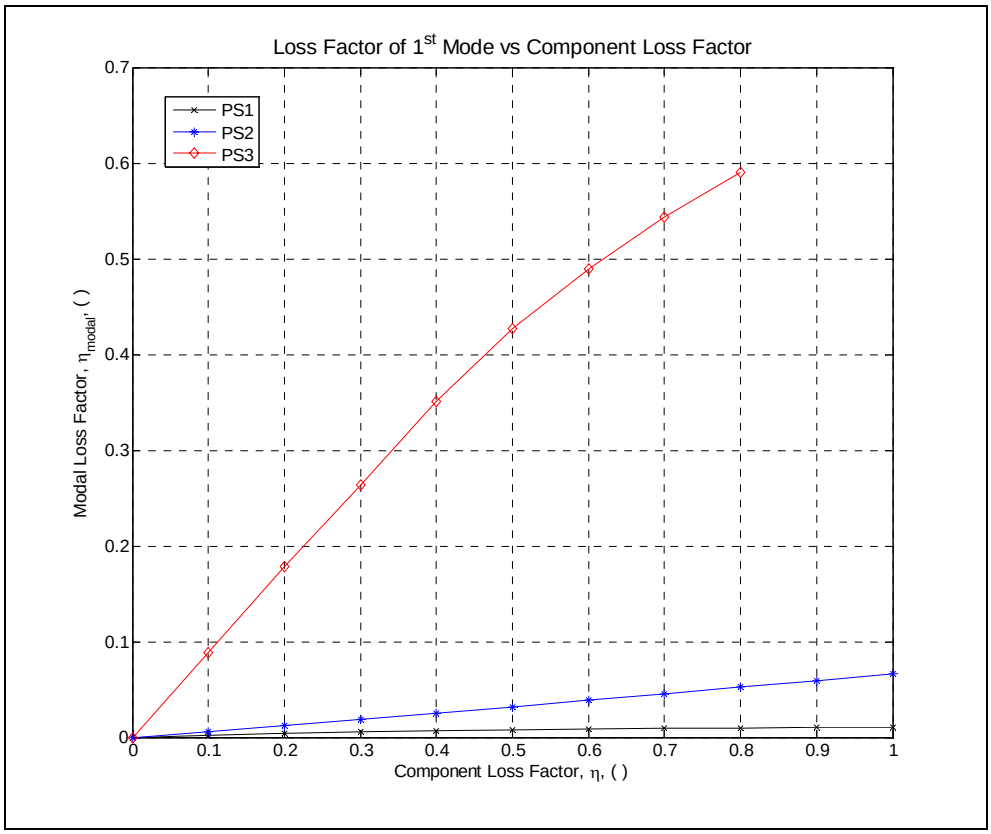

Figure 5.19: Modal loss factor of vibrating plate as a function of each contributing element. Solid line indicates the influence of the rotational spring loss factor, the dashed line indicates the effect of the linear spring's loss factor, and the dash-dot line indicates the beam loss factor's influence.

The results of these parametric studies clearly show that lossy plate behavior dominates damping behavior on a structural scale. It is therefore obvious that the most efficient means to achieve increased acoustic and vibrational isolation with a constrained plate is to increase the plate material loss factor. It must be stated that this study assumes that all other parameters remain equal, which is often difficult to achieve in reality. Indeed, increasing the material loss factor *usually* implies an undesired decrease in material strength: the classic material strength versus damping capacity dichotomy. Recent research suggests, however, that the introduction of certain trace microstructural heterogeneities can have marked effects on material damping behavior while minimally affecting material strength [18, 19, 21]. For this reason it is very interesting to study the

present nested multiscale modeling approach and its capacity to capture micro-scale influence on the structure-level damping behavior.

5.5 Microstructural influence on structural damping capacity

The final step in validating the proposed multiscale modeling approach is to inspect the influence of microstructural changes on structure level damping. The results of such a study will provide a complete picture of the role microstructure plays in structural damping for a vibrating sandwich plate. It will also illustrate how multiscale modeling lends designers high levels of control and insight at each individual scale and how changes at one level propagate through length scales. This section, therefore, endeavors to incorporate the SC micromechanical homogenization model developed in Chapter III into the multiscale model detailed in the prior sections and to show microstructural influence on structural behavior.

Previous sections have investigated the influence of material loss factors and sandwich geometry have on structural damping. Chapter IV made it abundantly obvious that changes in material microstructure can greatly increase material damping capacity by altering the amount of strain energy present in lossy components under identical loading conditions. The loads applied to windshield sandwich plates result from air-structure coupling, frame vibrations, and projectile impacts. All of these loads are fixed force/stress loads, as opposed to displacement or strain based loads. The simplest way to increase strain energy in lossy material components for such loading is to increase their compliance. Chapter IV illustrated that this can be achieved by introducing inclusions

into a viscoelastic material which are less rigid than the host. Voiding a material is the most efficient known means of increasing a composite viscoelastic compliance [64] and therefore voided viscoelastic material is subject of this study. The scope, however, is limited to isotropic bi-phase particulate composites resulting from a viscoelastic host material containing spherical voids.

Several points must be raised in regards to such a treatment for an automobile windshield. Voiding a windshield interlayer material has both positive and negative aspects. The most apparent drawback is that introducing heterogeneities of any kind will have a negative impact on the light transmission. The same scattering phenomena addressed in Chapter II with respect to acoustic waves are applicable to light waves when there is a material discontinuity. The major difference is that for light waves the *ka* value will be much larger and, consequentially, light scattering effects will be pronounced. Light scattering leads to poor windshield transparency and is a *major* restriction to the introduction of voids to achieve elevated windshield damping capacity. However, the physical mechanisms leading to enhanced energy dissipation, namely increasing strain energy in lossy components, are not restricted to voids. Ideally a material can be found to take the place of voids which has weak elastic constants but an index of refraction similar to the viscoelastic interlayer. This would eliminate light scattering problems. It is also possible that materials can be found which can analogously increase lossy behavior through the addition of only infinitesimal amounts of heterogeneity. A positive aspect of introducing voids into the interlayer material is that the resulting sandwich windshield will have a lower density. Lower overall density translates to increased energy efficiency which is a very desirable consequence.

5.5.1 Microstructure → Part level modeling

To study void fraction effect on part level behavior, it is interesting to re-visit the parametric studies shown in Section 5.3.1. That section investigated changes in the complex effective bending modulus, the flexural wavenumber, and the shear parameter as a function of the thickness ratio for several values of interlayer shear loss factor (Figure 5.4 – Figure 5.6). The plots showed that increasing interlayer material loss factor has a positive influence on the plate damping capacity. The most desirable result shown was that by only varying the material loss factor, i.e. no change in shear stiffness, the bending loss factor increased while very little change was observed in the real part of the effective bending modulus. Similar plots are shown below where the interlayer void fraction is varied in order to observe the effect on the complex effective flexural behavior.

Figure 5.20 clearly shows that the void fraction has a strong influence on the effective complex bending modulus. The reduction in real part, $\hat{B}'$, is rapid with increasing void fraction for any fixed thickness ratio, H. This is an undesirable result of adding voids to the interlayer material. Conversely, the bending modulus loss factor, $\hat{\eta}_p$, quickly increases as a function of void fraction.

Table 5.6: Material properties used to produce Figure 5.20-Figure 5.24 and Figure 5.26. The viscoelastic properties are calculated from (V.3.9) and the HN coefficients given in the associated paragraph for an exciting frequency of 1 kHz.

	$\mu_{VE}\,(GPa)$	ν_{VE} ( )	ρ (kg/m^3)	$E_p\,(GPa)$	ν_p ( )	ρ (kg/m^3)	μ_{void} (GPa)	ν_{void} ( )	ρ (kg/m^3)
Property / Geometry	0.133 (1+0.13j)	0.49	1115	72.0 (1+0.02j)	0.25	2469	$1\text{x}10^{-8}$	0.45	1.21

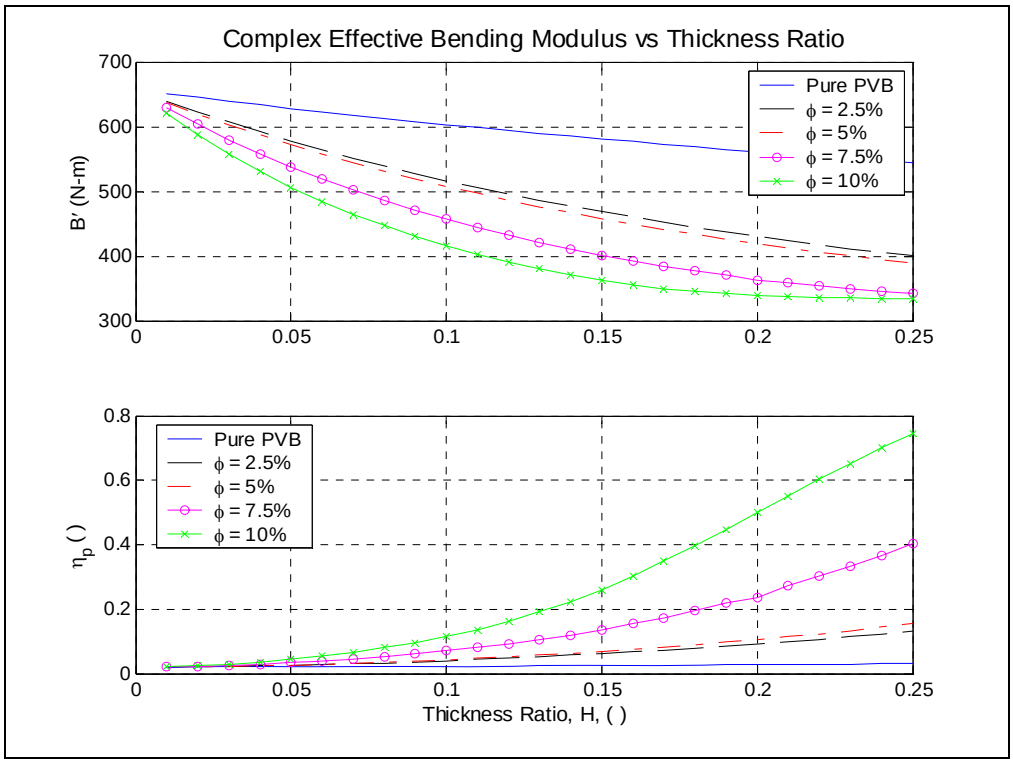

Figure 5.20: Effective bending modulus as a function of layer thickness ratio for varying values of interlayer void fraction at f = 1 kHz.

The increased damping capacity is further evidenced by inspecting the results in Figure 5.21 and Figure 5.22. The prior shows the effective complex flexural wave number and the latter a measure of the attenuation per flexural wavelength suggested by Kinsler *et al* [176], $\hat{\alpha}^{flex}/\hat{k}^{flex,'}$. The wavenumber plot shows two interesting aspects. The most obvious observation is that the magnitude of the flexural attenuation coefficient, $\hat{\alpha}^{flex}$, monotonically increases both for a fixed void fraction with increasing thickness ratio and for a fixed thickness ratio with increasing void fraction. This is due to the fact that both changes, increasing void fraction and increasing thickness ratio, result in increased plate flexural compliance. The increased compliance augments the strain energy present in the viscoelastic material for a fixed applied moment/stress, thereby increasing the plate's damping capacity. The less obvious result is the non-monotonic behavior of the real part,

$\hat{k}^{flex,'}$. For a fixed frequency, an increase in real part of the wavenumber implies a decrease in the wave speed, $\hat{c}^{flex}$, since $\hat{k} = \omega/\hat{c}$. Because the flexural wave speed is related indirectly to the inverse of the modulus through Eq. (V.3.2), it would seem apparent that a decrease in the real part of the flexural modulus would likewise lead to an increase in the wavenumber's real part. However, for high loss factor values, this is not always the case. The relationship between the real parts of these two quantities is *not* independent of the flexural modulus loss factor. It is for this reason that Figure 5.22 shows non-monotonic curves for $\hat{k}^{flex,'}$ and that the maximum value is observed for consecutively smaller thickness ratio values as the void fraction increases. The non-dimensional measure of attenuation plotted in Figure 5.22 clearly shows that the attenuation efficiency is a monotonic function of both the thickness ratio and the void fraction despite the increased wave speed for all values inspected. One further observation of effective plate behavior concerns the shear parameter. Figure 5.23 shows that values of $\hat{g}'$ decrease rapidly with increasing void fraction and thickness ratio. The RKU model is only valid when $\hat{g}' > 1$ implying that the RKU model may give erroneous values for thickness ratios exceeding ≈ 0.2.

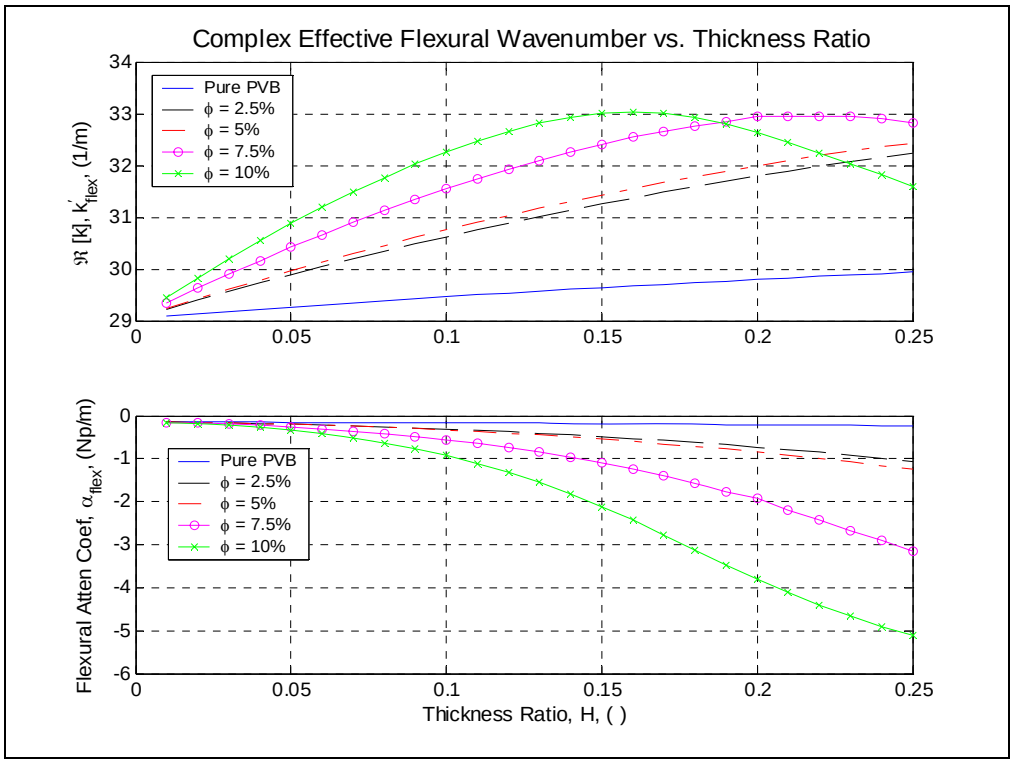

Figure 5.21: Effective flexural wavenumber as a function of the thickness ratio at f = 1 kHz for a several different void fractions.

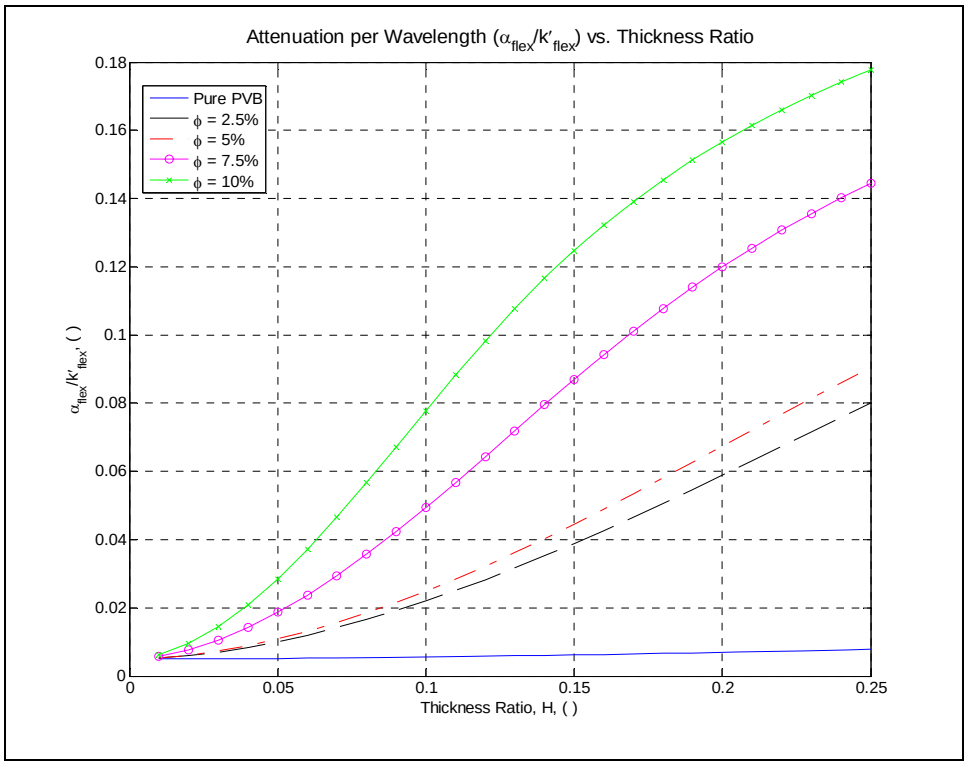

Figure 5.22: Measure of damping amplitude attenuation per flexural wavelength for layered plate homogenized using RKU model with a voided interlayer.

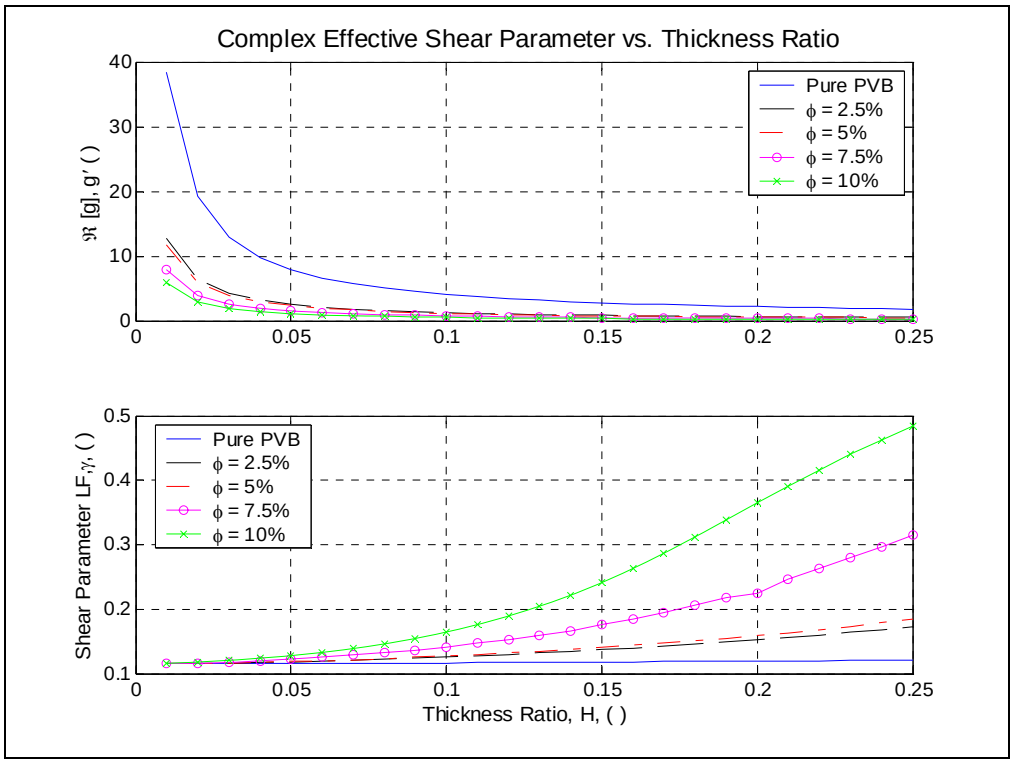

Figure 5.23: Effective shear parameter as a function of the layer thickness ratio for several values of interlayer void fraction at f = 1 kHz.

5.5.2 Microstructure → Structure level modeling

The final subject of interest is the influence of microstructural changes, in the form of void fraction, on structure-level damping. The results are presented in two different ways. First changes in the modal loss factor of a vibrating circular sandwich plate as a function of viscoelastic interlayer and boundary void fraction are shown. This yields insight into the increased capacity of the sandwich structure to damp resonant behavior. The second study approximates windshield transmission loss for an incident plane wave as a function of frequency. The results of this study will illustrate the relative acoustic isolation improvements a voided interlayer provides.

Section 5.4.1.2 presented the effects of different lossy elements on the damped behavior of a viscoelastically constrained circular plate. Though it was shown that the most efficient means to damp flexural vibrations is by elevating the beam loss factor, it is of interest to demonstrate the generality of the nested multiscale approach through a study that take into account the behavior of voided viscoelastic boundary conditions and sandwich interlayer. For this purpose the following studies the damped 1^{st} resonance of a circular sandwich plate embedded at $r = a$ in a voided viscoelastic material. The interlayer material is also assumed to contain voids with the same volume fraction. For this study the same materials and geometries are employed as those presented in Table 5.5 and the modal loss factor was again approximated using the half-power bandwidth method. Figure 5.24 shows interlayer and boundary material void fraction effects on the modal loss factor of the first mode. The plot clearly shows a quadratic correspondence, as was suggested in the RKU model sensitivity analysis presented in Section 5.3.2. This quadratic correspondence is due to the introduction of voids in the interlayer material, thereby increasing the loss factor of that layer. Section 5.4.1 showed that viscoelastic plate and B.C. behavior has only a quasi-linear influence on the modal loss factor, therefore the quadratic tendency observe in Figure 5.24 is a result of constrained layer damping of the sandwich plate. These results are encouraging and show that microstructural inhomogeneities can have noticeable influence on structure-level behavior.

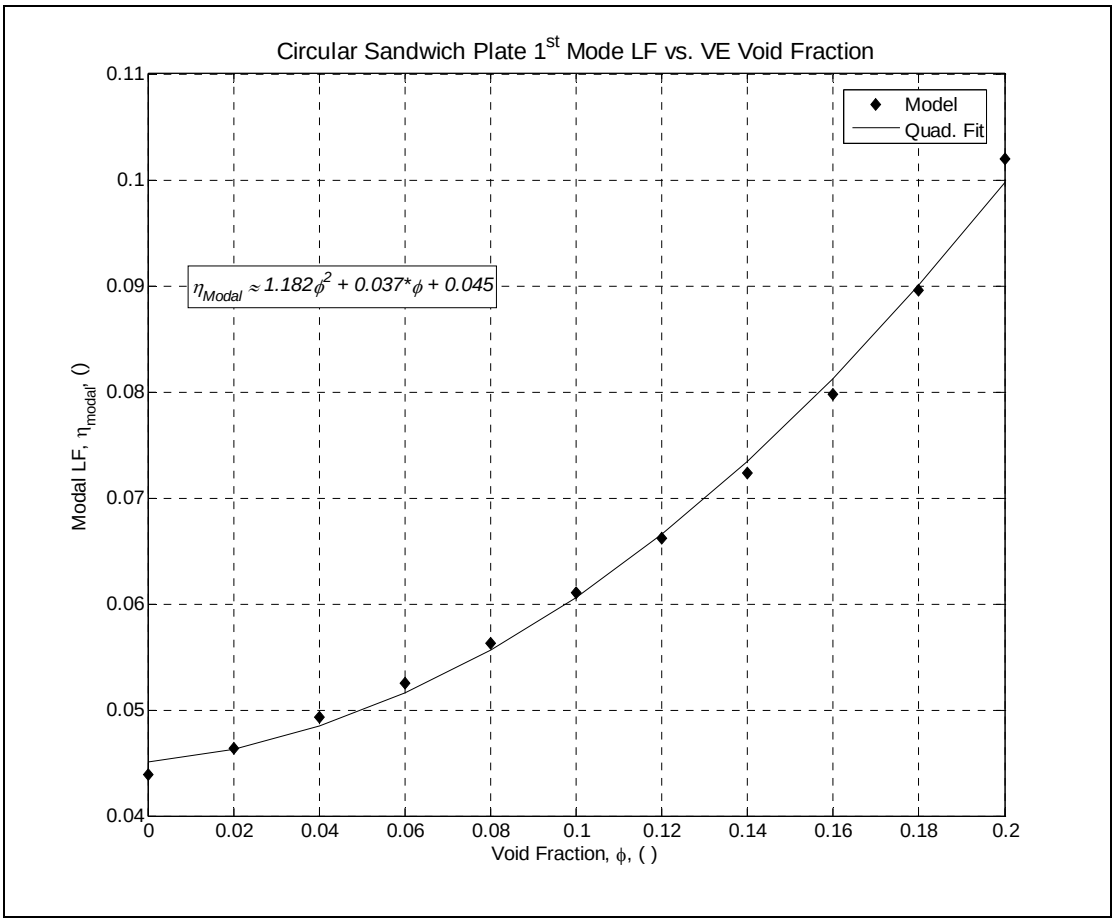

Figure 5.24: Variation of the loss factor of the 1st mode of vibration for a circular sandwich plate as a function of interlayer void fraction, ϕ.

Noise in an automobile interior has two distinctly different sources. A major contributing source is sound radiated by structure borne vibrations that originate from engine vibrations and, more importantly, the interaction between the road and the automobile [11]. The efficiency with which the windshield radiates this vibrational energy in the form of sound is dominated by its modal response. For this noise source, the previous study is more applicable. Figure 5.24 has clearly shown that increasing the void fraction of the viscoelastic interlayer and boundary materials displays the desirable ability to reduce resonant behavior. The second source of noise is sound originates outside the vehicle and is consequently transmitted through the windshield and other

acoustic paths. The quality of noise isolation is usually measured by the transmission loss (TL) discussed in previously. For a panel (homogeneous, sandwich, or otherwise) the general TL characteristics as a function of frequency are shown in Figure 5.25 [168].

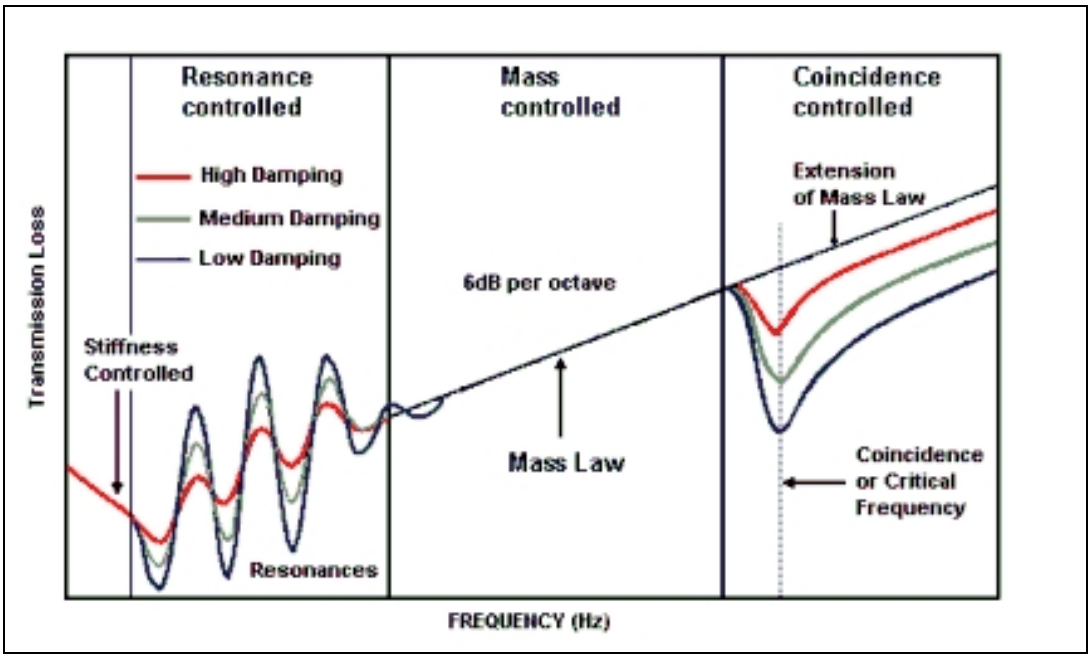

Figure 5.25: General characteristics of TL versus frequency for a panel (figure from Buerhle *et al* [168]).

This figure illustrates the four regimes of panel transmission loss. From left to right, the first is the stiffness controlled domain which is represents the quasi-static case for the *plate*, meaning acoustic wavelengths are much larger than the panel of interest. This regime is not of interest in the present work. The second regime, resonance controlled, is similar to the case studied above. It is reasonable to assume that behavior due to air-borne waves exciting resonance behavior will be damped in the same manner as structure borne vibrations and therefore this case was treated by the previous study. In the mass controlled TL regime, acoustic wavelengths are much smaller than the panel and the

panel is therefore approximated as a limp hanging panel with a known mass per unit area. The pressure gradient of the incident sound wave causes the panel to move as a whole and radiate sound on the other side. In this regime TL is dominated by the panel (windshield) mass and a doubling the frequency leads to a 6 *dB* TL increase [32]. It is obvious from this behavior that high density panels are ideal for noise isolation. The final TL regime is the coincidence controlled regime. In this frequency range the incident wavelength projected onto the panel matches the wavelength of flexural waves in the panel. Coincidence occurs when these two wavelengths match, resulting in near perfect transmission and a greatly diminished TL. The result is a sharp decrease in observed TL at a specific frequency depending on the air-borne plane wave angle of incidence. This region of high sound transmission is called the coincidence notch [32].

Microstructural effects of resonant behavior were previously shown for a vibrating plate so it is now interesting to inspect the effect of microstructural changes on windshield TL in the mass-controlled and coincidence-controlled regimes. Panel behavior in this frequency range is well approximated using the set of equations below [32].

$$\hat{\omega}_{coinc} = \frac{c_{air}^2}{\sqrt{\hat{K}}} \quad \text{where} \quad \hat{K} = \frac{\hat{B}^{eff}}{\rho^{eff} h^{tot}} \tag{V.5.1}$$

$$\hat{Z}_p = \omega \rho^{eff} h^{tot} \left\{ \hat{\eta}_p \left(\frac{\omega}{\hat{\omega}_{coinc}} \right)^2 \sin^4 \theta_1 - i \left[1 - \left(\frac{\omega}{\hat{\omega}_{coinc}} \right)^2 \sin^4 \theta_1 \right] \right\} \tag{V.5.2}$$

$$TL = 10\log_{10}\left[\left|1+\frac{\hat{Z}_p}{2(\rho c)_{air}}\cos\theta_I\right|^2\right] \qquad \text{(V.5.3)}$$

In these expressions c_{air} and ρ_{air} represent the speed of sound (343 *m/s*) and density (1.21 kg/m^3) of air, respectively, $\hat{\omega}_{coinc}$ is the coincidence frequency, $\hat{Z}_p$ represents the plate impedance, and the other variables have been previously introduced.

For a sandwich plate consisting of the same materials and geometry as for the resonance behavior discussed in Section 5.5.1, Figure 5.26 shows the approximate TL calculated from Eqns. (V.5.1)-(V.5.3). These results clearly show the expected mass and coincidence-controlled regimes. In the mass controlled regime the void fraction is small enough to have minimal detrimental effects on the TL. It also shows that the non-voided interlayer material already provides substantial coincidence notch reduction. The voided materials do enhance damping in this frequency range, but improvements are marginal at best and surely beyond the limits of human perceptibility in noise reduction.

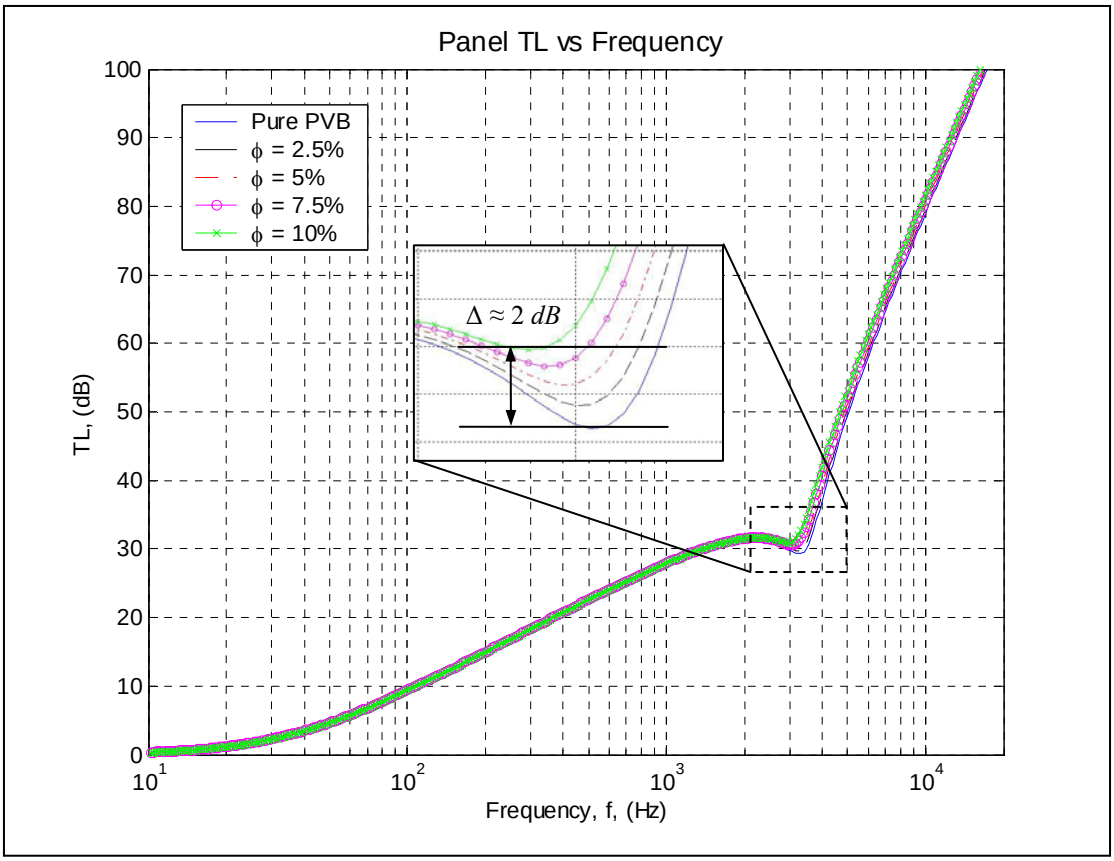

Figure 5.26: Theoretical TL of layered windshield as a function of frequency for an incident angle of $\theta_I = 60^o$. Slight improvements are predicted for voided PVB near coincidence frequency.

Unfortunately, the results of this study show only marginal damping improvements at the structure-level. This can be attributed to the fact that only traditional materials have been investigated. It is very possible that non-conventional inclusion materials or trace treatments of the interlayer material could translate to large effects on the structure-level damping capacity. One specific inclusion behavior leading to increased macroscopic material damping are negative stiffness inclusions. Lakes *et al* [18, 19, 21] have shown that "snap-through" phenomena observed in instable inclusion materials can be approximated as a negative stiffness. Their work has clearly shown that this extreme damping is due to large strains in the neighborhood of inclusions which exhibit "snap-through," or bi-stable material behavior. The most significant increases in macroscopic

lossy behavior result from inclusions whose modulus, $\hat{\mu}_I$, is related to the matrix modulus, $\hat{\mu}_M$, as $\hat{\mu}_I \approx -1.1\hat{\mu}_M$ [18]. It has been shown theoretically [18] and experimentally [19, 21] that treatments using inclusions displaying negative stiffness behavior can significantly increase lossy behavior with only trace amounts of the inhomogeneities, indeed, Lakes called such treatment "homeopathic." Figure 5.27 investigates structural behavior, in the form of sandwich windshield TL, when the interlayer contains small volume fractions of hypothetical negative stiffness inclusions whose modulus obeys $\hat{\mu}_I \approx -1.1\hat{\mu}_{PVB}$ at each frequency while all other materials and geometry are identical to those yielding Figure 5.26.

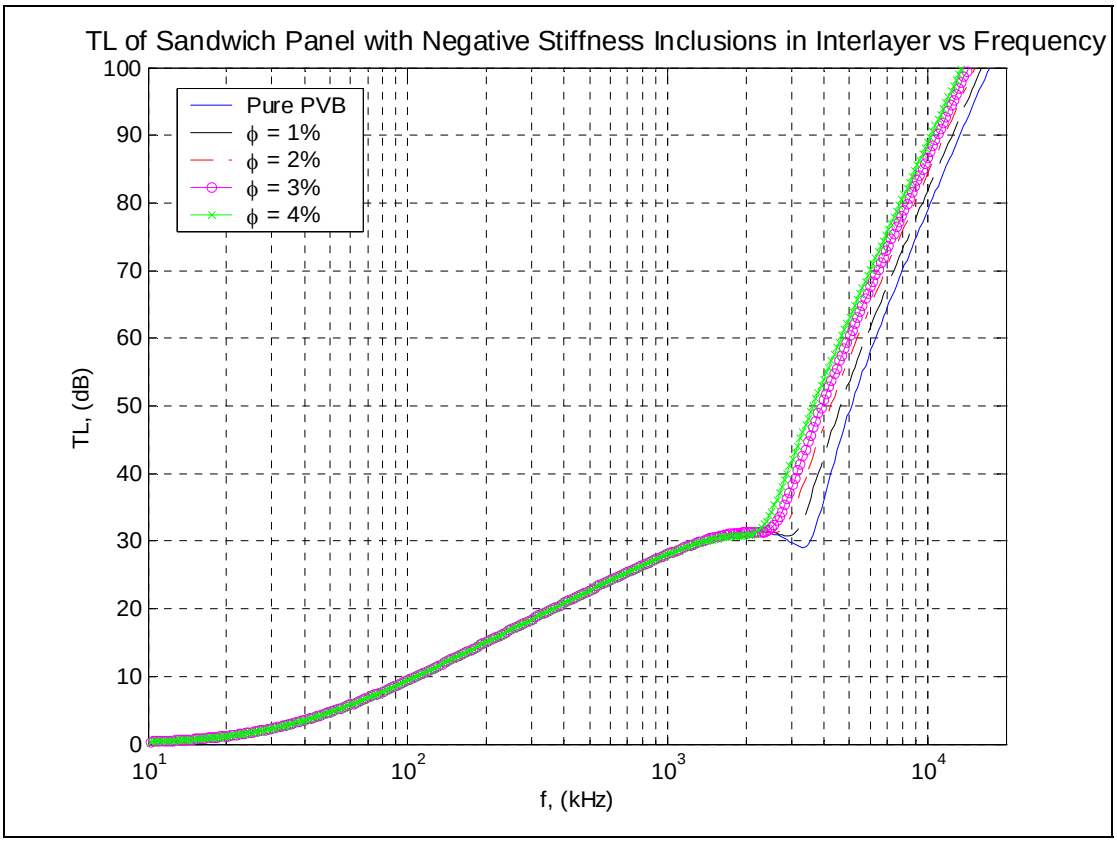

Figure 5.27: Transmission Loss of sandwich panel when PVB interlayer contains small volume fractions of negative stiffness inclusions ($\mu_I = -1.1\mu_{PVB}$). Coincidence notch moves to dramatically lower frequencies and nearly vanishes.

This plot shows a dramatic increase in observed structural level energy dissipation at coincidence. Indeed, the introduction of such inclusions nearly eliminates the coincidence notch while simultaneously moving coincidence to lower frequencies.

5.6 Chapter summary

Though the behavior shown in Figure 5.27 represents that of a hypothetical material, it is very interesting for future research to show that this behavior can be captured by a nested multiscale modeling technique such as the one presented in this

chapter. It also encourages further research in the design of materials with negative stiffness or "snap-through" behavior for use as treatments in structures where the dissipation of mechanical energy is important. More importantly for this work, the multiscale study of an automobile windshield gives merit to incorporating the SC micromechanical model into a materials design strategy and clears the way for more intense research on microstructural behaviors which have more pronounced effects on structural level damping. Chapter VI employs the nested multiscale modeling scheme developed in the introductory study of the current chapter and employs it in a decision based systems design strategy to explore the design space of an automobile windshield. Chapter VII then investigates the phenomenon of negative stiffness in more detail. Finally, Chapter VII integrates information gathered from the design process of Chapter VI to propose new inclusion structures and strategies which exploit negative stiffness behavior.

CHAPTER VI

MATERIALS DESIGN: COMPROMISE DESCISION SUPPORT AND MICROMECHANICS

6.1 Introduction

The purpose of this chapter is to implement a Decision-Based Design (DBD) technique for the purpose of exploring the design space of high loss materials. The DBD approach is taken in an effort to employ a systems design methodology to a material design problem. This is motivated by the observation that though materials design is a rapidly expanding area of research, the vast amount of existing materials design literature rarely represents design in the truest sense [6, 113]. The preponderance of material design research intently focuses on perfecting the understanding of material behavior based on its structure and processing. This understanding yields a more perfect knowledge of material behavior from first principles and is critical to the advance of the field of material design. However, the capacity to truly design materials must aim to develop and exploit existing knowledge and tools to specify material structure based on performance demanded by technology [113]. In other words, materials design must involve solving the inverse problem of specifying material structure and processing, at all length and time scales, based on properties needed to fulfill design requirements. These

two approaches are fundamentally different. The former is a deductive/bottom-up/manufacture for design approach which favors empiricism while the latter is better described as an inductive/top-down/design for manufacture approach which favors exploration, discovery, and creation [5, 6]. This statement does not imply that further study of material behavior is unwarranted or unneeded. To the contrary, fundamental understanding of material behavior at all scales is indispensable to the future of material design. However, perfection of the latter approach represents the highest promise to efficiently search for and ultimately create new materials to meet current and future technological needs. One well accepted top-down approach to material design aims to extend systems design methodologies to concurrently design materials for specific high importance components. This approach, which employs knowledge and tools from the fields of materials science, mechanical engineering, and engineering design, was pioneered by the Mechanical Properties Research Laboratory and Materials Council at Georgia Institute of Technology [2, 3, 6, 116, 117]. This chapter builds on their approach by employing a systems design construct together with the self-consistent micromechanical model developed in Chapter III to design an automobile windshield.

The following presents a design space exploration of an automobile windshield to improve its acoustic performance while simultaneously reducing weight and minimally reducing in-plane stiffness. The analysis serves two purposes. First, it is postulated that the results will shed light on sub-microscale behavior and structure that lead to significant enhancements of the macroscopic material damping. Second, the results will validate the integration of a top-down design methodology and micromechanical techniques to concurrently design structures and their constituent materials. This represents an effort to

employ a top-down methodology to design materials to the microscale *for optimal performance* by exploiting an existing robust multiscale micromechanical model [130]. The design methodology employed is a Compromise Decision Support Protocol (CDSP). CDSP is a general systems design technique which was developed by Mistree, Hughes, and Bras [177]. The technique was implemented by Bras and Mistree [118] and Seepersad *et al* [3] in the context of robust design and by Mistree, Smith, and Bras concerning concurrent design [119]. In a similar vein to the work proposed in this thesis, CDSP has been employed for composite material pressure vessel design by Karandikar *et al* [120], for the design of structures employing materials in combination by Edwards and Deng [121], and for the robust design of energetic materials by Choi *et al* [117]. These references give a representative example of the depth and breadth of problems that have been treated using this approach and gives promise to the integration of micromechanical models for the purpose of designing materials to the microscale.

6.2 System Specification

"Designing is a process of converting information that characterizes the needs and requirements for a product into knowledge about a product." In this statement, taken from the Handbook of the Systems Reliability Lab at Georgia Institute of Technology [178], the term *product* is used in its most general sense. In other words, not only can specific objects be designed, but processes can also be designed. For example, a designer may design a transducer and also design the process by which the design of the transducer is to be obtained. The approach to design which emphasizes the role of

designer decisions is called a decision support protocol. This technique holds that the principal role of a designer is to make decisions and thereby bridge the gap between an idea and reality. The Handbook continues to summarize what is meant by "design decisions" by using descriptive sentences. Those applicable to the current material-structure system are given below.

- Decisions in design are invariably multi-leveled and multi-dimensional in nature.
- Decisions involve information that comes from different sources and disciplines.
- Decisions are governed by multiple measures of merit and performance.

In this design approach, called Decision-Based Design, decisions serve as markers to identify the progression of a design from initiation to implementation to termination. The Compromise Decision Support Protocol is a construct created to aid the designer in implementing the DBD methodology. It is stressed that a *compromise decision* be defined as the process of determining the 'right' set of design variable values, such that the system is feasible with respect to system constraints and maximizes its performance. The support protocol is a construct which aids the designer to find this 'right' set of independent system variables. The example given in this chapter employs CDSP to design a multi-functional layered plate, an automobile windshield, in order to simultaneously improve performance of the plate with respect to noise isolation, in-plane stiffness, and area density. Though this chapter specifically models a windshield, the particular modeling approach may be employed for the design of any three layer plate

that exploits constrained layer damping as a mechanism to *passively* dissipate out-of-plane bending.

Multiscale modeling of the multi-layered plate is performed in a forward sense (material microstructure → macroscopic material behavior → structure) through a hierarchy of nested models as proposed in Chapter V. The frequency range of interest is the mass and coincidence controlled domains described in Section 5.5.2 of this thesis (or see Blackstock for a description [50]). CDSP and numerical optimization techniques are then applied to this hierarchy of models in order to efficiently "design" the microstructure of the plate materials based on system level goals (see Figure 6.1). The overall goals of windshield design considered in this work are to (*i*) reduce sound transmission, (*ii*) move the phenomenon of coincidence to a frequency outside the highly sensitive frequency range of human hearing, (*iii*) reduce the total windshield density, and (*iv*) maintain or improve the structural rigidity of the windshield.

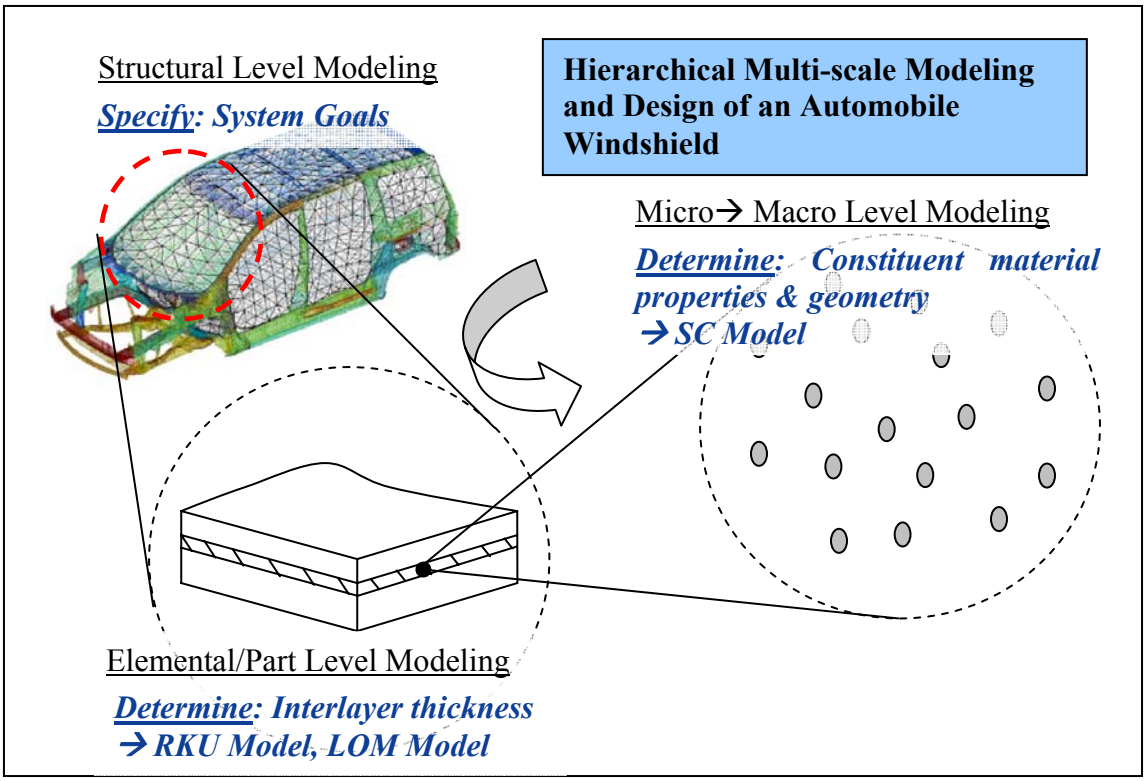

Figure 6.1: Visualization of the hierarchical modeling of an automobile windshield using different homogenization models. Curved arrow indicates the sense of the solution path of an inductive design methodology.

6.2.1 Design space description

The present section defines the design variables which fully define that automobile windshield design space using the proposed modeling approach. It is imperative to specify that CDSP lexicon differentiates between *design variables* and *system parameters*. Design variables are those system variables which are considered alterable from the initial state in order to improve system performance. Design variables are denoted with the vector **X**. System parameters describe any other model variables needed to fully describe the system but which cannot be altered from the initial system configuration due to design constraints or other considerations.

The layered plate behavior is modeled using four specific models implemented as schematized in Figure 6.2. First, the macroscopic material behavior is approximated through applicable micromechanical effective medium theories (EMT), specifically the self-consistent (SC) micromechanical model derived in Chapter III. This is the micro → macro modeling step. The modeling step employs Ross, Kerwin, and Ungar (RKU) model [31] and a simple law of mixtures (LOM) modeling approach. The RKU model approximates the enhanced damping of flexural waves traveling in the sandwich plate brought about by the high shear strain of the viscoelastic interlayer. The effective in-plane stiffness, denoted as $\hat{E}_{11}^{eff}$ or $\hat{E}_{22}^{eff}$, is simultaneously calculated using a LOM approach [179]. The details of these two models were discussed in Chapter V and Appendices E and F. This is the part level modeling. Finally, the modified mass-law (MML) given by Pierce [32] and detailed in Chapter V is employed to approximate the frequency dependent acoustic transmission loss (TL) of the sandwich plate. This is the structure level modeling of our system.

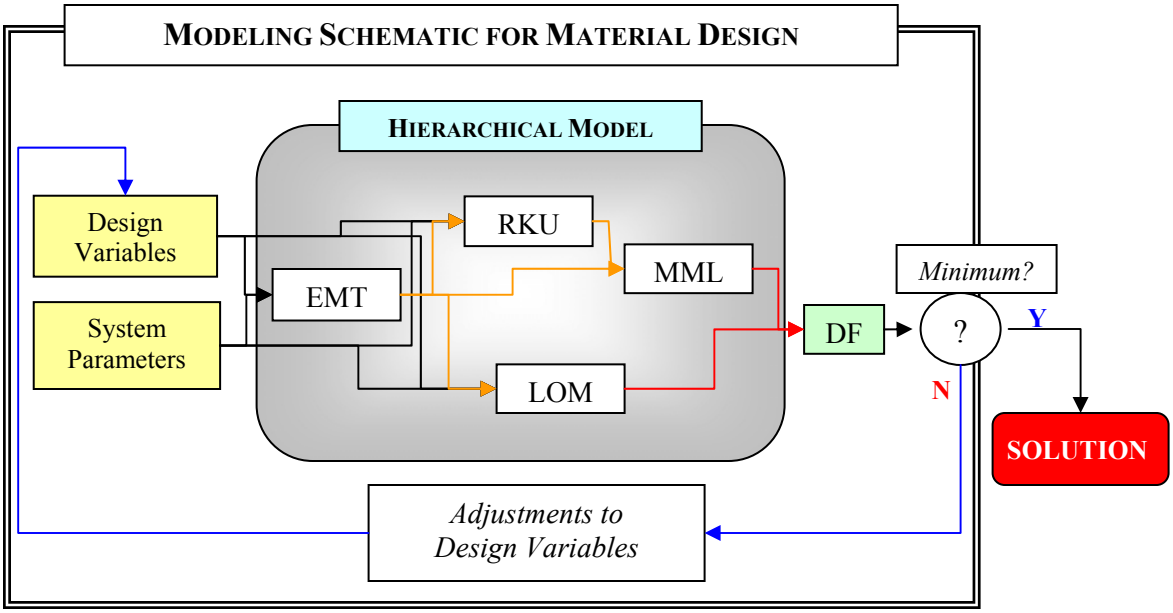

Figure 6.2: Schematic of the nested hierarchical modeling approach and solution scheme for material design employing micromechanics. EMT – Effective medium theory, RKU – Ross, Kerwin, Ungar Model, LOM – Law of mixtures, MML – Modified Mass Law, DF – Deviation Function

The CDSP design approach is then applied to this multi-scale system model to determine material microstructures that improve the performance of the sandwich plate. The CDSP is extremely important to solving this computationally intensive inverse problem as it has been devised to efficiently find design solutions for complex systems. The following sections describe in words the design space for the automobile windshield. As with all mathematical approximations of physical systems, each individual model described above introduces system variables and parameters, and imposes design space restrictions due to assumptions made in their formulation. These restrictions are described by the CDSP as either constraints or bounds. A complete list of design variables, their associated bounds and constraints, and all system parameters, is given in Section 6.2.2 which structures the design space exploration using CDSP.

6.2.1.1 Design variables, bounds, and constraints introduced by micromechanical modeling

Micromechanical effective medium theories represent very well-established mathematical schemes whose assumptions and domains of applicability are well understood. This section delineates the variables and parameters defining the design space occupied by the SC micromechanical model, which are listed in Table 6.1, and their associated constraints and bounds, which are listed in Table 6.2.

The SC model derived in Chapter III homogenizes the mechanical properties of a three-phase material consisting of a continuous matrix phase containing thinly coated inclusions. In the most general case, each phase of the heterogeneous material is assumed to have some frequency dependent viscoelastic behavior which is described by a complex valued fourth order stiffness tensor. The viscoelastic stiffness tensors of these phases are represented as $\hat{C}^{M}_{ijkl}$, $\hat{C}^{I}_{ijkl}$, and $\hat{C}^{C}_{ijkl}$, respectively. The current material design problem restricts material phase anisotropy to materials displaying transverse isotropy. It is important to note that the SC model does not require this restriction, but rather that it is a design constraint intended to reduce calculation time by reducing the size of the design space to be inspected. Transverse isotropy reduces the total number of independent material constants of each phase from nine to five, C_{11}, C_{12}, C_{13}, C_{22} (or C_{33}), and C_{44}. The symmetries and restrictions for transverse isotropy of **C** are given in Eq. (VI.2.1) using Voigt notation.

$$\mathbf{C} = \begin{bmatrix} C_{11} & C_{12} & C_{13} & 0 & 0 & 0 \\ C_{12} & C_{11} & C_{13} & 0 & 0 & 0 \\ C_{13} & C_{13} & C_{33} & 0 & 0 & 0 \\ 0 & 0 & 0 & C_{44} & 0 & 0 \\ 0 & 0 & 0 & 0 & C_{44} & 0 \\ 0 & 0 & 0 & 0 & 0 & 0.5\left(C_{11} - C_{12}\right) \end{bmatrix}$$

$$-OR- \qquad \text{(VI.2.1)}$$

$$= \begin{bmatrix} C_{11} & C_{12} & C_{12} & 0 & 0 & 0 \\ C_{12} & C_{22} & C_{23} & 0 & 0 & 0 \\ C_{12} & C_{23} & C_{22} & 0 & 0 & 0 \\ 0 & 0 & 0 & 0.5\left(C_{22} - C_{23}\right) & 0 & 0 \\ 0 & 0 & 0 & 0 & C_{44} & 0 \\ 0 & 0 & 0 & 0 & 0 & C_{44} \end{bmatrix}$$

In this chapter the term microstructure refers to a volume fraction of coated ellipsoidal inhomogeneities embedded in a continuous matrix having a given orientation distribution. It is proposed that micromechanical effective medium theories (EMT) be employed to predict the macroscopic material behavior as a function of this microstructure. The EMT employed is the previously derived self-consistent (SC) model which is based on the integral equations derived by Cherkaoui *et al* [23] and extended to the quasi-static frequency regime by Haberman *et al* [38]. It is important to emphasize that the CDSP material design approach is not restricted to the use of the SC model. Indeed it is entirely possible, and even preferable in some cases, to implement the models such as the differential effective medium (DEM) or and Mori-Tanaka (MT) schemes given in Appendix D.

Micromechanical models discussed in this work are strict mean-field approaches and therefore require that the inhomogeneities be "well mixed" in the continuous matrix.

In other words, the micromechanical models *are not* sensitive to the spatial distribution of inhomogeneous phases in the matrix or their relative proximity. Material microstructure specification is therefore limited to inhomogeneity volume fraction, ϕ, inclusion geometry described by their aspect ratios *a/b* and *a/c*, and their orientation distribution, $\Omega(\gamma,\theta,\psi)$ [150]. The inclusion volume fraction is physically restricted to the fall within the values of *0* and *1* but can be further constrained through designer specification or another physical property requirement, such as transparency, that is not considered here. The orientation distribution is fully described by the some probabilistic distribution of Euler angles. For the current application, it is assumed that this distribution is amply described using a three dimensional Gaussian distribution, $p(\sigma_\gamma,\sigma_\theta,\sigma_\psi)$, defined by the standard deviations of each Euler angle represented by $\sigma_\gamma,\sigma_\theta,$ and σ_ψ, respectively. All of the above restrictions result from the fact that mean-field theories are limited to predictions of material behavior at one scale, the macroscale for the current case, resulting from heterogeneities that exist at another, inferior, scale. The mathematical approach assumes that the macroscale behavior is a volume average of material properties at the inferior, microscopic, length scale. This assumption implicitly requires that the combination of heterogeneities in the matrix phase be well-mixed, that is, uniform from one representative volume element to the next, see Figure 6.3. If this is not true, then the EMT prediction of macroscopic behavior is only valid for the material domain having the assumed volume fraction and orientation distribution. Given these restrictions, the only variables available to describe the effective material behavior are the inclusion volume fraction, geometry, and orientation distribution.

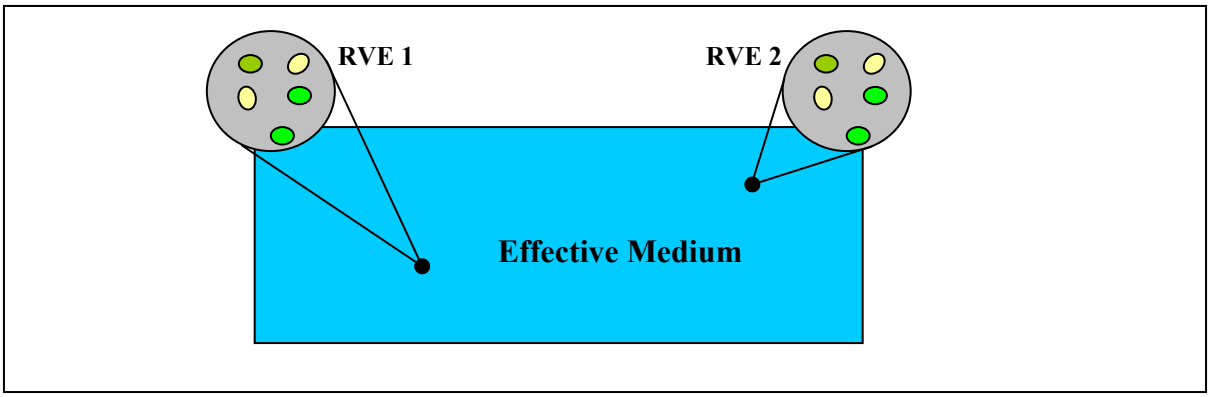

Figure 6.3: Schematic displaying continuity of RVE composition at any location in a material volume. Such continuity is required to expect valid results from mean-field EMT.

The SC model implemented in this study has been formulated such that the effects of thinly coated heterogeneities can be studied. The capability to include an inclusion coating is advantageous for several reasons. The first, most obvious, reason to model coated inclusions is that certain particulate composite materials consist of coated inclusions embedded in a continuous matrix [26, 180]. Another reason for including a coating phase is to improve modeling precision by the appearance of an "interphase" surrounding the material heterogeneity. Such is the case of the generalized self-consistent model developed by Christensen [80]. The SC model improves the generality of the design space exploration by allowing the effects of coated inclusion or interphase behavior to be considered. For coated inclusions, the volume fraction of coated inclusions is the sum of the volume fractions of the inclusion, f^I, and its coating, f^C.

$$\phi = f^I + f^C \approx f^I\left(1+\varepsilon\right) \qquad \text{(VI.2.2)}$$

The far right-hand side (RHS) of Eq. (VI.2.2) is an approximation that is valid when the coating is thin and "homothetic." For thinly coated inclusions, the coating percentage, ε, is well approximated with the formula $\varepsilon \approx 3\Delta a/a$. The term homothetic describes the case where the coating thickness along the primary axes of the ellipsoid denoted as Δa, Δb, and Δb are such that $\Delta a/a = \Delta b/b = \Delta c/c$. These are bounds placed on inputs to the SC model initially derived by Cherkaoui *et al* [23]. The CDSP design approach could, however, be implemented such that no inclusion coating is considered by introducing further design constraints.

One benefit of the micromechanical modeling technique proposed is the ability to account for microstructural variations resulting from fabrication processes and naturally randomness. Variability in inclusion orientation or coating thickness is easily approximated using the DSCT formulation described by Haberman *et al* [130]. Such variability has an effect on the final structure and is often a significant hurdle in material design. The topic of uncertainty and variability has been considered by several authors. Choi *et al* [116, 117, 181] and Panchal *et al* [182] have investigated the propagation of uncertainty through multi-scale models and its effect on robust design. While the effects of imprecise information on DBD has been investigated by Aughenbough and Paredis [183] and Aughenbough *et al* [184] in the context of information economics. The CDSP approach has been shown sufficiently flexible to consider degrees of randomness which can be traced to material variation, manufacturing processes, or even the non-deterministic nature of the model employed. These facts illustrate the power of the coupling of the robust micromechanical model with a systems design approach to explore material design possibilities. The former permits the exploration of many different

material properties and configurations and even variability while the latter provides a framework for logical and efficient design space exploration.

Table 6.1: Summary of quasi-static micromechanical modeling variables for a material consisting of a viscoelastic matrix containing thinly coated micro-inclusions.

Variable Model	*Description*	*Units*
	Inclusion	
$\hat{\mathbf{C}}^I$	Stiffness tensor	Pa
a/b	Aspect ratio	---
a/c	Aspect ratio	---
ρ^I	Density	kg/m^3
σ_γ^{IL}	Standard dev. of Euler angle, γ	radians
σ_θ^{IL}	Standard dev. of Euler angle, θ	radians
σ_ψ^{IL}	Standard dev. of Euler angle, ψ	radians
	Coating	
$\hat{\mathbf{C}}^C$	Stiffness tensor	Pa
ρ^C	Density	kg/m^3
$\Delta a/a$	Coating thickness ratio	---
	Matrix	
$\hat{\mathbf{C}}^M$	Stiffness tensor	Pa
ρ^M	Density	kg/m^3
	Overall	
ϕ	Volume fraction	---

Table 6.2: Summary of assumptions for micromechanical modeling in the quasi-static domain.

Assumption	*Description*
$\Delta a/a \ll 1$	▪ Thin coating approximation
$\Delta a/a = \Delta b/b = \Delta c/c$	▪ Homothetic approximation
$\left.\begin{matrix} k_L a \\ k_S a \\ k_{flex} a \end{matrix}\right\} \ll 1$	▪ Quasi-static approximation ▪ a is descriptive dimension of inclusion ▪ k_x represents the wavenumber of longitudinal, shear, or flexural waves in the matrix

6.2.1.2 Design variables, bounds, and constraints introduced by the RKU model and law of mixtures approximations

The part level modeling of the layered plate is achieved using two different models: the constrained layer damping model developed by Ross, Kerwin, and Ungar (RKU) [31] and LOM formulae derived in Appendix F. The purpose of the RKU model is to approximate the effective complex valued bending modulus, $\hat{B}^{eff}$, while the LOM formulae yields approximations of the in-plane Young's modulus of the plate, $\hat{E}_{11}^{eff}$. These models require inputs describing the material stiffness of each layer, denoted as $\hat{\mathbf{C}}^{IL}$, and $\hat{\mathbf{C}}^{g}$, the thickness of each layer, denoted as h_{IL}, and h_g, and the frequency of interest, ω. The multi-scale modeling scheme in Figure 6.2 shows that the inputs to these two models come from both the initial design parameters and from the outputs of micro → macro scale micromechanical modeling. The stiffness tensors of the interlayer and glass layers are functions of their respective microstructures which are determined using the SC micromechanical model. The RKU and LOM models rely on several simplifying assumptions, most of which are automatically satisfied by a typical automobile windshield. The most important of these is the restriction on the following Young's modulus ratio: $E_{11}^{',IL} / E_{11}^{',g} \ll 1$. This restriction implies that the interlayer will chiefly undergo shear deformation during the passage of a flexural wave. Shear deformation in this highly absorptive layer is the origin of the increased damping of the sandwich plate. The RKU model further requires that the overall thickness of the plate be much smaller than the wavelength of any waves (longitudinal, shear, or flexural) traveling in the plate. This assures that no standing waves are present and therefore that the multilayered plate

behavior is reasonably well approximated as a single entity. The last restriction of the RKU model is the assumption that the out-of-plane slope due to flexural motion is very small. This is required because the RKU model is based on Kirchhoff plate theory [185] (though this fact is not explicitly stated by the authors). Lastly, it is important to note that the restrictions placed on the RKU model are such that if they are satisfied, the restrictions placed on the LOM formulae will also be satisfied.

Several part level variables are restricted based on overall design considerations. One such variable is the overall thickness of the sandwich plate, h_{tot}, which must conform with pre-existing conditions, namely the windshield mounting. Another very important consideration is the effective in-plane stiffness, $E_{11}^{',eff}$. This stiffness variable has a direct impact on the structural soundness of the car frame. It is desirable that the effective in-plane stiffness be superior to some value. This is achieved by requiring that the in-plane Young's modulus not depart, in the negative sense, from that of the initial configuration by more than some ΔE_{11}, defined by the designer.

$$E_{11}^{',eff} - E_{11}^{',ref} \geq -\Delta E_{11}^{'} \qquad \text{(VI.2.3)}$$

where $E_{11}^{',ref}$ is the in-plane stiffness of the windshield before design changes. The value of $\Delta E_{11}^{'}$ is defined with respect to some admissible percentage decrease in in-plane stiffness which is a designer input. Table 6.3 and Table 6.4 summarize the model variables and assumptions introduced by the RKU and LOM models.

Table 6.3: Summary of RKU and LOM model variables.

Variable Model	*Description*	*Units*
$\hat{\mathbf{C}}^{IL}$	Stiffness tensor	Pa
$\hat{\mathbf{C}}^{g}$	Stiffness tensor	Pa
h_{IL}	Interlayer thickness	m
h_g	Glass layer thickness	m
ω	Frequency	rad./s

Table 6.4: Summary of RKU and LOM model assumptions to approximate the enhanced damping due to constrained layer damping.

Assumption	*Description*
$E_{11}^{',IL} / E_{11}^{',g} << 1$	▪ In plane stiffness of glass layers is much higher than that of the interlayer.
$\left.\begin{matrix}\lambda_L \\ \lambda_S \\ \lambda_{flex}\end{matrix}\right\} \gg h_{tot}$	▪ Wavelength, λ, of longitudinal, shear, and flexural waves in the sandwich plate are much larger than the total plate thickness.
$\left.\begin{matrix}\left.\frac{\partial z}{\partial x}\right\|_{neutral\ plane} \\ \left.\frac{\partial z}{\partial y}\right\|_{neutral\ plane}\end{matrix}\right\} \ll 1$	▪ The out of plane slope induced by traveling flexural waves must be very low in magnitude. This requirement is a result of the fact that the RKU model essentially employs Kirchhoff plate theory.
$h_2 = \text{Const}$ *Equivalent to:* $\lvert\hat{g}\rvert = \left\lvert \frac{\hat{\mu}_{\text{inter}}}{\hat{E}_{glass} h_{\text{inter}} h_{glass}} \sqrt{\frac{\hat{B}^{eff}}{\omega^2 \rho^{eff} h_{tot}}} \right\rvert \ll 1$	▪ The thickness of the central layer, h_2, of the sandwich plate is constant. This implies that no standing waves can be established in the central layer. This is quantified by the non-dimensional shear parameter, g.
$h_{tot} \ll \begin{cases} L \\ W \end{cases}$	▪ The total thickness of the plate must be far inferior to the length, L, and width, W, of the plate. This implies that edge effects are negligible.

6.2.1.3 Design variables, bounds, and constraints introduced by the modified mass law

The modified mass law was introduced in Chapter V to explore the effects of different materials on the transmission loss through a sandwich plate. This model

requires only the bending rigidity, $\hat{B}^{eff}$, thickness, h_{tot}, and density, ρ^{eff}, of the sandwich plate, the speed of sound in air, c_{air}, and the frequency of interest, ω. The effective bending rigidity is calculated by the RKU model, h_{tot} and ρ^{eff} are functions of the sandwich geometry, and $c_{air} = 343\ m/s$ at 20C. Though simple, this model provides a very accurate picture of the underlying physics governing the transmission of acoustic energy though the plate if several restrictions are applied. The first of these restrictions is on the wavelength. Specifically, the model is only valid when, regardless of frequency, the wavelength of a flexural wave in the plate is much larger than the plate thickness. This requirement is identical to that given for the RKU model in Section 6.2.1.2. The other is that the characteristic impedance of the plate be much larger than that in air, or: $\left|\left(\rho\hat{c}_L\right)_{plate}\right| \gg \left|\left(\rho\hat{c}_L\right)_{air}\right|$. This permits the approximation of the plate as a lumped mass that is moved by the pressure gradient presented by an incident acoustic wave. Table 6.5 summarizes these assumptions which are implemented as constraints in the CDSP design approach explained in Section 6.2.2.

Table 6.5: Summary of assumptions for TL approximation using the modified mass law. Note: these assumptions are automatically satisfied if the RKU model assumptions are satisfied.

Assumption	*Description*
$k_{flex}h_{tot} \ll 1$	▪ This inequality states that the flexural wavelength in the plate and in all layers is much longer than the total plate thickness, h_{tot}. Note: $k_{flex} = 2\pi/\lambda_{flex}$
$\left\|\left(\rho\hat{c}_L\right)_{plate}\right\| \gg \left\|\left(\rho\hat{c}_L\right)_{air}\right\|$	▪ The magnitude of the characteristic impedance of the plate, $\left\|\hat{Z}_{plate}\right\|$, must be much higher than that of air, $\left\|\hat{Z}_{air}\right\|$.

6.2.1.4 Overall bounds and constraints

It almost goes without saying that the constitutive material behavior of each layer must to obey the laws of physics. For the specific problem of material design for an automobile windshield, this statement implies that the stiffness tensor of the material comprising each layer must be positive definite. This requirement is a fundamental restriction placed on the strain energy function of any material which implies, according to Gibbs theorem, that the material is in a state of thermodynamic stability [185]. Any material not obeying this requirement is not in a "zero state" and is therefore thermodynamically unstable. However, the positive definite requirement only applies to the *macroscopic* stiffness tensor of each layer. Lakes and Drugan [186] and Wang and Lakes [187] have shown that it is admissible to consider the presence of inclusion materials whose stress tensor is not positive definite. This is possible because the material phase surrounding the instable material holds the unstable inclusion in a state of quasi-stability. The materials are said to be in quasi-stability, because they will become unstable if removed from the surrounding material. Such material behavior and its consequences are discussed in more detail in Chapter VII. For the purposes of CDSP design of an automobile windshield, it is sufficient to require that the macroscopic stiffness tensors of each plate layer be positive definite.

Table 6.6: Restrictions on the macroscopic material behavior of the system.

Assumption	*Description*
$C^{IL}_{ijkl} n_i n_k m_j m_l > 0$ $C^{g}_{ijkl} n_i n_k m_j m_l > 0$	▪ Macroscopic stiffness tensor of all plate materials must be positive definite. **n** and **m** represent any non-zero vector.

6.2.2 Structuring design space using CDSP

Now that all of the variables, restrictions, and assumptions of each model comprising the nested multi-scale modeling approach have been delineated, it is now possible to explore the design space using a CDSP. The CDSP is a mathematical construct to aid in the identification of design solutions in the presence of multiple conflicting goals. The generic CDSP is a hybrid formulation that incorporates concepts from both traditional mathematical programming and goal programming [177]. These two approaches are similar in that they refer to system constraints that must be satisfied. The difference between these approaches lays in the way the deviation or objective function is modeled. In the compromise DSP, as in goal programming, multiple objectives are formulated as system goals involving deviation variables, and the deviation function is modeled using deviation variables rather than system or decision variables. The CDSP is further tailored to handle common engineering design problems in which physical limitations are described as system constraints and bounds on the system variables.

The conceptual basis of the CDSP is to minimize the difference between that which is desired and that which can be achieved when *multiple* goals are considered [177]. The desired results are labeled the *goal*(*s*) and denoted as G_i while the achievement of those goals is denoted as $A_i(\mathbf{X})$. The goals are defined by the designer at the outset of the CDSP and the actual attainment of those goals is a function of the independent system variables, **X**, which are altered to improve performance. This is accomplished by minimizing a deviation function, *Z*, which depends on deviation

variables represented with in the vector ***d***. The deviation function provides an objective measure of the extent to which multiple, often conflicting, goals are achieved. In the CDSP, multiple goals are considered conventionally by formulating the deviation function in either an Archimedean or pre-emptive manner [177]. The Archimedean case assigns a weight, W_i, to the deviation variable, d_i, proportional to the importance level of the design goal, G_i. The pre-emptive case requires that n different pre-defined deviation functions, $f_k(d_i)$, be minimized sequentially. The CDSP contrasts with traditional mathematical programming which typically models the objective function as a single goal, by which the desirability of a design solution is measured and all other characteristics of the design are modeled as hard constraints. The formulation of a CDSP is achieved through a logical problem solving approach. A summary of the mathematical description of the generic CDSP is given in Table 6.7. The protocol is defined as consisting of four specific sections: *Given*, *Find*, *Satisfy*, and *Minimize*. The first section serves to define and initiate the design problem while the *Find* and *Satisfy* sections are solved using an iterative minimization scheme to arrive at the set of design variable values yielding the best system performance, see Figure 6.4. The minimization scheme is not specified by the CDSP and should be chosen by taking into consideration the specific system and associated design space. Sections 6.2.2.1 – 6.2.2.4 specify the implementation of a CDSP for the design of automobile windshield materials.

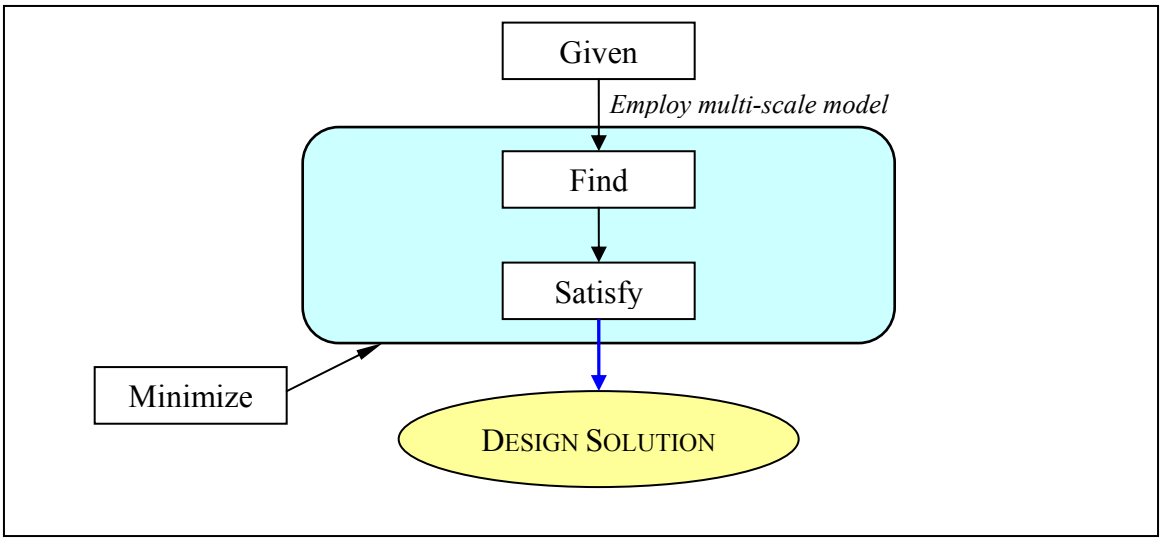

Figure 6.4: Schematic of CDSP steps. The given information corresponds to the initial product configuration and designer specified goals. The minimization loop contains the *Find* and *Satisfy* steps.

Table 6.7: Generic mathematical description of a compromise decision support protocol.

CDSP Summary
Given
An artifact to be improved in its initial configuration
n, number of system/design variables
p, number of equality constraints
q, number of inequality constraints
m, number of system goals
$g_i(\mathbf{X})$, constraint functions
G_i, system goals
$A_i(\mathbf{X})$, attainment values
$f_k(d_i)$, function of deviation variables to be minimized at priority level k (pre-emptive case)
W_i, Archimedean weight for the i^{th} goal (Archimedean case)
Find
$\mathbf{X}$, system variables
d_i^-, d_i^+, deviation variables

Table 6.7 (continued)

CDSP Summary
Satisfy
System constraints:
$g_i(\mathbf{X}) = 0 \quad i = 1,\ldots,p$
$g_i(\mathbf{X}) \le 0 \quad i = p+1,\ldots,p+q$
System goals:
$A_i(\mathbf{X})/G_i + d_i^- - d_i^+ = 1 \qquad i = 1,\ \ldots,\ m$
Bounds:
$X_j^{\min} \le X_j \le X_j^{\max} \qquad j = 1,\ \ldots,\ n$
$d_i^-,\ d_i^+ \ge 0$ and $d_i^- \cdot d_i^+ = 0 \quad i = 1,\ \ldots,\ m$
Minimize
Preemptive Minimization: $Z = \left[f_1(d_i^-, d_i^+) \quad \cdots \quad f_k(d_i^-, d_i^+) \right]$
Archimedean Minimization: $Z = \sum_{i=1}^{m} W_i (d_i^- + d_i^+)$ with $\begin{cases} \sum_{i=1}^{m} W_i = 1 \\ W_i \ge 0 \end{cases}$

6.2.2.1 Given

The *given* section of any design problem serves as the entry point for the iterative evaluation of the system model which employs the CDSP as a guide to improve the performance of any product. A symmetric three-layer sandwich plate consisting of two glass layers sandwiching a soft polymer interlayer with a fixed overall thickness, h_{tot}, is the product under consideration. The symmetric layer configuration will not altered in this work as is has been shown by Buerhle *et al* [188] to be optimal for noise isolation applications. The design aim is to search for changes in the material microstructure of each windshield layer that yields improved structural performance as defined by multiple, conflicting goals, G_i. The CDSP requires that all system parameters, system goals, and

the attainment of those goals by the initial artifact configuration, $A_i(\mathbf{X}_{init})$, be defined at this stage. The attainment of system goals by the initial configuration are calculated using the nested multi-scale modeling technique described in Figure 6.2 using the initial values of the independent system variables and the full set of system parameters. The initial values of the independent system variables, $\mathbf{X}_{init}$, are those of the traditional windshield configuration.

Table 6.8 lists the system parameters which must be defined in order to simulate the automobile windshield behavior as delineated in Figure 6.2. These are variables required for model implementation but they cannot be varied with respect to the original windshield configuration in order to improve system performance. Two very important system parameters are the stiffness tensors of the materials comprising the bulk material of each windshield layer. The detailed example given by this chapter allows the designer to select between three different polymers interlayer polymers. This is done to illustrate the practicality of applying this approach to a true design problem which could simultaneously consider both material selection and material design. It should be clear that the available number of bulk polymer and glass materials could easily be augmented to increase designer freedom.

Table 6.8: Table of system parameters.

X_i	*Description*	*Units*	*Comments*
	Interlayer Matrix		
$\hat{\mathbf{C}}^{M,IL}$	Interlayer matrix stiffness tensor $\hat{\mathbf{C}}^{IL}(f), \in \mathbb{C}$	Pa	Designer Selection, isotropic material
ρ_{IL}	Density	kg/m^3	Designer Selection
	Glass		
$\hat{\mathbf{C}}^{g,IL}$	Glass matrix stiffness tensor $\not\alpha f$, $\in \mathbb{C}$	Pa	Soda-Lime Glass, isotropic material
ρ_g	Density	kg/m^3	Soda-Lime Glass
	Air		
ρ_{air}	Density	kg/m^3	Given
c_{air}	Sound Speed	m/s	Given
	System		
h_{tot}	Plate thickness	m	Fixed

The pertinent material properties of soda-lime glass and three different polymers are givenin Table 6.9. These are the bulk materials whose microstructures are altered during the design process in order to improve the performance of the windshield as quantified by goals defined by the designer and given in Table 6.10. It is noted that, for simplicity, the results given in Section 6.4 only consider a PVB interlayer.

Table 6.9: Sandwich plate geometry and bulk material properties. The results given in Section 6.4 only consider a PVB interlayer.

	h (m)	μ (GPa)	v ( )	ρ (kg/m^3)
Glass	2.0 x 10^{-3}	29.5(1+0.02j)	0.23	2469
IL_{PVB} (@ 1kHz)	8.0 x 10^{-4}	0.133(1 + 0.13j)	0.40	1115
IL_{PNNL} (@ 1kHz)	8.0 x 10^{-4}	1.58(1 + 0.19j)	0.45	1100
IL_{BKT} (@ 1kHz)	8.0 x 10^{-4}	9.60(1 + 0.50j) x 10^{-3}	0.49	1090

The design goal values are set by the designer at the outset of the CDSP. Section 6.2 defined the windshield design goals in general terms as (*i*) reducing sound transmission, (*ii*) moving the phenomenon of coincidence to a frequency outside the highly sensitive frequency range of human hearing, (*iii*) reducing the total windshield density, and (*iv*) maintaining or improving the structural rigidity of the windshield. These goals are now specified with respect to the system model outputs as (*i*) ΔTL^{goal}, (*ii*) f_{coinc}^{goal}, (*iii*) ρ_{tot}^{goal}, and (*iv*) $\left(E_{11}^{ref} - E_{11}^{goal}\right)\Big/E_{11}^{ref}$, respectively. Goals (*iii*) and (*iv*) are straightforward calculations resulting from the multi-scale model. Goals, (*i*) and (*ii*), however, cannot be calculated directly from the multiscale model. These outputs are measures of the acoustic performance and must be found through analysis of the TL versus frequency curve. ΔTL measures the coincidence notch depth. It is defined as the difference between the TL measured at points *A* and *B* show in Figure 6.5. Point *A* is the first point of zero-slope encountered as a function of increasing frequency and point *B* is the second point of zero slope. f_{coinc} defines the frequency at which the TL is at its lowest point of the coincidence notch and is the frequency component of point *B*. These points must be found numerically through analysis of the TL versus frequency curve resulting from the nested multi-scale modeling. It is interesting to note that point *A* is a reasonable descriptor of the frequency at which the plate no longer obeys the mass-law. The simple diagram shown in Figure 6.5 illustrates ΔTL and f_{coinc}.

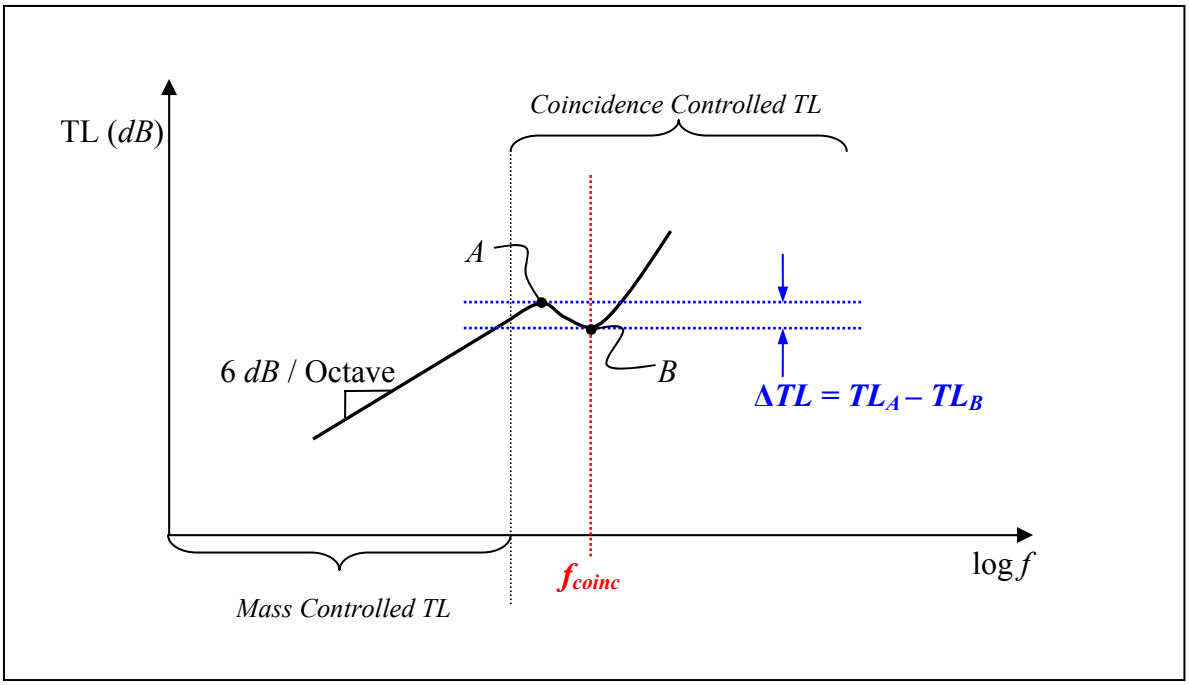

Figure 6.5: Idealized plot of a typical windshield TL vs. frequency curve. The diagram shows how the acoustic measures ΔTL and f_{coinc} are defined with respect to specific characteristics of this curve.

The actual values of ΔTL^{goal} and f_{coinc}^{goal} are defined via designer inputs which result from design decisions. The CDSP is implemented in this work using a Graphic Design Interface (GDI) created in Matlab which is described in Section 6.3. A summary of the design goals for an automobile windshield are summarized in Table 6.10.

Table 6.10: Table of system goals.

G_i	*Description*	*Units*	*Goal*
Air			
ρ_{tot}^{goal}	Overall plate density	kg/m^3	Minimize
f_{coinc}^{goal}	Coincidence notch frequency	Hz	Minimize
ΔTL^{goal}	Coincidence notch depth	dB	Minimize
$\left(E_{11}^{ref} - E_{11}^{goal}\right)/E_{11}^{ref}$	Variation of in-plane stiffness	---	Minimize

Given the initial design variable values, $\mathbf{X}_{init}$, the system parameter values, the designer specified system goals, G_i, and the initial attainment of those goals, $A_i\left(\mathbf{X}_{init}\right)$, it is now possible to employ the CDSP for the microstructural design of the windshield materials. This is addressed in Sections 6.2.2.2 – 6.2.2.4.

6.2.2.2 Find

The *find* section of CDSP is the first of the step to be calculated within the iterative minimization of the deviation function. This step involves the calculation of the deviation variables based on the n^{th} iteration of the independent system design variables, **X**. A complete list of independent system design variables, which was described in Section 6.2, is given in Table 6.11. The design variables describe the full design space of the windshield. In its most general form the design space consists of 38 independent variables. Regardless of the numerical minimization scheme employed, this size of design space coupled with the implicit nature of the SC model and the complexity of mean-field micromechanical modeling can lead to considerable design calculation times. This is an illustration of a common conundrum posed by conflicting requirements of material design. Specifically, material design requires complex models to correctly predict behavior at smaller and smaller scales but the penalty for increased information at smaller scales is an amplified calculation time. The goal in this chapter is to propose a middle path which introduces a satisfactorily high degree of microstructural complexity while allowing the designer to reduce calculation time to an acceptable level. For example, the size of design space can be reduced by only considering inclusions of

spheroidal geometry, *.i.e.* oblate, prolate, or spherical inclusions, by neglecting the role of inclusion coating, by neglecting the possibility of heterogeneities in a specific material layer, or any combination of the above. This chapter introduces methods by which such options are made available to the designer by prompting input in the form of pertinent design questions. Section 6.3 addresses the issue of calculation time through the creation of a GDI. This interface allows the designer to interactively restrict the number of variables in the design space. The result is an example of the practical use of mean-field micromechanical modeling as a tool for material design.

Table 6.11: Table of design variables, *X*.

X_i	*Description*	*Units*	*Constrained?*
	Interlayer Heterogeneities		
$\mathbf{C}^{I,IL}$ (2 or 5 variables)	Stiffness Tensor $\not\propto f$, $\notin \mathbb{C}$	Pa	Y
$(a/b)^{IL}$	Inclusion aspect ratio	---	Y
$(a/c)^{IL}$	Inclusion aspect ratio	---	Y
$\rho^{I,IL}$	Density	kg/m^3	Bounded
$\mathbf{C}^{C,IL}$ (2 or 5 variables)	Stiffness Tensor $\not\propto f$, $\notin \mathbb{C}$	Pa	Y
$\left(\Delta a/a\right)^{IL}$	Coating thickness measure	---	Y
$\rho^{C,IL}$	Density	kg/m^3	Y
σ_{γ}^{IL}	Euler Angle, γ, Standard Deviation	radians	Y
σ_{θ}^{IL}	Euler Angle, θ, Standard Deviation	radians	Y
σ_{ψ}^{IL}	Euler Angle, ψ, Standard Deviation	Radians	Y
	Glass Heterogeneities		
$\mathbf{C}^{I,g}$ (2 or 5 variables)	Stiffness Tensor $\not\propto f$, $\notin \mathbb{C}$	Pa	Y
$(a/b)^{g}$	Inclusion aspect ratio	---	Y
$(a/c)^{g}$	Inclusion aspect ratio	---	Y
$\rho^{I,g}$	Density	kg/m^3	Bounded
$\mathbf{C}^{C,g}$ (2 or 5 variables)	Stiffness Tensor $\not\propto f$, $\notin \mathbb{C}$	Pa	Y
$\left(\Delta a/a\right)^{g}$	Coating thickness measure	---	Y
$\rho^{C,g}$	Density	kg/m^3	Y
σ_{γ}^{g}	Euler Angle, γ, Standard Deviation	radians	Y
σ_{θ}^{g}	Euler Angle, θ, Standard Deviation	radians	Y
σ_{ψ}^{g}	Euler Angle, ψ, Standard Deviation	radians	Y
	Layers		
h_g/h_{IL}	Ratio of layer thicknesses	---	Bounded

The values of the deviation variables, d_i, are calculated once the values of the system design variables are determined for the n^{th} minimization iteration step. The manner in which these values are found is entirely dependent on the minimization scheme employed. The current CDSP implementation uses a Sequential Quadratic Programming (SQP) algorithm which is discussed in more detail in Section 6.2.2.4. The deviation variables describe the extent to which the system goals are achieved and have the characteristics defined by Eq. (VI.2.4).

$$d_i^-,\ d_i^+ \geq 0 \quad \text{and} \quad d_i^- \cdot d_i^+ = 0 \tag{VI.2.4}$$

In accordance with Table 6.7 there are *m* deviation variables, one corresponding to each design goal. The deviation variables corresponding to the current the system design goals are describe by Eqs. (VI.2.5).

$$d_i \equiv d_i^+ - d_i^- \equiv \frac{A_i(\mathbf{X})}{G_i} - 1 \quad \text{for} \quad i = 1,\ \ldots,\ 4 \tag{VI.2.5}$$

with

$$\frac{A_1(\mathbf{X})}{G_1} = \frac{\Delta TL^A}{\Delta TL^{goal}}; \qquad \frac{A_2(\mathbf{X})}{G_2} = \frac{f_{coinc}^A}{f_{coinc}^{goal}}$$

$$\frac{A_3(\mathbf{X})}{G_3} = \frac{\rho_{eff}^A}{\rho_{eff}^{goal}}; \qquad \frac{A_4(\mathbf{X})}{G_4} = \begin{cases} \dfrac{E_{11}^{ref} - E_{11}^A}{\Delta E_{11}^{goal}} & \text{if} \quad E_{11}^A < E_{11}^{ref} \\ 1 & \text{otherwise} \end{cases} \tag{VI.2.6}$$

Note that the superscript *A* denotes the value attained by the system at the current minimization step and the superscript *goal* denotes the desired design value. It is obvious that from these expressions the value of each deviation variable has a range of $\left[0 \quad \infty\right)$. This fact is very important for the minimization of the deviation function which is discussed in Section 6.2.2.4.

6.2.2.3 Satisfy

The *satisfy* section of the CDSP considers the (*i*) limitations of models implemented to approximate system behavior, (*ii*) limits defined by the designer, (*iii*) system bounds, and (*iv*) system design goals. Limitations described by points (*i*) and (*ii*) are called design constraints. Constraints are usually the result of model assumptions, but can also result from processing restrictions or from decisions taken by the designer for reasons ranging from materials sourcing to monetary cost. Constraints delimit the acceptable values which the independent design variables may assume during the deviation function minimization, see the illustration of a 2D design space shown in Figure 6.6. The figure illustrates how each point in the feasible design space, **X**, is linked

to a single point in the *m*-dimensional attainment space by system simulation methods. It is noted that the deviation variables defined in Eqs. (VI.2.5) and (VI.2.6) are a related to the *m* space vector difference between the goal point, $\mathbf{G}(\mathbf{X})$, and the attainment point, $\mathbf{A}(\mathbf{X})$, via relation (VI.2.7).

$$A_i(\mathbf{X}) - G_i = D_i(\mathbf{X}) \tag{VI.2.7}$$

Then, normalizing Eq. (VI.2.7) by G_i yields Eq. (VI.2.5).

$$\frac{A_i(\mathbf{X})}{G_i} - 1 = \frac{D_i(\mathbf{X})}{G_i} \equiv d_i(\mathbf{X}) \tag{VI.2.8}$$

The assumptions of each individual model employed in the current nested multi-scale windshield model are detailed in Sections 6.2.1.1 – 6.2.1.3. These system constraints can be altered by employing a different modeling scheme, or through designer decisions. The third item considered by this section is the design variable bounds. Bounds differ from constraints in the sense that they are not negotiable. For example, the density of any given constituent material cannot have a value of less than 0 kg/m^3. A less obvious bound is the positive definiteness requirement placed on the effective stiffness tensor of each layer material which was mentioned in Section 6.2.1.4. Lastly, this section considers system goals. The goal values are defined here in order to enter the minimization step which negotiates between what is wanted from the design and what is achievable based on the multi-scale model employed.

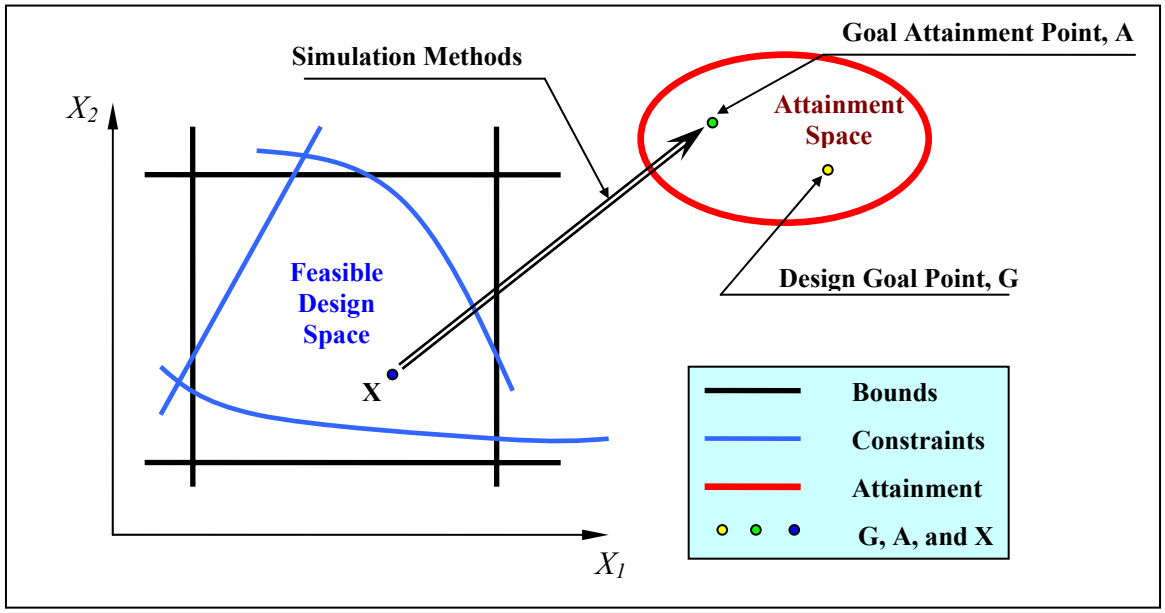

Figure 6.6: Visualization of system constraints and bounds. Simulation methods are shown bridging the design space to the aspiration space which includes the system goals.

The previous paragraph stated that system constraints must be satisfied for the solution to be feasible. Constraints are formulated as functions denoted as $g_i(\mathbf{X})$ and can be classified as either equality or inequality constraints. Constrain functions are described with Eq. (VI.2.9). It is important to note that the CDSP does not place restrictions on the linearity or convexity of either the system model or the constraint functions. This

$$g_i(\mathbf{X}) = 0 \qquad i = 1, \ \ldots, p$$
$$g_i(\mathbf{X}) \geq 0 \quad i = p+1, \ \ldots, p+q \tag{VI.2.9}$$

Equality constraints can be used to serve several purposes. The first would be the requirement that the independent design variables lie on some curve in the *n* dimensional design space. An example of this type of equality constraint is the relationship between the overall coated inclusion volume fraction, that of the individual constituents, and the shell thickness given by Eq. (VI.2.10) which employs a thin shell approximation.

$$\phi \approx f^I \left(1 + 3\frac{\Delta a}{a} \right) \tag{VI.2.10}$$

This relationship places restricts the possible values of f^I and $\Delta a/a$ for any given value of total volume fraction, ϕ. Equation (VI.2.10) can be expressed as an equality constraint in the form of Eq. (VI.2.9) as:

$$g\left(\phi, f^I, \frac{\Delta a}{a} \right) = \phi - f^I \left(1 + 3\frac{\Delta a}{a} \right) = 0 \tag{VI.2.11}$$

The other way an equality constraint can be employed is to effectively demote a design variable to a design parameter. For example, the following equality constraint function can be implemented if the designer desires to inspect the design space in the case where the coating thickness is fixed or neglected.

$$g\left(\frac{\Delta a}{a} \right) = \frac{\Delta a}{a} - x = 0 \tag{VI.2.12}$$

Where x is constant whose value is assigned by the designer and may assume any value, including zero. The second classification of system constraint is the inequality constraint. This is the type of constraint illustrated by the blue lines in Figure 6.6. These constraint functions limit the potential design variable values to lie on or above some n-1 dimensional surface in the n-dimensional design space. The system constraints for the windshield design problem are summarized in Table 6.12.

Table 6.12: Specification of system constraints.

X_i	***Description***	***Units***	***Constraint***
	Inclusion		
μ^I / μ^M	Shear modulus ratio	---	$\in [-2 \quad 1]$
ν^I	Inclusion Poisson Ratio	---	$\in [0.1 \quad 0.49]$
C_{11}^I	Stiffness tensor element	Pa	<u>*Design Decision*</u>: High: $\in \left[C_{11}^{I,low} \quad C_{11}^{I,hi} \right]$ Med: $\in \left[C_{11}^{I,low} \quad C_{11}^{I,hi} \right]$ Low: $\in \left[C_{11}^{I,low} \quad C_{11}^{I,hi} \right]$ Iso: $\in \left[C_{11}^{I,low} \quad C_{11}^{I,hi} \right]$
C_{33}^I	Stiffness tensor element	Pa	<u>*Design Decision*</u>: High: $\in \left[C_{33}^{I,low} \quad C_{33}^{I,hi} \right]$ Med: C_{11}^I Low: C_{11}^I Iso: C_{11}^I
C_{44}^I	Stiffness tensor element	Pa	<u>*Design Decision*</u>: High: $\in \left[\mu^{I,low} \quad \mu^{I,hi} \right]$ Med: $\in \left[\mu^{I,low} \quad \mu^{I,hi} \right]$ Low: $\in \left[\mu^{I,low} \quad \mu^{I,hi} \right]$ Iso: $\in \left[\mu^{I,low} \quad \mu^{I,hi} \right]$

Table 6.12 (continued)

X_i	*Description*	*Units*	*Constraint*
C_{12}^{I}	Stiffness tensor element	Pa	<u>*Design Decision*</u>: High: $\in \left[C_{12}^{I,low} \quad C_{12}^{I,hi} \right]$ Med: $\in \left[C_{12}^{I,low} \quad C_{12}^{I,hi} \right]$ Low: $\in \left[C_{12}^{I,low} \quad C_{12}^{I,hi} \right]$ Iso: $\in \left[C_{12}^{I,low} \quad C_{12}^{I,hi} \right]$
C_{13}^{I}	Stiffness tensor element	Pa	<u>*Design Decision*</u>: High: $\in \left[C_{13}^{I,low} \quad C_{13}^{I,hi} \right]$ Med: C_{12}^{I} Low: C_{12}^{I} Iso: C_{12}^{I}
a/c	Inclusion aspect ratio	---	<u>*Design Decision*</u>: High: $\in [0.1 \quad 10]$ Med: $\in [0.2 \quad 5]$ Low: $\in [0.5 \quad 2]$ Iso: 1
σ	Euler Angle Standard Deviation	radians	<u>*Design Decision*</u>: High: 0 Med: $\in [0.25 \quad 0.40]$ Low: $\in [0.40 \quad 1.00]$ Iso: *Not defined*
Coating			
μ^C / μ^M	Shear modulus ratio	---	$\in [-2 \quad 1]$
ν^C	Inclusion Poisson Ratio	---	$\in [0.1 \quad 0.49]$
C_{11}^{C}	Stiffness tensor element	Pa	<u>*Design Decision*</u>: High: $\in \left[C_{11}^{C,low} \quad C_{11}^{C,hi} \right]$ Med: $\in \left[C_{11}^{C,low} \quad C_{11}^{C,hi} \right]$ Low: $\in \left[C_{11}^{C,low} \quad C_{11}^{C,hi} \right]$ Iso: $\in \left[C_{11}^{C,low} \quad C_{11}^{C,hi} \right]$

Table 6.12 (continued)

X_i	*Description*	*Units*	*Constraint*
C_{33}^{C}	Stiffness tensor element	Pa	<u>*Design Decision*</u>: High: $\in\left[C_{33}^{C,low} \quad C_{33}^{C,hi}\right]$ Med: C_{11}^{C} Low: C_{11}^{C} Iso: C_{11}^{C}
C_{44}^{C}	Stiffness tensor element	Pa	<u>*Design Decision*</u>: High: $\in\left[\mu^{C,low} \quad \mu^{C,hi}\right]$ Med: $\in\left[\mu^{C,low} \quad \mu^{C,hi}\right]$ Low: $\in\left[\mu^{C,low} \quad \mu^{C,hi}\right]$ Iso: $\in\left[\mu^{C,low} \quad \mu^{C,hi}\right]$
C_{12}^{C}	Stiffness tensor element	Pa	<u>*Design Decision*</u>: High: $\in\left[C_{12}^{C,low} \quad C_{12}^{C,hi}\right]$ Med: $\in\left[C_{12}^{C,low} \quad C_{12}^{C,hi}\right]$ Low: $\in\left[C_{12}^{C,low} \quad C_{12}^{C,hi}\right]$ Iso: $\in\left[C_{12}^{C,low} \quad C_{12}^{C,hi}\right]$
C_{13}^{C}	Stiffness tensor element	Pa	<u>*Design Decision*</u>: High: $\in\left[C_{13}^{C,low} \quad C_{13}^{C,hi}\right]$ Med: C_{12}^{C} Low: C_{12}^{C} Iso: C_{12}^{C}
$\Delta a/a$	Coating thickness measure	---	$<< 1$ (model restriction) $\in\left[0 \quad 0.1\right]$
Interlayer & Glass Layers			
$E_{11}^{',IL}/E_{11}^{',g}$	Ratio of *in-plane* Young's moduli	---	$<< 1$ (model restriction) $\in\left(0 \quad 0.1\right]$
System			
h_{IL}/h_g	Layer thickness ratio	---	<u>*Design Decision*</u> $\in\left[0 \quad 0.05\right]$
ϕ	Volume fraction of coated inclusions	---	<u>*Design Decision*</u> $\in\left[0 \quad 0.05\right]$

Table 6.12 (continued)

X_i	*Description*	*Units*	*Constraint*
$\phi, f^I, \frac{\Delta a}{a}$	Volume fraction restriction	---	$\phi = f^I\left(1+3\frac{\Delta a}{a}\right)$

It is emphasized that this design space inspection is limited to the combinations of material anisotropy–inclusion geometry–inclusion orientation distribution combinations shown in Figure 6.7. The decision on admissible macroscopic anisotropy level (isotropic, low, medium, and high) is taken by the designer at the outset of the design problem. These particular combinations have been created to limit design calculation time. Introducing these limitations on the design space is not required per the generality of the micromechanical models, but rather implemented as practical measure to render design space exploration more efficient.

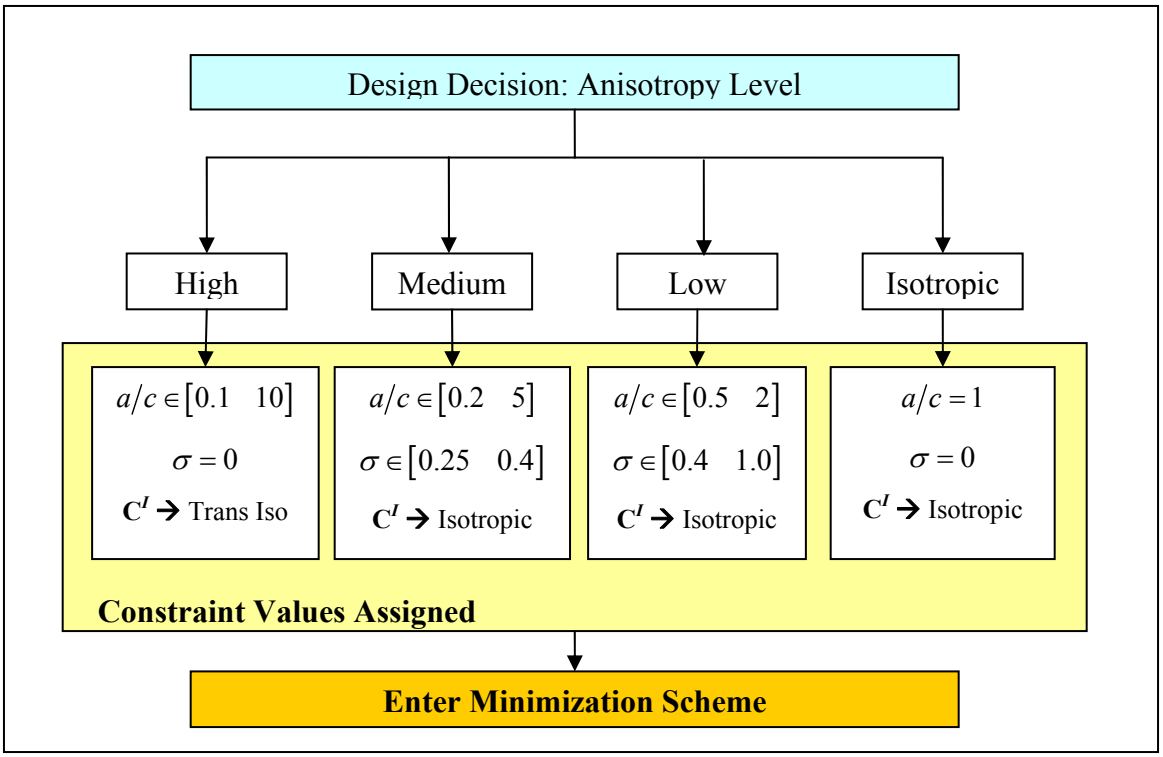

Figure 6.7: Flow chart of constraints placed on the geometry and material properties of inclusion and coating phases depending on design decisions pertaining to the macroscopicly permissible anisotropy level.

The different combinations shown in Figure 6.7 have been chosen based on observations of simulation results such as those given by Haberman *et al* [130, 150]. The limit values have been observed to induce anisotropic macroscopic material properties while minimally increasing calculation times. It must be noted that thought the statement that the calculation time is minimally increased *does not* mean that the calculation time is negligible. However, introducing these combinations of limit values allows the designer to explore various levels of macroscopic material anisotropy in the most time-efficient manner for the current nested multiscale model.

The limit values of the stiffness tensors in the isotropic case are determined from its classic representation shown in Eq. (VI.2.13) and the relationship between the Lamé constants and Poisson's ratio given by Eq. (VI.2.14).

$$C_{ijkl} = \lambda\delta_{ij}\delta_{kl} + \mu\left(\delta_{ik}\delta_{kl} + \delta_{il}\delta_{jk}\right) \tag{VI.2.13}$$

$$\lambda = \frac{2\mu\nu}{1-2\nu} \tag{VI.2.14}$$

Based on these expressions, the upper and lower constraint values for each element of stiffness tensor are estimated from isotropic property relations and isotropic initial guesses as shown in Eqs. (VI.2.15) and (VI.2.16). These equations employ Voigt notation.

$$\begin{aligned} C_{11,33}^{X,hi} &= 2\mu_{\max}^{X}\left(\frac{1-\nu_{\max}^{X}}{1-2\nu_{\max}^{X}}\right) \quad \text{if} \quad \mu_{\max}^{X} \geq 0 \quad C_{11,33}^{X,low} = 2\mu_{\min}^{X}\left(\frac{1-\nu_{\max}^{X}}{1-2_{\max}^{X}}\right) \quad \text{if} \quad \mu_{\min}^{X} < 0 \\ C_{11,33}^{X,hi} &= 2\mu_{\max}^{X}\left(\frac{1-\nu_{\min}^{X}}{1-2\nu_{\min}^{X}}\right) \quad \text{if} \quad \mu_{\max}^{X} < 0 \quad C_{11,33}^{X,low} = 2\mu_{\min}^{X}\left(\frac{1-\nu_{\min}^{X}}{1-2\nu_{\min}^{X}}\right) \quad \text{if} \quad \mu_{\min}^{X} \geq 0 \end{aligned} \tag{VI.2.15}$$

$$\begin{aligned} C_{12,13}^{X,hi} &= \frac{2\mu_{\max}^{X}\nu_{\max}^{X}}{1-2\nu_{\max}^{X}} \quad \text{if} \quad \mu_{\max}^{X} \geq 0 \quad C_{12,13}^{X,low} = \frac{2\mu_{\min}^{X}\nu_{\max}^{X}}{1-2\nu_{\max}^{X}} \quad \text{if} \quad \mu_{\min}^{X} < 0 \\ C_{12,13}^{X,hi} &= \frac{2\mu_{\max}^{X}\nu_{\min}^{X}}{1-2\nu_{\min}^{X}} \quad \text{if} \quad \mu_{\min}^{X} < 0 \quad C_{12,13}^{X,low} = \frac{2\mu_{\min}^{X}\nu_{\min}^{X}}{1-2\nu_{\min}^{X}} \quad \text{if} \quad \mu_{\min}^{X} \geq 0 \end{aligned} \tag{VI.2.16}$$

Where X of $C_{wx,yz}^{X,hi}$ represents either I or C and the comma denotes that the associated limit applies to both element wx and element yz. It is noted that the limits are dependent on the sign of the moduli to be considered. Because this chapter studies the effects of

negative moduli on the structural behavior of an automobile windshield, the above limit values apply to any given value of μ.

The lower and upper *bounds* on the system are now specified. As with many other design problems, most design variable bounds are not often encountered since variable constraints or generally more restrictive. The applicable upper and lower bounds on this problem are given in Table 6.13. There are three sets of bounds which may be active (which have not already been superseded by a constraint in Table 6.12) during design calculations. Those three are the inclusion and coating density bounds and the requirement that the effective stiffness tensor of the glass and interlayers be positive definite.

Table 6.13: Table of system bounds. These bounds are based on physical and geometric considerations and cannot be violated in any case.

X_i	*Description*	*Units*	*Bounds*
Inclusion			
σ_γ	Euler Angle, γ, Standard Deviation	radians	$\in [0 \quad \infty)$
σ_θ	Euler Angle, θ, Standard Deviation	radians	$\in [0 \quad \infty)$
σ_ψ	Euler Angle, ψ, Standard Deviation	radians	$\in [0 \quad \infty)$
ρ_I	Density	kg/m^3	$\in [0 \quad \infty)$
Coating			
ρ_C	Density	kg/m^3	$\in [0 \quad \infty)$
Interlayer & Glass Layers			
h_{IL}/h_g	Ratio of layer thickness	---	$\in (0 \quad \infty)$
$h_{tot} = 2h_g + h_{IL}$	Total thickness	m	fixed
$a_{ij}a_{kl}C_{ijkl}^{IL,eff}$ $a_{ij}a_{kl}C_{ijkl}^{g,eff}$	Measure of positive definiteness	N/A	> 0

Finally, the *system goal* values are considered in this section. More specifically, the designer is prompted to enter values for the system goals. Table 6.14 gives a list of suggested goal values. The reference value of each variable corresponds to that of the traditional sandwich windshield. The values of the coincidence notch frequency and depth for the reference case are given here since they are absolute values and are not relative measures. The reference coincidence frequency is approximately 4 kHz and notch depth is 3-4 dB. Because the coincidence phenomenon occurs at 4 kHz, which is within the most sensitive range of human hearing, significant acoustic performance improvements can be made by simply moving it to a lower frequency. Achievement of the system goal values in Table 6.14 will improve windshield performance with respect to weight reduction, structural rigidity, and acoustic isolations.

Table 6.14: Suggested system design goal values.

G_i	*Description*	*Units*	*Goal*
$100\left(\rho_{11}^{ref} - \rho_{11}^{goal}\right)/\rho_{11}^{ref}$	Reduction plate density	%	10%
f_{coinc}^{goal}	Coincidence notch frequency	Hz	1500
ΔTL^{goal}	Coincidence notch depth	dB	0.2
$100\left(E_{11}^{ref} - E_{11}^{goal}\right)/E_{11}^{ref}$	Maximum percent reduction of in-plane stiffness	%	2

This section has defined the constraints, bounds, and design goal values needed to design an automobile windshield having improved acoustic performance, reduced density, and minimally reduced structural rigidity. The following section closes the discussion of CDSP implementation for windshield design by detailing the minimization of the deviation function using Sequential Quadratic Programming.

6.2.2.4 Minimize

Deviation function minimization represents the final stage of a CDSP. The deviation function gives an objective measure of the difference between system attainment and system goals for any given set of independent design variables, **X**. The current CDSP implementation employs a deviation function having an Archimedean form. An Archimedean expression is one that sums the products of each deviation variable, defined in Eqs. (VI.2.5) and (VI.2.6), and their relative weights, W_i. The deviation function for the system goals specified in Section 6.2.2.1 is given by expression (VI.2.17).

$$Z = W_1 d_1 + W_2 d_2 + W_3 d_3 + W_4 d_4 \quad \text{with} \quad \begin{cases} \sum_{i=1}^{m} W_i = 1 \\ W_i \geq 0 \end{cases} \qquad \text{(VI.2.17)}$$

The individual deviation variable weights are specified by the designer. Equation (VI.2.17) states that the Archimedean weight values must be such that each weight is greater than zero and that all weights sum to unity. The current design problem determines these values through design decisions prompted by the GDI detailed in Section 6.3.2. Note that deviation function minimization implies that the CDSP is implemented in a manner such that the design solution is optimal. Other CDSP implementations exist, such as the robust design methodologies of Seepersad *et al* [3] and Choi *et al* [117], which take into consideration the sensitivity of the solution to input

variable noise. Robust solutions have not been considered as this work is primarily concerned with finding microstructural variables that lead to enhanced mechanical damping.

The minimization of any function of the design variables requires a robust numerical scheme and represents a key part of any design problem. Eq (VI.2.18) expresses the minimization problem in general terms.

$$\underset{\mathbf{X} \in \mathbb{R}^n}{\text{minimize}} \quad Z(\mathbf{X}) \tag{VI.2.18}$$

Where $\mathbf{X}$ is subject to the constraints and bounds defined in Table 6.7. Advances in computing power and numerical methods give the designer numerous options to efficiently minimize the deviation function and thereby determine the set of design variables yielding which improve windshield design. The major benefit of having numerous numerical minimization schemes available is the ability to select the scheme best suited for the deviation function defined in Eq. (VI.2.17). However, a high degree of scrutiny must be employed in choosing a numerical minimization scheme. Indeed, the use of some schemes can lead to very long evaluation times, erroneous results, or both.

An efficient and accurate solution to the minimization problem depends not only on the size of the problem in terms of the number of constraints and design variables but also on characteristics of the deviation function and constraints. When both the deviation function and the constraints are linear functions of the design variable, the problem is known as a Linear Programming (LP) problem. Quadratic Programming (QP) concerns the minimization (or maximization) of a quadratic deviation function that is linearly

constrained [189]. Reliable solution procedures are readily available for both the LP and QP problems [189]. The Nonlinear Programming (NP) problem is much more difficult to solve. A NP problem is one in which the deviation function and constraints can be nonlinear functions of the design variables. This is the case for the current design problem because the nested multiscale windshield model represents a non-linear relationship between the microstructural design variables and the deviation function. Finding a solution to a NP problem generally requires employing an iterative procedure which finds the solution to an LP or a QP sub-problem within some trust region in the design space [189]. The concept of a trust region is briefly discussed in the following paragraph. The present CDSP implementation employs an extremely robust NP problem solving method known as Sequential Quadratic Programming (SQP).

SQP methods represent the state of the art in nonlinear programming methods. For example, Schittkowski [190] has implemented and tested a version that outperforms every other tested method in terms of efficiency, accuracy, and percentage of successful solutions, over a large number of test problems. Based on the work of Biggs [191], Han[192], and Powell [193, 194], the method closely mimics Newton's method for constrained optimization of a NP problem. SQP makes an approximation of the Hessian and the Lagrangian function of the deviation function via a quasi-Newton updating method at each major SQP iteration. The update is then used to generate a QP sub-problem whose solution is used to form a search direction for a line search procedure. This is a type of trust region method. The basic idea of a trust region is to approximate the objective function, in this case $Z(\mathbf{X})$, with another function, $Z'(\mathbf{X})$, which reasonably reflects the behavior of $Z(\mathbf{X})$ in a neighborhood around the design point in *n*

dimensional design space. This neighborhood is known as the trust region. A trial step is then computed by finding the minimum of $Z'(\mathbf{X})$ within the trust region. The SQP method employed in this work computes $Z'(\mathbf{X})$, selects and modifies the trust region in the neighborhood of the design variable point, **X**, and determines the accuracy of the trust-region sub-problem through the BFGS QP algorithm. The BFGS algorithm is simply an QP technique named after contributing researchers Broyden [195], Fletcher [196], Goldfarb [197], and Shanno [198]. Further information regarding SQP and the BFGS algorithm can be found in Fletcher [189], Gill *et al.* [199], Powell [200], and Hock [201].

6.3 Strategy for design space exploration

The previous sections gave a description of how a CDSP can be implemented to employ the nested multiscale model for the design of an automobile windshield. This section develops and implements a strategy to explore the windshield design space and clearly illustrates how this information can be used to inform design decisions. Section 6.3.1 determines a set of parametric studies used to identify key material microstructural variables which influence windshield performance. The results of these parametric studies isolate specific microstructural variables and explore their influence on overall windshield performance. Section 6.3.2 then develops a basic graphic design interface (GDI) in order to (*i*) permit efficient evaluation of the parametric studies delineated in Section 6.3.1 and (*ii*) illustrate the how a correctly implemented CDSP can simplify design space exploration to yield useful multiscale modeling results. The second point is

very important for the future of material design as it this section shows that CDSP and similar techniques greatly aids in the process of inductive material design.

6.3.1 Parametric studies: Identifying trends and forming the design envelope

This section details a deliberate calculation strategy consisting of a set of parametric studies which aim to isolate the influence of individual microscale variables on windshield performance. Though each model making up the nested multiscale model and their associated assumptions include significant simplifications, design calculation time can still be considerable in the most general case. Further, finding a design solution in the most general case does not inform the designer of the of windshield performance sensitivity to individual microstructural variables. For these reasons it is highly desirable to create a calculation strategy. The calculation strategy yields data about the system performance as a function of microstructural variables. The data can be analyzed to predict what microstructural variable combinations provide superior performance, the performance sensitivity to each variable, and finally design specifications for material microstructure.

For any pair of glass and interlayer host materials, design constraints placed on macroscopic material anisotropy of each layer (no inclusions, isotropic, low, medium, and high anisotropy) result in twenty five possible bulk material configurations. These combinations are the result of the presence or absence of inclusions in both glass and interlayer materials, their geometry and orientation, and/or their inherent stiffness anisotropy. It is noted that one of those combinations is the reference case, *i.e.* no

inclusions present in any layer. Each combination results in different achievement levels for any given set of design goals and Archimedean weighting schemes. The overall performance of each configuration changes again when permitting higher inclusion volume fractions or by altering the importance levels of each design goal. As can be seen, the number of possible combinations is infinite. It is, therefore, important to limit the design exploration to the smallest set of microstructural variables and goal weighting schemes which gives a sufficiently complete picture of windshield performance.

This section employs the CDSP to minimize the deviation function having the same system goals for each of the twenty-five permissible macroscopic anisotropy level combinations at four different goal importance level combinations. In total, 100 different design calculations are carried out. The results of these calculations are given and analyzed in Section 6.4. It is first necessary to specify the design goals employed for every calculation considered. The system goals used for every design calculation are given in Table 6.15.

Table 6.15: Design goals used for each of 100 different design calculations in this chapter.

Goal	*Value*
ρ_{tot}^{goal}	$0.90\,\rho^{ref}$
f_{coinc}^{goal}	0.20 dB
ΔTL^{goal}	1500 Hz
E_{11}^{goal}	$\geq 0.98 E_{11}^{ref}$

It is noted that the overall plate density goal is a linear function of the interlayer thickness ratio given in Chapter V, $H = h_2/h_{1,3}$, the inclusion volume fraction in each layer, and the respective inclusion density given by Eq. (VI.3.1). The current design

problem holds the overall windshield thickness and thickness ratio fixed for these calculations.

$$\rho^{tot} = \rho^{M,g} + f^{I,g}(1-H)\left(\rho^{I,g} - \rho^{M,g}\right) + H\left[\left(\rho^{M,IL} - \rho^{M,g}\right) + f^{I,IL}\left(\rho^{I,IL} - \rho^{M,IL}\right)\right] \quad \text{(VI.3.1)}$$

Equation (VI.3.1) makes it obvious that any minimization scheme searching to reduce plate density would find the maximum volume fraction of inclusions having zero density. This is a trivial result and the variation in density goal importance is not considered here. It is important to point out, however, that *increased* effective in-plane stiffness indirectly translates to the potential for reduced windshield density as it would permit the fabrication of thinner windshields. Further, preliminary design space exploration gave the following observations which help limit the design space for more efficient exploration.

1. The presence of inclusion coating in the interlayer the glass layers or both did not improve overall system response. Inclusion coatings are not considered.
    a. The minimization scheme consistently "eliminated" the coating either by driving it to have the same material properties as that of the inclusion or by driving the coating thickness measure, $\Delta a/a$, to zero.
2. Overall anisotropy is the result of either anisotropic included material behavior, preferential orientation of non-spherical inclusions, inclusion aspect ratio, or a combination of these variables. Upon employing the constraints given in Table

6.12, no particular advantage was found in allowing simultaneous variation in both the inclusion geometry, a/c, and orientation distribution, σ. Further design space restrictions given in Table 6.16 reflect this observation while allowing significant freedom to inspect the design space.

Table 6.16: Restricted design space variables for both interlayer and glass layer inclusions to achieve macroscopic anisotropy levels qualified as isotropic, "low," "medium," and "high."

Macroscopic Anisotropy Level	a/c	σ
Isotropic	1	*Not defined*
Low	2	$\in [0.40 \quad 1.00]$
Medium	5	$\in [0.25 \quad 0.40]$
High	10	0

Finally, it is important to observe that the current nested multiscale model is deterministic. This essentially means that one set of inputs will always yield the same results. This is in contrast to probabilistic models which display model variability. This is an important subtle point as non-deterministic models require special consideration for CDSP implementation, see Choi *et al* [117]. Though the current modeling scheme is deterministic it is entirely possible to arrive at different deviation function minimums by varying initial guesses of microstructural variables. This variability in design results is the result of the minimization scheme and the complex relationship between microstructural variables and the deviation function. This complex relationship means that several local minima of the deviation may exist in the *n*-dimensional design space. Fortunately, preliminary design space exploration has shown the current model to be insensitive to initial guesses when they lie within the constraints placed on **X** given in Table 6.12.

It is now possible to delineate the design calculations necessary to provide a complete exploration of an automobile windshield. As previously stated, there are twenty-five potential combinations of material anisotropy levels for the effective behavior or the interlayer or glass layers. All twenty five possible combinations are given in Table 6.17. For each of these anisotropy level combinations it is necessary to determine the material microstructure of each layer that minimizes the deviation function for a given Archimedean weighting scheme.

Table 6.17: All possible anisotropy level combinations for glass layers (GL) and interlayer (IL). N – no inclusions, I – isotropic, L – low, M – medium, H – high.

GL	IL	GL	IL	GL	IL	GL	IL	GL	IL
N	N	I	N	L	N	M	N	M	N
“”	I	“”	I	“”	I	“”	I	“”	I
“”	L	“”	L	“”	L	“”	L	“”	L
“”	M	“”	M	“”	M	“”	M	“”	M
“”	H	“”	H	“”	H	“”	H	“”	H

The specific Archimedean weighting schemes must now be considered. It is proposed that four different weighting schemes be employed. Recall from Eq. (VI.2.17) that the deviation function is simply summation of the each deviation variable multiplied by its associated weight: $Z = W_1 d_1 + W_2 d_2 + W_3 d_3 + W_4 d_4$. In the first weighting scheme all design goals are assigned equal importance. In this case each deviation variable weight, W_i, is assigned the same value: 1/4. The other three weighting schemes give highest importance to one specific design goal and equal but lesser weights to the other goals. These weighting schemes are detailed in Table 6.18.

Table 6.18: Four different Archimedean weighting schemes investigated by calculations strategy.

Goal	*Equal Weight*	*High* f_{coinc}^{goal}	*High* ΔTL^{goal}	*High* E_{11}^{goal}
ρ_{tot}^{goal}	1/4	1/6	1/6	1/6
f_{coinc}^{goal}	1/4	1/2	1/6	1/6
ΔTL^{goal}	1/4	1/6	1/2	1/6
E_{11}^{goal}	1/4	1/6	1/6	1/2

The above proposed calculation strategy consists of 100 different design calculations in all. It is asserted that this strategy will provide a significant understanding of how to improve multi-objective windshield performance by manipulating the constituent material microstructure. Further, the results of this calculation strategy give sufficient data points quantify those microstructures using classic mechanical design lexicon such as design specifications and confidence intervals.

6.3.2 Design calculation facilitation through a graphic design interface

This section describes the material design graphic design interface (GDI) developed to implement the CDSP as specified in Section 6.2. The ultimate goal of this GDI is the facilitation of automobile windshield design space exploration for any designer. At present, the objective of its creation is to permit efficient implement of the calculation strategy detailed in the previous section. The GDI is divided into three main parts: (*i*) initial structure, (*ii*) design goal specification and importance, and (*iii*) design decisions. The following paragraphs define these sections and show the appropriate screen capture images of the GDI.

Figure 6.8 shows the first GDI section which allows the designer to enter the initial windshield structure. It is in this section that the bulk windshield layer materials and overall thickness are specified. The bulk layer materials are selected from a pull-down menu while the overall thickness is entered directly as shown in the figure. It is noted that adding to the list of available bulk layer materials is trivial. To further generalize the GDI, the option has been given to the designer to optimize interlayer thickness by checking the appropriate box in the bottom right-hand corner. This option has not been employed in the current design space exploration as the focus has been on microstructural variables. It is important to show, however, that coupling a GDI with a CDSP micromechanical design approach allows simultaneous consideration of variables at multiple length scales.

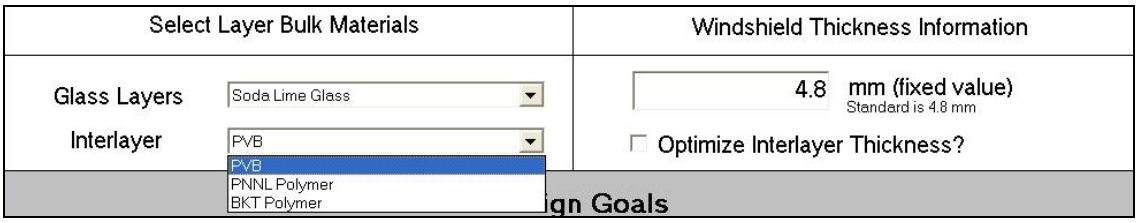

Figure 6.8: Initial structure section of GDI. Bulk layer materials are specified via pull-down menus while overall thickness is entered directly.

The next GDI section is the goal specification and importance section shown in Figure 6.9. This part of the GDI gives the designer the ability to directly enter the design goals. This is done via keyboard entry in the text boxes shown on the left-hand column. Notice that the values shown in Figure 6.9 are those specified in Table 6.15. The notes given in red text below each goal refer to a reference image similar to Figure 6.5 which is included in the GDI (see Figure 6.11).

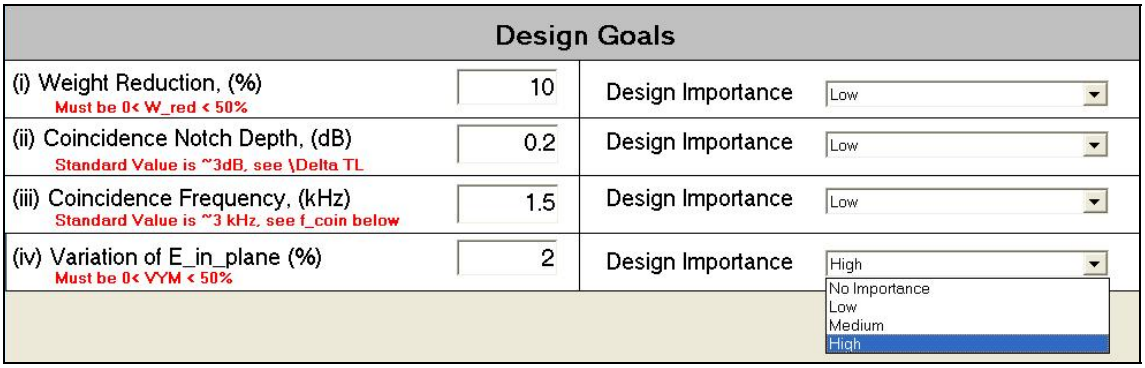

Figure 6.9: Design goal specification and importance section of the GDI. Actual goal values are entered directly and importance levels are chosen using drop-down menus.

The right column of this section allows the designer to specify the importance level of each goal by selection using drop-down menus having four different design importance levels, *DI*. Each term in the importance level drop-down menu corresponds to the following numeric values: *DI(No Importance) = 0*, *DI(Low) = 1*, *DI(Medium) = 2*, *DI(High) = 3*. The Archimedean weights for each goal are then determined using Eq. (VI.3.2).

$$W_i = DI_i \Big/ \sum_{i=1}^{4} DI_i \qquad \text{(VI.3.2)}$$

Figure 6.10 shows the final GDI section where the designer is prompted to make decisions regarding the permissible microstructure of each windshield layer. The designer uses this section to specify whether each layer can contain inclusions and what level of macroscopic anisotropy is permissible. Viewed from another standpoint, this section allows a designer to determine the best possible performance of an existing windshield if some manufacturing process is altered such that it may introduce impurities

into the structure. Decisions taken by the designer in this section also allow non-quantifiable considerations to be taken into account. For example, transparency is of paramount importance for a windshield and transparency is highly dependent on the presence and concentration of heterogeneities in each layer. However, the current multiscale model does not directly consider transparency. Fortunately, design decisions of maximal inclusion volume fraction (percentage by volume as shown in the GDI) can indirectly consider a parameter such as windshield transparency.

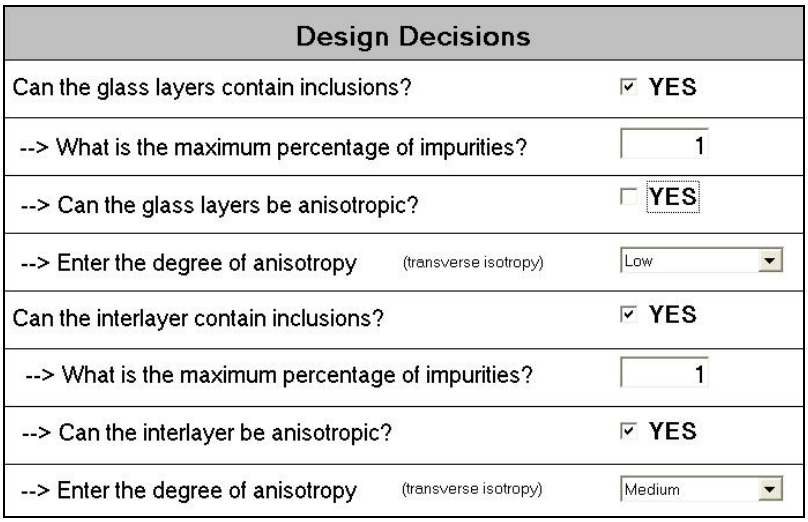

Figure 6.10: Design decisions section of the GDI. The designer is prompted make design decisions regarding inclusions and overall anisotropy of each layer.

Ultimately, design decisions taken in this section determine constraints placed on volume fraction, aspect ratio, orientation distribution, and inherent anisotropy of included phases. For example, the design decisions shown in Figure 6.10 set design constraints such that the glass layers can contain up to 1% by volume of isotropic spherical inclusions while the interlayer can contain up to 1% by volume of inclusions which induce a "medium" level of interlayer anisotropy. In accordance with Table 6.12 and Table 6.16, a medium

level of anisotropy requires the inclusion material to be isotropic with an aspect ratio $a/c = 5$ and orientation distribution described by an Euler angle standard deviation whose range is $\begin{bmatrix} 0.25 & 0.40 \end{bmatrix}$. These values can be changed by checking/unchecking the boxes on the right-hand side of this section and by choosing the appropriate anisotropy levels via the drop-down menus. Finally, the designer is then prompted to save the design results which are exported to a text file. Example contents of a text file for equal weighting is given in Table 6.19. It is in this manner that the twenty five different anisotropy level combinations given in Table 6.17 are investigated.

Table 6.19: Example of data output file from a single design calculation. This example assigns equal importance weights to each deviation variable.

Example Design Output File Data			
Date		19-Oct-06	
Time:		02:50.3	
Calculation Time (s)		760.158	
System Goals		**System Goal Archimedean Weights**	
$100\,\Delta\rho^{eff}/\rho^{ref}$ (%)	10	$W\left(\Delta\rho^{eff}\right) \le 1$	0.25
ΔTL^{goal} (dB)	0.2	$W\left(\Delta TL^{eff}\right) \le 1$	0.25
f_{coinc}^{goal} (Hz)	1500	$W\left(f_{coinc}^{eff}\right) \le 1$	0.25
$100\,\Delta E_{11}^{eff}/E_{11}^{ref}$ (%)	2	$W\left(\Delta E_{11}^{eff}\right) \le 1$	0.25
Final Attainment Values			
$\rho^{eff}\ \left(kg/m^3\right)$		2241	
$100\,\Delta\rho^{eff}/\rho^{ref}$ (%)		– 0.10	
ΔTL (dB)		0.20	
f_{coinc} (Hz)		1500	
E_{11}^{eff} (Pa)		43.63 x 10^9	
$100\,\Delta E_{11}^{eff}/E_{11}^{ref}$ (%)		15.2	
$Z_{\min}^{EW}\ (\ge 0)$		0.065	
$h_2\,(mm)$		0.768	
Glass Layer Inclusion Variables		**Interlayer Inclusion Variables**	
$\phi^{I,g}\ (\%)$	1.00	$\phi^{I,IL}\ (\%)$	1.00
Optimized Inclusion Material Properties			
$\mu^{I,g}/\mu^{M,g}$	– 0.76	$\mu^{I,IL}/\mu^{M,IL}$	– 1.09
$\mu^{I,g}$ (Pa)	– 22.35 x 10^9	$\mu^{I,IL}$ (Pa)	– 146 x 10^6
$\nu^{I,g}$ ( )	0.21	$\nu^{I,IL}$ ( )	0.40
Optimized Inclusion Geometry and Orientation			
$(a/c)^{I,g}$	1	$(a/c)^{I,IL}$	1
$\sigma_{az}^{I,g}$ (rad)	*N/A*	$\sigma_{az}^{I,IL}$ (rad)	*N/A*
Effective Material Properties			
$\hat{C}_{11}^{g,eff}$	$54.6(1-0.16i)\times10^9$	$\hat{C}_{11}^{IL,eff}$	$0.53(1-0.20i)\times10^9$
$\hat{C}_{12}^{g,eff}$	$9.39(1-0.20i)\times10^9$	$\hat{C}_{12}^{IL,eff}$	$0.28(1-0.07i)\times10^9$
$\hat{C}_{13}^{g,eff}$	$9.39(1-0.20i)\times10^9$	$\hat{C}_{13}^{IL,eff}$	$0.28(1-0.07i)\times10^9$
$\hat{C}_{33}^{g,eff}$	$54.6(1-0.16i)\times10^9$	$\hat{C}_{33}^{IL,eff}$	$0.53(1-0.20i)\times10^9$
$\hat{C}_{44}^{g,eff}$	$22.6(1-0.15i)\times10^9$	$\hat{C}_{44}^{IL,eff}$	$0.12(1-0.34i)\times10^9$

The GDI developed in this section provides a tool for intuitive and efficient automobile windshield design space exploration. The complete interface is shown in Figure 6.11. This GDI has been employed to execute the design strategy described by Section 6.3.1 and can likewise be employed to further investigate the design space in the future. The results of those calculations are given, analyzed, and discussed in the following section. The GDI illustrates one way in which micromechanical models and a CDSP can be combined to provide an intuitive and practical material design tool.

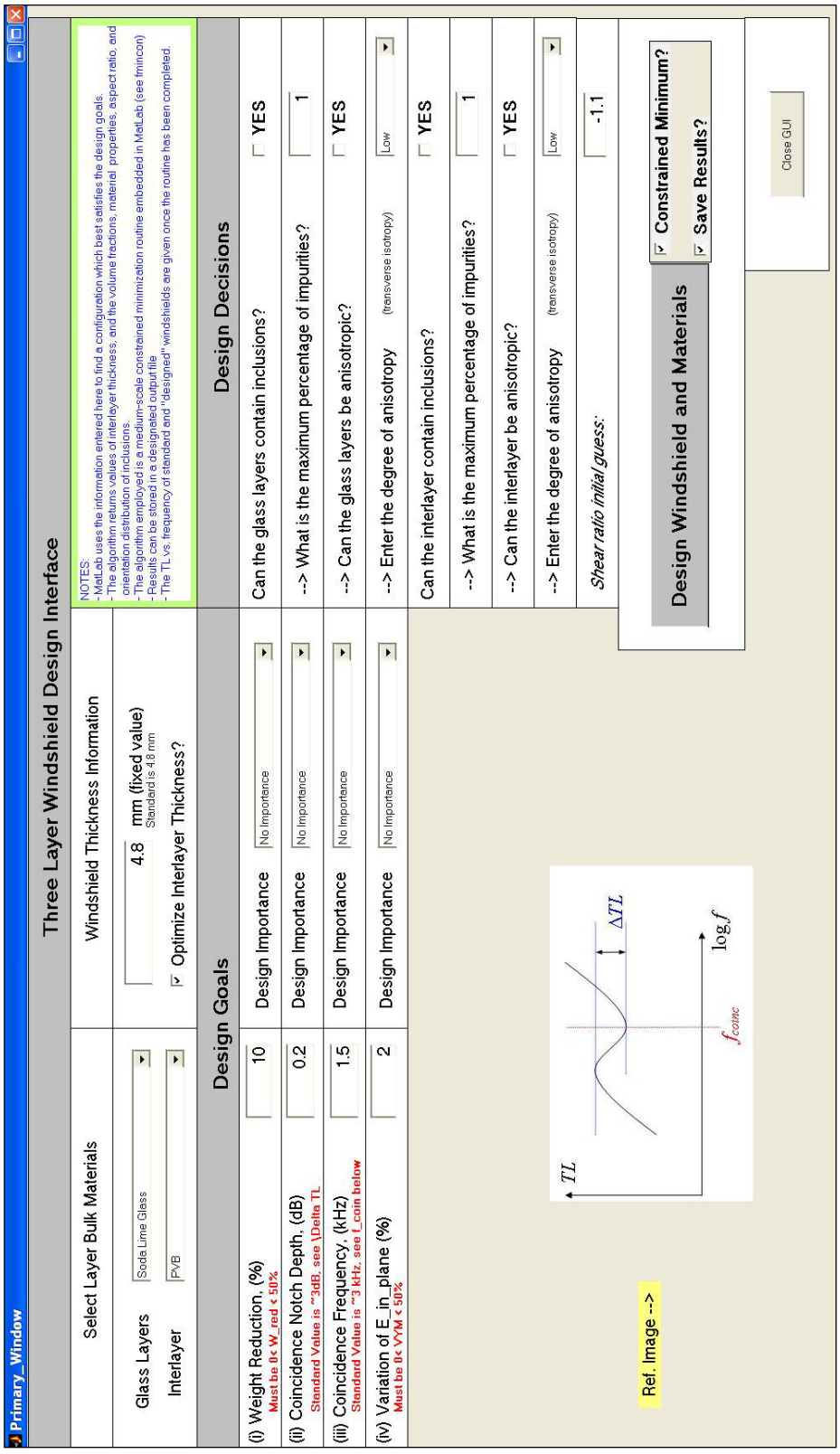

Figure 6.11: Complete image of the GDI created for the CDSP microstructural design of the constituent materials of an automobile windshield.

6.4 Design results and analysis

Completion of the calculation strategy detailed in Section 6.3.1 provides numerical design results for analysis on several different levels. First of all, it is possible to indicate which of these twenty five potential configurations yield the best system performance, analogous to the lowest deviation function value, for each Archimedean weighting scheme. These results also indicate the influence of layer microstructure and macroscopic anisotropy on overall system performance. The values of the minimized deviation function of each macroscopic anisotropy combination for all goal weighting schemes are given in Figure 6.12 and Figure 6.13. These are plots of the raw data given in Appendix H. The four different plots represent the four different weighting schemes listed in Table 6.18 and each data point on those plots corresponds to a single macroscopic anisotropy level combination from Table 6.17. Both figures show the same data, however Figure 6.12 displays the data as a function of interlayer anisotropy level while Figure 6.13 represents the data as a function of glass layer anisotropy. In total, each figures show four different plots each containing twenty five data points. Those data points make up five different curves. In Figure 6.12 each curve represents the minimal deviation function value attained at each interlayer anisotropy level for a given glass layer anisotropy level. The reverse is plotted in Figure 6.13. Note that the following representation has been employed to represent macroscopic material anisotropy: *0 = No inclusions*, *1 = Isotropic*, *2 = Low Anisotropy*, *3 = Medium Anisotropy,* and *4 = High Anisotropy*.

Inspection of these plots immediately clarifies several key points. First, it is apparent that a large percentage, 70%, of all materials designed using the coupled CDSP-micromechanics approach yield structural performances superior to that of a standard windshield. Superior performance is indicated when the minimized deviation function value is less than the reference value, represented in both figures with a bold horizontal blue line. These figures also clearly show that overall performance is highly dependent on interlayer anisotropy. Indeed, each curve of Figure 6.12 varies wildly with changing interlayer anisotropy. The same is not true of glass layer anisotropy. Figure 6.13 shows that for any given interlayer anisotropy level the designed structural response is much more consistent as a function of glass anisotropy. This is stated somewhat loosely as it is obvious, especially from Figure 6.13(b), that Z_{min} variability does change with glass anisotropy when interlayer anisotropy is high. These results also clearly indicate that the designed modifications of interlayer materials are more important than doing so to the glass layers. Figure 6.12 demonstrates this fact showing that data points coinciding with the case where glass layers do not contain inclusions show significantly improved system performance if the interlayer is designed to be isotropic or anisotropic. The opposite is not true. That is, if the interlayer is unmodified while glass layers are designed, the performance is roughly the same as that of the standard windshield configuration as indicated in Figure 6.13. A final general conclusion can be made from inspection of these plots. Namely that the best performance is observed, regardless of Archimedean weighting scheme, when both the interlayer and glass layers are constrained to be macroscopically isotropic. Similar attainment levels are possible if either the interlayer or glass layers display low levels of anisotropy, but in general the best performance was

recorded in all cases when all materials were constrained to be macroscopically isotropic. The following sections look more specifically at the designed microscopic inclusion variables and analyze the deviation function minimums attained by the designed system.

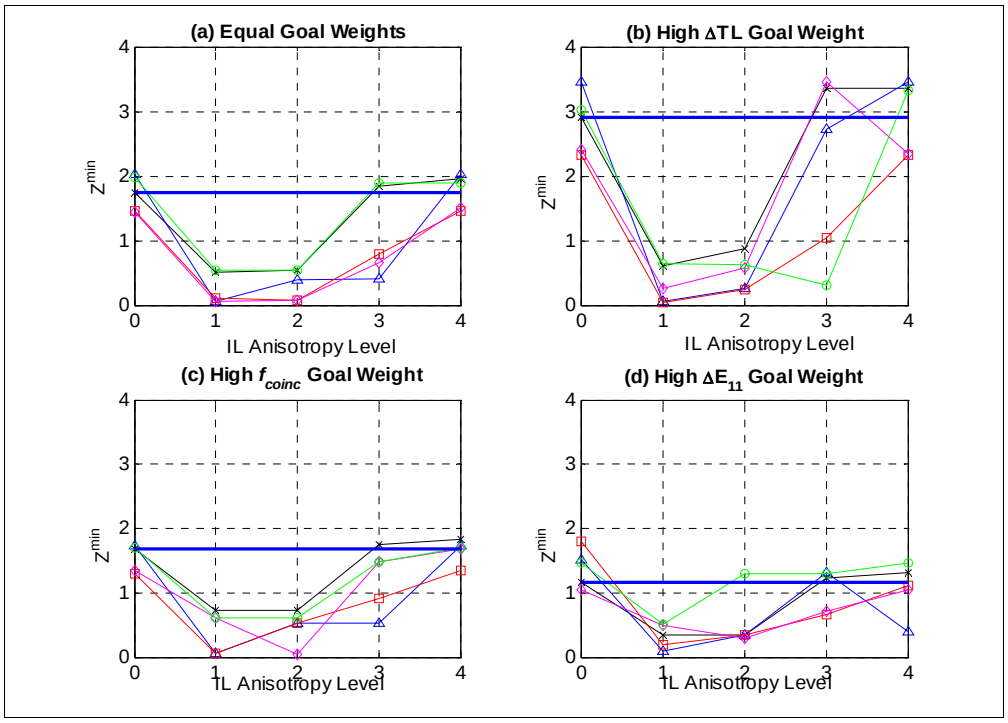

Figure 6.12: Parametric studies of Z_{min} for four different Archimedean weighting combinations. Each curve plots Z_{min} as a function of IL anisotropy level for five different anisotropy levels in glass layers. Bold blue line – Reference windshield performance; *— No inclusions in glass; Δ—Isotropic glass layer; □—Low anisotropy glass; ◊— Medium anisotropy glass; o—High anisotropy glass.

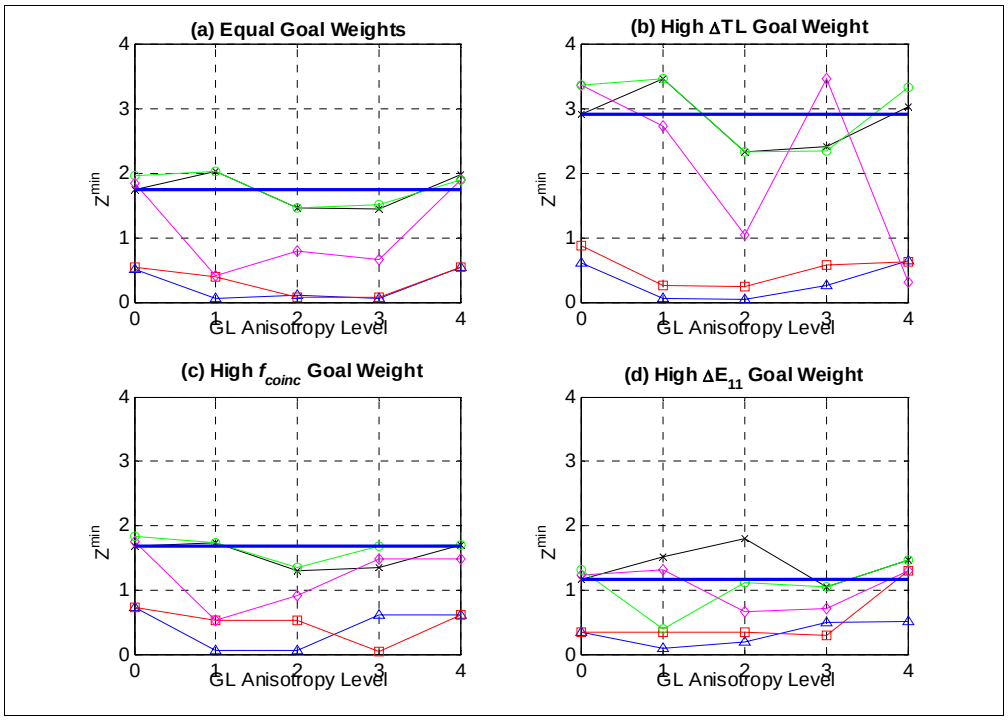

Figure 6.13: Parametric studies of Z_{min} for four different Archimedean weighting combinations. Each curve plots Z_{min} as a function of IL anisotropy level for five different anisotropy levels in glass layers. Bold blue line: Reference windshield performance; *— : No inclusions in IL; Δ— : Isotropic IL; □—: Low anisotropy IL; ◊— : Medium anisotropy IL; o— : High anisotropy IL.

6.4.1 Inclusion design specifications

The previous paragraph discussed the results of design calculations in terms of deviation function minimums and layer anisotropy. It is now of interest to inspect the microscale variables for both interlayer and glass layers which were calculated using the coupled micromechanics-CDSP methodology developed in this chapter. The results of Figure 6.12 and Figure 6.13 illustrate that the deviation function is much more sensitive to changes in the anisotropy level of the interlayer that that displayed by the glass layers. For this reason it is most meaningful to show the design results corresponding to each interlayer anisotropy level. The sample mean and standard deviation values of

microstructural variables resulting from calculations of each weighting scheme described in Table 6.18 are summarized below in Table 6.20–Table 6.23. The mean and standard deviation have been calculated for each interlayer anisotropy level with respect to the five different anisotropy levels in glass. Stated mathematically, the mean value of inclusion volume fraction in glass and interlayer for any given weighting scheme can be calculated from the raw design results using Eq. (VI.4.1).

$$\begin{aligned}\overline{\phi}^{I,g} &= \frac{1}{4}\left(\phi_{g,iso}^{I,g} + \phi_{g,L}^{I,g} + \phi_{g,M}^{I,g} + \phi_{g,H}^{I,g}\right) \\ \overline{\phi}^{I,IL} &= \frac{1}{5}\left(\phi_{g,N}^{I,IL} + \phi_{g,iso}^{I,IL} + \phi_{g,L}^{I,IL} + \phi_{g,M}^{I,IL} + \phi_{g,H}^{I,IL}\right)\end{aligned} \tag{VI.4.1}$$

Note that $\overline{\phi}^{I,X}$ represents the mean inclusion volume fraction in material *X*, and $\phi_{g,AL}^{I,X}$ represents the inclusion volume fraction in material *X* when the glass layers have an anisotropy level, *AL*. In accord with Table 6.17, the anisotropy levels are represented as *N – no inclusions*, *I – isotropic*, *L – low*, *M – medium*, *H – high*. The mean values of all designed inclusion variables for both the interlayer and glass layers are calculated in the same manner and tabulated in Table 6.20–Table 6.23. Inspection of the results shown in these tables allows the following observations.

- The most important factor influencing the windshield response is the shear modulus ratio in both the interlayer and glass layers.
    - For any given interlayer anisotropy level the absolute value of μ^I / μ^M is generally larger in glass layers than in the interlayer.

- The second most important factor influencing windshield behavior is the volume fraction of negative stiffness inclusions in glass and interlayers.
    - The performance is therefore highly sensitive to variations in inclusion stiffness and volume fraction of the stiffness. The impact of these two factors should be investigated using non-optimal CDSP design stragies such as a robust CDSP design methodology [3, 117].
- As a general rule increasing interlayer anisotropy leads to an increased value of μ^I / μ^M in both glass and interlayer. This presumably is a result of the minimization scheme trying to overcome the detrimental effect of interlayer anisotropy on performance.
- The deviation function minimization generally drives the both glass and interlayer inclusion volume fractions to the maximum inclusion fraction constraint value when the interlayer is constrained to be isotropic or have low levels of anisotropy.
    - At increased anisotropy levels the actual volume fraction is more random in glass layers. This is evidenced from lower mean values of $\phi^{I,g}$ with much higher standard deviations.
- When the interlayer is constrained to have high anisotropy, the minimization scheme drives the volume fraction to low values, even zero. This clearly indicates that increased interlayer anisotropy is detrimental to system performance.
- Poisson ratio of included phase is important and its value appears to reflect that of the host medium. Interlayer inclusions are generally ≥ 0.40 while those in glass

are ≥ 0.23, the respective bulk material values. It is observed that the designed Poisson ratio values tend to increase with increasing interlayer anisotropy.

- Macro- and microscopic anisotropy are not desirable for improved system performance.
- Standard deviation of Euler angles is driven towards the upper constraint limit in an effort to reduce macroscopic anisotropy.

Table 6.20: Mean and standard deviation values of designed inclusion variables when each design goal is ascribed equal weight. Values are given for each IL anisotropy level which are averaged across all glass layer anisotropy levels.

Designed Inclusion Variables – Equal Design Weights				
IL Anisotropy	Isotropic	Low	Med	High
IL Inclusion Variables				
σ_{IL} (radians)	---	0.62 ± 0.15	0.37 ± 0.07	---
$C_{44}^{I,IL} / \mu^{M,IL}$	-0.94 ± 0.10	-0.79 ± 0.16	-1.21 ± 0.48	-1.48 ± 0.08
$\nu^{I,IL}$	0.40 ± 0.01	0.45 ± 0.06	0.49 ± 0.00	---
$\phi^{I,IL}$	1.00 ± 0.01	0.99 ± 0.03	0.98 ± 0.04	0 ± 0
GL Inclusion Variables				
σ_g (radians)	0.46 ± 0.30	0.33 ± 0.11	0.46 ± 0.13	0.51 ± 0.37
$C_{44}^{I,g} / \mu^{M,g}$	-1.10 ± 0.25	-1.21 ± 0.16	-1.42 ± 0.44	-1.54 ± 0.32
$\nu^{I,g}$	0.31 ± 0.13	0.32 ± 0.16	0.40 ± 0.15	0.49 ± 0.01
$\phi^{I,g}$	1.00 ± 0.00	0.99 ± 0.01	0.61 ± 0.47	0.76 ± 0.23

Table 6.21: Mean and standard deviation values of designed inclusion variables when the coincidence notch depth goal is given highest importance. Values are given for each IL anisotropy level which are averaged across all glass layer anisotropy levels.

Designed Inclusion Variables – High ΔTL Weight				
IL Anisotropy	Isotropic	Low	Med	High
IL Inclusion Variables				
σ_{IL} (radians)	---	0.63 ± 0.22	0.36 ± 0.07	---
$C_{44}^{I,IL} / \mu^{M,IL}$	– 0.93 ± 0.11	– 0.99 ± 0.45	– 1.43 ± 0.66	– 1.64 ± 0.23
$\nu^{I,IL}$	0.42 ± 0.04	0.45 ± 0.06	0.32 ± 0.16	---
$\phi^{I,IL}$	0.96 ± 0.05	0.99 ± 0.02	0.60 ± 0.55	0.13 ± 0.29
GL Inclusion Variables				
σ_g (radians)	0.33 ± 0.10	0.38 ± 0.19	0.38 ± 0.18	0.45 ± 0.25
$C_{44}^{I,g} / \mu^{M,g}$	– 1.22 ± 0.33	– 1.25 ± 0.24	– 1.36 ± 0.52	– 1.68 ± 0.33
$\nu^{I,g}$	0.21 ± 0.05	0.35 ± 0.11	0.36 ± 0.11	0.47 ± 0.02
$\phi^{I,g}$	1.00 ± 0.00	0.98 ± 0.02	0.29 ± 0.44	0.53 ± 0.39

Table 6.22: Mean and standard deviation values of designed inclusion variables when the coincidence frequency goal is given highest importance. Values are given for each IL anisotropy level which are averaged across all glass layer anisotropy levels.

Designed Inclusion Variables – High f_{coinc} Weight				
IL Anisotropy	Isotropic	Low	Med	High
IL Inclusion Variables				
σ_{IL} (radians)	---	0.61 ± 0.25	0.40 ± 0.00	---
$C_{44}^{I,IL} / \mu^{M,IL}$	– 0.95 ± 0.08	– 1.02 ± 0.50	– 1.34 ± 0.12	– 1.47 ± 0.03
$\nu^{I,IL}$	0.41 ± 0.01	0.43 ± 0.07	0.47 ± 0.04	---
$\phi^{I,IL}$	0.99 ± 0.01	0.99 ± 0.01	0.99 ± 0.02	0.00 ± 0.00
GL Inclusion Variables				
σ_g (radians)	0.48 ± 0.28	0.43 ± 0.25	0.42 ± 0.24	0.52 ± 0.38
$C_{44}^{I,g} / \mu^{M,g}$	– 1.07 ± 0.17	– 1.46 ± 0.44	– 1.14 ± 0.29	– 1.48 ± 0.42
$\nu^{I,g}$	0.24 ± 0.05	0.34 ± 0.09	0.29 ± 0.18	0.42 ± 0.12
$\phi^{I,g}$	1.00 ± 0.01	0.95 ± 0.10	0.63 ± 0.38	0.57 ± 0.43

Table 6.23: Mean and standard deviation values of designed inclusion variables when the in-plane stiffness goal is given highest importance. Values are given for each IL anisotropy level which are averaged across all glass layer anisotropy levels.

Designed Inclusion Variables – High ΔE_{11} Weight				
IL Anisotropy	Isotropic	Low	Med	High
IL Inclusion Variables				
σ_{IL} (radians)	---	0.77 ± 0.23	0.40 ± 0.00	---
$C_{44}^{I,IL} / \mu^{M,IL}$	– 0.85 ± 0.27	– 1.05 ± 0.45	– 1.44 ± 0.04	– 1.23 ± 0.64
$\nu^{I,IL}$	0.41 ± 0.01	0.40 ± 0.14	0.49 ± 0.01	---
$\phi^{I,IL}$	0.96 ± 0.10	0.99 ± 0.02	0.94 ± 0.13	0.17 ± 0.28
GL Inclusion Variables				
σ_{g} (radians)	0.63 ± 0.53	0.33 ± 0.11	0.35 ± 0.07	0.33 ± 0.11
$C_{44}^{I,g} / \mu^{M,g}$	– 0.84 ± 0.27	– 1.23 ± 0.30	– 1.52 ± 0.37	– 1.20 ± 0.22
$\nu^{I,g}$	0.22 ± 0.12	0.47 ± 0.03	0.47 ± 0.03	0.49 ± 0.01
$\phi^{I,g}$	0.80 ± 0.37	0.87 ± 0.26	0.55 ± 0.42	0.57 ± 0.41

The design results above give the researcher and designer clear target values, or design specifications, on how to modify the microstructure of each material constituting an automobile windshield to achieve improved performance. It is postulated that this may be achieved by introducing specifically created heterogeneities or by modifying the glass or interlayer materials processing techniques. Several promising paths towards the creation of such materials are discussed more thoroughly in Chapter VII. The remainder of this chapter focuses on goal attainment, deviation function minimums, and the significance of the design results.

Table 6.24 shows the mean and standard deviation of the goal attainment values for all deviation function weighting schemes for a macroscopically isotropic interlayer material. These values were calculated by averaging the raw design results but could be reproduced using the average design results reported in the first column of Table 6.20–Table 6.23. It is in this sense that the inclusion property values reported in the previous

three tables serve as design specifications for improving the performance of an automobile windshield.

Table 6.24: Mean and standard deviation of attainment variables for each weighting scheme when the interlayer is constrained to remain isotropic.

Population Estimates of System Attainment Variables – Isotropic IL			
Weighting Scheme	ΔTL (dB)	f_{coinc} (Hz)	$100\,\Delta E_{11}^{eff} \,/\, E_{11}^{ref}$ (%)
Equal Weights	0.27 ± 0.09	2070 ± 805	21.5 ± 17.3
$\uparrow \Delta TL^{goal}$	0.26 ± 0.09	2300 ± 765	31.4 ± 27.3
$\uparrow f_{coinc}^{goal}$	0.30 ± 0.09	2300 ± 765	27.8 ± 18.6
$\uparrow E_{11}^{goal}$	0.29 ± 0.09	2300 ± 765	28.8 ± 19.7

The results of Table 6.24 show that the designed isotropic interlayer material satisfactorily attains the system goals given in Table 6.15. Section 6.4.2 examines this statement in further detail by exploring the statistical significance of the results and determining confidence intervals for improved performance. One striking result shown in Table 6.24 is in regards to ΔTL results. The table shows that the designed isotropic interlayer consistently reduces the coincidence notch depth, regardless of weighting scheme employed. These changes in ΔTL are very encouraging given that this parameter is a dominate indicator of sound transmission through the windshield. The results of the final attainment of the other variables are also encouraging. The mean coincidence frequency value for each weighting scheme is at least 1700 Hz below the standard value of 4 kHz while the mean value of effective in-plane stiffness ranges from 21-31% higher than the standard value. Noting that the standard coincidence frequency coincides with the most sensitive frequency range of human hearing [202], the significant decrease in f_{coinc} is important. The simultaneous reduction in ΔTL and f_{coinc} results in both an absolute and *perceived* noise reduction. The absolute decrease in sound transmission is reflected in the

decreased ΔTL value while the perceived decrease stems from decreases in both ΔTL and f_{coinc}. The 20% in-plane stiffness increase is important as it implies that the total windshield thickness can be reduced, thereby opening the door for significant weight reduction. Reduced automobile weight is a key component of increasing fuel efficiency in modern vehicles, of which the windshield is not an insignificant percentage. On its face, the increase in calculated in-plane stiffness by the addition of negative stiffness inclusions seems contradictory. However, this behavior has been noted and theoretically investigated Lakes and Drugan [186]. Their results point out that a stiffness increase is to be expected when the inclusion shear modulus ratio, μ^I/μ^M, is less than ~ -1.1. The designed microstructure data in Table 6.20-Table 6.23 make it apparent that the improved stiffness emanates from the presence of negative stiffness inclusion in the glass layers whose shear ratio is usually ≤ -1.1. These are very important results which should not be overlooked. Indeed, the simultaneous improvements in both in-plane stiffness, damping capacity, and perceived sound transmission which are afforded by the addition of trace amounts of negative stiffness materials is the most attractive result of this design space exploration.

It must be pointed out that the coincidence frequency and in-plane stiffness results do display substantial levels of variance. It is believed that the observed level of variation is largely due to the small sample size and the fact that the mean value has been obtained by averaging the effect of all glass anisotropy levels. The sample size has not been increased for two reasons. (*i*) Despite the many measures taken to reduce calculation time, design calculation remains a time-consuming task, requiring upwards of four hours to obtain a single set of design results. (*ii*) The reason for implementing this micromechanics-CDSP method was to illustrate the power of the method and not to exhaustively solve a design problem. The 100 sets of results issuing from the completion

of the calculation strategy described in Section 6.3.1 have given sufficient information to validate the design approach and to make matter of fact statements about the design of material microstructure for windshield design. Indeed Table 6.25 and Section 6.4.2 clearly show that despite these large variations the designed system performance displays a statistically significant improvement over those related to standard windshield materials.

Table 6.25: Mean and standard deviation values of deviation variable attainment. Reference deviation function values are: $Z^{EW} = 1.74$, $Z^{\Delta TL} = 2.92$, $Z^{f} = 1.68$, and $Z^{\Delta E} = 1.16$.

Minimum Deviation Function Values for Various IL Anisotropy Levels				
IL Anisotropy	Isotropic	Low	Med	High
$Z_{\min}^{EW}$	0.23 ± 0.23	0.29 ± 0.23	1.01 ± 0.70	1.56 ± 0.58
$Z_{\min}^{\Delta TL}$	0.32 ± 0.26	0.52 ± 0.24	2.18 ± 1.29	2.96 ± 0.52
$Z_{\min}^{f}$	0.41 ± 0.29	0.49 ± 0.24	1.23 ± 0.45	1.65 ± 0.16
$Z_{\min}^{\Delta E}$	0.33 ± 0.16	0.53 ± 0.39	1.04 ± 0.30	1.07 ± 0.37

6.4.2 Confidence intervals for superior system performance

The sample mean and standard deviation values given in Table 6.20 – Table 6.25 strongly suggest that a large percentage of the candidate material design configurations yield performance superior to that of a standard windshield. To place these estimates of mean performance on more solid ground, however, it is necessary to apply standard statistical analysis to these results. One very applicable concept from the fields of statistics and design is that of confidence intervals. A confidence interval gives an estimated range of values which is likely to include an unknown population parameter, such as the true mean value. The estimated range is calculated from a set of sample data

and is known as a confidence interval. The extent of the range is dependent on the probability (the confidence) that the unknown parameter will fall within the estimated range. Consider, for example, the unknown population parameter $\wp$ and an estimate of that value calculated from a set of sample data, $\overline{\wp}$. Equation (VI.4.2) shows that some value, *A*, must exist such that the probability that the true population parameter, $\wp$, lies within the range $\left[\overline{\wp} - A \quad \overline{\wp} + A\right]$ is 90%.

$$\Pr\left(\overline{\wp} - A \le \wp \le \overline{\wp} + A\right) = 0.9 \qquad \text{(VI.4.2)}$$

The present study is concerned with the performance of an automobile windshield as measured by the deviation functions $Z_{\min}^{EW}$, $Z_{\min}^{\Delta TL}$, $Z_{\min}^{f}$, and $Z_{\min}^{\Delta E}$. It is, therefore, of interest to determine such a confidence interval from the sample mean and standard deviation values given in Table 6.25 for the true mean deviation function value.

The most common method of constructing confidence intervals from sample estimates is the Student *t*-distribution [203]. Given the sample mean of a set of observations, which can reasonably be expected to have a normal distribution, it is possible to use Student's *t*-distribution to construct the confidence limits on the mean include some theoretically predicted value. The actual approach to constructing a confidence interval is to devise a null hypothesis which states that there is no difference between the attained deviation function values and that of the standard windshield configuration. The *t*-distribution is then employed to find the value *A* in Eq. (VI.4.2) such that the null hypothesis is *rejected* in $\left(1-\alpha\right)$% of the occurrences when the estimate

of the population parameter $\bar{\wp}$ falls within $\left[\bar{\wp}-A \quad \bar{\wp}+A\right]$, see Figure 6.14. The value A is related to the sample standard deviation, S, and t-distribution through Eq. (VI.4.3) [203].

$$A=\frac{t_{\alpha,n-1}S}{\sqrt{n}} \tag{VI.4.3}$$

Where $t_{\alpha,n-1}$ is the t-distribution variable value for a confidence level α of *accepting* the null hypothesis and n is the number of samples used to calculate the mean and standard deviation.

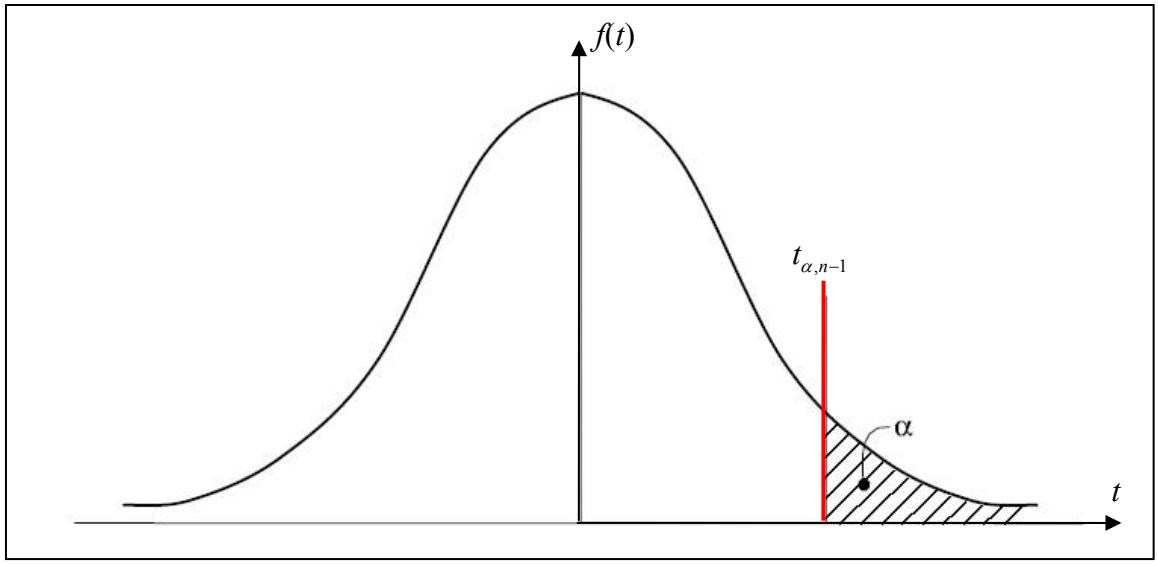

Figure 6.14: *t*-distribution showing confidence level *α* of accepting the null hypothesis.

The one-sided $(1-\alpha)$–upper confidence limit, $UCL_{1-\alpha}$, of the mean is then calculated using Eq. (VI.4.4).

$$UCL_{1-\alpha} = \bar{X}_n + \frac{t_{\alpha,n-1}S}{\sqrt{n}} \qquad \text{(VI.4.4)}$$

$UCL_{1-\alpha}$ represents the greatest average value that will occur for a given confidence interval and population size. In other words, given a mean of the set of observations, $\bar{X}_n$, the probability that the mean of the distribution is inferior to $UCL_{1-\alpha}$ is equal to the confidence level $1-\alpha$ [203]. The *t*-distribution values are readily available in any statistics text, several values relevant to the present design problem are: $t_{2.5\%,4}$ = 2.776, $t_{1\%,4}$ = 3.747, $t_{0.5\%,4}$ = 4.604. This information has been used to calculate the upper confidence limits of the minimum of each different deviation function considered in this work. The results are shown in Table 6.26.

Table 6.26: 99% Upper confidence limit of deviation variable attainment for designed IL inclusion variable values given in Table 6.20 – Table 6.23. Reference deviation function values are: Z^{EW} = 1.74, $Z^{\Delta TL}$ = 2.92, Z^{f} = 1.68, and $Z^{\Delta E}$ = 1.16. Highlighted values denote superior performance to reference windshield microstructure.

99% Upper Confidence Limit of Z_{min} for Various IL Anisotropy Levels				
IL Anisotropy	Isotropic	Low	Med	High
$UCL_{99\%}\left(Z_{\min}^{EW}\right)$	0.615	0.675	2.183	2.532
$UCL_{99\%}\left(Z_{\min}^{\Delta TL}\right)$	0.756	0.922	4.342	3.831
$UCL_{99\%}\left(Z_{\min}^{f}\right)$	0.896	0.892	1.984	1.918
$UCL_{99\%}\left(Z_{\min}^{\Delta E}\right)$	0.598	1.183	1.710	1.690

The values Table 6.26 in can be used to calculate the percent improvement, *PI*, of these 99% upper confidence limit over the reference deviation function variable using Eq. (VI.4.5).

$$PI\left(Z_{\min}\right) = 100\left[\frac{Z_{ref} - Z_{\min}}{Z_{ref}}\right] \qquad \text{(VI.4.5)}$$

Table 6.27: Percent improvement of UCL values over standard windshield configuration.

Improvement (%) of 99% Upper Confidence Limit Values over Reference				
IL Anisotropy	Isotropic	Low	Med	High
$PI\left(Z_{\min}^{EW}\right)$	65	61	– 25	– 46
$PI\left(Z_{\min}^{\Delta TL}\right)$	74	68	– 49	– 31
$PI\left(Z_{\min}^{f}\right)$	47	47	– 18	– 14
$PI\left(Z_{\min}^{\Delta E}\right)$	48	– 2	– 47	– 46

The results of Table 6.26 unequivocally show that a windshield designed to have isotropic or low-level transversely isotropic interlayer and inclusion in the glass layers having inclusion properties given in Table 6.20–Table 6.23 will indeed result in a statistically significant performance enhancement over the standard windshield material configuration. The same statement cannot be made when the interlayer displays a medium or high level of macroscopic anisotropy. However, it is possible that increasing the design sample size may reduce variability in the mean values calculated to ultimately show that designing medium and high interlayer anisotropy can yield improved performance. Obviously this would not be an ideal situation, but rather a case where it is impossible to eliminate macroscopic anisotropy. Most importantly, the results of this section have clearly shown that the material design tool devised in this chapter permits top-down design space exploration as well as design analysis. First, the design tool allows a designer to investigate the microscale variables which have an influence on multi-objective performance. Secondly, the same tool simplifies the task of executing a calculation strategy to perform meaningful analysis on expected achievement. This is a

very encouraging illustration of the promise in integrating micromechanical models and a CDSP design technique for material design.

6.4.3 Results summary

Chapters III and IV developed a robust self-consistent micromechanical model which has been shown capable of capturing the effects of microscopic behavior and structure on macroscopic damping capacity in the low frequency limit [38, 130, 150]. The previous sections of the present chapter have used this SC model in an optimal CDSP design methodology to create a design tool to explore the design space of an automobile windshield. The encouraging results were discussed in detail in Sections 6.4.1–6.4.2. Some key overall points deserve to be reiterated.

- ~70% of trial configurations yield superior performance to a standard windshield.
- ≤ 1% negative stiffness heterogeneities are required in each layer to achieve this improved performance.
- Up to 11 dB increase in *TL* at 4 kHz is predicted. A 10 dB drop in sound pressure level is equivalent to the difference in noise level on a street corner and that of a two person conversation.
- On average the in-plane stiffness is increased by 17%. Increased in-plane stiffness permits a decreased total thickness and, in turn, decreased weight. Weight reduction is a key thrust for increased automobile fuel efficiency.

- On average the coincidence moved from 4 kHz → 2.3 kHz. This leads to a significant decrease in the perceived sound transmission.

Figure 6.15 plots the TL versus frequency curves of the standard windshield together with the best design results of four different deviation functions. These curves clearly display the improved acoustic performance.

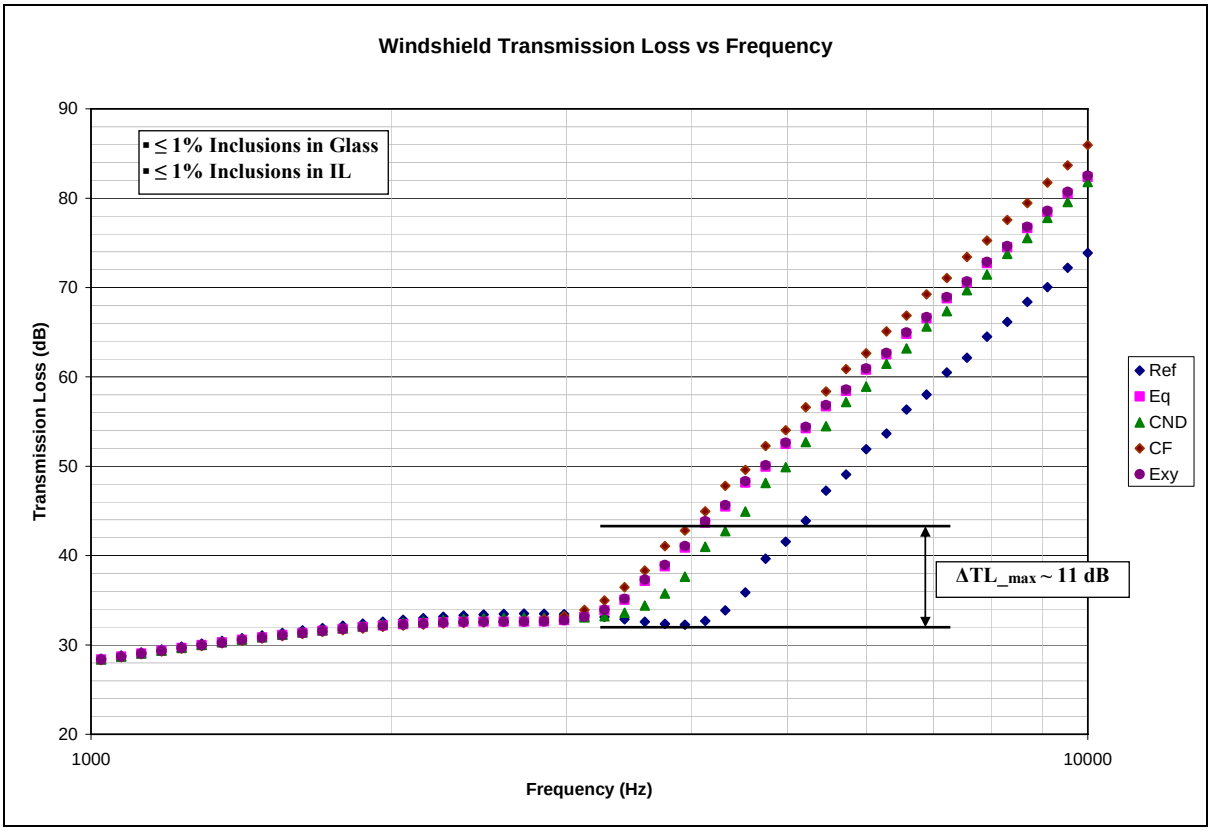

Figure 6.15: Best curves for four different design goal importance levels.

6.5 Chapter summary

This chapter has achieved several different goals. First and foremost it has detailed a successful integration of micromechanical modeling and a CDSP design methodology. Subsequently a simple, interactive, design tool was created and employed to carry out a calculation strategy to explore the windshield design space. The chapter serves as a concrete illustration of the ability to employ tools from both the field of mechanical design and material modeling to explore the design space of a material. This is extremely important as it simultaneously validates the inductive, or top-down, approach to material design and gives a blueprint of how to employ multiscale models in design protocols. It is further reasoned that this same technique may be employed to inform material design at smaller scales by extending the approach to include either comprehensive nanoscale analysis (such as Monte Carlo simulations) or nanoscale meta-models. Just as importantly, the design results given in Section 6.4 have shed considerable light on microstructural variable combinations which enhance the absorptive capacity of viscoelastic materials while simultaneously improving their structural rigidity. The results provide specific microstructural variable values, the acceptable variability of those variables, the associated system performance, and confidence intervals for achievement of those performance indices. This gives researchers who are trying to enhance lossy material behavior a much more specific set of target variables, some expected outcomes, and a methodology to further explore the design space. Moreover, the validation of the micromechanics-CDSP design approach opens the door to designing different materials for different applications such those modeled in Appendix I.

CHAPTER VII

NEGATIVE STIFFNESS MATERIALS, MECHANISMS, AND MODELING

7.1 Introduction

Chapter VI clearly demonstrated that coupling of micromechanical modeling and a CDSP design methodology provides a robust exploratory tool for material design. The chapter illustrated that fact by exploring the design space of an automobile windshield in an effort to simultaneously achieve multiple, conflicting, macroscale design goals by altering microscale material variables. The critical condition that emerges from those results is the need for minute quantities ($\leq$ 1% by volume) of heterogeneities displaying negative stiffness behavior. Indeed, negative stiffness regions proved to be the only means to simultaneously enhance the mechanical damping capacity of the windshield and increase its stiffness. The determination of the physical mechanisms which bring about negative stiffness phenomena and the understanding of how to exploit that behavior is, therefore, the crux of creating such extraordinary damping materials. This chapter explores negative stiffness behavior in several different aspects. First, it gives a detailed explanation of what exactly is meant by the term negative stiffness with respect to both material and structural behavior. Next, experimental and theoretical research from the

literature which is pertinent to understanding negative stiffness behavior is presented and discussed. Lastly, the chapter discusses several avenues to create negative stiffness inclusions in the future. In particular, a promising candidate inclusion structure and corresponding meta-modeling technique to approximate its negative stiffness behavior is proposed. The proposals and discussions of the chapter are limited to explanations of the causal mechanisms, physical principles, and potential means to generate this extraordinary behavior. Further targeted research is required to quantify and implement the proposals and ultimately to create high loss heterogeneous materials that exploit negative stiffness.

7.2 Defining negative stiffness behavior

What is meant by the term negative stiffness? Negative stiffness involves a reversal of the usual directional relationship between force and displacement in deformed objects. In the vast majority of cases, objects display positive stiffness by resisting deformation with a restoring force. The restoring force returns the deformable body to its neutral position upon removal of an imposed deformation. A negative stiffness object, on the other hand, *assists* the imposed deformation as a result of energy stored within or supplied to the object. The added energy could be the result of processing techniques [21, 204-206], pre-stressing/straining of elements in a discrete system [20, 207], or an external energy source, usually described as an active element [208, 209]. Negative stiffness can refer to the behavior of either a material or a structure because the term stiffness refers to the ratio of the generalized force to the generalized displacement. For a

structure such as a spring the stiffness is the ratio of the force to the displacement and is usually denoted as k. For a three-dimensional solid viewed as a continuum, the measure of stiffness is the ratio of the stress to the strain and referred to as a modulus or stiffness [185]. For this reason, the following discussion often employs simple structural elements to illustrate negative stiffness behavior in a clear manner. It is to be understood that these structures are analogous to specific cases of material behavior.

As an example of negative stiffness, consider the bistable buckled beam structure and corresponding transverse force versus displacement curves shown in Figure 7.1. The non-monotonic relationship observed between applied force and the resulting transverse displacement is indicative "snap-through" behavior and, therefore, negative stiffness.

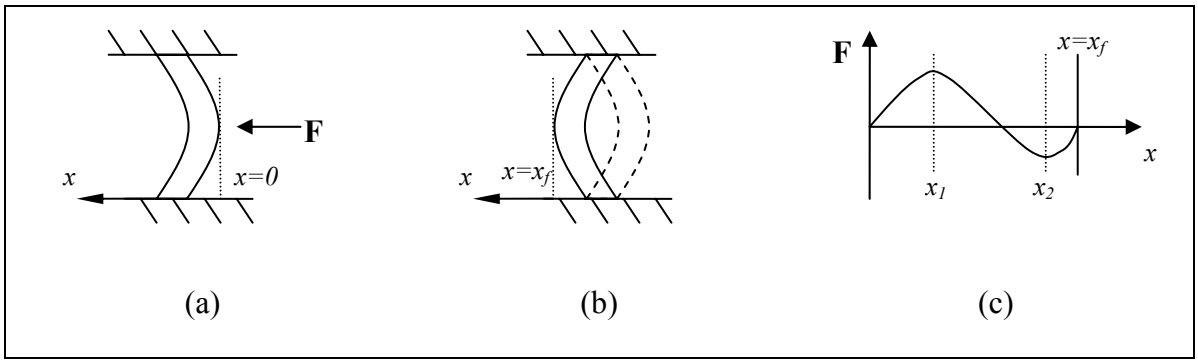

Figure 7.1: Structural analogue of negative stiffness: bistability of a laterally loaded post-buckled beam. (a) shows the buckled beam with an applied lateral load, (b) the beam has "snapped through" to the alternate stable configuration, and (c) is a qualitative representation of the force vs. lateral displacement curve.

The curve shown in Figure 7.1c is obtained by imposing a constant rate of displacement in the x-direction (as defined in Figure 7.1a) at the point of contact on the post-bucked beam and measuring the force required to obtain this displacement. Such behavior is common in micro-electromechanical systems (MEMS) devices and has been modeled by Saif [210] and experimentally observed by Qiu *et al* [211] and many others. Indeed the

MEMS community has successfully employed bistable structures to create many ingenious devices, such as an optical micro-switch devised by Texas Instruments [212] and a microscale gate valve for regulation of fluid delivery on the microscale [213]. It is important to emphasize that negative stiffness behavior is analogous to the portion of the force versus displacement curve possessing a negative slope, *not* negative force. This is the domain bounded by x_1 and x_2 in Figure 7.1c. It is for this reason that the axial displacement of buckled beams or tubes also displays negative stiffness behavior [19]. It has been shown that thin-shelled tubes display non-monotonic force versus displacement relationship upon the onset of buckling and negative stiffness post-buckling behavior [19, 214].

7.2.1 Thermodynamic equilibrium and negative stiffness

Negative stiffness is intuitively unfamiliar to the engineer, especially with respect to material behavior, because it rarely exists in nature. Its rarity stems from the fact that negative stiffness is inherently unstable when unconstrained in all but very few special cases and even when constrained it often is transient in nature. The unstability of negative stiffness materials or systems is rooted in their thermodynamic state, which is not in equilibrium with its environment. Recall that the thermodynamic state of a system is the set intensive properties such as temperature, density, and entropy, and the thermodynamic forces acting on the system, such as mechanical stresses and heat energy. The set of variables that fully describe the thermodynamic state of a system are known as the state variables. The state variables of the system can then be used to calculate

information such as its energy via classic thermodynamic expressions known as the equations of state [185].

It is instructive to consider the energy of a material volume or discrete system to understand why negative stiffness is usually thermodynamically unstable. If one considers quasi-static loading it is reasonable, though limiting, to approximate the total energy of any system as the sum of the internal energy of its parts. A more general analysis of the thermodynamic state of a system undergoing loading requires consideration of either the Helmholtz free energy function or the Gibbs thermodynamic potential [185]. Given this simplified quasi-static approach, the total internal energy, E, of a discrete system is calculated as the summation of the internal energies of each of its parts, E_i.

$$\text{energy} \approx E = \sum_{i=1}^{N} E_i \tag{VII.2.1}$$

For a continuous system such as a material volume, V, bounded by some surface, S, the total internal energy is represented by the volume integral given in Eq. (VII.2.2)

$$\text{energy} \approx E = \int_V \rho \mathcal{E} dV \tag{VII.2.2}$$

where $\mathcal{E}$ represents the internal energy *per unit mass*. Classic thermodynamics show that the strain, stress, temperature and entropy of the system is related to the change in internal energy through the equation of state given in Eq. [185].

$$d\mathcal{E} = Tds + \frac{1}{\rho}\sigma_{ij}d\varepsilon_{ij} \qquad \text{(VII.2.3)}$$

An isolated system is in a state of thermodynamic equilibrium when any thermodynamic force applied to the system leads to a variation in the total energy of the system, denoted here as δE, which is *positive*. In other words, thermodynamic equilibrium corresponds to a system configuration which attains some local energy minimum. The above statements describe Gibbs' theorem of thermodynamic stability in words [185, 215, 216]. The local minimum in energy represents a condition which requires work to be done on or heat, Q, to be added to the system in order to change its configuration, *i.e.* $\delta E = \text{work done} + \delta Q$.

Gibbs' theorem of stability stems from the requirement of the second law of thermodynamics which states that for any isolated system undergoing a thermodynamic process, the infinitesimal change in entropy will always be positive, $\delta s > 0$. This requirement is such that "for a system to be in thermodynamic equilibrium no change in boundary conditions is permissible and no spontaneous process which is consistent with the boundary conditions will occur in it [185]." This was first stated by J.W. Gibbs who showed that thermodynamic equilibrium of an isolated system having a given total energy corresponds to the thermodynamic state having entropy, s, that is maximum compared with respect to all neighboring states of the same energy. Equation (VII.2.4) states one form of the required condition for thermodynamic equilibrium.

$$s = \max \qquad \left(\mathcal{E} = \text{const.},\ \varepsilon_{ij} = \text{const.}\right) \tag{VII.2.4}$$

The conditions which satisfy Eq. (VII.2.4) which are particularly applicable to the mechanics of deformable bodies is given by Gibbs: "for the equilibrium of any isolated system it is necessary and sufficient that in all possible variations in the state of the system of which do not alter its entropy, the variation of its energy shall either vanish or be positive [216]."

$$\left(\delta\mathcal{E}\right)_{s=\text{const.}} \geq 0 \tag{VII.2.5}$$

One very important aspect of Gibbs' theorem of equilibrium is that it guarantees more than just equilibrium: it guarantees *stable* equilibrium. That is to say that a disturbed state neighboring equilibrium will tend to return the system to equilibrium. This is observable as the restoring force of a positive stiffness material or structure which returns it to the initial configuration. Negative stiffness behavior, by contrast, assists deformation when the system is perturbed from its initial state. The result is a net deformation when the perturbing strain, or stress, is removed. In so doing, negative stiffness employs its stored energy to do work on its surroundings, thereby violating conditions for *stable* equilibrium. Section 7.2.1.1 further explores and clarifies equilibrium conditions of a material with respect to the strain energy function and the stiffness tensor.

7.2.1.1 Thermodynamic equilibrium, the strain energy function, and constrained structures

Equation (VII.2.3) relates the variation of the internal energy of a system and its thermo-mechanical state. That expression implies that for any given stress and temperature conditions, the internal energy is a function of entropy and strain, $\mathcal{E}\left(s,\varepsilon_{ij}\right)$. Equation (VII.2.6) can then formulated by applying the rules of differentiation to Eq. (VII.2.3).

$$d\mathcal{E}=\left(\frac{\partial\mathcal{E}}{\partial s}\right)ds+\left(\frac{\partial\mathcal{E}}{\partial\varepsilon_{ij}}\right)d\varepsilon_{ij} \qquad \text{(VII.2.6)}$$

Recall also that the theory of elasticity often makes use of a strain energy function, *W*, of a continuous material defined by Eq. (VII.2.7) [185].

$$\frac{\partial W}{\partial\varepsilon_{ij}}\equiv\sigma_{ij} \qquad \text{(VII.2.7)}$$

Comparing Eqs. (VII.2.3) and (VII.2.6) gives the two equalities:

$$\rho\left(\frac{\partial\mathcal{E}}{\partial\varepsilon_{ij}}\right)_{s=\text{const.}}=\sigma_{ij} \qquad \rho\left(\frac{\partial\mathcal{E}}{\partial s}\right)_{\varepsilon_{ij}=\text{const.}}=T \qquad \text{(VII.2.8)}$$

The first equality of (VII.2.8) is compared with Eq. (VII.2.7) to give (VII.2.9) relating the internal energy of a system and the strain energy function for any revisable adiabatic process.

$$\rho\mathcal{E} = W \tag{VII.2.9}$$

The equality given in Eq. (VII.2.9) states that for a material satisfy Gibbs' equilibrium theorem its strain state must be such that the strain energy function is positive definite. This result is very important for the current discussion as it gives a direct relationship between the strain state of a system, which is related to its stiffness, and the internal energy of the system.

The strain energy function of a material is defined by the differential of Eq. (VII.2.7). That relationship can be re-arranged to $dW = \sigma_{ij} d\varepsilon_{ij}$ and then related to the stiffness of the system using the three dimensional form of Hooke's law. The result is then integrated with respect to any imposed strain to yield the classic quadratic form of the strain energy function given by Eq. (VII.2.10).

$$\begin{aligned} dW = C_{ijkl}\varepsilon_{kl} d\varepsilon_{ij} \Rightarrow W = \int_0^{\varepsilon_{ij}} dW \\ \Downarrow \\ W = C_{ijkl}\varepsilon_{ij}\varepsilon_{kl} \end{aligned} \tag{VII.2.10}$$

Equation (VII.2.10) clearly shows that the positive definiteness of C_{ijkl} is the only condition which must be satisfied in order to assure the positive definite nature of the

strain energy function (and therefore thermodynamic stability). In other words, stability is assured when the following classic condition is true.

$$C_{ijkl} n_i n_k m_j m_l > 0 \tag{VII.2.11}$$

Where **n** and **m** represent arbitrary non-zero vectors. For a homogeneous and elastically isotropic material, Eq. (VII.2.11) requires the following limits on the elastic constants [185].

$$\begin{gathered} K = \lambda + \frac{2}{3}\mu > 0 \qquad \mu > 0 \\ E > 0 \qquad -1 < \nu < \frac{1}{2} \end{gathered} \tag{VII.2.12}$$

The results of Eq. (VII.2.12) are found by applying restrictions to the classic relationships between elements of the stiffness tensor and the elastic moduli [215]. One final important observation that can be made with respect to Eq. (VII.2.10) is that the stiffness of a material or structure can be found by finding the curvature of the strain energy function. This gives insight to the discussion of Section 7.2.2.1.

7.2.2 Existence of negative stiffness

A very reasonable question surfacing from this analysis, especially relation (VII.2.12) is: How is it possible for negative stiffness to exist? The answer is not trivial. Indeed, a considerable amount of research has already been committed to understanding this phenomenon in the hopes of harnessing the desirable anomalies of negative stiffness. Of particular interest for this work are its effects on composite stiffness and damping properties which greatly exceeds those of the constituent materials. The literature presents two answers to the question:

i. Negative stiffness domains can conditionally exist within a multiscale system (discrete or continuous) where the remainder of the system consists of positive stiffness domains. Positive stiffness stabilizes the negative stiffness domains putting the system into a state of stable equilibrium.

ii. Negative stiffness behavior can be elicited by providing a system with enough energy to drive an otherwise positive stiffness domain to exhibit negative stiffness behavior. This behavior is *transient*. It is reversible under certain conditions.

The first answer has been studied in more detail with respect to composite material behavior. It has been theoretically demonstrated that domains of negative stiffness can exist *within* a system that constrains the negative stiffness domain with positive stiffness. Lakes and Drugan used both the Hashin-Shtrickman bounds [132] and finite deformation theory to show that it is theoretically admissible to consider negative stiffness domains within a multiscale material given that the resulting macroscopic

stiffness tensor is positive definite. Such a heterogeneous material obeys Gibb's theorem of stability and exhibits extremal stiffness and damping behavior. This is fact has been employed in Chapter VI to consider negative stiffness domains in the design of an automobile windshield. Wang and Lakes illustrated the same principle for discrete systems using Lyapunov's stability theorem [20, 217].

The ability of a positive stiffness matrix to stabilize a negative stiffness domain has been confirmed by calculating the effective behavior of a composite consisting of a positive stiffness viscoelastic matrix and small fractions of negative stiffness domains. The composite contained 2% by volume negative stiffness inclusions of varying negativity and the effective behavior was calculated using four different effective medium theories: the Hashin-Shtrickman lower bound (HS^-), the self-consistent model (SC), the Mori-Tanaka model (MT), and a differential effective medium model (DEM). The results shown in Figure 7.2 verify that the macroscopic behavior is *stable*. This is indicated by the fact that the ratio $\Re\left[\mu^{eff}\right]/\Re\left[\mu^{M}\right]$ is greater than zero for all ratios of $\mu^{I}/\Re\left[\mu^{M}\right]$. Figure 7.2 also validates observations in the literature that the absorptive capacity, tan δ, is very high in the neighborhood of $\mu^{I}/\Re\left[\mu^{M}\right]=-1.1$.

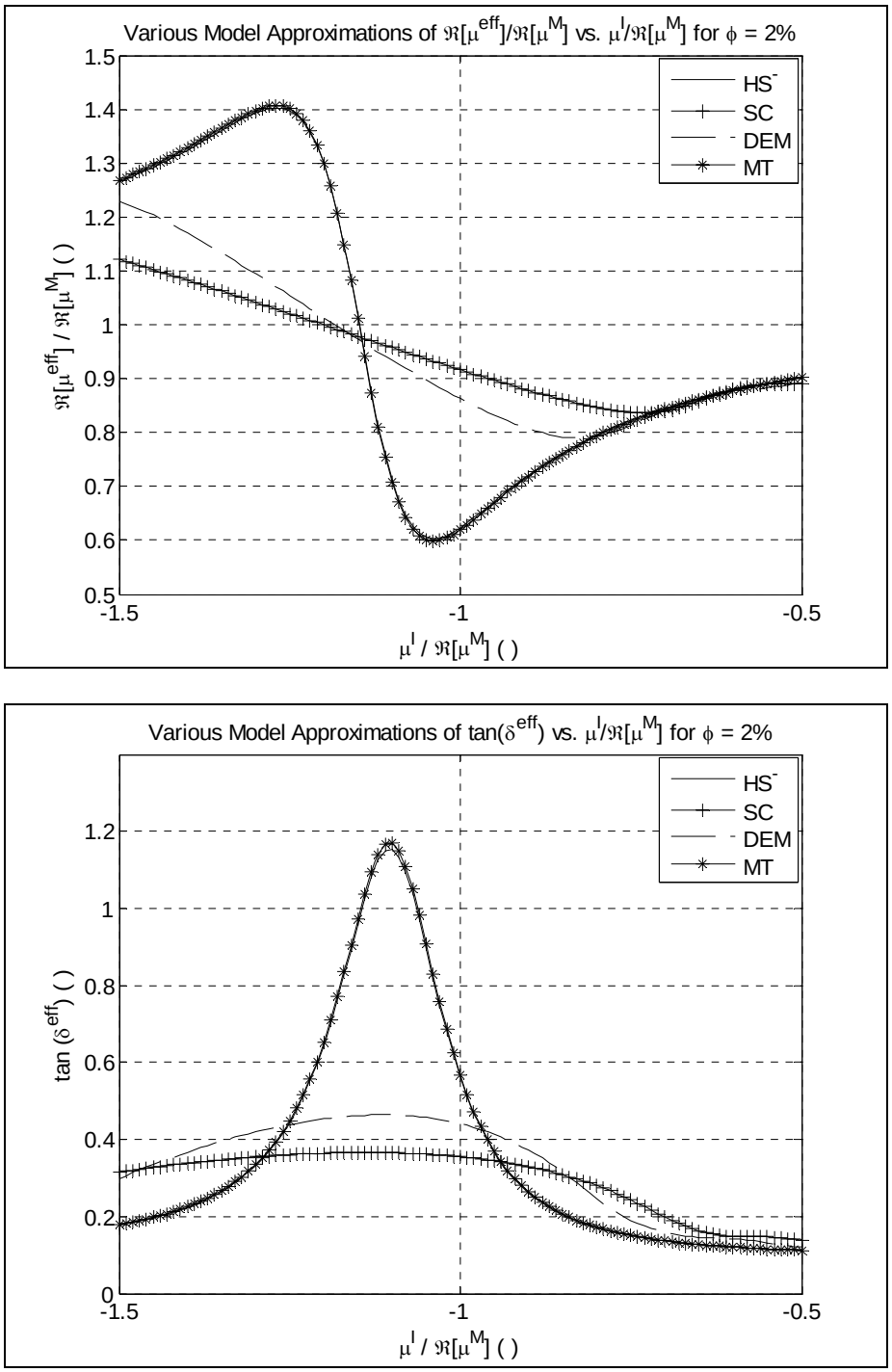

Figure 7.2: Effective shear modulus ratio and tan δ of a viscoelastic composite having a matrix with Poisson's ratio of ν = 0.3 and containing 2% by volume of negative stiffness inclusions. HS$^-$, SC, DEM, and MT models predictions.

One very important point concerning the theoretical consideration of negative stiffness domains presented by Lakes and Drugan [186] and Wang and Lakes [217] is that they

consider negative stiffness to exist *a priori*. In other words, their tacit assumption is that the system has been created in a manner such that stabilized negative stiffness domains co-exist within an otherwise positive stiffness system. Monte Carlo simulations of nanoscale behavior suggests that this may be possible [206, 218], but thus far the creation of such materials for realistic applications remains problematic.

Transient negative stiffness represents a behavior more familiar to the scientific community, though the behavior which can be described as displaying negative stiffness is rarely identified as such. In fact, transient negative stiffness behavior is exhibited by phenomena more commonly classified as a metastable, bistable, or "state switched." The snap through behavior of a buckled beam illustrated in Figure 7.1 is a simple example of a bistable system. As a general rule, the metastable, bistable, and state-switched processes are characterized two stable states that are related by nonlinear behavior. Specifically, such systems can be forced from one state to another by a small external input which elicits a large output. As the system goes from one stable state to another, negative stiffness behavior manifests itself and work is done on its environment. *The only materials and structures produced up to this point have exploited transient negative stiffness behavior as the physical mechanism of damping enhancement*. Metastable and bistable systems are present in many areas of science ranging from optics, to chemistry, to engineering controls, to weather systems. This work is specifically concerned with systems requiring small mechanical inputs which evoke large mechanical outputs. Section 7.2.2.1 explores this behavior in more detail by relating metastable and bistable systems to negative stiffness. Another, very specific, theoretical case of stable negative stiffness behavior is presented in Section 7.2.2.3.

7.2.2.1 Metastable and bistable systems

Any process that assists an externally imposed thermodynamic load will do more work on the system than that input into the system by the external source. This fact betrays the existence of energy stored within the material. These systems release some of their stored energy when the system is perturbed and work is done on the environment. It is in this manner that negative stiffness systems violate the conditions for thermodynamic equilibrium. It is also why they are very interesting. The fact that negative stiffness systems are able to do more work on their environment than that input by the external source is the causal mechanism of the extraordinary behavior observed by many authors [18-22, 186, 187, 204, 205, 207, 219]. *It is asserted here that the abnormal behavior of materials containing negative stiffness domains is only possible if those domains are initially constrained to some metastable state*. Metastability is an unstable and transient but relatively long-lived state of a physical system illustrated in the plot of energy, *E*, versus state variable, *X*, of Figure 7.3. A metastable state has an elevated internal energy which requires only small amounts of input energy to force the system into a state having another, lower, equilibrium energy level. Note that the time and energy required to force a system from state *1* to state *3* may vary wildly. For example, a diamond is simply a metastable form of graphite that persists for millennia while some chemical processes display metastable states that last milliseconds or less.

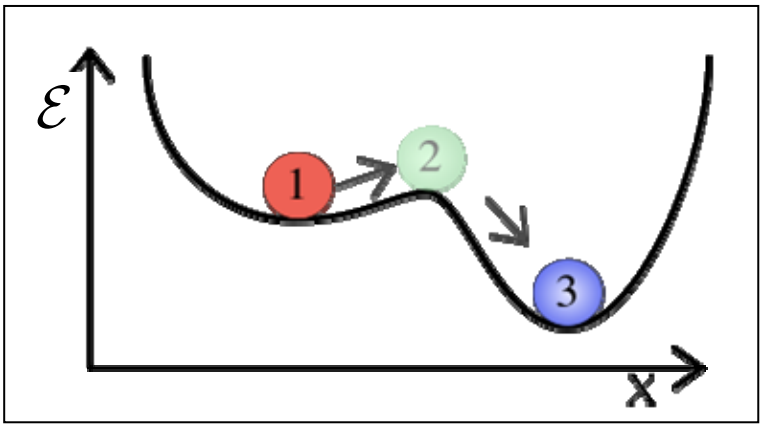

Figure 7.3: General illustration of metastability showing system energy, *E*, versus state the variable, *X*. Point *1* is metastable and point *3* is strongly stable. Point *2* represents the activation energy required to perturb the sytem from state *1* to state *3*.

The illustration in Figure 7.3 shows a metastable state, point *1*, and a strongly stable state, point *3*. When the system is perturbed by an external source that increases in internal energy equal to $\delta\mathcal{E}_{in} = \mathcal{E}_2 - \mathcal{E}_1$, the resulting net change in energy will be negative, namely $\delta\mathcal{E}_{tot} = \mathcal{E}_3 - \mathcal{E}_1 < 0$. The energy needed to drive the system from point *1* to point *3* is known as the activation energy. If the perturbation energy is greater than the activation energy, the metastable domain will release energy and do work on the environment. This is in violation of requirement (VII.2.5) for the domain to obey thermodynamic stability. Metastable systems, therefore, only *conditionally* obey thermodynamic equilibrium conditions. That is, they are stable only if the work done on the system is such that the internal energy is raised by a value $\delta\mathcal{E}_{in} < \mathcal{E}_2 - \mathcal{E}_1$.

A system displaying a behavior similar to that shown in Figure 7.3 is very interesting as it introduces the possibility of eliciting a large response from a system given a small input. Specific to the passage of a wave in a viscoelastic medium containing metastable domains, the behavior described above would provoke strain amplitudes in the neighborhood of the negative stiffness domain which are much larger

than those due to the stress wave alone. This is the physical mechanism which induces extremal damping in heterogeneous materials containing negative stiffness domains. Note that any system manifesting a large response due to a small input is inherently nonlinear. *Indeed, the concept of negative stiffness is simply a convenient meta-model researchers have used to approximate nonlinear small scale behavior*. It is also a potential source of discrepancy between observed behavior and micromechanical models which tacitly assume that behavior on the microscale can be related to that on the macroscale via a linear operator [54]. One problem with a metastable state such as the one illustrated in Figure 7.3 is that the energy required from the external source to push the system from state *1* to state *3* is different than that required to go from state *3* to state *1*: $\delta\mathcal{E}_{1\to 3} < \delta\mathcal{E}_{3\to 1}$. Previously observed negative stiffness behaviors, such as the collapse of isolated foam cells [220], do indeed display the same non-symmetry with respect to activation energy. This is problematic for practical damping purposes. Actual applications must rely on the presence of some disturbance to overcome the activation energy and elicit negative stiffness as the domain goes from state *1* to state *3*. All linear stress disturbances consist of high stress and low stress cycles which are equal in overall energy [32]. For this reason, a non-symmetric metastable system such as the one shown in Figure 7.3 may be driven from state *1* to state *3* but would require a different, higher amplitude, disturbance to return the system to state *1* from state *3*. The expected improved damping behavior would therefore be a one time occurrence. It is for this reason that bistability, a special case of metastability, is of interest and is the subject of the remainder of this section.

To illustrate the occurrence of bistability induced negative stiffness, consider the buckled beam shown in Figure 7.1. It is well known that upon removal of the displacement constraints positioned at the beam ends, the beam will spontaneously elongate to its free length via the energy stored in the buckled configuration. The free length, therefore, corresponds to its lowest internal energy configuration whose behavior is intuitive to the experience of the engineer. A transverse force versus transverse displacement plot for the unconstrained beam will no longer display the non-monotonic curve shown in Figure 7.1, effectively eliminating negative stiffness behavior. When, however, the beam is constrained either in displacement or via an axial load, P, the transverse force versus transverse displacement is altered as a function of the magnitude of that axial load. This behavior was explored in detail both theoretically and experimentally by Saif for micromachined beam which is assumed to be pinned at its endpoints [210]. Figure 7.4 shows an adaptation of the models derived by Saif describing the force applied at the midpoint of a beam which is required to induce transverse displacement for several different levels of axial load.

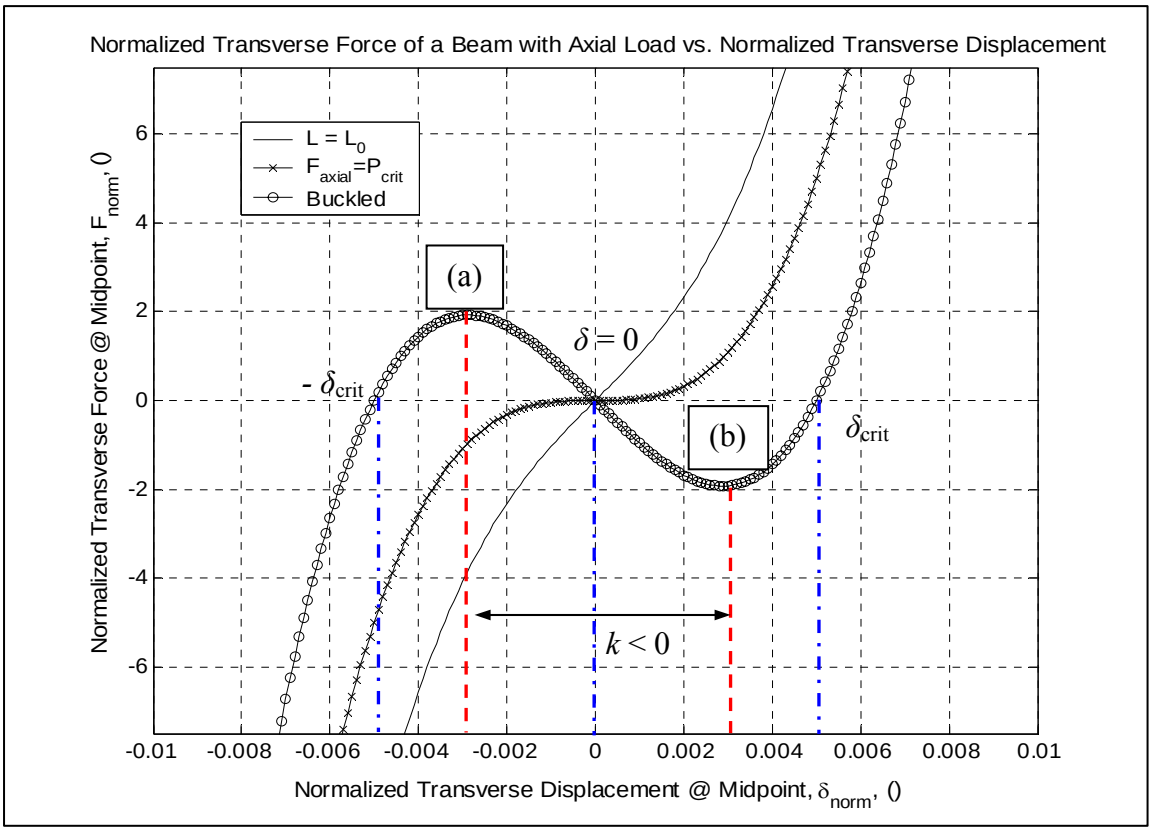

Figure 7.4: Normalized transversly force loaded applied at midpoint of a beam with axial load verus transverse displacement, adapted from Saif [210]. The solid curve shows behavior prior to buckling, the solid curve with crosses shows behavior when the axial load equals the critical buckling load, and the solid curve with circles shows behavior post-buckling. Vertical blue lines indicate equilibrium states and vertical red lines denote critical conditions for snap through.

The force versus displacement curves of Figure 7.4 provide a simple and clear illustration to aid in describing the mechanism of transient negative stiffness and how it significantly increases lossy behavior when embedded in a viscoelastic material. In Figure 7.4, the behaviors depicted by the solid line and solid line with crosses are consistent with usual engineering experience. Namely, in order to displace the midpoint in the positive or negative direction requires increasing the force applied the same direction, *i.e.* positive stiffness. It is possible recognize positive stiffness from direct observation of the required monotonic increase in force as a function of displacement. Recall from Eq. (VII.2.7) that the slope of the force versus displacement curve defines

the stiffness of the structure. The behavior of the buckled beam, represented by the solid line with circles, is no longer monotonic. The displacement values for which the curve has a negative slope are delineated by points labeled (a) and (b). For purposes of describing this behavior, the coordinates of point (a) and (b) are identified as $\left(-\delta_{act}, F_{\max}\right)$ and $\left(\delta_{act}, -F_{\max}\right)$, respectively. Between these two values, the beam displays transient negative stiffness behavior by snapping from one stable state, where the beam midpoint is located at $-\delta_{\text{crit}}$, to another, where the midpoint is located at δ_{crit}. A reasonable first order estimate of the negative stiffness value of the beam between points (a) and (b) is given by Eq. (VII.2.13).

$$k_{beam}^{a\to b} \approx -\frac{F_{\max}}{\delta_{act}} \tag{VII.2.13}$$

These two states and an intermediate unstable equilibrium position for a bistable buckled beam are identified in Figure 7.5.

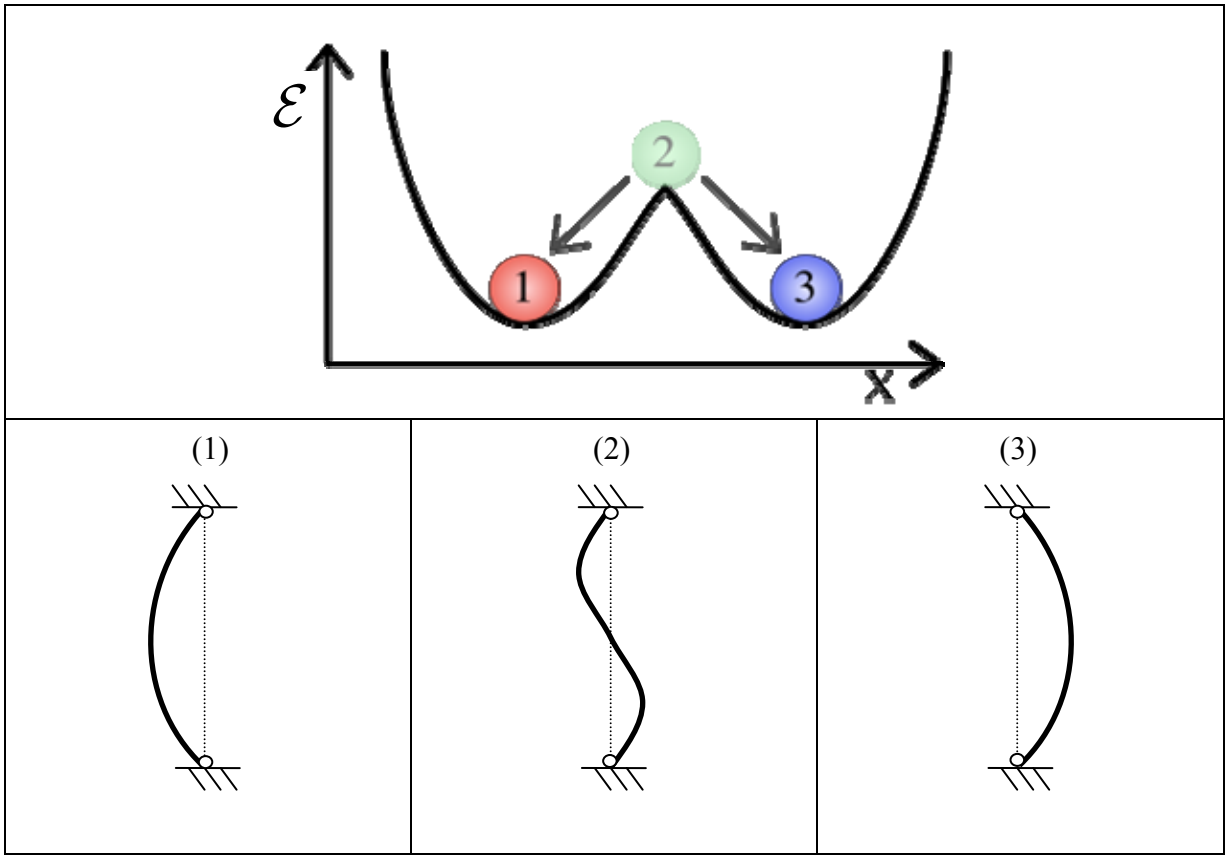

Figure 7.5: General illustration of bistability of a buckled beam. The upper plot shows system energy, *E*, versus state the variable, *X*, which is the displacement of the beam midpoint. Points *1* and *3* are both strongly stable and have the same stored energy. Point *2* represents an unstable equilibrium position.

As previously mentioned, for a bistable structure to pass from one stable equilibrium position to the other requires that the environment supply energy known as the activation energy, $\delta\mathcal{E}_{act}$. The activation energy is a key parameter for understanding how to induce negative stiffness behavior in true applications. If the work done on the bistable system is not adequate to induce snap-through from one bistable position to the other, only positive stiffness is observed. Figure 7.6 depicts both the case where (a) the supplied energy is sufficient to create snap through and (b) the supplied energy is insufficient and the beam displays positive stiffness behavior known as bounce-back.

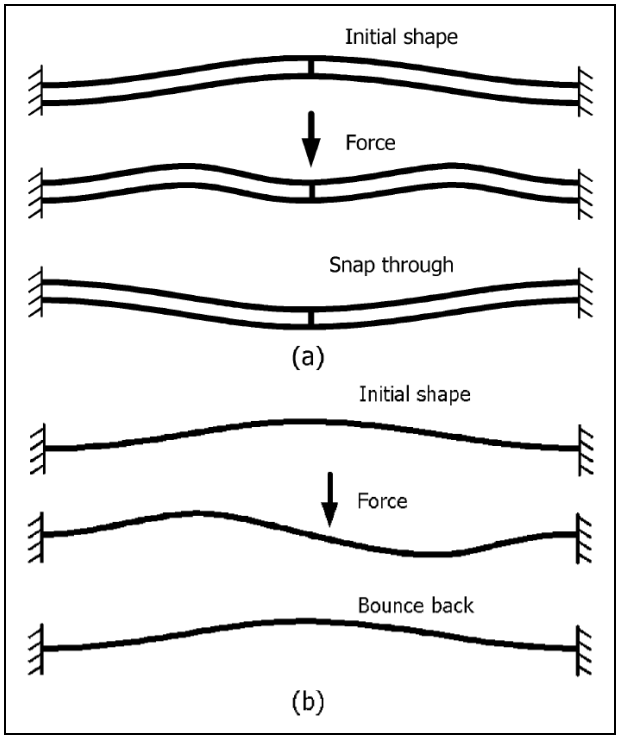

Figure 7.6: Two possible behaviors of a buckled beam when submitted to a transverse force at its midpoint. (a) Snap-through, or negative stiffness, behavior is observed if the product $F\delta = E_{act}$. (b) Bounce back, or positive stiffness, is observed if $F\delta < E_{act}$. Image from Qui *et al* [211].

To take advantage of the interesting properties of a bistable system brought about by transient negative stiffness, it is essential to understand what activation energy must be supplied to the system. Integration of the force versus displacement curves of Figure 7.4 shows that the activation energy required to cause beam snap through is given by Eq. (VII.2.14).

$$\delta\mathcal{E} = \mathcal{E}_2 - \mathcal{E}_1 = \int_{\delta=-\delta_{crit}}^{\delta=0} F(\delta)\,\delta d\delta \qquad \text{(VII.2.14)}$$

Indefinite integration of the force versus displacement curve yields a general expression for the internal energy of the strained beam as a function of transverse displacement. The result is an expression for the internal energy which is a fourth order function of the transverse displacement, δ, in the form of Eq. (VII.2.15) [210].

$$\mathcal{E}_{norm} = -K_1\delta_{norm}^2 + K_2\delta_{norm}^4 + C \qquad \text{(VII.2.15)}$$

K_1 and K_2 of Eq. (VII.2.15) represent stiffness terms related to the beam properties and geometry and C is a constant of integration related to the strain energy due to axial compression [210]. Neglecting the constant C, which results in vertical translation of the curve, Equation (VII.2.15) is plotted in Figure 7.7 for the same axial loads as those given in Figure 7.4.

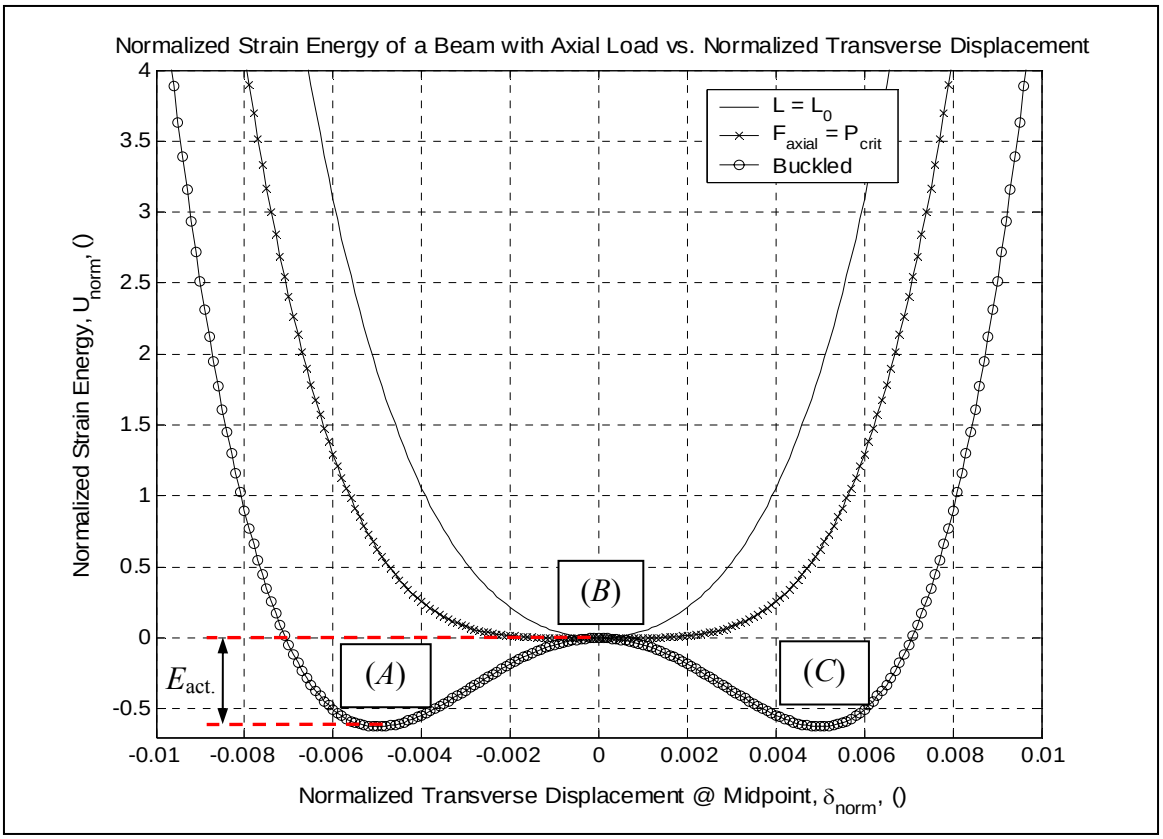

Figure 7.7: Normalized internal energy of a transversly loaded beam with axial load verus transverse displacement, adapted from Saif [210]. Points (*i*) and (*iii*) represent bistable half-wavelength buckled states while point (*ii*) represents a full wavelength "S-shape" unstable equilibrium position.

Figure 7.7 clearly shows that the bistable behavior of a buckled beam is consistent with expect behavior shown in Figure 7.5. Note that points (*A*), (*B*), and (*C*) of Figure 7.7 corresponds to the configurations represented by points (1), (2), and (3) of Figure 7.5, respectively. Point (*B*) is of particular interest as it represents a condition of unstable equilibrium where any perturbation drives the system to one of the lower energy configurations and elicits negative stiffness. In other words, the activation energy is *zero*. Obviously such behavior would be ideal for true applications since a disturbance of any magnitude would incite negative stiffness and the associated extremal behavior. Unfortunately, the ability to place a beam, or any other structure, in this precarious

configuration and then stabilize it is far from trivial, especially for material systems. Note, however, that research which assumes that negative stiffness exists *a priori* within a system assumes that the negative stiffness domains assumes an precarious configuration analogous to that of point (*B*). The stability of an idealized "beam" structure placed in the S-shaped configuration in is discussed in more detail in Section 7.2.2.2.

One very important observation of bistable behavior is that despite the fact that the system requires input energy to elicit negative stiffness, snap through results in net work being done on then environment. To clarify this point, consider the buckled beam with linear spring force attached at its midpoint shown in Figure 7.8. Note that this illustration is only valid if the restriction given in Eq. (VII.2.16) applies to the stiffness of the linear spring fixed to the left-hand side of the beam mid-point.

$$k < \left| k_{beam}^{a \to b} \right| \qquad \text{(VII.2.16)}$$

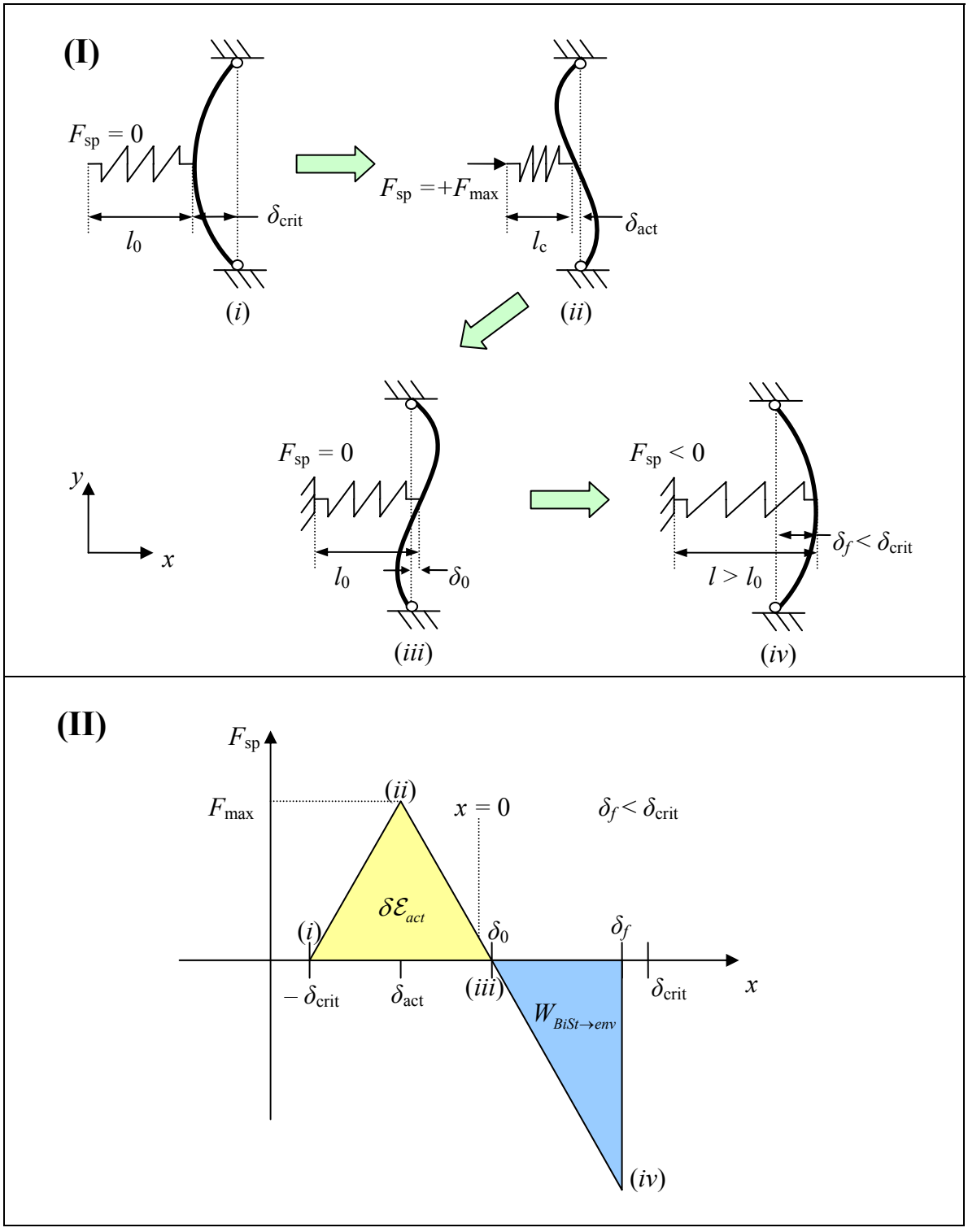

Figure 7.8: Schematic of transverse inducing snap through of a buckled beam. (I) Displays physical processes, and (II) displays the spring force generated at each point shown in (I). Net work is done on the spring.

Figure 7.8 represents four snap-shots of one possible transverse loading path on a buckled beam by an external source via a spring of stiffness k restricted by Eq. (VII.2.16). This is done to illustrate how a system displaying bistable behavior does work on its environment. The configuration labeled (*i*) depicts the buckled beam in its "free state." That is, its motion constrained in the y-direction, inducing bistability, but it is not yet loaded by the spring. Energy is then put into the beam by moving the left-hand side of the spring in the positive x-direction until the force in the spring reaches a value of $F_{\max}$. This process is depicted by configuration (*ii*). Note that a reasonable estimate of the compressed spring length, l_c, and the total travel of the left-hand side of the spring required to reach $F_{\max}$ can be determined from the model provided by Saif and the spring stiffness.

At this point it is reasonable to assume that the left-hand side of the spring is fixed if condition (VII.2.16) is met. The reason for imposing this restriction is that once $F_{\max}$ is attained, the force required at some incremental distance, δx, to the right of δ_{act} is still positive, though less than $F_{\max}$. If $k < F_{\max}/\delta_{act}$, it can be shown that the force in the linear spring will be sufficient to continue to displace the beam without requiring further imposed displacement on its left-hand side. The remainder of the beam travel will take place without further displacement input from the environment due to the bistability of the beam. However, the spring continues to deliver energy to the beam until the beam midpoint is such that the spring length attains its free length, which is illustrated as configuration (*iii*). At configuration (*iii*) the midpoint is located at some value denoted δ_0 which is ≥ 0 given that condition (VII.2.16) is met. At this point, the total energy

imparted to the beam by the linear spring, $\mathcal{E}_{sp}^{input}$, is given by Eq. (VII.2.17) and is related to Eq. (VII.2.15) and reference points (*A*) and (*B*) of Figure 7.7.

$$\mathcal{E}_{sp}^{input} = 2k\left(l_0 - l_c\right)^2$$
$$\mathcal{E}_{sp}^{input} \geq \delta\mathcal{E}_{A\to B} = -K_1\delta_{crit}^2 + K_2\delta_{crit}^4 \qquad \text{(VII.2.17)}$$

Further beam midpoint displacement is achieved solely due to beam bistability. Configuration (*iv*) depicts the buckled beam in its final location denoted as δ_f. Note that $\delta_f < \delta_{crit}$ due to the force generated in the linear spring. Equation then defines the work done on the spring by the bistable system, $W_{beam\to env}$, using the variables introduced in Figure 7.8.

$$W_{beam\to env} = k\left(\delta_f - \delta_0\right)^2 \qquad \text{(VII.2.18)}$$

A few important points should now be highlighted with respect to the idealized behavior shown in Figure 7.8 and discussed in the preceding paragraphs which can be generalized to any bistable system. First and foremost, it is essential to recognize that the bistable condition has clearly been shown capable of doing work on its environment, in this case the linear spring, after an the environment inputs the activation energy. The amount of work done on the environment depends on many factors which are specific to each bistable system and its environment. However, the inequality given in Eq. (VII.2.19) will always be satisfied.

$$W_{BiSt\to env} \le \delta\mathcal{E}_{act} \tag{VII.2.19}$$

Where $W_{BiSt\to env}$ represents the work done on the environment by the bistable system. Further, recall from Chapter II that if the environment is lossy described with a loss factor, η, the total energy dissipated, *D*, upon forcing the system through a cycle from configuration (*i*) → (*iv*) and back (*iv*) → (*i*) is reasonably well approximated with Eq. (VII.2.20).

$$D \approx \eta\left(\delta\mathcal{E}_{act} + W_{BiSt\to env}\right) \tag{VII.2.20}$$

This can be compared to the dissipation given in Eq. (VII.2.20) that of a lossy environment imparting a total strain energy, $\delta\mathcal{E}_{act}$, to a positive stiffness system. Equation (VII.2.21) shows that negative stiffness associated with bistability affords a percentage increase in absorption whose theoretical limit is 100%.

$$\begin{aligned}\left(\%\uparrow\right)_D &= 100\left[\frac{\left(\delta\mathcal{E}_{act} + W_{BiSt\to env}\right) - \delta\mathcal{E}_{act}}{\delta\mathcal{E}_{act}}\right] \\ \left(\%\uparrow\right)_D &= 100\left(\frac{W_{BiSt\to env}}{\delta\mathcal{E}_{act}}\right)\end{aligned} \tag{VII.2.21}$$

The enormous increase in dissipation is a direct result of the work done on the environment by the bistable system during snap through behavior. This is in concert with the discussion of Chapter II regarding strain energy and energy dissipation in viscoelastic materials.

One further informative point notes an observation by Lakes [18] which was confirmed in Figure 7.2. The observation being that the maximum increase in macroscopic damping due to negative stiffness inclusions in a lossy matrix occurs when the ratio of the inclusion shear modulus, μ^I, to matrix shear modulus, μ^M, is $-1.1 \approx \mu^I / \mu^M$. This analogous to restriction (VII.2.16) placed on the current example. Thus the simple one dimensional example of Figure 7.8 seems to confirm observation of three dimensional variational models. Further the 1D representation appears to provide an explanation for the behavior, namely that the absolute value of the inclusion modulus must be greater than that of the matrix in order to maximize the work done on the lossy matrix.

It is essential to stress that the concept if bistability is not restricted to structures, but that it can be generalized to the behavior of a continuous material. Indeed, Landau theory predicts that some crystalline materials, which are known as ferroelastic or co-elastic, experience bistability under specific thermomechanical loading conditions [221]. The bistability is a phase transformation where the crystalline structure of the ferroelastic exhibits a "spontaneous strain." Just as a buckled beam switches from one buckling mode to the next, the crystal strain appears when the environment imposes the activation energy necessary to drive a crystal from one state to another of equal energy. The phase transformation occurs as determined by a temperature dependent sixth order polynomial

of strain [222]. The crystalline state, and therefore bistable behavior, is dictated by the Helmholtz free energy of the crystal, $F(\varepsilon, T)$, which is given in simplified form by Eq. (VII.2.22).

$$F(\varepsilon, T) = \varepsilon^6 - \varepsilon^4 + \left[T + \frac{1}{4}\right]\varepsilon^2 \qquad \text{(VII.2.22)}$$

In Eq. (VII.2.22) ε represents that strain imposed on the crystal, and T is a temperature measure defined as $T = T_{env} - T_{crit} / T_{crit}$ where T_{env} is the environmental temperature and T_{crit} is the critical temperature at which phase transformation takes place in the absence of imposed strain. Representative Helmholtz free energy curves calculated using expression (VII.2.22) are shown in Figure 7.9 for four different normalized temperatures.

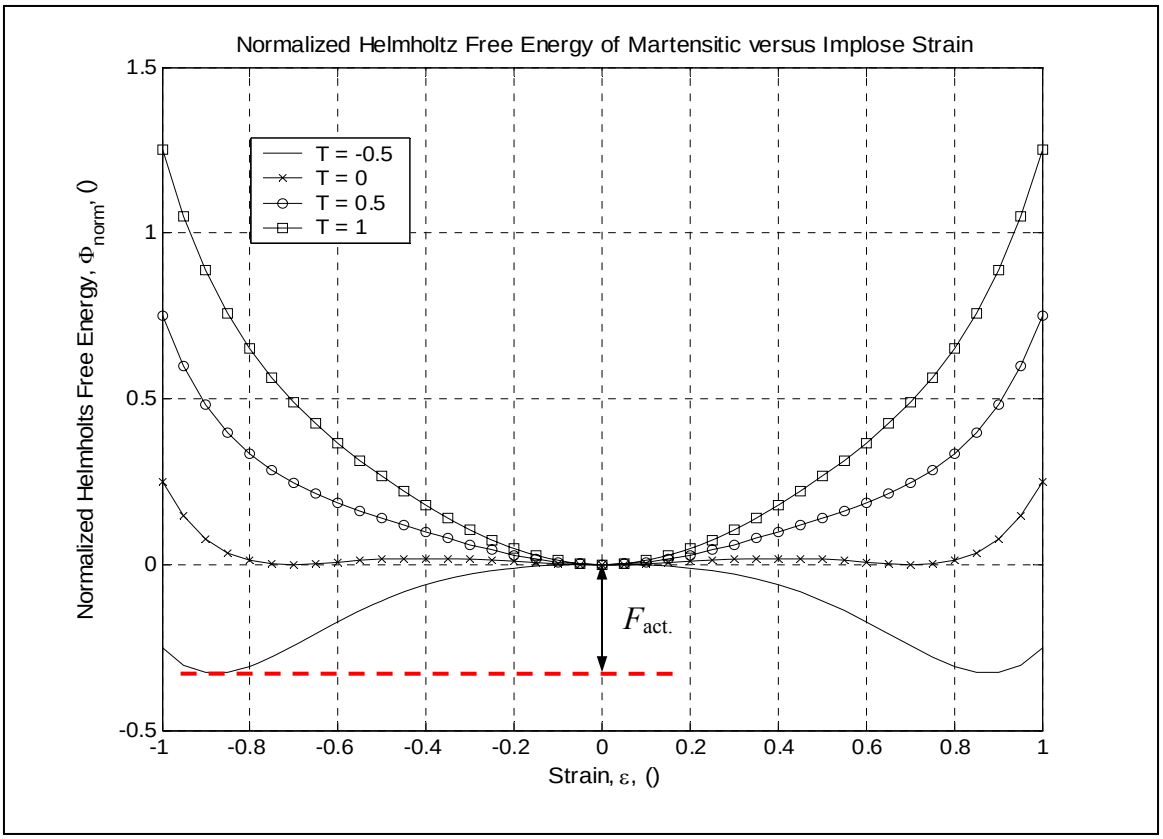

Figure 7.9: Normalized Helmholtz free energy, *F*, of a ferroelastic crystal as a function of strain for several values of temperature. Multiple energy wells when T = -0.5 show that multiple configurations exist which minimize the free energy, *i.e.* that are stable.

Analogous to the previously discussed bistable beam behavior, stable crystalline states are indicated by minimums in the energy function, $F(\varepsilon, T)$. Figure 7.9 clearly displays that for temperatures lower than the critical temperature, phase change can be induced by supplying the crystal with some activation energy. The crystal only has one stable state when above the critical temperature. Unfortunately, the activation energy required to drive phase transformation is much too large to be supplied by low amplitude stress waves and is therefore not of interest for quasi-static damping of harmonic vibrations. However, the figure also suggests that at or near the critical temperature, $T \approx 0$, spontaneous strain is induced for very small values of imposed strain. While the

system is at the critical temperature the ferroelastic material behavior exemplifies constrained unstable equilibrium position where negative stiffness exists *a priori.* Such a point is depicted as point 2 of Figure 7.5 and is discussed in Section 7.2.2.2. This is the phenomena that researchers have already employed to produce true materials displaying the hallmarks of microscopic negative stiffness behavior, namely extremal macroscopic damping [21, 204, 205]. Their studies validate the idea of employing negative stiffness to create high loss materials. The major drawback to employing ferroelastic materials as inclusions to induce extremal damping is that the desired negative stiffness behavior can only be observed when the system is near a specific temperature, T_{crit}. Another fact that restricts the use of ferroelastics is that negative stiffness behavior is only observed when single domains are embedded in a host matrix. This is not a trivial task. When multiple domains are present, phase transformation is coupled with the formation of twins which auto-accommodate and produce negligible spontaneous strain to do work on the environment [21, 221]. These facts make the use of martensitic phase transformation as the mechanism for negative stiffness exceedingly restrictive for the majority of applications.

7.2.2.2 Constrained negative stiffness and stability

It was previously stated that it is possible to constrain negative stiffness systems which would otherwise be unstable. To illustrate this point, consider the S-shaped buckled beam shown on the left-hand side of Figure 7.10 and the approximate spring model at right in the same figure adapted from the unconstrained case given by Wang and

Lakes [217]. The vertical springs are assumed to be pre-compressed to a load, f_0, which is always positive in the following discussion and whose magnitude is calculated from the spring stiffness of the beam in compression, k_b, the free length of that spring, l_{b0}, and its compressed length, l_b.

$$f_0 = k_b\left(l_{b0} - l_b\right) = k_b \Delta l_b \qquad \text{(VII.2.23)}$$

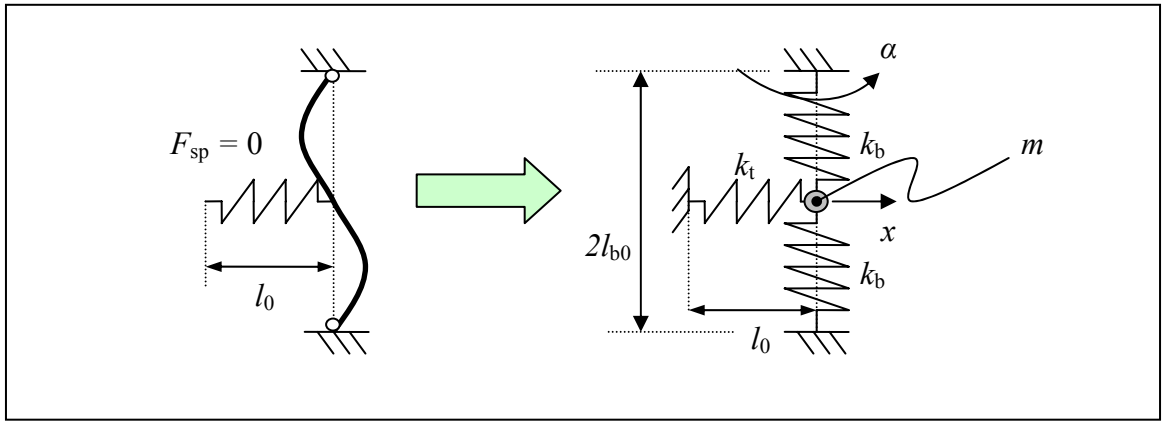

Figure 7.10: Simplified model of an S-shaped buckled beam permitting an elementary study of employing a spring to stabilize the system.

Lyapunov stability for any system is found by inspection of its free vibration state space description when it is perturbed from the equilibrium at $x = 0$. State space is the representation of any dynamic system in the form $\dot{\mathbf{x}} = [\mathbf{J}]\mathbf{x}$, where $\mathbf{x}$ is a vector of state variables and $\dot{\mathbf{x}}$ is the time derivative of $\mathbf{x}$. The eigenvalues of $[\mathbf{J}]$ define the stability of the system. If all eigenvalues of the system are real and negative, the system is asymptotically stable. If the real parts of the eigenvalues or zero, the system is stable when the imaginary part is non-zero [223].

Equation (VII.2.24) describes the free vibration of this system. It assumes small perturbation, $x \ll 1$, and that k_t is complex valued, that is that it can be represented as a spring-damper system. Recall that the Fourier transform can be employed to related the spring loss factor, η, to the viscous damping coefficient, c_v, at a given frequency, ω, through the relation $c_v = \eta k_t / \omega$.

$$m\ddot{x} + c_v\dot{x} + \left[2\frac{f_0}{l_{b0}} - k_t \right] x = 0 \qquad \text{(VII.2.24)}$$

Equation (VII.2.24) is represented in state space form given in Eq. (VII.2.25) by introducing the variable $q = \dot{x}$.

$$\begin{Bmatrix} \dot{q} \\ \dot{x} \end{Bmatrix} = \begin{bmatrix} -\frac{c_v}{m} & \frac{1}{m}\left[k_t - \frac{2f_0}{l_{b0}} \right] \\ 1 & 0 \end{bmatrix} \begin{Bmatrix} q \\ x \end{Bmatrix} \qquad \text{(VII.2.25)}$$

The stability of the system is now found by inspecting the eigenvalues of matrix $[\mathbf{J}]$ in Eq. (VII.2.25). The eigenvalues of $[\mathbf{J}]$ are given by the roots of expression (VII.2.26).

$$\lambda_{1,2} = -\frac{c_v}{2m}\left\{ 1 \mp \sqrt{1 - \frac{4m}{c_v^2}\left[k_t - \frac{2f_0}{l_{b0}} \right]} \right\} \qquad \text{(VII.2.26)}$$

The state of stability of this system is summarized by Eq. (VII.2.27). Note that stability is dependent on the spring stiffness ratio, the viscous damping coefficient, and the pre-compression of the vertical spring.

$$\text{asymtotically stable} \quad \ldots \quad \frac{k_t}{k_b} \geq \frac{2\Delta l_b}{l_{b0}} \tag{VII.2.27}$$

The eigenvalues of the system can then be written in terms of the constant $\mathfrak{Z}$ as shown by Eq. (VII.2.28)

$$\lambda_{1,2} = -\frac{c_v}{2m}\left\{1 \mp \sqrt{1 - \frac{8mf_o}{l_{b0}c_v^2}(\mathfrak{Z}-1)}\right\} \tag{VII.2.28}$$

Where

$$\mathfrak{Z} = \frac{k_t l_{b0}}{2f_0} = \frac{k_t l_{b0}}{2k_b \Delta l_b} \qquad \mathfrak{Z} \in [1 \quad \infty] \tag{VII.2.29}$$

These results are significant because they show that a negative stiffness system, which is unstable when unconstrained, can be constrained with a positive stiffness. In addition, relation (VII.2.27) *quantifies* the nature of constraint needed to stabilize negative stiffness behavior of a simple discrete system, in other words it gives stability criteria.

Though the analysis presented in this section for a mass-spring-damper system is relatively simple, such stability analysis is less obvious when extended to continuous material behavior. At present the only means to evaluate the stability of a composite material system is through evaluation of the positive definiteness of the macroscopic

material [186]. This is very useful knowledge, but it tells little about macroscopic stability in terms of constituent properties, material composition, and inclusion geometry. A significant contribution to the research of effective behavior of media containing *instable* heterogeneities would benefit from a conclusive study with regards to macroscopic stability as a function of instable microscopic behavior and geometry.

7.2.2.3 Unconstrained stable negative moduli?

Section 7.2.1.1 showed that unconstrained negative stiffness behavior is precluded from existence due to its thermodynamic unstability. Wang and Lakes have shown, however, that it is possible for a material with hierarchical structure to display an unconstrained negative bulk modulus under specific conditions [187]. At present these materials have not yet been created. Section 7.2.1.1 detailed the limits placed on the moduli of a homogeneous isotropic material and the physical principles from which these limits stem. If the isotropic material is heterogeneous and has a hierarchical structure, however, those limits can be slightly altered [185]. In this a case, Knowles and Sternberg have shown that requirement of positive definiteness of **C** leads to the following limits on the macroscopic isotropic constants [224]:

$$K > -\frac{4}{3}\mu \qquad \mu > 0$$

$$-\infty < E < \infty \qquad -\infty < \nu < \frac{1}{2} \text{ and } 1 < \nu \tag{VII.2.30}$$

Using this information, one observes that it is possible to have a heterogeneous material displaying negative bulk modulus if $\nu < -1$. Such materials are both macroscopically stable while unconstrained and strongly elliptic, meaning the material microstructure will not form shear bands (twins) [187, 224, 225]. It is encouraging to observe that Lakes and co-workers have created materials with Poisson ratios near –1 [226-228]. Their research coupled with the fact that theory does not exclude the existence of stable macroscopic materials is very exciting. However, further research must be carried out to validate these theories and create structured materials displaying this promising behavior.

7.2.3 Summary of negative stiffness behavior

This section has clarified the meaning of negative stiffness by discussing its existence with respect underlying physical mechanisms and thermodynamic stability. In brief, the reason negative stiffness is of interest is that it is an indicator of the underlying physical behavior of a system doing work on its surroundings. Negative stiffness is only observed after an external source perturbs a system from some metastable state. Therefore, the goal of producing materials that take advantage of negative stiffness is to create multiscale systems containing metastable domains. *It is asserted here that the most realistic manner to achieve this is by either exploiting systems that are bistable and have low actuation energies or by employing constraints to confine a system to an otherwise unstable state of equilibrium*. In the first case, the energy input to a system will drive the bistable system through an instability resulting in net work being done on

the environment by the bistable system. In the second case, input energy will temporarily force the system out of the constrained unstable equilibrium position. The system then does work on the environment and is returned to the constrained unstable equilibrium position. In both cases extremal behavior will be observed on the macroscale.

With the potential exception of negative bulk modulus/negative Poisson ratio materials discussed in Section 7.2.2.3, naturally occurring unconstrained negative stiffness materials are unstable or transient. Further, it has been shown that it is possible to constrain negative stiffness materials with a positive stiffness matrix, but the relationships between variables such as material moduli and inclusion fractions rendering the material macroscopically stable are not well understood. However, negative stiffness is much more prevalent than it may seem. One very interesting example is hair cell behavior in the inner ear of mammals. These cells have been observed to employ negative stiffness to enhance mechanical response to low amplitude signals. The actual mechanism creating this behavior is an active biological element driving the system between two stable states [209, 229]. Some other examples of phenomena that could be interpreted as displaying negative stiffness are bubble collapse [230-232], micro-bucking instability in single cells of cellular foams [186], phase transformation in single domain ferroelastic materials [21], and even active control [208]. This section has discussed the principles defining negative stiffness behavior and the underlying physical mechanisms leading to the extraordinary behavior observed when negative stiffness domains are present in a heterogeneous material or composite system. The next section briefly discusses the salient research pertinent to employing negative stiffness to enhance the absorptive capacity of a heterogeneous material.

7.3 Observation and modeling of negative stiffness behavior

A significant amount of recent research carried out by R. Lakes and his colleagues [18, 19, 21, 186] has shown that included materials possessing negative stiffness behavior can lead to extremely high macroscopic damping properties. This section explores past and ongoing research regarding negative stiffness behavior. Several types of systems which display negative stiffness have been thoroughly investigated. They fall into broad classes: (*i*) Materials undergoing phase transition, (*ii*) nanocomposites or nanostructured materials, and (*iii*) materials having domains undergoing structural failure. These three general domains are introduced in the following sections and their relevance for practical use in material damping applications is discussed.

7.3.1 Phase transition

Section 7.2.2.1 discussed ferroelastic crystals and their ability to display negative stiffness during phase transition. According to Landau theory, the existence of negative stiffness behavior during phase transformation is suggested by the presence of multiple local energy minimums, or energy wells, in the Helmholtz free energy of the crystal as a function of crystal strain [221, 222, 233]. Though multiple energy minimums, and therefore negative stiffness behavior, exist for all ferroelastic crystals, peaks in material damping are rarely observed in ferroelastic materials. This is due to the fact that the energy minimums described by Landau theory describe the behavior at the crystal level.

When multiple crystal domains exist and phase transformation occurs, each domain displays a spontaneous strain according to its own preference (auto-accommidation), twinning occurs, and bands form [221, 224]. The result is a macroscopic stress-strain curve that plateaus rather than showing the reduced stress with increasing strain characteristic of negative stiffness. Such are the macroscopic stress-strain curves of Shape Memory Alloys (SMA) and Transformation Induced Plasticity (TRIP) steels [234]. Lakes *et al* noted however, that it is possible for a single ferroelastic domain near the transition temperature, T_{crit}, to display negative stiffness behavior [21]. In the case of a single domain, the competition between surface and volume energy causes the ferroelastic domain to behave according to Landau theory and subsequently display negative stiffness [21]. Indeed, extreme damping behavior has been experimentally observed in bi-phase materials containing trace elements of single domain crystals undergoing phase transformation [21, 204, 205]. Phase transformation of single crystal domains appears to be the most straightforward way to induce negative stiffness behavior. Unfortunately, it is very impractical for most real-world applications phase transition only occurs at a very specific temperature in the presence of low amplitude stress disturbances. Employing phase transformation as the mechanisms to produce negative stiffness is therefore very useful to demonstrate and validate the use of negative stiffness to enhance damping, but exceedingly restrictive for the majority of applications.

7.3.2 Nanoparticles and nanostructure

One promising, but little investigated and highly theoretical, area of negative stiffness research involves the study of material nanostructures and nanoparticle embedding which lead to domains of negative stiffness in an otherwise homogeneous material. Examples include preliminary research conducted by Yoshimoto *et al* [206] and Papakonstantopoulos *et al* [218]. Yoshimoto *et al* investigated the effects of nanostructure of polymer glasses while Papakonstantopouls *et al* studied the effects of nanoparticle potentials on the local properties of nanocomposites. Both works employed molecular dynamics simulations to investigate local mechanical properties of their respective materials and found regions of negative stiffness. They employed Lennard-Jones potential functions and calculated local mechanical properties using techniques introduced by Lutsko [235] which were later augmented by Yoshimoto *et al* [236]. These two studies suggest that negative stiffness regions can be induced in a material that has the proper nanostructure. The ability to make homogeneous materials containing negative stiffness domains through processing techniques is extremely appealing for many reasons. Most importantly, however, is the fact that homogeneous materials with negative stiffness domains are not prone to the same types of failures, such as matrix-inclusion debonding and poor fatigue performance, as heterogeneous materials.

7.3.3 Single cell foam inclusions

Yet another negative stiffness mechanism was noted in articles by Moore *et al* [220] and Rosakis *et al* [237]. Their research on polymer foams from Foamade Industries (Auburn Hills, MI, USA), Foamex International (Eddystone, PA, USA), and

Scott Industrial Foam (Henderson, KY, USA) showed both theoretically and experimentally that single cells of polymer foams display negative stiffness upon buckling. It is interesting to note that these foams exhibit identical behavior on the macoscale as ferroelastic materials with multiple domains, and for the same reasons. That is, the buckling of large numbers of polymer foam cells is characterized by a macroscopic stress-strain plateau [220, 237]. A non-monotonic stress-strain relationship betraying negative stiffness is only observed when at the cell level. This implies that employing polymer foam cell buckling as the mechanism to induce negative stiffness is complicated by the need to produce materials with single isolated foam cells.

7.4 Proposed structures and research for damping applications

Section 7.3 recounted existing research regarding negative stiffness behavior with respect to extremal damping. It is obvious from this research that the mechanisms exploited to produce real materials exhibiting negative stiffness are quite impractical or very too poorly understood for implementation in everyday structures. For example, materials exploiting martensitic phase transformations as the negative stiffness mechanism do indeed display significant damping peaks, but only at a very specific temperature. Single cells of polymer foams may also display peaks in damping upon collapse, but their behavior requires high energy to instigate collapse. Negative stiffness behavior in polymer foams also require the extremely difficult task of creating isolated single cells within the viscoelastic matrix.

This section addresses the evident lack of true materials displaying negative stiffness which can be employed as inclusions. The purpose of this section is to employ the fundamental understanding of negative stiffness behavior given in Section 7.2 to *ideate* candidate materials and structures to produce negative stiffness inclusions. The ultimate aim is the creation of micro- and nanoscale structures for implementation in common materials and structures which are more practical than those delineated in Section 7.3. It is left to future work to create and validate the following proposals. Two potential candidate mechanisms are identified. The first is highly theoretical and proposes the creation of inclusions containing buckled nanotubes and the second proposes employing MEMS technology to produce bistable thin walled micro-tubes. Each proposal presents significant challenges, both theoretically and technically, and detailed study of each proposal would result in considerable knowledge contribution to their respective fields. Most importantly to the current study, the successful implementation of one or both of these proposed solutions would produce inclusions that display negative stiffness behavior in the presence of low amplitude disturbances and which do not display a high dependency on temperature variation. The proposed structures are therefore more practical for use in common structures. In short, each proposal represents a promising avenue to enhance material performance for a broad range of applications requiring high damping and high stiffness.

7.4.1 Inclusions employing buckled nanotubes

Scientific literature is raft with potential applications for carbon nanotubes which include mechanical reinforcement, micro-electronics, semiconductors, waste recycling, and thermal protection, to name just a few. Of specific interest to this work is their unique ability to undergo very large reversible buckling deformation without damage. Such behavior was theoretically predicted by Yakobson *et al* [238] and verified by Falvo *et al* [239]. The latter group experimentally buckled isolated nanotubes using a device designed by Topometrix Inc [240] and studied the resulting shapes. It is well known that the axial force required to deform a buckled *macroscopic* tube is not monotonic [214]. Indeed, Lakes employed a very simple experiment to show that cyclic axial loading of a buckled tube leads to negative stiffness behavior due to this non-monotonic axial force versus displacement relationship [19]. Theory suggests that non-monotonic axial force versus displacement relationships, and therefore negative stiffness, also exist at the nanoscale [238, 241], though to the author's knowledge this has not been confirmed experimentally. It is proposed that the possibility of creating inclusions containing buckled nanotubes be rigorously inspected. Ideally such inclusions could be created to display roughly isotropic negative stiffness behavior matched to the specific application per material design results such as those given in Chapter VI. The suggestion of creating inclusions containing buckled nanotubes is very ambitious due to the associated theoretical and technical challenges. Many unknowns are associated with this subject including, but in no way limited to: (*i*) detailed studies on their manipulation and associated forces and displacements, (*ii*) focused research on processing bundles of buckled tubes to create single "inclusions" having isotropic non-montonic stress-strain

curves, and (*iii*) the ability to include buckled tubes into a material to induce extremal macroscopic material behavior due to their negative stiffness behavior.

The next section proposes a more practical, though still highly challenging, approaches to creating negative stiffness inclusions. It is proposed that MEMS technology be employed to produce microtubes in a bistable energy configuration having low activation energies. Though the theoretical and fabrication challenges associated with these tubes are far from trivial, they represent a very promising avenue to creating negative stiffness inclusions for a broad range of applications. Due to the high level of control available in fabricating MEMS structures and their continuous improvement, it is submitted that microtubes may indeed represent a more promising means to achieve negative stiffness behavior than any mechanisms previously mentioned in this work.

7.4.2 Bi-stable microtubes

Section 7.2.2.1 discussed bistable mechanisms and their relationship to negative stiffness behavior in detail. The present section aims to make use of that knowledge to proposing the fabrication of microtubes which are bistable in ambient conditions, have low activation energies, and can be activated in the quasi-static domain due to acoustic or vibrational disturbances. The general processing structure to arrive at a bistable state is as follows. (*i*) A thin walled microtube having a length, L, thickness, h, and radius, R is created at temperature, T_H, from material *1*. (*ii*) A solid rod, concentric with the microtube, having of length, L, and radius, r, is created at temperature, T_H, from material *2*. (*iii*) Still at temperature, T_H, the microtube and rod are joined at top and bottom by

capping or other practical means. (*iv*) The microtube-rod composite structure is included into a matrix material. (*v*) The heterogeneous material is cooled to ambient temperature. The microtube-rod structure is illustrated Figure 7.11. The purpose of microtube-rod composite structure design is to define the tube and rod geometries and choose materials *1* and *2* such that when the composite microtube-rod structure is cooled to the ambient temperature the buckling load is achieved within the tube walls.

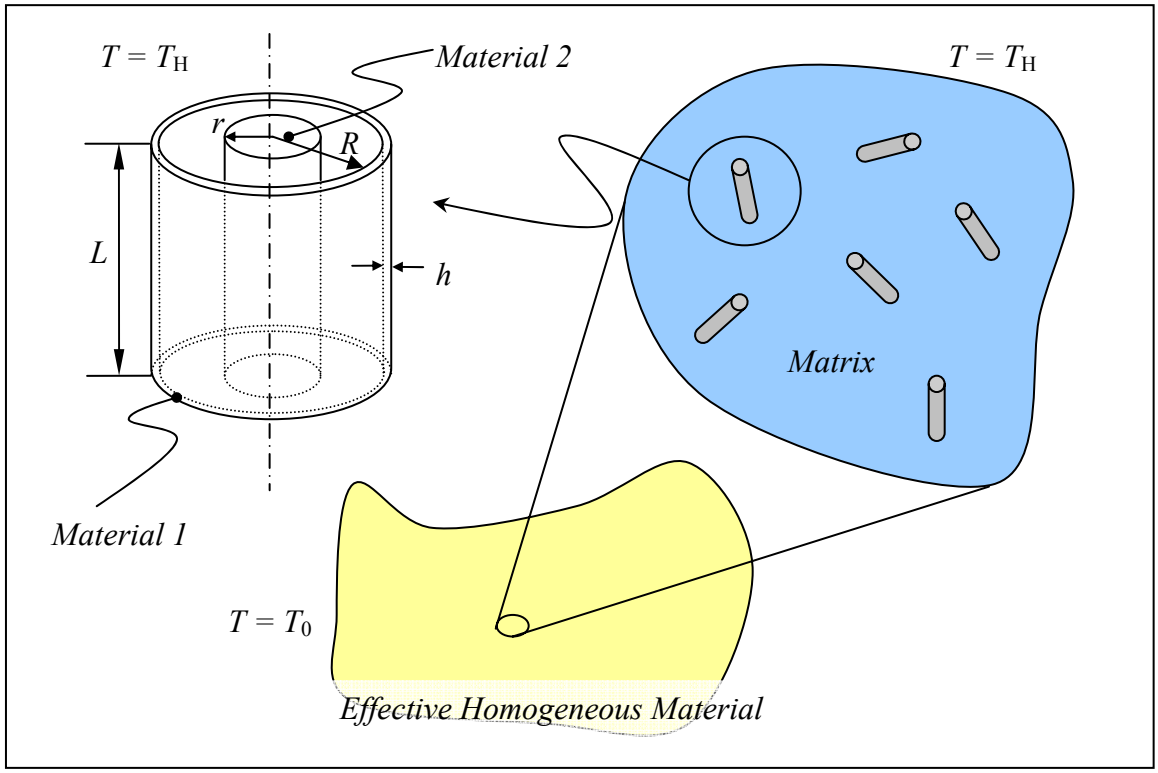

Figure 7.11: General representation of a microtube-rod composite structure to create bistable microtube shell walls. For clarity, tube caps are not shown.

The creation of microtubes is not trivial, but it is a well developed technology patented by the United States Air Force [242, 243]. The proposed structure is further complicated by the addition of a co-axial rod and adjoining surfaces which make the tube wall buckling upon cooling possible. Many practical issues will arise when trying to create this three

dimensional object which must withstand high stresses and many cycles of large strain. For the purposes of this section, which is ideation, it is assumed that a similar structure to that proposed can, or will, be fabricated.

At this stage it is important to give a general sense to modeling the behavior of the composite microtube. The remainder of this section provides an introductory analysis of the composite microtube to initiate tube modeling from an analytical standpoint. More detailed analysis, such as finite element methods, is left for future work. The literature is replete with theoretical and numerical studies concerning the complex buckling behavior of cylindrical shells. An excellent overview and literature survey for the behavior of thin walled shells is given by Wullschleger and references therein [214]. Other important references include Donnell [244], who provides a very approachable models for the buckling of thin-walled cylinders, a great overview of nonlinear shell modeling by Doyle [245], a concise theory regarding buckling and post-buckling behavior of Budiansky [246], and Markus' [247] complete summary and analysis of the shell vibrations. For the purposes of the current work, only a few basic relationships are necessary to illustrate how one would go about designing a bistable tubular structure to embed in a viscoelastic matrix.

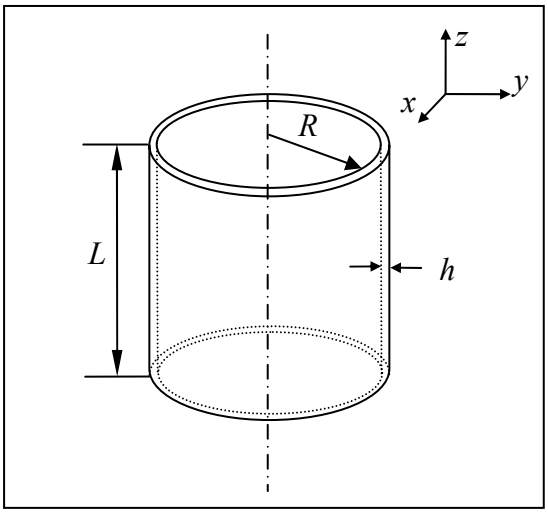

Figure 7.12: Schematic of thin walled cylinder having a height, *L*, radius, *R*, and thickness, *h*.

Consider thin walled cylinder having isotropic material properties and the geometry shown in Figure 7.12. When this structure is subjected to a linearly distributed axial compression load, *N*, the theoretical buckling load depends on both the geometry and material properties of the cylinder. Wullschleger shows that if the edges are hinged, the critical buckling load can be estimated by finding the minimum value for the axial load in given by Eq. (VII.4.1) [214].

$$N_{crit} = \min\left[\frac{Eh^3}{12\left(1-\nu^2\right)}\frac{\left(\beta^2+\eta^2\right)^2}{\beta^2}+\frac{Eh}{R^2}\frac{\beta^2}{\left(\beta^2+\eta^2\right)^2}\right] \qquad \text{(VII.4.1)}$$

Where β and η represent the number of axial half-wavelengths and complete wavelengths along the circumference of the post-buckled cylinder, respectively. They are represented in terms of their modal number, *n* and *m*, using Eq. (VII.4.2).

$$\beta = \frac{m\pi}{L} \qquad \eta = \frac{n}{R} \tag{VII.4.2}$$

Expression (VII.4.1) explicitly shows that the value of the critical axial load is quite complex and, interestingly, that many different buckling modes may be simultaneously induced when the critical load is reached. Indeed, for intermediate lengths of tube, that is those having a length to radius ratio that is neither $R/L \ll 1$ nor $R/L \gg 1$, buckling occurs upon satisfaction of Eq. (VII.4.3).

$$\frac{\left(\beta^2 + \eta^2\right)^2}{\beta^2} = \frac{2\sqrt{3\left(1-\nu^2\right)}}{hR} \tag{VII.4.3}$$

Substituting ing Eq. (VII.4.3) into expression (VII.4.1) and dividing by the thickness of the cylinder gives a critical compressive stress which will buckle the cylinder. The critical stress level can then be multiplied by the cross-sectional area of the cylinder, $A \approx 2\pi Rh$, to yield the compressive load required to buckle the thin walled cylinder. Expressions for both of these critical entities are given in Eq. (VII.4.4).

$$\sigma_{crit} = \frac{1}{\sqrt{3\left(1-\nu^2\right)}}\frac{Eh}{R} \qquad P_{cr} = \frac{2\pi Eh^2}{\sqrt{3\left(1-\nu^2\right)}} \tag{VII.4.4}$$

It is interesting to note that Eq. (VII.4.3) predicts buckling will occur with any number of modal number combinations. This fact may be problematic for actual implementation as the mode of interest corresponds to the $n = 0$, $m = 1$ bistable mode shown in Figure 7.13.

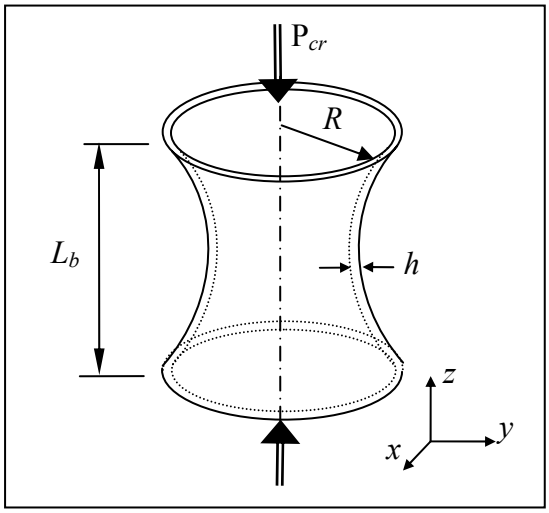

Figure 7.13: Bistable post-buckled axis-symmetric configuration for microstructures that can enhance damping through transient negative stiffness behavior.

Despite this potential difficulty, several points regarding post-buckled behavior are important. (*i*) Any buckling mode will have *at least* two alternate configurations. Negative stiffness will therefore be observed when external loading in the *x*-*y* plane exceeds the activation energy needed to switch between *any* alternate configuration of equal energy. This means that though more than the $n = 0$, $m = 1$ bistable mode will be present, enhanced damping due to transient negative stiffness is still observed. (*ii*) Higher modes (those with higher modal numbers) undergo smaller displacements when switching between states [214]. This more than likely will lead to decreased lossy behavior despite the presence of negative stiffness. Only further detailed research can quantify the extent of degradation to damping enhancement caused by the presence of higher modes. (*iii*) The simple linear analytical model employed to give Eq. (VII.4.1) and (VII.4.3) may neglect either geometric or material property aspects that limit the number of modes occurring upon after buckling. For example, it may be possible to

make a structure pre-disposed to a specific mode by alter the wall or internal stress profile. Again, further research must be conducted in order to gain a more detailed understanding of the resulting post-buckled configuration. This may permit the researcher to control the onset of buckling and the final post-buckled form.

Equation (VII.4.4) defines the theoretical axial stress level at which the tube will buckle. For the composite microtube-rod structure proposed here, the stress level in both elements is brought about uniquely by a mismatch in thermal expansion coefficients, β_{ij}, and the difference between the fabrication and ambient temperatures, $\Delta T = T_H - T_0$. To define the temperature at which tube wall buckling will occur a generalized form of Hooke's law which includes the effects of temperature must be employed [185].

$$\sigma_{ij} = C_{ijkl}\varepsilon_{kl} - \beta_{ij}\Delta T \qquad \text{(VII.4.5)}$$

Assuming the rod and tube are perfectly bonded requires equality of axial strain in both elements: $\varepsilon_{33}^{T} = \varepsilon_{33}^{R}$. The expression for the critical stress given in Eq. (VII.4.4) is then used in conjunction with Eq. (VII.4.5) and axial strain compatibility to define a material dependent expression for the temperature change required to induce tube buckling.

$$\Delta T = \left(\frac{E_2 - E_1}{\beta_2 E_1 - \beta_1 E_2} \right) \sigma_{crit} \qquad \text{(VII.4.6)}$$

Where the E_x is the Young's modulus of material x, $\beta_{1,2}$ represents one element of the matrix of thermal expansion coefficients β_{ij}, and the critical stress is defined with respect to the material properties and geometry of the tube.

$$\sigma_{crit} = \frac{1}{\sqrt{3\left[1-\left(\nu_1\right)^2\right]}} \frac{E_1 h}{R} \qquad \text{(VII.4.7)}$$

Equations (VII.4.6) and (VII.4.7) give an initial guideline to the choice of materials to employ to create bistable microtubes.

Several other important points, ideas, and potential problems should be considered for the designing of these microtube inclusions. They are listed here.

- The matrix surrounding the composite microtube must have a higher volumetric coefficient of thermal expansion to ensure that the bistable tube walls be pushed somewhere between either bistable two positions. This is an example of the creation of materials having negative stiffness domains which exist *a priori*.

- The proposed configuration introduces several difficulties, one of which is the need to induce large stress levels to put the microtube into its buckled state. Qiu *et al* [211] created a bistable beam mechanism by joining two curved beams at their mid-point. This was done because thermally induced buckling has been observed to be difficult using micro-manufacturing techniques. There is

considerable merit in exploring the extension of this technique to concentric cylinders.

- To eliminate the presence of higher buckling modes it may be of interest to study the feasibility and effect of adjusting tube wall profiles.

- Fatigue will pose a very real problem in the tube, rod, and matrix materials. All materials are under elevated cyclical stress levels and the tube walls will undergo large deformations. It is essential to consider fatigue problems when employing these or any other negative stiffness inclusions.

- Tube-matrix and tube-cap debonding will also pose a serious problem to implementing bistable structures for damping purposes. This problem is stems from negative stiffness behavior in general, namely the high strain amplitudes induced during snap through.

Though the creation of bistable microtubes present many challenges, the proposed structure has several significant benefits. First, the axis-symmetry of the induced bistability guarantees that negative stiffness will be activated in quasi-static loading conditions. Another important benefit of this structure is that it has much more promise the most other candidate materials that are known or theorized to display negative stiffness. Ferroelastics do display negative stiffness due to phase transformation. However that behavior only occurs at very specific temperatures which is a definite

impediment to their widespread use. Material heterogeneities displaying stable negative bulk moduli have also been proposed to enhance damping. Unfortunately such materials must simultaneously display Poisson ratios < -1, a material that has yet to be fabricated and represents a very significant technical challenge. One last benefit of the tubular structure is the ability to construct a transversely isotropic stiffness matrix to describe its behavior. This can be done by employing a finite element approximation of the post-buckled tube behavior and a procedure similar to that employed by Shen and Li [248]. They employ four stress-strain tests can be used to approximate the moduli of a tube. Specifically, axial tension yielding E_z and ν_{pz}, axial torsion giving μ_{pz}, biaxial plane stress applied in the plane of symmetry to obtain the plane stress bulk modulus, K_p, and biaxial shear test in the plan of symmetry to yield μ_p. Note that the transversely isotropic stiffness tensor, in Voigt notation, is written in terms of properties aligned with the plane of symmetry, *p*, and the *z* axis by Eq. (VII.4.8) [33].

$$C_{IJ} = \begin{bmatrix} \frac{1-\nu_{pz}^2}{E_p E_z \Delta} & \frac{\nu_p - \nu_{pz}^2}{E_p E_z \Delta} & \frac{\nu_{pz}\left(1-\nu_p\right)}{E_p^2 \Delta} & 0 & 0 & 0 \\ \frac{\nu_p - \nu_{pz}^2}{E_p E_z \Delta} & \frac{1-\nu_{pz}^2}{E_p E_z \Delta} & \frac{\nu_{pz}\left(1-\nu_p\right)}{E_p^2 \Delta} & 0 & 0 & 0 \\ \frac{\nu_{pz}\left(1-\nu_p\right)}{E_p^2 \Delta} & \frac{\nu_{pz}\left(1-\nu_p\right)}{E_p^2 \Delta} & \frac{1-\nu_p^2}{E_p^2 \Delta} & 0 & 0 & 0 \\ 0 & 0 & 0 & 2\mu_{zp} & 0 & 0 \\ 0 & 0 & 0 & 0 & 2\mu_{zp} & 0 \\ 0 & 0 & 0 & 0 & 0 & \frac{E_p}{1+\nu_p} \end{bmatrix} \quad \text{(VII.4.8)}$$

With

$$\Delta = \frac{\left(1+\nu_p\right)\left(1-\nu_p-2\nu_{zp}^2\right)}{E_p^2 E_z}$$

This stiffness matrix can then be employed in mean-field modes such as those developed and employed throughout this work. As an illustration, consider the acoustic wave amplitude attenuation per wavelength, $\alpha/k^{'}$, discussed in Section 5.5.4 for a PVB matrix containing 2% by volume of randomly oriented pin-shaped isotropic inclusions ($a/b=1 \quad a/c=1/10$). The material properties for PVB can be found in Chapters IV, V, and VI and the assumed inclusion Poisson ratio is $\nu^I = 0.20$. The Poisson ratio was chosen arbitrarily for the purposes of illustrating the ability to successfully integrate tubular shapes with negative bulk moduli to approximate peaks in lossy behavior. The results are encouraging for future research, displaying significant peaks in macroscopic damping capacity for bulk modulus ratios approximately $\in [-0.4 \quad 0.2]$.

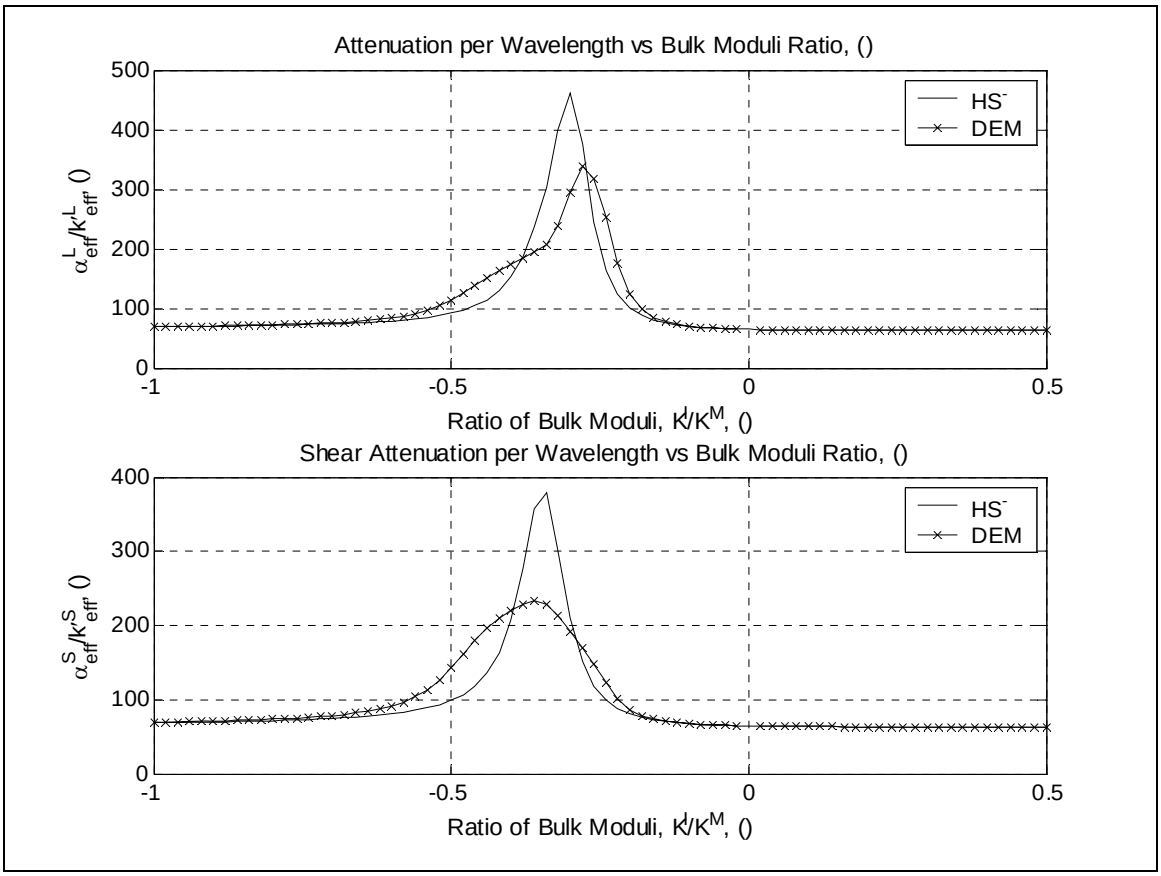

Figure 7.14: Effective compressional and shear wave amplitude attenuation per wavelength versus ratio of inclusion to matrix bulk moduli for a 2% inclusion fraction. The matrix material the PVB material employed as interlayer material in Chapters V and VI and the inclusion Poisson ratio is assumed to be $\nu^I = 0.20$.

7.5 Chapter summary

The ability to design and create inclusions displaying negative stiffness is crucial to the fabrication of high loss – high stiffness materials. This chapter explored the roots of negative stiffness behavior in detail, discussed existing research and observations of negative stiffness, and proposed two very different, but promising, avenues to create negative stiffness inclusions. Unfortunately, both proposals require significant focused research and technological advancement before they can be successful created. Research

on the creation of negative stiffness materials, however, is of high value both from theoretical and practical standpoints. The insight gained by searching to understand and implement mechanisms displaying negative stiffness will directly influence the creation of a generation of materials displaying previously unattainable property combinations.

One final note is in order regarding the proposals of this chapter. Namely: the insight gained in this chapter is a direct result of implementing a top-down design methodology to explore the multiscale design space of an automobile windshield. This chapter is, therefore, a confirmation of the power of the top-down/inductive material design approach to *efficiently* identify unique solutions paths for existing problems and to lend insight to the practical implementation scientific fundamentals.

CHAPTER VIII

GENERAL CONCLUSION

8.1 General conclusions and perspectives

The principal objective of this thesis is the derivation, development, and validation of a multiscale model to explore microstructural aspects that lead to enhanced damping behavior for future creation, design, and development of materials with high capacity to absorb mechanical energy.

The above statement recounts the principal thesis objective which was annunciated at the outset of this work. Satisfaction of the principal objective was accomplished by sequentially satisfying two secondary objectives. Those secondary objectives can be paraphrased as (*i*) a perfection of the understanding of heterogeneous multiscale viscoelastic material behavior, and (*ii*) an implementation of this understanding to improve the performance of structures requiring the absorption of mechanical energy. To achieve these objectives this thesis first concentrated on furthering the fundamental understanding of multiscale heterogeneous viscoelastic material behavior. Intertwined with the need for an understanding of this behavior is the ability to successfully model the effective lossy properties of a multiscale viscoelastic material. Of specific interest was the desire to understand the principal variables

governing the capacity of a material to absorb mechanical energy and how this could be applied to problems of wave propagation in absorptive media. These topics are the subjects of Chapters III and IV of this thesis. The pertinent results relating to the thesis objectives are summarized below in Sections 8.1.1 and 8.1.2. Next, it was postulated that the models developed and validated in Chapters III and IV could be integrated as a tool for the design of high loss materials and systems. To that end a nested multiscale model linking microstructural variables to structure level performance of an automobile windshield was created. A design strategy and methodology was then obtained from the systems design field. The desired characteristics of the design approach was one that aided in design space exploration to improve performance of a specific structure while simultaneously aiding in gaining knowledge on how to enhance the material damping capacity. Chapters V and VI detail the creation of the nested multiscale model and its implementation in an optimal design protocol, respectively. Subsequently, Chapter VII explores the intriguing results issuing from the design space exploration. The results relating to the satisfaction of this secondary objective are summarized in Sections 8.1.3 and 8.1.4.

It is obvious that the two objectives are not independent. Indeed design of lossy materials heavily depends on the designer having minimum level of understanding of the fundamentals of viscoelastic material behavior. Traditional design approaches placed a premium on material behavior knowledge, while the design approach was simply seen as an efficient means to optimize overall behavior in the face of conflicting goals [119]. Interestingly, the employment of certain types of design techniques can reciprocally yield significant insight into material behavior. Such is the case of inductive materials design.

Inductive design is a top-down design approach which lends easily exploration, discovery, and creation [5, 178]. This thesis has implemented and illustrated that the coupling of a robust multiscale modeling techniques with and inductive design approach provides a potent methodology to design materials to the microscale. Further, the results have shown that this particular combination allows the designer to efficiently gather knowledge of sub-microscale materials and mechanisms that significantly enhance the absorption of mechanical energy.

Because multiscale models represent the most powerful tools of a researcher for studying material behavior at all length and time scales, the development and study of multiscale material models is one of the most active research area of material design. Consequently, a significant portion of the research presented in this thesis concerns the derivation and developed a quasi-static self-consistent micromechanical model. The model was subsequently implemented as a tool in an inductive material design protocol to design of high loss materials. The material model and design protocol embody the satisfaction of the two secondary thesis objectives stated at the beginning of this section. The model, design protocol, and results ultimately lead to the achievement of the primary thesis objective, which required four distinct steps. The first step was the derivation of a robust quasi-static frequency domain micromechanical model for application to a wide range of VE particulate composite materials. Chapter III addressed model derivation by extending Cherkaoui's static SC coated inclusion model [23, 24] to include VE behavior of the constituent phases. The model was further developed via DSCT tensor formulation, thereby permitting the approximation of a broad range of VE particulate composites. The second step was the validation of the quasi-static SC model through

comparison with complex bounds and experimental data, the subject of Chapter IV. This chapter ensured that no laws were violated in model derivation and displayed model accuracy for both static and quasi-static applications. The third step in achieving the thesis objective was SC model implementation into a multiscale structural model. This was achieved in Chapter V through modeling the dynamic behavior of a viscoelastically constrained sandwich plate, representing an automobile windshield, through a hierarchy of nested models. The final step entailed the integration of the micromechanical model and nested structural model describing windshield material behavior into a compromise decision support protocol (CDSP) in Chapter VI. CDSP implementation allowed efficient design space exploration and yielded well defined design criteria to optimally enhance multi-objective windshield performance. In addition, design space exploration results *informed* the design process by showing negative stiffness behavior to be the variable of highest importance for absorptive material behavior. In consequence, Chapter VII gave a detailed investigation of the roots of negative stiffness behavior and suggested means to create inclusions displaying negative stiffness. The following subsections summarize the important contributions and developments of each section of this thesis, give perspectives on the results, and suggest future avenues for detailed study.

8.1.1 Quasi-static model development

Frequency dependent approximations of heterogeneous material damping properties depend strongly on the frequency range of interest. This thesis has been restricted to applications where mechanical loading in the frequency domain is well

represented as being spatially homogeneous and varying with time. It has been shown that this frequency range corresponds to heterogeneity length scales, a, which are much smaller than the incident wavelengths, λ. This frequency domain is called the "low frequency" limit, low *ka* scattering, or the Rayleigh scattering limit. It is well known that material behavior in this domain can be captured through static models by applying the elastic-viscoelastic correspondence principle. Based on this reasoning, this thesis proposed a micromechanical modeling approach rather than a scattering based model. Micromechanical modeling approximates macroscopic frequency dependent behavior uniquely through constituent material behaviors and neglects inertial effects present in scattering models. Despite the fact that such an approach limits modeling to the quasi-static domain, it greatly enhances the range of materials whose frequency dependent effective behavior is accurately approximated. It is for this reason that the micromechanical approach has been chosen to be developed as a material design tool.

The micromechanical model derived in Chapter III is an extension of the static coated inclusion self-consistent model introduced by Cherkaoui *et al* [23, 24]. Section 3.2 investigated modeling the simple case of coated ellipsoidal inclusions embedded in an infinite matrix. The model approximates the presence of inhomogeneities as a spatial variation of elastic constants in accordance with Zeller and Dederichs [68]. Application of this approach in the static domain yields an integral equation based on Green's formalism for the local strain field. The resulting Green's function relates material stiffness contrast between matrix, inclusion, and coating phases to a distribution of volume forces. Extension of the static model to the quasi-static frequency domain requires this distribution of volume forces to become time varying and integrates the

static integral equation across all frequencies. Finally, application of interfacial operators and volume averaging local strain fields yields a quasi-static SC micromechanical model for VE particulate composites containing coated ellipsoidal inclusions.

The quasi-static model derived in Section 3.2 is limited to the approximation of effective material behavior resulting from a host containing identical spherical or ellipsoidal inclusions which are identically orientated in space. This limitation is addressed in Section 3.3 where the model is generalized by extending the representative volume element to include multiple coated inclusion families, each having identical VE behavior, inclusion geometry, and spatial orientation. This is achieved through a dilute strain concentration tensor (DSCT) approximation scheme. Generalization through DSCT yields a much more flexible model which is capable of accommodating a vast range of materials containing coated inclusions with various VE behaviors, ellipsoidal geometries, and spatial orientation distributions.

8.1.2 Model validation

The quasi-static micromechanical model derived in Chapter III was first validated before attempting implementation of the model as a material design tool. Model validation and application was the aim of Chapter IV. The chapter first compared quasi-static SC estimates to complex bounds from the literature. Comparison with bounds has a two fold purpose. Bounds on the effective behavior of composite materials describe the limits of possible effective material properties based on minimal and maximal energy restrictions. They are dependent on constituent material properties, inclusion geometries,

and the volume fractions of each phase. Disagreement with bounds invalidates a material model as it implies that physical laws have been violated during model derivation. For this reason, verification that a proposed effective medium theory (EMT) falls within accepted bounds is a first order check of model validity. The second purpose for comparison with bounds is to check model optimality. Because bounds are derived based on upper and lower energy restrictions, the closer a model approximation lies upper or lower bounds, the closer that model is to describing optimal behavior due to phase composition, inclusion geometry, inclusion orientation, or any combination of these factors. The quasi-static SC model was compared with three specific complex bounding methods taken from the literature for these reasons. Section 4.2 clearly shows that the three phase model falls within the bounds proposed by Roscoe [137, 138] as a function of frequency and inclusion volume fraction. The two-phase isotropic SC model was then successfully compared with the variational and translational bounds for complex shear and bulk modulus introduced by Gibiansky and Lakes [144] and Milton and Berryman [143], respectively. This study validates the derivation given in Chapter III as well as the implementation of the resulting model in the quasi-static frequency domain.

8.1.2.1 Homogenization of composites containing oriented ellipsoidal inclusions

Section 4.3.2 employed the SC model to evaluate the effective VE constants of an isotropic VE matrix containing coated, ellipsoidal elastic inclusions. The lossy behavior of the resulting anisotropic composite was captured by introducing complex frequency dependent matrix material moduli. The section investigated the effects of constituent

phase properties, inclusion orientation, and inclusion aspect ratios through a series of parametric studies and comparison with experiment.

This validation step first investigated the transmission loss (TL) of a plane wave normally incident on a slab of VE composite submerged in water for oblate, coated, inclusions with aspects ratios ranging from 1.0 (spherical) to 2.5. For the range of material properties used, the effect of the inclusion geometry on the TL was modest, less than 2 dB, but agreement with the spherical inclusion approximation and experimental data taken from Baird *et al* [26] was good. Next, the variation of plane-wave attenuation coefficient was studied as a function of inclusion orientation angle for the same constituent material properties presented in the TL study. Directional dependence in accordance with the physical dissipation mechanisms were shown to be captured by the quasi-static SC model. The complex effective sound speed of the material was then evaluated as a function of frequency, constituent properties, and volume fraction. The effects of different inclusion geometries such as penny-shaped, needle-shaped, oblate, and prolate have also been studied. The results of all these studies clearly showed that the quasi-static SC model predicts directional variations of composite material lossy behavior induced by aligned ellipsoidal inclusions. The given calculations and discussion of Section 4.3.2 further verify that the quasi-static micromechanical model allows for a level of generality in modeling of lossy composites where scattering based approaches are limited. As such, it is possible that it could be a useful tool in the design of new anisotropic damping materials for numerous applications, including cases where the anisotropy of such materials is induced due to loading conditions or manufacturing processes.

8.1.2.2 Homogenization through DSCT formulation: Orientation distribution, multiple scale modeling, and coating thickness variations

The next validation step presented was an inspection of the quasi-static DSCT SC model. The SC model was modified in Section 3.3 though dilute strain concentration tensor formulation in order to allow for the approximation of the effective properties of composites with many disparate coated-inclusion properties, geometries, and orientation distributions. To illustrate the improved modeling flexibility of the DSCT formulation, several cases studies were presented in Sections 4.3.3, 4.3.4, and 4.3.5. Section 4.3.3.1 showed that DSCT SC approximation of the lossy properties of globally isotropic composites containing uniform orientation distributions of ellipsoidal inclusions has good qualitative agreement with a model proposed by Berryman [27]. The formulation was then shown in Section 4.3.3.2 to capture the effects of varying the orientational preference of ellipsoidal inclusions through a parametric study of the compressional wave attenuation coefficient of a bi-phase lossy composite. This is verified by comparison with experiment in Section 4.3.3.3. That section showed, through comparison with experimental values from Hornby *et al* [29], that the DSCT SC model has the ability to accurately homogenize composites containing multiple inclusion types together with preferential orientations of select inclusion phases. In Section 4.3.4, the multi-scale capability of the DSCT SC model was illustrated. A SiC-Al composite studied be Ledbetter and Datta [30] was idealized as consisting of three distinct length scales. The effective stiffness coefficients calculated using this formulation were shown to have good

agreement with experimental values. In both Sections 4.3.3.3 and 4.3.4.1 another strength of the coated-inclusion DSCT SC formulation was indicated, that being the simple extension to the form of a generalized SC model for bi-phase composites. The GSC scheme shows slight improvements of approximation without adding modeling difficulty. Finally, the DSCT SC model was shown capable of improving the accuracy of TL approximations for a previously studied composite [26, 38, 150] by taking variations in inclusion coating thickness into account. The comparisons detailed above illustrate the flexibility and level of generality achievable using the quasi-static DSCT SC model. The model is not without its drawbacks, however, and several points of caution must be addressed. First, it is known that SC models can display some numerical instability due to its implicit form. This drawback with respect to this particular model has been discussed at length and must be considered when modeling composites with high contrast phases. Another drawback of the model, which is also linked to its implicit nature, are the singularities observed in the imaginary part of the complex wavenumber around the threshold of rigidity for high contrast composites. With these drawbacks in mind, the level of achievable generality and accuracy of the DSCT SC model detailed above far outweigh these negative aspects in most cases. Indeed, given the ability of this formulation to capture the effects of such complex material microstructure in the static and quasi-static regimes, it is an ideal candidate for materials design studies for damping applications.

8.1.3 Implementation of the SC model as a material design tool

Chapter V investigated quasi-static SC model implementation as a material design tool by presenting and studying the damping behavior of a multi-scale structure. The aim of this chapter was to provide an introductory level example of quasi-static SC model implementation in the design of a lossy structure. This was accomplished by studying the damping properties of a simple structure: a vibrating constrained sandwich plate. A vibrating sandwich plate was chosen to represent an automobile windshield, a common structural element. Such a choice clearly shows practical implementation and the potential wide-range impact of the materials design approach. This study provided preliminary insight into the role the quasi-static SC model can play in a material design strategy and laid the groundwork for more detailed research.

A constrained sandwich plate was idealized as consisting of four distinct length scales. These length scales are, from shortest to longest: (*i*) the constituent material microstructure, (*ii*) the macroscopic plate material, (*iii*) the structural element, and (*iv*) the constrained structure. The lossy behavior of this structure was modeled using a nested hierarchy of models where each model was capable of making one or more scale transitions. The lossy behavior of the structure as a whole was approximated by the loss factor of the first mode of vibration calculated for a viscoelastically constrained sandwich plate or beam. Modal analysis was performed via classic methods discussed by Liessa [174]. This study quantified lossy behavior at the highest length scale. Structure level behavior required information about element level behavior in order to make the scale transition from length scales (*iii*) → (*iv*). The structural element of interest to this case study was represented by a sandwich plate and was modeled using a simple constrained layer damping model introduced by Ross, Kerwin, and Ungar (RKU) [31]. This simple

analytic model yielded insight into lossy sandwich plate behavior based on constituent plate layer material behavior and geometry. The RKU model was successfully employed to model the effective sandwich plate behavior as a function of frequency and made the scale transition from macroscopic plate materials and geometry to structural element, represented as length scales (*ii*) → (*iii*). The final model employed was the SC model which has already been discussed in detail and which performed the scale transition from constituent material microstructure to macroscopic material behavior, length scales (*i*) → (*ii*). This section showed that the SC model gives added design variables, design flexibility, and behavioral insight to the design process. The multi-scale structural behavior approximation via the nested hierarchy of models approach was verified by comparing results calculated for a viscoelastically constrained vibrating sandwich beam with finite element approximations that employed a model proposed by Daya and Potier-Ferry [166].

The case study presented next employed the SC model to enhance part and structural level damping capacity. The aim of this study was to quantify the effects of microstructural variations on part and structural damping properties. This was done by studying the effect of voiding the sandwich plate VE interlayer. The first effect of voiding the VE interlayer inspected was its influence on the damping properties of the structural element length scale. 5 – 10% increases in sandwich plate damping capacity, measured by amplitude attenuation per flexural wavelength, $\hat{\alpha}^{flex}/\hat{k}^{flex,'}$, were shown for interlayer void fractions of 10% or less. Though this is significant, the effects observed at the structural length scale were marginal. Calculations of circular sandwich plate modal loss factor showed a quadratic dependence on void fraction, but the magnitude of

this influence was minimal. Indeed, 10% interlayer void fraction was only shown to increase modal loss factor by ~2% over the non-voided interlayer case while the sandwich plate suffers a simultaneous significant reduction in flexural resistance upon introduction of voids. The effects of interlayer void fraction was also inspected via the frequency dependent TL of the sandwich plate using the nest multi-scale modeling approach coupled with fundamental acoustic relationships given by Pierce [32]. Interlayer voiding showed minimal TL improvement at coincidence. The improvement calculated was merely 2 *dB*, a level almost imperceptible to human hearing. Though the modeling approach was validated by this case study and microstructural influence was observed to propagate through lengths scales, these results were discouraging in terms of design benefit.

Fortunately, new research suggests that very small volume fractions of instable inclusions yield extreme increases in macroscopic damping behavior [18, 19, 21]. The set of material models was therefore solicited to approximate windshield TL for a sandwich plate whose interlayer contained trace amounts of a hypothetical instable material. The results of this multi-scale study showed the propagation of these microstructural variations through multiple length scales finally manifesting in very effective increases in structural level damping. Additions of only 1% instable inclusions nearly removed the TL coincidence notch, and 4% inclusions were shown completely damp coincidence phenomena. Though the material studied was hypothetical, such broadband material damping have been experimentally observed by Lakes *et al* [19, 21], and these results are therefore very encouraging for the design of high loss materials.

8.1.3.1 Integration of micromechanical model and a compromise decision support protocol

Top-down material design represents a very promising approach to material design. One such top-down approach is known as decision based design (DBD). Chapter VI employed a specific form of DBD, known as compromise decision support protocol (CDSP) to design materials for optimal performance of the automobile windshield discussed in Chapter V. The top-down CDSP approach gives a well-defined structure to efficiently solve the inverse problem of specifying material microstructure based on properties needed to fulfill design requirements. The specified design requirements were to improve its acoustic performance while simultaneously reducing weight and minimally reducing in-plane stiffness. The analysis served two purposes. First, the results shed light on sub-microscale behavior and structure that lead to significant enhancements of the macroscopic material damping. Second, the results validated the integration of a top-down design methodology and micromechanical techniques to concurrently design structures and their constituent materials. Some key design results issuing from the CDSP-SC model integration are listed below.

- ~70% of trial configurations yield superior performance to a standard windshield.
- ≤ 1% negative stiffness heterogeneities are required in each layer to achieve this improved performance.

- Up to 11 dB increase in *TL* at 4 kHz is predicted. (A 10 dB drop in sound pressure level is roughly equivalent to the difference in noise level between busy traffic and that of a two person conversation.)
- On average the in-plane stiffness is increased by 17%. Increased in-plane stiffness permits a decreased total thickness and, in turn, decreased weight. Weight reduction is a key thrust for increased automobile fuel efficiency.
- On average the coincidence moved from 4 kHz → 2.3 kHz. This leads to a significant decrease in the perceived sound transmission.

Chapter VI of this thesis achieved several different goals. Foremost it has detailed a successful integration of micromechanical modeling and a CDSP design methodology. It also resulted in the creation of a simple, interactive, design tool to carry out a calculation strategy to explore the windshield design space. This serves as a concrete illustration of the ability to employ tools from both the field of mechanical design and material modeling to explore the design space of a material. Furthermore, the design results provide specific microstructural variable values, the acceptable variability of those variables, the associated system performance, and confidence intervals for achievement of those performance indices. Chapter VI represents a significant contribution as it gives researchers who are trying to enhance lossy material behavior a much more specific set of target variables, some expected outcomes, and a methodology to further explore the design space.

8.1.4 Understanding and employing negative stiffness behavior

The most striking result of the studies presented in Chapters V and VI is the unmistakably important influence negative stiffness behavior has on macroscopic damping and stiffness. However, material and structural behavior characterized as displaying negative stiffness is complex. The mechanisms governing its influence on the overall behavior of multiscale materials are not generally understood. Chapter VII aimed to explain the intriguing behavior manifest by composites materials containing negative stiffness materials by investigating material behavior at one of its foundations: thermodynamics. The chapter clearly showed that negative stiffness behavior stems from an elevated thermodynamic energy state and the tendency of the system to lower its internal energy. It also showed that any system displaying a non-monotonic force versus displacement curve will display negative stiffness. Further research showed that negative stiffness usually exists as a transient, resulting from state switching between two bistable configurations, but that it can be constrained by a surrounding positive stiffness. The chapter concluded by proposing and discussing two promising avenues to create negative stiffness inclusions. The proposals are relatively simple, but well thought out, attempts to implement the observations from the beginning of the chapter in order to produce useful inclusions to improve the absorptive capacity of a material.

Although understanding the many different mechanisms leading to negative stiffness behavior and how to employ it is far from trivial, that understanding is of crucial importance. Indeed, a firm understanding of negative stiffness behavior and how to *practically* implement it is the gateway to the creation of materials exhibiting desirable

extremal behavior such as an elevated capacity to absorb energy: the focus of this work. The significant improvement in the performance of an automobile windshield predicted in Chapter VI is but one minor example of the plethora of structures that could be improved by the creating negative stiffness composites. Related work by other authors have shown that included phases with negative stiffness may also lead to extremal behavior with respect to macroscopic stiffness [186], thermal expansion, and piezoelectricity [219]. All of these results magnify the impetus to research the creation of materials having mechanisms that produce negative stiffness behavior. Chapter VII demonstrated that the ability to create composites containing negative stiffness heterogeneities for practical application is therefore an open, very active, and important area of research. The insight gained by searching to understand and implement mechanisms displaying negative stiffness will directly influence the creation of a generation of materials displaying previously unattainable property combinations.

8.2 Contributions

In summary, the original contributions that were made through the present thesis are:

1. Extension of the self-consistent model introduced by Cherkaoui *et al* [23, 24] to the quasi-static frequency regime and its generalization using dilute strain concentration tensors to the case of random or preferential distribution (coating thickness and orientation) of micro-inclusions. Model validated against elastic and acoustic experimental data and checked against known bounding techniques.

2. Implementation of the mean-field self-consistent model as a tool in a compromise decision support protocol to tackle a real-world multiple scale problem: a study of the influence of microscale material behavior and geometry on the macroscopic performance of an automobile windshield.

3. Detailed study of unstable material behavior (negative mechanical stiffness), its causal mechanisms, and its remarkable effects on the macroscopic damping properties of viscoelastic composites.

The publications that resulted from this work are listed in Appendix J. These contributions are important in the general areas of constitutive viscoelastic composite material modeling and the active field of materials design. The details of contribution (1) can be found in Chapters III and IV and is summarize in Sections 8.1.1 and 8.1.2 of this general conclusion and in references [38, 130, 150]. Contributions (2) and (3) are detailed chiefly in Chapter VI. Chapter VII also contains significant information regarding the fundamental mechanisms of negative stiffness behavior. A summary of the results pertinent to these contributions can also be found in Sections 8.1.3 and 8.1.4 of this conclusion.

8.3 Perspectives and suggestions for future work

The results developed in this thesis contribute to a better understanding of materials design. Mean-field models can be overlooked in the design process as they are only capable of describing a material as a function of volumetric microstructural measures (volume fraction, average aspect ratios, and average orientation distribution). However, this work has shown that mean field micromechanical models are very effective material design tools. They are easily incorporated into system design

strategies, such as the CDSP, via a nested hierarchy of models and deliver a significant amount of information regarding microstructural variables and their influence on structural performance. Specifically, the approach employed in Chapter VI gives considerable information and freedom to the design process and represents a significant step towards the integration of materials design into the overall design of any structure. Further, Chapter VII has shown that the results of integrating mean-field models into a top down design approach can yield tremendous insight into the discovery of microscale mechanisms to enhance overall performance. Indeed, the robust quasi-static self-consistent model derived, developed, and validated in this thesis has been shown to enhance knowledge of absorptive behavior as well as and the influence of microstructural behavior on damping at macroscopic, elemental, and structural length scales. This work has therefore given promising results which encourage the future development and integration of micromechanical tools for material design.

8.3.1 Suggestions for future work

It has been previously noted that the domain of materials design is rich for study. Future research in this domain could include a vast range of areas including the study of overarching design strategies, incorporation of fabrication processes and variability, studies of computationally efficient design, the design of collaborative systems, nano→micro scale modeling, and molecular dynamics and quantum approximations of sub-continuum material behavior. Specific to the design of absorptive materials discussed in this thesis, it has been noted that the most important factors influencing lossy

material behavior response is the inclusion/matrix shear modulus ratio and the volume fraction of negative stiffness inclusions in the matrix. Overall performance is, therefore, very sensitive to variations in inclusion stiffness and volume fraction of the stiffness. One rich open research area involves solving the problem of finding design solutions using non-optimal CDSP design stragies, such as the robust CDSP design methodology, to enhance overall mechanical and acoustic properties. Other suggestions for future research given here touch on effective medium theory improvement for wave propagation applications but are more specifically concerned with furthering the understanding and implementation of negative stiffness behavior. Yet another very exciting area of research where improvements in coupled material modeling and material design can have a significant impact is that of the *design of biomaterials*. The tools introduced and validated in this thesis have undeniable applicability to the design of materials for biological applications which also require materials conceived for specific applications which require the satisfaction of multiple objectives.

8.3.1.1 Effective medium theories for wave propagation

One limitation of the micromechanical model presented in this thesis is its limitation to quasi-static applications. This problem is specifically important when investigating wave propagation applications where the quasi-static approximation is no longer valid. This problem could be addressed using an approach similar to the micromechanical approach presented by this thesis without neglecting inertial terms in the first stages of model development. This is not a trivial modeling problem. Successful

evaluation of this problem would, however, yield a model capable of approximating both quasi-static and non-quasi-static material behavior while maintaining the generality of the quasi-static SC model presented in this work.

8.3.1.2 Negative stiffness, micro- and sub-microscale bistability

This work has clearly shown that micro- and sub-microscale instabilities represent an exciting mechanism to elicit extremal material behavior. However, the materials exhibiting this behavior are very rare and usually very impractical for broad application. For this reason it is of utmost interest to determine methods to *design* materials and structures that exhibit this behavior. Chapter VII gave a detailed description of the fundamental behavior which much be replicated and exploited to produce negative stiffness. It also made several inclusion design suggestions to achieve negative stiffness behavior. The remainder of this chapter discusses these proposals and poses some salient research questions which must be considered.

One promising, but little investigated and highly theoretical, area of negative stiffness research involves the study of material nanostructures and nanoparticle embedding which lead to domains of negative stiffness in an otherwise homogeneous material. Examples include preliminary research conducted by Yoshimoto *et al* [206] and Papakonstantopoulos *et al* [218]. Yoshimoto *et al* investigated the effects of nanostructure of polymer glasses while Papakonstantopouls *et al* studied the effects of nanoparticle potentials on the local properties of nanocomposites. Both works employed molecular dynamics simulations to investigate local mechanical properties of their

respective materials and found regions of negative stiffness. They employed Lennard-Jones potential functions and calculated local mechanical properties using techniques introduced by Lutsko [235] which were later augmented by Yoshimoto *et al* [236]. These two studies suggest that negative stiffness regions can be induced in a material that has the proper nanostructure. The ability to make homogeneous materials containing negative stiffness domains through processing techniques is extremely appealing for many reasons. Most importantly, however, is the fact that homogeneous materials with negative stiffness domains are not prone to the same types of failures, such as matrix-inclusion debonding and poor fatigue performance, as heterogeneous materials. Based on the research discussed about, three very obvious research questions can be formulated:

1. What is the affect of nanoscale negative stiffness regions on macroscopic damping and stiffness? How can they be quantified with respect to the nanostructure?
2. Is it possible to make such materials and exploit their advantageous damping and stiffness behavior? How?
3. Do any other possible nanostructures or nanocomposites induce negative stiffness regions?

These open questions are very intriguing from both theoretical and practical standpoints with potential for significant impact for a broad range of applications.

A second very interesting, though equally theoretical area of research concerns the creation of inclusions containing buckled nanotubes. Theoretical studies by Yakobson *et al* [238] suggest that the post-buckled behavior of nanotubes displays non-monotonic force versus displacement behavior. Further, nanotubes are known to undergo reversible buckling without permanent damage [239]. Successful creation of real

inclusions using buckled nanotubes, however requires a significant amount of research in many fields. Three pertinent research questions associated with determining the feasibility of using buckled nanotubes as the sources of negative stiffness are given below.

1. How can nanotubes be manipulated and their force versus displacement relationship measured?
2. Can nanotubes be processed or grown in a way that buckled tubes create single "inclusions" displaying non-montonic stress-strain curves?
3. How can buckled nanotubes be included into a matrix material in such a manner that their non-monotonic behavior can be employed to enhance macroscopic damping and strength?

The last promising and more immediately accessible research area concerns the construction of bistable microscale structures using MEMS technology. Bistable structures promise broadband negative stiffness behavior with little temperature dependence and low activities. Below are several important research questions regarding the creation of these negative stiffness "materials."

1. What materials and processes can be identified which permit reliable creation of bistable tubular inclusions?
2. How can finite element analysis be leveraged to determine the key parameters such as tube wall profile, axial load, and material properties that ensure only axis-symmetric buckling modes will be activated?
3. What procedures can be created to determine the effective stiffness tensor of a post-buckled thin walled tube? *i.e.* how can a meta-model be constructed for buckled microtube that can be implemented in material design? Are negative moduli sufficient for design purposes to capture the physical processes taking place at the microscale for this type of structure?

4. What processes, material properties, and geometries minimize the activation energy required to elicit negative stiffness behavior?

5. How can the bistable structure be bonded to the viscoelastic matrix in such a way that high amplitude strains evoked during snap through do not cause debonding?

6. Do high strain amplitudes damage the matrix material via crack initiation or otherwise?

Answering all of these research questions regarding the design of negative stiffness inclusions and materials presents many formidable challenges. However, their answers promise vast insight into the creation of materials with extraordinary damping and stiffness properties. The significant improvement in the performance of an automobile windshield is but one clear example of the multitude of structures that could be improved through the creation of negative stiffness composites.

APPENDIX A

EVALUATION OF MODIFIED GREEN'S TENSORS

Implementation of the mean-field micro-electromechanical modeling techniques requires the numerical approximation of the integration of modified Green's tensors. The Green's tensors describe the fields of displacement and electric potential when the surrounding matrix is anisotropic (this includes cases when the actual material phases are anisotropic or when the inclusions are ellipsoidal and oriented). Numerical evaluation is accomplished via Fourier transform (FT) techniques as explained by Berveiller *et al* [71]. For evaluation using the FT technique, the assumption is made that the displacement field caused by the presence of the inclusion can be represented by the superposition of an infinite sum of spatially regular fields. This assumption, by the very nature of the FT, implies that the spacing of inclusions is regular. Though this can be a gross estimate, the method has been proven to provide very good approximations to true composite material behavior [54]. Simply stated, the technique involves using the Fourier integral to transform the ellipsoidal heterogeneity into a sphere in Fourier domain (where the transform variable is the "wavenumber" of the spatial regularity of the strain field in an infinite homogeneous medium resulting from the presence of inclusions). The

transformation allows for numerical evaluation of volume and surface integrals using numerical techniques to evaluate Eqs. (A.1.1)-(A.1.4). The integrals of interest are:

$$T^I_{ijkl}\left(\mathbf{C}^X\right) = \frac{1}{V_I}\int_{V_I}\int_{V_I}\Gamma^X_{ijkl}\left(\mathbf{r}-\mathbf{r}'\right)d\mathbf{r}'d\mathbf{r} \tag{A.1.1}$$

$$t^I_{ij}\left(\mathbf{C}^X\right) = \frac{1}{V_I}\int_{V_I}\int_{V_I}\gamma^X_{ij}\left(\mathbf{r}-\mathbf{r}'\right)d\mathbf{r}'d\mathbf{r} \tag{A.1.2}$$

$$B^I_{ijk}\left(\mathbf{C}^X\right) = \frac{1}{V_I}\int_{V_I}\int_{S_I}G^X_{ij,k}\left(\mathbf{r}-\mathbf{r}'\right)d\mathbf{r}'d\mathbf{r} \tag{A.1.3}$$

$$b^I_{ij}\left(\boldsymbol{\kappa}^X\right) = \frac{1}{V_I}\int_{V_I}\int_{S_I}g^X_{,i}\left(\mathbf{r}-\mathbf{r}'\right)n_j\left(\mathbf{r}'\right)d\mathbf{r}'d\mathbf{r} \tag{A.1.4}$$

A.1 Derivation of $\mathbf{T^I(C^X)}$

The fourth order tensor, $T^I_{ijkl}\left(\mathbf{C}^X\right)$, is the volume average of the volume integral of the modified Green's Tensor, $\Gamma_{ijkl}\left(\mathbf{r}-\mathbf{r}'\right)$ defined by Eq. (A.1.1). Numerical evaluation of this tensor greatly simplifies implementation of the any mean-field micromechanical model when the material surrounding heterogeneities is anisotropic or preferentially oriented ellipsoidal inclusions induce macroscopic anisotropy. First, let the Fourier transform of the Green's tensor in the reference material *X* and its inverse be defined as follows:

$$\tilde{G}_{km}^{X}\left(\vec{k}\right)=\int_{-\infty}^{\infty}G_{km}^{X}\left(\vec{r}\right)e^{i\vec{k}\cdot\vec{r}}d\vec{r}$$
$$G_{km}^{X}\left(\vec{r}\right)=\frac{1}{\left(2\pi\right)^{3}}\int_{-\infty}^{\infty}\tilde{G}_{km}^{X}\left(\vec{k}\right)e^{-i\vec{k}\cdot\vec{r}}d\vec{k} \tag{A.1.5}$$

where the vector $\vec{k}$ is the Fourier variable that represents the periodicity of the displacement (and therefore strain) field in an infinite homogeneous medium due to the presence of the material heterogeneity. This variable is analogous to the wavenumber in wave propagation problems. From the derivation of the effective material properties, it is known that the Green's tensor must satisfy the differential equation given in Eq. (A.1.6).

$$C_{ijkl}^{X}G_{km,lj}^{X}\left(\mathbf{r}-\mathbf{r}'\right)+\delta_{im}\delta\left(\mathbf{r}-\mathbf{r}'\right)=0 \tag{A.1.6}$$

Applying the Fourier transform to Eq. (A.1.6) gives Eq. (A.1.7).

$$C_{ijkl}^{X}k_{l}k_{j}\tilde{G}_{km}^{X}\left(\vec{k}\right)=\delta_{im} \tag{A.1.7}$$

It is convenient to define elements of the vector $\vec{k}$ using spherical coordinate convention shown in Figure A.1 using Eq. (A.1.8).

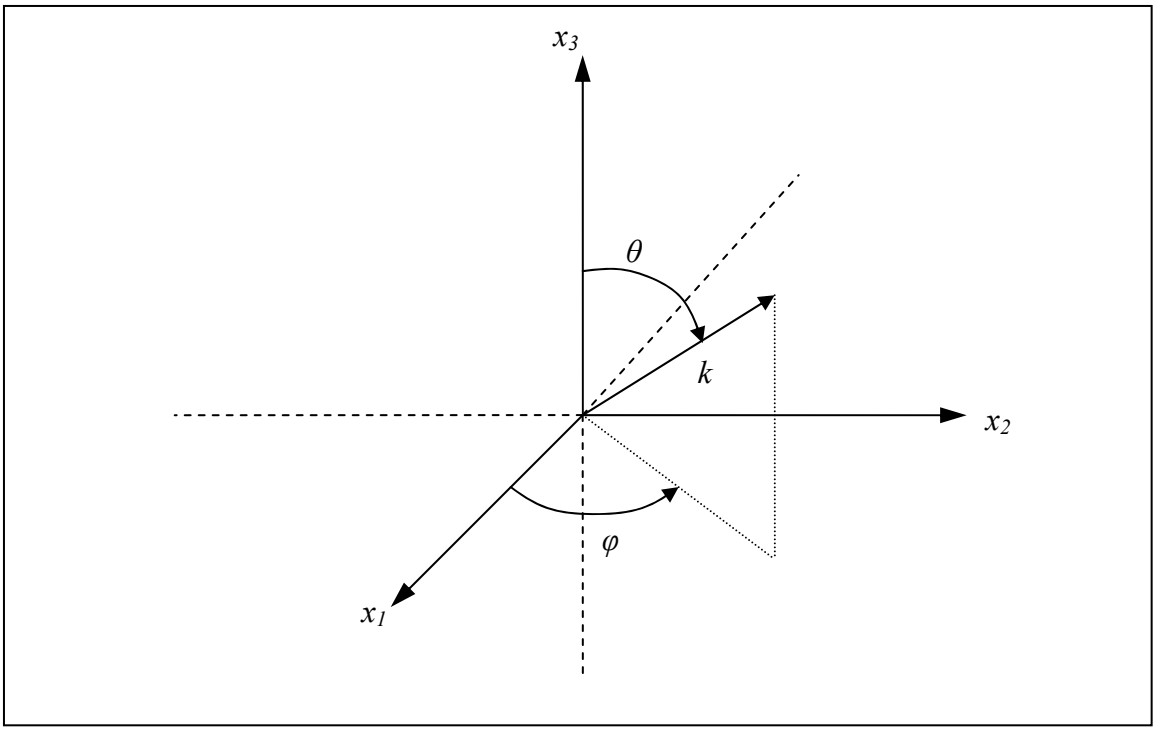

Figure A.1: Spherical coordinate convention employed for Green's tensor evaluation.

$$\vec{k} \;=\; \begin{Bmatrix} k_1 \\ k_2 \\ k_3 \end{Bmatrix} \;=\; k \begin{Bmatrix} \sin\theta\cos\varphi \\ \sin\theta\sin\varphi \\ \cos\theta \end{Bmatrix} = k\vec{\chi} \qquad \text{(A.1.8)}$$

Where k is the wavenumber magnitude and the elements of the vector in the far right-hand side of Eq. (A.1.8) are the direction cosines, defined for $\theta \in [0,\pi]$, $\varphi \in [0,2\pi]$. The following shows a complete derivation for the numerical evaluation of Eq. (A.1.1) for a spherical inclusion geometry.

A.1.1 Spherical inclusions

The numerical evaluation of $T^I_{ijkl}\left(\mathbf{C}^X\right)$ for the case when inclusions are spherical gives insight to the evaluation of for the ellipsoidal inclusion case. Equation (A.1.9) recalls the expression for the integral of the modified Green's tensor in three different forms.

$$\begin{aligned} T^I_{klmj}\left(\mathbf{C}^X\right) &= \frac{1}{V_I}\int_{V_I}\int_{V_I}\Gamma^X_{klmj}\left(\mathbf{r}-\mathbf{r}'\right)d\mathbf{r}'d\mathbf{r} \\ &= \frac{1}{V_I}\int_{V_I}\int_{V_I}-\frac{1}{2}\left[G^X_{km,lj}\left(\mathbf{r}-\mathbf{r}'\right)+G^X_{lm,kj}\left(\mathbf{r}-\mathbf{r}'\right)\right]d\mathbf{r}'d\mathbf{r} \\ &= \frac{1}{V_I}\left(T^{I,p}_{klmj}+T^{I,p}_{lkmj}\right) \end{aligned} \qquad \text{(A.1.9)}$$

Using the FT and inverse FT of the Green's tensor given in Eq. (A.1.5), Eq. (A.1.9) can be written as follows:

$$T^I_{klmj}=\frac{1}{V_I}\frac{1}{8\pi^3}\int_{V_I}\int_{V_I}-\frac{1}{2}\left\{\int_{-\infty}^{\infty}k_lk_j\tilde{G}^X_{km}\left(\mathbf{k}\right)e^{-i\mathbf{k}\cdot\left(\mathbf{r}-\mathbf{r}'\right)}d\mathbf{k}+\int_{-\infty}^{\infty}k_mk_l\tilde{G}^X_{kj}\left(\mathbf{k}\right)e^{-i\mathbf{k}\cdot\left(\mathbf{r}-\mathbf{r}'\right)}d\mathbf{k}\right\}d\mathbf{r}'d\mathbf{r}$$

(A.1.10)

It is now possible to use Eq. (A.1.10) to arrive at an expression that depends only on the direction cosines and the magnitude of the tensor, M_{km}, defined by the Green's tensor expression given in Eq. (A.1.7).

$$\begin{aligned} M_{ik} &= \chi_l\chi_jC^X_{ijkl} \\ k^2\tilde{G}^X_{km} &= \delta_{im}M^{-1}_{ik} \end{aligned} \qquad \text{(A.1.11)}$$

Each term of Eq. (A.1.10) can now be re-written in terms of M_{km} and direction cosines in the following form:

$$T_{klmj}^{I,p} = -\frac{1}{16\pi^3}\int_{V_I}\int_{V_I}\int_{-\infty}^{\infty} \chi_l \chi_j M_{km}^{-1} e^{-i\mathbf{k}\cdot(\mathbf{r}-\mathbf{r}')} d\mathbf{k} d\mathbf{r}' d\mathbf{r} \tag{A.1.12}$$

Note that the inner product $\mathbf{k}\cdot\mathbf{r} = \mathbf{k}\cdot\mathbf{r}' = kr$ since,

$$\begin{aligned} \mathbf{k}\cdot\mathbf{r} &= kr\left\{\sin^2\theta\cos^2\varphi + \sin^2\theta\sin^2\varphi + \cos^2\theta\right\} \\ &= kr\left\{\sin^2\theta\underbrace{\left(\cos^2\varphi + \sin^2\varphi\right)}_{=1} + \cos^2\theta\right\} \\ &\qquad\qquad\qquad

where the limits of integration for the magnitude of the Fourier variable, k, have changed because spherical coordinates are employed. Evaluating the final integral on the RHS of Eq. (A.1.15) gives:

$$\begin{aligned}\int_{V_I} e^{ikr'}dr' &= \int_0^{\pi}\int_0^{2\pi}\int_0^{a}(r')^2\sin\theta e^{ikr'}dr'd\theta d\varphi \\ &= \frac{4\pi}{k^3}\left\{\begin{array}{l}\left[2ka\cos(ka)+\left((ka)^2-2\right)\sin(ka)\right]+ \\ \quad i\left[-\left((ka)^2-2\right)\cos(ka)+2ka\sin(ka)-2\right]\end{array}\right\}\end{aligned} \tag{A.1.16}$$

It is now important to make several statements regarding this result. The first is the requirement that the result be purely real. This is required as the result for the integral of the modified Green's tensor must first be evaluated for the purely elastic case. Viscoelasticity can then be modeled using the correspondence principle by inserting complex valued stiffness tensors into expressions derived for the purely elastic solution[33]. Therefore, only the real part of Eq. (A.1.16) is conserved. The second observation regards the change of scale and the assumption that the strain in the inclusion is uniform. Due to these restrictions, it is only necessary to retain the lowest order of the non-dimensional variable ka, in other words, all terms of $O(ka)^2$ or higher. Doing so yields a model that is only capable of capturing displacement fields that vary slowly (spatially) in comparison to the inclusion radius, a. This follows the reasoning of Mead[249] which simplified the otherwise unwieldy result given by Kneer[250]. It is also noted that $\mathbb{R}\mathrm{e}\left[\int e^{ikr}d\mathbf{r}\right] = \mathbb{R}\mathrm{e}\left[\int e^{-ikr}d\mathbf{r}\right]$. Substituting the result given in Eq. (A.1.16)

with the above approximations yields the following expression for the product of the final two terms of Eq. (A.1.15).

$$\mathbb{R}\mathrm{e}\left[\int e^{-ikr}d\mathbf{r}\right]\cdot\mathbb{R}\mathrm{e}\left[\int e^{ikr}d\mathbf{r}\right]=\frac{16\pi^2}{k^6}\left\{\sin(ka)-ka\cos(ka)\right\}^2 \qquad \text{(A.1.17)}$$

This expression then must be integrated with respect to the Fourier variable, *k*.

$$\mathbf{Y}=\frac{1}{\pi}\int_0^\infty\left(\frac{1}{k^4}\right)\left\{\sin(ka)-ka\cos(ka)\right\}^2 dk \qquad \text{(A.1.18)}$$

In the above expression **Y** is a constant which includes the leading constant on the RHS of Eq. (A.1.15). The result of this integral is detailed in Eq. (A.1.19)

$$\begin{aligned}\mathbf{Y}&=\frac{1}{\pi}\left\{\frac{1}{6k^3}\left[\left(k^2a^2+1\right)\cos(2ka)-3k^2a^2-1+2k^3a^3Si(2ka)+3ka\sin(ka)\right]\right\}\Bigg|_{k=0}^{k=\infty}\\&=\frac{1}{\pi}\left\{\frac{\pi}{6}a^3\right\}\\&=\frac{a^3}{6}\end{aligned} \qquad \text{(A.1.19)}$$

Note that $Si(x)$ is the sine integral function. The resulting simplified version of Eq. (A.1.15) is then:

$$T_{klmj}^{I,p} = \frac{a^3}{6}\int_0^{\pi}\int_0^{2\pi} \chi_l \chi_j M_{km}^{-1} \sin\theta d\theta d\varphi$$
$$T_{klmj}^{I} = \frac{3}{4\pi a^3}\left(T_{klmj}^{I,p} + T_{lkmj}^{I,p}\right) \tag{A.1.20}$$

Note that the constant $1/V_I$ on the RHS of Eq. (A.1.33) renders $T_{klmj}^{I}\left(\mathbf{C}^X\right)$ a function of the matrix anisotropic material properties alone. Equation (A.1.20) can now be evaluated numerically using *n* point Gauss–Legendre (G-L) quadrature. It has been observed that 9 or 10 point quadrature gives acceptable results. Recall that a double integral, **I**, of any function $f(\theta,\varphi)$ is approximated by G-L quadrature as follows:

$$\mathbf{I} = \int_{\theta_a}^{\theta_b}\int_{\varphi_a}^{\varphi_b} f(\varphi,\theta)\, d\varphi d\theta \approx m_\theta m_\varphi \sum_{i=1}^{n}\sum_{j=1}^{m} w_i^\varphi w_j^\theta f\left(c_\theta + m_\theta t_i^\theta, c_\varphi + m_\varphi t_j^\varphi\right)$$
$$\text{where} \quad \begin{cases} c_x = \frac{1}{2}\left(x_b + x_a\right) \\ m_x = \frac{1}{2}\left(x_b - x_a\right) \end{cases} \tag{A.1.21}$$

Were *x* represents the integration variable θ or φ, the coefficients *c* and *m* appear because of the change of variables requiring $t_{i,j} \in [-1, 1]$, and w_i represents the G-L quadrature weights which can be found in any standard numerical methods text. This numerical evaluation permits the calculation of the $T_{ijkl}^{I}\left(\mathbf{C}^X\right)$ for the case of spherical inclusions embedded in an isotropic or anisotropic matrix. The following section delineates the same approach when inclusions are ellipsoidal.

A.1.2 Ellipsoidal inclusions

Consider the case of an ellipsoidal anisotropic inclusion embedded in an anisotropic host medium. In such a case, it is convenient to introduce the following change of variables:

$$\mathbf{r} = \begin{Bmatrix} x_1 \\ x_2 \\ x_3 \end{Bmatrix} \Rightarrow \mathbf{R} = \begin{Bmatrix} X_1 = x_1 \\ X_2 = \dfrac{a}{b} x_2 \\ X_3 = \dfrac{a}{c} x_3 \end{Bmatrix} \quad \text{and} \quad \mathbf{k} = \begin{Bmatrix} k_1 \\ k_2 \\ k_3 \end{Bmatrix} \Rightarrow \mathbf{K} = \begin{Bmatrix} K_1 = k_1 \\ K_2 = \dfrac{b}{a} k_2 \\ K_3 = \dfrac{c}{a} k_3 \end{Bmatrix} \qquad \text{(A.1.22)}$$

Where a general ellipsoid is shown in Figure A.2.

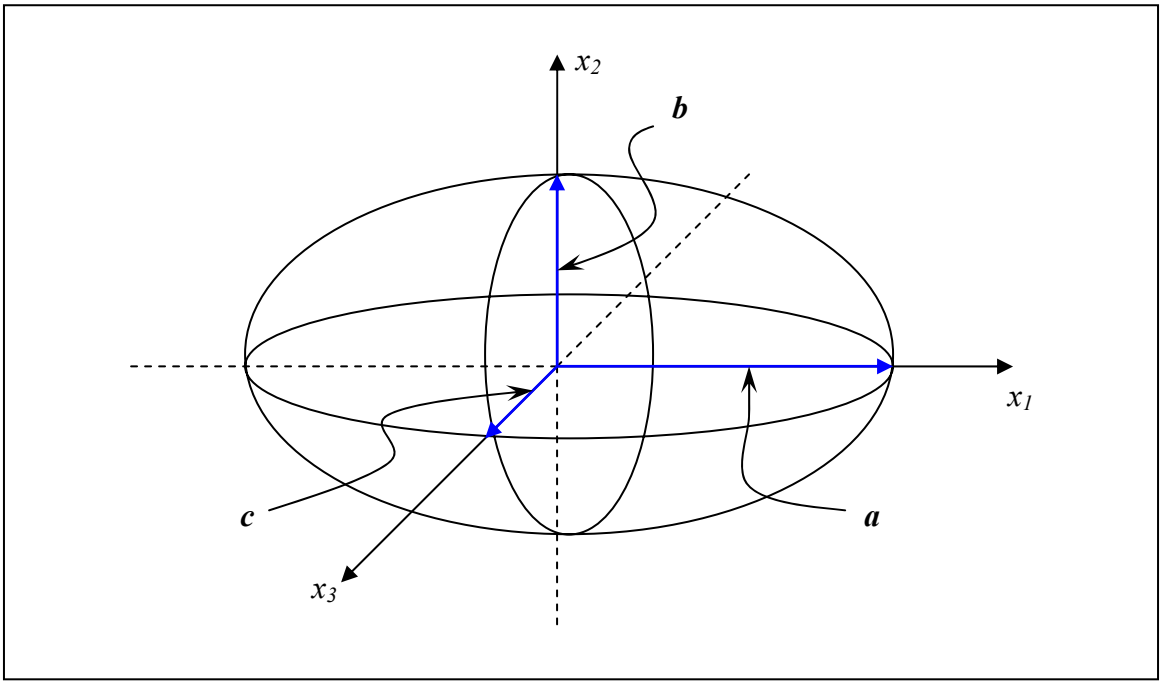

Figure A.2: Ellipsoidal inclusion aligned with its local coordinate system. Minor axes are labeled *a*, *b*, and *c* which are in the x_1, x_2, and x_3 directions, respectively.

This change of variables is useful as the following inner product remains constant

$$\mathbf{k}\cdot\mathbf{r}=\mathbf{K}\cdot\mathbf{R} \tag{A.1.23}$$

The change of variables given in Eq. (A.1.22) can be expressed using Eqs. (A.1.24) and (A.1.25).

$$k_i=\Phi_{ij}K_j \quad \text{where:} \quad \Phi_{ij}=\begin{bmatrix}1 & 0 & 0\\ 0 & \frac{a}{b} & 0\\ 0 & 0 & \frac{a}{c}\end{bmatrix} \tag{A.1.24}$$

$$x_i=\Psi_{ij}X_j \quad \text{where:} \quad \Psi_{ij}=\begin{bmatrix}1 & 0 & 0\\ 0 & \frac{b}{a} & 0\\ 0 & 0 & \frac{c}{a}\end{bmatrix} \tag{A.1.25}$$

It is also important to relate the differential volume elements for the change of variables.

$$d\mathbf{r}=\frac{bc}{a^2}d\mathbf{R};\quad d\mathbf{k}=\frac{a^2}{bc}d\mathbf{K} \tag{A.1.26}$$

Equation (A.1.12) is then written:

$$T_{klmj}^{I,p} = -\frac{1}{16\pi^3}\int_{V_I^t}\int_{V_I^t}\int_{-\infty}^{\infty} \Phi_{lt}K_t\Phi_{ju}K_u\tilde{G}_{km}\left(\mathbf{K}\right)e^{-i\mathbf{K}\cdot\left(\mathbf{R}-\mathbf{R}'\right)}\left(\frac{bc}{a^2}\right)d\mathbf{K}d\mathbf{R}'d\mathbf{R} \quad \text{(A.1.27)}$$

Note that these integrals are performed over the transformed volumes, V_I^t, which is a sphere of radius a. Equation (A.1.7) can then be expressed as for the case of an ellipsoidal inclusion:

$$C_{ijkl}^X K_t\Phi_{lt}K_u\Phi_{ju}\tilde{G}_{km}^X\left(\mathbf{k}\right) = \delta_{im} \quad \text{(A.1.28)}$$

Then, defining $K_i = K\chi_i$, where K is the magnitude and χ_i are the direction cosines, leads to:

$$\begin{aligned} C_{ijkl}^X\Phi_{lt}\Phi_{ju}\chi_t\chi_u &= M_{ki} \\ K^2\tilde{G}_{km}^X &= M_{km}^{-1} \end{aligned} \quad \text{(A.1.29)}$$

which depends only on the direction cosines of the vector K and the stiffness tensor of the host material. Finally, we are left with the relationships given below.

$$T_{klmj}^{I,p} = -\frac{1}{16\pi^3}\frac{bc}{a^2}\int_{V_I^t}\int_{V_I^t}\int_{-\infty}^{\infty} \chi_t\Phi_{lt}\chi_u\Phi_{ju}M_{km}^{-1}e^{-i\mathbf{K}\cdot\left(\mathbf{R}-\mathbf{R}'\right)}d\mathbf{K}d\mathbf{R}'d\mathbf{R} \quad \text{(A.1.30)}$$

Note that the differential volume of the changed of variables are analogous to Eq. (A.1.14):

$$\begin{aligned} d\mathbf{K} &= K^2 \sin\theta d\theta d\varphi dK \\ d\mathbf{R} &= R^2 \sin\theta d\theta d\varphi dR \end{aligned} \tag{A.1.31}$$

Equation (A.1.30) then becomes:

$$T_{klmj}^{I,p} = -\frac{1}{16\pi^3}\frac{bc}{a^2}\int_0^{\pi}\int_0^{2\pi} \chi_t \Phi_{lt} \chi_u \Phi_{ju} M_{km}^{-1} \sin\theta d\varphi d\theta \int_0^{\infty} K^2 dK \int_{V_I^t} e^{-iKR} d\mathbf{R} \int_{V_I^t} e^{iKR'} d\mathbf{R}' \tag{A.1.32}$$

The same approximations and evaluation procedure applies to the last two integrals on the RHS of Eq. (A.1.32) as given in Section A.1.1. The result is the following relation for $t_{ijkl}^{I,p}$, which is equally easily evaluated as for the case of spherical inclusions by using numerical techniques such as G-L quadrature.

$$\begin{aligned} T_{klmj}^{I,p} &= \frac{abc}{6}\int_0^{\pi}\int_0^{2\pi} \chi_t \Phi_{lt} \chi_u \Phi_{ju} M_{km}^{-1} \sin\theta d\varphi d\theta \\ T_{klmj}^{I}\left(\mathbf{C}^X\right) &= \frac{3}{4\pi abc}\left(T_{klmj}^{I,p} + T_{lkmj}^{I,p}\right) \end{aligned} \tag{A.1.33}$$

Note that the constant $1/V_I$ on the RHS of Eq. (A.1.33) renders $T_{klmj}^{I}\left(\mathbf{C}^X\right)$ a function of the matrix anisotropic material properties and the ellipsoidal aspect ratios.

A.2 Evaluation of $\mathbf{t^I(\kappa^X)}$

The second order tensor, $t_{ij}^{I}\left(\kappa^{X}\right)$, is the volume integral of the integral over the inclusion volume of the modified Green's function, $\gamma_{ij}\left(\mathbf{r}-\mathbf{r}'\right)$ defined by Eq. (A.1.2). The evaluation of this tensor using numerical techniques is developed analogously to the development of the fourth order tensor $T_{ijkl}^{I}\left(\mathbf{C}^{X}\right)$ discussed in Section A.1. As with $T_{ijkl}^{I}\left(\mathbf{C}^{X}\right)$, numerical evaluation of $t_{ij}^{I}\left(\kappa^{X}\right)$ greatly simplifies the implementation of any mean-field micro-electromechanical model when the material surrounding heterogeneities is anisotropic or preferentially oriented ellipsoidal inclusion induce macroscopic anisotropy. First, let the Fourier transform of the Green's function in the reference material *X* and its inverse be defined as follows:

$$\begin{aligned}\tilde{g}^{X}\left(\vec{k}\right) &= \int_{-\infty}^{\infty} g^{X}\left(\vec{r}\right) e^{i\vec{k}\cdot\vec{r}}\, d\vec{r} \\ g^{X}\left(\vec{r}\right) &= \frac{1}{\left(2\pi\right)^{3}} \int_{-\infty}^{\infty} \tilde{g}^{X}\left(\vec{k}\right) e^{-i\vec{k}\cdot\vec{r}}\, d\vec{k}\end{aligned} \tag{A.2.1}$$

Here the vector $\vec{k}$ is the Fourier variable that represents the periodicity of the electric potential (and therefore electric field) in an infinite homogeneous medium due to the presence of the deposited charge. This variable is analogous to the wavenumber in wave propagation. From the derivation of the effective material properties, it is known that the Green's function must satisfy the differential equation given in Eq. (A.2.2).

$$\kappa_{ij}^{X} g_{,ji}^{X}\left(\mathbf{r}-\mathbf{r}'\right)+\delta\left(\mathbf{r}-\mathbf{r}'\right)=0 \tag{A.2.2}$$

Applying the Fourier transform to Eq. (A.2.2) give expression (A.2.3).

$$\kappa_{ij}^{X} k_j k_i \tilde{g}^{X}\left(\vec{k}\right)=1 \tag{A.2.3}$$

The vector $\vec{k}$ is defined in spherical coordinates according to the convention shown in Figure A.1 of the previous section and related to the Cartesian system with Eq. (A.1.8). Section A.2.3 derives a method to numerically evaluate Eq. (A.1.2) for a spherical inclusion.

A.2.3 Spherical inclusions

Equation (A.2.4) recalls the expression for the integral of the modified Green's function in three different forms.

$$\begin{aligned} t_{ij}^{I}\left(\kappa^{X}\right) &= \frac{1}{V_I}\int_{V_I}\int_{V_I}\gamma_{ij}^{X}\left(\mathbf{r}-\mathbf{r}'\right)d\mathbf{r}'d\mathbf{r} \\ &= \frac{1}{V_I}\int_{V_I}\int_{V_I}-\frac{1}{2}\left[g_{,ij}^{X}\left(\mathbf{r}-\mathbf{r}'\right)+g_{,ji}^{X}\left(\mathbf{r}-\mathbf{r}'\right)\right]d\mathbf{r}'d\mathbf{r} \\ &= \frac{1}{V_I}\left(t_{ij}^{I,p}+t_{ji}^{I,p}\right) \end{aligned} \tag{A.2.4}$$

Using the FT and inverse FT of the Green's function given in Eq. (A.2.1), Eq. (A.2.4) can be written as follows:

$$t_{ij}^{I} = \frac{1}{V_I}\frac{1}{8\pi^3}\int_{V_I}\int_{V_I} -\frac{1}{2}\left\{\int_{-\infty}^{\infty} k_i k_j\left(\mathbf{k}\right)e^{-i\mathbf{k}\cdot(\mathbf{r}-\mathbf{r}')}d\mathbf{k} + \int_{-\infty}^{\infty} k_j k_i \tilde{g}^{X}\left(\mathbf{k}\right)e^{-i\mathbf{k}\cdot(\mathbf{r}-\mathbf{r}')}d\mathbf{k}\right\} d\mathbf{r}'\, d\mathbf{r} \quad \text{(A.2.5)}$$

It is now possible to use Eq. (A.2.5) to arrive at an expression that depends only on the direction cosines and the magnitude of the scalar value, *m*, defined by the Green's function expression given in Eq. (A.2.3).

$$\begin{aligned} m &= \chi_i \chi_j \kappa_{ij}^{X} \\ k^2 \tilde{g}^{X} &= m^{-1} \end{aligned} \quad \text{(A.2.6)}$$

Each term of Eq. (A.2.5) can now be re-written in terms of *m* and direction cosines in the following form:

$$t_{ij}^{I,p} = -\frac{1}{16\pi^3}\int_{V_I}\int_{V_I}\int_{-\infty}^{\infty} \chi_i \chi_j m^{-1} e^{-i\mathbf{k}\cdot(\mathbf{r}-\mathbf{r}')}d\mathbf{k}d\mathbf{r}'\,d\mathbf{r} \quad \text{(A.2.7)}$$

Note that the inner product $\mathbf{k}\cdot\mathbf{r} = \mathbf{k}\cdot\mathbf{r}' = kr$ since,

$$\mathbf{k}\cdot\mathbf{r} = kr\left\{\sin^2\theta\cos^2\varphi + \sin^2\theta\sin^2\varphi + \cos^2\theta\right\}$$
$$= kr\left\{\underbrace{\sin^2\theta\underbrace{\left(\cos^2\varphi + \sin^2\varphi\right)}_{=1} + \cos^2\theta}_{=1}\right\} \tag{A.2.8}$$

and that the following describes the differential volume elements $d\mathbf{k}$ and $d\mathbf{r}$:

$$d\mathbf{k} = k^2\sin\theta\ dk\ d\theta\ d\varphi$$
$$d\mathbf{r} = r^2\sin\theta\ dr\ d\theta\ d\varphi \tag{A.2.9}$$

Expanding (A.2.7) gives:

$$t_{ij}^{I,p} = -\frac{1}{16\pi^3}\int_0^{\pi}\int_0^{2\pi}\chi_i\chi_j m^{-1}\sin\theta d\varphi d\theta\int_0^{\infty}k^2 dk\int_{V_I}e^{-ikr}d\mathbf{r}\int_{V_I}e^{ikr'}d\mathbf{r}' \tag{A.2.10}$$

where the limits of integration for the magnitude of the Fourier variable, k, have changed because spherical coordinates are employed. Evaluating the final integral on the RHS of Eq. (A.1.15) gives:

$$\int_{V_I}e^{ikr'}dr' = \int_0^{\pi}\int_0^{2\pi}\int_0^{a}(r')^2\sin\theta e^{ikr'}dr'd\theta d\varphi$$
$$= \frac{4\pi}{k^3}\left\{\begin{array}{l}\left[2ka\cos(ka) + \left((ka)^2 - 2\right)\sin(ka)\right] + \\ \qquad i\left[-\left((ka)^2 - 2\right)\cos(ka) + 2ka\sin(ka) - 2\right]\end{array}\right\} \tag{A.2.11}$$

It is noted that the exact same arguments regarding the size of the non-dimensional variable *ka* apply for the electrostatic case for the change of scale involved in micro → macroscopic averaging as discussed at length in Section A.1.1 for the simplification of Eq. (A.1.16). The resulting version of Eq. (A.2.10) is then:

$$\begin{aligned} t_{ij}^{I,p} &= \frac{a^3}{6}\int_0^{\pi}\int_0^{2\pi} \chi_l \chi_j m^{-1} \sin\theta d\theta d\varphi \\ t_{ij}^{I} &= \frac{3}{4\pi a^3}\left(t_{ij}^{I,p} + t_{ji}^{I,p}\right) \end{aligned} \tag{A.2.12}$$

Note that the constant $1/V_I$ on the RHS of Eq. (A.1.33) renders $T_{klmj}^{I}\left(\mathbf{C}^{X}\right)$ a function of the matrix anisotropic material properties. Equation (A.2.12) can now be evaluated numerically using *n* point G-L quadrature. It has been observed that 9 or 10 point quadrature gives acceptable results. Recall that a double integral, **I**, of any function $f(\theta,\varphi)$ is approximated by G-L quadrature as follows:

$$\mathbf{I} = \int_{\theta_a}^{\theta_b}\int_{\varphi_a}^{\varphi_b} f(\varphi,\theta)\, d\varphi d\theta \approx m_\theta m_\varphi \sum_{i=1}^{n}\sum_{j=1}^{m} w_i^{\varphi} w_j^{\theta} f\left(c_\theta + m_\theta t_i^{\theta}, c_\varphi + m_\varphi t_j^{\varphi}\right)$$

$$\text{where} \quad \begin{cases} c_x = \dfrac{1}{2}\left(x_b + x_a\right) \\ m_x = \dfrac{1}{2}\left(x_b - x_a\right) \end{cases} \tag{A.2.13}$$

Were *x* represents the integration variable θ or φ, the coefficients *c* and *m* appear because of the change of variables requiring $t_{i,j} \in [-1,\ 1]$, and w_i represents the G-L quadrature

weights which can be found in any standard numerical methods text. This numerical evaluation permits the calculation of the $t_{ij}^{I}\left(\kappa^{X}\right)$ for the case of spherical inclusions embedded in an isotropic or anisotropic matrix. The following section give the results of the same the same approach when inclusions are ellipsoidal.

A.2.4 Ellipsoidal inclusions

Consider the case of an ellipsoidal anisotropic inclusion embedded in an anisotropic host medium. In such a case, the derivation for the electrostatic Green's function is identical to that given in Section A.1.2. For this reason, the derivation with not repeated. The resulting expression for ellipsoidal inclusions embedded in an anisotropic matrix is given in Eq. (A.2.14).

$$\begin{aligned} t_{ij}^{I,p} &= \frac{abc}{6}\int_{0}^{\pi}\int_{0}^{2\pi} \chi_t \Phi_{it} \chi_u \Phi_{ju} m^{-1} \sin\theta d\varphi d\theta \\ t_{ij}^{I} &= \frac{3}{4\pi abc}\left(t_{ij}^{I,p} + t_{ji}^{I,p}\right) \end{aligned} \tag{A.2.14}$$

Note that the constant $1/V_I$ on the RHS of Eq. (A.1.33) renders $T_{klmj}^{I}\left(\mathbf{C}^{X}\right)$ a function of the matrix anisotropic material properties and the ellipsoidal aspect ratios. This expression can be evaluated using G-L quadrature to yield a good approximation of the analytical solution to Eq. (A.1.2).

A.3 Evaluation of $\mathbf{B^I(C^X)}$

The third order tensor, $B^I_{ijk}\left(\mathbf{C}^X\right)$, is the volume average of the surface integral of the spatial derivative of the Green's tensor, $G^X_{ij,k}\left(\mathbf{r}-\mathbf{r}'\right)$, defined by Eq. (A.1.3). This term is crucial for the calculation of the macroscopic effect of electromechanical coupling that occurs at the inclusion level. As in the previous sections, evaluation of this integral is not possible when the matrix surrounding the heterogeneity is anisotropic. Fortunately, the Fourier transform technique delineated in Section A.1 can also be applied to the evaluation of this tensor.

Given the Fourier transform of the Green's tensor, $G^X_{ij}\left(\mathbf{r}-\mathbf{r}'\right)$, and inverse defined in Eq. (A.1.5), Eq. (A.1.3) can be written as:

$$\begin{aligned} B^I_{ijk}\left(\mathbf{C}^X\right) &= \frac{1}{V_I}\int_{V_I}\int_{S_I} G^X_{ij,k}\left(\mathbf{r}-\mathbf{r}'\right)d\mathbf{r}'d\mathbf{r} \\ &= \frac{1}{8\pi^3}\frac{1}{V_I}\int_{V_I}\int_{S_I}\int_{-\infty}^{\infty}\tilde{G}_{ij}\left(\mathbf{k}\right)\left(-ik_k\right)e^{i\mathbf{k}\cdot\left(\mathbf{r}-\mathbf{r}'\right)}d\mathbf{k}d\mathbf{r}'d\mathbf{r} \end{aligned} \tag{A.3.1}$$

The Green's tensor must satisfy differential equation given by Eq. (A.3.2)

$$C^X_{ijkl}G^X_{km,lj}\left(r-r'\right)+\delta_{im}\delta\left(r-r'\right)=0 \tag{A.3.2}$$

Using this knowledge and known properties of the Fourier transform, Eq. (A.3.2) can be written as:

$$\begin{aligned}\left[\mathrm{FT}\left\{G^X_{km,l}\right\}\right]\left(-ik\chi_j\right)C^X_{ijkl}+\delta_{im}&=0\\ \mathrm{FT}\left\{G^X_{km,l}\right\}&=\frac{1}{ik}\left[\chi_j C^X_{ijkl}\right]^{-1}\delta_{im}\end{aligned}\tag{A.3.3}$$

Using the Fourier transform, it is known that $\mathrm{FT}\left\{G^X_{km,l}\right\}=\left(-ik\right)\chi_l\tilde{G}^X_{km}$ which allows Eq. (A.3.1) to be written as a function of the matrix stiffness tensor, the direction cosines, and the magnitude of the vector **k**.

$$B^I_{ijk}\left(\mathbf{C}^X\right)=\frac{1}{8\pi^3 V_I}\int_0^{\pi}\int_0^{2\pi}\left[\chi_r C^X_{jrik}\right]^{-1}\sin\theta\, d\varphi\, d\theta\int_0^{\infty}k^2\left\{\int_{V_I}e^{ikr}d\mathbf{r}\int_{S_I}\frac{1}{ik}e^{ikr'}d\mathbf{r}'\right\}dk \tag{A.3.4}$$

It must be known noted that the tensor $\chi_r C^X_{jrik}$ is *third order* and therefore that its inverse can only be found using singular value decomposition to find its pseudo-inverse.

A.3.5 Spherical inclusions

Section A.1.1 showed that the following approximation is valid for the evaluation of the volume integral of the complex exponential.

$$\mathbb{R}\mathrm{e}\left\{\int_{V_I}e^{ikr'}dr'\right\}\approx\frac{4\pi}{k^3}\left\{ka\cos\left(ka\right)-\sin\left(ka\right)\right\} \tag{A.3.5}$$

To determine $B_{ijk}^{I}\left(\mathbf{C}^{X}\right)$ it is necessary to evaluate the surface integral given in expression (A.3.6).

$$\begin{aligned}\int_{S_I}\frac{1}{ik}e^{ikr'}d\mathbf{r}' &= a^2\int_0^{\pi}\int_0^{2\pi}\left(\frac{1}{ik}\right)e^{-ika}\sin\theta d\varphi d\theta \\ &= \frac{-4\pi a^2}{k}\left[\sin\left(ka\right)+i\cos\left(ka\right)\right]\end{aligned} \tag{A.3.6}$$

Because the solution must be purely real for the evaluation of the electrostatic solution, it is only necessary to retain the real part of this solution. It is then necessary to evaluate the integral over the magnitude of the Fourier variable, *k*.

$$\begin{aligned}\int_0^{\infty}k^2\left\{\int_{V_I}e^{ikr}d\mathbf{r}\int_{S_I}\frac{1}{ik}e^{ikr'}d\mathbf{r}'\right\}dk &= \int_0^{\infty}\frac{1}{k^2}\left\{1-\cos\left(2ka\right)-ka\sin\left(2ka\right)\right\}dk \\ &= \left(\frac{1}{k}\right)\left[\cos\left(2ka\right)+\left(ka\right)\mathrm{Si}\left(ka\right)-1\right]\Big|_0^{\infty}\end{aligned} \tag{A.3.7}$$

Finally yielding an numerically integrable expression for $B_{ijk}^{I}\left(\mathbf{C}^{X}\right)$

$$B_{ijk}^{I}\left(\mathbf{C}^{X}\right)=\frac{1}{12\pi}\int_0^{\pi}\int_0^{2\pi}\left[\chi_m C_{imjk}^{X}\right]^{-1}\sin\theta d\varphi d\theta \tag{A.3.8}$$

Eq. (A.3.8) gives the approximate value of Eq. (A.1.3) after numerical integration using G-L quadrature.

A.3.6 Ellipsoidal inclusions

The evaluation of $B_{ijk}^{I}\left(\mathbf{C}^{X}\right)$ for ellipsoidal inclusion geometry follows directly from the approach given in Section A.1.2. Using that change of variables for an ellipsoidal inclusion geometry described in it is possible to show:

$$B_{ijk}^{I}\left(\mathbf{C}^{X}\right)=\frac{1}{12\pi}\int_{0}^{\pi}\int_{0}^{2\pi}\left[\chi_{t}\Phi_{mt}C_{imjk}^{X}\right]^{-1}\sin\theta d\varphi d\theta \tag{A.3.9}$$

This expression can then be evaluated using G-L quadrature to yield and approximate solution to the integral given in Eq. (A.1.3).

A.4 Evaluation of $\gamma^{I}(\kappa^{X})$

The second order tensor, $b_{ij}^{I}\left(\kappa^{X}\right)$, is the volume average of the surface integral of the spatial derivative of the Green's function, $g_{,i}^{X}\left(\mathbf{r}-\mathbf{r}'\right)$, multiplied by the normal to the inclusion defined by Eq. (A.1.4). This term is crucial for the calculation of the macroscopic effect of electromechanical coupling that occurs at the inclusion level. As in the previous sections, evaluation of this integral is not possible when the matrix surrounding the heterogeneity is anisotropic. Evaluation of this tensor is greatly aided by first applying the divergence theorem as shown in Eq. (A.4.1).

$$
\begin{aligned}
b_{ij}^{I}\left(\kappa^{X}\right) &= \int_{V_I}\int_{S_I} g_{,i}^{X}\left(\mathbf{r}-\mathbf{r}'\right) n_j\left(\mathbf{r}'\right) d\mathbf{r}' d\mathbf{r} \\
&= \int_{V_I}\int_{V_I} g_{,ij}^{X}\left(\mathbf{r}-\mathbf{r}'\right) d\mathbf{r}' d\mathbf{r} \\
&= -2t_{ij}^{I,p}
\end{aligned}
\tag{A.4.1}
$$

It is important to note that this does not violate any physical law and that the application of the divergence theorem is physically objective [251]. Due to this convenience, it is not necessary to derive approximate solutions for $b_{ij}^{I}\left(\kappa^{X}\right)$ but simply to apply the methods given in Section A.2 for either spherical or ellipsoidal inclusions.

APPENDIX B

TENSOR ROTATION AND EULER ANGLES

According to Euler's rotation theorem, any rotation may be described using three angles. If the rotations are written in terms of rotation matrices **B**, **C**, and **D**, then a general rotation can be written as the product of those rotations [129].

$$\mathbf{R} = \mathbf{BCD} \tag{B.1.1}$$

The three angles giving the three rotation matrices are called Euler angles. There are several conventions for Euler angles, depending on the axes about which the rotations are carried out. One of the most common conventions is the "*x*"-convention which has been employed in this thesis and is illustrated in Figure B.1.

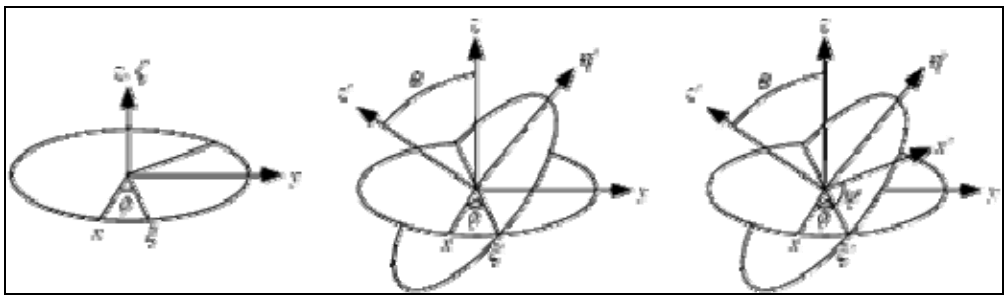

Figure B.1: Visualization of Euler angles employed in the *x*-convention [129].

The rotations associated with this convention consist of a rotation, φ, about the z-axis, followed by a rotation, θ, about the new x-axis and finally a rotation, ψ, about the new z-axis. In general the Euler angles, (φ, θ, ψ), can take the following values:

$$\begin{aligned} \varphi &\in [0 \quad 2\pi] \\ \theta &\in [0 \quad \pi] \\ \psi &\in [0 \quad 2\pi] \end{aligned} \tag{B.1.2}$$

The individual rotation matrices are defined in Eqns. (B.1.3)-(B.1.5).

$$\mathbf{B} = \begin{bmatrix} \cos\psi & \sin\psi & 0 \\ -\sin\psi & \cos\psi & 0 \\ 0 & 0 & 1 \end{bmatrix} \tag{B.1.3}$$

$$\mathbf{C} = \begin{bmatrix} 1 & 0 & 0 \\ 0 & \cos\theta & \sin\theta \\ 0 & -\sin\theta & \cos\theta \end{bmatrix} \tag{B.1.4}$$

$$\mathbf{D} = \begin{bmatrix} \cos\varphi & \sin\varphi & 0 \\ -\sin\varphi & \cos\varphi & 0 \\ 0 & 0 & 1 \end{bmatrix} \tag{B.1.5}$$

The resulting components of the rotation matrix **R** are detailed in Eqns. (B.1.6).

$$
\begin{aligned}
R_{11} &= \cos\psi\cos\varphi - \cos\theta\sin\varphi\sin\psi \\
R_{12} &= \cos\psi\sin\varphi + \cos\theta\cos\varphi\sin\psi \\
R_{13} &= \sin\psi\sin\theta \\
R_{21} &= -\sin\psi\cos\varphi - \cos\theta\sin\varphi\cos\psi \\
R_{22} &= -\sin\psi\sin\varphi - \cos\theta\cos\varphi\cos\psi \\
R_{31} &= \sin\theta\sin\varphi \\
R_{32} &= -\sin\theta\cos\varphi \\
R_{33} &= \cos\theta
\end{aligned}
\tag{B.1.6}
$$

The rotation of any second order tensor, X_{rs}, from one coordinate system to its representation in another, $\tilde{X}_{ij}$, using the rotation matrix, **R**, is shown in Eq. (B.1.7) below.

$$
\tilde{X}_{ij} = R_{ir}R_{js}X_{rs} \tag{B.1.7}
$$

The rotation of any fourth order tensor, X_{nmpq}, from one coordinate system to its representation in another, $\tilde{X}_{ijkl}$, which is related by the above Euler angles is given in Eq. (B.1.8).

$$
\tilde{X}_{ijkl} = R_{im}R_{jn}R_{kp}R_{lq}X_{nmpq} \tag{B.1.8}
$$

APPENDIX C

COMPLEX BOUNDS SUMMARY

C.1 Roscoe's bounds

The equations used to derive the complex bounds proposed by Roscoe are analogous to the statements of potential energy which are the basis of the extremum principles used to find the bounds for elastic composites, see Voigt [60] and Reuss [61]. The following analysis employs the notation used by Roscoe. First the isotropic and deviatoric parts of the relevant tensors are separated in order to simplify the derivation. Doing so yields the following classic relations for the stress and strain in a material.

$$\sigma_{ij} = \sigma\delta_{ij} + s_{ij} \tag{C.1.1}$$

$$\sigma_{ij} = \varepsilon\delta_{ij} + e_{ij} \tag{C.1.2}$$

In the equations above the hydrostatic and deviatoric stress values are denoted as σ and **s** respectively, the analogous strain values are assigned the variables ε and **e**, respectively, and δ_{ij} is the Kronecker delta function. In the low frequency limit the elastic-VE

correspondence principle can be employed and the well-known stress-strain relationship for the r^{th} phase is given as [137, 138].

$$\mathbf{s}_r = 2\mu_r^*\mathbf{e}_r \qquad \sigma_r = 3\kappa_r^*\varepsilon_r \tag{C.1.3}$$

$$\mathbf{e}_r = \frac{1}{2}j_r^*\mathbf{s}_r \qquad \varepsilon_r = \frac{1}{3}l_r^*\sigma \tag{C.1.4}$$

In these expressions an asterisk, *, denotes that the quantity has a complex value, μ_r and κ_r represent the shear and bulk moduli and j_r and l_r represent the deviatoric and isotropic compliances of the r^{th} phase. The two elementary extremum principles used for classic elastic composites [60, 61] and applied here to VE composites are summarized with the two points below.

1. Assume $\langle s\rangle = s_r$ and $\langle\sigma\rangle = \sigma_r$ for each phase, r, where $\langle s\rangle$ and $\langle\sigma\rangle$ are the global deviatoric and isotropic stresses respectively.
2. Assume $\langle\mathbf{e}\rangle = \mathbf{e}_r$ and $\langle\varepsilon\rangle = \varepsilon_r$ for each phase, r, where $\langle\mathbf{e}\rangle$ and $\langle\varepsilon\rangle$ are the global deviatoric and isotropic strains respectively.

Applying assumption 1 to the expression for strain energy yields Eq. (C.1.5) below.

$$\frac{1}{2}j_{eff}^*\langle s_{ij}\rangle\langle\bar{s}_{ij}\rangle + \frac{1}{3}l_{eff}^*\langle\sigma_{ij}\rangle\langle\bar{\sigma}_{ij}\rangle = \frac{1}{V}\sum_r\int\left(\frac{1}{2}j_r^*s_{ij}\bar{s}_{ij} + \frac{1}{3}l_r^*\sigma_{ij}\bar{\sigma}_{ij}\right)dV_r \tag{C.1.5}$$

A bar over any quantity in the above expression denotes the complex conjugate of that quantity and V_r is the volume of the r^{th} phase with $V = \sum_r V_r$. Similarly, for assumption 2, the strain energy relationship is written:

$$2\mu^*_{eff}\left\langle e_{ij}\right\rangle\left\langle \overline{e}_{ij}\right\rangle + 3\kappa^*_{eff}\left\langle \varepsilon_{ij}\right\rangle\left\langle \overline{\varepsilon}_{ij}\right\rangle = \frac{1}{V}\sum_r \int \left(2\mu^*_r e_{ij}\overline{e}_{ij} + 3\kappa^*_r \varepsilon_{ij}\overline{\varepsilon}_{ij}\right) dV_r \qquad \text{(C.1.6)}$$

It is important to note that Eqns. (C.1.5) and (C.1.6) each represent two separate relationships each of which relate the real or imaginary parts of macroscopic material behavior and mechanical loading to the analogous quantities of the constituent phases. Denoting the real and imaginary parts of a complex quantity as $x^* = x' + ix''$, these relationships are shown below.

$$\frac{1}{2} j'_{eff}\left\langle s_{ij}\right\rangle\left\langle \overline{s}_{ij}\right\rangle + \frac{1}{3} l'_{eff}\left\langle \sigma_{ij}\right\rangle\left\langle \overline{\sigma}_{ij}\right\rangle = \frac{1}{V}\sum_r \int \left(\frac{1}{2} j'_r s_{ij}\overline{s}_{ij} + \frac{1}{3} l'_r \sigma_{ij}\overline{\sigma}_{ij}\right) dV_r \qquad \text{(C.1.7)}$$

$$2\mu'_{eff}\left\langle e_{ij}\right\rangle\left\langle \overline{e}_{ij}\right\rangle + 3\kappa'_{eff}\left\langle \varepsilon_{ij}\right\rangle\left\langle \overline{\varepsilon}_{ij}\right\rangle = \frac{1}{V}\sum_r \int \left(2\mu'_r e_{ij}\overline{e}_{ij} + 3\kappa'_r \varepsilon_{ij}\overline{\varepsilon}_{ij}\right) dV_r \qquad \text{(C.1.8)}$$

VE analogues to the elastic Reuss and Voigt bounds are then found by matching terms on the LHS and RHS of relations (C.1.7) and (C.1.8). These bounds are simply the weighted harmonic average and weighted average of the constituent phase properties given below:

$$\mu_{RL}^{'''} = \left(\sum_r \frac{f_r}{\mu_r^{'''}} \right)^{-1} \qquad \kappa_{RL}^{'''} = \left(\sum_r \frac{f_r}{\kappa_r^{'''}} \right)^{-1} \tag{C.1.9}$$

$$\mu_{RU}^{'''} = \sum_r f_r \mu_r^{'''} \qquad \kappa_{RU}^{'''} = \sum_r f_r \kappa_r^{'''} \tag{C.1.10}$$

In the above relationships, *RL* and *RU* denote Roscoe's lower and upper bounds, respectively. It is now important to note that due to energy considerations the following is true:

$$\begin{gathered} \mu_{RU}^{'''} \geq \mu_{eff}^{'''} \quad \kappa_{RU}^{'''} \geq \kappa_{eff}^{'''} \\ j_{RL}^{'''} \geq j_{eff}^{'''} \quad l_{RL}^{'''} \geq l_{eff}^{'''} \end{gathered} \tag{C.1.11}$$

An important aspect of these complex bounds is the lack of restrictions with respect to the frequency inspected, the total number of constituent VE phases, *r*, or the total volume fraction, φ. This logic leads to the following restrictions on the possible values for the effective VE moduli:

$$\begin{gathered} \mu_{RL}^{'''}(\omega,\varphi) \leq \mu_{eff}^{'''}(\omega,\varphi) \leq \mu_{RU}^{'''}(\omega,\varphi) \\ \kappa_{RL}^{'''}(\omega,\varphi) \leq \kappa_{eff}^{'''}(\omega,\varphi) \leq \kappa_{RU}^{'''}(\omega,\varphi) \end{gathered} \tag{C.1.12}$$

where ω is the frequency of interest and φ is the total volume fraction of inclusion phases. Note: $f_{matrix} = 1 - \varphi$.

C.2 Complex bulk modulus bounds

According to the work of Gibiansky and Lakes [144], the effective complex valued bulk modulus of the isotropic VE composite is constrained to a "lens-shaped" region in the complex bulk modulus plane. This region is bounded by the outer-most pair of four circular arcs, each of which correspond to the four min-max variational principles proposed by Cherkaev and Gibiansky [139] and Milton [140]. The equations defining these arcs are calculated from Eqns. (C.2.1) – (C.2.5) below.

$$\kappa^{(n)}\left(f,\gamma\right)=f\kappa_1+\left(1-f\right)\kappa_2-\frac{f\left(1-f\right)\left(\kappa_1-\kappa_2\right)^2}{\left(1-f\right)\kappa_1+f\kappa_2+y^{(n)}\left(\gamma\right)} \tag{C.2.1}$$

for $n=1, 2, 3, 4$

For this relation *f*, where $f\in[0,1]$ and represents the volume fraction of phase *2*, is fixed and γ varies along the real axis from [0, 1]. Functions $y^{(n)}(\gamma)$ are the previously mentioned *Y*-transforms and are defined for the bulk modulus as shown below.

$$y^{(1)}=\frac{4}{3}\left(\gamma\mu_1+\left(1-\gamma\right)\mu_2\right) \tag{C.2.2}$$

$$y^{(2)}\left(\gamma\right)=\frac{4}{3}\left(\frac{\gamma}{\mu_1}+\frac{\left(1-\gamma\right)}{\mu_2}\right)^{-1} \tag{C.2.3}$$

$$y^{(3)}(\gamma) = -\kappa_1 + \left[\left(\frac{4\mu_1}{3} + \kappa_1\right)\left(\frac{4\mu_2}{3} + \kappa_1\right)\right] * \left[\gamma\left(\frac{4\mu_2}{3} + \kappa_1\right) + (1-\gamma)\left(\frac{4\mu_1}{3} + \kappa_1\right)\right]^{-1} \tag{C.2.4}$$

$$y^{(4)}(\gamma) = -\kappa_2 + \left[\left(\frac{4\mu_1}{3} + \kappa_2\right)\left(\frac{4\mu_2}{3} + \kappa_2\right)\right] * \left[\gamma\left(\frac{4\mu_2}{3} + \kappa_2\right) + (1-\gamma)\left(\frac{4\mu_1}{3} + \kappa_2\right)\right]^{-1} \tag{C.2.5}$$

C.3 Complex shear modulus bounds

Milton and Berryman derived bounds for the complex shear modulus of a bi-phase isotropic complex composite material using the variational principles introduced by Cherkaev et Gibiansky [139]. Application of these bounds is achieved through the following algorithm. Given the complex valued bulk and shear moduli of the constituent phases, κ_1, κ_2, μ_1, μ_2, the algorithm calculates the bounds in the transformed complex plane. Note that the same notation for VE composite composition and material properties is used for these bounds as for the complex bulk modulus bounds derived by Gibiansky and Lakes [144]. The algorithm begins by defining a range of angles which represent the phase angle of the shear modulus bounds in *Y*-transform space must be defined [143]:

$$\theta \in \left[\theta_L \quad \theta_U\right]$$

with

(C.3.1)

$$\begin{cases} \theta_L = -\pi + \max\left\{\arg(\kappa_1), \arg(\kappa_2), \arg(\mu_1), \arg(\mu_2)\right\} \\ \theta_U = \min\left\{\arg(\kappa_1), \arg(\kappa_2), \arg(\mu_1), \arg(\mu_2)\right\} \end{cases}$$

Because both real and imaginary parts of the moduli are forced to be positive for the evaluation of these bounds, the values of θ_U and θ_L will always fall between 0 and π, and – π and 0, respectively. In the *Y*-transform space the bounds are defined by some single valued function, $f^{+,-}$, represented in Eq. (C.3.2) in the most general terms possible [143].

$$y = f^{+,-}(x), \quad \text{if and only if } z^{+,-} = x + iy \in \partial B^{+,-} \tag{C.3.2}$$

$\partial B^{+,-}$ in Eq. (C.3.2) represents the upper and lower boundary, respectively, of the set of all admissible values of $z^{+,-}$ in complex *Y*-space, *x* and *y* are the real and imaginary parts of the complex shear modulus in *Y*-space on that boundary, and the complex number, $z^{+,-}$, is some as function of the VE composite's constituent properties and composition. The resulting bounds can now be plotted either in the *Y*-transformed space or complex shear modulus space via the relationships given below. First, $z^{+,-}$ must be defined in terms of the VE constituent properties and the *Y*-space phase angle θ with the equations below [143]:

$$z^{-}(\theta)=\frac{\mu_i(8+9c_1)}{6(2+c_1)}+\frac{5(\kappa_j-c_1\mu_i)}{3(2+c_1)^2}$$

$$z^{+}(\theta)=\left[\frac{6(2+c_2)}{\mu_k(8+9c_2)}+\frac{60c_2}{(8+9c_2)}\left(\frac{c_2}{\kappa_l}-\frac{1}{\mu_k}\right)\right]^{-1} \tag{C.3.3}$$

where

$$c_1=\frac{\mathrm{Im}\left[\kappa_j e^{-i\theta}\right]}{\mathrm{Im}\left[\mu_i e^{-i\theta}\right]} \text{ and } c_2=\frac{\mathrm{Im}\left[e^{i\theta}/\mu_k\right]}{\mathrm{Im}\left[e^{i\theta}/\kappa_l\right]} \tag{C.3.4}$$

For z^{-}, the variables μ_i and κ_j are defined as:

$$\begin{aligned}\mu_i&=\begin{cases}\mu_1, & \text{if } \mathrm{Im}\left[(\mu_1-\mu_2)e^{-i\theta}\right]\le 0\\ \mu_2, & \text{otherwise}\end{cases}\\ \kappa_j&=\begin{cases}\kappa_1, & \text{if } \mathrm{Im}\left[(\kappa_1-\kappa_2)e^{-i\theta}\right]\le 0\\ \kappa_2, & \text{otherwise}\end{cases}\end{aligned} \tag{C.3.5}$$

and, for z^{+}, the variables μ_k and κ_l are defined as:

$$\begin{aligned}\mu_k&=\begin{cases}\mu_1, & \text{if } \mathrm{Im}\left[(1/\mu_1-1/\mu_2)e^{i\theta}\right]\ge 0\\ \mu_2, & \text{otherwise}\end{cases}\\ \kappa_l&=\begin{cases}\kappa_1, & \text{if } \mathrm{Im}\left[(1/\kappa_1-1/\kappa_2)e^{i\theta}\right]\ge 0\\ \kappa_2, & \text{otherwise}\end{cases}\end{aligned} \tag{C.3.6}$$

Upon implementation of this algorithm either $c_1 \rightarrow \infty$ or $c_2 \rightarrow \infty$. The former occurs when one of the shear moduli determines either of the limiting angles in Eq. (C.3.5) and

the latter occurs when one of the bulk moduli determines either of the limiting angles in Eq. (C.3.6). It should also be noted that the evaluation of the above equations does not always lead to a closed space. This problem is eliminated by extending tangent lines from the limiting angles using the following relationships [143]:

$$z^{-} = z^{-}(\theta_U) + se^{i\theta_U}, \qquad z^{-} = z^{-}(\theta_L) - se^{i\theta_L} \tag{C.3.7}$$

$$z^{+} = \left[z^{+}(\theta_U) + se^{-i\theta_U}\right]^{-1}, \qquad z^{+} = \left[z^{+}(\theta_L) - se^{-i\theta_L}\right]^{-1} \tag{C.3.8}$$

The variable s in Eqns. (C.3.7) and (C.3.8) represents a real variable that can takes any value in the range $[0\ \infty)$ required to close the upper and lower bounds. The Y-transform space bounds given by Eqns. (C.3.1) – (C.3.8) can then be transformed to the complex shear modulus space using the following relationship [143].

$$\mu^{+,-} = \sum_{n=1}^{2}\left[\frac{f_n}{\mu_n + z^{+,-}}\right]^{-1} - z^{+,-} \tag{C.3.9}$$

In the above expression, f_n and μ_n denote the volume fraction and shear modulus of phase n.

APPENDIX D

DERIVATION OF DIFFERENTIAL AND MORI-TANAKA EFFECTIVE MEDIUM SCHEMES

D.1 Introduction

Equation (D.1.1) gives an expression for the effective material behavior of a particulate composite having a dilute volume fraction of coated inclusions using the concentration tensors derived in the thesis.

$$\mathbf{C}^{eff} = \mathbf{C}^{M} + f^{I}\Delta\mathbf{C}^{I-M} : \mathbf{A}^{IM}\left(\mathbf{C}^{M}\right) + f^{C}\Delta\mathbf{C}^{C-M} : \mathbf{A}^{CM}\left(\mathbf{C}^{M}\right) \qquad \text{(D.1.1)}$$

In this expression, $\Delta\mathbf{C}^{X-Y} = \mathbf{C}^{X} - \mathbf{C}^{Y}$ and $\mathbf{A}^{IM}$ and $\mathbf{A}^{CM}$ represent the strain localization tensors for the inclusion and coating phases, respectively (see Chapter III for the derivation and expressions representing these tensors). When the concentration of coated inclusions is low enough to assume that the interaction between inclusions is negligible, Eq. (D.1.1) yields a reasonable estimate of the effective material behavior. This approximation should not be used for volume fractions above 10%. A well established method of overcoming the ability of this formulation to approximate effective material behavior for higher inclusion volume fractions is to employ a self-consistent scheme.

This scheme assumes that the coated inclusions are surrounded by the effective material which has unknown material properties [23, 150]. This results in an implicit set of tensor equations as the strain localization tensors shown in Eq. (D.1.1) become functions of the effective material, shown in Eq. (D.1.2) below.

$$\mathbf{C}^{eff} = \mathbf{C}^{M} + f^{I}\Delta\mathbf{C}^{I-M} : \mathbf{A}^{I}\left(\mathbf{C}^{eff}\right) + f^{C}\Delta\mathbf{C}^{C-M} : \mathbf{A}^{C}\left(\mathbf{C}^{eff}\right) \qquad \text{(D.1.2)}$$

The above formulation permits approximation of effective material behavior at elevated coated inclusion volume fractions. Unfortunately, the solution scheme is implicit and significant convergence problems have been encountered, specifically when inclusion rigidity is significantly lower than matrix rigidity [150]. The root of this is the large difference between the upper and lower strain energy bounds of the composite medium when inclusion phases are much less rigid than the matrix phase [252, 253]. Because of the inconvenience posed by numerical evaluation of the self-consistent model for such cases, it is sometimes desirable to use volume averaged strain fields and strain localization tensors found in previous works to derive direct evaluation models. Two well accepted and versatile schemes are the Differential Effective Medium (DEM) and Mori-Tanaka (MT) methods. In what follows these models are for the specific case of a matrix containing coated ellipsoidal inclusions.

D.2 Differential effective medium theory

A Differential Effective Medium (DEM) theory can be developed from Eq (D.1.1) for the non-dilute case as follows. This derivation closely follows classic DEM theory discussed by Garboczi and Berryman [254] and Norris [255]. For a non-dilute concentration of coated inclusions, we can assume that the macroscopic behavior of the material has an elastic response described by $\mathbf{C}^{eff,I}$. The representative volume element, having a volume V_0, of this material contains volume fractions of matrix material, f^M, inclusion, f^I, and coating, f^C, such that:

$$1 = f^M + f^I + f^C = f^M + \varphi \tag{D.2.1}$$

If the coated inclusion geometry is restricted to the thin shell homothetic case ($\Delta a/a = \Delta b/b = \Delta c/c << 1$) it can further be shown that the coated inclusion concentration, φ, is given by:

$$\varphi \approx f^I \left(1 + \varepsilon\right) \tag{D.2.2}$$

where

$$f^C \approx \varepsilon f^I = 3\left(\frac{\Delta a}{a}\right) f^I \tag{D.2.3}$$

The DEM can now be developed through a constant volume process. We can assume that a very small representative volume of material, dV_0, is removed from the non-dilute representative volume element (RVE), V_0. This representative differential volume is assumed to have the same composition as the non-dilute representative volume element,

that is: $dV_0 = dV_M + dV_I + dV_C$ where $df^X = f^X\left(dV_0/V_0\right)$ and X represents any of the constituent materials. We then assume that removed composite volume of composite material is replaced with the same volume of purely coated inclusion. The new effective material properties due to this change in composition can now be predicted using the dilute concentration formula given in Eq. (D.1.1) where $\mathbf{C}^M$ is replaced by $\mathbf{C}^{eff,1}$.

$$\begin{aligned}\mathbf{C}^{eff,2} &= \mathbf{C}^{eff,1} + d\mathbf{C} \\ &= \mathbf{C}^{eff,1} + f^I\left\{\Delta\mathbf{C}^{I-eff,1} : \mathbf{A}^I\left(\mathbf{C}^{eff,1}\right) + \varepsilon\Delta\mathbf{C}^{C-eff,1} : \mathbf{A}^C\left(\mathbf{C}^{eff,1}\right)\right\} \\ &= \mathbf{C}^{eff,1} + \frac{\varphi}{1+\varepsilon}\left\{\Delta\mathbf{C}^{I-eff,1} : \mathbf{A}^I\left(\mathbf{C}^{eff,1}\right) + \varepsilon\Delta\mathbf{C}^{C-eff,1} : \mathbf{A}^C\left(\mathbf{C}^{eff,1}\right)\right\}\end{aligned} \tag{D.2.4}$$

Where it is noted that c only represents the additional concentration of coated inclusion material added: $\varphi = dV_0/V_0$. It is for this reason the dilute approximation can be employed. Equation (D.2.4) can now be rearranged to find an expression for $d\mathbf{C}$.

$$d\mathbf{C} = \left(\frac{dV_0}{V_0}\right)\frac{1}{1+\varepsilon}\left\{\Delta\mathbf{C}^{I-eff,1} : \mathbf{A}^I\left(\mathbf{C}^{eff,1}\right) + \varepsilon\Delta\mathbf{C}^{C-eff,1} : \mathbf{A}^C\left(\mathbf{C}^{eff,1}\right)\right\} \tag{D.2.5}$$

Note that when the differential volume element was removed from the RVE only a percentage of that volume is matrix material. The relationship relating the differential volume and the change in matrix inclusion fraction is given below in Eq. (D.2.6).

$$df^M = -f^M\frac{dV_0}{V_0} \quad \Rightarrow \quad \frac{dV_0}{V_0} = -\frac{df^M}{f^M} \tag{D.2.6}$$

This knowledge is then used to find the following differential equation describing the rate of change in effective elastic constants with respect to the matrix volume fraction.

$$\frac{d\mathbf{C}}{df^M} = \frac{-1}{f^M\left(1+\varepsilon\right)}\left\{\Delta\mathbf{C}^{eff} : \mathbf{A}^I\left(\mathbf{C}^{eff}\right) + \varepsilon\Delta\mathbf{C}^{eff} : \mathbf{A}^C\left(\mathbf{C}^{eff}\right)\right\} \tag{D.2.7}$$

The effective material properties at any matrix material volume fraction can then be calculated by evaluating the following integral.

$$\mathbf{C}^{eff}\left(f^{M,2}\right) = \mathbf{C}^{eff}\left(f^{M,1}\right) + \int_{f^{M,1}}^{f^{M,2}}\left(\frac{d\mathbf{C}}{df^M}\right)df^M \tag{D.2.8}$$

Where it is noted that $f^M = 1$ corresponds to the pure matrix material case, which has know material properties. The final relationship describing the effective material properties is given below in Eq. (D.2.9).

$$\mathbf{C}^{eff}\left(f^M\right) = \mathbf{C}^M - \frac{1}{1+\varepsilon}\int_1^{f^M}\left(\frac{1}{f^{M'}}\right)\left\{\Delta\mathbf{C}^{eff} : \mathbf{A}^I\left(\mathbf{C}^{eff}, f^{M'}\right) + \varepsilon\Delta\mathbf{C}^{eff} : \mathbf{A}^C\left(\mathbf{C}^{eff}, f^{M'}\right)\right\}df^{M'} \tag{D.2.9}$$

Equation (D.2.9) must be evaluated numerically since the strain localization tensors are functions of the effective material behavior at any $f^{M'}$ and they cannot be integrated analytically except for special cases (such as spherical coated inclusions).

D.3 Mori-Tanaka model

The Mori-Tanaka (MT) modeling scheme is another well-established mean field model. The advantage of MT formulation over both the SC and DEM models is that it is not only explicit, but it also does not require numeric integration to the volume fraction of interest. It must be noted, however, that the MT scheme for multiphase has been shown to violate Hashin-Shtrikman bounds for certain three-phase composites, and that it should therefore be employed with caution [256].

A Mori-Tanaka scheme can be derived from the integral equation expressions for the strain field in the inclusion and coating phases and expressions for the volume average of stress and strain in the heterogeneous materials [23]. The MT model assumes that the average strain present in the matrix phase is equal to the macroscopically applied strain ($\overline{\varepsilon}^{M} = \mathbf{E}$) [54], therefore, the volume average strain expression give in Eq. (D.3.1) can be rearranged into the form given in Eq. (D.3.2).

$$\mathbf{E} = f^{M}\overline{\varepsilon}^{M} + f^{I}\overline{\varepsilon}^{I} + f^{C}\overline{\varepsilon}^{C} \tag{D.3.1}$$

$$\mathbf{E} = f^{M}\overline{\varepsilon}^{M} + f^{I}\overline{\varepsilon}^{I} + f^{C}\overline{\varepsilon}^{C} = \left[f^{M}\mathbf{I} + f^{I}\mathbf{A}^{IM} + f^{C}\mathbf{A}^{CM} \right] : \mathbf{E} = \overline{\varepsilon}^{M} \tag{D.3.2}$$

Note that the following is also assumed for the macroscopically observed stress, Σ.

$$\Sigma = f^M \bar{\sigma}^M + f^I \bar{\sigma}^I + f^C \bar{\sigma}^C \tag{D.3.3}$$

Hooke's law is valid in each constituent phase, so Eq. (D.3.3) can be re-written as:

$$\Sigma = \left[(1-\varphi)\mathbf{C}^M + f^I \mathbf{A}^{IM} : \mathbf{C}^I + f^C \mathbf{A}^{CM} : \mathbf{C}^C \right] : \mathbf{E} \tag{D.3.4}$$

Where the coated inclusion volume fraction is denoted as $\varphi = f^I + f^C$ and Hooke's law and the strain concentration tensors have been employed to calculate the average stress in each phase. It is now assumed that the composite obeys Hooke's law according to its effective viscoelastic stiffness as:

$$\Sigma = \mathbf{C}^{eff} : \mathbf{E} = \mathbf{C}^{eff} : \bar{\varepsilon}^M \tag{D.3.5}$$

Where the middle expression is true in all micromechanical approaches, and the far RHS expression is only true for the MT approximation. If the RHS equality in Eq. (D.3.2) and Eq. (D.3.4) are inserted into Eq. (D.3.5), the following expression results.

$$\left[(1-\varphi)\mathbf{C}^M + f^I \mathbf{A}^{IM} : \mathbf{C}^I + f^C \mathbf{A}^{CM} : \mathbf{C}^C \right] : \mathbf{E} = \mathbf{C}^{eff} : \left[(1-\varphi)\mathbf{I} + f^I \mathbf{A}^{IM} + f^C \mathbf{A}^{CM} \right] : \mathbf{E} \tag{D.3.6}$$

Equation (D.3.6) implies the following expression to approximate the effective viscoelastic stiffness tensor of the composite.

$$\mathbf{C}^{eff} = \left[\left(1-\varphi\right)\mathbf{C}^{M} + f^{I}\mathbf{A}^{IM} : \mathbf{C}^{I} + f^{C}\mathbf{A}^{CM} : \mathbf{C}^{C}\right] : \left[\left(1-\varphi\right)\mathbf{I} + f^{I}\mathbf{A}^{IM} + f^{C}\mathbf{A}^{CM}\right]^{-1} \tag{D.3.7}$$

It is obvious from Figure D. 1 and Figure D. 2 that the MT method also provides good approximations of the effective behavior of heterogeneous materials. It is also important to note that for a bi-phase composite, the MT model corresponds with lower bounds derived by Hashin and Shtrikman [18, 132].

D.4 Model validation

A few examples are given here as a check of the DEM and MT formulation. Huang and Gibson created and tested a polymer matrix material containing hollow glass spheres [180]. Curves showing the effective viscoelastic Young's and shear moduli as a function of voided sphere fraction, $\varphi = f^{I} + f^{C}$, are shown below in Figure D. 1 and Figure D. 2. Note that the SC model has been shown to be a reliable predictor of the elastic material behavior of this composite by Cherkaoui [127]. The viscoelastic material properties are given in Table D. 1.

Table D. 1: Material properties of composites studied by Huang and Gibson [180].

	Matrix	Coating	Inclusion
μ (GPa)	1.75(1-0.4*i*)	28.5(1-0.1*i*)	0
ν ()	0.40	0.23	0

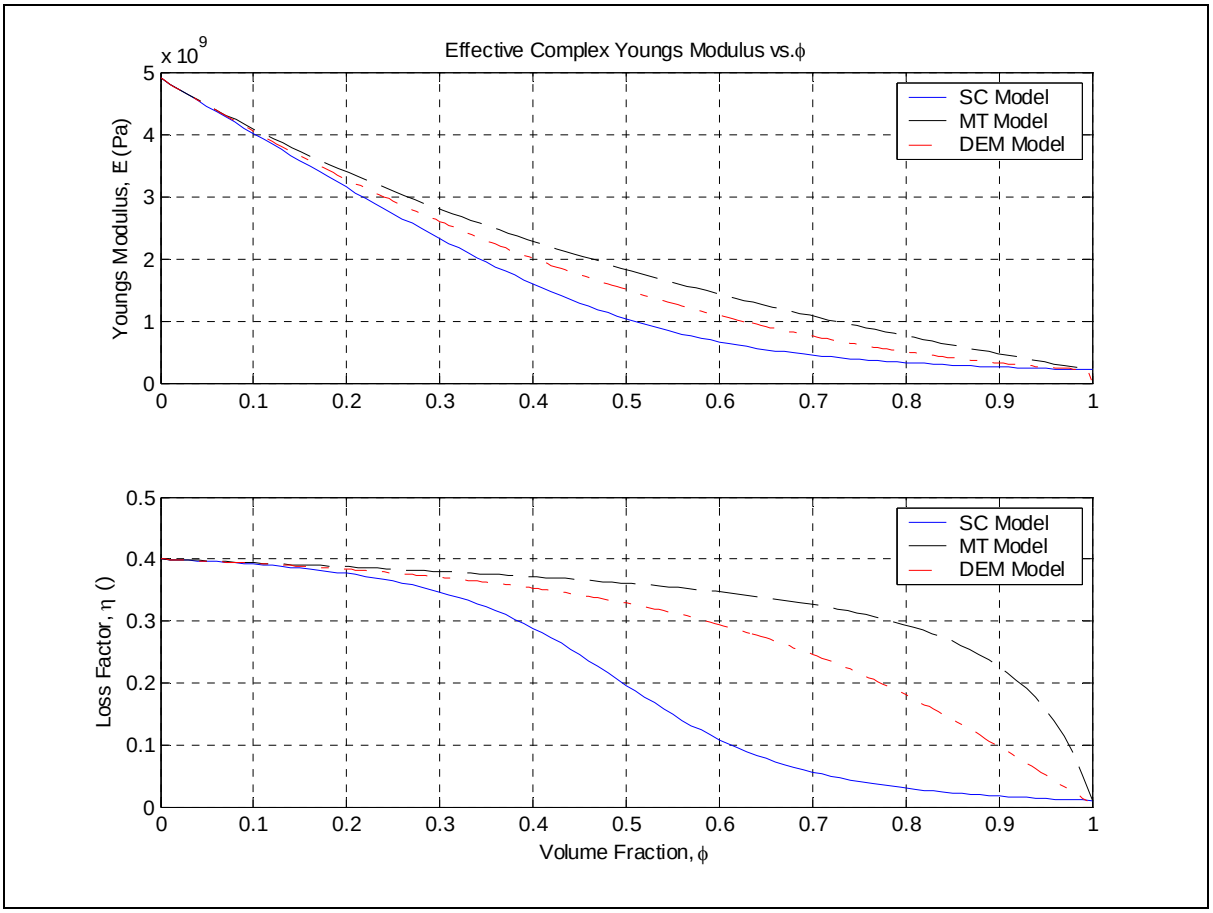

Figure D. 1: Effective Young's modulus predicted by self-consistent (SC), Mori-Tanaka (MT), and differential schemes (DEM).

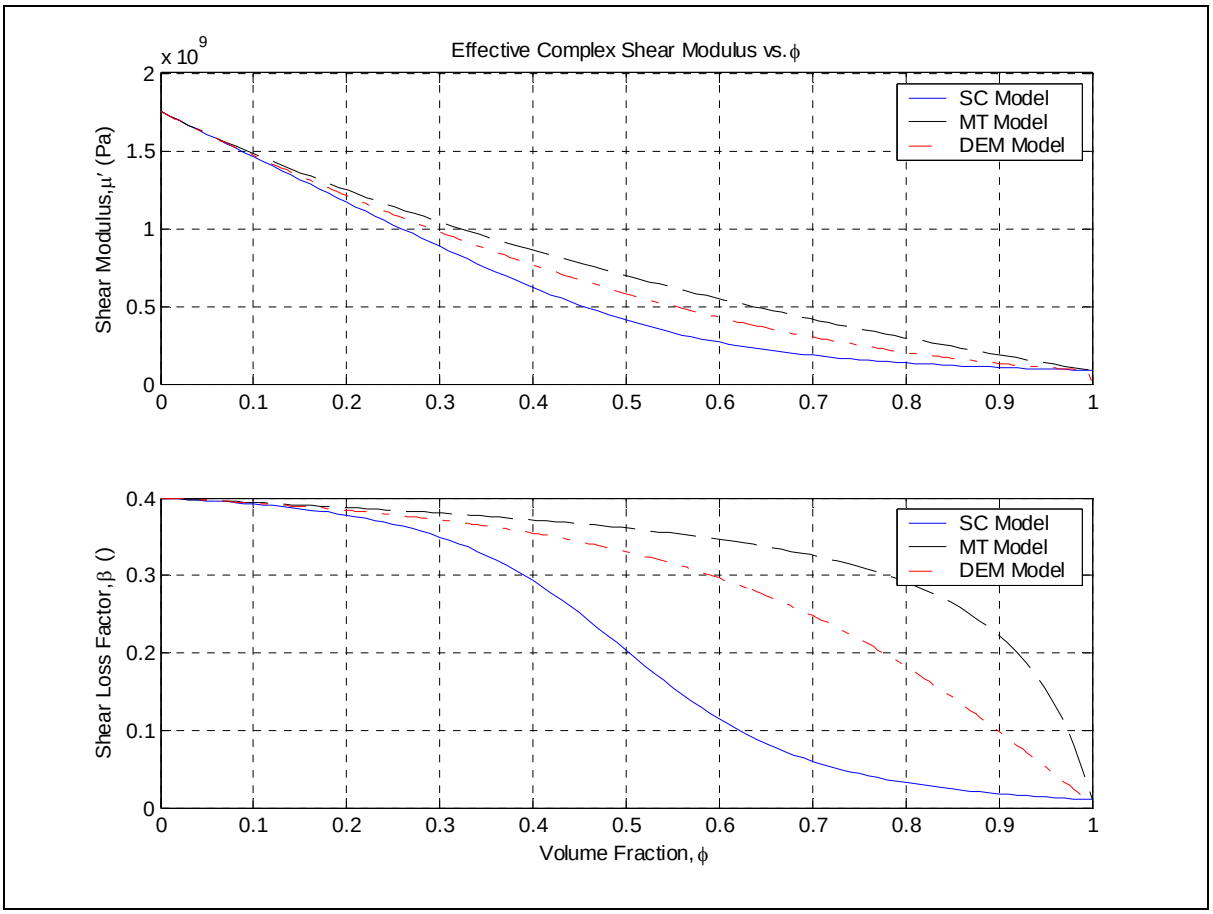

Figure D. 2: Effective shear modulus predicted by self-consistent (SC), Mori-Tanaka (MT), and differential schemes (DEM).

The two proceeding plots show strong correlation between the established SC model (whose agreement with experimental data associated with this composite material has been shown [127, 257]) and the DEM formulation derived in this section. It is noted that agreement between the models presented here, DEM, Mori-Tanaka (MT), and SC, diverges with increasing composite inclusion volume fraction. This is to be expected as each model is based on different assumptions of macroscopic behavior and numerical evaluation schemes. The DEM model has been shown by several authors to yield reliable results for composites where SC solution scheme encounters difficulties [255, 258, 259]. This is especially true when a matrix contains voids or cracks. Another attractive

property of the DEM formulation over the SC model is its explicit nature. This renders the solution scheme stable while approximating very similar effective composite properties, especially at lower volume fractions. All of these attributes make the DEM EMT solution scheme a good candidate for exploration of material microstructures in a materials design strategy.

The fact that the bi-phase MT model corresponds to the lower HS bound is verified by comparing the effective material behavior of a viscoelastic matrix containing negative stiffness inclusions. Figure D. 3 and Figure D. 4 below show that the MT predictions of the effective shear modulus and tan δ overlay the HS lower bounds. It is also evident that the SC and DEM models predict a similar, though moderated, behavior noted by Lakes [18].

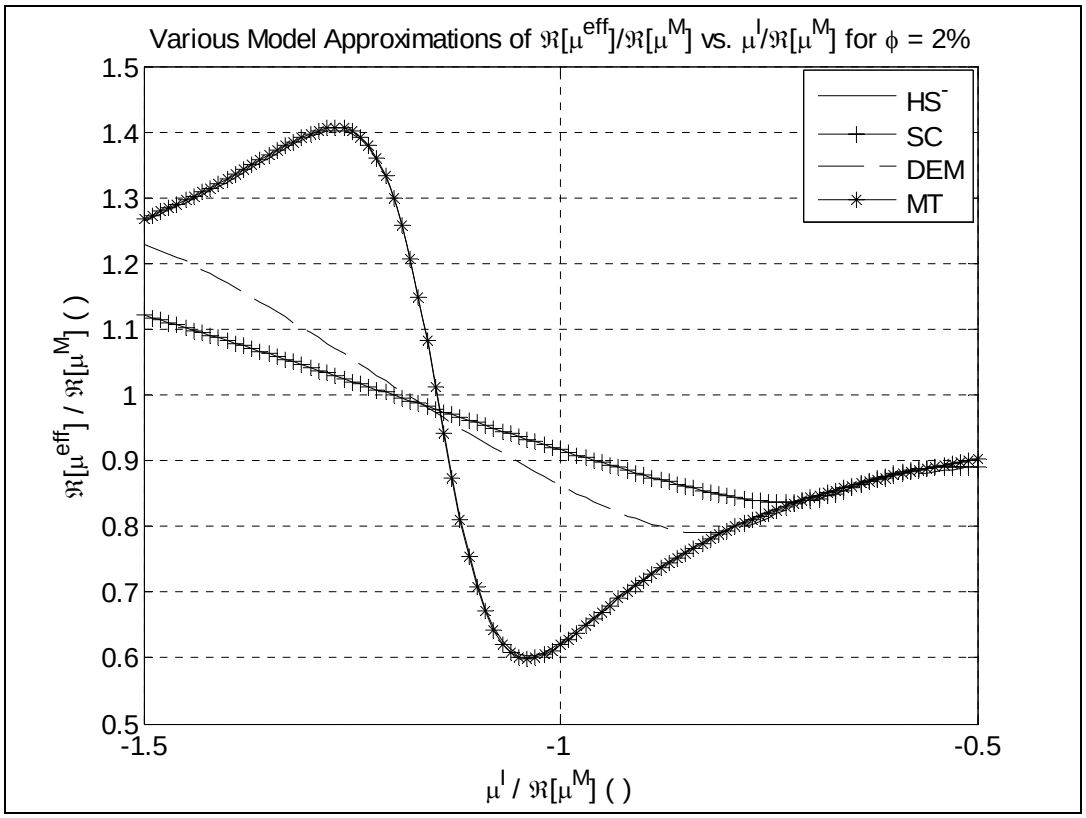

Figure D. 3: Effective shear modulus of viscoelastic matrix containing 2% negative stiffness inclusions and $\nu = 0.3$. Predictions by HS$^-$ [18], SC, DEM, and MT models.

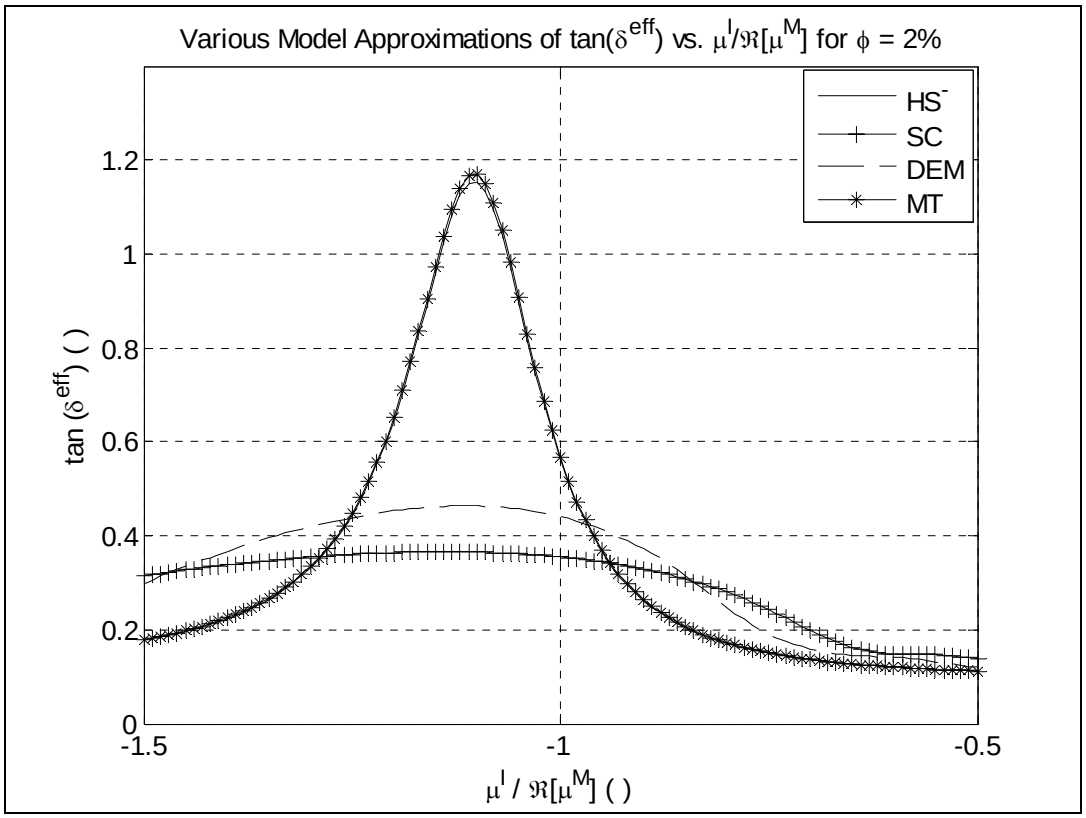

Figure D. 4: Effective tan δ of viscoelastic matrix containing 2% negative stiffness inclusions and ν = 0.3. Predictions by HS$^-$ [18], SC, DEM, and MT models.

These models can also be implemented using the DSCT formulation. Table D. 2shows DEM DSCT model predictions of the effective behavior of the composite shales studied by Hornby *et al* [29] and Jones and Wang [28] and discussed in Chapter IV.

Table D. 2: Measured values and model approximations of the effective stiffness tensor of a cretacious shale studied.

	Observed (GPa)	*Hornby et al (GPa)*	*DSCT SC (GPa)*	*DSCT DEM (GPa)*
C_{11}	34.3 ± 1.4	34.7	37.3	33.2
C_{22}	34.3 ± 1.4	34.7	37.3	33.2
C_{33}	22.7 ± 0.9	22.2	21.7	21.9
C_{44}	5.4 ± 0.8	6.0	5.2	6.5
C_{55}	5.4 ± 0.8	6.0	5.2	6.5
C_{66}	10.6 ± 1.6	10.8	11.1	9.7
C_{12}	*Not reported*	*Not reported*	13.1	13.2
C_{13}	10.7 ± 5.4	11.5	12.1	13.1
C_{23}	10.7 ± 5.4	11.5	12.1	13.1

From this table it is obvious that the DEM model provides a reasonable alternative to the SC model when convergence issues arise.

APPENDIX E

RKU MODEL EVALUATION ALGORITHM

The effective flexural modulus relation derived by Ross *et al* [31] is given in Eqns. (E.1.1)–(E.1.3). In order to efficiently evaluate these implicit equations and to simplify sensitivity analyses, it is desirable to find analytical expressions for both the real and imaginary parts of the bending modulus and shear parameter denoted as: $\hat{B}^{eff,'}$, $\hat{\eta}_p$, $\hat{g}'$, and $\hat{\gamma}'$.

$$\hat{B}^{eff} = \frac{1}{6}\hat{E}h^3\left(1+6Y\left(\frac{\hat{g}}{1+2\hat{g}}\right)\right) = \hat{B}^{eff,'}\left(1+j\hat{\eta}_p\right) \tag{E.1.1}$$

In the above expression Y denotes the geometric parameter and $\hat{g}$ is the complex shear parameter. These parameters are calculated using Eqns. (E.1.2) and (E.1.3), respectively.

$$Y = \left(1+H\right)^2 \tag{E.1.2}$$

$$\hat{g} = \frac{1}{h^2}\left(\frac{\hat{\mu}_2}{\hat{E}H}\right)\sqrt{\frac{1}{\omega^2}\frac{\hat{B}^{eff}}{h^{tot}\rho^{eff}}} = \hat{g}'\left(1+j\hat{\gamma}\right) \tag{E.1.3}$$

In these equations, H is the ratio of interlayer thickness to the thickness of the top and bottom plates ($H = H_2/h$), $\hat{\mu}_2$ is the complex shear modulus of the viscoelastic interlayer where $\hat{\mu}_2 = \hat{\mu}_2^{'}\left(1 + j\hat{\beta}\right)$, $\hat{E}$ is the complex Young's modulus of the upper and lower plates with $\hat{E} = \hat{E}^{'}\left(1 + j\hat{\eta}\right)$, ω is the frequency of interest, h^{tot} is the thickness of the sandwich plate, and ρ^{eff} is the effective sandwich plate density.

The following relationship is given which permits the calculation of this implicit relationship for the effective flexural modulus of the sandwich plate. Given the material properties and sandwich plate geometry, a rough estimate of the sandwich plate effective bending modulus is: $B^{eff,i} \approx \frac{1}{6}Eh^2 = B^{eff,',i}\left(1 + j\eta_p^i\right)$. This represents the resistance of the top and bottom plates to flexure about their bottom plane. Using this estimate the evaluation loop described by Eqns. (E.1.4) – (E.1.11) will yield the effective flexural modulus at each frequency and plate geometry of interest. Note: frequency dependence denoted by "^" is not included in these inclusions.

$$Y = \left(1 + H\right)^2 \tag{E.1.4}$$

Define:

$$x = \sqrt{1 + \sqrt{1 + \eta_p^i}} \tag{E.1.5}$$

$$g^{',i} = \frac{1}{h^2}\frac{\mu_2^{'}}{EH}\sqrt{\frac{B^{',i}}{\omega^2 h_{tot}\rho_{eff}}}\left\{\frac{\sqrt{2}}{2}\left(\frac{1}{1+\eta^2}\right)\left[x\left(1 + \eta_p^i\beta\right) - \frac{\eta_p^i}{x}\left(\beta - \eta\right)\right]\right\} \tag{E.1.6}$$

$$\gamma^i = \left\{ x^i \left(\beta - \eta\right) + \frac{1}{x^i} \eta_p^i \left(1 + \eta\beta\right) \right\} \Big/ \left\{ x^i \left(1 + \eta\beta\right) - \frac{1}{x^i} \eta_p^i \left(\beta - \eta\right) \right\} \qquad \text{(E.1.7)}$$

$$A_r^i = \left\{ g^{',i} \left(1 + 2g^{',i}\right) + 2g^{',i} \left(\gamma^i\right)^2 \right\} \Big/ \left\{ \left(1 + 2g^{',i}\right)^2 + \left(2g^{',i}\gamma^i\right)^2 \right\} \qquad \text{(E.1.8)}$$

$$A_s^i = \left\{ \gamma \left(1 + 2g^{',i}\right) - 2g^{',i}\gamma^i \right\} \Big/ \left\{ \left(1 + 2g^{',i}\right)^2 + \left(2g^{',i}\gamma^i\right)^2 \right\} \qquad \text{(E.1.9)}$$

$$B^{',i+1} = \frac{1}{6} E' h^3 \left[1 + 6Y \left(A_r^i - \eta A_s^i \right) \right] \qquad \text{(E.1.10)}$$

$$\eta_p^{i+1} = \left\{ \eta \left(1 + 6A_r^i Y\right) + 6A_s^i Y \right\} \Big/ \left\{ 1 + 6Y \left(A_r^i - \eta A_s^i \right) \right\} \qquad \text{(E.1.11)}$$

$$B^{eff,i+1} = B^{',i+1} \left(1 + j\eta_p^{i+1}\right)$$

This model is well-behaved and simple root finding techniques such as bi-section reliably converge. One suggested convergence criteria is given in (E.1.12).

$$\varepsilon = \frac{\left| \left| B^{eff,i+1} \right| - \left| B^{eff,i} \right| \right|}{\left| B^{eff,i} \right|} \qquad \text{(E.1.12)}$$

APPENDIX F

APPROXIMATE BEHAVIOR OF LAYERED MEDIA

F.1 Effective moduli of a symmetric sandwich plate

This appendix derives the effective in-plane and out-of-plane moduli for a symmetric sandwich plate such as an automobile windshield. The typical dimensions of windshields are such that it is reasonable to assume that a state of plane stress exists in the plate. This is the result of the fact that $h_{tot}/L \ll 1$, where h_{tot} is the total thickness and L represents either the length or width of the plate. Further, the symmetry of the plate about its neutral axis and the out-of plane axis yields transverse isotropy. This state of symmetry reduces the total number of independent material constants needed to describe the material behavior to five. The resulting stress-strain relationship, written in compliance matrix form, is then written as shown in Eq. (F.1.1).

$$\begin{Bmatrix} \varepsilon_{11} \\ \varepsilon_{22} \\ \varepsilon_{33} \\ \varepsilon_{23} \\ \varepsilon_{13} \\ \varepsilon_{12} \end{Bmatrix} = \begin{bmatrix} \frac{1}{E_{11}} & -\frac{\nu_{12}}{E_{11}} & -\frac{\nu_{13}}{E_{33}} & 0 & 0 & 0 \\ -\frac{\nu_{12}}{E_{11}} & \frac{1}{E_{11}} & -\frac{\nu_{13}}{E_{33}} & 0 & 0 & 0 \\ -\frac{\nu_{13}}{E_{11}} & -\frac{\nu_{13}}{E_{11}} & \frac{1}{E_{33}} & 0 & 0 & 0 \\ 0 & 0 & 0 & \frac{1}{2\mu_{13}} & 0 & 0 \\ 0 & 0 & 0 & 0 & \frac{1}{2\mu_{13}} & 0 \\ 0 & 0 & 0 & 0 & 0 & \frac{1}{2\mu_{12}} \end{bmatrix} \begin{Bmatrix} \sigma_{11} \\ \sigma_{22} \\ \sigma_{33} \\ \sigma_{12} \\ \sigma_{13} \\ \sigma_{23} \end{Bmatrix} \qquad \text{(F.1.1)}$$

Where the independent material constants are E_{11}, E_{33}, ν_{12}, ν_{13}, and μ_{13}. μ_{12} is not an independent material constant for a transversely isotropic plate. It can be shown that transverse isotropy requires μ_{12} to be a function of the stiffness tensor elements, C_{11} and C_{12} given in Eq. (F.1.2)[33].

$$2\mu_{12} = \frac{1}{2}\left(C_{11} - C_{12}\right) \qquad \text{(F.1.2)}$$

where

$$C_{11} = \frac{1-\left(\nu_{13}\right)^2}{E_{11}E_{33}\Delta} \qquad C_{12} = \frac{\nu_{12}+\left(\nu_{13}\right)^2}{E_{11}E_{33}\Delta} \qquad \text{(F.1.3)}$$

and

$$\Delta = \frac{1-(\nu_{12})^2 - 2(\nu_{13})^2 - \nu_{12}(\nu_{13})^2}{(E_{11})^2 E_{33}} \tag{F.1.4}$$

Combining the expressions above gives the following result for μ_{12} in terms of the independent material constants E_{11}, ν_{12}, and ν_{13}.

$$2\mu_{12} = \left(\frac{E_{11}}{2}\right)\frac{1-\nu_{12}-2(\nu_{13})^2}{1-(\nu_{12})^2 - 2(\nu_{13})^2 - \nu_{12}(\nu_{13})^2} \tag{F.1.5}$$

The following expressions will derive independent material properties of the transversely isotropy sandwich plate using law of mixture approximations for the stress and strain.

F.1.1 Determination of E_{11}

Consider the case where the bonding at the interface of each layer is perfect. The strain resulting from a uni-axial stress imposed in x_1 or x_2 direction must then be identical each layer (i.e., $\varepsilon_{11}^{g} = \varepsilon_{11}^{IL}$ and $\varepsilon_{22}^{g} = \varepsilon_{22}^{IL}$). This strain is measured by some change in length of the plate in the direction of the uniaxial stress.

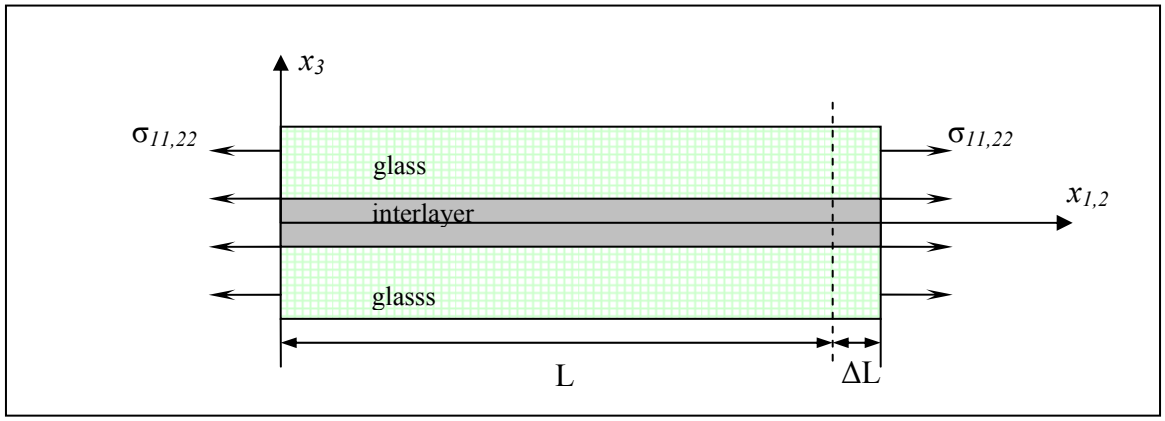

Figure F. 1: Schematic used to approximate the effective Young's modulus E_{11}.

The total force applied on the sandwich plate is given by:

$$F_1 = \sigma_{11} A_1 = \sigma_{11}^{IL} A_1^{IL} + 2\sigma_{11}^{g} A_1^{g} \tag{F.1.6}$$

where A_1^{IL} and A_1^{g} are the cross sectional areas of the interlayer and the glass layers, respectively. For this case, the effective Young's modulus along the x_1 and x_2 directions is well approximated as follows.

$$E_{11} = \frac{\sigma_{11}}{\varepsilon_{11}} = \frac{F_{11}/A_1}{\varepsilon_{11}} = \frac{\sigma_{11}^{IL} A_1^{IL} + 2\sigma_{11}^{g} A_1^{g}}{\varepsilon_{11} A_1}$$

$$E_{11} = f^{IL} E_{11}^{IL} + f^{g} E_{11}^{g} \tag{F.1.7}$$

where f^{IL} and f^{g} represent the volume fractions of the interlayer and glass layers, respectively. In this case the plate behaves as two springs in parallel. The effective

modulus is known as the volume average of the constituent material constants. Note that the volume fraction of the glass and interlayer is related to their respective thicknesses as shown by Eq. (F.1.8).

$$\frac{1}{h_{tot}}\left(2h^{g}+h^{IL}\right)=f^{g}+f^{IL}=1 \tag{F.1.8}$$

F.1.2 Determination of E_{33}

The effective Young's modulus in the out of plane, x_3, direction, is derived in this section. As in the previous section, it is assumed that the layers are perfectly bonded and that the stress in the glass layers and interlayer are the same along the x_3 (i.e. $\sigma_{33}^{g}=\sigma_{33}^{IL}=\sigma_{33}$) when the lamina is subjected to a uniaxial force as shown below.

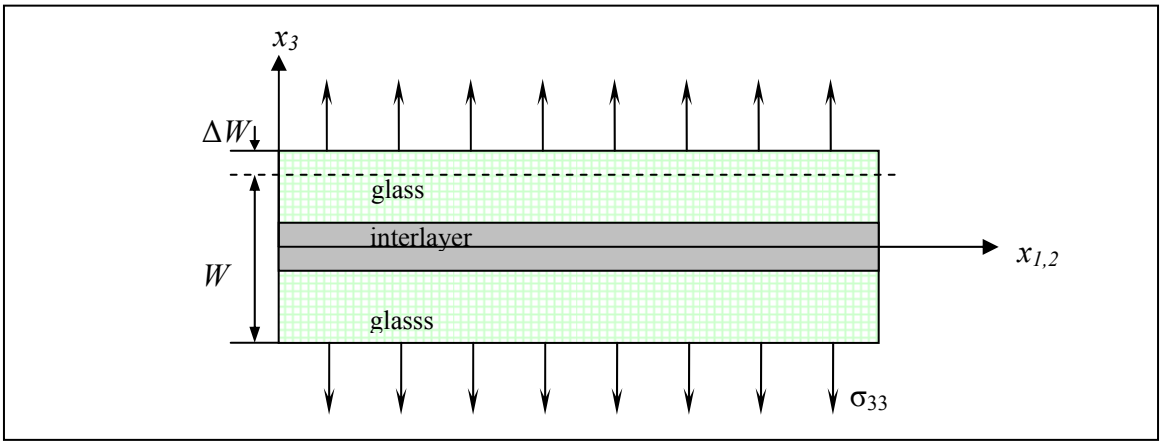

Figure F. 2: Schematic used to approximate the effective Young's modulus E_{33}.

It is noted that in this case the total strain in the x_3 direction is the sum strains of the glass layers and interlayer. This can be reasonably approximated in by employing the volume average of strains given by Eq. (F.1.9).

$$\varepsilon_{33} = f^{IL}\varepsilon_{33}^{IL} + f^{g}\varepsilon_{33}^{g} \tag{F.1.9}$$

Then the effective Young's modulus E_{33} can be calculated using Eq. (F.1.9) and the fact that $\sigma_{33}^{g} = \sigma_{33}^{IL} = \sigma_{33}$ as shown in Eq. (F.1.10).

$$E_{33} = \frac{\sigma_{33}}{\varepsilon_{33}} = \frac{\sigma_{33}}{f^{IL}\varepsilon_{33}^{IL} + f^{g}\varepsilon_{33}^{g}} = \left[\frac{f^{IL}\varepsilon_{33}^{IL}}{E_{33}^{IL}\varepsilon_{33}^{IL}} + \frac{f^{g}\varepsilon_{33}^{g}}{E_{33}^{g}\varepsilon_{33}^{g}}\right]$$

$$E_{33} = \frac{E_{33}^{IL}E_{33}^{g}}{f^{IL}E_{33}^{IL} + f^{g}E_{33}^{g}} \tag{F.1.10}$$

In this case, the fibers and the matrix act like two springs in series and the effective properties are the harmonic average of constituent properties.

F.1.3 Determination of ν_{13}

The derivation of the effective Poisson ratio ν_{13} employs Figure F. 3.

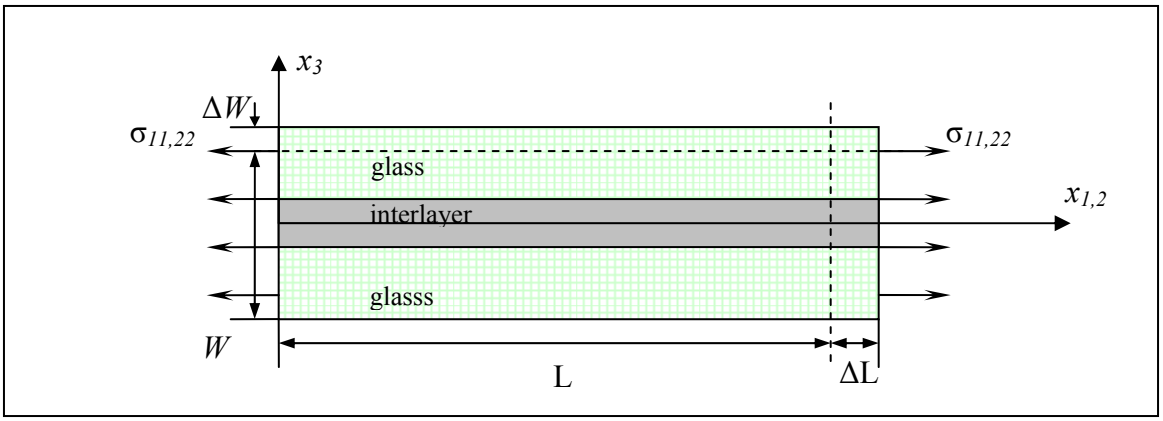

Figure F. 3: Schematic used to approximate the effective Poisson ratio v_{13}.

The Poisson's ratio ν_{13} is defined as ratio of the out of plane strain, ε_{33}, to the in plane strain, ε_{33}, resulting from an stress imposed in the x_1 (or x_2) direction. ν_{13} is described mathematically using in Eq. (F.1.11).

$$\nu_{13} = -\frac{\varepsilon_{33}}{\varepsilon_{11}} \tag{F.1.11}$$

Section F.1.1 explained that the imposition of a uni-axial stress, σ_{11}, requires that

$$\varepsilon_{11} = \varepsilon_{11}^{g} = \varepsilon_{11}^{IL} \tag{F.1.12}$$

Using the same rational as Section F.1.2, the total out of plane strain is approximated as the sum of the out of plane strains in each layer using Eq. (F.1.13).

$$\varepsilon_{33} = f^{IL}\varepsilon_{33}^{IL} + f^{g}\varepsilon_{33}^{g}$$

$$\varepsilon_{33} = -\left(f^{IL}\nu_{13}^{IL}\varepsilon_{11}^{IL} + f^{g}\nu_{13}^{g}\varepsilon_{11}^{g}\right) \tag{F.1.13}$$

The final result giving the effective Poisson ratio, ν_{13}, is given in Eq. (F.1.14).

$$\varepsilon_{33} = -\left(f^{IL}\nu_{13}^{IL} + f^{g}\nu_{13}^{g}\right)\varepsilon_{11}$$

$$\nu_{13} = f^{IL}\nu_{13}^{IL} + f^{g}\nu_{13}^{g} \tag{F.1.14}$$

F.1.4 Determination of ν_{12}

The derivation of the effective Poisson ratio ν_{12} employs Figure F. 4.

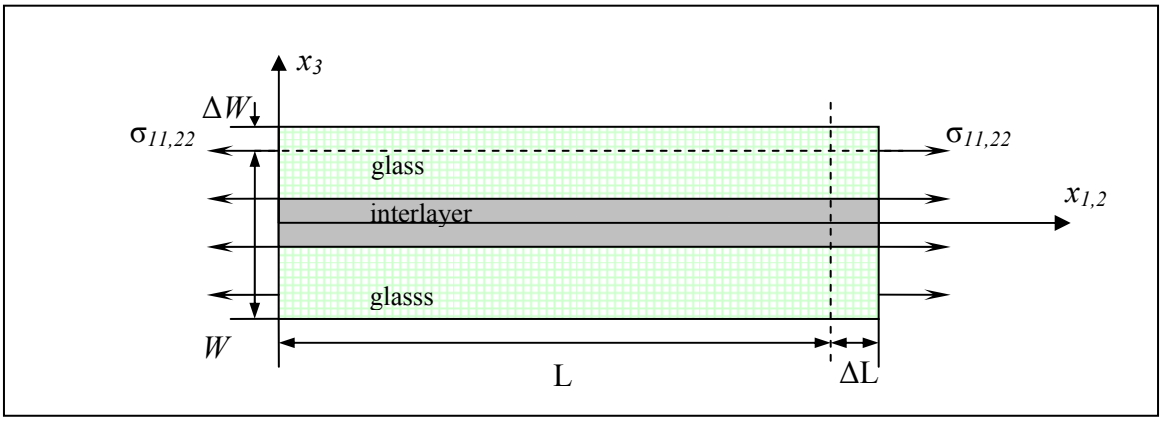

Figure F. 4: Schematic used to approximate the effective Poisson ratio ν_{12}.

ν_{12} is defined as ratio of the in plane strain, ε_{22}, to the orthogonal in plane strain, ε_{11}, which results from an stress imposed in the x_1 direction. ν_{12} is described mathematically using in Eq. (F.1.11).

$$\nu_{12} = -\frac{\varepsilon_{22}}{\varepsilon_{11}} \tag{F.1.15}$$

Section F.1.1 explained that the imposition of a uniaxial stress, σ_{11}, requires that

$$\varepsilon_{11} = \varepsilon_{11}^{g} = \varepsilon_{11}^{IL} \tag{F.1.16}$$

Using the same rational, the in plane strain orthogonal to the imposed stress is also identical in each layer as described by Eq. (F.1.17). It is imperative to note here that allowing the existence of strain in the x_2 direction implicitly relaxes the plain strain assumption asserted at the beginning of the appendix. It is, however, reasonable to do so in order to approximate the effective plate behavior in three dimensions.

$$\varepsilon_{22} = \varepsilon_{22}^{g} = \varepsilon_{22}^{IL} \tag{F.1.17}$$

Recalling the law of mixtures approximation of the in plane stress and Young's modulus from Section F.1.1.

$$\text{(a)} \quad E_{11} = f^{IL} E_{11}^{IL} + f^{g} E_{11}^{g}$$
$$\text{(b)} \quad \sigma_{11} = f^{IL} \sigma_{11}^{IL} + f^{g} \sigma_{11}^{g} \tag{F.1.18}$$

The stress in each material layer along the x_1 direction can now be represented as a function of the constituent material properties, the strain along x_2, and the stress imposed on each layer as shown in Eq. (F.1.19).

$$\begin{aligned} \sigma_{11} &= -E_{11} \frac{\varepsilon_{22}}{\nu_{12}} \\ \sigma_{11}^{IL} &= -E_{11}^{IL} \frac{\varepsilon_{22}^{IL}}{\nu_{12}^{IL}} \\ \sigma_{11}^{g} &= -E_{11}^{g} \frac{\varepsilon_{22}^{g}}{\nu_{12}^{g}} \end{aligned} \tag{F.1.19}$$

The above expressions for stress in each material phase can then be inserted into Eq. (F.1.18)b yielding expression .

$$\varepsilon_{22} \left(\frac{E_{11}}{\nu_{12}} \right) = f^{IL} \varepsilon_{22}^{IL} \left(\frac{E_{11}^{IL}}{\nu_{12}^{IL}} \right) + f^{g} \varepsilon_{22}^{g} \left(\frac{E_{11}^{g}}{\nu_{12}^{g}} \right) \tag{F.1.20}$$

Noting that $\varepsilon_{22} = \varepsilon_{22}^{g} = \varepsilon_{22}^{IL}$, making use of Eq. (F.1.18)a, and rearranging the result gives the following approximation of the effective Poisson ratio, ν_{12}.

$$\nu_{12} = \frac{\nu_{12}^{IL}\nu_{12}^{g}\left[f^{IL}E_{11}^{IL} + f^{g}E_{11}^{g} \right]}{f^{IL}\nu_{12}^{IL}E_{11}^{IL} + f^{g}\nu_{12}^{g}E_{11}^{g}} \tag{F.1.21}$$

F.1.5 Determination of μ_{13}

It is possible to assume that the shear stress, σ_{13}, in each layer is identical based on the same argument used in Section F.1.2. Figure F. 5 gives a schematic showing the approximate behavior used to find the effective value of μ_{13}.

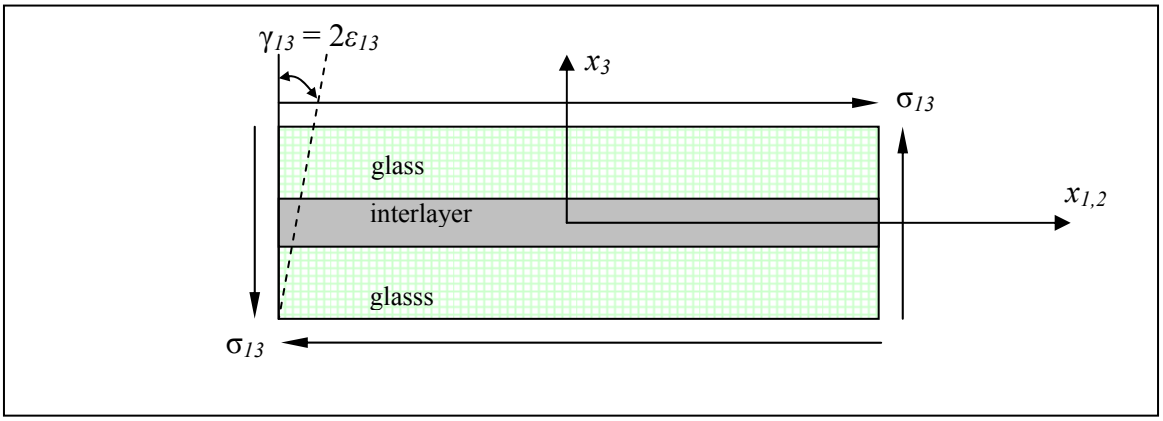

Figure F. 5: Schematic used to approximate the effective shear modulus μ_{13}.

The shear stress of the sandwich plate and in each layer is mathematically given as $\sigma_{13} = 2\mu_{13}\varepsilon_{13} = 2\mu_{13}^{g}\varepsilon_{13}^{g} = 2\mu_{13}^{IL}\varepsilon_{13}^{IL}$. The total resulting shear strain is approximated as the sum of the contributions of each layer, which are proportional to their respective volume fractions.

$$\varepsilon_{13} = f^{IL}\varepsilon_{13}^{IL} + f^{g}\varepsilon_{13}^{g} \tag{F.1.22}$$

The overall shear modulus μ_{13} is then approximated as the harmonic average of the constituent properties given in Eq.(F.1.23).

$$\mu_{13} = \frac{\mu_{13}^{g}\mu_{13}^{IL}}{f^{IL}\mu_{13}^{IL} + f^{g}\mu_{13}^{g}} \tag{F.1.23}$$

F.1.6 Determination of μ_{12}

It is possible to assume that the shear stress, σ_{12}, in each layer is identical based on the same argument used in Section F.1.1. Figure F. 6 looks down on the x_1-x_2 plane to show a square section of layered plate which shows the approximate behavior used to find the effective value of μ_{12}.

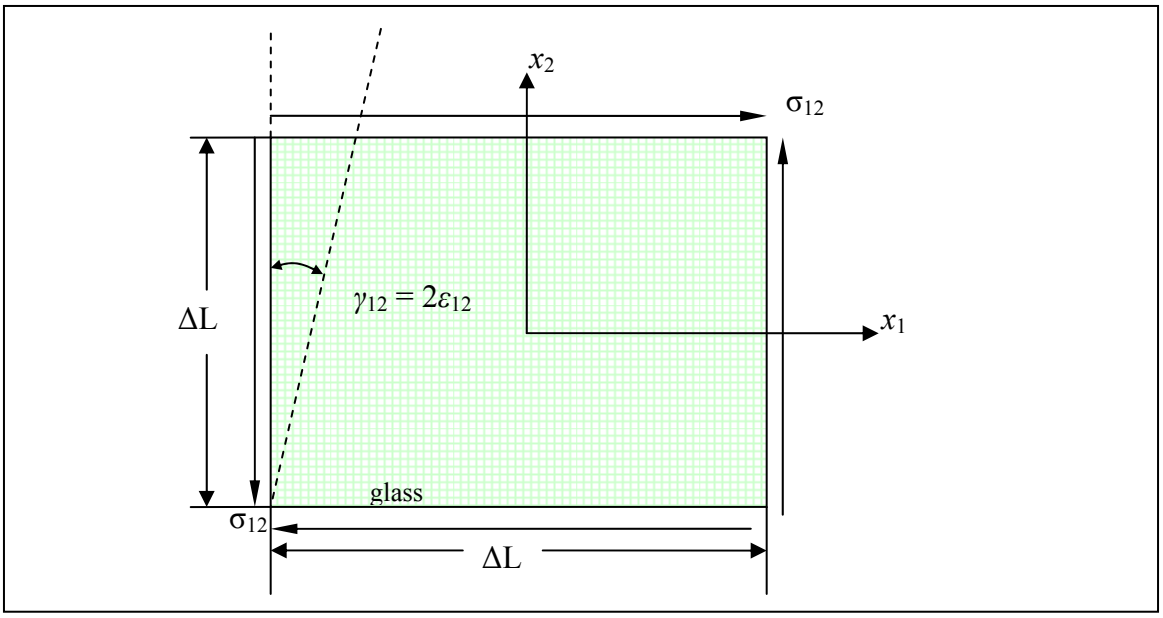

Figure F. 6: Schematic used to approximate the effective shear modulus μ_{12}.

The shear strain of the sandwich plate and in each layer is mathematically given as $\varepsilon_{12} = \varepsilon_{12}^{g} = \varepsilon_{12}^{IL}$. The total shearing *force* applied to each edge of the cut plate is approximated as the sum of the contributions of each layer. The shearing force present in each layer proportional to their respective cross sectional areas as shown by Eq. (F.1.24).

$$\begin{aligned} F_{12} = \quad \sigma_{12}A_{12} &= \quad \sigma_{12}^{IL}A_{12}^{IL} + 2\sigma_{12}^{g}A_{12}^{g} \\ \sigma_{12}h\Delta L &= \quad \sigma_{12}^{IL}h^{IL}\Delta L + 2\sigma_{12}^{g}h^{g}\Delta L \end{aligned} \tag{F.1.24}$$

where A_{12}^{IL} and A_{12}^{g} are the cross sectional areas of the interlayer and the glass layers normal to the x_1-x_2 plane, respectively. For this case, the effective shear modulus, μ_{12}, is well approximated with expression (F.1.25).

$$\mu_{12} = \frac{\sigma_{12}}{\varepsilon_{12}} = \frac{F_{12}/A_{12}}{\varepsilon_{12}} = \frac{\sigma_{12}^{IL} h^{IL} + 2\sigma_{12}^{g} h^{g}}{\varepsilon_{12} h}$$

$$\mu_{12} = f^{IL}\mu_{12}^{IL} + f^{g}\mu_{12}^{g} \qquad \text{(F.1.25)}$$

where f^{IL} and f^{g} represent the volume fractions of the interlayer and glass layers, respectively. In this case the plate behaves as two springs in parallel.

APPENDIX G

FORCED VIBRATION OF ELASTICALLY CONSTRAINED BEAMS AND CIRCULAR PLATES

G.1 Frequency response of an elastically constrained beam

This section finds the solution for the *y*-displacement for a uniform forcing pressure as a function of frequency for the general case of a beam with uniform cross-section and material properties in the *x*-direction and elastic boundary conditions at $x = 0$ and $x = L$. The diagram in Figure G. 1 shows this case:

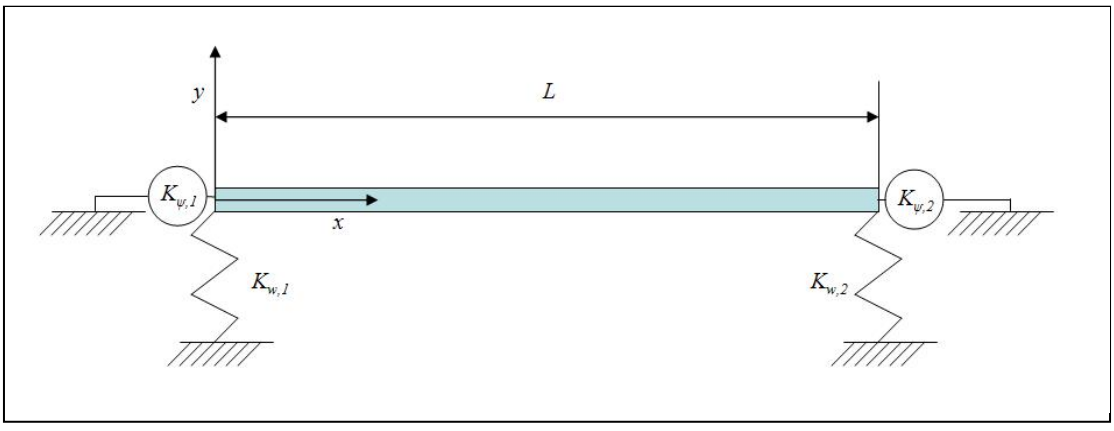

Figure G. 1: Schematic of elastically constrained circular plate.

The well known differential equation for the space and time varying out of plane displacement, *y(x,t)*, for a vibrating beam of uniform cross section and material properties along its length, which is found via the dynamics of beam elements using the Euler-Bernoulli beam bending assumptions [171], is given below in Eq. (G.1.1).

$$EI\frac{\partial^4 y(x,t)}{\partial x^4}+\rho bh\frac{\partial^2 y(x,t)}{\partial t^2}=p(x,t)b \tag{G.1.1}$$

In this equation E is the Young's modulus of the beam, I is the beam's area moment of inertia ($I=bh^3/12$), ρ is the mass per unit volume of the beam, b is the width of the beam cross section, h is the beam's height, and $p(x,t)$ is the space and time varying forcing pressure. The first step in solving this partial differential equation to first take the Fourier transform of the out of plane displacement with respect to time, yielding the non-homogeneous ordinary differential equation below.

$$\frac{d^4\hat{y}(x)}{dx^4}-\beta^4\hat{y}(x)=\frac{\hat{p}(x)b}{EI} \tag{G.1.2}$$

Where $\beta^4=\omega^2\rho bh/EI=12\omega^2\rho/Eh^2$ and represents the flexural wave number in the beam. One arrives at the solution to this ordinary differential equation through the resolution of the homogeneous and particular parts. For simplification of the solution of the particular part, exciting pressure is assumed to be constant in space and a harmonic of

the form $p(r,\theta,t) \rightarrow p(t) = p_o \cos(\omega t) = \mathrm{Re}\left[p_o e^{-i\omega t} \right]$. The resulting general solution is shown below in Eq. (G.1.3).

$$y(x,t) = \left[b_1 \cos(\beta x) + b_2 \sin(\beta x) + b_3 \cosh(\beta x) + b_4 \sinh(\beta x) - \frac{p_o}{\omega^2 \rho h} \right] \cos(\omega t) \quad \text{(G.1.3)}$$

The undetermined coefficients of the relationship given in Eq. (G.1.3) are dependent on the specific boundary conditions of the beam, and are found through the resolution of the following four boundary conditions.

G.1.1 Resolution of system for elastic boundary conditions

For the elastically constrained plate shown in Figure G. 1, the determination of the coefficients $b_1 - b_4$ require expressions for the shear and moment at the extents of the beam. The boundary conditions are expressed below in the four relations given in (G.1.4).

$$\begin{aligned} &(i) \quad M(0,t) = -K_{\psi,1} \frac{dy(0,t)}{dx} \qquad (iii) \quad M(L,t) = K_{\psi,2} \frac{dy(L,t)}{dx} \\ &(ii) \quad \mathrm{V}(0,t) = K_{w,1} y(0,t) \qquad (iv) \quad \mathrm{V}(L,t) = -K_{w,1} y(L,t) \end{aligned} \quad \text{(G.1.4)}$$

Where $K_{\psi,1,2}$ are the rotational spring coefficients on the left and right limits respectively (having the units of N·m) and $K_{w,1,2}$ are the linear displacement spring coefficients at the left and right limits respectively (having units of N/m). Approximate values for the linear

and rotational springs are approximated using the conventions shown in Figure G. 2. These shear and moment sign conventions for beam bending shown below in Figure G. 3.

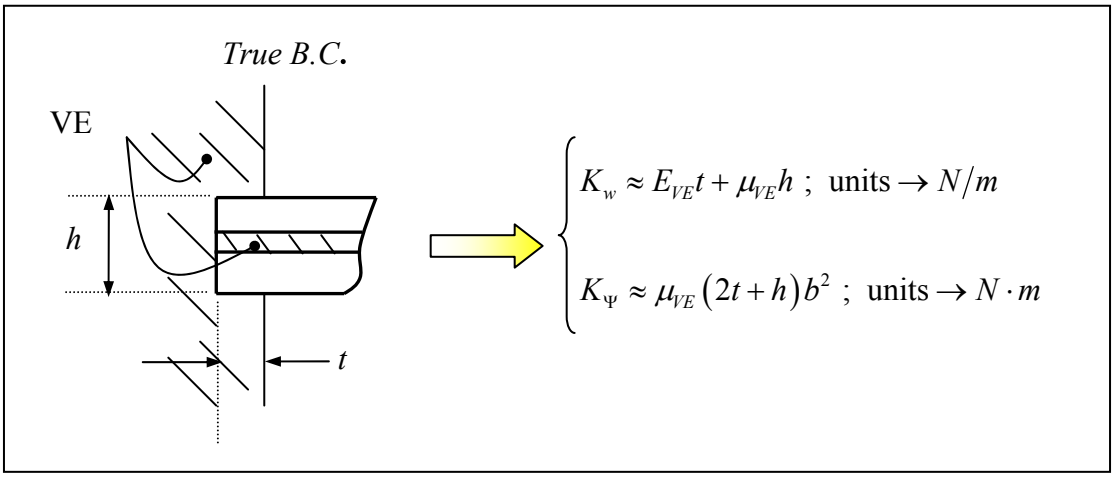

Figure G. 2: Approximation of boundary conditions as linear spring and rotational spring. *b* is the beam width.

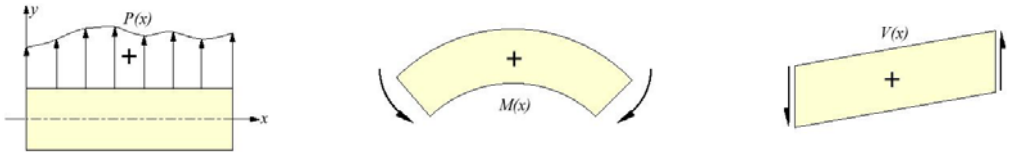

Figure G. 3: Sign conventions used in the derivation of the beam bending problem.

Expressions for the shear and moment can also be derived from the deflection expression using the following [179].

$$M(x,t) = EI\frac{\partial^2 y(x,t)}{\partial x^2}$$

$$V(x,t) = \frac{\partial M(x,t)}{\partial x} = EI\frac{\partial^3 y(x,t)}{\partial x^3} \quad \text{(G.1.5)}$$

Inserting expression (G.1.3) for the out of plane displacement into the RHS of the boundary conditions given in Eq. (G.1.4) where the LHS is determined using the relations for shear and moment given in Eq. (G.1.5) yields a system of four equations having four unknowns. These four unknowns are the undetermined coefficients $b_{1,\ldots,4}$ and can be resolved in terms of the specific beam material and geometry specified by E, ρ, b, h, and L, the elastic boundary conditions: $K_{w,1,2}$, and $K_{\psi,1,2}$, and the loading conditions p_o, and ω. Useful in this derivation are the following spatial derivations.

$$\begin{aligned}
\frac{d\hat{y}(x)}{dx} &= -b_1\beta\sin(\beta x) + b_2\beta\cos(\beta x) + b_3\beta\sinh(\beta x) + b_4\beta\cosh(\beta x) \\
\frac{d^2\hat{y}(x)}{dx^2} &= -b_1\beta^2\cos(\beta x) - b_2\beta^2\sin(\beta x) + b_3\beta^2\cosh(\beta x) + b_4\beta^2\sinh(\beta x) \\
\frac{d^3\hat{y}(x)}{dx^3} &= b_1\beta^3\sin(\beta x) - b_2\beta^3\cos(\beta x) + b_3\beta^3\sinh(\beta x) + b_4\beta^3\cosh(\beta x)
\end{aligned} \tag{G.1.6}$$

Using all of this information, the following system of equations results:

$$\begin{bmatrix}
-EI\beta & K_{\psi,1} & EI\beta & K_{\psi,1} \\
-K_{w,1} & -EI\beta^3 & -K_{w,1} & EI\beta^3 \\
-EI\beta\cos(\beta L) + K_{\psi,2}\sin(\beta L) & -EI\beta\sin(\beta L) - K_{\psi,2}\cos(\beta L) & EI\beta\cosh(\beta L) - K_{\psi,2}\sinh(\beta L) & EI\beta\sinh(\beta L) - K_{\psi,2}\cosh(\beta L) \\
EI\beta^3\sin(\beta L) + K_{w,2}\cos(\beta L) & -EI\beta^3\cos(\beta L) + K_{w,2}\sin(\beta L) & EI\beta^3\sinh(\beta L) + K_{w,2}\cosh(\beta L) & EI\beta^3\cosh(\beta L) + K_{w,2}\sinh(\beta L)
\end{bmatrix}
\begin{Bmatrix} b_1 \\ b_2 \\ b_3 \\ b_4 \end{Bmatrix}
= \begin{Bmatrix} 0 \\ -K_{w,1} \\ 0 \\ K_{w,2} \end{Bmatrix} \frac{p_o}{\rho h\omega^2} \tag{G.1.7}$$

The system is characterized as a function of frequency by solving this system of equations for the unknown coefficients ($\{b\} = [A]^{-1}\{c\}$) at each exciting frequency. Or, more simply, a search for the zeros of the characteristic equation of the *[A]* matrix yields the resonant frequencies for any system that can be simulated using the elastic boundary

conditions above (which includes, cantilevered, simply-supported – simply supported, clamped – simply-supported, etc). Using this system of equations, the above model was verified by checking the first three calculated eigenvalues, βL, with those tabulated in the literature [172] which employs an Rayleigh quotient method. This is summarized in Table G. 1 below.

Table G. 1: First three eigenvalues taken from literature and comparison with current model.

	Cantilevered (C. – F.)		S.S. – S.S.		C. – S.S.	
	Ref. [172]	Model	Ref. [172]	Model	Ref. [172]	Model
$(\beta L)_1$	1.875	1.875	π	3.142	3.927	3.927
$(\beta L)_2$	4.694	4.694	2π	6.286	7.069	7.069
$(\beta L)_3$	7.855	7.855	3π	9.425	10.210	10.210

It is important to note that the conditions at $x = 0$ and $x = L$ required to approximate a clamped B.C. were that $K_{w,1,2} = 1 \times 10^{10}$ N/m and $K_{\psi,1,2} = 1 \times 10^{10}$ N·m, and for the simply-supported B.C., $K_{w,1,2} = 1 \times 10^{10}$ N/m and $K_{\psi,1,2} = 0$ N·m were used. As can be seen from this table, this model is easily adaptable to different boundary conditions by simply varying the values of the elastic constants at the extents of the beam. This can now be employed in order to study the effects of viscoelastic elements on the modal damping of the system. The most straightforward manner to quantify modal damping using the system response relations above is the half-power bandwidth method.

G.2 Frequency response of an elastically constrained circular plate

The general case of a plate having uniform cross-section and material properties in the *r*- and θ-directions and having elastic boundary conditions at $r = a$. The diagram in Figure G. 4 shows this case:

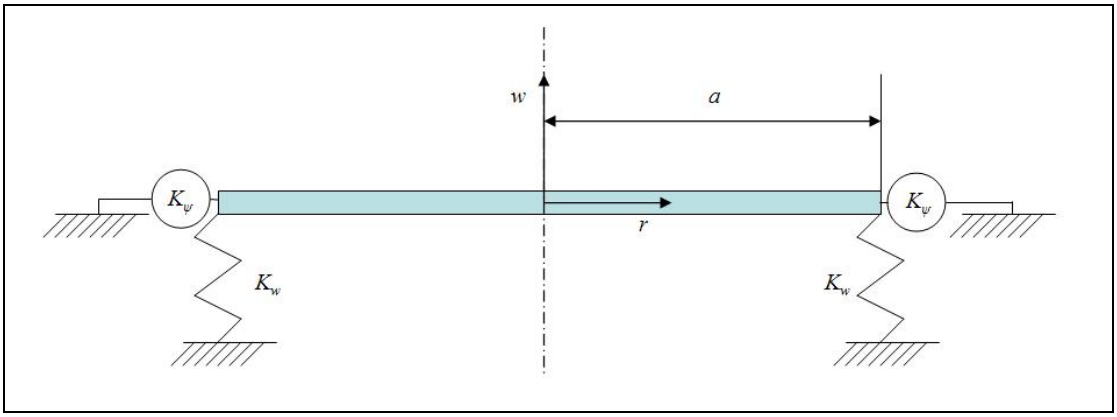

Figure G. 4: Schematic of elastically constrained circular plate.

For a vibrating plate of uniform cross section and material properties in the *r*- and θ-directions, the well known differential equation for the space and time varying out of plane displacement, *w(x,t),* which is found via the dynamics of plate elements using classic Kirchhoff plate theory [174], is given below in Eq. (G.2.1).

$$\hat{B}\nabla^4\hat{w}(r,\theta,t)+\rho h\frac{\partial^2\hat{w}(r,\theta,t)}{\partial t^2}=\hat{p}(r,\theta,t) \qquad \text{(G.2.1)}$$

Where B is the frequency dependent bending modulus described by the relationship $\hat{B}=\hat{E}h^3/12(1-\nu^2)$, w is the out of plane displacement, ρ is the mass per unit volume, h is the thickness of the plate, and p is the forcing pressure. Now, making the simplifying assumption that the forcing pressure is a harmonic and constant in space as shown in Eq. (G.2.2)

$$\hat{p}(r,\theta,t) \rightarrow \hat{p}(t) = p_o \cos(\omega t) = \mathrm{Re}\left[\hat{p}_o e^{-i\omega t}\right] \tag{G.2.2}$$

Taking the Fourier transform with respect to time of Eq. (G.2.1), the result is Eq. (G.2.3).

$$\nabla^4 \hat{w}(r,\theta) - \hat{k}^4 \hat{w}(r,\theta) = \frac{\hat{p}}{\hat{B}} \tag{G.2.3}$$

Where $\hat{k}^4 = \rho h \omega^2 / \hat{B}$ and is the bending wave number. The general solution to this partial differential equation is done by first finding the solution to the homogeneous part as follows. The LHS of the above equation can first be factored into two Laplacian operator relations.

$$\left(\nabla^2 - \hat{k}^2\right)\left(\nabla^2 + \hat{k}^2\right)\hat{w}_h(r,\theta) = 0 \tag{G.2.4}$$

Now, due to symmetry, we know that $\hat{w}_h$ must be periodic in θ i.e. $\hat{w}(r,\theta=0) = \hat{w}(r,\theta=2\pi)$. Therefore, in taking a separation of variables approach such that $\hat{w}_h(r,\theta,t) = R(r)\Theta(\theta)e^{-i\omega t}$, it is apparent that $\Theta(\theta)$ must be of the form:

$$\Theta(\theta) = \begin{Bmatrix} \cos(n\theta) \\ \sin(n\theta) \end{Bmatrix} \tag{G.2.5}$$

Then, returning Eq. (G.2.4), the two similar relations below will require solutions:

$$\nabla^2\left\{R(r)\Theta(\theta)\right\}-\hat{k}^2\left\{R(r)\Theta(\theta)\right\}=0 \tag{G.2.6}$$

$$\nabla^2\left\{R(r)\Theta(\theta)\right\}+\hat{k}^2\left\{R(r)\Theta(\theta)\right\}=0 \tag{G.2.7}$$

Now, applying the Laplacian operator in cylindrical coordinates and noting that the form of $\Theta(\theta)$ given in Eq. (G.2.5) requires $\Theta''(\theta)=-n^2\Theta(\theta)$, the following two equations result.

$$R''(r)+\left(\frac{1}{r}\right)R'(r)-\left(\hat{k}^2+\frac{n^2}{r^2}\right)R(r)=0 \tag{G.2.8}$$

$$R''(r)+\left(\frac{1}{r}\right)R'(r)+\left(\hat{k}^2-\frac{n^2}{r^2}\right)R(r)=0 \tag{G.2.9}$$

These are identified as equations whose solutions are respectively the regular and modified Bessel and Neuman functions of the first kind. The complete solution for the homogeneous out-of-plane displacement is therefore described with the following complete solution.

$$\hat{w}_h(r,\theta,t)=\left[\begin{Bmatrix}J_n(\hat{k}r)\\N_n(\hat{k}r)\end{Bmatrix}+\begin{Bmatrix}I_n(\hat{k}r)\\K_n(\hat{k}r)\end{Bmatrix}\right]\begin{Bmatrix}\cos(n\theta)\\\sin(n\theta)\end{Bmatrix}e^{-i\omega t} \tag{G.2.10}$$

Now, the solution can be simplified by noting specifics of the geometry. First, due to the symmetry about the *z*-axis, we can discard one of the two functions in θ. Secondly, because the plate is continuous at $r = 0$, the regular and modified Neuman functions must be discarded. This leaves the following relationship for the solution to the homogeneous part of Eq. (G.2.3).

$$\hat{w}_h(r,\theta,t) = \left\{ \sum_{n=0}^{\infty} \left[A_n J_n\left(\hat{k}r\right) + B_n I_n\left(\hat{k}r\right) \right] \cos(n\theta) \right\} e^{-i\omega t} \qquad \text{(G.2.11)}$$

Note that there are two unknown coefficients which must be determined from the shear and moment boundary conditions imposed at $r = a$.

To find the particular solution, we must take into account that the exciting pressure is uniform in space and harmonic. This leads to the simple hypothesis that the particular solution be simply of the form $\hat{w}_p(r,\theta,t) \to \hat{w}_p(t) = C\cos(\omega t) = \mathrm{Re}\left[Ce^{-i\omega t} \right]$. Substituting this solution into Eq. (G.2.3), we have the following.

$$\nabla^4\left(\hat{C}e^{-i\omega t}\right) - \hat{C}\hat{k}^4 e^{-i\omega t} = \frac{p_o}{\hat{B}} e^{-i\omega t} \qquad \text{(G.2.12)}$$

The first term on the LHS of Eq. (G.2.12) is zero, and the remaining terms yield an expression for the constant, *C*, in terms of the forcing pressure. The final general solution of (G.2.3) is then given below.

$$\hat{w}(r,\theta,t)=\left\{\sum_{n=0}^{\infty}\left[A_n J_n\left(\hat{k}r\right)+B_n I_n\left(\hat{k}r\right)\right]\cos(n\theta)-\frac{p_o}{\rho h\omega^2}\right\}e^{-i\omega t} \qquad \text{(G.2.13)}$$

G.2.2 Resolution of system for elastic boundary conditions

For the elastically constrained plate shown in Figure G.4, the determination of the coefficients A_n and B_n require expressions for the shear and moment at the extents of the plate. The boundary conditions are expressed below in relations (G.2.14) and (G.2.15).

$$\hat{M}_r(a,\theta,t)=K_\psi\frac{\partial\hat{w}(a,\theta,t)}{\partial r} \qquad \text{(G.2.14)}$$

$$\hat{V}_r(a,\theta,t)=-K_w\hat{w}(a,\theta,t) \qquad \text{(G.2.15)}$$

Where the linear and rotational spring values are approximated from the true boundary conditions using the convention shown in Figure G. 5.

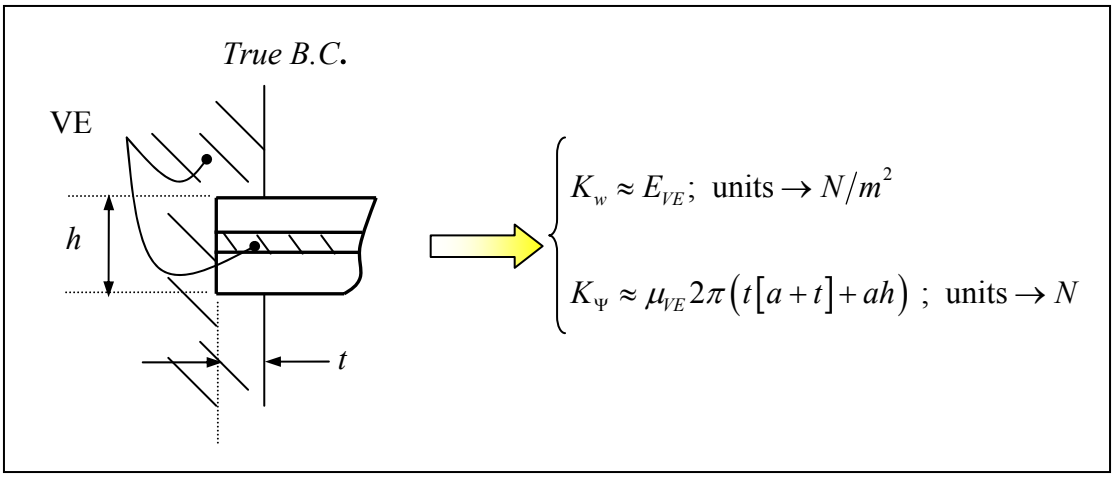

Figure G. 5: Approximation of boundary conditions as linear spring and rotational spring. *a* is the plate radius, *h* is the plate thickness, and *t* is the radial thickness that the plate is embedded in the elastic boundary.

As was done in the previous example, the resolution of the problem requires expressions relating the shear and moment to the displacement equation derived above and given in Eq. (G.2.13). The necessary classic plate relations for this problem were taken from Liessa [174] and are given below in Eqns. (G.2.16) – (G.2.19) describing the plate bending moments, the transverse shearing forces, and the Kelvin-Kirchhoff edge reactions in terms of the out-of-plane displacement.

$$\hat{M}_r = -\hat{B}\left[\frac{\partial^2 \hat{w}}{\partial r^2} + \nu\left(\frac{1}{r}\frac{\partial w}{\partial r} + \frac{1}{r^2}\frac{\partial^2 \hat{w}}{\partial \theta^2}\right)\right] \tag{G.2.16}$$

$$\hat{M}_{r\theta} = -\hat{D}\left(1-\nu\right)\frac{\partial}{\partial r}\left(\frac{1}{r}\frac{\partial \hat{w}}{\partial \theta}\right) \tag{G.2.17}$$

$$\hat{Q}_r = -\hat{B}\frac{\partial}{\partial r}\left(\nabla^2 \hat{w}\right) \tag{G.2.18}$$

$$\hat{V}_r = \hat{Q}_r + \frac{1}{r}\frac{\partial \hat{M}_{r\theta}}{\partial \theta} \tag{G.2.19}$$

The evaluation of the boundary conditions will lead to two simultaneous equations at $r = a$ that can then be solved for the undetermined coefficients A_n and B_n. The system of equations is given below in Eqns. (G.2.20) – (G.2.24).

$$\begin{bmatrix} \hat{L}_n\left(\hat{ka}\right) & \hat{M}_n\left(\hat{ka}\right) \\ \hat{R}_n\left(\hat{ka}\right) & \hat{S}_n\left(\hat{ka}\right) \end{bmatrix} \begin{Bmatrix} \hat{A}_n \\ \hat{B}_n \end{Bmatrix} = \begin{Bmatrix} 0 \\ 1 \end{Bmatrix} \frac{K_w p_o}{\hat{B}k^3 \rho h \omega^2} \tag{G.2.20}$$

Where the frequency dependent functions in the matrix of the LHS are specified below. Note that in the following the "^" designation has been removed for clarity, but that all entities are still dependent on the frequency:

$$L_n\left(ka\right) = J_n^{''}\left(ka\right) + \left(\frac{\nu}{ka} + \frac{K_\psi a}{Bka}\right) J_n^{'}\left(ka\right) - \frac{\nu n^2}{\left(ka\right)^2} J_n\left(ka\right) \tag{G.2.21}$$

$$M_n\left(ka\right) = I_n^{''}\left(ka\right) + \left(\frac{\nu}{ka} + \frac{K_\psi a}{Dka}\right) I_n^{'}\left(ka\right) - \frac{\nu n^2}{\left(ka\right)^2} I_n\left(ka\right) \tag{G.2.22}$$

$$R_n\left(ka\right) = J_n^{'''}\left(ka\right) + \frac{1}{ka} J_n^{''}\left(ka\right) - \frac{1+\nu n^2}{\left(ka\right)^2} J_n^{'}\left(ka\right) + \left\{\frac{n^2\left(1+\nu\right)}{\left(ka\right)^3} - \frac{K_w a^3}{B\left(ka\right)^3}\right\} J_n\left(ka\right)$$

(G.2.23)

$$S_n(ka) = I_n'''(ka) + \frac{1}{ka} I_n''(ka) - \frac{1+\nu n^2}{(ka)^2} I_n'(ka) + \left\{ \frac{n^2(1+\nu)}{(ka)^3} - \frac{K_w a^3}{B(ka)^3} \right\} I_n(ka)$$

(G.2.24)

Solving relationship (G.2.20) for A_n and B_n in terms of the forcing function and the elastic boundary conditions yields the following expressions.

$$A_n = \frac{-p_o K_w}{Bk^3 \rho h \omega^2} \frac{M_n(ka)}{\Delta(ka)} \tag{G.2.25}$$

$$B_n = \frac{p_o K_w}{Bk^3 \rho h \omega^2} \frac{L_n(ka)}{\Delta(ka)} \tag{G.2.26}$$

Where $\Delta(ka)$ is the characteristic equation of the matrix in Eq. (G.2.20).

$$\Delta(ka) = L_n(ka) S(ka) - M_n(ka) R_n(ka) \tag{G.2.27}$$

From Eqns. (G.2.25) – (G.2.27) it is obvious that resonance is reached when the characteristic equation of the coefficient matrix of Eq. (G.2.20) is equal to zero as would be expected. Eqns. (G.2.20) – (G.2.27) give a complete solution for a thin circular plate with a uniform harmonic exciting pressure and allow modeling of the forced frequency

response of the system for a large variety of boundary conditions. It is important to note that for simple implementation of these relationships, it is convenient to use the following recursion relationships for the regular and modified Bessel functions taken from Blackstock [50].

$$\mathrm{X}_{n+1}(ka) = \frac{2n}{ka}\mathrm{X}_n(ka) - \mathrm{X}_{n-1}(ka) \tag{G.2.28}$$

$$\mathrm{X}_n^{'}(ka) = \frac{1}{2}\left[\mathrm{X}_{n-1}(ka) - \mathrm{X}_{n+1}(ka)\right] \tag{G.2.29}$$

$$\frac{d}{d(ka)}\left[(ka)^n \mathrm{X}_n(ka)\right] = (ka)^n \mathrm{X}_{n-1}(ka) \tag{G.2.30}$$

Where $X_n(ka)$ represents either the regular or modified Bessel or Neumann function of the first kind.

To verify the formulation outlined by Eqns. (G.2.20) – (G.2.27), the first few eigenvalues of circular plates having different boundary conditions has been checked with models derived by Leissa [174] for the specific case given. The results are given below in Table G. 2-Table G. 4.

Table G. 2: First four eigenvalues of clamped circular plate taken from literature [174] and comparison with current model. ν = 0.30

	Plate Clamped at $r = a$, with ν = 0.30					
	n = 0		n = 1		n = 2	
$\beta_{n,s}^2$	Ref. [174]	Model	Ref. [174]	Model	Ref. [174]	Model
$\beta_{n,0}^2$	10.2	10.22	21.2	21.26	34.8	34.80
$\beta_{n,1}^2$	39.7	39.76				

Table G. 3: First four eigenvalues of a simply-supported circular plate taken from literature [174] and comparison with current model. ν = 0.30

	Plate Simply-Supported at $r = a$, with ν = 0.30					
	n = 0		n = 1		n = 2	
$\beta_{n,s}^2$	Ref. [174]	Model	Ref. [174]	Model	Ref. [174]	Model
$\beta_{n,0}^2$	4.9	4.94	13.9	13.90	25.6	25.61
$\beta_{n,1}^2$	29.7	29.72				

Table G. 4: First five eigenvalues of free circular plate taken from literature [174] and comparison with current model. ν = 0.25

	Free Plate with ν = 0.25							
	n = 0		n = 1		n = 2		n = 3	
$\beta_{n,s}^2$	Ref. [174]	Model	Ref. [174]	Model	Ref. [174]	Model	Ref. [174]	Model
$\beta_{n,0}^2$					5.513	4.600	12.75	12.71
$\beta_{n,1}^2$	8.892	8.884	20.41	19.97	35.28	33.60		

Here the index s indicates the number of nodal circles on the plate (not including the boundary). It is important to note that the conditions at $r = a$ required to approximate a clamped B.C. were that $K_w = 1 \times 10^9$ N/m^2 and $K_\psi = 1 \times 10^9$ N, and for the simply-supported B.C., $K_w = 1 \times 10^9$ N/m^2 and $K_\psi = 0$ N were used. As can be seen from the results, the model derived here yields results for three extremely different boundary conditions which are acceptably close, though not identical, to the specific individual models of Liessa [174]. The model is therefore ideal for studies on the effects of various elastic (and VE) boundary conditions on the lossy behavior of the system.

APPENDIX H

RAW WINDSHIELD DESIGN RESULTS

Table H. 1: Initial calculations. All design goals are assigned equal importance levels. Weight Reduction Goal: 10%, Coincidence Notch Goal: 0.2 dB, Coincidence Frequency Goal: 1.5 kHz, Variation in Young's Modulus Goal: 2%. Green shading indicates the standard configuration, light blue shading indicates superior performance to standard configuration, orange shading indicates inferior performance to standard configuration.

Glass Layer Settings	IL Settings	$Z_{\min}^{EW}$
No inclusions	No inclusions	1.738
""	1 %, isotropic	0.511
""	1%, low anisotropy	0.544
""	1%, med anisotropy	1.850
""	1%, high anisotropy	1.959
1%, isotropic	No inclusions	2.022
""	1 %, isotropic	0.065
""	1%, low anisotropy	0.385
""	1%, med anisotropy	0.409
""	1%, high anisotropy	2.020
1%, low anisotropy	No inclusions	1.455
	1 %, isotropic	0.102
""	1%, low anisotropy	0.070
""	1%, med anisotropy	0.792
""	1%, high anisotropy	1.457
1%, med anisotropy	No inclusions	1.446
	1 %, isotropic	0.066
""	1%, low anisotropy	0.067
""	1%, med anisotropy	0.656
""	1%, high anisotropy	1.508
1%, high anisotropy	No inclusions	1.976
	1 %, isotropic	0.547
""	1%, low anisotropy	0.536
""	1%, med anisotropy	1.891
""	1%, high anisotropy	1.891

Table H. 2: Investigation of design goal importance (1): Coincidence notch depth goal has highest importance, others have equal (low) importance. Weight Reduction Goal: 10%, Coincidence Notch Goal: 0.2 dB, Coincidence Frequency Goal: 1.5 kHz, Variation in Young's Modulus Goal: 2%. Green shading indicates the standard configuration, light blue shading indicates superior performance to standard configuration, orange shading indicates inferior performance to standard configuration.

Glass Layer Settings	IL Settings	$Z_{\min}^{\Delta TL}$
No inclusions	No inclusions	2.915
""	1 %, isotropic	0.606
""	1%, low anisotropy	0.869
""	1%, med anisotropy	3.356
""	1%, high anisotropy	3.356
1%, isotropic	No inclusions	3.459
""	1 %, isotropic	0.055
""	1%, low anisotropy	0.260
""	1%, med anisotropy	2.732
""	1%, high anisotropy	3.459
1%, low anisotropy	No inclusions	2.332
	1 %, isotropic	0.046
""	1%, low anisotropy	0.248
""	1%, med anisotropy	1.042
""	1%, high anisotropy	2.319
1%, med anisotropy	No inclusions	2.408
	1 %, isotropic	0.265
""	1%, low anisotropy	0.582
""	1%, med anisotropy	3.459
""	1%, high anisotropy	2.334
1%, high anisotropy	No inclusions	3.029
	1 %, isotropic	0.645
""	1%, low anisotropy	0.623
""	1%, med anisotropy	0.306
""	1%, high anisotropy	3.323

Table H. 3: Investigation of design goal importance (1): Coincidence frequency goal has highest importance, others have equal (low) importance. Weight Reduction Goal: 10%, Coincidence Notch Goal: 0.2 dB, Coincidence Frequency Goal: 1.5 kHz, Variation in Young's Modulus Goal: 2%. Green shading indicates the standard configuration, light blue shading indicates superior performance to standard configuration, orange shading indicates inferior performance to standard configuration.

Glass Layer Settings	IL Settings	$Z^{f}_{\min}$
No inclusions	No inclusions	1.681
""	1 %, isotropic	0.720
""	1%, low anisotropy	0.720
""	1%, med anisotropy	1.757
""	1%, high anisotropy	1.829
1%, isotropic	No inclusions	1.725
""	1 %, isotropic	0.055
""	1%, low anisotropy	0.523
""	1%, med anisotropy	0.525
""	1%, high anisotropy	1.725
1%, low anisotropy	No inclusions	1.302
	1 %, isotropic	0.061
""	1%, low anisotropy	0.530
""	1%, med anisotropy	0.920
""	1%, high anisotropy	1.347
1%, med anisotropy	No inclusions	1.353
	1 %, isotropic	0.608
""	1%, low anisotropy	0.038
""	1%, med anisotropy	1.482
""	1%, high anisotropy	1.674
1%, high anisotropy	No inclusions	1.695
	1 %, isotropic	0.612
""	1%, low anisotropy	0.615
""	1%, med anisotropy	1.478
""	1%, high anisotropy	1.695

Table H. 4: Investigation of design goal importance (1): In-plane Young's Modulus goal has highest importance, others have equal (low) importance. Weight Reduction Goal: 10%, Coincidence Notch Goal: 0.2 dB, Coincidence Frequency Goal: 1.5 kHz, Variation in Young's Modulus Goal: 2%. Green shading indicates the standard configuration, light blue shading indicates superior performance to standard configuration, orange shading indicates inferior performance to standard configuration.

Glass Layer Settings	IL Settings	$Z_{\min}^{\Delta E_{11}}$
No inclusions	No inclusions	1.158
""	1 %, isotropic	0.342
""	1%, low anisotropy	0.342
""	1%, med anisotropy	1.234
""	1%, high anisotropy	1.306
1%, isotropic	No inclusions	1.516
""	1 %, isotropic	0.099
""	1%, low anisotropy	0.349
""	1%, med anisotropy	1.309
""	1%, high anisotropy	0.396
1%, low anisotropy	No inclusions	0.108
	1 %, isotropic	0.191
""	1%, low anisotropy	0.335
""	1%, med anisotropy	0.656
""	1%, high anisotropy	1.114
1%, med anisotropy	No inclusions	1.046
	1 %, isotropic	0.082
""	1%, low anisotropy	0.298
""	1%, med anisotropy	0.718
""	1%, high anisotropy	1.053
1%, high anisotropy	No inclusions	1.472
	1 %, isotropic	0.510
""	1%, low anisotropy	1.302
""	1%, med anisotropy	1.302
""	1%, high anisotropy	1.472

APPENDIX I

MEAN FIELD MODELLING OF PIEZOELECTRET FOAMS

I.1 Introduction and motivation

Innovative closed cell polymer foams with piezoelectric properties, also known as piezoelectrets, have recently gained interest in the scientific community [260]. These foams consist of a polymer matrix, often polypropylene (PP), containing a high volume fraction of voids, see Figure I. 1. The foams are processed in such a way that the large elliptical voids carry surface charge on their interior void surface thereby creating large dipoles within the material [260]. The coupling of these large dipoles with the relatively high foam compliance leads to high piezoelectric coupling of the foam as a whole. The d_{33} piezoelectric coupling coefficient of these materials is quite high, with experimentally measured values ranging from 100-200 pC/N in cellular polypropylene [260]. Modeling the effective behavior of the foams has proven to be a difficult task. Past modeling attempts have been limited, employing only one dimensional electrostatic models to approximate the d_{33} coefficient while neglecting the estimation of the coupled mechanical properties [261, 262]. Further development of these closed cell polymer foams requires

an interdisciplinary approach drawing from scientific fields including material science, acoustics, electrostatics, plasma physics, mechanics, and manufacturing. To enhance the ability to improve the behavior of piezoelectrets, this work proposes a general modeling approach to improve the understanding of their electromechanical behavior and to create a tool for the researcher desiring to improve their behavior.

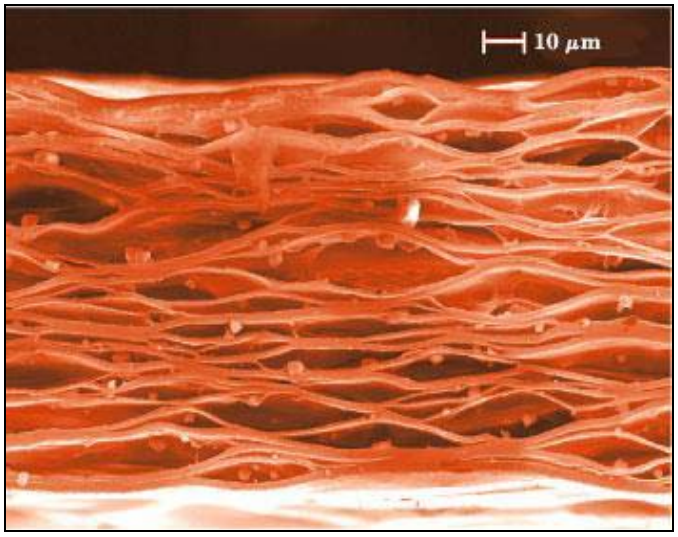

Figure I. 1: Micrograph showing structure of a closed-cell piezoelectret foam. Image from Bauer *et al* [260].

Addressing the behavior of piezoelectrets at a fundamental level requires a robust model that considers the void shape, polarization, and coupled electromechanical response. This work investigates the physical behavior at the void scale, derives a micro-electromechanical model of the effective behavior of these foams, and provides a validation of the model by calculating the effective properties and comparing them with experimental observations. The resulting model predicts the effective viscoelastic, dielectric, and piezoelectric properties of the foams as a function of void shape, orientation, surface charge density and the polymer matrix material properties. The aim

of deriving and implementing this model is to aid in the future design and development of piezoelectrets and to improve an understanding of their complex behavior.

I.2 Model development

Mean field modeling of a heterogeneous medium is accomplished in two discrete steps. The first step is known as localization. The localization step consists of finding expressions for the field variables, in this case that of strain and electric field, on the smallest scale of interest, which is the scale of the voids for these foams. This is done using Green's function techniques. The local field expressions are found in Sections I.2.1 and I.2.2. The second step is known as homogenization. Homogenization is the process of approximating the macroscopic response of the heterogeneous medium as a volume average of the local fields found in the localization step. The homogenization step is detailed in Sections I.2.3 and I.2.4.

I.2.1 Localization

Modeling of piezoelectric closed cell polymer foams starts with the analogous relations of stress equilibrium and Gauss's law:

$$\begin{array}{cc} \text{(a) Mechanical} & \text{(b) Electrostatic} \\ \sigma_{ij,j}(\mathbf{r}) + f_i(\mathbf{r}) = \vec{0} & P_{i,i}(\mathbf{r}) + \rho^b(\mathbf{r}) = 0 \end{array} \qquad \text{(I.2.1)}$$

In these expressions $\boldsymbol{\sigma}$ denotes the Cauchy stress tensor, f_i is the body force associated with the charge deposited in the closed cells, P_i is the polarization density in the heterogeneous material, and ρ^b represents the deposited (bound) charge density (having units C/m^3). Note that the above equations employ Einstein's notation and that the comma denotes the spatial derivative. The formulation of Eq. (I.2.1)a neglects inertial effects and Eq. (I.2.1)b assumes that no free charge is present in the composite dielectric. The electrostatic expression follows from the differential form of Gauss' Law in the absence of free charge and the expression for electric displacement [263]. Gauss' Law states that the surface integral of the flux of electric field through a surface is equal to the total charge contained in the volume surrounded by that surface. This is stated mathematically in both integral and differential forms by Eq. (I.2.2).

$$\begin{aligned} \varepsilon_0 \int_S E_i(\mathbf{r}) n_i dS &= \int_V \rho(\mathbf{r}) dV \\ \varepsilon_0 E_{i,i}(\mathbf{r}) &= \rho^f(\mathbf{r}) + \rho^b(\mathbf{r}) \end{aligned} \tag{I.2.2}$$

It is also known that the divergence of the electric displacement at a point in space is equal to the free charge at that point, or: $D_{i,i}(\mathbf{r}) = \rho^f(\mathbf{r})$. The following relationships between the electric displacement field, the electric field, the polarization density, and the material properties of the dielectric are also very useful.

$$D_i(\mathbf{r}) = \varepsilon_0 E_i(\mathbf{r}) + P_i(\mathbf{r}) = \varepsilon E_i(\mathbf{r}) = \varepsilon_0 \kappa_{ij} E_j(\mathbf{r}) \tag{I.2.3}$$

$$P_i(\mathbf{r}) = \varepsilon_0 \left[\chi_{ij}^{(1)}(\mathbf{r}) E_j(\mathbf{r}) + \chi_{ijk}^{(2)}(\mathbf{r}) E_j(\mathbf{r}) E_k(\mathbf{r}) + \cdots \right] \tag{I.2.4}$$

In Eq. (I.2.3) E_i represents the electric field, ε_0 the permittivity of free space, ε is the permittivity of the dielectric material, κ_{ij} is the dielectric constant, D_i the electric displacement field, and ρ the total charge which is the sum of the free, ρ^f, and bound, ρ^b, charge density [263]. Eq. (I.2.4) gives the important relationship between the polarization density, the electric field, and the material constants. In this expression $\chi_{ij}^{(1)}$ is the electric susceptibility of the heterogeneous medium and $\chi_{ijk}^{(2)}$ is the second order Pockel's effect. In the discussion that follows, the relationship between the polarization density and electric field will be limited to first order effects and therefore the susceptibility will be denoted simply as $\chi_{ij}^{(1)} \to \chi_{ij}$. Equations (I.2.3) and (I.2.4) can now be combined to show that the susceptibility of a medium is related to its dielectric permittivity, κ_{ij}, as follows.

$$\begin{gathered} \kappa_{ij}(\mathbf{r}) = \left[\delta_{ij} + \chi_{ij}(\mathbf{r}) \right] \\ \Downarrow \\ \chi_{ij}(\mathbf{r}) = \kappa_{ij}(\mathbf{r}) - \delta_{ij} \end{gathered} \tag{I.2.5}$$

Where δ_{ij} is the Kronecker delta.

It is now assumed that the heterogeneous composite material can be represented mathematically as a homogeneous material whose electromechanical properties vary with position (this is similar to the approach taken by Hill [135] and Zeller and Dederichs

[68]). It is first necessary to introduce the following expressions for the electromechanical material properties:

$$C_{ijkl}(\mathbf{r}) = C^0_{ijkl} + \delta C_{ijkl}(\mathbf{r}) \tag{I.2.6}$$

$$\chi_{ij}(\mathbf{r}) = \chi^0_{ij} + \delta\chi_{ij}(\mathbf{r}) \tag{I.2.7}$$

$\mathbf{C}(\mathbf{r})$ represents the fourth order position dependent viscoelastic stiffness tensor. This tensor is decomposed into a spatially uniform reference stiffness, $\mathbf{C}^0$, and a stiffness variation about the reference value that is a function of position, $\delta\mathbf{C}(\mathbf{r})$. Likewise $\boldsymbol{\chi}(\mathbf{r})$ represents the second order position dependent electric susceptibility tensor. The electric susceptibility has also been decomposed into a spatially uniform reference susceptibility, $\boldsymbol{\chi}^0$, and some variation about this reference value, $\delta\boldsymbol{\chi}(\mathbf{r})$, which is a function of position. Equations (I.2.8) and (I.2.9) follow from the application of the constitutive analogous mechanical and electrostatic laws given in Eq. (I.2.1) to a material having these spatially dependent properties.

$$C^0_{ijkl}u_{k,lj}(\mathbf{r}) = \left[-\delta C_{ijkl}(\mathbf{r})\varepsilon_{kl}(\mathbf{r})\right]_{,j} - f^p_i(\mathbf{r}) \tag{I.2.8}$$

$$\varepsilon_0\chi^0_{ij}\phi_{,ji}(\mathbf{r}) = \left[\varepsilon_0\delta\chi_{ij}(\mathbf{r})E_j(\mathbf{r})\right]_{,i} - \rho^b(\mathbf{r}) \tag{I.2.9}$$

$\varepsilon_{ij}(\mathbf{r})$ given in the expression (I.2.8) is the small strain tensor which is defined as the gradient of the displacement field in the material, $u_i(\mathbf{r})$, by the classic relation: $\varepsilon_{ij}(\mathbf{r}) = \frac{1}{2}\left[u_{i,j}(\mathbf{r}) + u_{j,i}(\mathbf{r})\right]$. Note that the strain tensor is symmetric: $\varepsilon_{ij}(\mathbf{r}) = \varepsilon_{ji}(\mathbf{r})$. Analogously, $E_i(\mathbf{r})$ is the electric field at any field point and can be calculated from the gradient of the its electric potential: $E_i(\mathbf{r}) = -\phi_{,i}(\mathbf{r})$.

It is now possible to *define* a body force due to the variation in viscoelastic stiffness, $f_i^M(\mathbf{r})$, and a charge density, $\rho^E(\mathbf{r})$, resulting from the spatial variation in electromechanical properties as shown in Eqs. (I.2.10) and (I.2.11).

$$f_i^M(\mathbf{r}) = \left[\delta C_{ijkl}(\mathbf{r})\varepsilon_{kl}(\mathbf{r})\right]_{,j} \tag{I.2.10}$$

$$\rho^E(\mathbf{r}) = -\left[\varepsilon_0 \delta\chi_{ij}(\mathbf{r})E_j(\mathbf{r})\right]_{,i} \tag{I.2.11}$$

These definitions simplify Eqs. (I.2.8) and (I.2.9) to the following:

$$C^0_{ijkl}u_{k,lj}(\mathbf{r}) = -\left[f_i^M(\mathbf{r}) + f_i(\mathbf{r})\right] \tag{I.2.12}$$

$$\varepsilon_0\chi^0_{ij}\phi_{,ji}(\mathbf{r}) = -\left[\rho^E(\mathbf{r}) + \rho^b(\mathbf{r})\right] \tag{I.2.13}$$

The form of the stress equilibrium equation and Gauss's law by given be Eqs. (I.2.12) and (I.2.13) are differential equation that can be solved by employing Green's functions. This is done through the second order Green's tensor, $G_{km}^{0}\left(\mathbf{r}-\mathbf{r}'\right)$, and the scalar Green's function, $g^{0}\left(\mathbf{r}-\mathbf{r}'\right)$, respectively. The superscript *0* denotes that the resulting solution propagates the effect of the body force and charge density distributions through the reference medium whose properties have not yet been found. In this case, Green's *tensor* calculates the displacement in the *k* direction at the point **r** due to a time varying force, $f_i^{tot}\left(\mathbf{r},t\right)=\mathbb{R}\mathrm{e}\left\{\left[f_i^{M}\left(\mathbf{r}\right)+f_i\left(\mathbf{r}\right)\right]e^{-i\omega t}\right\}$, acting in the *m* direction and located at the point **r**'. Analogously, the scalar Green's function calculates the electric potential at the point **r** due to a time varying charge density, $\rho\left(\mathbf{r},t\right)=\mathbb{R}\mathrm{e}\left\{\left[\rho^{E}\left(\mathbf{r}\right)+\rho^{b}\left(\mathbf{r}\right)\right]e^{-i\omega t}\right\}$, located at the point **r**'.

The Green's tensor and function are found by solving the differential Eqs. (I.2.14) and (I.2.15):

$$C_{ijkl}^{0}G_{km,lj}^{0}\left(\mathbf{r}-\mathbf{r}'\right)+\delta_{im}\delta\left(\mathbf{r}-\mathbf{r}'\right)\delta\left(\omega-\omega'\right)=0 \qquad \text{(I.2.14)}$$

$$\varepsilon_0\chi_{ij}^{0}g_{,ji}^{0}\left(\mathbf{r}-\mathbf{r}'\right)+\delta\left(\mathbf{r}-\mathbf{r}'\right)\delta\left(\omega-\omega'\right)=0 \qquad \text{(I.2.15)}$$

for the boundary conditions on the external surface of the homogeneous medium, *S* [71]. In these equations, δ_{im} is the Kronecker delta, $\delta\left(\omega-\omega'\right)$ is the frequency domain Dirac delta function, and $\delta\left(\mathbf{r}-\mathbf{r}'\right)$ is the three dimensional Dirac delta function [71]. By

modifying the work of Berveiller *et al* [71] to take the time variation of the distributed body force and charge density into account, it can be shown that the solution to Eqs. (I.2.14) and (I.2.15) are given by the integral equations below.

$$\begin{aligned} u_m(\mathbf{r}) &= u_m^0 + \int_{-\infty}^{\infty}\int_V G_{im}^0(\mathbf{r}-\mathbf{r}')\, f_i^{tot}(\mathbf{r}')\, d\mathbf{r}'\, d\omega' \\ u_m(\mathbf{r}) &= u_m^0(\mathbf{r}) + \int_{-\infty}^{\infty}\int_V G_{im}^0(\mathbf{r}-\mathbf{r}')\left\{\left[\delta C_{ijkl}(\mathbf{r}')\,\varepsilon_{kl}(\mathbf{r}')\right]_{,j'} + f_i(\mathbf{r}')\right\} d\mathbf{r}'\, d\omega' \end{aligned} \tag{I.2.16}$$

$$\begin{aligned} \phi(\mathbf{r}) &= \phi^0 + \int_{-\infty}^{\infty}\int_V g^0(\mathbf{r}-\mathbf{r}')\, h(\mathbf{r}')\, d\mathbf{r}'\, d\omega' \\ \phi(\mathbf{r}) &= \phi^0 + \int_{-\infty}^{\infty}\int_V g^0(\mathbf{r}-\mathbf{r}')\left\{\left[\varepsilon_0\delta\chi_{ij}(\mathbf{r}')\,E_j(\mathbf{r}')\right]_{,i'} + \rho^b(\mathbf{r}')\right\} d\mathbf{r}'\, d\omega' \end{aligned} \tag{I.2.17}$$

Integrating (I.2.16) and (I.2.17) by parts yields the following displacement and potential fields:

$$u_m(\mathbf{r}) = u_m^0(\mathbf{r}) - \int_{-\infty}^{\infty}\int_V \left\{G_{im,j'}^0(\mathbf{r}-\mathbf{r}')\left[\delta C_{ijkl}(\mathbf{r}')\,\varepsilon_{kl}(\mathbf{r}')\right] - G_{im}^0(\mathbf{r}-\mathbf{r}')\, f_i(\mathbf{r}')\right\} d\mathbf{r}'\, d\omega' \tag{I.2.18}$$

$$\phi(\mathbf{r}) = \phi^0(\mathbf{r}) - \int_{-\infty}^{\infty}\int_V \left\{g_{,i'}^0(\mathbf{r}-\mathbf{r}')\left[\varepsilon_0\delta\chi_{ij}(\mathbf{r}')\,E_j(\mathbf{r}')\right] - g^0(\mathbf{r}-\mathbf{r}')\,\rho^b(\mathbf{r}')\right\} d\mathbf{r}'\, d\omega' \tag{I.2.19}$$

Recalling the following properties of Green's functions:

$$G^0_{im,j'} = \frac{\partial G^0_{im}\left(\mathbf{r}-\mathbf{r}'\right)}{\partial x_j'} = -\frac{\partial G^0_{im}\left(\mathbf{r}-\mathbf{r}'\right)}{\partial x_j} = -G^0_{im,j} \tag{I.2.20}$$

Relations (I.2.18) and (I.2.19) represent the local fields of displacement and electric potential. These equations can be modified to yield the local expressions for strain and electric field by taking the spatial derivative. The result can be simplified to the representation given in Eqs. (I.2.21) and (I.2.22) by evoking the small strain approximation and the integral property of the Dirac delta function, $x(\omega) = \int_{-\infty}^{\infty} x(\omega')\delta(\omega-\omega')d\omega'$ [68, 125]:

$$\varepsilon_{ij}\left(\mathbf{r}\right) = \varepsilon^g_{ij} - \int_V \Gamma^0_{ijkl}\left(\mathbf{r}-\mathbf{r}'\right)\delta C_{klmn}\left(\mathbf{r}'\right)\varepsilon_{mn}\left(\mathbf{r}'\right)d\mathbf{r}' + \int_V G^0_{ij,k}\left(\mathbf{r}-\mathbf{r}'\right)f_k\left(\mathbf{r}'\right)d\mathbf{r}' \tag{I.2.21}$$

$$E_i\left(\mathbf{r}\right) = E^g_i - \int_V \gamma^0_{ij}\left(\mathbf{r}-\mathbf{r}'\right)\varepsilon_0\delta\chi_{jk}\left(\mathbf{r}'\right)E_k\left(\mathbf{r}'\right)d\mathbf{r}' + \int_V g^0_{,i}\left(\mathbf{r}-\mathbf{r}'\right)\rho^b\left(\mathbf{r}'\right)d\mathbf{r}' \tag{I.2.22}$$

In the above expressions, ε^g_{ij} and E^g_i represent the macroscopic strain and electric fields of the reference medium, respectively. These fields have no spatial dependence. $\Gamma^0_{ijkl}\left(\mathbf{r}-\mathbf{r}'\right)$ and $\gamma^0_{ij}\left(\mathbf{r}-\mathbf{r}'\right)$ are called the modified Green's tensor and function,

respectively. The modified Green's tensor is related to the previously introduced second order Green's tensor through Eq. (I.2.23) while the modified Green's function is defined by Eq. (I.2.24).

$$\Gamma^0_{ijkl}\left(\mathbf{r}-\mathbf{r}'\right) = -\frac{1}{2}\left[G^0_{ki,jl}\left(\mathbf{r}-\mathbf{r}'\right) + G^0_{kj,il}\left(\mathbf{r}-\mathbf{r}'\right)\right] \tag{I.2.23}$$

$$\gamma^0_{ij}\left(\mathbf{r}-\mathbf{r}'\right) = -\frac{1}{2}\left[g^0_{,ij}\left(\mathbf{r}-\mathbf{r}'\right) + g^0_{,ji}\left(\mathbf{r}-\mathbf{r}'\right)\right] \tag{I.2.24}$$

Relations (I.2.21) and (I.2.22) specifically show that the strain and electric fields at the macroscopic length scale can be approximated by averaging the effects of material property variations within the volume, V. This reinforces Christensen's statement that multiscale modeling requires the effects of discontinuities at the microscopic length scale to have only an average effect on the macroscopic behavior [33].

It is now useful to define the spatial variation of the viscoelastic stiffness and electric susceptibility. This spatial variation can be mathematically expressed using the Heaviside step function $\theta\left(\mathbf{r}\right)$ as shown below.

$$\delta\mathbf{C}\left(\mathbf{r}\right) = \left(\mathbf{C}^I - \mathbf{C}^0\right)\theta^I\left(\mathbf{r}\right) = \Delta\mathbf{C}^{I0}\theta^I\left(\mathbf{r}\right) \tag{I.2.25}$$

$$\delta\chi\left(\mathbf{r}\right) = \left(\chi^I - \chi^0\right)\theta^I\left(\mathbf{r}\right) = \Delta\chi^{I0}\theta^I\left(\mathbf{r}\right) \tag{I.2.26}$$

In the above expression, $\mathbf{C}^I$ and $\boldsymbol{\chi}^I$ represent the stiffness tensor and electric susceptibility of the closed cell. Further, the step function is defined as:

$$\theta^I(\mathbf{r}) = \begin{cases} 1 & \text{if } \mathbf{r} \in V_I \\ 0 & \text{if } \mathbf{r} \notin V_I \end{cases} \tag{I.2.27}$$

It is also noted that the strain and electric fields inside the close cells can be assumed to be spatially uniform. This is the implementation of Eshelby's assumption and its electrostatic analogue [58]. Note also that the body force, $f_i(\mathbf{r})$, and charge density, $\rho^b(\mathbf{r})$, due to the charge deposited on the interior surface of the closed cells coincide with the location of these cells and can be *approximated as being uniform surface density entities collocated with the inner cell surface*. This is done by employing the Dirac delta distribution on the surface of the inclusion, S_I, represented as $\delta(S_I)$.

$$\int_{V_I} \mathbf{u}(\mathbf{r}) : f_i^p(\mathbf{r}) \delta(S_I) dV = \int_{S_I} \mathbf{u}(\mathbf{r}) : f_i^{surf}(\mathbf{r}) dS \tag{I.2.28}$$

$$\int_{V_I} \mathbf{u}(\mathbf{r}) \rho^b(\mathbf{r}) \delta(S_I) dV = \int_{S_I} \mathbf{u}(\mathbf{r}) \rho^{b,surf}(\mathbf{r}) dS \tag{I.2.29}$$

In these equations, $\mathbf{u}(\mathbf{r})$ represents any n^{th} order tensor, f_i^{surf} a force per unit area in the i direction (a traction), and $\rho^{b,surf}$ a surface charge density. Both the traction and surface charge density only at the material point, $\mathbf{r}$, located on the void-polymer interface.

Equations (I.2.25), (I.2.26), (I.2.28), and (I.2.29) can now be substituted into expressions for the local strain and electric field, Eqs. (I.2.21) and (I.2.22), to yield the following integral equations for the strain and electric field anywhere in the heterogeneous dielectric material.

$$\varepsilon_{ij}\left(\mathbf{r}\right)=\varepsilon_{ij}^{g}-\int_{V_I}\Gamma_{ijkl}^{0}\left(\mathbf{r}-\mathbf{r}'\right)\Delta C_{klmn}^{I0}\overline{\varepsilon}_{mn}^{I}d\mathbf{r}'+\int_{S_I}G_{ij,k}^{0}\left(\mathbf{r}-\mathbf{r}'\right)f_i^{surf}\left(\mathbf{r}\right)d\mathbf{r}' \qquad \text{(I.2.30)}$$

$$E_i\left(\mathbf{r}\right)=E_i^{g}-\int_{V_I}\gamma_{ij}^{0}\left(\mathbf{r}-\mathbf{r}'\right)\Delta\chi_{jk}^{I0}\overline{E}_k^{I}d\mathbf{r}'+\int_{S_I}g_{,i}^{0}\left(\mathbf{r}-\mathbf{r}'\right)\overline{\rho}^{b,surf}d\mathbf{r}' \qquad \text{(I.2.31)}$$

The following section will investigate the physical origin of f_i^{surf} and $\rho^{b,surf}$ and their relation to the deposited charge, void geometry, the applied electric and strain fields.

I.2.2 Derivation of piezoelectric coupling terms

The piezoelectric effect displayed by closed cell polymer foams is the result of the interaction of the charge bound to the interior of the closed cells with applied electric and strain fields. This interaction is intuitively simple to understand, but is less simple to describe mathematically. The purpose of this section is to derive f_i^{surf} and $\rho^{b,surf}$ as functions of the deposited surface charge density, cell geometry, and the applied electromechanical fields.

I.2.2.1 Approximation of the traction at the void-matrix interface

The force f_i^{surf} represents the force per unit area acting in the *i* direction at the void-polymer interface and it has two major contributors. The first is the net *Coulomb force* per unit area at each material point on the interface resulting from the existence of the deposited opposite charges on each side of the void. This is analogous to the attractive force between the two plates of a charged parallel plate capacitor. The second is a *Lorentz force* resulting from the interaction of the applied electric field and the deposited bound charge density. Further, there are two consequences of the Coulomb force. The first is a pre-stress induced by the existence of the deposited charge and will be denoted as denoted as σ_{ij}^{pre}. This stress does not affect the stiffness behavior of the foam, but *may affect* the piezoelectric coupling behavior by changing the initial separation distance between charged surfaces. This initial separation distance governs the strength of the polarization density and thus the piezoelectric effect. Studies by Wegener *et al* [264] show the influence of internal void pressure, which is simply an internal pre-stress, on the piezoelectric coupling hint that this may be the case. The second consequence of the Coulomb force is a change in the observed effective stiffness of the foam even in the absence of an electric field. The change in stiffness is brought about by the difference in separation distance between material points on the surface of the void when the foam is strained. In other words, a voided polymer having charge deposited on the void surfaces will have a different stiffness than that of a non-charged voided polymer. The Lorentz force component gives the voided polymer its piezoelectric effect by generating stress inside the material when an external electric field is applied

across the foam. It is imperative that this force be quantified in order to approximate the effective piezoelectric coupling coefficients of the foam. Finally, it is important to note that the fact that force associated with the presence of deposited charge coincides with a material surface means that f_i^{surf} is analogous to the traction vector of continuum mechanics. This statement is in accordance with the observations of Rinaldi and Brenner that the Maxwell stress tensor is not a physically objective Cauchy stress, but rather that body forces resulting electrostatic behavior can only be correctly represented as force at a distance entities [251]. Because the traction vector f_i^{surf} is derived from force-at-a-distance approximations of electrostatic behavior and resolved using volume integrals, the above derivation has not violated any of the fundamental assumptions of continuum mechanics.

The resultant force per unit area at each material point must be found through a surface integral of the contributing forces. The first component, the Coulomb force, is investigated first. In a vacuum, the Coulomb force, **F**, exerted on one charged particle by another can be calculated from Eq. (I.2.32).

$$\mathbf{F}(\mathbf{r},\mathbf{r}') = \frac{q(\mathbf{r})q(\mathbf{r})}{4\pi\varepsilon_0}\frac{\mathbf{r}-\mathbf{r}'}{|\mathbf{r}-\mathbf{r}'|^3} = \frac{q(\mathbf{r})q(\mathbf{r}')}{4\pi\varepsilon_0}\frac{\mathbf{r}_d}{|\mathbf{r}_d|^3} \qquad \text{(I.2.32)}$$

In this expression q represents the charge, in Coulombs, at material points $\mathbf{r}$ and $\mathbf{r}'$, respectively and $\mathbf{r}_d = \mathbf{r} - \mathbf{r}$. The value of $1/4\pi\varepsilon_0$ is known to be 8.9876 x 10^9 (N m^2)C^{-2}. For gas filled voids, this value is a reasonable approximation of true permittivity. This

force component can be related to the deposited charge density and void geometry, shown below in Figure I. 2 as follows.

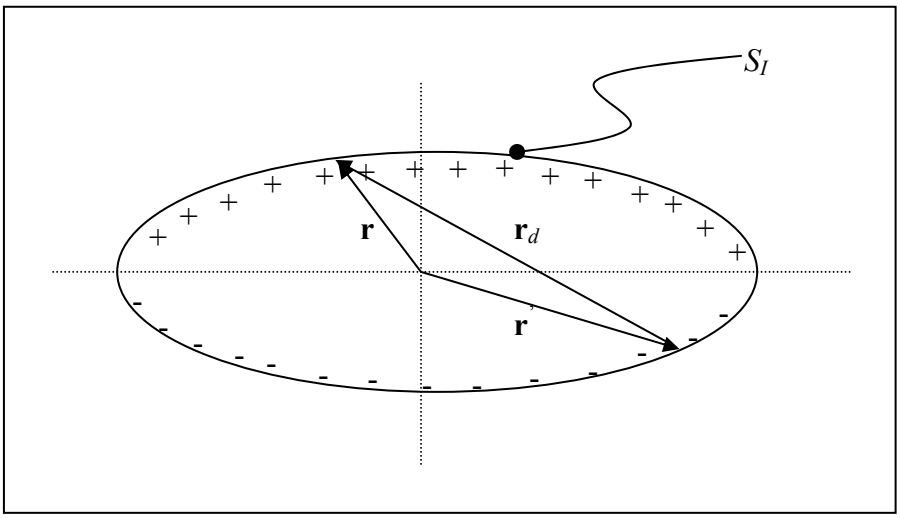

Figure I. 2: Diagram of a single oblate ellipsoidal closed-cell void with a charge deposited on the interior surface. The diagram is used in this section to derive the piezoelectric coupling terms.

The Coulomb force is decomposed into unstrained and strain components. The unstrained component is a function of the void geometry and the surface charge density alone, while the strained component also depends on the imposed strain state. This is shown explicitly in Eq. (I.2.33).

$$\mathbf{F}^{tot} = \mathbf{F}_1\left(\mathbf{r}, \rho^{surf}\right) + \mathbf{F}_2\left(\mathbf{r}, \rho^{surf}, \varepsilon_{ij}\right) \tag{I.2.33}$$

Note that $\mathbf{F}_1$ created a pre-stress in the material while $\mathbf{F}_2$ changes the overall stiffness. In a strained state, the displacement, **u**, of each material point can be described using the usual small strain approximation as $u_i\left(\mathbf{r}\right) = \varepsilon_{ij}\left(\mathbf{r}\right) r_j$. The vectors $\mathbf{r}_\delta$ and $\mathbf{r}_\delta^{'}$ pointing to

material points initially found at the positions $\mathbf{r}$ and $\mathbf{r}'$, respectively, are then easily found.

$$r_i^{X\delta} = \left[\delta_{ij} + \varepsilon_{ij}\left(\mathbf{r}_X\right)\right] r_j^{\delta} \tag{I.2.34}$$

Where $\mathbf{r}_X \Leftrightarrow r_i^X$ and X represents either d, or a prime or non-primed value. The vector pointing between material points $\mathbf{r}$ and $\mathbf{r}'$ is then represented in Eq (I.2.35).

$$r_i^{d\delta} = r_i^d + \left[\varepsilon_{ij}\left(\mathbf{r}\right) r_j - \varepsilon_{ij}\left(\mathbf{r}'\right) r_j'\right] \tag{I.2.35}$$

This expression can now be simplified through the application of Eshelby's assumption that the strain in an void is well approximated as being uniform, $\bar{\varepsilon}_{ij}^I$, yielding the following.

$$r_i^{d\delta} = \left[\delta_{ij} + \bar{\varepsilon}_{ij}^I\right] r_j^d \tag{I.2.36}$$

Inserting expression (I.2.36) into (I.2.32) gives a relation for the total Coulomb force at any material point as a function of strain.

$$\mathbf{F}\left(\mathbf{r},\mathbf{r}'\right) = \frac{q\left(\mathbf{r}\right)q\left(\mathbf{r}'\right)}{4\pi\varepsilon_0}\frac{\mathbf{r}_d^{\delta}}{\left|\mathbf{r}_d^{\delta}\right|^3} \approx \frac{q\left(\mathbf{r}\right)q\left(\mathbf{r}'\right)}{4\pi\varepsilon_0}\frac{\left(\delta_{ij} + \bar{\varepsilon}_{ij}^I\right) r_j^d}{\left|\mathbf{r}_d\right|^3}\left(1-3K\right) \tag{I.2.37}$$

Where K is a constant that depends on the elements of the strain tensor and the vector $\mathbf{r}$.

$$K = \frac{1}{\left|\mathbf{r}_d\right|^2}\left\{r_1^d\left[r_1^d\bar{\varepsilon}_{11}^I + r_2^d\bar{\varepsilon}_{12}^I + r_3^d\bar{\varepsilon}_{13}^I\right] + r_2^d\left[r_1^d\bar{\varepsilon}_{21}^I + r_2^d\bar{\varepsilon}_{22}^I + r_3^d\bar{\varepsilon}_{23}^I\right] + r_3^d\left[r_1^d\bar{\varepsilon}_{31}^I + r_2^d\bar{\varepsilon}_{32}^I + r_3^d\bar{\varepsilon}_{33}^I\right]\right\}$$
$$= \frac{1}{\left|\mathbf{r}_d\right|^2}\bar{\varepsilon}_{ij}^I r_i^d r_j^d \tag{I.2.38}$$

Using these equations it is now possible to show that the total Coulomb force reduces to the following expression.

$$\begin{aligned} F_i\left(\mathbf{r},\mathbf{r}'\right) &= \bar{F}\left(\mathbf{r},\mathbf{r}'\right)\left\{r_i^d + \bar{\varepsilon}_{ij}^I r_j^d - \frac{3r_m^d r_n^d \bar{\varepsilon}_{mn}^I r_i^d}{\left|\mathbf{r}_d\right|^2}\right\} \\ &= \bar{F}\left(\mathbf{r},\mathbf{r}'\right)r_i^d + \bar{F}\left(\mathbf{r},\mathbf{r}'\right)\left[\delta_{ij} - \frac{3r_i^d r_j^d}{\left|\mathbf{r}_d\right|^2}\right]\bar{\varepsilon}_{jk}^I r_k^d \end{aligned} \tag{I.2.39}$$

with

$$\bar{F}\left(\mathbf{r},\mathbf{r}'\right) = q\left(\mathbf{r}\right)q\left(\mathbf{r}'\right)\Big/4\pi\varepsilon_0\left|\mathbf{r}_d\right|^3 \tag{I.2.40}$$

It is important to note that the force is attractive (in the opposite direction as the position vector) when the charged particles have opposite charges. Inspection of Eq. (I.2.39) clearly shows that the total force due to Coulomb attraction/repulsion is divided into the unstrained component, represented by the first term on the RHS of Eq. (I.2.39) and the strained component represented by the second term in the same equation. The first term contributes to the initial stress state of the heterogeneous material and the second term

changes the overall stiffness of the material. It is also important to note that the force given by Eq. (I.2.39) is in units of Newtons and that the charges, q, are total charges in Coulombs, while a force per unit area, a traction, as a function of the known deposited surface charge density is needed. This traction can be described in terms of the deposited surface charge density as follows. First the variable $\mathfrak{I}_i\left(\mathbf{r}\middle|\mathbf{r}'\right)$ is defined having units of N/m^4.

$$\mathfrak{I}_i\left(\mathbf{r}\middle|\mathbf{r}'\right)=\frac{\rho^{surf}\left(\mathbf{r}\right)\rho^{surf}\left(\mathbf{r}'\right)}{4\pi\varepsilon_0\left|\mathbf{r}_d\right|^3}\left[r_i^d+\left\{\delta_{ij}-\frac{3r_i^d r_j^d}{\left|\mathbf{r}_d\right|^2}\right\}\overline{\varepsilon}_{jk}^I r_k^d\right] \tag{I.2.41}$$

Equation (I.2.41) is simply a restatement of Eq. (I.2.39) where the total charge, q, has be replaced with the surface charge density at the same material point. The force entity $\mathfrak{I}\left(\mathbf{r}\middle|\mathbf{r}'\right)$ calculates the force per m^4 exerted at $\mathbf{r}$ due to a surface charge density at any other point, $\mathbf{r}'$. The total traction due to Coulomb interaction at any point $\mathbf{r}$ is now determined by summing the contributions to this force from all possible contributing material points, $\mathbf{r}'$, on the interior surface of the void. This is achieved by performing the following surface integral.

$$\begin{aligned} f_i^{C,surf}\left(\mathbf{r}\right)&=\int_{S_I}\mathfrak{I}_i\left(\mathbf{r}\middle|\mathbf{r}'\right)d\mathbf{r}' \\ \text{where}&\begin{cases}\mathbf{r},\mathbf{r}'\in S_I\\ \mathbf{r}\neq\mathbf{r}'\end{cases}\end{aligned} \tag{I.2.42}$$

Where the *C* of the superscript denotes the Coulomb contribution to the traction at $\mathbf{r}$.

The resolution of the Lorentz force per unit area is much simpler to deduce. It is known that the Lorentz force acting on any charged particle in the absence of magnetic field and having a particle velocity much lower than the speed of light is related to the charge and electric field as follows [263].

$$\mathbf{F} = \int_V \rho \mathbf{E} dV \tag{I.2.43}$$

Where ρ is the charge density per unit volume and **E** is the electric field. From this relation, it is obvious that the traction at the material point **r** due to a surface charge density at the same point is given as follows.

$$f_i^{L,surf}(\mathbf{r}) = \rho^{surf}(\mathbf{r}) E(\mathbf{r}) \tag{I.2.44}$$

Finally, the total traction at any material point is calculated as the sum of the Coulomb and Lorentz components.

$$f_i^{surf}(\mathbf{r}) = f_i^{C,surf}(\mathbf{r}) + f_i^{L,surf}(\mathbf{r}) \tag{I.2.45}$$

It is now possible to turn attention to the development of the polarization density in the void related to the geometry, surface charge density, and strain.

I.2.2.2 Approximation of the surface charge density

An analysis of the surface charge density must begin with a remark concerning the form of Gauss' Law employed in Eq. (I.2.1). The integral form of this equation can be employed to show that the normal component of the polarization density is equal to the surface charge density at each material surface point. This is only true when no charge exists within the volume surrounded by the surface that includes the material point. This is stated mathematically as follows.

$$\rho^{surf}\left(\mathbf{r}\right) = P_i\left(\mathbf{r}\right) n_i\left(\mathbf{r}\right) \tag{I.2.46}$$

Where **n** is the vector pointing normal to the surface at the material point **r**. Further, the average polarization density of a void, $\overline{\mathbf{P}}^I$, is reasonably well approximated as the volume average of all dipole moments within the void as follows.

$$\overline{\mathbf{P}}^I = \frac{1}{V_I}\left\langle \frac{1}{2}\left(\left|q\left(\mathbf{r}\right)\right| + \left|q\left(\mathbf{r}'\right)\right|\right)\mathbf{r}_d \right\rangle \tag{I.2.47}$$

Where V_I is the void volume, $\mathbf{r}_d$ is the separation distance between any two material points on the void surface, and q is the charge at the material points **r** and $\mathbf{r}'$. Due to the symmetry of the voids present in the voided closed-cell polymer electrets modeled in this work, this polarization density of the voids can be acceptably well using the following description.

$$\overline{\mathbf{P}}^I = \frac{1}{2V_I}\left(\left|q_{top}\right| + \left|q_{bottom}\right|\right)\mathbf{r}_D^{ave} \tag{I.2.48}$$

With

$$\begin{aligned} q_{top} &= \int_{S_I^{top}} \rho_{top}^{surf}(\mathbf{r})\, d\mathbf{r} \\ &\approx \frac{1}{2}\overline{\rho}_{top}^{surf} S_I \end{aligned} \quad \& \quad \begin{aligned} q_{bottom} &= \int_{S_I^{bottom}} \rho_{bottom}^{surf}(\mathbf{r})\, d\mathbf{r} \\ &\approx \frac{1}{2}\overline{\rho}_{bottom}^{surf} S_I \end{aligned} \tag{I.2.49}$$

Where $\mathbf{r}_D^{ave}$ is the area average separation distance between the top and bottom surfaces of the void. The effect of strain is included using the small strain approximation elicited earlier, $r_i^{\delta D} = \left[\delta_{ij} + \overline{\varepsilon}_{ij}^{I}\right] r_j^D$. It is now possible to approximate the void polarization and piezoelectric coupling based on the above analysis.

$$\begin{aligned} &\overline{P}_i^I = \frac{S_I}{2V_I}\left|\overline{\rho}^{surf}\right|\left(\delta_{ij} + \overline{\varepsilon}_{ij}^{I}\right) r_j^{D,ave} \\ &\text{if} \quad \left|\overline{\rho}_{top}^{surf}\right| \approx \left|\overline{\rho}_{bottom}^{surf}\right| \approx \left|\overline{\rho}^{surf}\right| \end{aligned} \tag{I.2.50}$$

The value of $\left|\overline{\rho}^{surf}\right|$ is a model input that depends on experimental values of actual charge deposition. It is important to note, however, that variable can be calculated from a known charge density distribution, $\rho^{surf}(\mathbf{r})$, using area averaging.

$$\overline{\rho}^{surf} = \frac{1}{S}\int_S \rho^{surf}(\mathbf{r})\, d\mathbf{r} \quad \text{with} \quad \mathbf{r} \in S \tag{I.2.51}$$

Where S represents any area. Note that for spheres, and oblate and prolate ellipsoids, the term S_I/V_I reduces to the following [129].

$$\frac{S_I^{sphere}}{V_I^{sphere}} = \frac{3}{a} \tag{I.2.52}$$

$$\frac{S_I^{oblate}}{V_I^{oblate}} = \frac{3}{2c} + \frac{3c}{4a^2 e_{OB}} \ln\left[\frac{1+e_{OB}}{1-e_{OB}}\right] \tag{I.2.53}$$

$$\frac{S_I^{prolate}}{V_I^{prolate}} = \frac{3}{2c} + \frac{3}{2ae_{PR}} \sin^{-1}\left(e_{PR}\right) \tag{I.2.54}$$

with

$$e_{OB} = \sqrt{1-\frac{c^2}{a^2}} \qquad e_{PR} = \sqrt{1-\frac{a^2}{c^2}} \tag{I.2.55}$$

Where a and c represent the major and minor axis' respectively, and e is known as the ellipticity of the ellipsoid. Equation (I.2.50) clearly shows that the result of the deposited charge is to induce a pre-polarization in the voided polymer and to induce an electromechanical coupling where the polarization, and consequently the electric displacement, depends on the imposed strain. The above analysis of the electromechanical behavior in the void is sufficient to proceed to the final step of mean-field modeling: volume averaging.

I.2.3 Volume averaging

The integral equations derived above used techniques introduced by Zeller and Dederichs [68] and Walpole [73] and emphasizes one of the most basic requirements of multiscale modeling given by Christensen [33]. The requirement is that inhomogeneities, representing the smallest length scale, only have an average effect on the behavior observed at the macroscopic scale. Though this is approximation is arguably not representative of the structure of piezoelectric closed cell polymers which are the subject of this study, mean field methods have been shown to have reasonable agreement with macroscopic material behavior even at elevated inclusion fractions. See, for example, Ledbetter and Datta [30], Hornby *et al* [29], and Haberman *et al* [130]. For this reason, there is merit in continuing the mean field approach pursued to this point by employing the integral equation representations (I.2.30) and (I.2.31), which describe the local strain and electric fields, to approximate the effective behavior of the heterogeneous medium at the macroscopic scale. This is achieved by calculating the volumetric average of $\varepsilon_{ij}(\mathbf{r})$ and $E_i(\mathbf{r})$.

The volume average of the strain and electric fields in the closed cells, $\overline{\varepsilon}_{ij}^{I}$ and $\overline{E}_i^{I}$ respectively, must first be defined.

$$\overline{\varepsilon}_{ij}^{I} = \frac{1}{V_I}\int_{V_I} \varepsilon_{ij}(\mathbf{r})\,d\mathbf{r}$$
$$\overline{E}_i^{I} = \frac{1}{V_I}\int_{V_I} E_i(\mathbf{r})\,d\mathbf{r} \qquad \text{(I.2.56)}$$

The volume average of Eqs. (I.2.30) and (I.2.31) with respect to the inclusion gives [24]:

$$\bar{\varepsilon}_{ij}^{I} = \varepsilon_{ij}^{g} - \frac{1}{V_I}\int_{V_I}\int_{V_I} \Gamma_{ijkl}^{0}\left(\mathbf{r}-\mathbf{r}'\right)\Delta C_{klmn}^{I0}\bar{\varepsilon}_{mn}^{I}\, d\mathbf{r}'\, d\mathbf{r} + \frac{1}{V_I}\int_{V_I}\int_{S_I} G_{ij,k}^{0}\left(\mathbf{r}-\mathbf{r}'\right)\bar{f}_{k}^{surf}\, d\mathbf{r}'\, d\mathbf{r} \tag{I.2.57}$$

$$\bar{E}_{i}^{I} = E_{i}^{g} - \frac{1}{V_I}\int_{V_I}\int_{V_I} \gamma_{ij}^{0}\left(\mathbf{r}-\mathbf{r}'\right)\varepsilon_0\Delta\chi_{jk}^{I0}\bar{E}_{k}^{I}\, d\mathbf{r}'\, d\mathbf{r} + \frac{1}{V_I}\int_{V_I}\int_{S_I} g_{,i}^{0}\left(\mathbf{r}-\mathbf{r}'\right)\bar{P}_{j}^{I} n_j\left(\mathbf{r}'\right) d\mathbf{r}'\, d\mathbf{r} \tag{I.2.58}$$

Where $\bar{\varepsilon}_{mn}^{I}$, $\bar{f}_{k}^{surf}$, $\bar{E}_{k}^{I}$, and $\bar{P}_{j}^{I}$ have been approximated as constants within the void. Future equation manipulation can simplified by defining the following tensors which denote the various volume averages of the second Green's tensor and function. Approximation of these terms using Fourier transform techniques is given in Appendix A of this thesis.

$$\begin{aligned} T_{ijkl}^{I}\left(\mathbf{C}^0,\mathbf{r}\right) &= \frac{1}{V_I}\int_{V_I}\int_{V_I} \Gamma_{ijkl}^{0}\left(\mathbf{r}-\mathbf{r}'\right) d\mathbf{r}' \quad \text{if} \quad \mathbf{r}' \in V_I \\ B_{ijk}^{I}\left(\mathbf{C}^0,\mathbf{r}\right) &= \frac{1}{V_I}\int_{V_I}\int_{S_I} G_{ij,k}^{0}\left(\mathbf{r}-\mathbf{r}'\right) d\mathbf{r}' \quad \text{if} \quad \mathbf{r}' \in S_I \end{aligned} \tag{I.2.59}$$

$$\begin{aligned} t_{ij}^{I}\left(\kappa^0,\mathbf{r}\right) &= \frac{1}{V_I}\int_{V_I}\int_{V_I} \gamma_{ij}^{0}\left(\mathbf{r}-\mathbf{r}'\right) d\mathbf{r}' \qquad \text{if} \quad \mathbf{r}' \in V_I \\ b_{ij}^{I}\left(\kappa^0,\mathbf{r}\right) &= \frac{1}{V_I}\int_{V_I}\int_{S_I} g_{,i}^{0}\left(\mathbf{r}-\mathbf{r}'\right) n_j\left(\mathbf{r}'\right) d\mathbf{r}' \quad \text{if} \quad \mathbf{r}' \in S_I \end{aligned} \tag{I.2.60}$$

Note that the average over the volume of the inclusion of the fourth order tensor $\mathbf{T}^I\left(\mathbf{C}^0\right)$ is related to Eshelby's tensor, **S**, as shown below [58, 71]:

$$\mathbf{S} = \mathbf{T}^I\left(\mathbf{C}^0\right) : \mathbf{C}^0 \tag{I.2.61}$$

Now, because $\overline{\varepsilon}_{mn}^I$, $\overline{f}_k^{surf}$, $\overline{E}_k^I$, and $\overline{P}_j^I$ have been approximated as constants in the inclusion volume or on the inclusion surface, Eqs. (I.2.57) and (I.2.58) simplify to the following useful expressions.

$$\overline{\varepsilon}_{ij}^I = \varepsilon_{ij}^g - T_{ijkl}^I\left(\mathbf{C}^0\right)\Delta C_{klmn}^{I0}\overline{\varepsilon}_{mn}^I + B_{ijk}^I\left(\mathbf{C}^0\right)\overline{f}_k^{surf} \tag{I.2.62}$$

$$\overline{E}_i^I = E_i^g - t_{ij}^I\left(\varepsilon_0\chi^0\right)\varepsilon_0\Delta\chi_{jk}^{I0}\overline{E}_k^I + b_{ij}^I\left(\varepsilon_0\chi^0\right)\overline{P}_j^I \tag{I.2.63}$$

I.2.4 Homogenization of local expressions

The integral equations derived above provide a means to calculate the local strain fields given the loading conditions imposed at the representative volume element (RVE) boundary. The first homogenization step defines the volumetric composition of the composite material. The total volume of the particulate composite is decomposed into portions that are occupied by the closed cells, V_I, and the matrix material, V_M, according to $V = V_M + V_I$. This equation yields the volume fraction relation below.

$$f^M + f^I = 1 \tag{I.2.64}$$

Here f^X is the volume fraction of phase *X* and is related to the total volume fraction of the composites by $f^X = V^X / V$.

The uniform stress, strain, polarization density, and electric fields of the heterogeneous material, σ_{ij}^g, ε_{ij}^g, P_i^g and E_i^g, must be defined in terms of their local analogues, $\sigma_{ij}(\mathbf{r})$, $\varepsilon_{ij}(\mathbf{r})$, $P_i(\mathbf{r})$, and $E_i(\mathbf{r})$. The classic approach defines the macroscopic fields as the volumetric average of the local fields defined by (I.2.65) and (I.2.66) [54].

$$\text{(a)}\ \varepsilon_{ij}^g = \frac{1}{V}\int_V \varepsilon_{ij}(\mathbf{r})\,d\mathbf{r} \qquad \text{(b)}\ \sigma_{ij}^g = \frac{1}{V}\int_V \sigma_{ij}(\mathbf{r})\,d\mathbf{r} \tag{I.2.65}$$

$$\text{(a)}\ E_i^g = \frac{1}{V}\int_V E_i(\mathbf{r})\,d\mathbf{r} \qquad \text{(b)}\ P_i^g = \frac{1}{V}\int_V P_i(\mathbf{r})\,d\mathbf{r} \tag{I.2.66}$$

Homogenization begins by introducing the macroscopic canonical equations for the behavior of piezoelectric material [156, 265] modified to take into account pre-stress and pre-polarization brought about by the existence of deposited charge.

$$\sigma_{ij}^g = C_{ijkl}^{eff}\varepsilon_{kl}^g - e_{kij}^{eff}E_k^g + \sigma_{ij}^{g,pre} \tag{I.2.67}$$

$$\begin{aligned} D_i^g &= e_{ijk}^{eff}\varepsilon_{jk}^g + \varepsilon_0 E_i^g + P_i^g + P_i^{g,pre} \\ &= e_{ijk}^{eff}\varepsilon_{jk}^g + \varepsilon_0\left(\delta_{ij} + \chi_{ij}^{eff}\right)E_j^g + P_i^{g,pre} \end{aligned} \tag{I.2.68}$$

In the above equations, $\mathbf{C}^{eff}$, $\mathbf{e}^{eff}$, and $\boldsymbol{\chi}^{eff}$ denote the effective viscoelastic stiffness, piezoelectric coupling, and electric susceptibility tensors of the heterogeneous material, respectively, and D_i^g is the macroscopic electric displacement. Recall that the electric displacement, in the absence of piezoelectric coupling, is related to the polarization density and macroscopic electric field through the expression analogous expressions.

$$D_i^g = \varepsilon_0 E_i^g + P_i^g = \varepsilon_0\left(\delta_{ij} + \chi_{ij}^{eff}\right)E_j^g + P_i^{pre} \tag{I.2.69}$$

The concept of a localization tensor is now introduced. These tensors relate the macroscopic strain and electric fields to the local strain and electric fields as shown below in Eqs. (I.2.70) and (I.2.71) [69, 75].

$$\varepsilon_{ij}\left(\mathbf{r}\right) = A_{ijkl}^{\varepsilon}\left(\mathbf{r}\right)\left[\varepsilon_{kl}^g + \varepsilon_{kl}^{g,pre}\right] + A_{ijk}^{\varepsilon E}\left(\mathbf{r}\right)E_k^g \tag{I.2.70}$$

$$E_i\left(\mathbf{r}\right) = A_{ijk}^{E\varepsilon}\left(\mathbf{r}\right)\varepsilon_{jk}^g + A_{ij}^{E}\left(\mathbf{r}\right)\left[E_j^g + E_j^{g,pre}\right] \tag{I.2.71}$$

It is now assumed that the average macroscopic strain, stress, electric displacement, and electric fields can be approximated as volume averages of

corresponding fields in the constituent phases and the pre-existing fields resulting from the deposited charges. These equations are given by Eqs. (I.2.72) and (I.2.73) [54].

$$\text{(a)}\ \ \sigma_{ij}^{g} = f^{M}\bar{\sigma}_{ij}^{M} + f^{I}\bar{\sigma}_{ij}^{I} + \sigma_{ij}^{g,pre} \qquad \text{(b)}\ \ \varepsilon_{ij}^{g} = f^{M}\bar{\varepsilon}_{ij}^{M} + f^{I}\bar{\varepsilon}_{ij}^{I} + \varepsilon_{ij}^{g,pre} \quad \text{(I.2.72)}$$

$$\text{(a)}\ \ D_{i}^{g} = f^{M}\bar{D}_{i}^{M} + f^{I}\bar{D}_{i}^{I} + D_{i}^{g,pre} \qquad \text{(b)}\ \ E_{i}^{g} = f^{M}\bar{E}_{i}^{M} + f^{I}\bar{E}_{i}^{I} + E_{i}^{g,pre} \quad \text{(I.2.73)}$$

Recall the constitutive mechanical and electrostatic laws for each material phase:

$$\text{(a)}\ \ \bar{\sigma}_{ij}^{M} = C_{ijkl}^{M}\bar{\varepsilon}_{kl}^{M} + \bar{\sigma}_{ij}^{M,pre} \qquad \text{(b)}\ \ \bar{\sigma}_{ij}^{I} = C_{ijkl}^{I}\bar{\varepsilon}_{kl}^{I} + \bar{\sigma}_{ij}^{I,pre} \qquad \text{(I.2.74)}$$

$$\text{(a)}\ \ \bar{D}_{i}^{M} = \varepsilon_{0}\left(\delta_{ij} + \chi_{ij}^{M}\right)\bar{E}_{j}^{M} + \bar{P}_{i}^{M,pre} \qquad \text{(b)}\ \ \bar{D}_{i}^{I} = \varepsilon_{0}\left(\delta_{ij} + \chi_{ij}^{I}\right)\bar{E}_{j}^{I} + \bar{P}_{i}^{I,pre} \qquad \text{(I.2.75)}$$

It is noted that volume averages of Eqs. (I.2.70) and (I.2.71) can be found for the matrix or inclusion phases via relations similar to (I.2.56). Combining constitutive equations of the form (I.2.74) and (I.2.75) with such volume averaging yields simplified relationships between the average local stress or electric displacement field in material *X*, where *X* is either *I* or *M*, and the analogous macroscopic fields. The relationships are given below in Eqs. (I.2.76) and (I.2.77).

$$\bar{\sigma}_{ij}^{X} = C_{ijkl}^{X}\left(A_{klmn}^{X,\varepsilon}\left[\varepsilon_{mn}^{g} + \varepsilon_{kl}^{g,pre}\right] + A_{klm}^{X,\varepsilon E}E_{m}^{g}\right) + \bar{\sigma}_{ij}^{X,pre} \qquad \text{(I.2.76)}$$

$$\bar{D}_i^X = \varepsilon_0\left(\delta_{ij} + \chi_{ij}^X\right)\left(A_{jkl}^{X,E\varepsilon}\varepsilon_{kl}^g + A_{ij}^{X,E}\left[E_j^g + E_j^{g,pre}\right]\right) + \bar{P}_i^{X,pre} \qquad \text{(I.2.77)}$$

The average strain and electric fields in the matrix can now be expressed by inserting inclusion volume averages of Eqs. (I.2.70) and (I.2.71) into relations (I.2.72)(b) and (I.2.73)(b), respectively. These results can be combined with the stress and electric displacement fields in the matrix expressed by applying the constitutive laws given in Eqs. (I.2.74)(a) and (I.2.75)(a). The results of these operations are given below in expressions (I.2.78) – (I.2.81).

$$\bar{\varepsilon}_{ij}^M = \frac{1}{f^M}\left[\left(I_{ijkl} - f^I A_{ijkl}^{I,\varepsilon}\right)\varepsilon_{kl}^g - f^I A_{ijk}^{I,\varepsilon E}E_k^g - \left(I_{ijkl} + f^I A_{ijkl}^{I,\varepsilon}\right)\varepsilon_{kl}^{g,pre}\right] \qquad \text{(I.2.78)}$$

$$\bar{\sigma}_{ij}^M = \frac{1}{f^M}C_{ijkl}^M\left[\left(I_{klmn} - f^I A_{klmn}^{I,\varepsilon}\right)\varepsilon_{mn}^g - f^I A_{klm}^{I,\varepsilon E}E_m^g - \left(I_{klmn} + f^I A_{klmn}^{I,\varepsilon}\right)\varepsilon_{mn}^{g,pre}\right] + \bar{\sigma}_{ij}^{M,pre} \qquad \text{(I.2.79)}$$

$$\bar{E}_i^M = \frac{1}{f^M}\left[\left(\delta_{ij} - f^I A_{ij}^{I,E}\right)E_j^g - f^I A_{ijk}^{I,E\varepsilon}\varepsilon_{jk}^g - \left(\delta_{ij} - f^I A_{ij}^{I,E}\right)E_j^{g,pre}\right] \qquad \text{(I.2.80)}$$

$$\bar{D}_i^M = \frac{1}{f^M}\varepsilon_0\left(\delta_{ij} + \chi_{ij}^M\right)\left[\begin{array}{r}\left(\delta_{jk} - f^I A_{jk}^{I,E}\right)E_k^g - f^I A_{jkm}^{I,E\varepsilon}\varepsilon_{km}^g \\ -\left(\delta_{jk} - f^I A_{jk}^{I,E}\right)E_{jk}^{g,pre}\end{array}\right] + \bar{P}_i^{M,pre} \qquad \text{(I.2.81)}$$

The average stress and electric displacement in the matrix material can also be found by combining Eqs. (I.2.72)(a) and (I.2.73)(a) with and stress and electric displacement localization equations in the form of (I.2.76) and (I.2.77) together with the assumed macroscopic behavior given by (I.2.67) and (I.2.68), respectively [24]. The results are shown in (I.2.82) and (I.2.83).

$$\bar{\sigma}_{ij}^{M} = \frac{1}{f^{M}}\left[\begin{array}{r}\left(C_{ijmn}^{eff} - f^{I}C_{ijkl}^{I}A_{klmn}^{I,\varepsilon}\right)\varepsilon_{mn}^{g} - \left(e_{mij}^{eff} + f^{I}C_{ijkl}^{I}A_{klm}^{I,\varepsilon E}\right)E_{m}^{g} \\ + \left(1-f^{I}\right)C_{ijkl}^{I}A_{klmn}^{I,\varepsilon}\varepsilon_{mn}^{g,pre}\end{array}\right] \tag{I.2.82}$$

$$\bar{D}_{i}^{M} = \frac{1}{f^{M}}\left[\begin{array}{r}\left[e_{ikl}^{eff} - f^{I}\varepsilon_{0}\left(\delta_{ij}+\chi_{ij}^{I}\right)A_{jkl}^{I,E\varepsilon}\right]\varepsilon_{kl}^{g} + \\ \varepsilon_{0}\left[\left(\delta_{ik}+\chi_{ik}^{eff}\right) - f^{I}\left(\delta_{ij}+\chi_{ij}^{I}\right)A_{jk}^{I,E}\right]E_{k}^{g} \\ + \varepsilon_{0}\left[\delta_{ij} + \left(1-f^{I}\right)\chi_{ij}^{I}\right]A_{jk}^{I,E}E_{k}^{g,pre}\end{array}\right] \tag{I.2.83}$$

The effective piezoelectric material properties of the heterogeneous closed cell foam is finally found by using the dilute approximation by equating equation pairs (I.2.79) – (I.2.82) and (I.2.81) – (I.2.83) then matching terms to solve for $\mathbf{C}^{eff}$, $\mathbf{D}^{eff}$, $\mathbf{e}^{eff}$, and $\boldsymbol{\chi}^{eff}$ [24].

$$C_{ijkl}^{eff} = C_{ijkl}^{M} + f^{I}\left(C_{ijmn}^{I} - C_{ijmn}^{M}\right)A_{mnkl}^{I,\varepsilon} \tag{I.2.84}$$

$$e_{mij}^{eff} = -f^{I}\left(C_{ijkl}^{I} - C_{ijkl}^{M}\right)A_{klm}^{I,\varepsilon E} \tag{I.2.85}$$

$$e_{ijk}^{eff} = f^{I}\varepsilon_{0}\left(\chi_{il}^{I} - \chi_{il}^{M}\right)A_{ljk}^{I,E\varepsilon} \tag{I.2.86}$$

$$\chi_{ij}^{eff} = \chi_{ij}^{M} + f^{I}\left(\chi_{ik}^{I} - \chi_{ik}^{M}\right)A_{kj}^{I,E} \tag{I.2.87}$$

The strain and electric field localization tensors, $\mathbf{A}^{I,\varepsilon}$, $\mathbf{A}^{I,\varepsilon E}$, $\mathbf{A}^{I,E\varepsilon}$, and $\mathbf{A}^{I,E}$, must be found to complete this model. These tensors are dependent on the volumetric composition of the composite, the geometry of the closed cells, the constituent material electromechanical properties, and the material properties of the reference material. Expressions for these terms must be found via the previously derived integral equations. This is done by first re-arranging (I.2.62) and (I.2.63) as shown below in Eqs. (I.2.88) and (I.2.89).

$$\varepsilon_{ij}^{g} = \left[I_{ijmn} + T_{ijkl}^{I}\left(\mathbf{C}^{0}\right)\Delta C_{klmn}^{I0}\right]\overline{\varepsilon}_{mn}^{I} - B_{ijk}^{I}\left(\mathbf{C}^{0}\right)\overline{f}_{k}^{surf} \tag{I.2.88}$$

$$E_{i}^{g} = \left[I_{ik} + t_{ij}^{I}\left(\varepsilon_{0}\chi^{0}\right)\varepsilon\Delta\chi_{jk}^{I0}\right]\overline{E}_{k}^{I} - b_{ij}^{I}\left(\varepsilon_{0}\chi^{0}\right)\overline{P}_{j}^{I} \tag{I.2.89}$$

It is crucial to recognize that $\overline{f}_{i}^{surf}$ can be decomposed as follows.

$$\overline{f}_{i}^{surf} = \underbrace{\overline{f}_{i}^{C,surf\,1}}_{pre-stress} + \underbrace{\overline{f}_{i}^{C,surf\,2}\left(\overline{\varepsilon}_{ij}^{I}\right)}_{\delta\mathbf{C}^{eff}} + \underbrace{\overline{f}_{i}^{L,surf}\left(\overline{E}_{i}^{I}\right)}_{electro-mech\ coupling} \tag{I.2.90}$$

with

$$
\begin{aligned}
&\text{(a) } \overline{f}_i^{C,surf\,1} = \overline{F}_i^{C,1} \\
&\text{(b) } \overline{f}_i^{C,surf\,2} = \overline{F}_{ijk}^{C,2}\overline{\varepsilon}_{jk}^{I} \\
&\text{(c) } \overline{f}_i^{L,surf} = \frac{1}{S_I}\overline{E}_i^{I}\int_{S_I}\rho^{surf}\left(\mathbf{r}\right)d\mathbf{r} \approx 2\left|\overline{\rho}^{surf}\right|\overline{E}_i^{I}
\end{aligned}
\tag{I.2.91}
$$

$\overline{F}^{C}$ and $\overline{F}_{ijk}^{C,2}$ and are defined with respect to the deposited chargzqe density and void geometry as described by Eq. (I.2.92). Note as well that the far RHS of Eq. (I.2.91)(c) is only true if the boundary condition is such that there is no displacement at the bottom of the foam; $u_3 = 0$.

$$
\begin{aligned}
\overline{F}_i^{C,1} &= \frac{1}{4\pi\varepsilon_0 S_I}\int_{S_I}\int_{S_I}\frac{\rho^{surf}\left(\mathbf{r}\right)\rho^{surf}\left(\mathbf{r}'\right)r_i^d}{\left|\mathbf{r}_d\right|^3}dS'dS \\
\overline{F}_{ijk}^{C,2} &= \frac{1}{4\pi\varepsilon_0 S_I}\int_{S_I}\int_{S_I}\frac{\rho^{surf}\left(\mathbf{r}\right)\rho^{surf}\left(\mathbf{r}'\right)}{\left|\mathbf{r}_d\right|^3}\left[\delta_{ij}r_k^d - \frac{3r_i^d r_j^d r_k^d}{\left|\mathbf{r}_d\right|^2}\right]dS'dS
\end{aligned}
\tag{I.2.92}
$$

Where $\mathbf{r}_d = \mathbf{r} - \mathbf{r}'$ and the surface averaged Coulomb traction, $\overline{F}_i^{C,1}$, and third order Coulomb "force" tensor, $\overline{F}_{ijk}^{C,2}$, must be calculated numerically. These values are dependent on the charge distribution and geometry of the ellipsoid. It may also be possible to calculate the average distance vector $\left|\mathbf{r}_d^{ave}\right|$ using a probabilistic approach such at the one outlined by Parry and Fischbach [266], this is not, however, employed in the current implementation. Inserting expressions (I.2.90)–(I.2.92) for the average surface traction on the inclusion into Eq. (I.2.88) and matching terms with Eq. (I.2.70) yields the following expressions for the localization tensors $A_{ijkl}^{I,\varepsilon}$ and $A_{ijk}^{I,\varepsilon E}$ as well as the

macroscopic pre-strain and stress resulting from the charge deposited on the interior of the closed cells.

$$A_{ijkl}^{I,\varepsilon} = \left[I_{ijkl} + T_{ijmn}^{I}\left(\mathbf{C}^{0}\right)\Delta C_{mnkl}^{I0} - B_{ijr}^{I}\left(\mathbf{C}^{0}\right)\bar{F}_{rkl}^{C,2} \right]^{-1} \tag{I.2.93}$$

$$A_{ijk}^{I,\varepsilon E} = 2A_{ijkl}^{I,\varepsilon} B_{lmn}^{I}\left(\mathbf{C}^{0}\right)\left|\bar{\rho}^{surf}\right| A_{mn}^{I,E} \tag{I.2.94}$$

$$\begin{aligned} \varepsilon_{ij}^{g,pre} &= -B_{ijk}^{I}\left(\mathbf{C}^{0}\right)\bar{F}_{k}^{C,1} \\ &\Downarrow \\ \sigma_{ij}^{g,pre} &= C_{ijkl}^{eff}\varepsilon_{kl}^{g,pre} \end{aligned} \tag{I.2.95}$$

Note that the strain localization tensor $A_{ijkl}^{I,\varepsilon}$ reduces to a the classical strain localization tensor of a bi-phase material when no charge is deposited because $\bar{F}_{ijk}^{C,2} = 0$ when $\bar{\rho}^{surf}\left(\mathbf{r}\right) = 0$ for $\mathbf{r} \in S_I$. This expression also verifies the intuitive observation that the effective stiffness of the foam will depend on the charge deposited on the interior surface of the voids. Further, it is observed that the pre-strain is null when no charge is deposited inside the closed cells.

It is now necessary to insert the components of the void polarization, $\bar{P}_{j}^{I}$, derived in described by (I.2.50) into Eq. (I.2.89) to find the localization tensors $A_{ij}^{I,E}$ and $A_{ijk}^{I,E\varepsilon}$ as well as the macroscopic pre-polarization. Matching terms of Eq. (I.2.71) with results of the operations described in the previous sentence yields the following localization tensors and pre-polarization.

$$A_{ij}^{I,E} = \left[\delta_{ij} + t_{ik}^{I} \left(\varepsilon_0 \chi^0 \right) \varepsilon_0 \Delta \chi_{kj}^{I0} \right]^{-1} \tag{I.2.96}$$

$$A_{ijk}^{I,E\varepsilon} = A_{il}^{I,E} b_{lm}^{I} \left(\varepsilon_0 \chi^0 \right) \left(\frac{S_I}{2V_I} \right) \left| \overline{\rho}^{surf} \right| r_i^{D,ave} A_{mijk}^{I,\varepsilon} \tag{I.2.97}$$

$$\begin{gathered} E_i^{g,pre} = -b_{ij}^{I} \left(\varepsilon_0 \chi^0 \right) \left| \overline{\rho}^{surf} \right| \left(\frac{S_I}{2V_I} \right) r_j^{D,ave} \\ \Downarrow \\ D_i^{g,pre} = \varepsilon_0 \left(\delta_{ij} + \chi_{ij}^{eff} \right) E_j^{g,pre} \end{gathered} \tag{I.2.98}$$

Equations (I.2.84)–(I.2.87), (I.2.93)–(I.2.98), (I.2.91), and (I.2.92) constitute the micromechanical model approximating the piezoelectric behavior of closed-cell polymer foams. It is noted that the piezoelectric coupling coefficients d_{kij}^{eff} can now be found via the following relation.

$$d_{kij}^{eff} = e_{kmn}^{eff} \left[C_{mnij}^{eff} \right]^{-1} \tag{I.2.99}$$

I.2.5 Model implementation

This section describes the derivation of several terms needed to evaluate the effective piezoelectric material properties of the foam. The terms that must be evaluated

are $r_i^{D,ave}$, $\overline{F}_i^{C,1}$, and $\overline{F}_{ijk}^{C,2}$. These entities are evaluated here for direct implementation of the effective medium theory.

$r_i^{D,ave}$ is the surface average of the distance separating the top and bottom surfaces *i.e.* twice the *z*-value of all points falling on the surface of the ellipsoid as shown in the diagram shown in Figure I. 3.

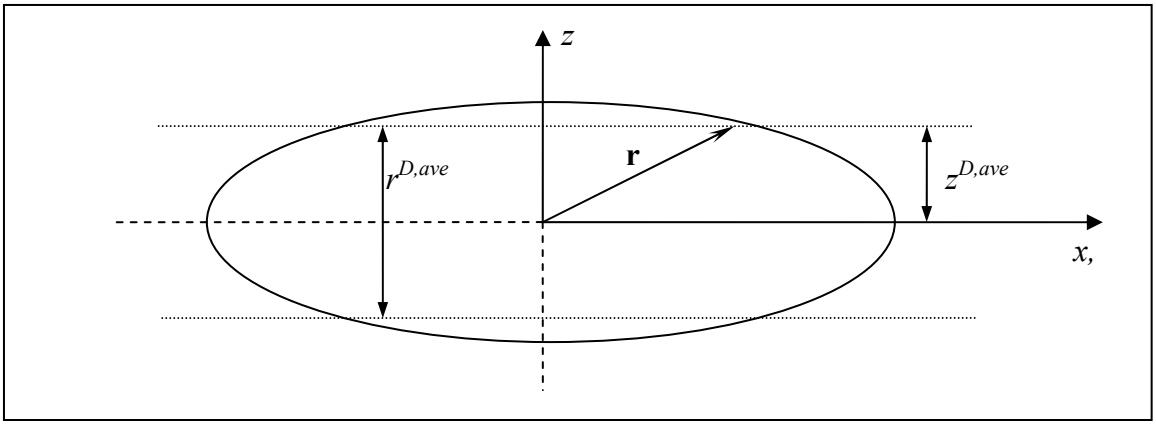

Figure I. 3: Diagram displaying the average *z*-distance, with respect to the local coordinate system, and average top-bottom distance of an ellipsoid.

The value of $r_i^{D,ave}$ average can be calculated analytically through by using Eq. (I.2.100).

$$r^{D,ave} = \frac{4}{S_I} \int_{S_I/2} z dS \qquad \text{(I.2.100)}$$

This expression can be evaluated for spherical, oblate and prolate inclusion geometries where it is noted that *dS* is given by Eq. (I.2.101) for an ellipsoid with *z*-axis symmetry.

$$dS = 2\pi a\sqrt{1+\frac{(a-c)(a+c)z^2}{c^4}}dz \tag{I.2.101}$$

The results are given below in Eq. (I.2.102).

$$\begin{aligned} r_{sphere}^{D,ave} &= a \\ r_{spheroid}^{D,ave} &= \frac{8\pi ac\left(a^3-c^3\right)}{3S_I\left(a^2-c^2\right)} \end{aligned} \tag{I.2.102}$$

Where the surface area of oblate and prolate spheroids are given below.

$$\begin{aligned} S_I^{oblate} &= 2\pi a^2 + \frac{\pi c^2}{e_{OB}}\ln\left[\frac{1+e_{OB}}{1-e_{OB}}\right] \\ S_I^{prolate} &= 2\pi a^2 + \frac{2\pi ac}{e_{PR}}\sin^{-1}\left(e_{PR}\right) \end{aligned} \tag{I.2.103}$$

The calculation of the Coulomb terms given in Eq. (I.2.92) must be achieved through numerical integration. The integral on the surface of a spheroid having $a = b \neq c$ of the function $f(u,v)$ (prolate or oblate spheroids), denoted F^{int}, is given in Eq. (I.2.104).

$$F^{\text{int}} = \int_0^{\pi}\int_0^{2\pi} f(u,v)\underbrace{\sqrt{E(u,v)G(u,v)-F(u,v)^2}dudv}_{dS} \tag{I.2.104}$$

Where the values or $E(u,v)$, $F(u,v)$, and $G(u,v)$ are values of the first fundamental form. For a spheroid with *z*-axis symmetry, these variables reduce to functions of the angle *v* and are defined in Eq. (I.2.105)[129].

$$\begin{aligned} E(v) &= a^2 \sin^2 v \\ F &= 0 \\ G(v) &= \frac{1}{2}\left\{a^2 + c^2 + \left(a^2 - c^2\right)\cos(2v)\right\} \end{aligned} \tag{I.2.105}$$

It is also noted that the Cartesian coordinates are given below.

$$\mathbf{r} = \begin{Bmatrix} x \\ y \\ z \end{Bmatrix} = \begin{Bmatrix} a\sin v\cos u \\ a\sin v\sin u \\ a\cos v \end{Bmatrix} \quad \text{with} \quad \begin{matrix} v \in [0 \quad 2\pi] \\ u \in [0 \quad \pi] \end{matrix} \tag{I.2.106}$$

The constants $\bar{F}_i^{C,1}$ and $\bar{F}_{ijk}^{C,2}$ can then be evaluated by noting that *R* falls on the surface of an ellipsoid having symmetry about the z-axis when

$$R = a\sqrt{1 - \left(\frac{z}{a}\right)^2} = \sqrt{x^2 + y^2} \tag{I.2.107}$$

and by setting $f(u,v)$ equal to expression (I.2.108)and (I.2.109), respectively.

$$f_i(u,v) = \frac{1}{4\pi\varepsilon_0 S_I} \frac{\rho^{surf}(\mathbf{r})\rho^{surf}(\mathbf{r}')r_i^d}{|\mathbf{r}_d|^3} \tag{I.2.108}$$

$$f_{ijk}(u,v) = \frac{1}{4\pi\varepsilon_0 S_I} \frac{\rho^{surf}(\mathbf{r})\rho^{surf}(\mathbf{r}')}{|\mathbf{r}_d|^3}\left[\delta_{ij}r_k^d - \frac{3r_i^d r_j^d r_k^d}{|\mathbf{r}_d|^2}\right] \tag{I.2.109}$$

Where the angle v is determined from the expression $v = \cos^{-1}(z/c)$.

I.2.5.1 Model simplification

Evaluation of the above model requires several simplifying matters. The first, and most important, is the approximation of the surface traction, $\overline{f}_k^{surf}$, Eq. (I.2.57) as $\overline{f}_k^{surf} \approx \overline{f}^{surf} n_k$. This is a reasonable approximation, especially for the closed-cell foams in question, due to the symmetry of the inclusions. Doing so alters the form of Eq. (I.2.60) to the following:

$$B_{ijk}^I(\mathbf{C}^0) \Rightarrow B_{ij}^I(\mathbf{C}^0) = \frac{1}{V_I}\int_{V_I}\int_{S_I} G_{ij,k}^0(\mathbf{r}-\mathbf{r}')n_k d\mathbf{r}'d\mathbf{r} \tag{I.2.110}$$

Application of the divergence theorem to Eq. (I.2.110) yields the simpler expression.

$$B_{ijk}^I(\mathbf{C}^0) \Rightarrow B_{ij}^I(\mathbf{C}^0) = \frac{1}{V_I}\int_{V_I}\int_{V_I} G_{ij,kk}^0(\mathbf{r}-\mathbf{r}')d\mathbf{r}'d\mathbf{r} \tag{I.2.111}$$

Such an alteration then changes expressions for the localization, pre-strain and pre-polarization tensors listed in Eqs. (I.2.93)-(I.2.98). Those expressions are listed in Eqs. (I.2.112)-(I.2.117).

$$A_{ijkl}^{I,\varepsilon} = \left[I_{ijkl} + T_{ijmn}^{I}\left(\mathbf{C}^{0}\right)\Delta C_{mnkl}^{I0} - B_{ij}^{I}\left(\mathbf{C}^{0}\right)\bar{F}_{kl}^{C,2} \right]^{-1} \tag{I.2.112}$$

$$A_{ijk}^{I,\varepsilon E} = 2A_{ijmn}^{I,\varepsilon} B_{mn}^{I}\left(\mathbf{C}^{0}\right)\left|\bar{\rho}^{surf}\right|\delta_{3r}A_{rk}^{I,E} \tag{I.2.113}$$

$$\begin{gathered} \varepsilon_{ij}^{g,pre} = -B_{ij}^{I}\left(\mathbf{C}^{0}\right)\bar{F}^{C,1} \\ \Downarrow \\ \sigma_{ij}^{g,pre} = C_{ijkl}^{eff}\varepsilon_{kl}^{g,pre} \end{gathered} \tag{I.2.114}$$

$$A_{ij}^{I,E} = \left[\delta_{ij} + t_{ik}^{I}\left(\varepsilon_0\chi^{0}\right)\varepsilon_0\Delta\chi_{kj}^{I0} \right]^{-1} \tag{I.2.115}$$

$$A_{ijk}^{I,E\varepsilon} = \left\{ \left(\frac{S_I}{2V_I} \right)\left|\bar{\rho}^{surf}\right| \right\} A_{il}^{I,E} b_{lm}^{I}\left(\varepsilon_0\chi^{0}\right) r_r^{D,ave} A_{mrjk}^{I,\varepsilon} \tag{I.2.116}$$

$$\begin{gathered} E_i^{g,pre} = -b_{ij}^{I}\left(\varepsilon_0\chi^{0}\right)\left|\bar{\rho}^{surf}\right|\left(\frac{S_I}{2V_I} \right) r_j^{D,ave} \\ \Downarrow \\ D_i^{g,pre} = \varepsilon_0\left(\delta_{ij} + \chi_{ij}^{eff}\right)E_j^{g,pre} \end{gathered} \tag{I.2.117}$$

Where the average force terms given in Eq. (I.2.92) are approximated by assuming that the spheroid is reasonably well represented as a parallel plate capacitor having separation distance $\mathbf{r}^{D,ave}$, whose only non-zero component is along the x_3 axis with respect to the inclusion center. The actual value of $\mathbf{r}^{D,ave}$ is found by evaluating Eq. (I.2.102). The resulting simplified force terms are given in Eqs. (I.2.118) and (I.2.119), below.

$$\overline{F}^{C,1} = \frac{Q^{top} Q^{bottom}}{4\pi\varepsilon_0 \left|\mathbf{r}^{D,ave}\right|^2} \tag{I.2.118}$$

$$\overline{F}_{ij}^{C,2} = \frac{Q^{top} Q^{bottom}}{4\pi\varepsilon_0 \left|\mathbf{r}^{D,ave}\right|^2} \left[\delta_{i3}\delta_{3j} - \frac{3 r_i^{D,ave} r_j^{D,ave}}{\left|\mathbf{r}^{D,ave}\right|^2} \right] \tag{I.2.119}$$

Where δ_{3j} is a specific form of the Kronecker delta which can be represented in matrix form as

$$\delta_{i3}\delta_{3j} = \begin{bmatrix} 0 & 0 & 0 \\ 0 & 0 & 0 \\ 0 & 0 & 1 \end{bmatrix} \tag{I.2.120}$$

And Q^{top} and Q^{bottom} are the total charge deposited on the top and bottom surfaces, respectively. These constants are related to the average surface charge density, $\overline{\rho}^{surf}$, through expression .

$$Q^X = S_I^X \overline{\rho}^{surf,X} \tag{I.2.121}$$

Where X represented either the top or bottom surface. All terms necessary to evaluate the effective piezoelectric material properties have now been defined. Section I.2.5.2 defines a differential effective medium scheme to evaluate those properties as a function of the constituent material properties, the deposited charge density, and the volume fraction and geometry of ellipsoidal voids.

I.2.5.2 Differential effective medium scheme

Employing methodology described in Appendix D

$$\mathbf{C}^{eff}\left(f^M\right) = \mathbf{C}^M - \int_1^{f^M} \left(\frac{1}{f^{M'}}\right) \Delta\mathbf{C}^{eff} : \mathbf{A}^{I,\varepsilon}\left(f^{M'}\right) df^{M'} \tag{I.2.122}$$

$$\chi^{eff}\left(f^M\right) = \chi^M - \int_1^{f^M} \left(\frac{1}{f^{M'}}\right) \Delta\chi^{eff} : \mathbf{A}^{I,E}\left(f^{M'}\right) df^{M'} \tag{I.2.123}$$

$$\mathbf{e}^{eff}\left(f^M\right) = \mathbf{e}^M + \int_1^{f^M} \left(\frac{1}{f^{M'}}\right) \Delta\mathbf{C}^{eff} : \mathbf{A}^{I,\varepsilon E}\left(f^{M'}\right) df^{M'} \tag{I.2.124}$$

$$\mathbf{e}^{eff}\left(f^M\right) = \mathbf{e}^M - \int_1^{f^M} \left(\frac{1}{f^{M'}}\right) \Delta\chi^{eff} : \mathbf{A}^{I,E\varepsilon}\left(f^{M'}\right) df^{M'} \tag{I.2.125}$$

Equations (I.2.122)-(I.2.125) completes the DEM micro-electromechanical mean-field model derivation for the behavior of closed-cell piezoelectret foams. The following sections show and modeling results and suggest future study.

I.3 Results and discussion

The model derived in this work has greatly enhanced the ability to predict the effective coupled electromechanical behavior of piezoelectret foams. This section explores the insight that such increases in predictive power gives to researchers who strive to improve foam performance using methods such as those explored in this thesis. The following highlights several salient modeling results which illustrate the strengths of the micro-electromechanical model developed in this appendix. Unless stated otherwise, the model inputs employed to calculate the results are those detailed in Table I. 1.

Table I. 1: Material properties and void variables employed to calculate the effective behavior of a closed-cell piezo-electret foam.

Material Properties		
	Polypropylene (PP)	Air
$K \ \left(\mathrm{Pa}\right)$	2.50×10^{9}	1.42×10^{5}
$\mu \ \left(\mathrm{Pa}\right)$	5.36×10^{8}	1
$\kappa \ \left(\mathrm{F/m}\right)$	1.5	1.000536
$\rho \ \left(\mathrm{kg/m^3}\right)$	850	1.21
Void Variables		
$q^{surf} \ \left(\mathrm{C/m^2}\right)$	30×10^{-6}	
$a/\mathrm{c} \ \left(\ \right)$	6	
$a \ \left(\mathrm{m}\right)$	37.5×10^{-6}	
$\phi^{I} \ \left(\ \right)$	0.65	
$f^{NC} \ \left(\%\right)$	30	

The polymer and air material properties can be found in various locations. The values above have been taken from a reliable online database called MatWeb [267]. The polypropylene (PP) is assumed to be an unfilled homopolymer. It should be noted, however, that many different types of PP's exist, each displaying vastly different stiffness values. This must be taken into consideration when creating new foams. Unfortunately such input value certainty does not exist with respect to the other void variables listed in Table I. 1. The experimental values reported in the literature for these variables display a considerable amount of uncertainty. The reason for assigning the values given in Table I. 1 must, therefore, be explained in more detail.

One of the most difficult variables to quantify is the value of surface charge density present on the interior void surface. Gerhard-Multhaupt *et al* [268] and Paajanen *et al* [269] and the references therein provide a detailed description of the corona discharge process employed to breakdown gases within the closed cells and thereby deposit charge on their interior surfaces. The gas breakdown is dependent on many variables including, but not limited to, the gas within the voids, internal pressure, void height, temperature, and the applied electric field. Paajanen *et al* employed Paschen's Law to approximate the resulting deposited surface charge density due to a given applied voltage [269]. Their results suggest maximum surface charge densities ranging from 430–730 $\mu C/m^2$. It is well known, however, that deposited charge decays rapidly, nearly exponentially, to nearly half of that charge during the first two to five days until reaching a quasi-stable charge density [270, 271]. A value of 30 $\mu C/m^2$ has been chosen as a very conservative estimate to validate the model with respect to predicted trends and orders of

magnitude. It should be noted that the results given in Section I.3.7 suggest that increasing the estimate of surface charge density will linearly increase the predicted piezoelectric coupling coefficient. Further, other void variables that have a significant influence on the overall piezoelectric coupling coefficient, such as the aspect ratio, a/c, and percentage of voids which do not have a deposited charge are equally difficult to quantify. For these reasons and for the purposes of this study, a conservative estimate q^{surf} of is sufficient.

The percentage of voids which do not carry a deposited charge is the other variable which is exceedingly difficult to quantify. The work of Sessler and Hillenbrand suggested that a larger percentage of voids, by number, are too small to be charged during corona discharging [262]. Paschen's Law void predicts that voids having an average height $\leq 2\mu m$ will not be charged during Corona discharging [261]. In order to approximate the volume fraction of voids not being charged, the average void aspect ratio and the overall void fraction, a image processing has been performed of a micrograph given in reference [262]. The original image and processed image are shown in Figure I. 4. The corresponding void height versus length data points are shown in Figure I. 5. The analysis agree with the literature showing that the height and lengths fall within the range of 1-5 and 10-100 μm, respectively [269]. It is also possible to approximate the average void aspect ratio from the scatter plot in Figure I. 5, $a/c \in [6 \quad 8]$. Note that it is also possible to approximate the void fraction and percentage of voids not carrying charge from the same image analysis. The values employed to calculate the curves given in the remainder of this section are given in Table I. 1.

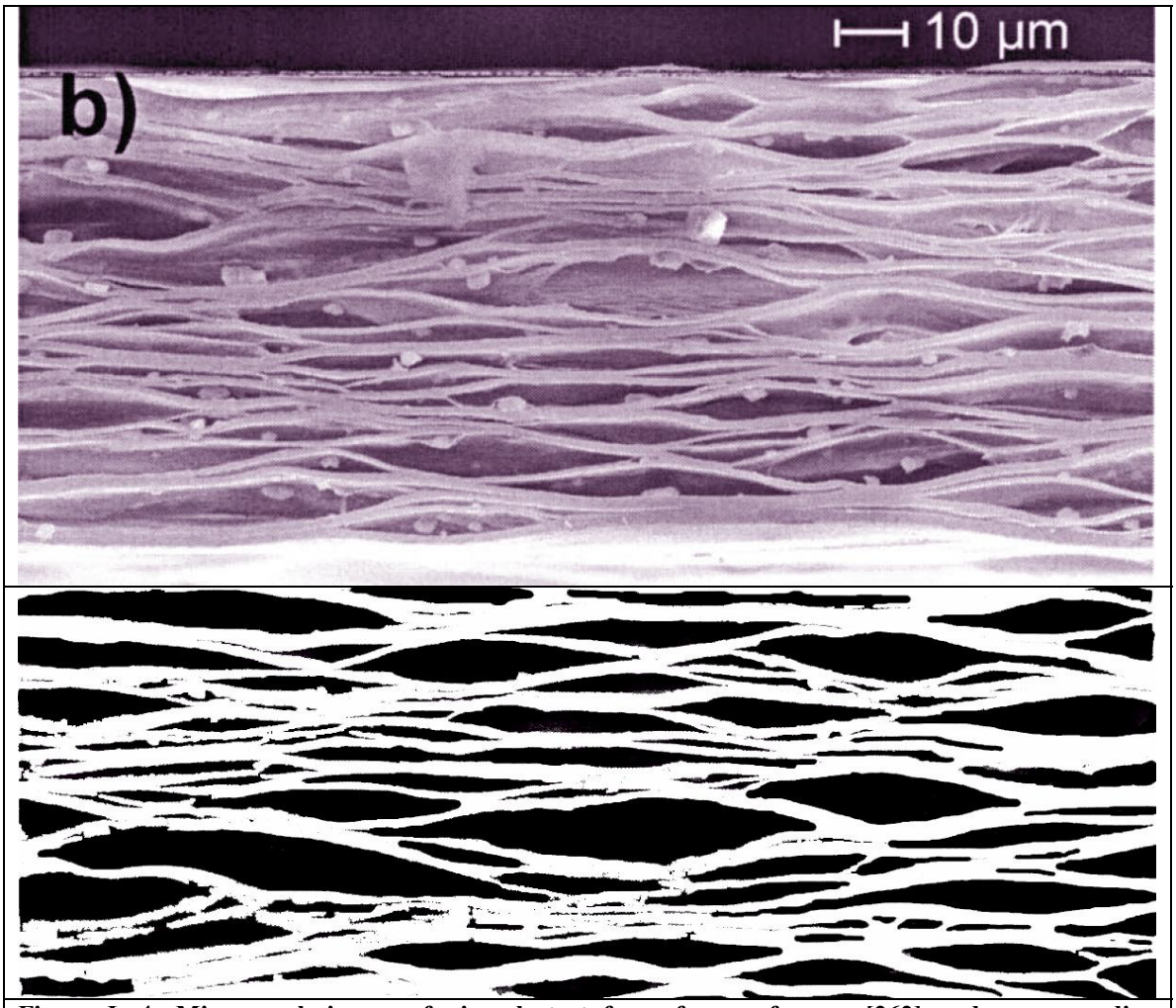

Figure I. 4: Micrograph image of piezoelectret foam from reference [262] and corresponding analyzed image.

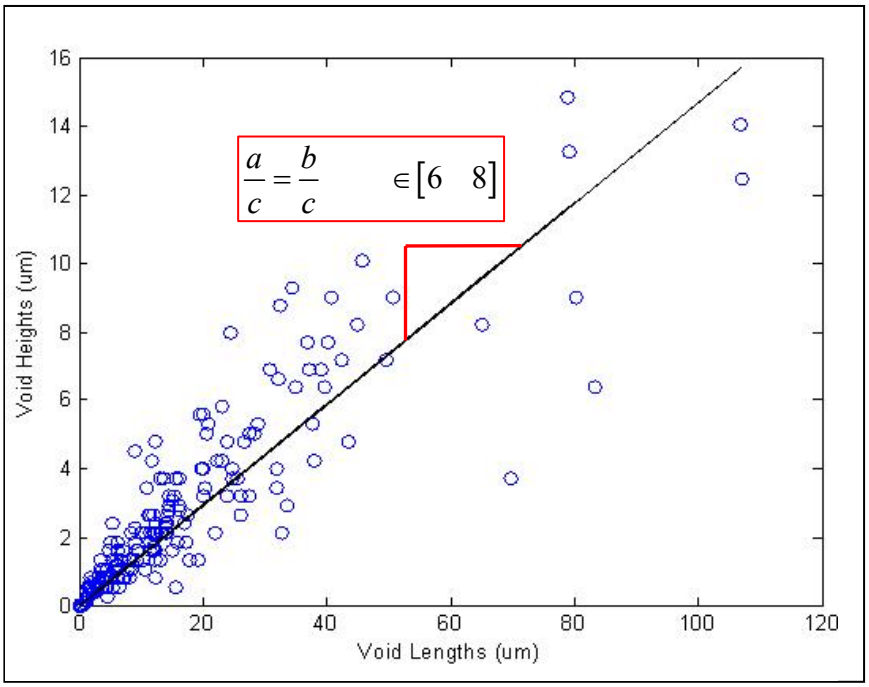

Figure I. 5: Void height and length data point results from image processing.

The following sub-sections explore the influence of various parameters on the piezoelectret coupled effective electromechanical behavior. Their influence on the piezoelectric coupling coefficient, d_{33}^{eff}, is of specific interest as it is a descriptor of the electromechanical coupling sensitivity of the foam. It is important to point out that the following results are in agreement with experimental observations in every aspect. This validates the previously derived modeling approach and illustrates its power to be applied towards efficient performance optimization. Such a model permits researchers to explore foam behavior numerically before committing significant time, effort, and funds to experimentally determine such behavior.

I.3.6 Calculation of effective materialproperties

The first interesting results are those showing the effective macroscale material properties as a function of void fraction. These results are explored first to verify the model is in accordance with traditional micromechanical modeling trends. The effective material properties of a heterogeneous material, both elastic and electrostatic, along principal directions follow well known trends. These trends are functions of the constituent material properties and the particulate (void) geometry but are independent of the employed modeling scheme [52, 139]. The specific modeling scheme is important for the precision in approximating the effective behavior depending on constituent properties, heterogeneity fraction, and many other considerations. A complete discussion regarding the "correct" choice of micromechanical modeling scheme to apply for a given particulate composite material is one of the main focuses of the field of micromechanics and is beyond the scope of appendix. The reader is referred to references [33, 52, 54, 151, 272] and references therein for a detailed discussion and analysis of micromechanical modeling approximations.

In general the expected trends are as follows. The overall material properties correspond to those of the matrix material, which is PP in this case, when the void fraction, ϕ^I, is zero and to that of the void when $\phi^I = 1$. Overall anisotropy is a result of two different factors: (*i*) constituent material anisotropy and (*ii*) the geometry and preferential orientation of heterogeneities. The foams studied here display highly anisotropic behavior or, to be more specific, a *high degree of transverse isotropy*. The anisotropy is a result of the presence of highly preferentially oriented oblate heterogeneities as the matrix material and heterogeneities of a piezoelectret are isotropic. It must be noted, however, that the general model derived in Section I.2 *is not* restricted

to only consider isotropic constituent material properties. Figure I. 6 plots the effective Young's moduli in the three principal directions predicted by the DEM model given in Section I.2.5.2. The effective Young's moduli are given as the curves for the other effective elastic moduli (*i.e.* shear, bulk, and plane wave moduli) yield similar trends. It therefore suffices to explore the results of the effective Young's modulus.

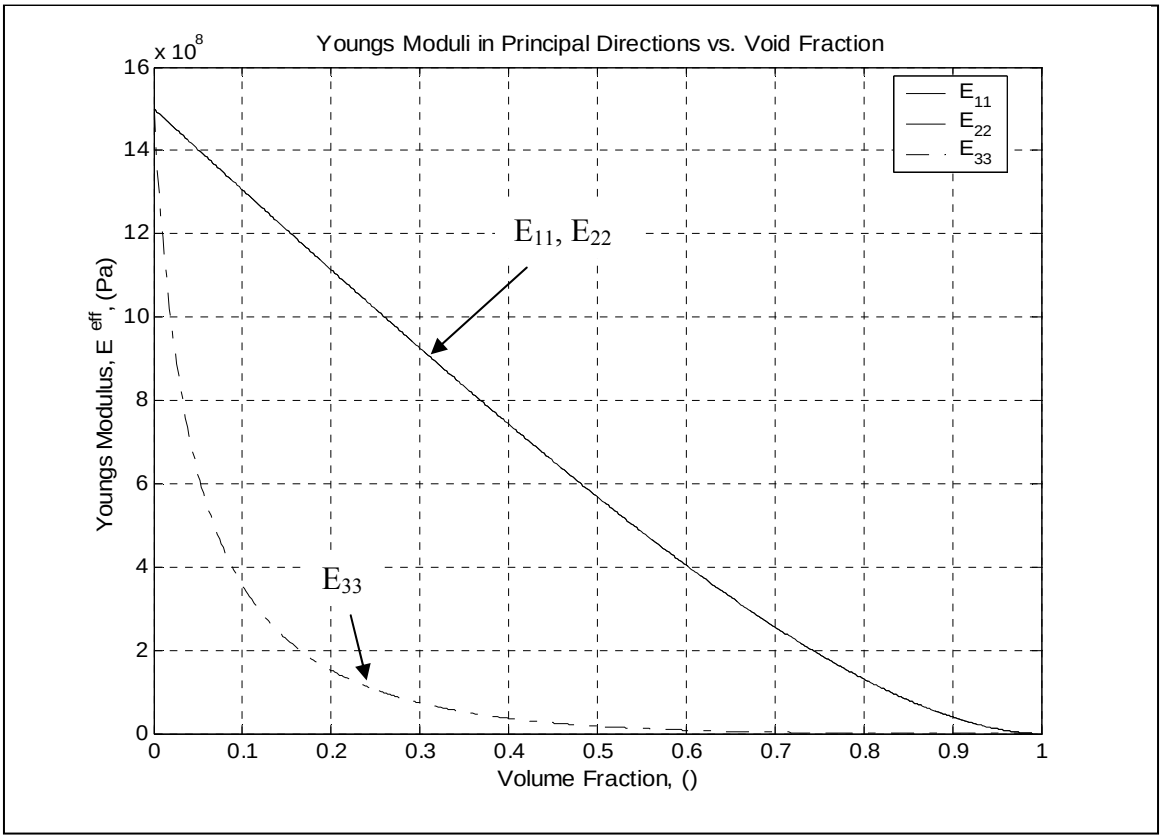

Figure I. 6: Effective Young's modulus along principal directions of piezoelectret as a function of void fraction.

The results of Figure I. 6 are encouraging. Foremost, recall that experimental measurements of typical foam elastic moduli along the x_3-axis give values of 1-10 MPa [260]. The proposed modeling approach falls agrees with experiment as the value approximated by the DEM model at $\phi^I = 0.65$ is $E_{33} \approx 5.25$ MPa. It is noted, however,

that Hillenbrand and Sessler [261] employed the second harmonic of the thickness resonance to experimentally estimate the Young's modulus of a PP foam to be ~0.95 MPa. Their value is only 20% of that estimated in the current modeling attempt. The source of this discrepancy may be the actual stiffness of the PP, errors in void fraction estimates, or experimental error.

It is of interest to discuss the influence the average void aspect ratio has on the elastic (and electrostatic) properties in the principal directions. Specifically, the magnitude of the difference between E_{33}^{eff} and E_{11}^{eff} (or E_{22}^{eff}) at any given void fraction is dependent on the void aspect ratio. When $a/c \in [1 \quad \infty]$, the voids are oblate spheroids and the ratio $E_{33}^{eff}/E_{11}^{eff}$ monotonically decreases. When $a/c = 1$, the voids are spherical and the macroscopic material behavior is isotropic and $E_{11}^{eff} = E_{22}^{eff} = E_{33}^{eff}$. Finally, when $a/c \in [0 \quad 1]$, the voids are prolate inclusions and the ratio $E_{33}^{eff}/E_{11}^{eff}$ monotonically increases.

One would also expect to observe, both intuitively and from the model derived in Section I.2, that the Young's modulus in the thickness direction would be altered after charge deposition. The current model does predict that a difference exists between these two cases. Figure I. 7 shows that the difference is a complicated function of voids fraction but that the difference is negligible for engineering calculations.

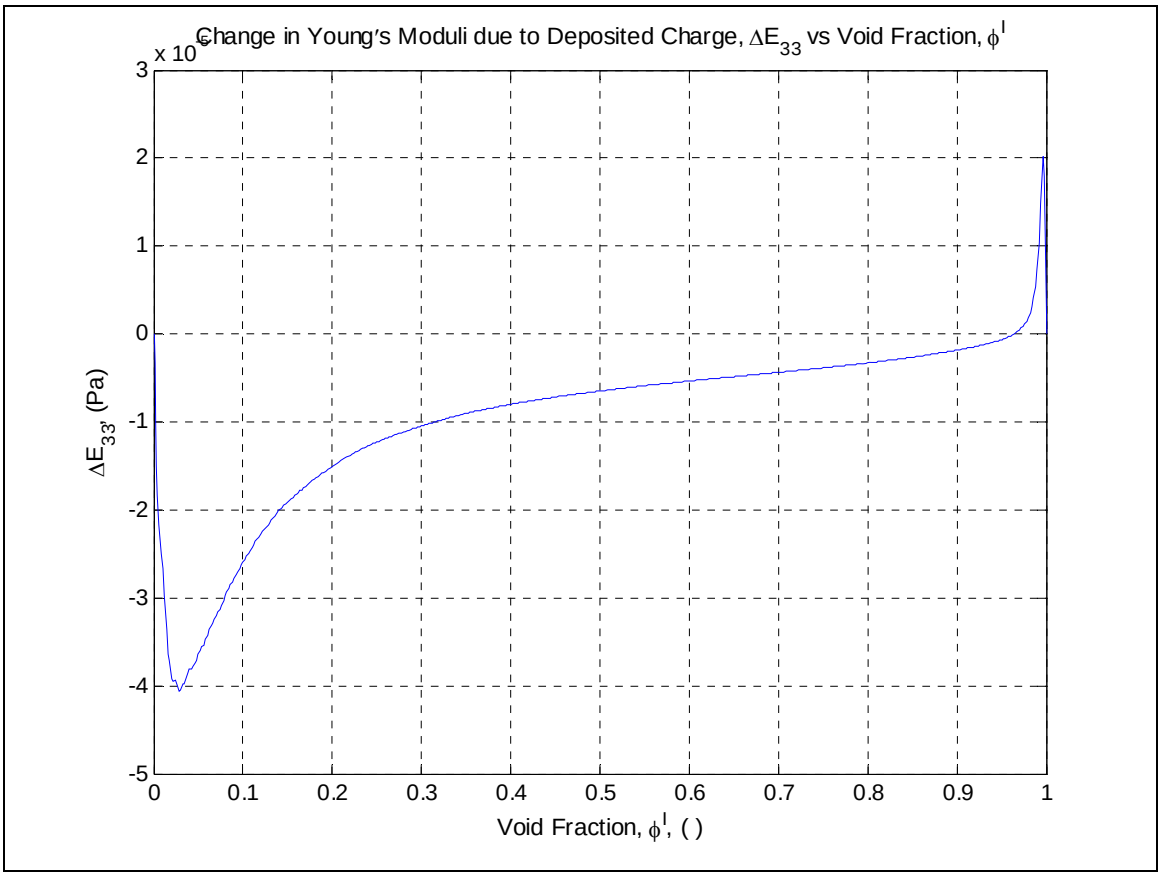

Figure I. 7: Difference in E_{33} between a foam having charge deposited within its voids and one without i.e.: $\Delta E_{33} = E_{33}(NC) - E_{33}(C)$. NC represents a foam having uncharged voids while C represents a foam having charged voids. The maximal value of difference is a negligible – 40 µPa.

The effective dielectric material properties are also accessible and of interest. Figure I. 8 shows the effective dielectric constant of the piezoelectret as a function of void fraction. As should be expected, the trends observed for the anisotropic effective dielectric constant, κ_{ij}^{eff}, are identical to those of the elastic properties. Indeed, the same observations regarding the ratio Young's modulus ratio $E_{33}^{eff}/E_{11}^{eff}$ as a function of void aspect ratio apply to the predicted dielectric constant ratio $\kappa_{33}^{eff}/\kappa_{11}^{eff}$. Mean field modeling results for material properties other than elastic have been previously noted by many others, notably Hashin [273] and Cherkaev *et al* [139], and others [158, 274].

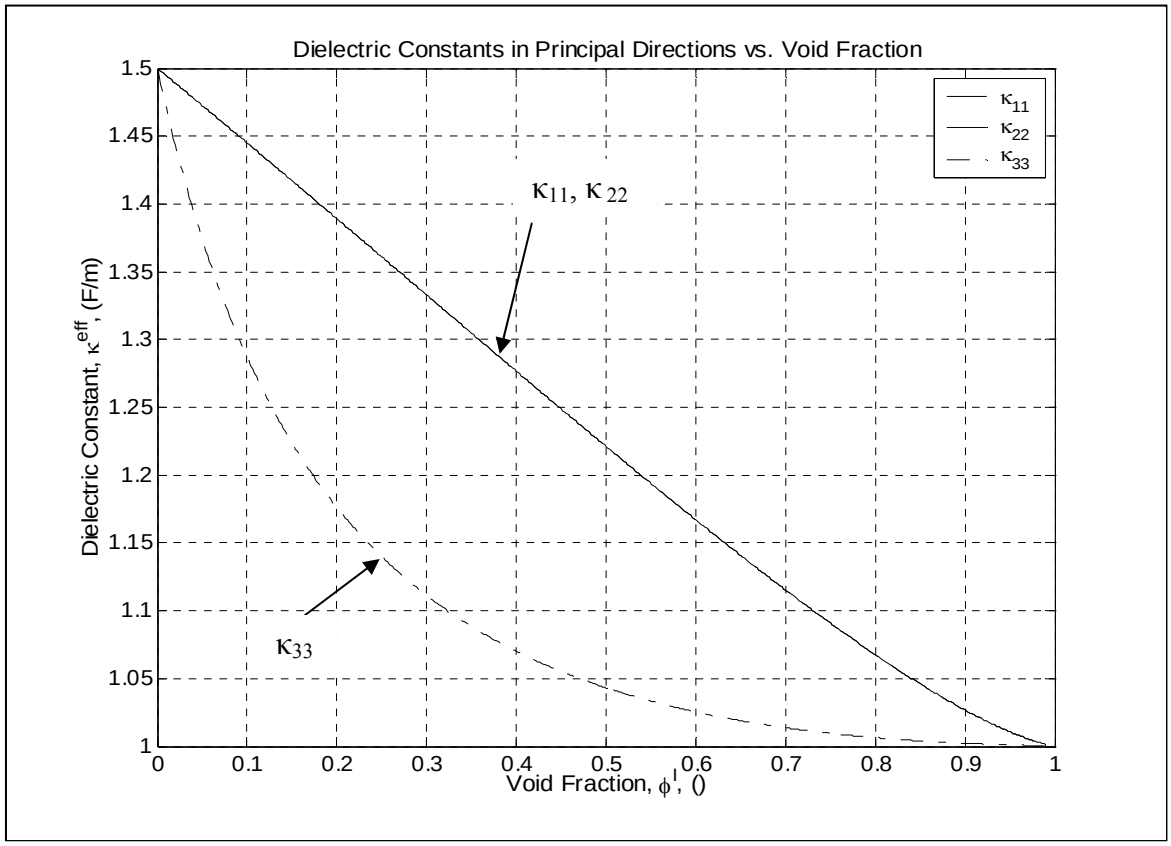

Figure I. 8: Effective dielectric constant along principal directions of piezoelectret as a function of void fraction.

Of high interest for this study are the values effective piezoelectric coupling coefficient d_{ij}^{eff}. Figure I. 9 shows the predicted effective piezoelectric coupling coefficient along the principal directions of the foam.

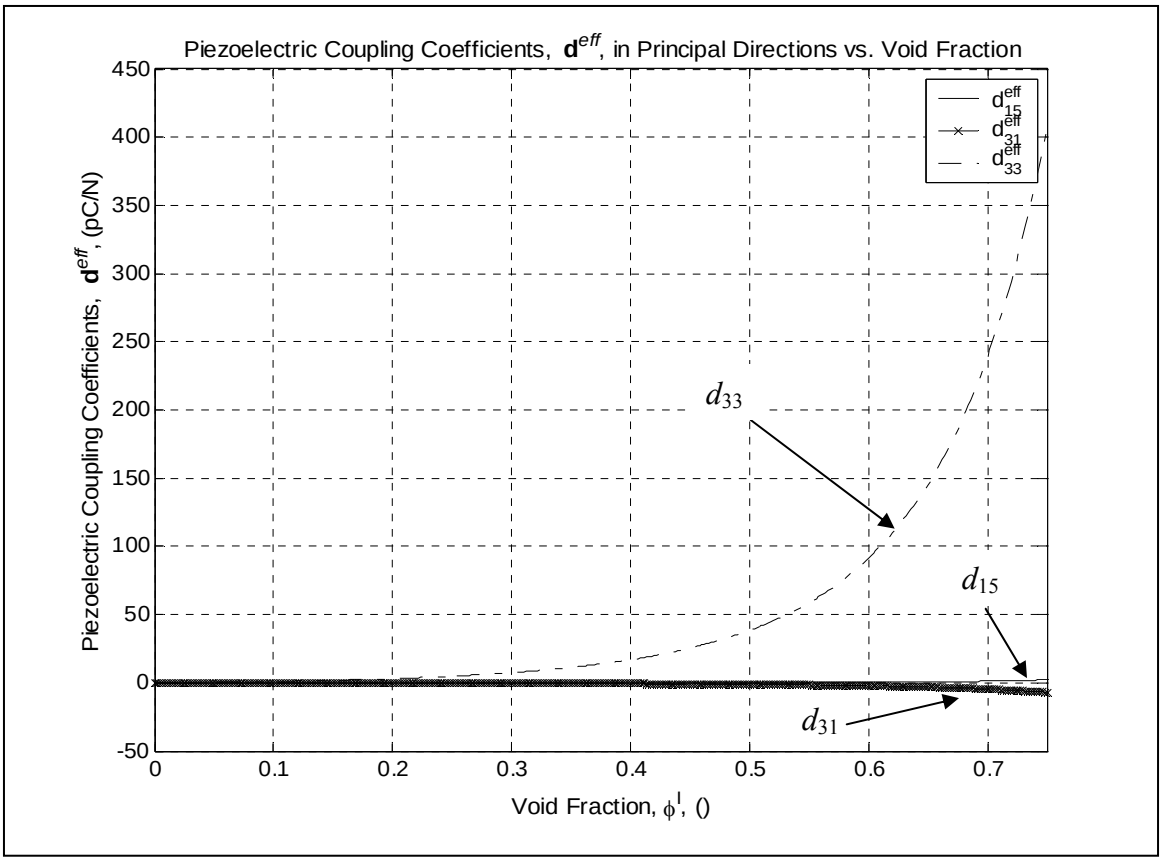

Figure I. 9: Effective piezoelectric coupling coefficient, [d^{eff}], along principal directions of piezoelectret as a function of void fraction.

The non-zero terms resulting from the model derived in Section I.2 are d_{31}^{eff}, d_{15}^{eff}, and d_{33}^{eff} (using Voigt notation). Recall that, in the absence of applied stress, the constitutive piezoelectric equations relate the observed strain of a material to the applied electric field by Eq. (9.3.1).

$$\begin{aligned} \varepsilon_1 &= d_{31}E_3 \quad \varepsilon_2 = d_{31}E_3 \quad \varepsilon_3 = d_{33}E_3 \\ \varepsilon_4 &= d_{15}E_1 \quad \varepsilon_5 = d_{15}E_2 \quad \varepsilon_6 = 0 \end{aligned} \tag{9.3.1}$$

Some key points to observe relevant to the developed mean-field model and the corresponding piezoelectret properties are now highlighted. Most importantly, the model predicts that d_{33}^{eff} will have the only non-negligible magnitude, in agreement with experimental observation. This was not explicitly required per the modeling approach, but stems from the manner in which the microscale physics of the problem have been considered. To emphasize that point, observed that all elements of d_{ij}^{eff} go to zero when the void fraction goes to zero. This is a model check. The viability of the three dimensional modeling is validated through the approximation of d_{31}^{eff}. Note that the value calculated is small in magnitude ($d_{31}^{eff} << d_{33}^{eff}$) and negative. This corresponds to the Poisson effect a inducing a very small in-plane constriction when an electric field is applied in the thickness direction. On the other hand, the fact that d_{15}^{eff} is non-zero is not coherent with observations. This is probably an artifact of model assumptions and numerical evaluation. In any case the calculated value is negligible even with respect to d_{31}^{eff}.

A few further useful observations can be made concerning the calculated effective d_{33}^{eff}. It is noted that the magnitude of d_{33}^{eff} is highly dependent on overall void fraction. The precipitous increase in d_{33}^{eff} is the result of both the increase in the number of voids "working" when an electric field is applied and the simultaneous decrease in stiffness in the same direction. The influence of polymer stiffness on effective piezoelectric coupling is investigated in Section I.3.7. Figure I. 9 suggests that one very efficient means of increasing the sensitivity of a piezo-electret foam would be to increase the void fraction while maintaining the percentage of voids with deposited charge and their aspect of ratio.

I.3.7 Sensitivity of effective piezoelectric coupling to various variables

The design/optimization of piezoelectret performance will often focus on maximizing the thickness coupling coefficient, d_{33}^{eff}. For this reason, it is interesting to inspect the influence of different parameters on the d_{33}^{eff}. These studies will simultaneously give insight on those parameters having the highest influence on electromechanical coupling and demonstrate the versatility of the mean field modeling technique derived in this work. For all of these studies the input variables are given in Table I. 1 except for the variable on which piezoelectric sensitivity is being solicited.

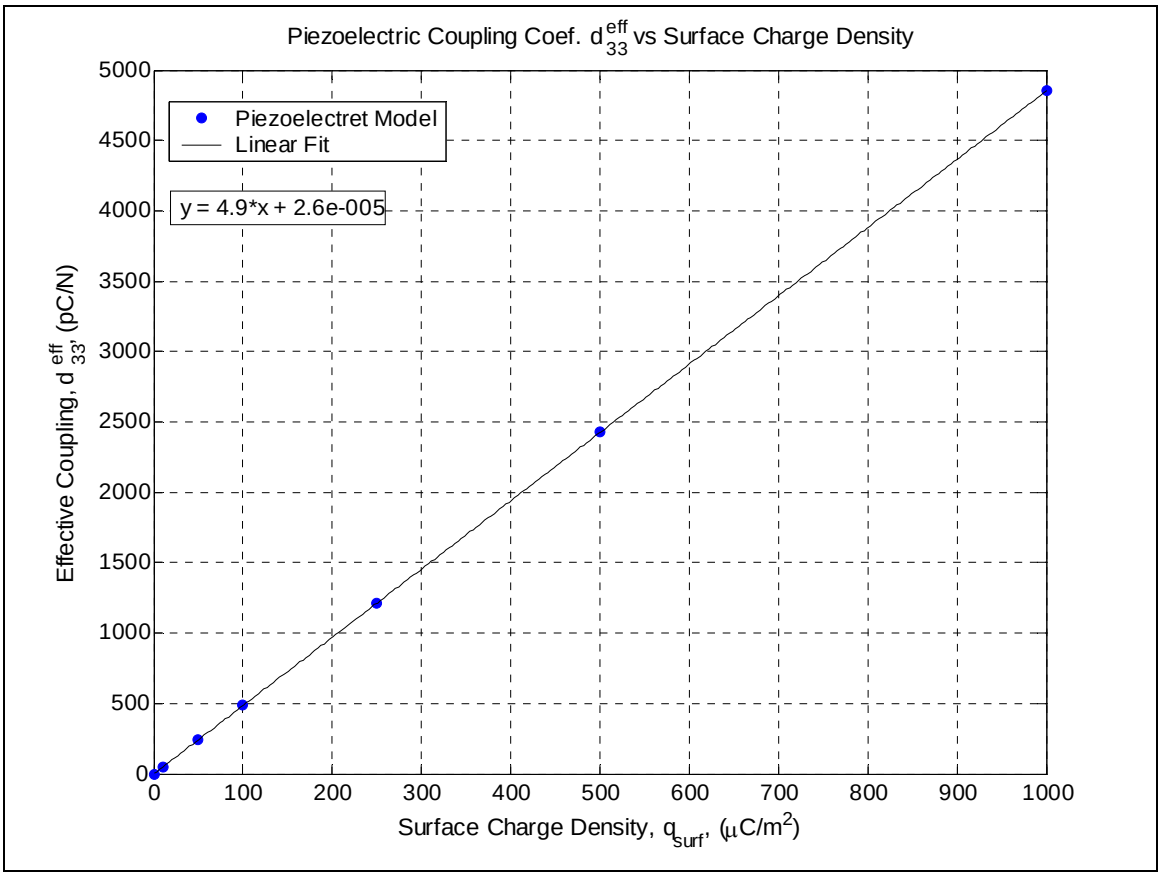

Figure I. 10: Effective piezoelectric coupling coefficient along x_3-direction, d^{eff}, as a function of surface charge density. Solid circles represent the mean field model points and the line is a least squares linear fit of the data.

Figure I. 10 shows the modeling results of calculating d_{33}^{eff} as a function of surface charge density deposited on the interior of the voids. All other variables given in Table I. 1 are held constant. The results clearly show that the relationship between q^{surf} and d_{33}^{eff} is linear. The model correctly predicts that a value of $q^{surf} = 0$ corresponds to a null value for d_{33}^{eff}. This plot confirms intuition showing that the value of d_{33}^{eff} is *highly* dependent on the surface charge density. Indeed, inspection of the remainder of the plots in this section shows that increasing the surface charge density is the most efficient means to increase piezoelectric coupling. A few other important points should be made

which were observed by varying the other input variables, but which are not explicitly shown here. The slope of the linear relationship will increase for the following changes in the other variables: $\uparrow a/c$, $\uparrow \phi^I$, $\downarrow f^{NC}$, and $\downarrow \delta E^{\%}$. Where f^{NC} represents the percentage of voids, per volume, which do not hold charge, and $\delta E^{\%}$ is a measure of the difference between the actual polymer matrix stiffness and that of PP which is defined in Eq. (9.3.2).

$$\delta E^{\%} = 100\left(\frac{E^{polymer} - E^{PP}}{E^{PP}}\right) \tag{9.3.2}$$

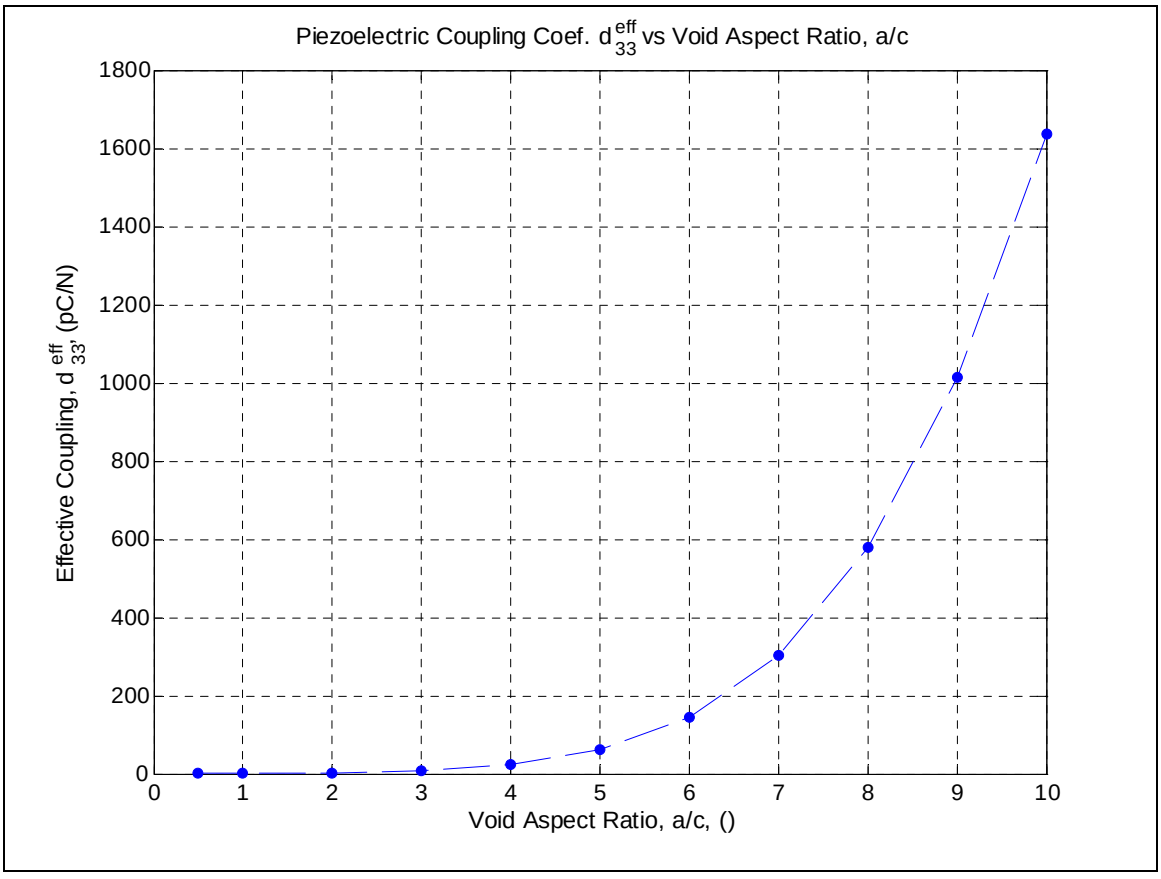

Figure I. 11: Effective piezoelectric coupling coefficient along x_3-direction, d^{eff}, as a function of the aspect ratio, a/c, when a = b.

Next the dependence of d_{33}^{eff} on the void aspect ratio has been calculated. Figure I. 11 shows a strong dependence of d_{33}^{eff} on the aspect ratio of charged voids. The strong dependence stems from two coupled causes: (*i*) As the aspect ratio increases, the conversion of Lorentz force to strain in the thickness direction, x_3, becomes more efficient due to the increases parallelism of void normals with the x_3- axis. (*ii*) For a fixed void fraction an increase in void aspect ratio yields decreased stiffness in the thickness direction. This was discussed with respect to the results given in Figure I. 6. Note also that calculations of d_{33}^{eff} as a function of the aspect ratio, a/c, has been carried out for the case where the major radius, *a*, was held constant and for the case where the void volume, V^I was held constant. Though neither of these cases exactly reflects reality, they yield virtually same results. It is clear that as the dominant variable is simply the aspect ratio, a/c. Another important observation relates the results of Figure I. 11 to the work of Wegener *et al* concerning the effect of void inflation [264]. They discovered that inflating voids to the point where they are nearly spherical results in extremely poor electromechanical coupling behavior. An aspect ratio of $a/c = 1$ corresponds to spherical voids. Figure I. 11 confirms that the mean field model derived here predicts very low magnitude piezoelectric coupling when voids are spherical.

Wegener *et al* also studied the variation in measured C_{33}^{eff} and d_{33}^{eff} due to controlled void inflation [264]. Their results reported the variation in stiffness and piezoelectric coupling as a function of the relative density which is simply the ratio,

ρ^{eff}/ρ^{PP}. The effective density is easily found as a function of void fraction through the law of mixtures relationship (9.3.3)

$$\rho^{eff} = \rho^{PP} + \phi^{I}\left(\rho^{gas} - \rho^{PP}\right) \tag{9.3.3}$$

Reported experimental observations showed a relative maximum in piezoelectric coupling when $\rho^{eff}/\rho^{PP} \approx 0.43$. The choice of ρ^{eff}/ρ^{PP} as independent variable seems, at first, to imply that the inflation process simply induces an increase in foam void fraction. In which case $\rho^{eff}/\rho^{PP} \approx 0.43$ would imply a void fraction of $\phi^{I} \approx 0.57$. Figure I. 9 shows, however, that one should expect to observe a *monotonic* decrease in d_{33}^{eff} with increasing relative density. Note however, that the main objective of void inflation is to increase the void height and in so doing, their aspect ratio, to allow efficient charge deposition. It is therefore hypothesized that the non-monotonic curves reported by Wegener *et al* [264] are a result of the complex interaction of simultaneously increasing void fraction, which increases d_{33}^{eff}, and increasing aspect ratio, which tends to decrease d_{33}^{eff}. Indeed it may be very enlightening to quantify, either through modeling or experiment, the dependency of void fraction and aspect ratio on the inflation pressure for a given matrix material. This may provide and elegant manner to approximate d_{33}^{eff} as a function of the internal void pressure.

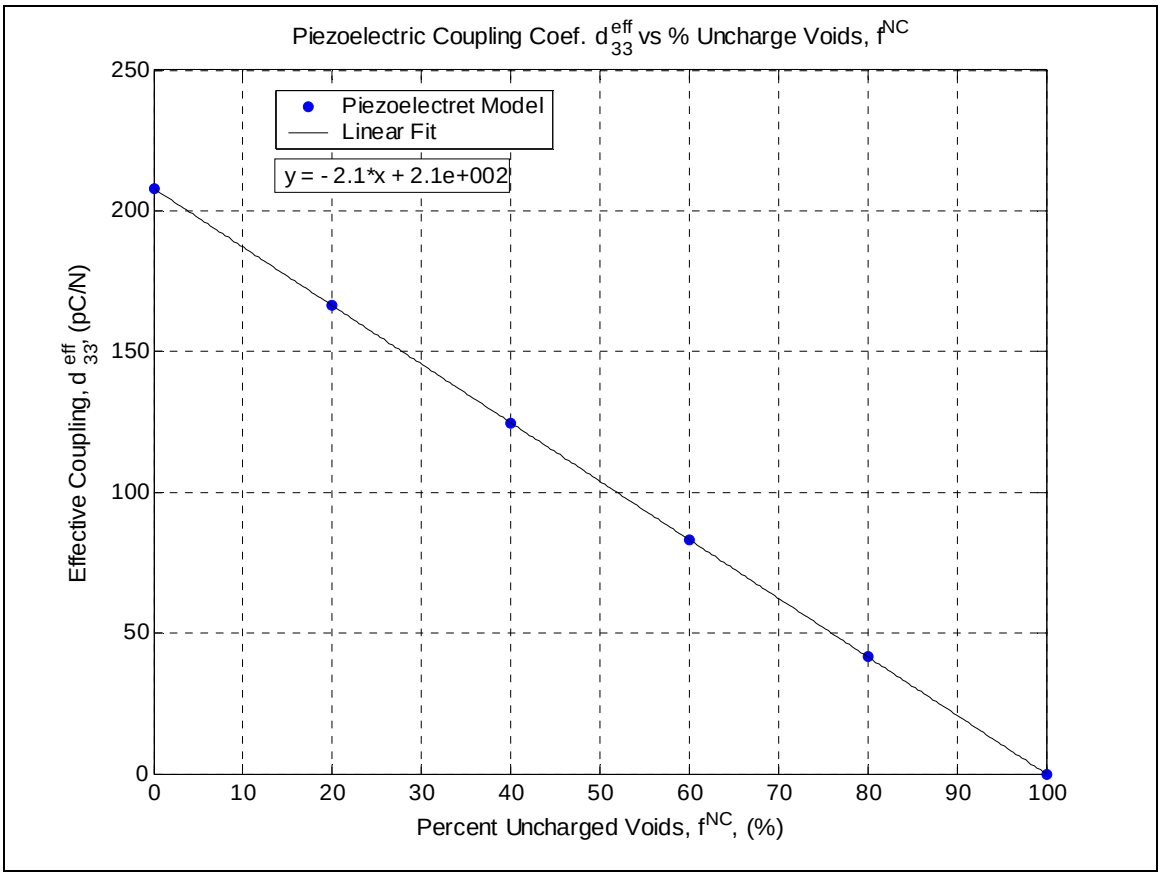

Figure I. 12: Effective piezoelectric coupling coefficient along x_3-direction, d^{eff}, as a function of the percentage of void which are not charge during the Corona discharging process. Solid circles represent the mean field model points and the line is a least squares linear fit of the data.

Another variable that influences the effective piezoelectric coupling coefficient is the percentage of voids not carrying charge. Figure I. 12 shows the relationship between d_{33}^{eff} and the percentage, per volume, of voids which are uncharged, f^{NC}. The calculated relationship is very linear with d_{33}^{eff} decreasing with increasing f^{NC}. The sensitivity of d_{33}^{eff} to the percentage of uncharged voids is much lower than its sensitivity to surface charge density. As a model confirmation, a value of $f^{NC} = 100$ corresponds to a null value of d_{33}^{eff} and, conversely, d_{33}^{eff} max is observed when all voids have a deposited charge: $f^{NC} = 0$. As with the results shown in Figure I. 10, the slope and intercept value

of this line are highly dependent on other independent variables. Specifically, the magnitude of the slope and the intercept value both increase when $\uparrow a/c$, $\uparrow \phi^{l}$, $\uparrow q^{surf}$, and $\downarrow \delta E^{\%}$.

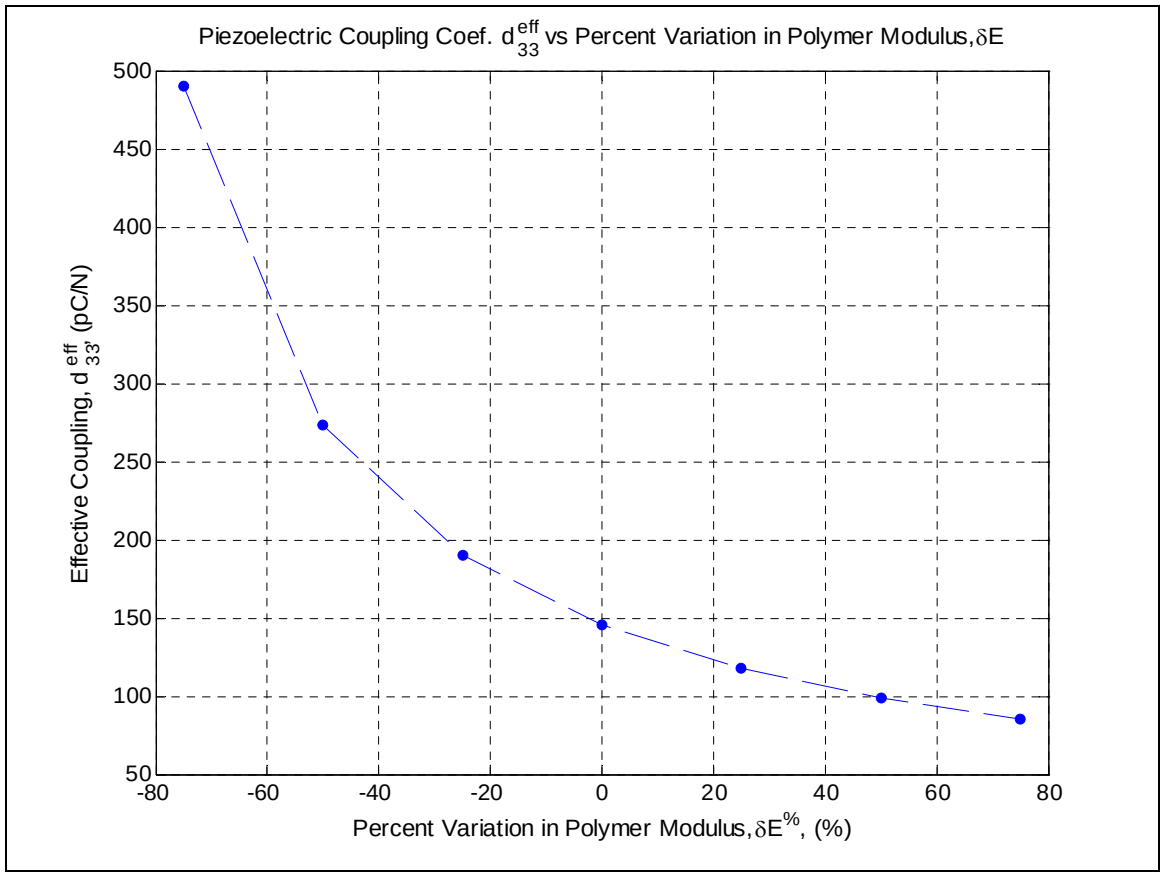

Figure I. 13: Effective piezoelectric coupling coefficient along x_3-direction, d^{eff}, as a function of the percent variation, with respect to E^{PP}, of the Young's modulus of the polymer matrix.

The final variable impacting the effective piezoelectric coupling coefficient that is inspected here is the variation in polymer matrix Young's modulus defined by Eq. (9.3.2) . The results are shown in Figure I. 13. All other variables given in Table I. 1 are held constant. The results agree with intuition that, all other variables remaining equal, a softer polymer host material yields better electromechanical coupling. A final, related

point should be made regarding polymer stiffness and the resulting piezoelectric coupling. Thermo-mechanical processing of polymers, such as those often imposed on closed cell polymer foams, can induce large variations in their final mechanical stiffness [149]. Figure I. 13 illustrates that the resulting piezoelectric coupling coefficient will be significantly impacted by variations in polymer matrix stiffness. It is, therefore, very important to consider the influence of polymer processing when designing and seeking to optimize the piezoelectric properties of piezoelectrets.

I.4 Conclusions on mean-field modeling and results

This appendix has derived and validated a three dimensional mean-field micro-electromechanical DEM model predicting the behavior of closed cell piezoelectret foams. This model is very general and significantly improves upon the existing one-dimensional models from the literature. It is also important to note that this work has only modeled the effective properties when the voids are assumed to have the same orientation, aspect ratio, and surface charge density. However, it is straightforward to extend the model derived in Section 1.2 using the dilute strain concentration formulation (DSCT) employed by Haberman *et al* [130]. DSCT formulation allows the researcher to more closely mimic true foam composition and therefore more closely approximate the true material behavior. Even when the voids are assumed to be identical and identically oriented, model prediction improvements stem from the ability to take into account the three-dimensionality of the medium, to directly model the interaction of different input variables, and a to provide a more realistic description of the physical processes taking

place at the void scale. The resulting model provides a very strong tool for the design and optimization of the viscoelastic, dielectric, and piezoelectric properties of these exciting heterogeneous materials. The results given in Section I.3 agree with experimental results in every aspect. That section illustrated the capacity of the model to perform intricate numerical studies and encourages the use of the micro-electromechanical DEM model for efficient improvement of piezoelectret behavior by design and to explore their complex behavior as a function of multiple independent variables.

APPENDIX J

THESIS RELATED SCIENTIFIC COMMUNICATIONS

J.1 Refereed journal articles

M. Haberman, Y. Berthelot, M. Cherkoui, "Micro-electromechanical modeling of piezoelectret foams," *in preparation*, Journal of Applied Physics

M. Haberman, Y. Berthelot, M. Cherkoui, "Design of high loss composites through micromechanics and a Compromise Decision Support Protocol," *in preparation*, Journal of Computer-Aided Materials Design

Y. Koutsawa, M. Haberman, E. M. Daya, M. Cherkaoui, "Modal behavior of a rectangular sandwich plate supported at extents by a viscoelastic material with a heterogeneous viscoelastic core," *submitted* January 2007 to the Journal of Sound and Vibration.

M. Haberman, Y. Berthelot, M. Cherkaoui, "Micromechanical modeling of particulate composites for damping of acoustic waves," Journal of Engineering Materials Technology, **128**, 2006, pgs. 320-329.

M. Haberman, Y. Berthelot, M. Cherkaoui, "Transmission loss of viscoelastic materials containing oriented ellipsoidal, coated microinclusions," The Journal of the Acoustical Society of America, **118** (5), 2005, pgs. 2984-2992.

M. Haberman, Y. Berthelot, J. Jarzynski, and M. Cherkaoui, "Micromechanical modeling of viscoelastic voided composites in the low frequency approximation," The Journal of the Acoustical Society of America, **112** (5), Pt. 1, 2002, pgs 1937 – 1943.

J.2 Articles in conference proceedings

M. Haberman, Y. H. Berthelot, J. M. Vander Weide, "Micro-electromechanical modeling of closed cell piezo-polymer foams," Proceedings of the International Congress on Ultrasonics, Vienna, Austria, April 9-12, 2007.

M. Haberman, Y. Berthelot, M. Cherkaoui, E. M. Daya, "Modélisation des plaques sandwich pour l'amélioration de la performance acoustique," Actes du 17ème Congrès Français de Mécanique, Troyes, France, Aug. 29-Sept 2, 2005.

J.3 Presentations

Y. Koutsawa, M. Haberman, E. M. Daya, M. Cherkaoui, "Modélisation Multi-échelles des Structures Sandwich Verre/Viscoélastique/Verre," accepted for presentation at the 8ème Congrès Marocaine de Mécanique, El Jadida, Morocco (April 17-20, 2007).

M. Haberman, J. Vander Weide, Y. Berthelot, "Micromechanical Predictions of Cellular Electret Material Properties," Presented at the 8th European Conference on Applications of Polar Dielectrics, Metz, France, (September 5-8, 2006).

M. Haberman, Y. Berthelot, M. Cherkaoui, "Micromechanical modeling of particulate composites for acoustic damping purposes," Invited Speaker, Laboratoire de Physique et Mécanique des Matériaux, Metz, France, (November 18, 2005).

M. Haberman, Y. Berthelot, M. Cherkaoui, "Acoustic performance of composite materials containing micro-inclusions," Presented at the Workshop on Acoustical Imaging of Complex Media: Applications in Medicine, Seismology, and Oceanography, Institut d'Etudes Scientifiques de Cargèse, Cargèse, France, (July 4 – 9, 2005).

M. Haberman, Y. Berthelot, M. Cherkaoui, "Micromechanical modeling of particulate composites for acoustic damping purposes," Presented at the Workshop on Damping in Shape Memory Alloys, Composites, and Foams, Georgia Tech Lorraine, Metz, France, (May 2005).

M. Haberman, Y. Berthelot, and M. Cherkaoui, "Transmission loss of a submerged viscoelastic slab containing oblate spheroidal coated microinclusions," Presented at the 147th meeting of the Acoustical Society of America, New York, NY (May 2004).

M. Haberman, Y. Berthelot, "Acoustic performance of composite materials containing micro-inclusions," Presented at the Symposium for Mechanical Modeling: ENSAM – GT, Metz, France, (March 2004).

REFERENCES

1. Olson, G.B., *Computational Design of Hierarchically Structured Materials.* Science, 1997. **277**(5330): p. 1237-1242.

2. McDowell, D.L. and T.L. Story, *New Directions in Materials Design Science and Engineering (MDS&E)*. 1999, U.S. National Science Foundation Workshop Report: Georgia Institute of Technology Materials Council, Atlanta, GA.

3. Seepersad, C.C., B.M. Dempsey, J.K. Allen, F. Mistree, and D.L. McDowell, *Design of Multifunctional Honeycomb Materials.* AIAA Journal, 2004. **42**(5): p. 1025-1033.

4. Ashby, M.F., *Materials Selection in Mechanical Design*. 1999, Oxford, UK: Butterworth-Heinmann.

5. Olson, G.B., *Designing a new material world.* Science, 2000. **288**(5468): p. 993-998.

6. Mistree, F. *Are We Designing Materials?* in *Workshop on Inverse Techniques in Materials Design*. 2004. Atlanta, GA.

7. Smith, C.S., *A Search for Structure*. 1981, Cambridge, MA: MIT Press.

8. Seepersad, C.C., *A Robust Topological Preliminary Design Exploration Method with Materials Design Applications*, in *Mechanical Engineering*. 2004, Georgia Institute of Technology: Atlanta, GA. p. 526.

9. Qian, Z., C.C. Seepersad, V.R. Joseph, J.K. Allen, and C.F.J. Wu, *Building surrogate models based on detailed and approximate simulations.* Journal of Mechanical Design, 2005, *in Press*.

10. Mixson, J.S. and C.A. Powell, *Review of recent research on interior noise of propeller aircraft.* Journal of Aircraft, 1985. **22**(11): p. 931-949.

11. Moore, T.C. and A.B. Lovins. *Vehicle design strategies to Meet and Exceed PNGV goals*. in *SAE Future Transportation Technology Conference* 1995. Costa Mesa, CA: Society of Automotive Engineers.

12. Wilson, C.E., *Noise Control: Measurement, Analysis, and Control of Sound and Vibration*. 1994, Melbourne, FL: Krieger Publishing Co.

13. Varanasi, K.K. and S.A. Nayfeh. *Vibration damping by coupling to lossy low-wave-speed media*. in *Smart Structures and Materials: Damping and Isolation*. 2003. San Diego, CA: SPIE.

14. Lilly, J.G., *Recent advances in acoustical glazing*, in *Sound and Vibration*. 2004. p. 8-13.

15. Jarzynski, J., *A Review of the Mechanisms of Sound Attenuation in Materials.* Sound and Vibration Damping with Polymers, ed. R.D. Corsaro and L.H. Sperling. Vol. 424. 1990, Washington D.C.: American Chemical Society. 116-207.

16. Christensen, R.M., *Viscoelastic properties of heterogeneous media.* Journal of the Mechanics and Physics of Solids, 1969. **17**: p. 23-41.

17. Hashin, Z., *Viscoelastic behavior of heterogeneous media.* Journal of Applied Mechanics, 1965. **32**: p. 630-635.

18. Lakes, R.S., *Extreme damping in composite materials with a negative stiffness phase.* Physical Review Letters, 2001. **86**(13): p. 2897-2900.

19. Lakes, R.S., *Extreme damping in compliant composites with a negative-stiffness phase.* Philosophical Magazine Letters, 2001. **81**(2): p. 95-100.

20. Wang, Y.-C. and R.S. Lakes, *Stable extremely-high-damping discrete viscoelastic systems due to negative stiffness elements.* Applied Physics Letters, 2004. **84**(22): p. 4451-4453.

21. Lakes, R.S., T. Lee, A. Bersie, and Y.C. Wang, *Extreme damping in composite materials with negative-stiffness inclusions.* Nature, 2001. **410**: p. 565-567.

22. Wang, Y.C., M. Ludwigson, and R. Lakes, *Deformation of extreme viscoelastic metals and composites.* Materials Science and Engineering A, 2004. **370**: p. 41-49.

23. Cherkaoui, M., H. Sabar, and M. Berveiller, *Micromechanical Approach of the coated inclusion problem and applications to composite materials.* Journal of Engineering Materials and Technology, 1994. **116**: p. 274-278.

24. Cherkaoui, M., H. Sabar, and M. Berveiller, *Elastic composites with coated reinforcements: A micromechanical approach for nonhomothetic topology.* International Journal of Engineering Science, 1995. **33**(6): p. 829-843.

25. 3M, *3M Microspheres*. 2003.

26. Baird, A.M., F.H. Kerr, and D.J. Townend, *Wave propagation in a viscoelastic medium having fluid-filled microspheres.* Journal of the Acoustical Society of America, 1999. **105**: p. 1527-1538.

27. Berryman, J.G., *Long-wavelength propagation in composite elastic media II. Ellipsoidal Inclusions.* Journal of the Acoustical Society of America, 1980. **68**(6): p. 1820-1831.

28. Jones, L.E.A. and H.F. Wang, *Ultrasonic velocities in Cretaceous shales from the Williston Basin.* Geophysics, 1981. **46**: p. 288-297.

29. Hornby, B.E., L.M. Schwartz, and J.A. Hudson, *Anisotropic effective-medium modeling of the elastic properties of shales.* Geophysics, 1994. **59**(10): p. 1570-1583.

30. Ledbetter, H.M. and S.K. Datta, *Effective wave speeds in an SiC-particle reinforced Al composite.* Journal of the Acoustical Society of America, 1986. **79**(2): p. 239-248.

31. Ross, D., E.E. Ungar, and E.M. Kerwin, *Damping of Plate Flexural Vibrations by Means of Viscoelastic Laminae*, in *Structural Damping - A Colloquium held at the ASME Annual Meeting*, A.S.o.M. Engineers, Editor. 1959, American Society of Mechanical Engineers: Atlantic City, New Jersy. p. 49-87.

32. Pierce, A.D., *Acoustics, and Introduction to Its Physical Principles and Applications*. 5th ed. 1991, Woodbury, NY: Acoustical Society of America.

33. Christensen, R.M., *Mechanics of Composite Materials*. Reprint ed. 1991, Melbourne, FL: Krieger Publishing Company. 348.

34. Lakes, R.S., *Viscoelastic Solids*. Mechanical Engineering. Vol. 9. 1998, New York, NY: Taylor & Francis CRC Press. 496.

35. Haddad, Y.M., *Viscoelasticity of Engineering Materials*. 1st ed. 1995: Chapman & Hall.

36. Ferry, J., *Viscoelastic Properties of Polymers*. 1970, New York, NY: John Wiley & Sons.

37. Christensen, R.M., *Restrictions Upon Viscoelastic Relaxation Functions and Complex Moduli.* Transactions of the Society of Rheology, 1972. **16**(4): p. 603-614.

38. Haberman, M., Y. Berthelot, J. Jarzynski, and M. Cherkaoui, *Micromechanical modeling of viscoelastic composites in the low frequency approximation.* Journal of the Acoustical Society of America, 2002. **112**(5): p. 1937-1943.

39. Hwang, S.J. and R.F. Gibson, *The use of strain energy-based finite element techniques in the analysis of various aspects of damping of composite materials and structures.* Journal of Composite Materials, 1992. **26**(17): p. 2585-2605.

40. Hwang, S.J. and R.F. Gibson, *Micromechanical modeling of damping in discontinuous fiber composites using a strain energy/finite element approach.* Journal of Engineering Materials and Technology, 1987. **109**(1): p. 47-52.

41. Guan, H. and R.F. Gibson, *Micromechanical models for damping in woven fabric-reinforced polyer matrix composites.* Journal of Composite Materials, 2001. **35**(16): p. 1417-1434.

42. Ungar, E.E. and E.M. Kerwin, *Loss factors of viscoelastic systems in terms of strain energy.* Journal of the Acoustical Society of America, 1962. **34**(2): p. 954-958.

43. Lin, R.M. and M.K. Lim, *Complex eigensensitivity-based characterization of structures with viscoelastic damping.* Journal of the Acoustical Society of America, 1995. **100**(5): p. 3182-3191.

44. Soni, M.L., *Finite element analysis of viscoelastically damped sandwich structures.* Shock and Vibration Bulletin, 1981. **55**(1): p. 97-109.

45. Mead, D.J. and S. Markus, *The forced vibration of three-layer damped sandwich beam with arbitrary boundary conditions.* Journal of Sound and Vibration, 1969. **10**: p. 163-175.

46. Sun, C.T. and Y.P. Lu, *Vibration Damping of Structural Elements*. 1995, Englewood Cliff, NJ: Prentice Hall.

47. Nashif, A.D., *Control of Noise and Vibration with Damping Materials*, in *Sound and Vibration Magazine*. 1983. p. 28-36.

48. McDaniel, J.G. and J.H. Ginsberg, *A simple test of the modal strain energy method.* Journal of the Acoustical Society of America, 1993. **93**(4): p. 2388.

49. Malvern, L.W., *Introduction to the Mechanics of a Contiuous Medium*. 1st ed. 1977, Englewood Cliff, NJ: Prentice Hall. 713.

50. Blackstock, D.T., *Fundamentals of Physical Acoustics*. 2000, New York: Wiley.

51. Achenbach, J.D., *Wave propagation in elastic solids*. 7th ed. Applied Mathematics and Mechanics, ed. J.D. Achenbach, et al. Vol. 16. 1999, Amsterdam, NL: North-Holland - Elsevier. 426.

52. Böhm, H.J., *A short introduction to basic aspects of continuum micromechanics*. 1998, A Report to: The Vienna Institute of Technology: Christian Doppler Labratory for Functionally Oriented Materials: Vienna, Austria.

53. LeGonidec, Y., D. Gibert, and J.-N. Proust, *Multiscale analysis of waves reflected by complex interfaces: Basic principles and experiments.* Journal of Geophysical Research - Solid Earth, 2002. **107**(B9): p. 2184.

54. Mura, T., *Micromechanics of Defects in Solids*. 2nd ed. 1987: Kluwer Academic.

55. Bradshaw, R.D., F.T. Fisher, and L.C. Brinson, *Fiber waviness in nanotube-reinforced polymer composites - II: modeling via numerical approximation of the dilute strain concentration tensor.* Composites Science and Technology, 2003. **63**: p. 1705-1722.

56. Fisher, F.T., R.D. Bradshaw, and L.C. Brinson, *Fiber waviness in nanotube-reinforced polymer composites-I: Modulus predictions using effective nanotube properties.* Composites Science and Technology, 2003. **63**: p. 1689-1703.

57. Odegard, G.M., T.S. Gates, K.E. Wise, C. Park, and E.J. Siochi, *Constitutive modeling of nanotube-reinforced polymer composites.* NASA/CR-2002-211760, ICASE Report No. 2002-27, 2002.

58. Eshelby, J.D., *The determination of the elastic field of an ellipsoidal inclusion, and related problems.* Proceedings of the Royal Society of London, A, 1957. **241**: p. 376-396.

59. Song, G.Q., Q.P. Sun, and M. Cherkaoui, *Micromechanics modeling of composite with ductile matrix and SMA reinforcement.* International Journal of Solids and Structures, 2000. **37**: p. 1577-1594.

60. Voigt, W., *Uber die beziehung zurischen den beiden elastizitäts konstanten isotroper körper.* Wied. Ann, 1889. **38**.

61. Reuss, A., *Berechnung der fliessgrenze von mischkristallan auf grund der plastizitätsbedingung fur einkristall.* Z. Ang. Math. Mech., 1929. **9**.

62. Kröner, E., *Elastic moduli of perfectly disordered composite materials.* Journal of the Mechanics and Physics of Solids, 1967. **15**(5): p. 319-329.

63. Lu, Y. and P.K. Liaw, *Effects of particle orientation in silicon carbide particulate reinforced aluminum matrix composite extrusions on ultrasonic velocity measurement.* Journal of Composite Materials, 1995. **29**(8): p. 1096-1116.

64. Wu, T.T., *The effect of inclusion shape on the elastic moduli of a two-phase material.* International Journal of Solids and Structures, 1966. **2**: p. 1-8.

65. Kröner, E., *Berechnug der elastishen konstanten des vielkristalles aus den konstanten des einkristalls.* Zeitschrift fur Physik, 1958. **151**: p. 504-518.

66. Budiansky, B., *On the elastic moduli of some heterogeneous materials.* Journal of the Mechanics and Physics of Solids, 1965. **13**(4): p. 223-227.

67. Mori, T. and K. Tanaka, *Average stress in the matrix and average elastic energy of materials with misfitting inclusions.* Acta Metallurgica, 1973. **21**: p. 571-574.

68. Zeller, R. and P.H. Dederichs, *Elastic constants of polycrystals.* Physica Status Solidi B, 1973. **55**: p. 831-842.

69. Mura, T., *Displacement and plastic distortion fields produced by dislocations in anisotropic media.* Journal of Applied Mechanics, 1971. **38**: p. 865-868.

70. Willis, J.R., *Stress fields produced by dislocations in anisotropic media.* Philosophical Magazine, 1970. **21**: p. 931-949.

71. Berveiller, M., O. Fassi-Fehri, and A. Hihi, *The problem of two plastic and heterogeneous inclusions in an anisotropic medium.* International Journal of Engineering Science, 1987. **25**(6): p. 691-709.

72. Hill, R., *Interfacial operators in the mechanics of composite media.* Journal of the Mechanics and Physics of Solids, 1983. **31**(4): p. 347-357.

73. Walpole, L.J., *The elastic field of an inclusion in an anisotropic medium.* Proceedings of the Royal Society of London, A, 1967. **300**: p. 270-289.

74. Cherkaoui, M., D. Muller, H. Sabar, and M. Berveiller, *Thermoelastic behavior of composites with coated reinforcements: a micromechanical approach and applications.* Computational Materials Science, 1996. **5**(1-3): p. 45-52.

75. Nemat-Nasser, S. and M. Hori, *Micromechanics: Overall properties of heterogeneous materials*. 1999, Amsterdam, Netherlands: Elsevier.

76. Molinari, A. and M.E. Mouden, *The problem of elastic inclusions at finite concentration.* International Journal of Solids and Structures, 1996. **33**(20-22): p. 3131-3150.

77. Hill, R., *A self-consistent mechanics of composite materials.* Journal of the Mechanics and Physics of Solids, 1965. **13**: p. 213-222.

78. Hill, R., *Continuum micro-mechanisms of elastoplastic polycrystals.* Journal of the Mechanics and Physics of Solids, 1965. **13**(2): p. 89-101.

79. Berveiller, M. and A. Zaoui. *Méthodes self-consistentes en mécanique des solides hétérogènes*. in *15^e Colloque du Groupe Français de Rhéologie: Comportement Rhéologique des Matériaux*. 1980.

80. Christensen, R.M. and K.H. Lo, *Solutions for effective shear properties in three phase sphere and cylinder models.* Journal of the Mechanics and Physics of Solids, 1979. **27**(4): p. 315-330.

81. Jasiuk, I. and M.W. Kouider, *The effect of an inhomogeneous interphase on the elastic constants of transversly isotropic composites.* Mechanics of Materials, 1993. **15**(1): p. 53-63.

82. Hervé, E. and A. Zaoui, *n-layered inclusion-based micromechanical modeling.* International Journal of Engineering Science, 1993. **31**(1): p. 1-10.

83. Hashin, Z., *Complex moduli of viscoelastic composites - I: General theory and application to particulate composites.* International Journal of Solids and Structures, 1970. **6**: p. 539-552.

84. Hashin, Z., *Complex moduli of viscoelastic composites II: Fiber reinforced materials.* International Journal of Solids and Structures, 1970. **6**: p. 797-807.

85. Ying, C.F. and R. Truell, *Scattering of plane longitudinal waves by a spherical obstacle in an isotropically elastic fluid.* Journal of the Acoustical Society of America, 1956. **27**: p. 1086-1097.

86. Chaban, I.A., *Self-consistent field approach to calculation of the effective parameters of microinhomogeneous media.* Soviet Physical Acoustics, 1965. **10**: p. 298-304.

87. Kuster, G.T. and M.N. Toksöz, *Velocity and attenuation of seismic waves in two-phase media: Theoretical Formulation.* Geophysics, 1974. **39**: p. 587-606.

88. Kligman, R.L., W.M. Madigosky, and J.R. Barlow, *Effective dynamic properties of composite viscoelastic materials.* Journal of the Acoustical Society of America, 1981. **70**(5): p. 1437-1444.

89. Gaunaurd, G.C. and H. Überall, *Resonance theory of the effective properties of perforated solids.* Journal of the Acoustical Society of America, 1982. **71**(2): p. 282-295.

90. Kerr, F., *The scattering of a plane elastic wave by a spherical elastic inclusions.* International Journal of Engineering Science, 1992. **30**: p. 169-186.

91. Mal, A.K. and L. Knopoff, *Elastic wave velocities in two-component systems.* Journal of the Institute of Mathematics and its Applications, 1967. **3**: p. 376-387.

92. Norris, A.N., *Scattering of elastic waves by spherical inclusions with applications to low frequency wave propagation in composites.* International Journal of Engineering Science, 1986. **24**: p. 1271-1282.

93. Aggelis, D.A., S.V. Tsinopoulos, and D. Polyzos, *An iterative effective medium approximation (IEMA) for wave dispersion and attenuation predictions in particulate composites, suspensions, and emulsions.* Journal of the Acoustical Society of America, 2004. **116**(6): p. 3343-3452.

94. Gaunaurd, G.C. and H. Überall, *Theory of resonant scattering from spherical cavities in elastic and viscoelastic media.* Journal of the Acoustical Society of America, 1978. **63**(6): p. 1699-1712.

95. Berryman, J.G., *Long-wavelength propagation in composite elastic media I: Spherical Inclusions.* Journal of the Acoustical Society of America, 1980. **68**(6): p. 1809-1819.

96. Anson, L.W. and R.C. Chivers, *Ultrasonic scattering from spherical shells including viscous and thermal effects.* Journal of the Acoustical Society of America, 1993. **93**(4): p. 1687-1699.

97. Varadan, V.K., Y. Ma, and V.V. Varadan, *A multiple scattering theory for elastic wave propagation in discrete random media.* Journal of the Acoustical Society of America, 1985. **77**: p. 375-385.

98. Foldy, L.L., *The multiple scattering of waves.* Physical Review Letters, 1945. **67**: p. 107-119.

99. Lax, M., *Multiple scattering of waves.* Reviews of Modern Physics, 1952. **23**: p. 287-310.

100. Waterman, P.C. and R. Truell, *Multiple scattering of waves.* Journal of Mathematical Physics, 1961. **2**: p. 513-537.

101. Bose, S.K. and K. Mal, *Elastic waves in a fiber-reinforced composite.* Journal of the Mechanics and Physics of Solids, 1976. **22**: p. 217-229.

102. Lloyd, P. and M.V. Berry, *Wave propagation through an assembly of spheres. IV: Relations between different multiple scattering theories.* Proceedings of the Royal Society of London, A, 1967. **91**: p. 678-688.

103. Twersky, V., *On scattering of waves by random distributions. I: Free-space scatterer formalism.* Journal of Mathematical Physics, 1962. **3**(4): p. 700-724.

104. Twersky, V., *On scattering of waves by random distributions, II: Two-space scatterer formalism.* Journal of Mathematical Physics, 1962. **3**(4): p. 724-734.

105. Twersky, V., *Multiple scattering of waves and optical phenomena.* Journal of the Optical Society of America, 1962. **52**: p. 145-171.

106. Epstein, P.S. and R.R. Carhart, *The absorption of sound in suspensions and emulsions. I: Water fog in Air.* Journal of the Acoustical Society of America, 1953. **51**(5): p. 553-565.

107. Allegra, J.R. and A. Hawley, *Attenuation of sound in suspensions and emulsions, theory and experiment.* Journal of the Acoustical Society of America, 1972. **51**: p. 1545-1564.

108. Anson, L.W. and R.C. Chivers, *Ultrasonic propagation in suspensions: A comparison of a multiple scattering and effective medium approach.* Journal of the Acoustical Society of America, 1989. **85**(2): p. 535-540.

109. Yang, R.-B., *A dynamic generalized self-consistent model for wave propagation in particulate composites.* Journal of Applied Mechanics, 2003. **70**(4): p. 575-582.

110. Pahl, G. and W. Beitz, *Engineering Design: A Systematic Approach*. 2nd ed. 1996, New York, NY: Springer-Verlag.

111. Ashbey, M.F., *Materials Selection in Mechanical Design*. 1999, Oxford, UK: Butterworth-Heinmann.

112. Cohen, M., *Unknowables in the essence of materials science and engineering.* Materials Science and Engineering, 1976. **25**: p. 3-4.

113. Eberhart, M.E. and D.P. Clougherty, *Looking for design in materials design.* Nature Materials, 2004. **3**(10): p. 659-661.

114. *Innovations in Ultrahigh-Strength Steel Technology*, ed. G.B. Olson, M. Azrin, and E.S. Wright. 1990, Washington, DC: Government Printing Office (GPO).

115. Stupp, S.I. and P.V. Braun, *Molecular manipulation of microstructures: Biomaterials, ceramics, and semiconductors.* Science, 1997. **277**(f): p. 1242-1248.

116. Choi, H.-J., R. Austin, J.K. Allen, D.L. McDowell, and F. Mistree. *An approach for robust micro-scale materials design under unparametreizable variability*. in *10th AIAA/ISSMO Multidisciplinary Analysis and Optimization Conference*. 2004. Albany, NY: AIAA.

117. Choi, H.-J., R. Austin, J.K. Allen, D.L. McDowell, and F. Mistree, *An approach for robust design of reactive powder metal mixtures based on non-deterministic micro-scale shock simulation.* Journal of Computer-Aided Materials Design, 2005. **12**(1): p. 57-85.

118. Bras, B. and F. Mistree, *Robust design using compromise decision support problems.* Engineering Optimization, 1993. **21**: p. 213-239.

119. Mistree, F., W. Smith, and B. Bras, *A Decision-Based Approach to Concurrent Engineering*, in *Handbook of Concurrent Engineering*, H.R. Parsaei and W.G. Sullivan, Editors. 1993: New York. p. 127-158.

120. Karandikar, H., R. Srinivasan, F. Mistree, and W.J. Fuchs, *Compromise: An effective approach for the design of pressure vessels using composite materials.* Computers and Structures, 1989. **33**(6): p. 1465-1477.

121. Edwards, K.L. and Y.-M. Deng, *Supporting design decision-making when applying materials in combination.* Materials & Design, 2007. **28**: p. 1288-1297.

122. Cochran, J.K., K.J. Lee, D.L. McDowell, and T.H. Sanders. *Low density monolithic honeycombs by thermal chemical processing*. in *4th Conference on Aerospace Materials, Processes, and Environmental Technology*. 2000. Huntsville, AL.

123. Randle, V., *http://www.swan.ac.uk/mateng/microstructure/*. 2004.

124. Piscanec, S., *http://www-g.eng.cam.ac.uk/edm/index.html*. 2004.

125. Eshelby, J.D., *Elastic Inclusions and Inhomogeneities*. Progress in Solid Mechanics. Vol. 2. 1961, Amsterdam: North-Holland. 140.

126. Lipinski, P., E.H. Barhdadi, and M. Cherkaoui, *Micromechanical modeling of an arbirary ellipsoidal multi-coated inclusion.* Philosophical Magazine, *submitted March* 2005.

127. Cherkaoui, M., *Comportement Thermoélastique Global des Composites à Renforts Enrobés : Modélisation Micromécanique et Applications*. 1995, Université de Metz: Metz, France.

128. Havriliak, S. and S. Negami, *A complex plane analysis of α-dispersions in some polymer systems.* Journal of Polymer Science: Part C, 1966. **14**: p. 99-117.

129. Weisstein, E.W., *CRC Conscise Encyclopedia of Mathematics*. 2nd ed. 2003, Boca Raton, FL: Chapman & Hall/CRC. 3252.

130. Haberman, M., Y. Berthelot, and M. Cherkaoui, *Micromechanical modeling of particulate composites for damping of acoustic waves.* Journal of Engineering Materials and Technology, 2006. **128**: p. 320-329.

131. Willis, J.R., *Bounds and self-consistent estimates for the overall properties of anisotropic composites.* Journal of the Mechanics and Physics of Solids, 1977. **25**: p. 185-202.

132. Hashin, Z. and S. Shtrikman, *A variational approach to the theory of the elastic behavior of multi-phase materials.* Journal of the Mechanics and Physics of Solids, 1963. **11**: p. 127-140.

133. Walpole, L.J., *On the bounds for the overall elastic moduli of inhomogeneous systems I.* Journal of the Mechanics and Physics of Solids, 1966. **14**: p. 151-162.

134. Hill, R., *The elastic behavior of a crystalline aggregate.* Proceedings of the Physical Society, A, 1952. **65**: p. 349.

135. Hill, R., *Elastic Properties of reinforced solids: some theoretical principles.* Journal of the Mechanics and Physics of Solids, 1963. **11**: p. 357-372.

136. Hashin, Z., *Analysis of composite materials.* Journal of Applied Mechanics, 1983. **50**: p. 481-505.

137. Roscoe, R., *Bounds for real and imaginary parts of the dynamic moduli of composite viscoelastic systems.* Journal of the Mechanics and Physics of Solids, 1969. **17**: p. 17-22.

138. Roscoe, R., *Improved bounds for real and imaginary parts of complex moduli of isotropic viscoelastic composites.* Journal of the Mechanics and Physics of Solids, 1972. **20**: p. 91-99.

139. Cherkaev, A.V. and L.V. Gibiansky, *Variational principles for complex conductivity, viscoelasticity, and similar problems I: Media with complex moduli.* Journal of Mathematical Physics, 1994. **35**(1): p. 127-145.

140. Milton, G.W., *On characterizing the set of possible effective tensors of composites: The variational method and the translation method.* Communs Pure Applied Mathematics, 1990. **43**: p. 63-125.

141. Miller, M.N., *Bounds for effective electrical, thermal, and magnetic properties of heterogeneous materials.* Journal of Mathematical Physics, 1969. **10**: p. 1988-2005.

142. Gibiansky, L.V. and G.W. Milton, *On the effective viscoelastic moduli of two-phase media. I: Rigorous bounds on the complex bulk modulus.* Proceedings of the Royal Society of London, A, 1993. **440**: p. 163-188.

143. Milton, G.W. and J.G. Berryman, *On the effective viscoelastic moduli of two-phase media. II: Rigorous bounds on the complex shear modulus in three dimensions.* Proceedings of the Royal Society of London, A, 1997. **453**: p. 1849-1880.

144. Gibiansky, L.V. and R.S. Lakes, *Bounds on the complex bulk modulus of a two-phase viscoelastic composite with arbitrary volume fractions of the components.* Mechanics of Materials, 1993. **16**: p. 317-331.

145. Gibiansky, L.V. and R.S. Lakes, *Bounds on the complex bulk and shear moduli of a two-dimensional two-phase viscoelastic composite.* Mechanics of Materials, 1997. **25**: p. 79-95.

146. Gibiansky, L.V. and S. Torquato, *New method to generate three-point bounds on effective properties of composites: Application to viscoelasticity.* Journal of the Mechanics and Physics of Solids, 1998. **46**(4): p. 749-783.

147. Krönig, R. and A. Kramers, *Absorption and dispersion in X-Ray spectra.* Zeitschrift fur Physik, 1928. **48**: p. 174.

148. Yeh, P., *Optical Waves in Layered Media*. 1988, New York, NY: John Wiley & Sons.

149. Ferry, J.D., *Viscoelastic Properties of Polymers*. 3rd ed. 1980, New York, NY: Wiley & Sons.

150. Haberman, M., Y. Berthelot, and M. Cherkaoui, *Transmission loss of viscoelastic materials containing oriented, ellipsoidal, coated microinclusions.* Journal of the Acoustical Society of America, 2005. **118**(5): p. 2984-2992.

151. Christensen, R.M., *A critical evaluation for a class of micromechanics models.* Journal of the Mechanics and Physics of Solids, 1990. **38**(3): p. 379-404.

152. Mavko, G., T. Mukerji, and J. Dvorkin, *The Rock Physics Handbook: Tools for Seismic Analysis of Porous Media*. 2003, New York, NY, USA: Cambridge University Press.

153. Merkel, S., A.P. Jephcoat, J. Shu, H.K. Mao, P. Gillet, and R.J. Hemley, *Equation of state, elasticity and shear strength of pyrite under high pressure.* Physics and Chemistry of Minerals, 2002. **29**: p. 1-9.

154. Spearot, D.E., K.I. Jacob, and D.L. McDowell, *Non-local seperation constitutive laws for interfaces and their relation to nanoscale simulations.* Mechanics of Materials, 2004. **36**(9): p. 825-847.

155. Dvorak, G.J. and M.V. Srinivas, *New Estimates of Overall Properties of Heterogeneous Solids.* Journal of the Mechanics and Physics of Solids, 1999. **47**: p. 899-920.

156. Odegard, G.M., *Constitutive modeling of piezoelectric polymer composites.* Acta Materiala, 2004. **52**(18): p. 5315-5330.

157. Press, W.H., B.P. Flannery, S.A. Teukolsky, and W.T. Vetterling, *Numerical Recipes in Fortran: The Art of Scientific Computing*. 1992, New York, NY: Press Syndicate of the University of Cambridge.

158. Davies, J.M., *Lightweight Sandwich Construction*. 2001: Blackwell Science, Ltd. 370.

159. Kerwin, E.M., *Damping of Flexural Waves by a constrained viscoelastic layer.* Journal of the Acoustical Society of America, 1959. **31**(7): p. 952-962.

160. Ungar, E.E., *Structural Damping*, in *Noise and Vibration Control Engineering: Principles and Applications*, L.L. Beranek and I.L. Vér, Editors. 1992, Wiley-Interscience: Hoboken, NJ.

161. Ditaranto, R.A. and W. Blasingame, *Composite damping of vibrating beams.* Journal of Engineering Industry, 1967. **89B**: p. 633-638.

162. Yan, M.J. and E.H. McDowell, *Governing equations for vibrating constrained-layer damping sandwich plates and beams.* Journal of Applied Mechanics, 1972. **94**: p. 1041-1047.

163. Cupial, P. and J. Niziol, *Vibration and damping analysis of thee-layer composite plate with viscoelastic mid-layer.* Journal of Sound and Vibration, 1995. **183**(1): p. 99-114.

164. Johnson, C.D. and D.A. Kienholz, *Finite element prediction of damping in beams with constrained viscoelastic layer.* Shock and Vibration Bulletin, 1981. **51**(1): p. 71-81.

165. Rikards, R., A. Chate, and E. Barkanov, *Finite element analysis of damping the vibrations of laminated composites.* Computers and Structures, 1993. **46**(6): p. 1005-1015.

166. Daya, E.M. and M. Potier-Ferry, *A shell finite element for viscoelastically damped sandwich structures.* Revue Européene des Eléments Finis, 2002. **11**(1): p. 39-56.

167. Austin, E.M., *Variations on Modeling of Constrained-Layer Damping Treatments*, in *The Shock and Vibration Digest*. 1999. p. 275-280.

168. Buehrle, R.D., J. Klos, and G.P. Gibbs. *Damped windows for aircraft interior noise control*. in *Noise-Con 2004*. 2004. Baltimore, Maryland.

169. Haberman, M., Y. Berthelot, M. Cherkaoui, and E.M. Daya. *Modèlisation des plaques sandwiches pour l'amélioration de la performance acoustique*. in *17ème Congrès Français de Mécanique*. 2005. Troyes, France.

170. Williams, D.E., *Technical Memo: Saflex 3G Master Curves*. 2001.

171. Tongue, B.H., *Principles of Vibrations*. 2nd ed. 2002, New York, NY: Oxford University Press. 518.

172. Angloulvant, F., *Caractérisation dynamique des matériaux composites: Étude de l'amortissement*, in *Génie Mécanique*. 1998, Université de Maine: Le Mans. p. 243.

173. S.A.E., *J1400: Laboratory Measurement of the Airborne Sound Barrier Performance of Automotive Materials and Assemblies*, A.M. Committee, Editor. 1990, Society of Automotive Engineers International.

174. Leissa, A., *Vibration of Plates*. 1993, Melville, NY: American Institute of Physics.

175. Koutsawa, Y., M. Haberman, E.M. Daya, and M. Cherkaoui, *Modal behavior of a rectangular sandwich plate supported at extents by a viscoelastic material with heterogeneous viscoelastic core.* Journal of Sound and Vibration, *submitted January* 2007.

176. Kinsler, L.E., A.R. Frey, A.B. Coppens, and J.V. Sanders, *Fundamentals of Acoustics*. 4th ed. 2000, Hoboken, NJ: John Wiley & Sons, Inc. 560.

177. Mistree, F., O.F. Hughes, and B. Bras, *Compromise Decision Support Problem and the Adaptive Linear Programming Algorithm*, in *Structural Optimization: Status and Promise*, M.P. Kamat, Editor. 1993, AIAA: Washington D.C. p. 251-290.

178. Mistree, F., B. Bras, J.K. Allen, D. Rosen, and C.J.J. Paredis, *Learning How to Design: A Minds-On, Hands-On, Decision-Based Approach*. 2006, Systems Realization Laboratory, George W. Woodruff School of Mechanical Engineering: Atlanta, GA.

179. Gere, J.M., *Mechanics of Materials*. 5th ed. 2003, Toronto, Canada: Thomson-Engineering.

180. Huang, J.S. and L.J. Gibson, *Elastic moduli of a composite of hollow spheres in a matrix.* Journal of the Mechanics and Physics of Solids, 1993. **41**(1): p. 55-75.

181. Choi, H.-J., J.K. Allen, D. Rosen, D.L. McDowell, and F. Mistree. *An inductive design exploration method for the integrated design of multi-scale materials and products*. in *Proceedings of the Design Engineering Technical Conferences (DETC'05)*. 2005. Long Beach, CA: ASME.

182. Panchal, J.H., H.-J. Choi, J. Shepherd, J.K. Allen, D.L. McDowell, and F. Mistree. *A strategy for Simulation-Based Design of multi-scale, multi-functional products and associated design processes*. in *Proceedings of the Design Engineering Technical Conferences (DETC'05)*. 2005. Long Beach, CA: ASME.

183. Aughenbaugh, J.M. and C.J.J. Paredis. *The value of using imprecise probabilities in engineering design*. in *Proceedings of the Design Engineering Technical Conferences (DETC'05)*. 2005. Long Beach, CA: ASME.

184. Aughenbaugh, J.M., J. Ling, and C.J.J. Paredis. *Applying information economics and imprecise probabilities to data collection in design*. in *ASME International Mechanical Engineering Congress & Exposition*. 2005. Orlando, FL: ASME.

185. Fung, Y.C. and P. Tong, *Classical and Computational Solid Mechanics*. Advanced Series in Engineering Science. Vol. 1. 2005, Hackensack, New Jersey: World Scientific Publishing Co. Pte. Ltd. 930.

186. Lakes, R.S. and W.J. Drugan, *Dramatically stiffer elastic composite materials due to a negative stiffness phase?* Journal of the Mechanics and Physics of Solids, 2002. **50**: p. 979-1009.

187. Wang, Y.C. and R. Lakes, *Composites with inclusions of negative bulk modulus: Extreme damping and negative Poisson's ratio.* Journal of Composite Materials, 2005. **39**(18): p. 1645-1657.

188. Buehrle, R.D., G.P. Gibbs, J. Klos, and M. Mazur. *Modeling and validation of damped plexiglass windows for noise control*. in *44th AIAA/ASME/ASCE/AHS/ASC Structures, Structural Dynamics, and Materials Conference*. 2003. Norfolk, VA: AIAA.

189. Fletcher, R., *Practical Methods of Optimization*, in *Unconstrained and Constrained Optimization* R. Fletcher, Editor. 1980, John Wiley and Sons: New York.

190. Schittkowski, K., *A FORTRAN-Subroutine Solving Constrained Nonlinear Programming Problems.* Annals of Operations Research, 1985. **5**: p. 485-500.

191. Biggs, M.C., *Constrained Minimization Using Recursive Quadratic Programming*, in *Towards Global Optimization*, L.C.W. Dixon and G.P. Szergo, Editors. 1975, North-Holland: Amsterdam. p. 341-349.

192. Han, S.P., *A globally convergent method for nonlinear programming.* Journal of Optimization Theory and Applications, 1977. **22**: p. 297.

193. Powell, M.J.D., *The Convergence of Variable Metric Methods for Nonlinearly Constrained Optimization Calculations*, in *Nonlinear Programming 3*, O.L. Mangasarian, R.R. Meyer, and S.M. Robinson, Editors. 1978, Academic Press: London.

194. Powell, M.J.D., *A Fast Algorithm for Nonlinearly Constrained Optimization Calculations*, in *Numerical Analysis*, G.A. Watson, Editor. 1978, Springer Verlag: Berlin.

195. Broyden, C.G., *The convergence of a class of double-rank minimization algorigthms.* Journal of the Institute of Mathematics and its Applications, 1970. **6**: p. 76-90.

196. Fletcher, R., *A new approach to variable metric algorithms.* Computer Journal, 1970. **13**: p. 317-322.

197. Goldfarb, D., *A family of variable metric updates derived by variational means.* Mathematics of Computing, 1970. **24**: p. 22-26.

198. Shanno, D.F., *Conditioning of quasi-Newton methods for function minimization.* Mathematics of Computing, 1970. **24**: p. 647-656.

199. Gill, P.E., W. Murray, and M.H. Wright, *Practical Optimization*. 1981, London: Academic Press.

200. Powell, M.J.D., *Variable Metric Methods for Constrained Optimization*, in *Mathematical Programming: The State of the Art*, A. Bachem, M. Grotschel, and B. Korte, Editors. 1983, Springer Verlag: Berlin. p. 288-311.

201. Hock, W. and K. Schittkowski, *A comparative performance evaluation of 27 nonlinear programming codes.* Computing, 1983. **30**: p. 335.

202. Harris, C.M., ed. *Handbook of Acoustical Measurements and Noise Control*. 3rd ed. 1997, Acoustical Society of America: Sewickley, PA. 600.

203. Mendenhall, W. and T. Sincich, *Statistics for Engineering and the Sciences*. 5th ed. 2006, Englewood Cliffs, NJ: Prentice Hall. 1072.

204. Jaglinski, T., P. Franscone, B. Moore, D.S. Stone, and R. Lakes, *Internal friction due to negative stiffness in the indium-thallium martensitic phase transformation.* Philosophical Magazine, 2006. **86**(27): p. 4285-4303.

205. Jaglinski, T. and R. Lakes, *Anelastic instability in composites with negative stiffness inclusions.* Philosophical Magazine Letters, 2004. **84**(12): p. 803-810.

206. Yoshimoto, K., T.S. Jain, K.V. Workum, P.F. Nealey, and J.J.d. Pablo, *Mechanical heterogeneities in model polymer glassses at small length scales.* Physical Review Letters, 2004. **93**(17): p. 175501-1 - 4.

207. Wang, Y.-C. and R. Lakes, *Negative stiffness-induced extreme viscoelastic mechanical properties: stability and dynamics.* Philosophical Magazine, 2004. **84**(35): p. 3785-3801.

208. Mizuno, T., T. Toumiya, and M. Takasaki, *Vibration isolation system using negative stiffness.* JSME International Journal, 2003. **46**(3): p. 807-812.

209. Martin, P., A.D. Mehta, and A.J. Hudspeth, *Negative hair-bundle stiffness betrays a mechanism for mechanical amplification by the hair cell.* Proceedings of the National Academy of Sciences of the United States of America, 2000. **97**(22): p. 12026-12031.

210. Saif, M.T.A., *On a tunable bistable MEMS - Theory and experiment.* Journal of Microelectricomechanical Systems, 2000. **9**(2): p. 157-170.

211. Qiu, J., H. Lang, and A.H. Slocum, *A curved-beam bistable mechanism.* Journal of Microelectricomechanical Systems, 2004. **13**(2): p. 137-146.

212. Hornbeck, L.J., T.R. Howell, R.L. Knipe, and M.A. Mignardi, *Digital micromirror device-Commercialization of massively parallel MEMS technology.* Proceedings ASME International Mechanical Engineering Congress and Exposition, 1997. **DSC-62**(HTD-354): p. 3-8.

213. Luharuka, R. and P.J. Hesketh, *Design of fully compliant, in-plane rotary, bistable mechanisms for MEMS applications.* Sensors and Actuators A, 2007. **134**(1): p. 231-238.

214. Wullschleger, L., *Numerical Investigation of the Buckling Behavior of Axially Compressed Circular Cylinders Having Parametric Initial Dimple Imperfections*, in *Department of Technical Sciences*. 2006, Swiss Federal Institute of Technology - Zurich: Zurich, Switzerland.

215. Born, M. and K. Huang, *Dynamical Theory of Crystal Lattices*. Oxford Classic Texts in the Physical Sciences. 1988, Oxford: Oxford University Press.

216. Gibbs, J.W., *The Collected Works of J. Willard Gibbs*. Vol. 1. 1908. Reprinted 1948, New Haven, CT: Yale University Press.

217. Wang, Y.C. and R. Lakes, *Extreme stiffness systems due to negative stiffness elements.* American Journal of Physics, 2004. **72**(1): p. 40-40.

218. Papakonstantopoulos, G.J., K. Yoshimoto, M. Doxastakis, P.F. Nealey, and J.J.d. Pablo, *Local mechanical properties of polymeric nanocomposites.* Physical Review E, 2005. **72**(031801): p. 1-6.

219. Wang, Y.C. and R. Lakes, *Extreme thermal expansion, piezoelectricity, and other coupled field properties in composites with a negative stiffness phase.* Journal of Applied Physics, 2001. **90**(12): p. 6458-6465.

220. Moore, B., T. Jaglinski, D.S. Stone, and R.S. Lakes, *Negative incremental bulk modulus in foams.* Philosophical Magazine Letters, 2006. **86**(10): p. 651-659.

221. Salje, E., *Phase Transitions in Ferroelastic and Co-elastic Crystals*. 1990, Cambrdige, MA: Cambridge University Press.

222. Falk, F., *Model free energy, mechanics, and thermodynamics of shape memory alloys.* Acta Metallurgica, 1980. **28**: p. 1773-1780.

223. Chen, C.-T., *Linear System Theory and Design*. 3rd ed. 1999, New York, NY: Oxford University Press.

224. Knowles, J.K. and E. Sternberg, *On the failure of ellipticity and the emergence of discontinuous gradients in plane finite elastostatics.* Journal of Elasticity, 1978. **8**: p. 329-379.

225. Milton, G.W., *Composite materials with Poisson's ratios close to -1.* Journal of the Mechanics and Physics of Solids, 1992. **40**: p. 1105-1137.

226. Lakes, R., *Deformation mechanisms of negative Poisson's ratio materials: Structural Aspects.* Journal of Material Science, 1991. **26**: p. 2287-2292.

227. Lakes, R., *Materials with structural hierarchy.* Nature, 1993. **361**: p. 511-515.

228. Lakes, R., *Advances in negative Poisson ratio materials.* Advanced Materials, 1993. **5**(293-295).

229. Goff, L.L., D. Bozovic, and A.J. Hudspeth, *Adaptive shift in the domain of negative stiffness during spontaneous oscillation by hair bundles from the internal ear.* Proceedings of the National Academy of Sciences of the United States of America, 2005. **102**: p. 16996-17001.

230. Bogoyavlenskiy, V.A., *Differential criterion of a bubble collapse in viscous liquids.* Physical Review E, 1999. **60**(1): p. 504-508.

231. Copeland, E.J., M. Gleiser, and H.-R. Müller, *Oscillons: Resonant configurations during bubble collapse.* Physical Review D, 1995. **52**(4): p. 1920-1933.

232. Flannigan, D.J., S.D. Hopkins, C.G. Camara, S.J. Putterman, and K.S. Suslick, *Measurement of pressure and density inside a single sonoluminescing bubble.* Physical Review Letters, 2006. **96**(204301).

233. Falk, F., *Ginzburg–Landau theory of static domain walls in shape memory alloys.* Zeitschrift fur Physik B, 1983. **51**: p. 177-185.

234. Patoor, E. and M. Bervieller, *Technologie des Alliages à Mémoire de Forme*. Traité des Nouvelles Technologies, série Matériaux. 1994, Paris, France: Hermès. 339.

235. Lutsko, J.F., *Stress and elastic constants in anisotropic solids: Molecular dynamics techniques.* Journal of Applied Physics, 1988. **64**(3): p. 1152-1154.

236. Yoshimoto, K., G.J. Papakonstantopoulos, J.F. Lutsko, and J.J.d. Pablo, *Statistical calculation of elastic moduli for atomistic models.* Physical Review B, 2005. **71**(18): p. 184108.

237. Rosakis, P., A. Ruina, and R.S. Lakes, *Microbuckling instability in elastomeric cellular solids.* Journal of Material Science, 1993. **28**: p. 4667-4672.

238. Yakobson, B.I., C.J. Brabec, and J. Bernholc, *Nanomechanics of carbon nanotubes: Instabilies beyond linear response.* Physical Review Letters, 1996. **76**(14): p. 2511-2514.

239. Falvo, M.R., G.J. Clary, R.M.T. II, V. Chi, F.P.B. Jr., S. Washburn, and R. Superfine, *Bending and buckling of carbon nanotubes under large strain.* Nature, 1997. **389**: p. 582-584.

240. Taylor, R.M., W. Robinett, V.L. Chi, J. R.P. Brooks, W.V. Wright, R.S. Williams, and E.J. Snyder. *The nanomanipulator: A virtual reality interface for a scanning tunneling microscope*. in *20th Annual International Conference on Computer Graphics and Interactive Techniques*. 1993. Anaheim, California.

241. Sears, A. and R.C. Batra, *Buckling of multiwalled carbon nanotubes under axial compression.* Physical Review B, 2006. **73**: p. 085410.

242. *Encyclopedia of Smart Materials*, ed. M. Schwartz. 2001: Wiley-Interscience. 1200.

243. Hoffman, W.P., *Microscopic Tube Devices and Method of Manufacture*. 2001, The United States of America as represented by the Secretary of the Air Force (Washington, DC): United States of America.

244. Donnell, L.H., *A new theory for the buckling of thin cylinders under axial compression and bending.* Transactions of the ASME, 1934. **56**: p. 795-806.

245. Doyle, J.F., *Nonlinear Analysis of Thin-Walled Structures*. Mechanical Engineering. 2001, New York: Springer.

246. Budiansky, B., *Theory of buckling and post-buckling behavior of elastic structures.* Advances in Applied Mechanics, 1974. **14**: p. 1-65.

247. Markus, S., *The Mechanics of Vibrations of Cylindrical Shells*. Studies in Applied Mechanics. Vol. 17. 1988, Bratislava: Elsevier.

248. Shen, L. and J. Li, *Transversely isotropic elastic properties of single-walled carbon nanotubes.* Physical Review B, 2004. **69**: p. 045414.

249. Morris, P.R., *Iterative scheme for calculating polycrystal elastic constants.* International Journal of Engineering Science, 1971. **9**(10): p. 917-920.

250. Kneer, G., *Uber die Berechnung der Elastizitäsmoduln vielkristalliner Aggregate mit Textur.* Physica Status Solidi B, 1965. **9**(3): p. 825-838.

251. Rinaldi, C. and H. Brenner, *Body versus surface forces in continuum mechanics: Is the Maxwell stress tensor a physically objective Cauchy stress?* Physical Review E, 2002. **65**: p. 036615 1-4.

252. Jiang, M., K. Alzebdeh, I. Jasiuk, and M. Ostoja-Starzewski, *Scale and boundary conditions effects in elastic properties of random composites.* Acta Mechanica, 2001. **148**: p. 63-78.

253. Jiang, M., M. Ostoja-Starzewski, and I. Jasiuk, *Scale-dependent bounds on effective elastoplasitic response of random composites.* Journal of the Mechanics and Physics of Solids, 2001. **49**: p. 655-673.

254. Garboczi, E.J. and J.G. Berryman, *Elastic moduli of a material containing composite inclusions: Effective medium theory and finite element computations.* Mechanics of Materials, 2001. **33**(2001): p. 455-470.

255. Norris, A.N., *A differential scheme for the effective moduli of composites.* Mechanics of Materials, 1985. **4**: p. 1-16.

256. Norris, A.N., *An examination of the Mori-Tanaka effective medium approximation for multiphase composites.* Journal of Applied Mechanics, 1989. **56**: p. 83-88.

257. Haberman, M., *Frequency dependent micromechanical model of viscoelastic materials with coated inclusions*, in *Woodruff School of Mechanical Engineering*. 2001, Georgia Institute of Technology: Atlanta, GA. p. 118.

258. Hashin, Z., *The differential scheme and its application to cracked materials.* Journal of the Mechanics and Physics of Solids, 1988. **36**(6): p. 719-734.

259. Norris, A.N., A.J. Callegari, and P. Sheng, *A generalized differential effective medium theory.* Journal of the Mechanics and Physics of Solids, 1985. **33**(6): p. 525-543.

260. Bauer, S., R. Gerhard-Multhaupt, and G.M. Sessler, *Ferroelectrets: Soft electroactive foams for transducers*, in *Physics Today*. 2004. p. 37-43.

261. Hillenbrand, J. and G.M. Sessler, *Piezoelectricity in cellular electret films.* IEEE Transactions on Dielectrics and Electrical Insulation, 2000. **7**(4): p. 537-542.

262. Sessler, G.M. and J. Hillenbrand, *Electromechanical response of cellular electret films.* Applied Physics Letters, 1999. **75**(21): p. 3405-3407.

263. Landau, L.D., *The Classical Theory of Fields*. 4th ed. Course of Theoretical Physics. Vol. 2. 1987, Oxford: Butterworth-Heinmann. 402.

264. Wegener, M., W. Wirges, R. Gerhard-Multhaupt, M. Dansachmüller, R. Schwödiauer, S. Bauer-Gogonea, S. Bauer, M. Paajanen, H. Minkkinen, and J. Raukola, *Controlled inflation of voids in cellular polymer ferroelectrets: Optimizing electromechanical transducer properties.* Applied Physics Letters, 2004. **84**(3): p. 392-394.

265. Dunn, M.L. and M. Taya, *Micromechanics predictions of the effective electroelastic moduli of piezocomposites.* International Journal of Solids and Structures, 1993. **30**(2): p. 161-175.

266. Parry, M. and E. Fischbach, *Probability distribution of distance in a uniform ellipsoid: Theory and applications to physics.* Journal of Mathematical Physics, 2000. **41**(4): p. 2417-2433.

267. *MatWeb, Material Property Data*. 2007, http://www.matweb.com/, Automation Creations, Inc.

268. Gerhard-Multhaupt, R., W. Künstler, T. Görne, A. Pucher, T. Weinhold, and M. Seiss, *Porous PTFE Space-charge electrets for piezoelectric applications.* IEEE Transactions on Dielectrics and Electrical Insulation, 2000. **7**(4): p. 480-488.

269. Paajanen, M., M. Wegener, and R. Gerhard-Multhaupt, *Understanding the role of the gas in the voids during corona charging of cellular electret films - A way to enhance their piezoelectricity.* Journal of Physics D: Applied Physics, 2001. **34**: p. 2482-2488.

270. Sessler, G.M., *Electrets: Recent developments.* Journal of Electrostatics, 2001. **51-52**: p. 137-145.

271. Xia, Z., R. Gerhard-Multhaupt, W. Kunstler, A. Wedel, and R. Danz, *High surface-charge stability of porous polytetrafluoroethylene electret film at room and elevated temperatures.* Journal of Physics D: Applied Physics, 1999. **32**: p. L83-L85.

272. Wijeyewickrema, A.C. and S. Leungvichcharoen. *A review of analytical methods to determine effective mechanical properties of composites with spherical inclusions*. in *JSPS-DOST Regional Symposium on Construction Materials & Testing*. 2003. Manila, Philippines.

273. Hashin, Z. and S. Shtrikman, *A variational approach to the theory of the effective magnetic permeability of multiphase materials.* Journal of Applied Physics, 1962. **33**(10): p. 3125-3131.

274. Keller, J.B. and J. F.C. Karal, *Effective dielectric constant, permeability, and conductivity of a random medium and the velocity and attenuation coefficient of coherent waves.* Journal of Mathematical Physics, 1966. **7**(4): p. 661-670.

VITA

MICHAEL R. HABERMAN

Michael Haberman was born in Jerome, Idaho where he attended elementary and high school. He received a B.S. in Mechanical Engineering from the University of Idaho in Moscow, Idaho, in 2000. Michael then continued his education with Georgia Institute of Technology (GIT), receiving his M.S. in Mechanical Engineering in 2001 after receiving instruction on both the Georgia Tech Lorraine (GTL) and Atlanta campuses. Michael then took a research and development mechanical engineering position with Beltone Electronics/GN ReSound in Chicago, Illinois. In 2003 Michael returned to the GTL campus of GIT to simultaneously pursue a Ph.D. in Mechanical Engineering and Diplôme de Doctorat from the Université Paul Verlaine in Metz, France. At the same time, Haberman helped grow graduate level research at GTL by assisting Dr. Yves Berthelot in the development of an ultrasonics and advanced materials laboratory. Michael received his Diplôme de Doctorat in April 2003 with highest honors ("Mention très Honorable et Félicitations du Jury"). Michael has accepted a post-doctoral fellow position at Applied Research Labs at the University of Texas starting in August 2007. When not working on research, Michael enjoys enjoys traveling, running, and hiking.